ANL-6868

Argonne National Laboratory

ANNUAL REPORT FOR 1963

METALLURGY DIVISION

Price $5.50 . *Available from the Office of Technical Services, Department of Commerce, Washington 25, D.C.*

ANL-6868
Metals, Ceramics,
and Materials
(TID-4500, 29th Ed.)
AEC Research and
Development Report

ARGONNE NATIONAL LABORATORY
9700 South Cass Avenue
Argonne, Illinois 60440

ANNUAL REPORT FOR 1963

METALLURGY DIVISION

Frank G. Foote, Director
Haim H. Chiswik, Associate Director
Robert E. Macherey, Associate Director

The last three Annual Reports

ANL-6330	1960
ANL-6516	1961
ANL-6677	1962

Operated by The University of Chicago
under
Contract W-31-109-eng-38
with the
U. S. Atomic Energy Commission

TABLE OF CONTENTS

PART I - ENGINEERING METALLURGY

TABLE OF CONTENTS

TABLE OF CONTENTS

TABLE OF CONTENTS

TABLE OF CONTENTS

TABLE OF CONTENTS

PART II - BASIC METALLURGY

TABLE OF CONTENTS

TABLE OF CONTENTS

PART I

ENGINEERING METALLURGY

A. Fast Reactor Fuel Element Development and Fabrication

1. Properties of Metallic Fuels and Jacket Materials

a. Properties of Uranium-Plutonium-Fizzium Alloys

(L. R. Kelman, R. J. Dunworth, H. Savage, and E. R. Gilbert)

The uranium-plutonium-fizzium alloys are being studied as possible metal fuels for fast breeder reactors. During the past year, the properties of the U-10 w/o Pu-10 w/o Fz alloy have been investigated, principally because of its better irradiation stability[1] and a higher melting point. Some properties of this alloy are listed in Table I and compared with uranium and the U-20 w/o Pu-10 w/o Fs alloy. In this table the alloys not only have different plutonium contents but also different alloy compositions (Fs - low Zr; Fz - high Zr).[2]

Table I

PROPERTIES OF URANIUM AND URANIUM-PLUTONIUM FUELS

Property	Uranium	U-10 w/o Pu-10 w/o Fz	U-20 w/o Pu-10 w/o Fs
Density, g cm^{-3}	19.0	16.8	17.0
Hardness DPH, kg mm^{-2}	220	254/471(a)	498(a)
Tensile Strength, kg mm^{-2}			
500°C	10	21	
600°C	4	7	
Solidus, °C		≈920	820
Liquidus, °C	1132	≈1100	1010
Thermal Expansion Coef, $°C^{-1} \times 10^6$	20	≈16	16
Thermal Conductivity, W cm^{-1} $°C^{-1}$			
500°C	0.36	0.26	0.23
600°C	0.39	0.29	0.26
Enthalpy, 25°C to m. p., cal g^{-1}	52	44(b)	

(a) Converted from Rockwell A by means of steel conversion table.

(b) Heats of transformation estimated at 90% of the uranium values.

[1] Horak, J. A., Kittel, J. H., and Dunworth, R. J., The Effects of Irradiation on Uranium-Plutonium-Fissium Fuel Alloys, ANL-6429 (July 1962).

[2] Annual Report for 1962, Metallurgy Division, ANL-6677, pp. 9-14.

The fizzium content of this alloy results from the EBR-II melt refining process, which removes most, but not all, of the fission-produced elements from the irradiated fuel. The elements remaining which make up the 10 w/o Fz composition are 2.80 w/o Zr, 2.75 w/o Mo, 2.95 w/o Ru, 0.50 w/o Rh, and 1.00 w/o Pd. The data obtained with these alloys have been reported previously.[2-5] During the past year additional information has been obtained on the liquidus and solidus temperatures, the heat content, transformation kinetics, thermal cycling, tensile properties, brittleness, thermal stresses and creep in fuel pins, and compatibility with potential clads.

Liquidus and Solidus (R. J. Dunworth)

The solidus and liquidus boundaries of U-20 w/o Pu-10 w/o Fs and U-10 w/o Pu-15 w/o Mo alloys were determinded by thermal analysis. The results are listed in Table II. The data for the U-20 w/o Pu-10 w/o Fs alloy agree quite well with those reported earlier by Kruger[5] except that the liquidus value is lower by 20°C. The values for the U-10 w/o Pu-15 w/o Mo are lower than those reported by Mardon et al.,[6] for an alloy of slightly lower plutonium content. A difference of 20°C exists for the liquid + molybdenum isotherm. The liquidus for this alloy is estimated to be about 1320°C.

Table II

SOLIDUS AND LIQUIDUS TEMPERATURES* OF U-Pu ALLOYS

	Temp (°C)
U-20 w/o Pu-10 w/o Fs	
Solidus	820
Liquidus	990
U-10 w/o Pu-15 w/o Mo	
Liquid + gamma (solidus)	1055
Liquid + Mo (isotherm)	1180
Liquidus (estimated)	1320

* All temperatures have an estimated accuracy of ±10°C.

Heat Content (H. Savage)

The heat contents of U-10 w/o Pu and U-10 w/o Pu-10 w/o Fz alloys were measured in a drop calorimeter.[3] The heat content of U-10 w/o Pu alloy was measured through its fusion temperature to 1190°C, and the heat content of U-10 w/o Pu-10 w/o Fz alloy was determined to 910°C. In the alpha temperature region, the heat contents of uranium are the same as the values for U-10 w/o Pu but lower than those for U-10 w/o Pu-10 w/o Fz. Similar results have been found for uranium and uranium-fissium alloys.[7] The data are shown in Tables III and IV. Figure 1 graphically presents the heat contents of U-10 w/o Pu alloy and Figure 2 that of U-10 w/o Pu-10 w/o Fz alloy. Compositions of the specimens are listed in Table V.

[3] Annual Report for 1961, Metallurgy Division, ANL-6516, pp. 9-16, 407.

[4] Annual Report for 1960, Metallurgy Division, ANL-6330, pp. 9-18.

[5] Annual Report for 1959, Metallurgy Division, ANL-6099, pp. 9-11.

[6] Mardon, P. G., Evans, J. P., Hodkin, D. J., North, J. M., Pearce, J. H., "The Constitution and Fabrication of Uranium-Molybdenum-Plutonium Fuels," Plutonium 1960, 329-352, Cleaver-Hume Press, Ltd., London (1961).

[7] Savage, H., and Seibel, R. D., Heat Capacity Studies of Uranium and Uranium-Fissium Alloys ANL-6702 (Sept 1963).

Table III

HEAT CONTENT OF U-10 w/o Pu ALLOY

Temp (°C)	Heat Content ±2% (cal/g)	Temp (°C)	Heat Content ±2% (cal/g)
348	10.0	659	25.3
364	11.2	716	28.0
425	13.1	723	27.9
447	14.4	766	34.6
514	16.7	805	36.0
544	18.1	854	37.6
566	19.7	894	40.0
574	20.0	938	40.9
589	21.9	1047	48.2
591	21.2	1105	56.4
604	23.6	1150	58.7
625	24.4	1190	60.6

Figure 1. Heat Content of U-10 w/o Pu Above 25°C

Table IV

HEAT CONTENT OF U-10 w/o Pu-10 w/o Fz ALLOY

Temp (°C)	Heat Content ±2% (cal/g)	Temp (°C)	Heat Content ±2% (cal/g)
331	11.0	666	26.3
353	11.5	672	26.9
394	13.0	714	29.2
417	13.9	752	30.6
485	16.8	766	30.6
498	17.5	805	33.2
537	19.1	847	35.5
578	22.0	848	35.4
590	23.3	895	38.7
619	24.5	912	39.4

Figure 2. Heat Content of U-10 w/o Pu-10 w/o Fz Above 25°C

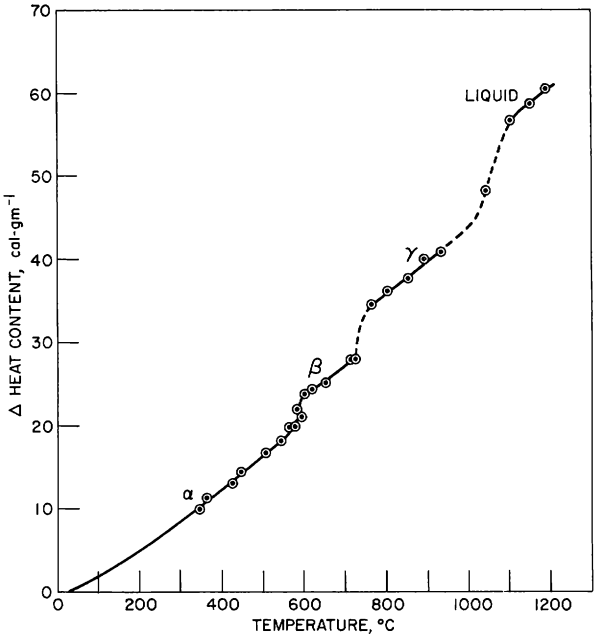

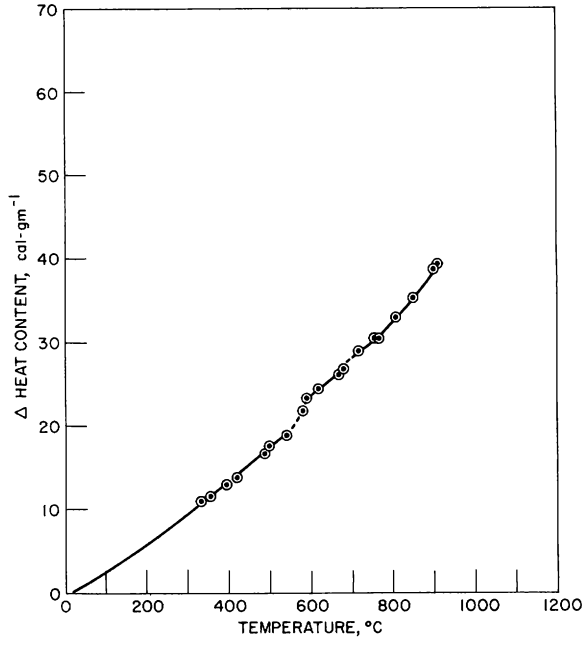

Table V

COMPOSITION OF SPECIMENS USED IN MEASUREMENTS OF HEAT CONTENT

Element	U-10 w/o Pu Charged* (w/o)	U-10 w/o Pu-10 w/o Fz	
		Charged (w/o)	Analyzed
U	90.0	80.0	79.8 ± 0.4 w/o
Pu	10.0	10.0	10.3 ± 0.2 w/o
C		-	52 ppm
H		-	8 ppm
O		-	129 ppm
Mo		2.75	3.08 ± 0.06 w/o
Rh		0.50	0.52 ± 0.03 w/o
Ru		2.95	3.21 ± 0.13 w/o
Pd		1.00	1.02 ± 0.05 w/o
Zr		2.80	2.75 ± 0.14 w/o
Other			< 66 ppm

* Starting material for this charge consisted of high-purity uranium and plutonium.

In the U-10 w/o Pu alloy, the $\alpha \rightarrow \beta$, $\beta \rightarrow \gamma$, and $\gamma \rightarrow$ liquid transformations occur over a range of temperatures. The heat of the $\alpha \rightarrow \beta$ transformation was 2.9 ± 0.3 cal/g and of the $\beta \rightarrow \gamma$ was 4.7 ± 0.5 cal/g. These heats were calculated in the middle of the two-phase regions and agree with those for pure uranium.[8] The heat of fusion of the binary alloy was 10.2 ± 1.0 cal/g as compared with 12.2 ± 1.0 cal/g for pure uranium.[7]

The phase transformations in the U-10 w/o Pu-10 w/o Fz alloy are largely suppressed because of the rapid cooling rate obtained in the drop calorimeter; nevertheless, heat effects are recorded and indicate the transformation temperatures. The full heat content is obtained only up to the first transformation at about 535°C. The heat contents above 535°C are low by the amount of heat retained in the untransformed phases.

Transformation Kinetics (H. Savage)

The transformation kinetics of the U-10 w/o Pu-10 w/o Fz alloy are being investigated as an aid in fabrication, for understanding of mechanical properties, and behavior under thermal and irradiation conditions.

The study to date is based on hardness changes occurring in isothermally quenched specimens. The data obtained are shown in Figure 3. The alloys were homogenized for 10 days at 850°C, air cooled, reheated to 700°C for 0.5 hr, and isothermally quenched to 450, 500, or 550°C.

Figure 3. Hardness of U-10 w/o Pu-10 w/o Fz Alloys vs Annealing Time

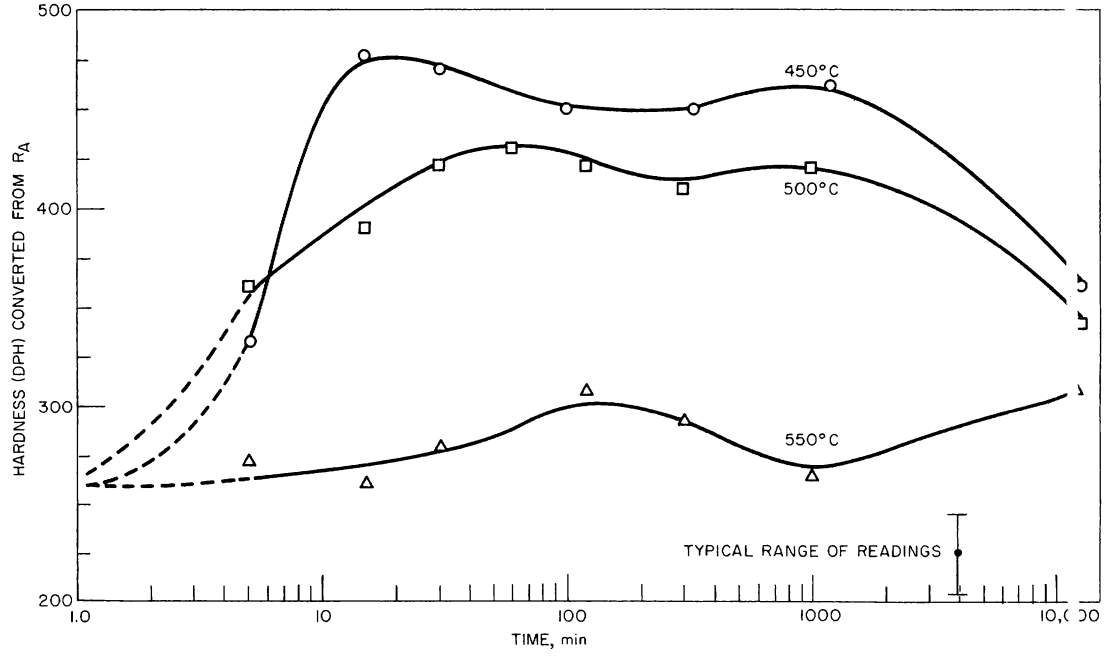

[8] Ginnings, D. C., and Corruccini, R. J., Heat Capacity Studies at High Temperature of Uranium, Uranium Trichloride and Uranium Tetrachloride, J. Research Natl. Bur. Stds., 39, 309 (1947).

The specimens were held at temperature for the times shown in Figure 3 and quenched in oil to room temperature. Five Rockwell A hardness values were obtained and averaged for each point on the graph. The Rockwell A numbers were converted to DPH values by use of the steel conversion chart.

The double hump in the hardness curve is similar to that shown in the U-Pu-Mo system.[9] The first hump is probably due to a precipitation-hardening mechanism. At the annealing time corresponding to the second hump, a lamellar structure, observable at high magnification, develops. The isothermal anneal at 550°C is above the first transformation temperature.

Table VI

COMPOSITION OF THERMALLY CYCLED ALLOYS

U (w/o)	Pu (w/o)	Fz (w/o)
90	10	
80	10	10
75	15	10
70	20	10

Thermal Cycling
(R. J. Dunworth)

Injection cast U-Pu and U-Pu-Fz alloy pins, 0.36 mm (0.144 in.) in diameter, of the compositions shown in Table VI were tested for thermal-cycling stability. Pins were cycled 100 times for the times and at the temperatures listed in Table VII. About 15-min transfer times were used for both heating and cooling. The holding times were considered to be adequate to transform both high- and low-temperature phases. The specimens were submerged in a large volume of NaK to minimize temperature gradients.

Table VII

THERMAL-CYCLING TESTS

Property	Test Cycle	U-10 w/o Pu	U-10 w/o Pu-10 w/o Fz	U-15 w/o Pu-10 w/o Fz	U-20 w/o Pu-10 w/o Fz
% Density Change	1	-35.2	+0.67	-0.07	
	2	-28.9	+0.53	+0.07	
	3		+0.33		-0.67
	3		+0.96		-0.68
% Length Change	1	+29.8	-0.25	-1.0	
	2	+25.1	+0.10	-0.3	
	3		+0.02		+1.5
	3		+0.45		+1.9
% Diameter Change	1	+10.6*	-0.83	+0.55	
	2	+ 7.2*	+0.28	+0.55	
	3		+0.22		-
	3		+0.64		+2.34

* Average values.

Test Cycle 1 - 100 cycles, 20 min at 700°C, 15 min at 450°C; 1 hr total cycle time.
Test Cycle 2 - 100 cycles, 1 hr at 700°C, 4-1/2 hr at 450°C; 6 hr total cycle time.
Test Cycle 3 - 100 cycles, 1 hr at 750°C, 4 hr at 500°C; 5-1/2 hr total cycle time.
On all cycles the heating and cooling times were 15 min each.

9 Mardon, P. G., "Authors' Comments to Papers on Ternary Alloys," Plutonium 1960, p. 387, Cleaver-Hume Press, Ltd., London (1961).

None of the fizzium alloys showed significant dimensional or density changes; however, the U-10 w/o Pu alloy lengthened 33%, swelled 9% in diameter, and decreased 32% in density. It is not clear why this U-10 w/o Pu casting behaved so badly on thermal cycling. These results were considerably different from those obtained upon cycling uranium.[10]

Tensile Properties (H. Savage)

The tensile properties of U-10 w/o Pu-10 w/o Fz alloy were measured from room temperature to 810°C. Unalloyed uranium and U-10 w/o Pu alloy were included in the investigation to evaluate the specimen preparation and the methods of testing, and to determine the effect of plutonium additions to uranium.

The apparatus used for the measurements consisted of a 10,000-kg tensile machine which had its work table enclosed in an alpha-active glovebox.[3] A vacuum furnace contained the specimen. The pull rods were led through bellows seals at the ends of the furnace. Clamps on the specimen transmitted movement through linkage to a microformer extensometer in a cooler area of the vacuum chamber. The output of this instrument was amplified and plotted as extension.

Tensile test specimens were prepared from injection cast rods, 400 mm long and 10.5 mm in diameter, as shown in Figure 4. Porosity in the castings caused obvious premature failure in some cases, especially when the material was brittle. Specimens were rejected if gross amounts of porosity were present.

Figure 4. U-10 w/o Pu-10 w/o Fz Injection Casting, Top, and Machined Tensile Test Specimens, Bottom.

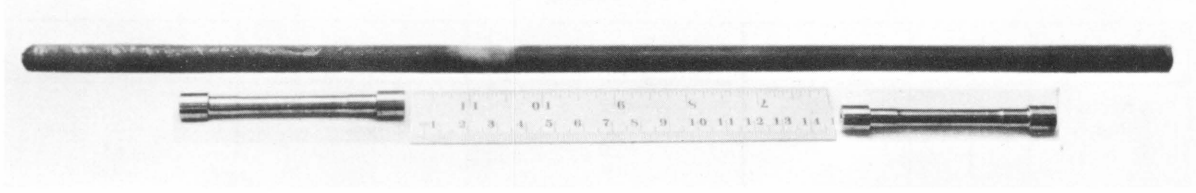

Macro 37889

The injection cast specimens were tested in both as-cast and heat-treated conditions. The U-10 w/o Pu-10 w/o Fz specimens were homogenized at 850°C for one week and quenched in oil or air cooled. One specimen was transformed at 500°C before testing. The uranium and U-10 w/o Pu specimens were tested in the cast condition only, since heat treatment does not change the tensile values.

---

[10] Hayward, B. R., Dimensional Changes Resulting from Alpha-Beta Thermal Cycling of Uranium and Uranium Alloys, NAA-SR-1434 (1957).

Testing conditions were maintained constant for all the compositions. A strain rate of 1.65 mm/min was measured by the extensometer and by cross-head motion. For all specimens, the gage length was 25.4 mm and the diameter was 6.35 mm. Both threaded and button-head specimens were used. The latter proved to be more desirable, especially in the case of the brittle specimens. A vacuum of 6×10^{-6} mm Hg was maintained during the tests.

The tensile property data are summarized in Tables VIII, IX, and X. The variation of ultimate tensile strength (U.T.S.) with temperature is shown in Figure 5. The general trend in the data indicates, that the tensile strength decreases and the elongation increases with increasing temperature.

Table VIII

TENSILE PROPERTIES OF INJECTION CAST URANIUM AS A FUNCTION OF TEMPERATURE

Temp (°C)	U.T.S. (kg mm^{-2})	Y.S.* (kg mm^{-2})	Reduction in Area (%)	Elongation in 25.4 mm (%)	Modulus (10^3 kg mm^{-2})
23.0	50.1 ± 1%	22.9 ± 1%	≈1	4 ± 5%	23.2 ± 1%
202	38.7 ± 1%	21.5 ± 1%	20 ± 5%	35 ± 5%	23.2 ± 1%
298	21.8 ± 1%	12.7 ± 1%	73 ± 5%	19 ± 5%	23.4 ± 1%
503	11.8 ± 1%	10.1 ± 1%	67 ± 5%	38 ± 5%	
550	6.05 ± 1%	5.29 ± 1%	80 ± 5%	30 ± 5%	5.4 ± 8%
550	6.02 ± 1%	5.57 ± 1%	>90	47 ± 5%	6.19 ± 8%
551	7.13 ± 1%	6.37 ± 1%	34 ± 5%	44 ± 5%	7.17 ± 8%
647	3.46 ± 1%	2.97 ± 1%	>90	56 ± 5%	4.32 ± 8%
652	2.59 ± 1%	1.98 ± 1%	>90	50 ± 5%	4.49 ± 8%
680	6.40 ± 1%		>90	38 ± 5%	7.45 ± 8%
812	0.120 ± 1%		>70	>63	

*Yield strength at 0.2% offset.

Table IX

TENSILE PROPERTIES OF INJECTION CAST U-10 w/o Pu AS A FUNCTION OF TEMPERATURE

Temp (°C)	U.T.S. (kg mm^{-2})	Y.S.† (kg mm^{-2})	Reduction in Area (%)	Elongation in 25.4 mm (%)	Modulus (10^3 kg mm^{-2})
23.5	26.4 ± 1%		<1	0.625 ± 5%*	13.4 ± 1%
305	23.0 ± 1%		<1	<1	
454	16.3 ± 1%	14.8 ± 1%	<1	0.900* ± 5%	10.9 ± 8%
502	13.3 ± 1%	11.9 ± 1%	<1	0.725* ± 5%	9.14 ± 8%
548**	8.15 ± 1%	7.38 ± 1%	≈1	6.3 ± 5%	6.47 ± 8%
550	9.36 ± 1%	9.34 ± 1%	<1	0.700* ± 5%	10.1 ± 8%
589	10.4 ± 1%		<1	0.300* ± 5%	15.7 ± 8%
651	6.75 ± 1%		<1	0.275* ± 5%	5.13 ± 8%
700	5.82 ± 1%	5.69 ± 1%	<1	0.687* ± 5%	0.70 ± 8%

* Fracture strain includes elastic-plastic components.
** High purity
† Yield strength at 0.2% offset.

Table X

TENSILE PROPERTIES OF INJECTION CAST U-10 w/o Pu-10 w/o Fz AS A FUNCTION OF TEMPERATURE

Temp (°C)	U.T.S. (kg mm^{-2})	Y.S. (kg mm^{-2})	Reduction in Area (%)	Elongation in 25.4 mm (%)	Modulus (10^3 kg mm^{-2})	Remarks
23.0	23.7 ± 1%		<1	<1	9.07 ± 1%	As cast.
23.0	58.6 ± 1%		<1	<1	8.23 ± 1%	Homogenized at 850°C for 1 wk. Quenched in oil.
23.0	19.7 ± 1%		<1	<1	14.8 ± 1%	Homogenized at 850°C for 1 wk. Quenched, 500°C 1 day.
197	27.8 ± 1%		<1	<1	8.8 ± 8%	As cast.
298	37.0 ± 1%		<1	0.5 ± 5%	8.0 ± 8%	Homogenized at 850°C for 1 wk. Gas cooled.
300	33.5 ± 1%		<1	<1	6.8 ± 8%	As cast.
427	22.8 ± 1%		<1	<1	7.5 ± 8%	As cast.
501	22.4 ± 1%		<1	<1	5.1 ± 8%	As cast.
552	13.2 ± 1%		<1	1.0 ± 5%	3.3 ± 8%	Homogenized at 850°C for 1 wk. Gas cooled.
605	6.81 ± 1%	5.99 ± 1%	≈20	10 ± 5%	4.1 ± 8%	Homogenized at 850°C for 1 wk. Gas cooled.
653	4.22 ± 1%	4.20 ± 1%	5 ± 5%	23 ± 5%		Homogenized at 850°C for 1 wk. Quenched, ingot top.
655	4.06 ± 1%	3.73 ± 1%	15 ± 5%	31 ± 5%	1.3 ± 8%	Homogenized at 850°C for 1 wk. Quenched, ingot bottom.
656	4.63 ± 1%	3.88 ± 1%	>80	53 ± 5%	2.8 ± 8%	Homogenized at 850°C for 1 wk. Gas cooled.
702	3.07 ± 1%	2.05 ± 1%	3 ± 5%	9 ± 5%	2.4 ± 8%	As cast.
810	1.21 ± 1%			>5	0.7 ± 8%	As cast.

Figure 5. Ultimate Tensile Strength vs Temperature for Injection Cast U-Pu-Fz Alloys

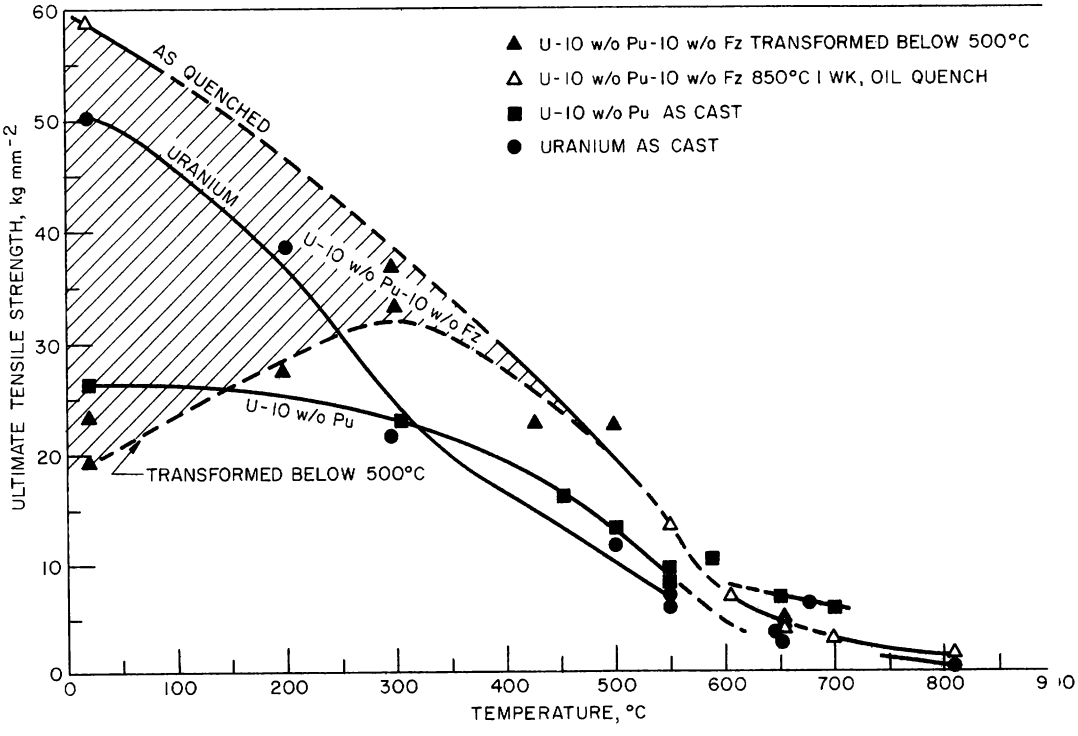

The discontinuity in the strength of uranium (associated with a decrease in ductility) in the beta-phase temperature region indicates the strong dependence of tensile properties on the phases present. Porosity in the uranium castings has negligible effect on tensile properties since uranium is relatively ductile.

The tensile strength of the U-10 w/o Pu alloy is similar to that of uranium at elevated temperatures. The salient difference is the small elongation and brittleness at all the temperatures of the tests. The room-temperature strength is only 50% of the uranium values. One high-purity specimen was more ductile at 548°C, but the 6% elongation was still only one-sixth that of uranium.

There is more variation in the tensile properties of the U-10 w/o Pu-10 w/o Fz alloy because quenching retains upper-temperature phases. At room temperature the tensile strength and the modulus depend on the amount of retained phases. Different degrees of transformation produce values between the high and low limits. The tensile strength of quenched specimens is higher than that of uranium for equivalent conditions, but the modulus of elasticity and the elongation are lower. In the transformed state, the alloy exhibits almost double the modulus and half of the tensile strength compared with the quenched values. Extreme brittleness characterizes the transformed state, so that reliable tensile values were not obtained due to premature fracturing.

The elongation improves above 600°C but, as with uranium, the strength is very low. The elongation increases to about 50% at about 650°C, but decreases at 700 and 800°C. The strength continues to drop at higher temperatures, and a form of hot-shortness seems to cause the low elongation.

In summary, lack of ductility characterizes the plutonium-bearing alloys at low temperature, and low strength with modest ductility characterizes these alloys in the gamma-phase region. In the 600°C temperature region the U-10 w/o Pu-10 w/o Fz alloy exhibits high ductility compared with that of the U-10 w/o Pu, for reasons not understood. At low temperatures, the alloys are all reasonably strong, but notch sensitive.

Brittleness (E. R. Gilbert)

The brittleness of U-Pu-Fz alloy castings influences methods of handling during fabrication and is related to the mechanical stability of the fuel under thermal shock and stresses in an operating reactor. The effect of heat treatment on the brittleness of U-10 w/o Pu, U-10 w/o Pu-10 w/o Fz and U-20 w/o Pu-10 w/o Fz through impact, bend, and hardness tests have been studied. Elastic modulus data were derived from the bend tests.

The alloys studied were induction melted in yttria-coated graphite crucibles under 2×10^{-6} mm Hg vacuum and injection cast into Vycor molds coated with yttria. Specimens were machined to 0.794-cm (5/16-in.)-diameter by 4.45-cm (1-3/4-in.)-long rods. For heat treating, specimens were wrapped in tantalum foil and encapsulated in Vycor tubes at a pressure of 2×10^{-6} mm Hg.

The large tensile stresses are near the surface of the fuel pin and were calculated for a 0.366-cm-diameter fuel pin by use of values for the terms of Eqs. 1, 2, and 3 given in Table XIII. The stresses in the three directions were then converted into an effective stress $\bar{\sigma}$,[12] which is given by

$$\bar{\sigma} = \frac{1}{\sqrt{2}}\left[(\sigma_r - \sigma_t)^2 + (\sigma_r - \sigma_\ell)^2 + (\sigma_t - \sigma_\ell)^2\right]^{1/2} \quad (4)$$

and is tabulated in column five of Table XIV.

Table XIII

VALUES OF FUEL PROPERTIES USED IN CALCULATION OF THERMAL STRESSES

Alloy	Temp Range (°C)	Coef of Linear Thermal Expansion $\alpha(10^{-6}\ ^oC^{-1})$	Elastic Modulus $E(10^6$ psi)	Thermal Conductivity $K(W\ cm^{-1}\ ^oC^{-1})$	Poisson's Ratio ν
U-10 w/o Pu-10 w/o Fz	300-450	16*	9	0.23[2]	0.38*
	400-550	17*	8	0.25[2]	0.39*
	450-600	19*	7	0.26[2]	0.40*
	550-700	21*	7	0.29[2]	0.42*
U-10 w/o Pu	300-450	18*	14	0.27*	0.30*
	550-700	24*	11	0.23*	0.34*
Uranium	300-450	21[13]	22[14]	0.32[15]	0.25[14]
	550-700	28[13]	19[14]	0.39[15]	0.30[14]

*Estimated

Table XIV

CALCULATED EFFECTIVE SURFACE STRESS AND FUEL PIN CREEP BEHAVIOR

Alloy	Surface Temp (°C)	Power per Volume of Fuel (W cm^{-3})	ΔT[a] (°C)	Effective Surface Stress (kg mm^{-2})	Time for 1% Strain at Effective Stress (hr)	Time for 1% Strain with Decreasing Stress (hr)	Time for Stress to Decrease to Zero (hr)	Strain for Stress to Decrease to Zero (%)
U-10 w/o Pu-10 w/o Fz as Injection Cast	300	1375	50	4.07	5600[b]	-	-	-
	300	4000	145	11.9	21[b]	-	-	-
	300	4125	150	12.2	15[b]	-	-	-
	410	1495	50	3.94	238	[c]	19	0.267
	410	4000	134	10.5	49	[c]	23	0.713
	410	4485	150	11.7	29	[c]	23	0.799
	450	1555	50	3.87	3200	[c]	1302	0.233
	450	4000	129	9.98	86	[c]	731	0.602
	450	4664	150	11.7	33	[c]	573	0.703
	550	1735	50	4.43	3.5	[c]	3340	0.43
	550	4000	115	10.3	2.9×10^{-3}	3350	3350	1.00
	550	5205	150	13.1	9.3×10^{-5}	106	3350	1.28
U-10 w/o Pu as Injection Cast	300	1615	50	6.33	55	-	-	-
	300	4000	124	15.7	1.2	-	-	-
	300	4845	150	19.1	1.5×10^{-1}	-	-	-
	550	1975	50	6.47	4.3×10^{-2}	-	-	-
	550	4000	101	13.1	3.2×10^{-3}	-	-	-
	550	5925	150	19.4	7.2×10^{-4}	-	-	-
Uranium Beta Quenched	300	1915	50	10.8	278	-	-	-
	300	4000	104	22.6	11.1	-	-	-
	300	5745	150	32.4	2.3	-	-	-
	550	2330	50	13.4	6.2×10^{-3}	-	-	-
	550	4000	85	22.9	6.9×10^{-4}	-	-	-
	550	6990	150	40.0	6.4×10^{-5}	-	-	-

[a] ΔT is the difference between the center and surface temperatures. [b] Estimated from tensile tests. [c] Stress decreases to zero before strain reaches %.

[12] Dorn, J. E., Jelinek, J. J., Latter, A. J., and Thomsen, E. G., Plastic Flow in Metals, Research Report OPRD No. W-200 (May 1954).

[13] Foote, F. G., "Physical Metallurgy of Uranium," Progress in Nuclear Energy, 1 (V), 109, Pergamon Press, London and New York (1956).

[14] Reactor Handbook, Materials, 1, 2nd Ed., Interscience Publishers, London and New York, 12 [illegible] (1960).

[15] Zegler, S. T., and Nevitt, M. V., Structures and Properties of Uranium-Fissium Alloys, ANL-6116 (1961).

The calculated thermal stresses for uranium, U-10 w/o Pu, and U-10 w/o Pu-10 w/o Fz are below the yield strength, so that plastic deformation takes place by creep. U-10 w/o Pu and U-10 w/o Pu-10 w/o Fz are brittle below 550°C with total creep elongations of 1 to 3%. If the amount of creep in the fuel pin reaches the fracture strain, cracks would be expected to form. The calculation which is perhaps most appropriate for this situation is the time for 1% strain and the maximum amount of creep which can occur.

Creep tests are conducted with constant load or stress. The stress in the fuel pin continuously decreases as it deforms. Conventional stress-relaxation measurements involve decreasing stress as strain remains constant. Neither conventional creep measurements nor conventional stress-relaxation measurements seem to apply directly to the case of the fuel pin in which stresses decrease as the fuel pin deforms. To overcome these difficulties, creep measurements were made under both constant stress and under decreasing stress while the specimen was permitted to deform.

With this information the time for 1% deformation was calculated for several temperatures and temperature gradients. The time for the stress to decrease to zero and the corresponding strain were also calculated. The power of 4000 W/cm^3 of fuel corresponds to an EBR-II operating level.[16] The results of these calculations are given in Table XIV. For comparison, the time for 1% deformation is also given for the case in which the stress in the fuel pin does not decrease, but remains the same as the initial calculated stress.

The results of the calculations show that the thermal stresses decrease to zero and creep stops before the fracture strain is reached.

b. Compatibility of Uranium-5 w/o Fissium with Type 304 Stainless Steel (C. M. Walter)

A study of the interdiffusion of the EBR-II, Core-I fuel, U-5 w/o Fs with its clad material, Type 304 stainless steel, was completed in 1963. Most of the results were reported last year.[17]

Electron microprobe analysis was performed with two diffusion couples (35 days at 550 and 650°C) to determine if there is significant penetration beyond that revealed by metallographic examination. None was found.

The results of this study indicate a total diffusion band width of 6.4 x 10^{-3} cm for 90 days at 550°C of EBR-II operation. Of this, only about 5%, or 3 x 10^{-4} cm, is into the 2.3 x 10^{-2}-cm clad. As the temperature increases, the diffusion band widens rapidly, more than doubling with each 50°C temperature increment until at 700°C it becomes 8.6 x 10^{-2} cm in 90 days.

[16] Koch, L. J., et al., Summary Report on the Hazards of the EBR-II, ANL-5719, pp. 6, 8 (May 1957).

[17] Annual Report for 1962, Metallurgy Division, ANL-6677, p. 14.

c. Dip Studies of the Penetration Rate of Clad Materials by Molten Fuel (C. M. Walter and L. R. Kelman)

A study of the rate of penetration of molten plutonium-containing metal fuels through prospective jacket materials is in progress in the gloveboxed equipment that has been previously described.[18] Results of earlier studies of the penetration rate of molten U-5 w/o Fs alloy, uranium, and U-36 a/o Fe eutectic through stainless steel and iron have been reported.[19,20] Further data have been obtained to aid in the interpretation of some unexpected, but reproducible, changes in penetration rate with temperature that were found in these systems. The old and new data are summarized in Table XV and Figure 6.

Table XV

PENETRATION OF ARMCO IRON BY MOLTEN URANIUM, URANIUM-36 a/o Fe EUTECTIC, AND U-77 a/o Fe EUTECTIC

Melt Material:	Uranium				Uranium-36 a/o Iron				Uranium-77 a/o Iron			
Wall Thickness (μ):	380		760		380		760		380		76	
Temp (°C)	Time (sec)	Rate (μ/sec)	Time (sec)	Rate (μ/sec)	Time (sec)	Rate (μ/sec)	Time (sec)	Rate (μ/sec)	Time (sec)	Rate (μ/sec)	Time (sec)	Rate (μ/sec)
740							176,400	4.3×10^{-3}				
850							2,340	3.2×10^{-1}				
950							600	1.3				
1050					84	4.5	216	3.6				
1070							198	3.8				
1085					0.6	630	1.4	540				
1100											199	3.8
1115							0.67	1100				
1138			0.9	850								
1150	0.5	760	1.0	760			1.1	690	53.0	7.2	138	5.5
1169			1.0	690								
1187			1.5	530			1.55	490				
1206			4.4	170								
1229	3.1	120	5.7	130			3.7	210				
1244			5.2	150			5.95	130			134	5.7
1300			3.7	210	1.7	220	4.4	170	22.7	17	53.5	14

Figure 6. Penetration Rates of Armco Iron by Uranium and U-Fe Eutectics

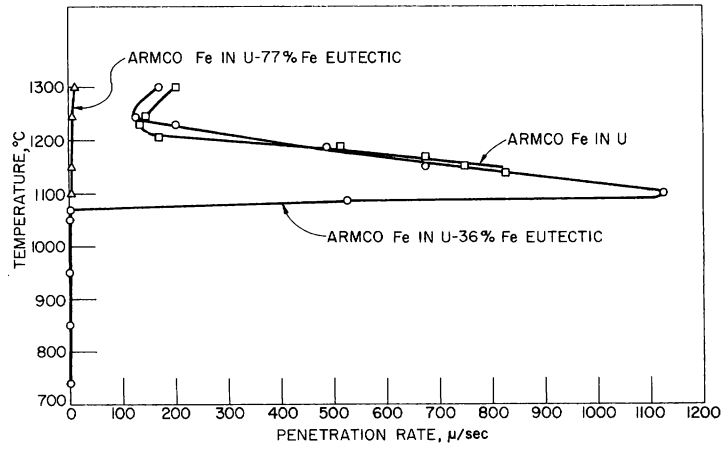

18 Annual Report for 1961, Metallurgy Division, ANL-6516, p. 21.

19 Walter, C. M., and Kelman, L. R., Penetration Rate Studies of Stainless Steel by Molten Uranium and Uranium-Fissium Alloy, J. Nuc. Matls. 6 281-290 (1962).

20 Annual Report for 1962, Metallurgy Division, ANL-6677, pp. 16-17.

For all tests below 1080°C and above 1235°C the penetration rate increased with increasing temperature; however, at and just above 1080°C, penetration was extremely rapid. At higher temperatures, up to 1235°C, the rate of penetration decreased with increasing temperature.

Figure 7a shows the microstructure of the U-36 a/o Fe eutectic reaction with iron at 1070°C. It is typical of microstructures of all tests below 1080°C, showing a thin continuous layer of UFe_2 compound on the iron surface backed up by particles of UFe_2 in U-36 a/o Fe eutectic.

The very rapid increase in penetration at about 1080°C is attributed to the formation of molten U-77 a/o Fe eutectic which results from the reaction of UFe_2 compound with iron at that temperature.

Figure 7b shows the microstructure of the U-36 a/o Fe eutectic reaction with iron at 1150°C. It is typical of microstructures of tests of molten uranium and of U-36 a/o Fe eutectic above 1080°C, showing a layer of U-77 a/o Fe eutectic backed up by UFe_2 compound. Further attention is being given to the kinetics of the reactions where the penetration rate decreases with increasing temperature.

The importance of the formation of UFe_2 in this process was verified by a series of tests of molten U-77 a/o Fe eutectic alloy against iron. As was expected for this system, which contains no compounds, the penetration rate of iron by the U-77 a/o Fe eutectic increased smoothly and continuously with increasing temperature. Figure 7c shows the microstructure of the U-77 a/o Fe eutectic reaction with iron at 1150°C. Note that the structure consists only of the U-77 a/o Fe eutectic adjacent to iron with no excess compound. At 1100°C the rate was 3.8 μ/sec, and 14 μ/sec at 1300°C. Note that the penetration rate of the U-36 a/o Fe eutectic is 3.8 μ/sec at 1070°C, just below the temperature at which the rate increases very rapidly. In spite of the difference in composition, the two eutectics are not much different in their aggressiveness toward iron as long as the above-described complications do not enter the picture.

Penetration behavior similar to that described above would be expected in any binary system wherein an intermetallic compound of higher melting temperature than the lower-melting element forms an eutectic with the other element. The refractory metals now under consideration as jacket materials do not form such systems with uranium or plutonium. Some other systems which may show this behavior and which will be checked if time permits are U-Ni, U-Mn, Pu-Fe, Fe-Nb, Cu-Mg, Sn-U, and Sn-Zr.

Figure 7. Microstructures Showing Products of the Reaction of Molten U-36 a/o Fe and U-77 a/o Fe Eutectics with Iron below and above 1080°C

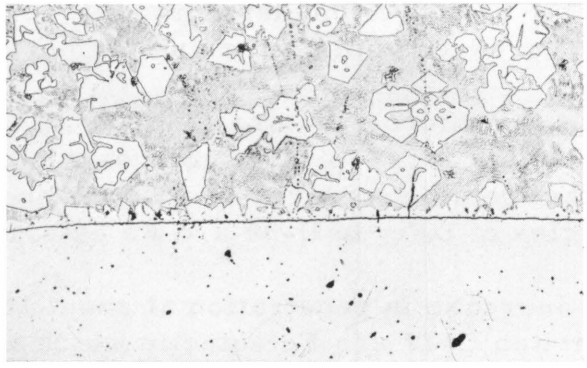

UFe_2 + U-36 a/o Fe Eutectic

Iron

Micro 37429 150X

a. U-36 a/o Fe Eutectic-Iron Reaction at 1070°C.

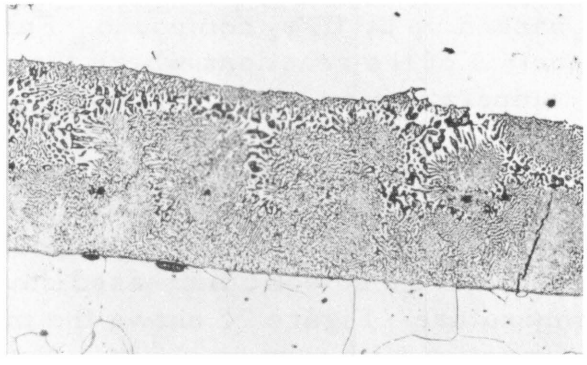

UFe_2

U-77 a/o Fe Eutectic

Iron

Micro 37428 150X

b. U-36 a/o Fe Eutectic-Iron Reaction at 1150°C.

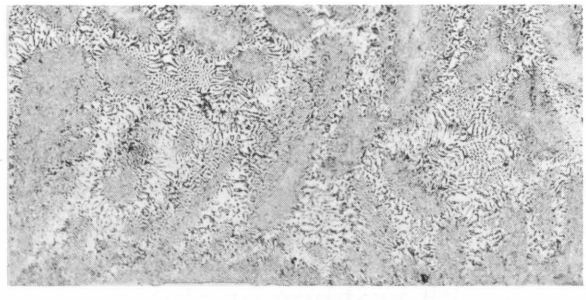

U-77 a/o Fe Eutectic

Iron

Micro 37432 150X

c. U-77 a/o Fe Eutectic-Iron Reaction at 1150°C.

d. TREAT Study of the Penetration Rate of Stainless Steel by Molten Uranium and Uranium-5 w/o Fissium (C. M. Walter and L. R. Kelman)

A study of the penetration rate of molten uranium and U-5 w/o Fs through Type 304 stainless steel has been extended by performing a series of experiments in the TREAT reactor. These experiments were made to more closely duplicate reactor conditions, namely, actual fuel element geometry, heat generation within the fuel itself, a sodium bond between fuel and cladding, and the presence of an oxide film on the surface of the fuel pins.

An experimental capsule (see Figure 8) containing two fuel elements, one bonded with sodium and one unbonded, was placed in the reactor. TREAT was given a predetermined power pulse such that the fuel element came to the desired temperature above the melting point of the fuel. The molten fuel then penetrated the clad and contacted a metal sheath around the fuel element. This produced an electrical signal which was the indication of failure time. The starting time was taken as the time at which the fuel became molten and was determined from the temperature trace. A typical temperature trace with the reactor power curve superimposed is shown in Figure 9. The difference between these two times is the penetration time.

The test results for the bonded uranium and U-5 w/o Fs fuel elements are summarized in Table XVI. The data are arranged in the order of increasing severity of the transients, because of the uncertainty of the temperature measurements. The data obtained from the unbonded elements were very erratic.

Figure 8. TREAT Test Assembly

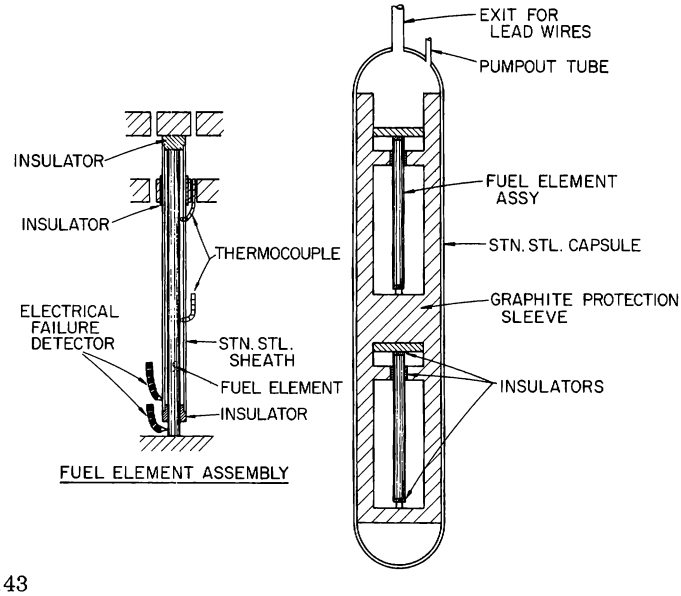

106-7143

Figure 9. Typical Test Run Showing Temperature and Reactor Power on the Same Time Base (Transient # 528 U-5 w/o Fs)

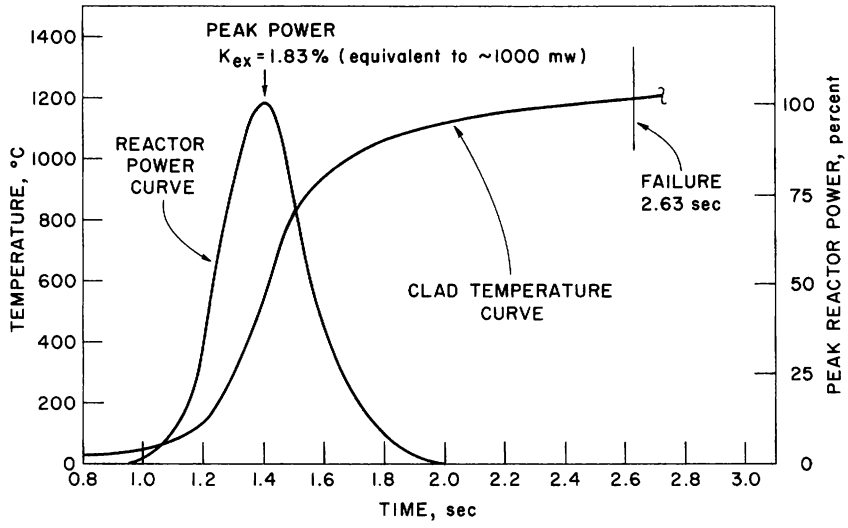

Table XVI

FAILURE OF 0.23-mm-WALL, TYPE 304 STAINLESS STEEL CLADDING IN BONDED ELEMENTS

Uranium-5 w/o Fissium Fuel				Uranium Fuel			
$k_{ex}(0)$ (%)	Recorded Temp (°C)	Failure Time (sec)	Penetration Rate (μ/sec)	$k_{ex}(0)$ (%)	Recorded Temp (°C)	Failure Time (sec)	Penetration Rate (μ/sec)
1.77	1100	1.7	140	1.57	1025	1.2	1[illegible]0
1.79	1150	0.8	290	1.57	1130	1.1	2 0
1.86	1200	1.2	190	1.61	1075	1.0	2 0
1.95	1150	0.7	330	1.61	1050	0.9	2 0
2.07	*	<0.1	>2000	1.65	1150	0.8	2[illegible]0
2.13	*	<0.1	>2000	1.74	1150	0.9	2 0

* Ruptured during rapid heating. Maximum recorded temperature at the time of failure was about 1150°C.

A comparison of the results from TREAT and the results of laboratory dip experiments[19] performed previously indicate that there is excellent agreement at 1150°C. The penetration rate of molten uranium and U-5 w/o Fs through 304 stainless steel in TREAT was about 250 μ/sec and in the laboratory furnace experiments was about 300 to 350 μ/sec. In the U-5 w/o Fs fuel samples, the penetration rate appears to decrease about 50°C above and 50°C below 1150°C (penetration time increases), which is the same phenomenon observed in the laboratory experiments.

The excellent correlation between these two very different types of experiments makes it possible to use the relatively simple dip test to survey several combinations of materials and TREAT to test the most promising of them.

e. Compatibility of Jacket Materials with Uranium-Plutonium-Fizzium (C. M. Walter)

This program began as a preliminary determination of compatibility of U-20 w/o Pu-10 w/o Fs with several refractory metals and alloys in the temperature range from 550 to 800°C. Tentative results of this study, which were of a preliminary nature and were primarily intended for weeding out potential cladding materials for a projected 90-day operation in EBR-II, were reported previously.[21] No attempt was made to determine direction of penetration.

The study has developed into a more general approach as part of a continued program to develop metal fuels for future fast reactors. The fuel-clad combinations now being studied are U-10 w/o Pu and U-20 w/o Pu-10 w/o Fz with niobium and U-10 w/o Pu-10 w/o Fz with niobium, Nb-1 w/o Zr, molybdenum, vanadium, V-10 w/o Ti, V-20 w/o Ti, 304 stainless steel, and Hastelloy-X. These combinations are being studied by annealing diffusion couples in the temperature range from 550 to 650°C for 7, 17, and 42 days. Metallographic examination and electron microprobe analysis of the diffusion bands are being used to determine the extent of interdiffusion.

Preliminary results on several of these combinations are summarized in Table XVII. The niobium versus U-10 w/o Pu-10 w/o Fz

Table XVII

COMPATIBILITY OF U-Pu-Fz ALLOYS WITH POTENTIAL CLAD MATERIALS

Material (w/o)	Temp (°C)	Interdiffusion Band Width (μ) Time (days)			Direction
		7	17	42	
Nb vs U-10 Pu-10 Fz	550 600 650	3 7 15	5 10 30	6 16 80	Total band width. Almost 100% into the clad.
Nb-1 Zr vs U-10 Pu-10 Fz	550 600 650	3 6 13	6 10 29	8 16 76	Total band width. Almost 100% into the clad.
Nb vs U-20 Pu-10 Fz	550 600 650	6 12 25	9 20 75	13 37 170	Total band width. Almost 100% into the clad.
Nb vs U-10 Pu	550 600 650	nil nil nil	nil nil nil	nil nil nil	No evidence for penetration.
304 SS vs U-10 Pu-10 Fz	550 600 650	2 5 11	3 7 16	5 10 22	Penetration into the clad. Also evidence for major diffusion into the fuel.
Hasteloy-X vs U-10 Pu-10 Fz	550 600 650	- - -	- 10 -	- 18 39	Penetration into the clad. Also evidence for major diffusion into the fuel.
Mo vs U-10 Pu-10 Fz	550 600 650	3 6 -	6 9 17	- 13 25	Total band width. Penetration mostly into the fuel.
V vs U-10 Pu-10 Fz	550 600 650	- - -	4 6 -	6 9 -	Total band width. Penetration mostly into the fuel.

[21] Annual Report for 1960, Metallurgy Division, ANL-6330, pp. 15-19.

and Nb-1 w/o Zr versus U-10 w/o Pu-10 w/o Fz showed almost identical band widths. Niobium versus U-20 w/o Pu-10 w/o Fz showed an interdiffusion band width of about twice that of niobium versus U-10 w/o Pu-10 w/o Fz for all temperatures tested (see Figure 10). The penetration was almost 100% into the cladding for all three combinations. No evidence was found for interdiffusion in niobium versus U-10 w/o Pu.

Figure 10. Penetration Time vs Total Band Width of Nb/U-Pu-Fz Couples

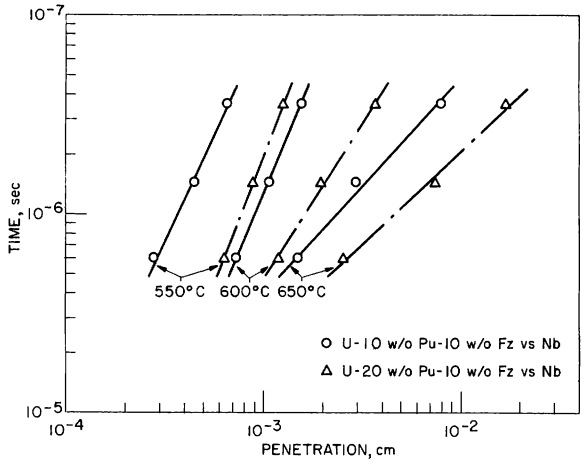

For equivalent times and temperatures the U-10 w/o Pu-10 w/o Fz alloy penetrated Hastelloy-X about 1-1/2 to 2 times as deep as it penetrated 304 stainless steel. Evidence was found for major diffusion into the fuel in both these combinations, but the etches tried to date have not delineated this zone, so no values are given for diffusion into the fuel. Molybdenum versus U-10 w/o Pu-10 w/o Fz showed a relatively narrow interdiffusion band, with the majority into the fuel.

The results for vanadium versus U-10 w/o Pu-10 w/o Fz also showed a relatively narrow diffusion band with penetration almost all into the fuel. The high oxygen content of the vanadium (1300 ppm) and the appearance of the diffusion band suggest that the fuel is gettering oxygen from the clad to form an oxide which inhibits further diffusion. Samples of vanadium containing lower amounts of oxygen are being used to investigate this possibility.

Work is proceeding to fill in the gaps in Table XVII and to clarify the questions which have arisen from this study. We are also in the process of running U-10 w/o Pu-10 w/o Fz with V-10 w/o Ti and V-20 w/o Ti alloys.

f. Compatibility of Plutonium-1.25 w/o Aluminum with Zircaloy (C. M. Walter)

The study of the compatibility of Pu-1.25 w/o Al fuel with Zircaloy-2 clad for EBR-I, Core IV was completed in 1963. Preliminary results were reported last year[22] for diffusion couples annealed at 500, 550, and 600°C for 7, 17, and 42 days and at 650°C for 42 days. Metallographic examination did not reveal any interdiffusion but did indicate that bonding occurred between the fuel and clad materials. The plutonium-zirconium

[22] Annual Report for 1962, Metallurgy Division, ANL-6677, p. 6 .

phase diagram shows that delta-plutonium (the stable phase in Pu-1.25 w/o Al alloy in the temperature range from 500 to 650°C) has an extensive solubility for zirconium, and vice versa. Neither metallographic nor microhardness studies revealed evidence of solid solubility.

Electron microprobe analysis (work done at Mound Laboratory in Miamisburg, Ohio) proved to be a very useful tool in the study of this solid solution penetration. The couple annealed at 600°C for 42 days which represented a condition far more severe than reactor conditions (the projected operation temperature of Core IV is 500°C), was selected for investigation. Also, the relatively high annealing temperature and long annealing time should assure a good bond and deep enough interpenetration to produce reasonable experimental resolution.

The plot in Figure 11 shows that some penetration of plutonium into Zircaloy-2 occurred but that very little diffusion took place in the opposite direction. The total penetration into the clad was about 9 μ.

Figure 11. Pu-Lα and Zr-Lα X-ray Intensity vs Distance Across a Pu-1.25 w/o Al vs Zr-2 Diffusion Couple Annealed at 600°C for 42 Days

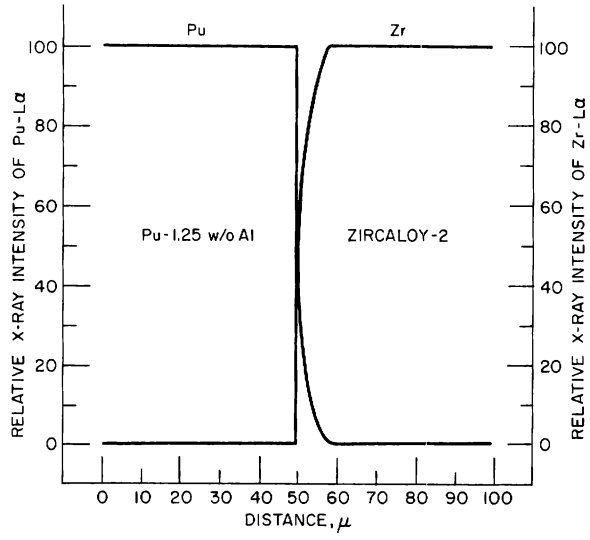

The diffusion couple tested represents the condition in the reactor which would promote maximum penetration at 600°C for 42 days. Considerably less penetration for equivalent time at the lower operating temperature of Core IV fuel elements would be expected. From a compatibility standpoint, Zircaloy-2 is, therefore, a very adequate jacket material for Pu-1.25 w/o Al.

g. Properties of Zero-power Uranium-Plutonium Metal Fuels (L. R. Kelman and H. V. Rhude)

Currently there is considerable interest in a plutonium fuel for zero-power fast critical experiments. A fuel alloy having a U^{238} to Pu^{239} atom ratio of 2:1 with as little dilution as possible from other elements is preferred from physics considerations. Unfortunately, binary uranium-plutonium alloys of this composition are pyrophoric and extremely brittle. The influence of small amounts of alloying additions on pertinent properties, especially pyrophoricity and workability, of U-30 a/o Pu alloys are of interest.

With the same goal in mind, the French have been studying the influence of small iron additions on the properties of U-25 w/o Pu alloy.[23]

[23]Zaleski, C P., private communication.

A patent by Schonfeld and Coffinberry of LASL[24] suggested the potential of this alloy. The French have found that 1 and 1.5 w/o iron additions greatly improve the resistance of the U-25 w/o Pu alloy to air oxidation whereas 0.5 w/o iron does not.

The effects of several alloying elements (including aluminum, carbon, copper, iron, molybdenum, and zirconium) on the pyrophoric tendencies of U-30 a/o Pu alloy are being studied. These elements were chosen mainly on the basis of their beneficial effect on resistance of uranium and/or plutonium to air corrosion. Specimens for ignition studies by G. Schnizlein of ANL Chemical Engineering Division were prepared by tilt pour chill casting ternary alloys containing 6 a/o (about equivalent to 1.5 w/o Fe) of the above elements with 67 a/o U-27 a/o Pu. The specimens were machined into right cylinders, 6 mm in diameter and 6 mm long, with a thermocouple hole drilled in one end. The ignition tests were made in dry air and in air saturated with moisture by the burning-curve method.[25] The iron and the molybdenum alloys were found to have high ignition temperatures, whereas the ignition temperatures of the aluminum and copper alloys were not much different than the 157°C ignition temperature (in dry air) reported for the binary U-30 a/o Pu alloy.[26] The carbon and zirconium alloys showed self-heating at relatively low temperatures, which makes results obtained with them questionable.[26]

The air-oxidation resistance of specimens similar to those used for the ignition study are under investigation. Results of one-month exposure to flowing room air at 15 cfm, 24°C, and 25 to 56% relative humidity are summarized in Table XVIII.

Table XVIII

EFFECT OF ROOM AIR CORROSION ON URANIUM AND URANIUM-PLUTONIUM-BASE ALLOYS

Alloy (a/o)	Original Weight (gm)	Weight after 1 Month (gm)	Remarks
Uranium	3.20	3.20	No change in weight. Slightly tarnished.
U-30 Pu	6.85	7.50	Began gaining weight on 2nd day. Completely disintegrated by 6th day.*
U-27 Pu-6 Al	6.87	7.78	Began gaining weight on 2nd day. Completely disintegrated by 6th day.*
U-27 Pu-6 C	3.23	3.62	No gain in weight first 5 days. Gained 0.03 gm 6th day. Completely disintegrated by 6th day.*
U-27 Pu-6 Cu	4.45	4.79	Did not begin gaining weight until 7th day. Although showed some signs of swelling and initial disintegration on 6th day. Completely disintegrated on 21st day.*
U-27 Pu-6 Fe	2.95	2.95	No change in weight. Slightly tarnished.
U-27 Pu-6 Mo	3.49	3.49	No change in weight. Slightly tarnished.
U-27 Pu-6 Zr	3.75	3.75	No change in weight. Slightly tarnished.
U-20 Pu-10 Fz**	0.10	0.10	No change in weight. Slightly tarnished.

* Still gaining weight after 30 days.

** U-20 Pu-10 Fz in w/o.

---

[24] Schonfeld, F. W., and Coffinberry, A. S., Plutonium-Uranium Alloy, U. S. Patent No. 2,905,362 (Sept 1, 1959).

[25] Chemical Engineering Division Summary Report, April-June 1961, ANL-6379, p. 192.

[26] Schnizlein, J. G., Jr., private communication.

Specimens of U, U-30 a/o Pu, and U-20 w/o Pu-10 w/o Fz are also being tested for comparison. The condition of the specimens after 21 days is shown in Figure 12. Since this is a weeding-out test, only rough weights are being followed. The U-30 a/o Pu alloy was completely disintegrated to a powder in 6 days. The aluminum and carbon alloys behaved in about the same manner. The copper alloy started to powder in 6 days and was completely powdered in 21 days. The iron, molybdenum, and zirconium alloys (as well as the U and U-20 w/o Pu-10 w/o Fz) were slightly tarnished but showed no appreciable weight change after 30 days.

Figure 12. Pyrophoricity Samples after 21 Days in Air

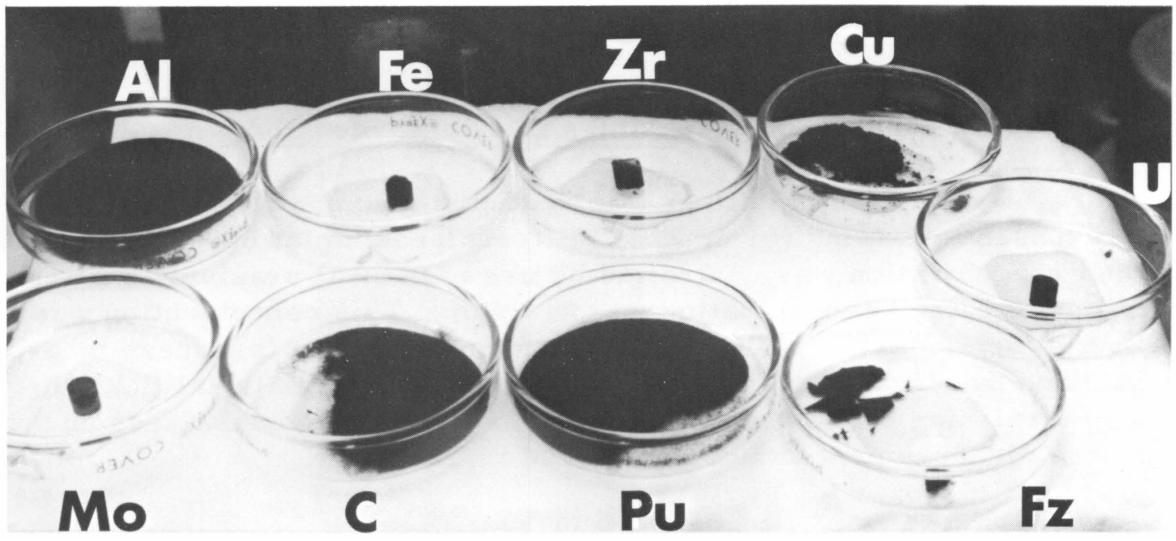

Macro 37668

Top Row: U-27 a/o Pu-6 a/o Al, U-27 a/o Pu-6 a/o Fe, U-27 a/o Pu-6 a/o Zr, U-27 a/o Pu-6 a/o Cu.

Extreme Right: Uranium.

Bottom Row: U-27 a/o Pu-6 a/o Mo, U-27 a/o Pu-6 a/o C, U-30 a/o Pu, U-20 w/o Pu-10 w/o Fz.

Metallographic examination of the chill-cast U-27 a/o Pu-6 a/o Fe alloy has shown it to be an extremely fine-grained two-phase structure. A much heavier rod of this alloy was also prepared by injection casting to obtain tensile specimens. This was found to be extremely coarse grained and showed localized corrosion even in our nitrogen glovebox atmosphere containing a few hundred ppm water and oxygen. The phases in these alloys are being determined by metallography, X-ray diffraction, and electron microprobe analysis.

Further work is in progress to determine the dependence of pyrophoric tendency on microstructure. Also, the fabricability of promising alloys is being studied.

2. Corrosion of Refractory Metals Alloys in Sodium (H. A. Levin, S. Greenberg)

The design and construction of specialized equipment to study the corrosion behavior of refractory metal and alloys in sodium containing controlled amounts of oxygen and carbon are in progress. Pending completion of this equipment, a Reactor Engineering Division sodium loop capable of operation at 650°C has been reactivated. This is serving as a screening facility for commercial and developmental alloys and for combinations of potential interest.

In addition, evaluation of vanadium-base alloys exposed by Reactor Engineering Division personnel to low-oxygen sodium has been completed.[27]

a. Vanadium-base Alloys in Low-oxygen Sodium

Vanadium alloys (fabricated at Armour Research Foundation) were exposed to flowing (61 cm/sec [2 ft/sec]) sodium at 650°C for 2 days. Oxygen concentration was controlled by use of natural uranium as a getter. The reported Na_2O concentration was 1-5 ppm. This concentration was measured semiquantitatively by means of tantalum tabs (hardness measurements) and by visual inspection of the uranium getter material (i.e., there was no tarnishing of the uranium). The results of oxygen analyses and hardness measurements are summarized in Table XIX.

Table XIX

EFFECT OF LOW-OXYGEN SODIUM ON VANADIUM-BASE ALLOYS (650°C) FOR 21 DAYS

Alloy (w/o)	Weight Gain (mg/cm^2)	Oxygen Concentration (ppm)[a]		Hardness, DPH - 100-g Load					
				Edge			Center		
		As Received	Tested	As Received	Tested	Annealed[b]	As Received	Tested	Annealed
V-10 Ti-3 Nb	0.21	665	1400	240	650	200	240	190	2[illegible]
V-10 Ti-3 Ta	0.24	570	1800	240	450	200	240	195	2[illegible]
V-5 Ti-20 Nb	0.05	530	1200	275	680	245	275	235	2[illegible]

[a] Bulk sample concentration. Average of two analyses.

[b] Annealed in vacuum at 850°C for 23 hr.

Each of the three alloys V-10 w/o Ti-3 w/o Nb, V-10 w/o Ti-3 w/o Ta, and V-50 w/o Ti-20 w/o Nb showed a distinct surface layer approximately 10 μ in thickness. Adjacent to this was a darkly etched layer, approximately 40 μ in thickness (bulk of the sample), containing a second phase. This is illustrated for the case (typical) of the V-5 w/o Ti-20 w/o Nb alloy in Figure 13. The untested materials exhibited homogeneous structures (similar to the central portions of the exposed samples).

[27] Annual Report for 1962, Metallurgy Division, ANL-6672, pp. 27-31.

Figure 13. V-5 w/o Ti-20 w/o Nb Exposed to Flowing Low-oxygen Sodium at 650°C for 21 Days

Micro 38101 Etchant - 40% HNO_3, 20% HF 640X

An electron diffraction study of the exposed V-5 w/o Ti-20 w/o Nb sample was unsuccessful in determining the identity of the surface layer. X-ray powder patterns of this surface layer material showed two sets of diffraction lines. One set corresponded to the base material (V-5 w/o Ti-20 w/o Nb). The other could not be indexed on the basis of any of the simple oxides of the alloy constituents.

Microhardness measurements showed the edge hardnesses of the exposed specimens to be much greater than the center hardness. This is attributed to oxygen pickup. Inasmuch as the oxygen data in Table XIX represents the average oxygen concentration for an entire sample, it is reasonable to suppose, based on the hardness data, that the oxygen concentration at the sample surfaces was considerably higher than the average values reported.

The hardness data in Table XIX indicate that some stress relief occurred at the test temperature. No mechanical-property tests were performed with the exposed samples because of lack of material.

b. Screening Tests in High-oxygen Sodium

The Reactor Engineering Division loop operates at 650°C. A sodium flow of 15 cm/sec (0.5 ft/sec) is maintained past samples suspended in a stainless steel wire basket. Zirconium turnings in the same basket were used to control the oxygen level which, for different runs, ranged between 100 and 200 ppm.

This relatively high oxygen content imposes more severe conditions than are likely to be encountered in any real reactor system. (For example, it is planned to maintain EBR-II oxygen concentration at about 40 ppm with cold-trap operation at about 150°C.) However, tests under conditions of relatively high oxygen concentration are useful for at least two reasons.

First, during the expected lifetime of a core loading (i.e., 1-2 years) it does not appear unreasonable to expect at least several days of operation at oxygen levels higher than specified. Short-time tests in a high-oxygen environment will thus give an indication of the effects of accidental contamination.

Second, in conjunction with the planned studies in sodium of much lower oxygen concentration, the results of these tests may help lead to an understanding of the mechanism of corrosive attack in oxygen-containing sodium.

Another variable of potential importance is that of surface-to-volume ratio. With respect to refractory metals considered for use as fuel-cladding material, this ratio is twenty times as great in the test loop as it will be in EBR-II. The actual importance of this variable depends on the method of reactor operation and will be considered for the case of two extremes.

If the reactor is considered to be a closed system with a limited amount of available oxygen, the extent of oxidation (or other oxygen-sensitive corrosion reaction) will obviously decrease with increasing surface-to-volume ratio for any initial oxygen concentration. For such a case the environment of the EBR-II is more severe than that of the test loop. If, on the other hand, in-leakage and other factors produce a constant oxygen concentration during operation (i.e., an equilibrium exists between oxygen supply and oxygen removal by cold traps, getters, etc.), the surface-to-volume ratio is of no consequence. This is the condition which has existed in the test loop and the condition, it is believed, which will exist in a reactor.

The behaviors of a group of cold-rolled niobium-base alloys were tested in this loop. The results, summarized in Table XX, indicate that all samples had high rates of metal loss. In addition, the Nb-1 w/o Zr, Nb-5 w/o Zr, Nb-5 w/o Mo, and Nb-2.37 w/o Cr samples were severely split apart at the edges (see Figure 14).

Microhardness measurements taken across the transverse sections of the samples showed varying profiles, ranging from a constant hardness increase in the case of the Nb-1 w/o Zr and Nb-5 w/o Mo samples (about 30 DPH units) to very steep hardness gradients at the surface (in a 200-300 μ-thick layer) for the Nb-39 w/o V-1 w/o Ti samples. The Nb-2.37 w/o Cr sample showed a shallow hardness gradient from edge to center;

the edge was 50 DPH harder than the center. It is obvious that none of these materials are suitable for service under the conditions of the test.

Table XX

BEHAVIOR OF COLD-ROLLED NIOBIUM-BASE ALLOYS IN HIGH-OXYGEN SODIUM: 650°C AND 15-cm/sec FLOW RATE

Alloy (w/o)	Exposure Time (days)	Oxygen Conc of Sodium (ppm)	Rate of Weight Loss ($mg/cm^2/mo$)[a]	Equivalent Metal Loss Rate[b]	
				($cm/mo \times 10^3$)	(mils/mo)
Nb-39 V-1 Ti	7.0	200[c]	93.5	12.5	4.92
Nb-39 V-1 Ti	7.0	200[c]	58.8	7.85	3.08
Nb-1 Zr	7.0	200[c]	364		
Nb-5 Zr	7.0	200[c]	220		
Nb-1 Zr	13.7	140	136		
Nb-5 Zr	13.7	140	81.6		
Nb-5 Mo	13.7	140	62.9		
Nb-39 V-1 Ti	13.7	140	50.0	6.66	2.62
Nb-5 Mo	12.8	100-125[d]	26.7		
Nb-2.37 Cr	12.8	100-125[d]	128		
Nb-39 V-1 Ti	12.8	100-125[d]	41.4	5.52	2.18

(a) Cleaned of sodium with alcohol and water. Nonadherent oxide removed with soft brush.
(b) Calculated for those samples which maintained reasonable integrity. Any remaining oxide film assumed negligible.
(c) Estimated. Analytical facility not in operation.
(d) Estimated. Analytical value of 350 ppm known to be in error.

Figure 14. Niobium-base Alloys Exposed to Flowing High-oxygen Sodium at 650°C

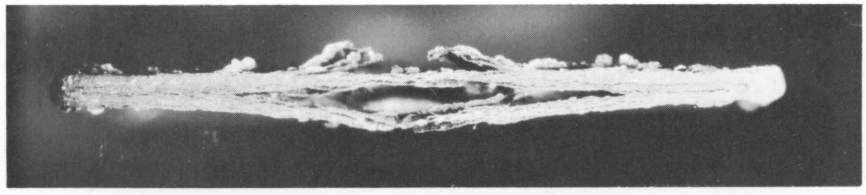

Micro 38098 Nb-1 w/o Zr - 140 ppm Oxygen - 13.7 Days 8.5X

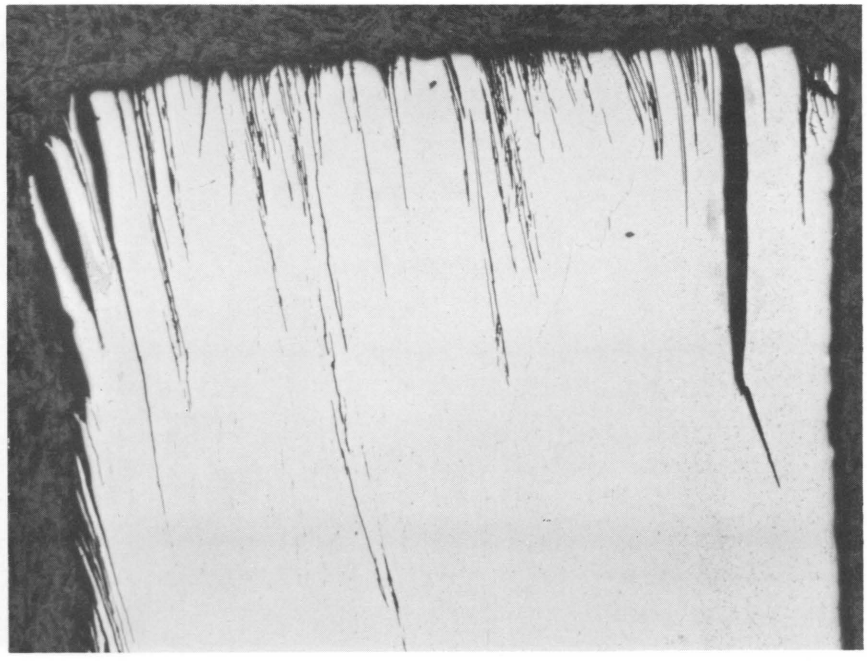

Micro 38100 Nb-5 w/o Mo - 100-125 ppm Oxygen - 12.8 Days 70X

The effect of metallurgical condition on a group of niobium- and vanadium-base alloys is summarized in Table XXI.

Table XXI

BEHAVIOR OF NIOBIUM- AND VANADIUM-BASE ALLOYS IN HIGH-OXYGEN SODIUM: 650°C AND 15-cm/sec FLOW RATE

Alloy (w/o)	Exposure Time (days)	Oxygen Conc of Sodium (ppm)	Rate of Weight Loss ($mg/cm^2/mo$)[a]	Equivalent Metal Loss Rate[b]	
				($cm/mo \times 10^3$)	(mils/mo)
Nb-5 Mo (SR)[c]	7.0	120	55.6		
Nb-5 Mo (Rx)[d]	7.0	120	43.4		
Nb-10 Ti-5 Zr (SR)	7.0	120	17.1		
Nb-10 Ti-5 Zr (Rx)	7.0	120	80.7		
Nb-18 Ti-4 V (SR)	7.0	120	50.6		
Nb-18 Ti-4 V (Rx)	7.0	120	66.0		
Nb-10 W-2.5 Zr (SR)	7.0	120	13.1		
Nb-10 W-2.5 Zr (Rx)	7.0	120	38.6		
Nb-3 Mo-9 Ti (SR)	7.0	120	72.8		
Nb-3 Mo-9 Ti (Rx)	7.0	120	63.7		
V-10 Ti (SR)	9.0	195	3.23	0.92	0.37
V-10 Ti (Rx)	9.0	195	2.76	0.76	0.29
V-20 Ti (SR)	9.0	195	3.33	0.72	0.29
V-20 Ti (Rx)	9.0	195	3.72	0.83	0.32
Nb (SR)	9.0	195	41.6	4.94	1.95
Nb (Rx)	9.0	195	52.8	6.55	2.58

[a] Cleaned of sodium with alcohol and water. Nonadherent oxide removed with soft brush.
[b] Calculated for those samples which maintained reasonable integrity. Any remaining oxide film assumed negligible. Includes allowance for oxygen dissolved in metal (see Table XXII).
[c] Stress relieved.
[d] Recrystallized.

All the niobium-base alloys showed varying degrees of intergranular attack. The most extreme example was that of the recrystallized Nb-10 w/o W-2.5 w/o Zr sample, illustrated in Figure 15.

Figure 15. Recrystallized Nb-10 w/o W-2.5 w/o Zr Exposed to Flowing Sodium (650°C and 7.0 Days) Containing 120 ppm Oxygen

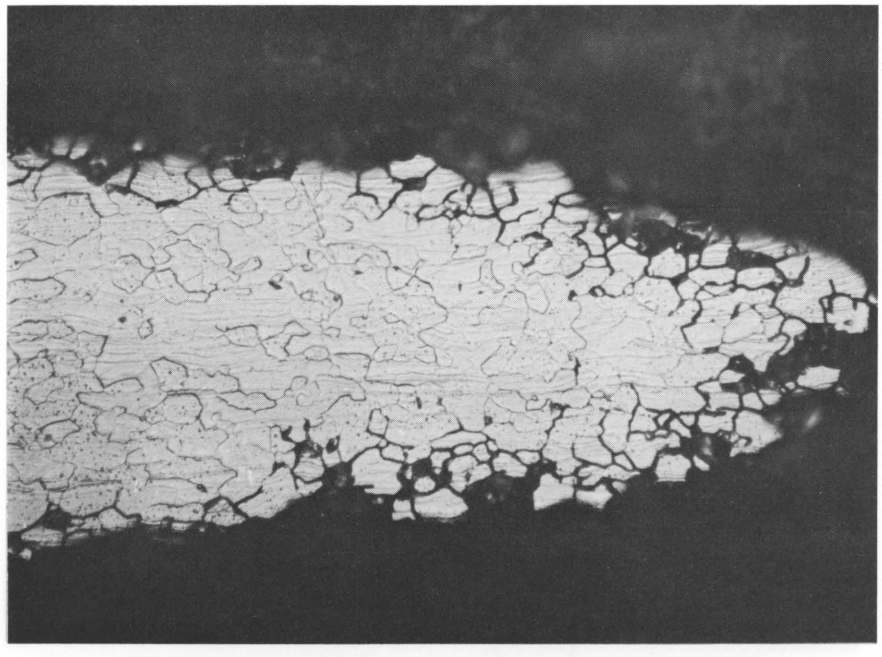

Micro 38097 Etchant - 40 v/o HNO_3, 20 v/o HF 200X

The greatly increased attack experienced by recrystallized samples of the Nb-10 w/o Ti-5 w/o Zr and Nb-10 w/o W-2.5 w/o Zr alloys is due to extensive grain-boundary corrosion and consequent physical loss of many grains. However, it should be noted that the effect of the recrystallization heat treatment is not uniformly severe for all the alloys tested. Microhardness measurements taken across the transverse sections of the samples showed varying profiles, but there were no distinct differences between the hardness profiles of the stress-relieved and recrystallized samples.

The data in Table XXI show that the vanadium-titanium alloys experienced a rate of weight loss less by about an order of magnitude than that apparently typical of niobium-base alloys exposed under similar conditions. The effect of the sodium environment on the room-temperature hardness of the recrystallized vanadium-titanium alloys is illustrated in Figures 16 and 17. The behavior of the stress-relieved samples is similar except that the base hardness values are slightly higher. Changes in physical and mechanical properties may be associated with oxygen and/or carbon pickup from the sodium environment. Preliminary data for the vanadium-titanium alloys and pure niobium (for comparison) are summarized in Table XXII.

Figure 16. Effect of Flowing Sodium on Room-temperature Hardness of Recrystallized V-10 w/o Ti

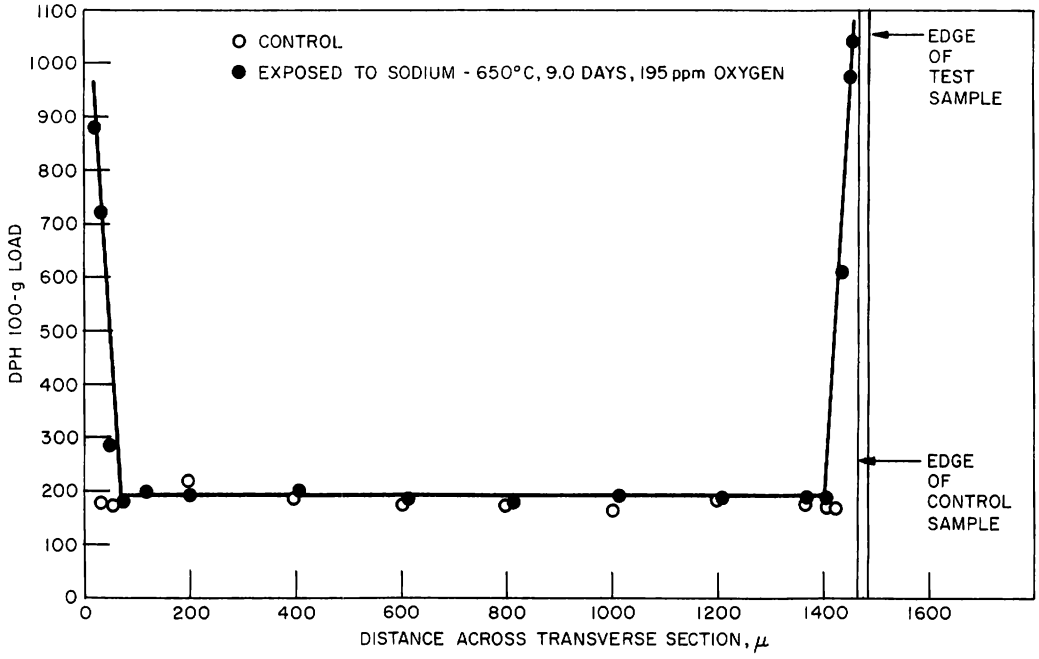

Figure 17. Effect of Flowing Sodium on Room-temperature Hardness of Recrystallized V-20 w/o Ti

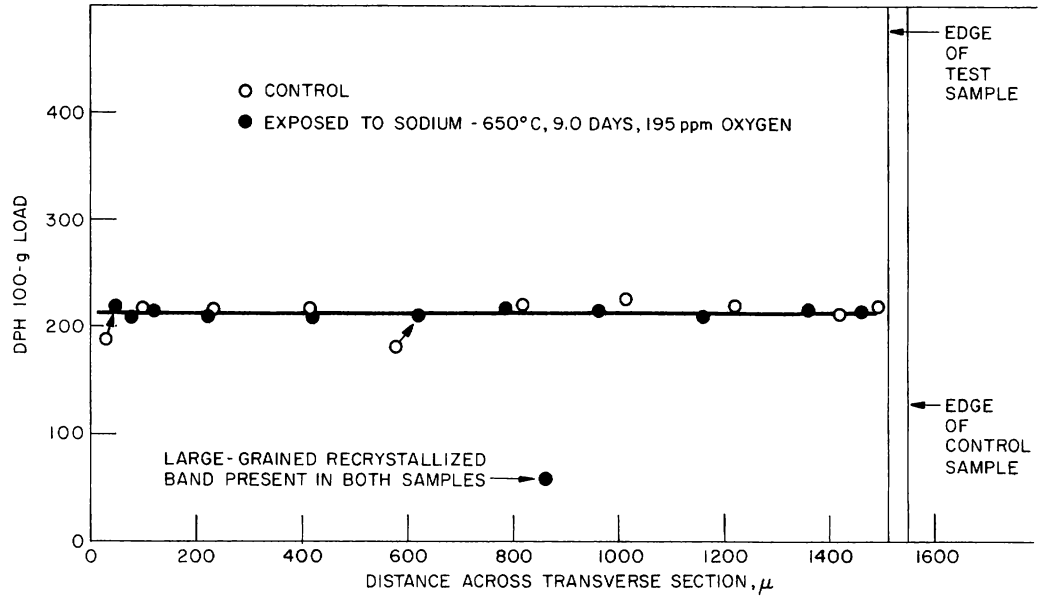

Table XXII

OXYGEN AND CARBON PICKUP OF VANADIUM-TITANIUM ALLOYS AND NIOBIUM EXPOSED TO FLOWING SODIUM (CONTAINING 195 ppm OXYGEN) AT 650°C FOR 9 DAYS

Alloy (w/o)	Initial Impurity Conc (ppm)(a)		Final Impurity Conc (ppm)(a)		
			O		C
	O	C	SR	Rx	Rx
V-10 Ti	800	486	2400	2080	
V-20 Ti	800	435	1465	1500	509
Nb	65	38	240	205	28

(a) Bulk sample concentration. Average of two analyses.

As shown in Figures 16 and 17, the V-10 w/o Ti, bu not the V-20 w/o Ti alloy, had a surface layer considerably harder than the bulk material. This may be associated with the higher oxygen conte it of the former alloy and implies the existence of a surface layer of con ider- ably higher oxygen concentration than the bulk value reported. The behavior of these alloys during longer exposures, particularly with regard to forma- tion and growth of surface layers apparently rich in oxygen, will be studied. The relatively low value for the oxygen pickup of the niobium sampl is unexpected.

The reasons for the apparent superiority of the vanadium-titanium alloys are not understood at present. Some speculation which indicates the direction of future work is in order. Thermodynamic considerations indicate that niobium and vanadium have comparable oxidation potentials in oxygen-containing sodium. Under similar conditions, titanium could be expected to show an even greater tendency to oxidize. However, titanium is known to be an oxidation-resistant material (at least in air), presumably because of the formation of a protective film. Rather simple considerations lead to the picture of protective films formed on solid solution alloys containing more than a minimum (unknown at the time) amount of titanium. Increasing the titanium content could lead to a decrease in the diffusion rate of oxygen with the metal.

In addition to the refractory alloys which have been discussed, a Nb-1 w/o Zr sample clad with a 0.127-mm-thick, plasma-sprayed, 304 stainless steel coating has been tested. The sample was exposed to flowing (15 cm/sec) sodium containing 100-125 ppm oxygen at 650°C for 12.8 days. The stainless steel coating proved to be an effective barrier to diffusion of oxygen into the refractory alloy, and there was no attack of the stainless steel. A cross section through the sample is shown in Figure 18. There is only a mechanical bond between the coating and base metal. Lack of a metallurgical bond casts doubt on the adequacy of such a structure under the cycling conditions typical of reactor operation.

Figure 18. 304 Stainless Steel-clad Nb-1 w/o Zr Exposed to Flowing Sodium (Containing 100-125 ppm Oxygen) for 12.8 Days at 650°C

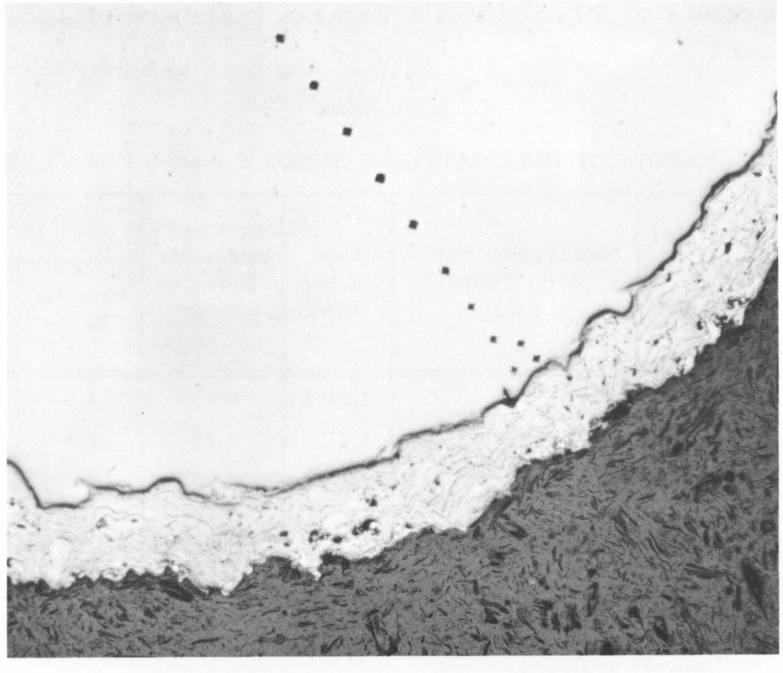

Micro 38099 50X

3. Irradiation of Fast Reactor Fuel Elements and Structures

a. Irradiation of EBR-II Core-I Fuel Elements (C. F. Reinke)

A series of capsules containing U-Fs and U-Fs-Zr alloy fuel rods jacketed with 0.023-cm-thick, Type 304 stainless steel and bonded with a 0.015-cm annulus of sodium were irradiated in the MTR. Dimensions and assembly of the rods were identical with reference EBR-II Core-I fuel elements.

The results of the postirradiation examination of the jacketed rods have been reported.[28] The postirradiation measurements of density of the jacketed rods indicated a slight increase in overall volume. This volume increase was equivalent to a uniform diameter increase of less than 0.0025 cm. Work continued during 1963 on the examination of these rods. Radiographs of the jacketed fuel cores indicated that the U-5 w/o Fs alloy cores decreased in length. The U-5 w/o Fs-2.5 w/o Zr alloys showed a scatter in the data, with some cores increasing in length, some decreasing, and some not changing at all.

Dejacketing of representative elements has been completed. A comparison of the diameter, length, and volume changes based on density measurements for both the jacketed elements and fuel cores is given in Table XXIII. In general, there is an increase in diameter and volume. The measured increases of diameter of the fuel pins are less than is required to completely fill the jacketed assembly. It appears that the jacketed EBR-II Core-I fuel elements can be expected to increase slightly in diameter before the fuel core has expanded against the jacket. Fuel can undergo a diameter increase of 30 mm and a volume increase of 16% before it will contact the jacket.

Table XXIII

PHYSICAL CHANGES OF IRRADIATED REFERENCE EBR-II FUEL ELEMENTS

Element No.	Composition[a] (w/o)		Max Irradiation[b] Fuel Temp (°C)	Max Burnup (a/o)	Jacketed Assembly Volume Change (%)	Fuel Core		
	Fs	Zr				Max Dia Change (%)	Length Change (%)	Volume Change (%)
ET-3-14	5	-	370	1.8[c]	0.43	4.9	-1.4	4.4
ET-1-8	5	-	210	1.2[d]	0.25	2.8	-1.3	2.9
ET-2-2	5	2.5	280	1.1[d]	0.26	4.2	-0.5	4.4
ET-2-6	5	2.5	260	1.0[d]	0.26	2.1	+0.4	3.8
ET-2A-14	5	2.5	180	0.5[d]	0.27	1.4	+0.8	2.6

[a] Balance is uranium.
[b] Based on the fission rate necessary to give the analyzed burnup.
[c] Based on technetium-99 analyses.
[d] Based on mass spectrometric analyses of the uranium isotopes.

[28] Annual Report for 1961, Metallurgy Division, ANL-6516, pp. 27-28.

b. Irradiations of Prototype Fuel Elements - Refractory Alloy-clad Uranium-Plutonium-Fissium Alloys (W. N. Beck)

The EBR-II plutonium alloy fuel element is a 3.6-mm (0.144-in.)-diameter injection cast pin of U-Pu-Fs alloy, sodium bonded to cladding sufficiently strong to restrain fuel swelling. The desired operating surface temperature of the cladding is 580°C, corresponding to a maximum fuel temperature of ≈680°C. The minimum desired fuel burnup is 2 a/o.

Earlier experiments have shown that the fuel alloy swells catastrophically at temperatures above 350°C. The cladding, therefore, is highly stressed when the fuel has achieved the desired burnup at design conditions. Irradiations of prototype fuel elements are being made in instrumented capsules in the CP-5 reactor to evaluate various cladding materials and fuel element design modifications.

During 1963 a total of 36 irradiated prototype EBR-II fuel elements were examined in the hot cells. A significant improvement was noted in the performance of these specimens compared with observations in previous experiments. A sizable fraction of the specimens survived burnups exceeding 2.0 a/o at EBR-II design temperatures. The cladding thickness on all specimens was 0.23 mm (0.009 in.).

Capsule CP-21 contained specimens clad in Nb-1 w/o Zr and Ta-0.1 w/o W alloy tubing. The void space within the cladding was 25% of the fuel volume. A lower temperature than reference (maximum 600°C) was used during irradiation. One specimen (CP-21-6) was purposely assembled without bond sodium. All six specimens had failed by the time 1.9 a/o burnup had been attained. The unbonded specimen showed no significant differences compared to the bonded specimen.

Capsule CP-25 contained specimens clad with Nb-1 w/o Zr, Ta-0.1 w/o W, and Nb-33 w/o Ta-1 w/o Zr alloy. The principal difference between these specimens and previous ones is that the void space was increased to 51%. The maximum fuel temperature was 680°C. During the 5-month irradiation a burnup of 2.4 a/o was achieved before erratic temperature readings indicated failed specimens. Two of the six specimens were found to be intact when the capsule was opened. Failures of the other four specimens were considerably less drastic than had been observed in previous specimens.

Capsule CP-27 was identical with CP-25, except that the cladding was perforated to prevent buildup of gas pressure in the void space above the fuel. The specimens operated to a burnup of 2.1 a/o at a maximum temperature of 660°C with no apparent difficulty. At this time the capsule was damaged during handling at the reactor and irradiation was discontinued. It was found that, although one specimen had developed a split in the cladding, the other five were still intact.

Capsule CP-28 was distinguished from its predecessors by the inclusion of four specimens clad with a duplex cladding - Hastelloy-X coated on the ID with 0.04 mm (0.0015 in.) of tungsten. A photograph of this type of tubing can be seen in Figure 19. The other two specimens were clad with Nb-1 w/o Zr alloy for comparison. Void volume was either 51 or 57%. The maximum fuel temperature during irradiation was 670°C. After 4 months of irradiation to a burnup of 2.6 a/o, the capsule was opened for examination. Both Nb-1 w/o Zr alloy-clad specimens had failed. One of the Hastelloy-X-clad specimens showed severe failure, evidently accompanied by eutectic formation. Another Hastelloy-X-clad specimen showed a pinhole failure, with evidence of eutectic formation. Failure of the two Hastelloy-X specimens evidently occurred as a result of defects in the tungsten coating rather than as a result of overstressed cladding. The other two Hastelloy-X-clad specimens were intact. Photographs of four of the irradiated specimens in this capsule can be seen in Figure 20.

Figure 19. Hastelloy-X Tubing with Tungsten-coated Inner Diameter

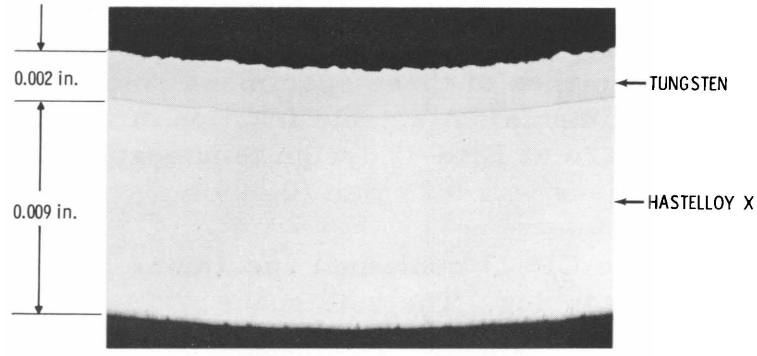

106-7001

Capsule CP-29 contained three specimens clad in Nb-4 w/o V alloy and three specimens having Hastelloy-X coated on the ID with 0.04 mm (0.0015 in.) of tungsten. The void volume within the cladding was equivalent to 57% of the fuel volume. The specimens were irradiated at a maximum fuel temperature of 560°C to 2.4 a/o fuel burnup. All specimens were intact; there were no significant dimensional changes. The fuel material had elongated in the clad an average of 10%. There was no evidence that eutectic formation had locally penetrated the Hastelloy-X claddings. A photograph of these specimens is shown in Figure 21.

Capsule CP-30 contained six specimens of U-Pu-Fs and U-Pu alloys clad in Nb-1 w/o Zr alloy. The void volume in all the specimens was 57% of the fuel volume. Four different fuel compositions were irradiated: (a) U-10 w/o Pu, (b) U-15 w/o Pu, (c) U-10 w/o Pu-10 w/o Fs, and (d) U-15 w/o Pu-10 w/o Fs. The specimens were irradiated at a maximum clad temperature of 560°C, with a maximum fuel temperature of 640°C. The maximum fuel burnup was 2.5 a/o. The postirradiation

Figure 20. Typical Refractory Alloy-clad U-20 Pu-10 Fs Alloy Specimens after 2.6 a/o Burnup, Max Irradiation Temp of 670°C, and Max Clad Temp of 590°C.

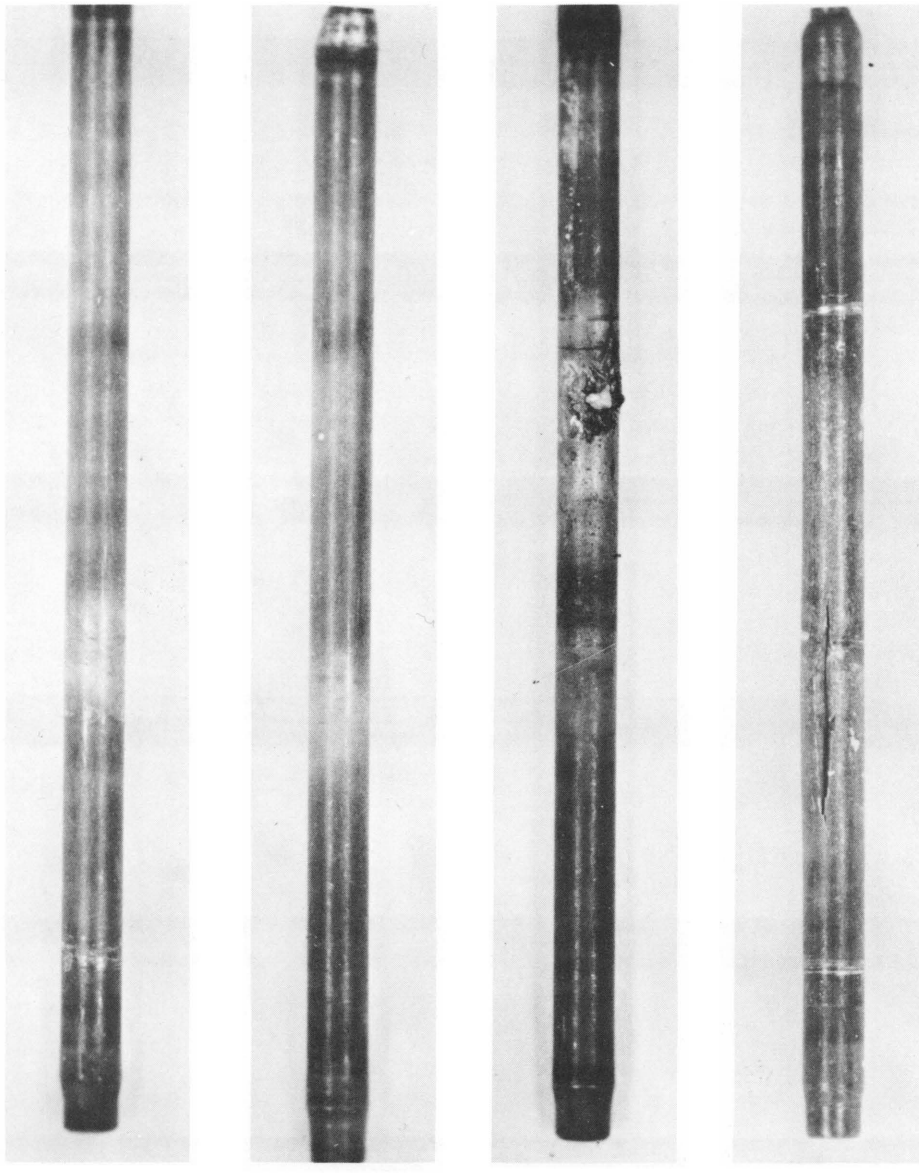

106-7309

W-coated Hastelloy-X Cladding

Nb-1 Zr Cladding

Figure 21. U-20 w/o Pu-10 w/o Fs Alloy Specimens after 2.4 a/o Burnup at a Fuel Temperature of 560°C and a Clad Temperature of 485°C. The Clad Thickness is 0.23 mm (0.009 in.).

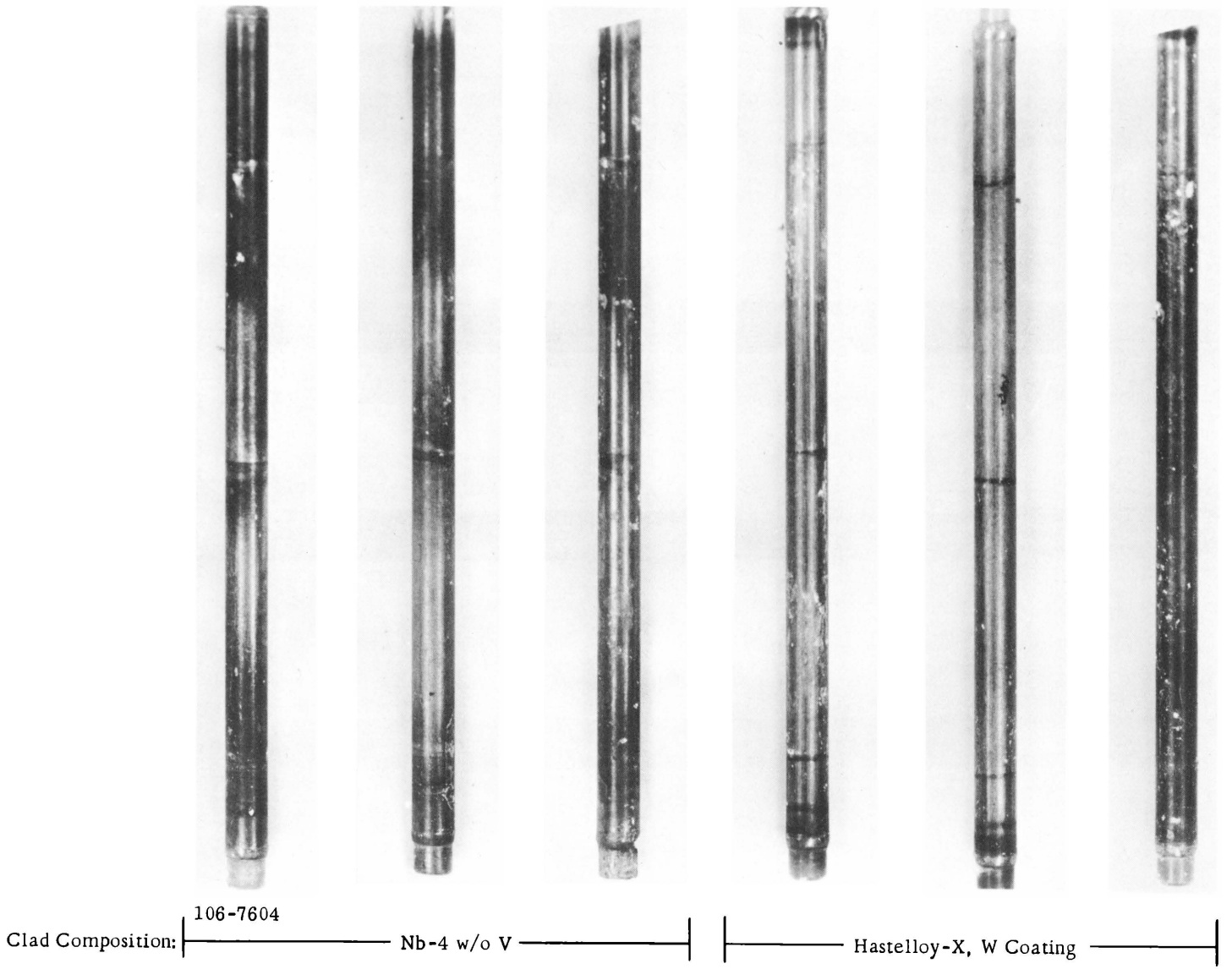

examination showed that the two U-15 w/o Pu-10 w/o Fs specimens had developed localized cladding failures. The other four specimens were intact. Irradiation data and photographs of these irradiated specimens are shown in Figure 22.

The results of these irradiations indicate that fuel burnups exceeding 2 a/o can be successfully achieved in plutonium alloy fuels at temperatures above 600°C. Experiments currently in progress indicate that with somewhat thicker cladding (0.38 mm, or 0.015 in.) fuel burnups beyond 3 a/o can be obtained without clad failure or distortion. Future irradiations will emphasize the use of the promising V-20 w/o Ti (TV-20) alloy. The irradiation performance needs to be established for this alloy, which gives indications of corrosion resistance to sodium, compatibility with the fuel, and fabricability.

c. Irradiations of Full-length EBR-II Fuel Elements - Refractory Alloy-clad Uranium-Plutonium-Fissium Alloy (W. F. Murphy and C. C. Crothers)

Irradiation of full-length [45-cm (18-in.)] EBR-II fuel elements of refractory alloy-clad U-20 w/o Pu-10 w/o Fs alloys is being made in the MTR. The temperature in the irradiation capsules is controlled by varying the composition of a helium-nitrogen mixture in an annulus surrounding the fuel specimens.

The first capsule, ANL-46-4, contained a fuel rod sodium bonded to 0.23-mm (0.009-in.)-thick Nb-1 w/o Zr alloy cladding. At the reactor site the capsule was incorrectly connected to its control circuit. As a result, on reactor startup fuel temperatures exceeded the melting point of the fuel alloy (820°C). The fuel element was subsequently irradiated to 1.5 a/o burnup with a cladding temperature of 700°C. It was then removed from the capsule for examination. The cladding was found to have split over about two-thirds of the length of the fuel element, with evidence of fuel melting. It is believed that most of the damage was caused during the initial temperature excursion.

Capsule ANL-55-5 is a duplicate of ANL-46-4, both with respect to fuel composition and cladding. To date it has been irradiated to about 0.75 a/o burnup at cladding temperatures near 500°C without evidence of failure.

Capsule ANL-55-6 is the same type of capsule, but it contains three U-20 w/o Pu-10 w/o Fs fuel pins clad with 0.23 mm (0.009 in.) of Nb-1 w/o Zr alloy. These fuel elements have accumulated 1.7 a/o burnup at cladding temperatures near 500°C without evidence of failure.

Figure 22. Effect of Irradiation on Plutonium Fuel Alloys Clad with 0.23-mm (0.009-in.) Nb-1 w/o Zr Alloy

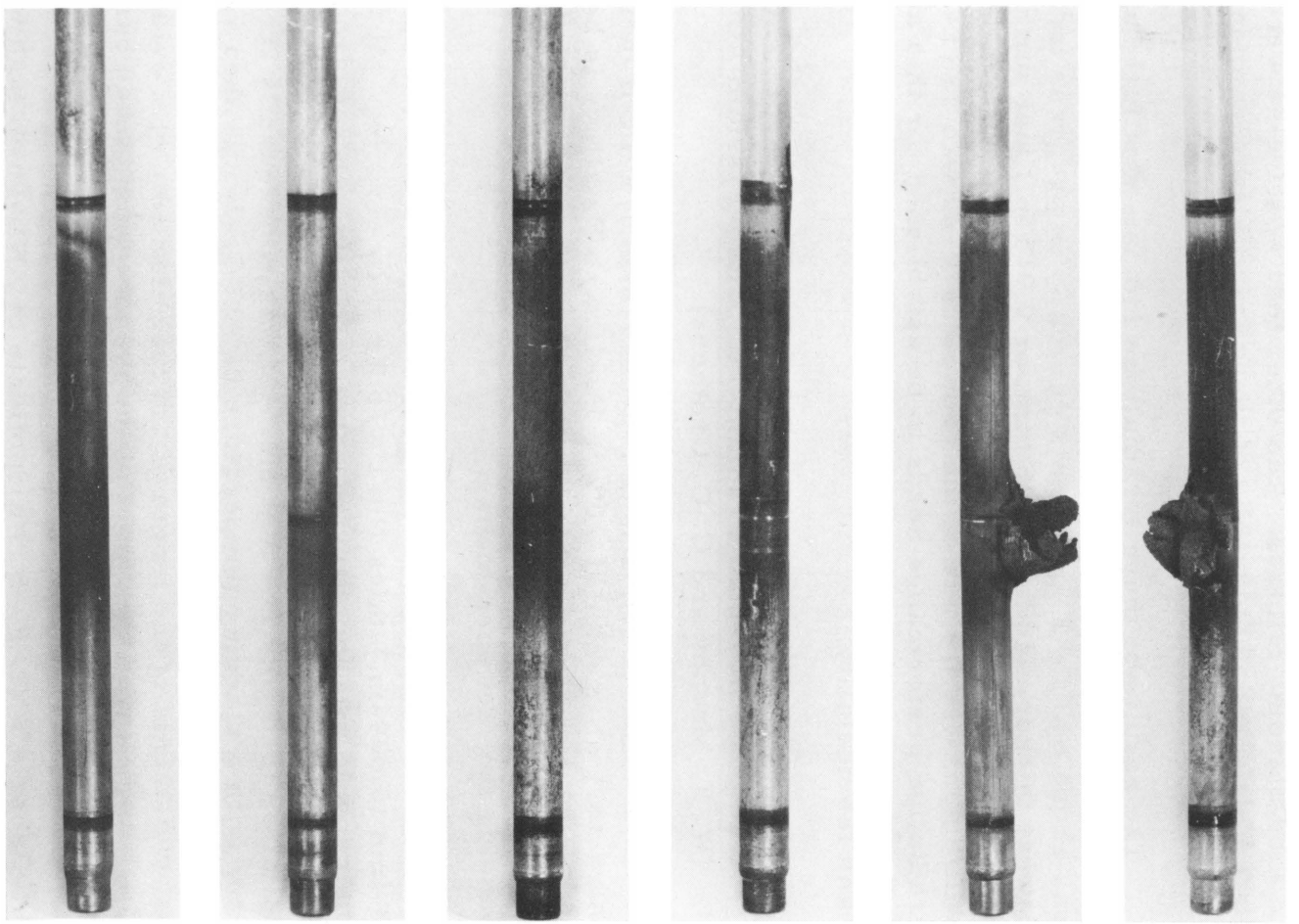

106-7603

Fuel Composition, w/o	U-10 Pu	U-10 Pu-10 Fs	U-10 Pu-10 Fs	U-15 Pu	U-15 Pu-10 Fs	U-15 Pu-10 Fs
Burnup, a/o	1.7	1.5	1.5	2.6	2.5	2.5
Max Fuel Temp, °C	600	600	600	600	640	600
Max Clad Temp, °C	525	525	525	525	560	525

Capsule ANL-55-7 is presently being assembled to contain three fuel pins of U-15 w/o Pu-10 w/o Fz alloy. Cladding materials on each of the pins are, respectively: 0.38 mm (0.015 in.) of Nb-1 w/o Zr, 0.38 mm (0.015 in.) of vanadium, and 0.23 mm (0.009 in.) of Hastelloy-X internally coated with 0.0015 in. of tungsten.

d. Preparation and Irradiation of Thin-disk, Central Void Specimens for Irradiation Swelling Studies

Preparation of Thin-disk Specimens (L. R. Kelman and H. V. Rhude)

The irradiation behavior of metal fuels that have been provided with radial and axial paths to encourage the venting of fission gases is under study. The specimens designed for this study consist of very thin disks of 20% enriched uranium stacked to simulate rods, thus providing for radial venting between the disks. The minimum diffusion distance was limited only by the limits in fabrication capability for thin uranium foil. The influence of foil thickness, and therefore of diffusion distance, was included in the study by using both 0.025- and 0.15-mm (0.001- and 0.006-in.)-thick disks. Another purpose in using this design was to provide relatively good radial thermal conductivity through the simulated metal fuel rod. A central void provided for axial venting of fission gases.

Disks of 3.86-mm (0.152-in.) diameter with a central 1.42-mm (0.056-in.)-diameter hole were stamped from 0.025- and 0.15-mm-thick, 20% enriched, rolled uranium foil. These were stacked as shown in Figure 23 and then compressed to make a simulated fuel rod 25.40 mm (1.000 in.) long.

Two types of specimens were prepared. One type was clad in Nb-1 w/o Zr with three different goemetries for different degrees of restraint. The other type, an essentially unrestrained assembly, was made by using an open cage, as shown in Figure 24. A second set was clad in 3.96-mm (0.156-in.)-ID, 0.23-mm (0.009-in.)-wall tubing with sodium as a thermal bond. The clad for the third set was similar to the second except for a 1.02-mm (0.040-in.)-diameter vent hole through the clad above the fuel.

Solid rod specimens with axial holes were also prepared for comparison purposes. The specimens were machined from a rolled plate with the long axis transverse to the rolling direction.

The assembled disks and the rods were β heat treated and quenched to randomize the highly oriented rolled structure, thus minimizing directional growth under irradiation.

Thin disks have been prepared from U-20 w/o Pu-10 w/o Fz foils for a follow-up to the above study. The low swelling temperature (approximately 370°C)[29] of this alloy will permit irradiation testing at temperatures lower than that for the unalloyed uranium. The rolling of 0.025- and 0.15-mm foil and subsequent stamping of disks required considerable effort because of the brittleness of this alloy.

Figure 23. Stacked Thin Disks Prior to Encapsulation

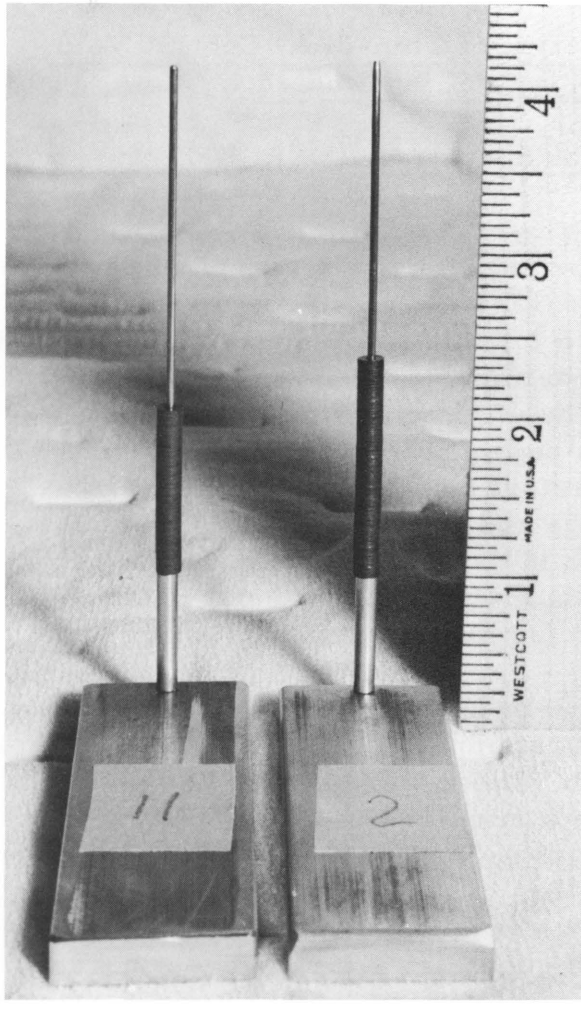

106-7109

Irradiation of Thin-disk Specimens (W. N. Beck, R. Carlander)

The foil specimens described above have been irradiated and are being examined in the hot cells. The objective of the experiment was to evaluate the swelling behavior of metallic fuel with a selective number of paths for fission gas release. Venting within the fuel was obtained both radially and axially by stacking circular foils as previously discussed. For comparison purposes, solid specimens of fuel of identical internal and outer diameters were also irradiated. Six specimens were irradiated in a single high-temperature capsule containing sodium.

One specimen of each foil thickness and one of the solid specimens was irradiated in cladding with a vent hole to permit released fission gas to escape from the cladding. The other group of three specimens was irradiated in cladding which had been partially cut away to form an open cage for the fuel. Swelling could thus occur with a minimum of restraint. A third group of three specimens, not yet under irradiation, is in sealed cladding. A photograph of the specimens before irradiation is shown in Figure 24.

---

[29] Horak, J. A., Kittel, J. H., and Dunworth, R. J., The Effects of Irradiation on Uranium-Plutonium-Fissium Fuel Alloys, ANL-6429 (July 1962) p. 17.

Figure 24. Thin-disk, Central Void Fuel Pin Assemblies as Submitted for Irradiation Testing. Three at left are completely clad. Three at right are caged.

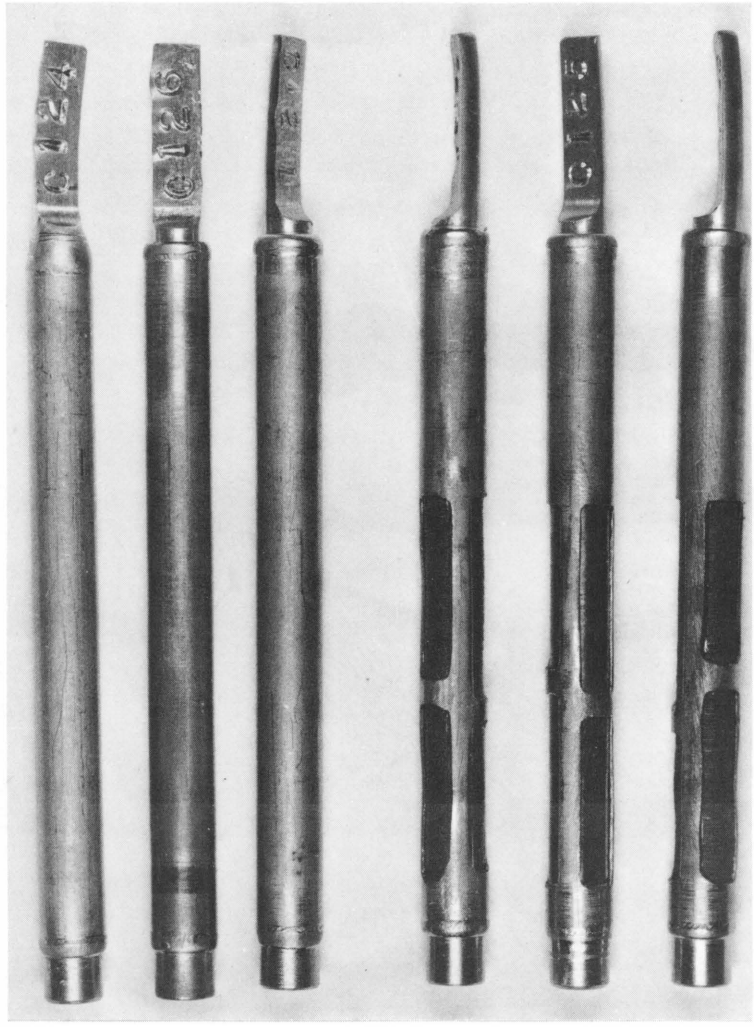

EI-1084 2X

During irradiation the thermocouples adjacent to the caged specimens were observed to increase slowly in temperature, as would be expected if the fuel were swelling. The capsule was removed from the reactor after 0.7 a/o burnup was achieved. The maximum fuel temperature recorded was 590°C. A photograph of the clad irradiated specimens is shown in Figure 25; a photograph of the caged specimens is presented in Figure 26.

Neutron radiography of the capsule confirmed that the caged specimens had swelled, particularly the solid specimen and the 150-μ foil specimen. The axial holes in all caged specimens were discernible, with the clearest indication in the 25-μ foil specimen. The axial holes in the specimens with continuous cladding appeared to be completely filled.

Figure 25. Photographs (1-1/2X) and Data Pertaining to Specimens with Vented Cladding

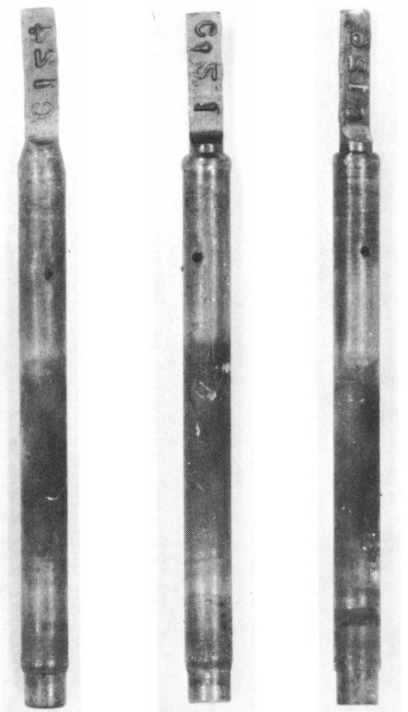

	EI-1376	EI-1378	EI-1377
Specimen No.	31-1	31-3	31-2
Foil Thickness (mm)	0.025	0.150	Solid
No. of Foils in Stack	970	167	-
Max Fuel Temp (^{o}C)	590	590	590
Avg Max Fuel Temp (^{o}C)	570	570	570
Max Surface Temp (^{o}C)	560	560	560

Figure 26. Photographs (1-1/2X) and Data Pertaining to Caged Specimens

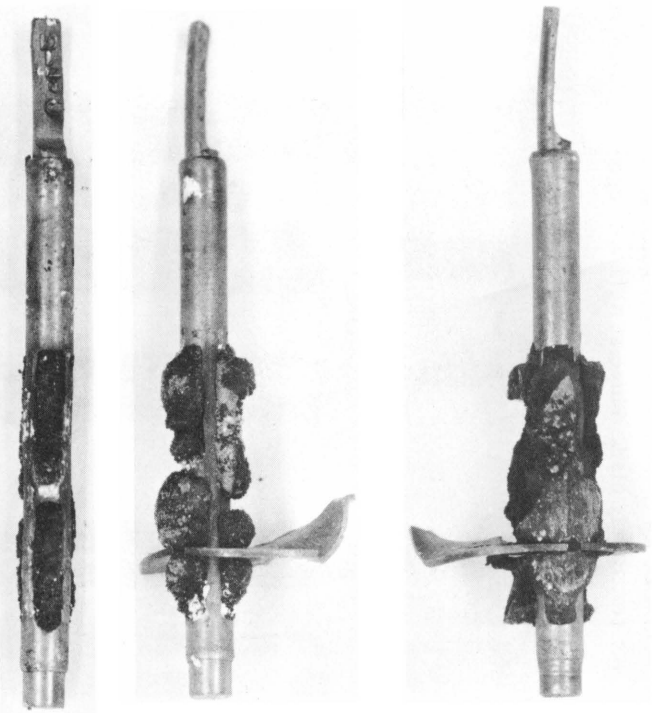

	EI-1379	EI-1382*	EI-1381*
Specimen No.	31-4	31-6	31-5
Foil Thickness (mm)	0.025	0.150	Solid
No. of Foils in Stack	940	171	-
Max Fuel Temp (^{o}C)	590	590	590
Avg Max Fuel Temp (^{o}C)	570	570	570
Max Surface Temp (^{o}C)	560	560	560

*Part of capsule spacer plate at lower portion of specimen could not be removed without damaging fuel.

Metallographic examinations were performed on transverse and longitudinal sections from both the clad and the caged foils. It was possible to determine the original interfaces of the foils in only a limited number of areas. In these regions the foils were severely distorted and had grown together to form a single mass of material. The only areas in which the individual foils could be distinguished as separate from the main body of the fuel were at areas of least restraint, the axial hole and adjacent to the cladding. Pores, presumably resulting from bubbles of fission gas, were evident. The thickness of the foils and the relative extent of swelling had no apparent effect upon the size and distribution of pores. It appeared, however, that the size of the pores was greater in the caged specimens than in the restrained specimens. In addition, the single sample in which the axial hole had been completely closed due to swelling was the solid restrained specimen. The microstructural characteristics of a porous mass of material which was noted at the outer surfaces of the 150-μ (0.006-in.) and solid caged samples could not be determined, although it was generally nonmetallic in nature.

e. Irradiation of PuC and UC-20 w/o PuC (L. A. Neimark and R. Carlander)

Two vibratory-compacted specimens of PuC and four vibratory-compacted specimens of a physical mixture of UC-20 w/o PuC powders in both Type 304 stainless steel and Nb-1 w/o Zr alloy claddings have been examined after irradiation in a thermocouple-instrumented capsule in the CP-5 reactor. The specimens had EBR-II geometry, 4.42-mm (0.174-in.) OD and 0.23-mm (0.009-in.) cladding, with a 5-cm (2-in.)-long fuel section compacted to about 80% of theoretical density. The size ratios of the powders in all specimens were 60 w/o 20/40 mesh, 20 w/o 120/200 mesh, and 20 w/o -325 mesh. The 120/200 mesh fraction in the mixed carbide specimens was PuC. Normal uranium was used in these specimens. Fabrication of these specimens is discussed later in this report (Sect. A-8, p. 102).

Neutron radiographs of the specimens while in the irradiation capsule indicated that: (1) no cladding failures had occurred and the fuel was completely contained, (2) the fuel did not appear to change in length, (3) the mixed carbides remained inhomogeneous during irradiation, and (4) a thin irregular central void may exist in at least two of the UC-PuC specimens. The capsule was then opened for direct examination of the specimens.

A summary of the irradiation conditions and results of the postirradiation examination for these six specimens and a single specimen to be discussed later appear in Table XXIV. Specimen clad temperatures, heat generation, and burnup were determined from thermocouple temperature data. The data are subject to correction by subsequent isotopic burnup analyses.

Table XXIV

SUMMARY OF IRRADIATION RESULTS ON VIBRATORY-COMPACTED PuC AND UC-20 w/o PuC POWDERS

Specimen No.	Nominal Composition	C (w/o)	Cladding	Burnup		Clad Surface Temp (°C)		Mean Surface Heat Flux (W/cm²)	Maximum Dia Increase (mm)	Volume Increase of Clad Specimen (%)	Fis Release (% Theoret)
				MWd/MT	Fiss/cc x 10^{20}	Mean	Maximum				
C-69	UC-20 w/o PuC	5.14 (6.42)[a]	Nb-1 Zr	18,000	5.0	370	405	100	0.023	0.31	3.5
C-74	UC-20 w/o PuC	4.54 (3.40)	Nb-1 Zr	20,000	5.4	400	455	220	0.015	0.49	20.8
C-44	PuC	3.40	Nb-1 Zr	26,000	7.1	515	625	290	0.023	0.28	34.1
F-21	UC-20 w/o PuC	4.53 (3.40)	304 SS	20,000	5.4	395	430	220	0.020	0.22	20.9
F-18	UC-20 w/o PuC	5.14 (6.42)	304 SS	23,000	6.2	455	505	250	0.015	0.63	4.9
F-7	PuC	4.24	304 SS	23,000	6.2	450	495	250	0.046	1.10	29.4
F-6	PuC	6.22	304 SS	48,000	13.0	550	625	280	0.036	-	-

[a]Percent carbon on PuC fraction.

From the location of black, suspected-oxide coating on the Nb-1 w/o Zr alloy claddings, it appears that the top halves of the specimens operated at higher surface temperatures than the lower halves. This condition probably resulted from temperature stratification in the NaK between the horizontal spacers that centered the specimens and held the thermocouples. Since the thermocouples extended slightly into the lower, cooler region, the maximum temperatures given in Table XXIV are probably conservative. The stainless steel-clad specimens were bright compared with the black coatings on the Nb-1 w/o Zr alloy. Two typical irradiation specimens are shown in Figures 27 and 28.

Measurements showed that changes in diameter were no greater than 0.05 mm (0.002 in.), or 1%. Volume changes measured by immersion were of the order of 0.5% for the UC-PuC pins and up to 1.1% for the PuC pins. The magnitude of these changes is too small, however, to make meaningful comparisons between the PuC and UC-PuC specimens, or between the stainless steel and Nb-1 w/o Zr alloy claddings.

The pins were punctured for fission gas release, and the results are also given in Table XXIV. The PuC pins released the greatest amount of gas, 29.4 and 34.1% of theoretical. The UC-20 w/o PuC pins in which the PuC contained 3.4 w/o C released 20.8 and 20.9%, and the UC-20 w/o PuC with 6.42 w/o C in the PuC released 3.5 and 4.9%. The effects of irradiation temperature and burnup on the gas release were overshadowed by the effect of carbon content in the PuC.

Preliminary metallographic examination of the pins showed that the PuC powders had sintered, or melted, almost out to the cladding. The UC-PuC pins contained the original particles of PuC in the UC matrix with only very slight sintering to adjacent UC particles. No central voids were found in the specimens examined to date. A 0.03-mm-thick layer of an unidentified phase was found on the fuel side of the PuC-(Nb-1 w/o Zr)

interface in specimen C-44. The layer was not continuous and appeared only in a few areas. The metallographic examination of these specimens is continuing.

Figure 27

Specimen C-44, PuC (3.4 w/o C) in Nb-1 w/o Zr Cladding. Burnup was 7.1 x 10^{20} fiss/cc (26,000 MWd/MT) at a maximum cladding temperature of 625°C.

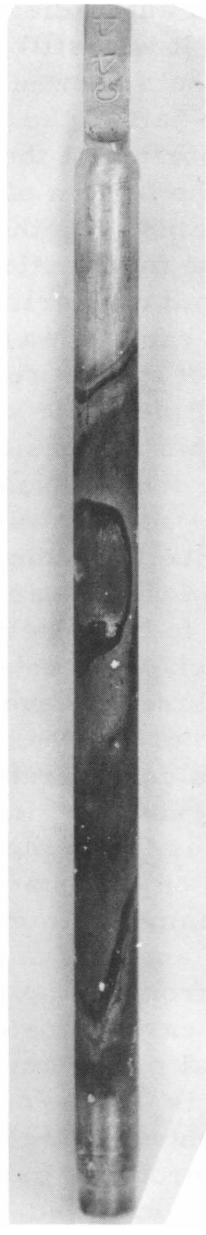

EI-1616 2X

Figure 28

Specimen F-18, UC-20 w/o PuC (6.42 w/o C) in Type 304 Stainless Steel Cladding. Burnup was 6.2 x 10^{20} fiss/cc (23,000 MWd/MT) at a maximum cladding surface temperature of 505°C.

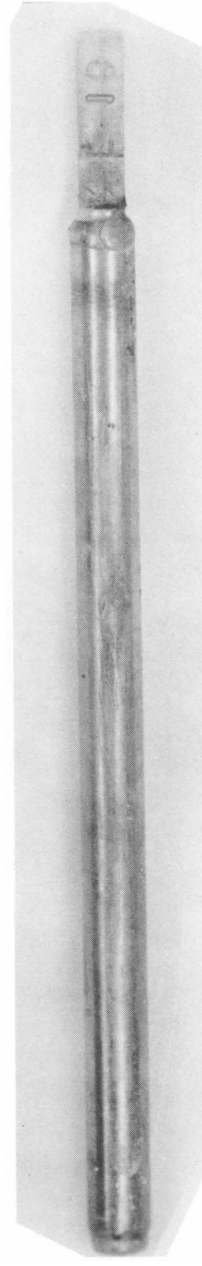

EI-1614 2X

The postirradiation examination of a single vibratory-compacted PuC specimen, F-6, taken to a burnup of 1.3 x 10^{21} fiss/cc (48,000 MWd/MT) has been partially completed. This specimen also had the EBR-II fuel element cross section geometry and was clad with Type 304 stainless steel. The fuel contained 6.22 w/o C. The maximum indicated cladding surface temperature was 625°C; the mean surface temperature for the irradiation period was 550°C. The specimen failed sometime during irradiation, but the occurrence of failure was not identifiable from the thermocouple data.

Figure 29. Specimen F-6, PuC (6.22 w/o C) in Type 304 Stainless Steel Cladding. Burnup was 13.0 x 10^{20} fiss/cc (48,000 MWd/MT) at a maximum cladding surface temperature of 625°C.

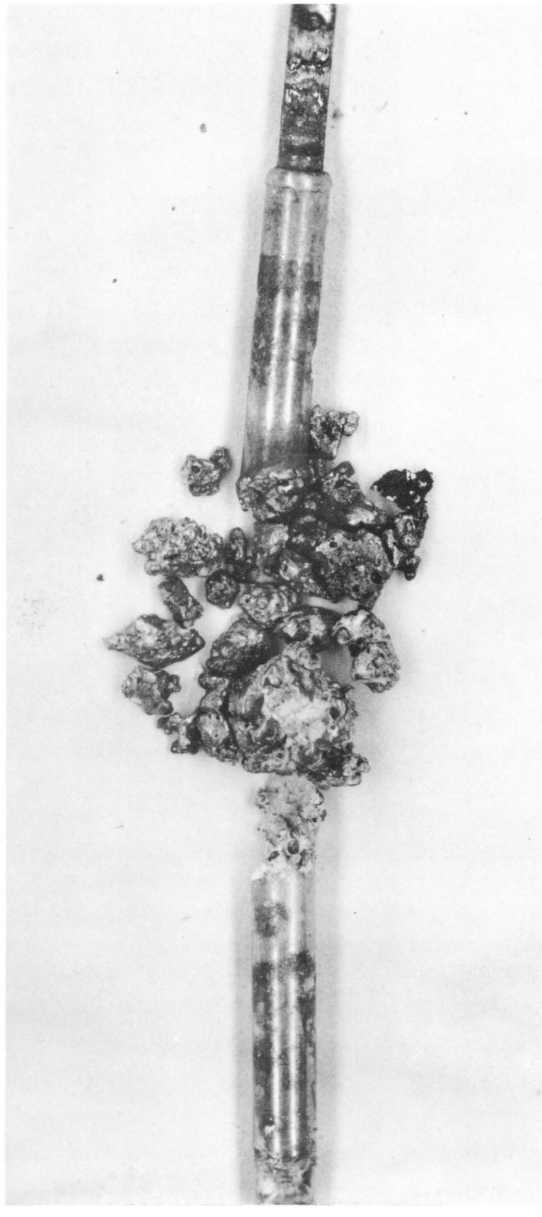

EI-1327 2X

An autoradiograph of the failed pin while it was still inside the irradiation capsule showed the failure to be in the top half of the fuel section. Only a small portion of the fuel filtered down to the bottom of the capsule. The rest remained together in the upper part of the fuel section, although distorted from cylindrical geometry. When the capsule was opened and the remains of the pin removed, large and small pieces of sintered or fused PuC containing considerable gas bubbles were found. No cladding for the upper fuel section was evident. The edge of intact cladding adjacent to the top of the failure was rounded and appeared to have melted. The edge of intact cladding adjacent to the bottom of the failure, however, was ragged, indicative of a stress rupture. The fact that a considerable internal pressure did exist is evidenced by the large gas bubbles in the pieces of fuel. Measurements on the intact cladding areas showed diameter increases of 0.02 mm. Chemical analysis of the ragged edge of cladding from the bottom intact section showed a carbon content of 0.32 w/o; the normal maximum in Type 304 stainless is 0.08 w/o. The cladding carbon content in the hotter failed region was probably much higher before the failure occurred. The reconstructed specimen is shown in Figure 29. A metallographic examination of the specimen is to begin in the near future.

An instrumented capsule containing six vibratory-compacted PuC and UC-20 w/o PuC specimens of miniature EBR-II size is now under irradiation in the MTR with cladding surface temperatures averaging between 500°C and 600°C. Cladding materials are 304 stainless steel and Nb-1 w/o Zr alloy. The burnup achieved to date is about 1.8×10^{20} fiss/cc (6700 MWd/MT), and satisfactory performance is indicated. Target burnup for specimens in this capsule is 2.7×10^{21} fiss/cc (100,000 MWd/MT).

f. Effect of Irradiation on Cladding Materials (W. F. Murphy)

Currently, this program is concerned with the effects of neutron irradiation on the properties of materials proposed for use as cladding for EBR-II fuel elements. Since fuel rod irradiations have indicated that internal pressure is a major factor in cladding failures, a burst test seemed to afford the best approximation to the conditions of use. Tests at room temperature with oil as a pressurizing medium were initially planned. A system with a pressure limit of 12,000 psi has been set up. Equipment with a greater pressure capacity is being procured.

One capsule with tubular burst test specimens was irradiated for 417 MWd in CP-5. The unperturbed epicadmium flux in the location of irradiation was 4.2×10^{13} nv. Irradiation temperature was in the range from 310 to 500°C, with a brief excursion to 750°C. An unirradiated control capsule was given approximately the same temperature history over an equivalent period of time.

These two capsules contained burst test specimens of Inconel X, vanadium, Type 304 stainless steel, niobium, niobium-1 w/o zirconium, and tantalum-0.1 w/o tungsten alloy. Small pellets for checking hardness were also included. All specimens were submerged in sodium. The irradiated capsule has not yet been opened. The control capsule was opened and some discoloration of the specimens was evident. One control specimen of tantalum-0.1 w/o tungsten was accidentally dropped. The specimen broke adjacent to the weld for the end plug, with the fracture surface consisting of large grains.

g. Irradiation Surveillance Program for EBR-II Structural Materials (W. F. Murphy)

The Metallurgy Division and the Reactor Engineering Division are cooperating in a surveillance program of radiation damage and the effect of high-temperature sodium on structural materials used within the primary tank of EBR-II.

Metallurgy Division personnel will be responsible for pre-irradiation measurements, and measurements or tests on controls and irradiated specimens. The type of measurement or test to be applied to a

particular material is determined by the use of the material. Tensile, hardness, impact, and bend test specimens have been specified where needed. Weight and density changes will be measured. Metallography will be included. Compression tests on some helical and Belleville springs are also included.

Some specimens will be encapsulated in sealed stainless steel tubes without sodium; others will be in capsules with holes in the walls to admit sodium. Nineteen capsules will be irradiated in a subassembly. Irradiation of ten subassemblies is planned.

Procurement of materials for the specimens has been started and capsule and subassembly parts are being collected.

h. Development of Experimental Irradiation Facilities in EBR-II (W. F. Murphy and J. H. Kittel)

With the assistance of the Reactor Engineering Division, a subassembly was designed in which 19 encapsulated specimens would be simultaneously irradiated in EBR-II. The facility is usable for irradiating experimental fuel rods (or nonfissile specimens) up to 50 cm (20 in.) long. Recently, the design has been altered to accommodate specimens up to approximately 95 cm (38 in.) long. An extensive series of experimental fuel rods are in preparation for irradiation in the special subassemblies. These experimental fuel elements include uranium-plutonium-fissium alloys in various cladding materials, thorium-base alloy fuels, and ceramic fuel rods of UC-PuC and US. A shielded cask has been designed to accommodate shipment of the special subassemblies from Idaho to Lemont.

4. Development of Remote Refabrication Methods and Equipment for Fast Reactor Fuel Elements

a. Development of Methods and Equipment for Remote-controlled Refabrication of Irradiated Reactor Fuel

(N. J. Carson, H. F. Jelinek, R. H. Olp, A. P. Grunwald, G. J. Pokorny, and A. B. Shuck)

This program was initiated in 1956 to cover the development of all EBR-II processes and remote refabrication equipment. The purposes of the program are as follows:

(1) to investigate processes and requirements for remote refabrication of irradiated reactor fuel;

(2) to develop and test in production a process adaptable for refabrication of the EBR-II fuel;

(3) to design, construct, and pretest a complete system of fuel-refabrication equipment to be installed in the EBR-II Fuel Cycle Facility.

The EBR-II fuel cycle incorporates partial fission product removal by pyrometallurgical refining. The highly radioactive billets from the refining operation must be refabricated into 0.366-cm-diameter by 36.12-cm-long fuel pins. The fuel pins are sodium bonded in stainless steel jackets forming the fuel rods. Ninety-one of these are assembled by remote control between upper and lower depleted uranium blanket subassemblies in hexagonal stainless steel tubes by remote-controlled assembly procedures.

Preliminary investigations and engineering studies to develop the requirements for remote refabrication and assembly were completed by 1961. These included the calculation of the expected temperature levels,[30] radiation testing of components,[31,32] and the development of requirements for an architect/engineer.

The process flow diagram (see Figure 30), based upon injection casting, was developed and equipment to test the process was

---

[30] Lazar, N. M., Feldman, M. J., Mahagin, D. E., and Carson, N. J., Self-heating of Fuel Arrays in the EBR-II Fuel Cycle, ANL-6791 (in preparation).

[31] Pokorny, G. J., and Ayer, J. E., The Performance of a Special Differential Transformer and an Eddy Current Coil in a High Gamma Flux Environment, ANL-5988 (1959), pp. 12-14.

[32] Ayer, J. E., and Pokorny, G. J., The Performance of a Motor, A Switch, and Two Types of Pressure Pickup in a High-Gamma Flux Environment, ANL-6347 (1961), pp. 15, 16.

designed, constructed, and installed in Building 6 by mid-1961. In this process, batches of 100 or more fuel pins are gas-pressure injection cast in thoria-coated precision Vycor-glass molds. The molds are crushed from the castings which have only to be sheared to length and inspected to produce finished fuel pins. Demolding, shearing, weighing, and gaging are accomplished in a pin-process and -inspection machine. The inspected rods are inserted in stainless steel jacket tubes which have been preloaded with a measured quantity of sodium. The fuel rods are heated to above the melting point of the sodium and pins settled down into position by means of gentle agitation. The upper closure plugs are inserted and welded to the jacket. The operations with the radioactive fuel rods must be done in an inert atmosphere to prevent oxidation of the fuel and burning of the sodium. After welding, the rods are transferred to an air-atmosphere cell where they are leak detected by a pressure method, impact bonded at 450 to 500°C, and bond tested to eliminate those rods containing unbonded voids between the fuel pins and jackets. The upper and lower blanket sections of the fuel rods are assembled from nonradioactive materials outside the shielded cell. They are transferred into the cell and placed in a fuel-element-assembly machine where they are assembled with 91 fuel pins in the hexagonal tube and fittings to form the fuel elements.

Figure 30. Flow Diagram for EBR-II Fuel Cycle

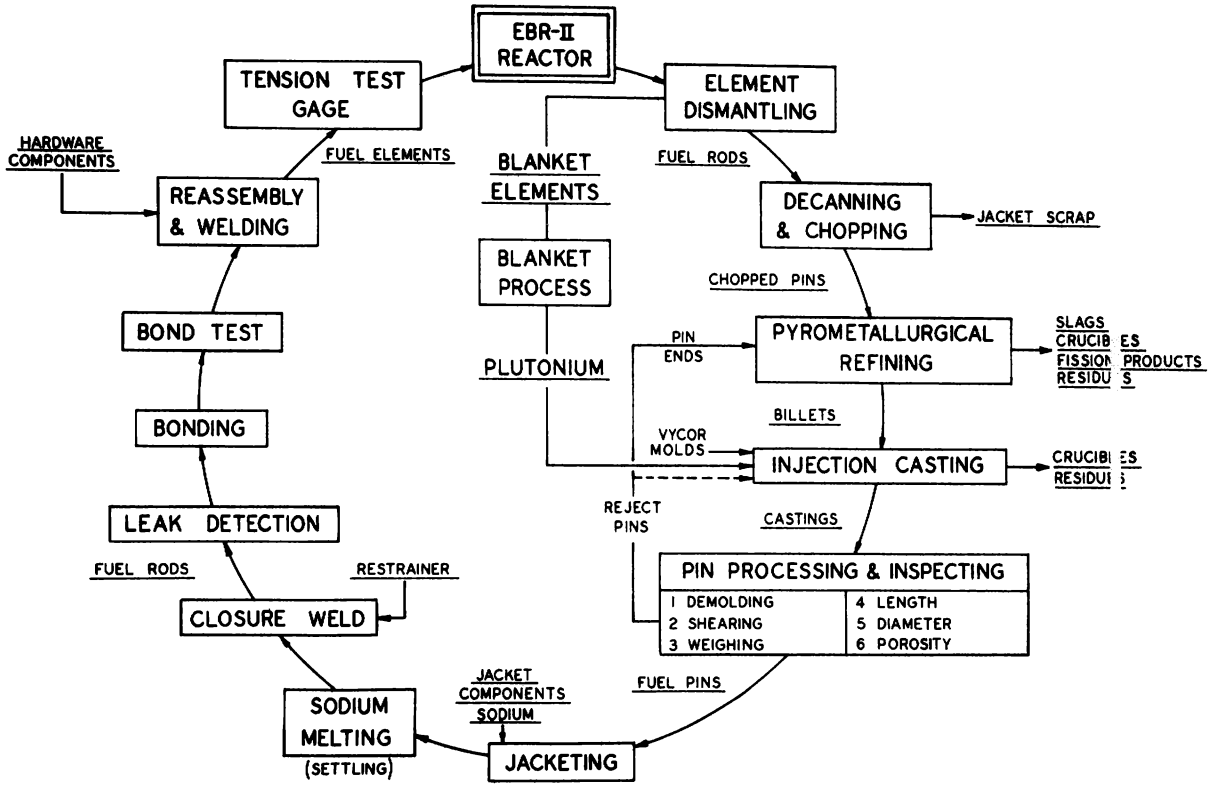

350-611

The processes and developmental equipment were tested first by the production of approximately 3,000 natural uranium-5 w/o fizzium

alloy fuel rods in 1961. Production of Core I for EBR-II was completed in 1962 with the production of 11,107 enriched uranium-5 w/o fissium alloy fuel rods. These fuel rods were assembled into ninety-seven fuel elements (each containing 91 fuel rods), fourteen (61-rod) control elements, and six safety elements.[33] A total of 3,579 additional depleted uranium-fissium rods were cast, of which 2,700 were assembled into fuel rods for Fuel Cycle Facility startup tests.[34]

As soon as the process steps had been proved, remotely controlled equipment was designed for the EBR-II Fuel Cycle Facility. The injection casting furnaces, sodium "settlers," and bonding machines were completed in late 1962 and shipped to Idaho.

Progress in 1963

Equipment for eight of the operations shown in Figure 30 was completed during 1963 and shipped to Idaho. This included: (1) a remote-controlled beam scale, (2) a charge-preparation station, (3) injection casting mold-loading and -unloading equipment, (4) two pin-process machines, (5) fuel-element-assembly equipment, (6) two welders, (7) a five-station leak detector, and (8) a bond tester for determining voids in the sodium bonds.

The beam scale was a modification of a commercial design. It consisted of a compound-lever beam with a poise driven by a ball screw and radiation-resistant stepping motor. Beam position was sensed by a linear-variable-differential transformer (LVDT). The unbalance signal of the LVDT was converted to pulses which were fed to the stepping motor to drive it in the direction to balance the beam by electrical circuitry developed by the ANL Electronics Division. Each step represented 0.5 gm. Grams were "counted" by a second stepping motor in the control box geared to a counter. The beam scale was enclosed in a lead-shielded box to increase radiation resistance and protect against radiation damage.

The furnace-charge-preparation station contained features for billet dumping, for dumping the heel from the crucible, and tongs for handling billets and crucibles. A falling-weight breaker was also provided to reduce crucible heels for recharging.

The mold-loading and -unloading station consists of containers and fixtures for positioning furnace pallets, empty molds, and gravid

---

[33] Carson, N. J., Grant, N. R., Hessler, N. F., Jelinek, H. F., Olp, R. H., and Shuck, A. B., Fabrication of EBR-II, Core I Fuel Elements, ANL-6276 (1962), p. 5.

[34] Carson, N. J., Jelinek, H. F., and Shuck, A. B., The Manufacture of Supplemental Depleted Fuel Rods for FCF Startup, ANL-6550 (1963), p. 5.

molds after casting. The loading and unloading operations are performed by master-slave manipulators. A stand is provided to hold a magazine for the pin-process machine.

The pin-process machine is shown in Figure 31. It demolds the castings and crops the casting ends to produce fuel pins of the correct length. It then successively measures the length and weight of each pin, and scans the pins lengthwise with a diameter gage and eddy current probe. Signals from the inspection devices are fed into a data processor which computes length, weight, average diameter, volume, and density, and plots a strip chart record of length versus diameter and the differential eddy current signal. Considerable difficulty was experienced

Figure 31. Pin-process Machine Showing Plug-in Modular Stations

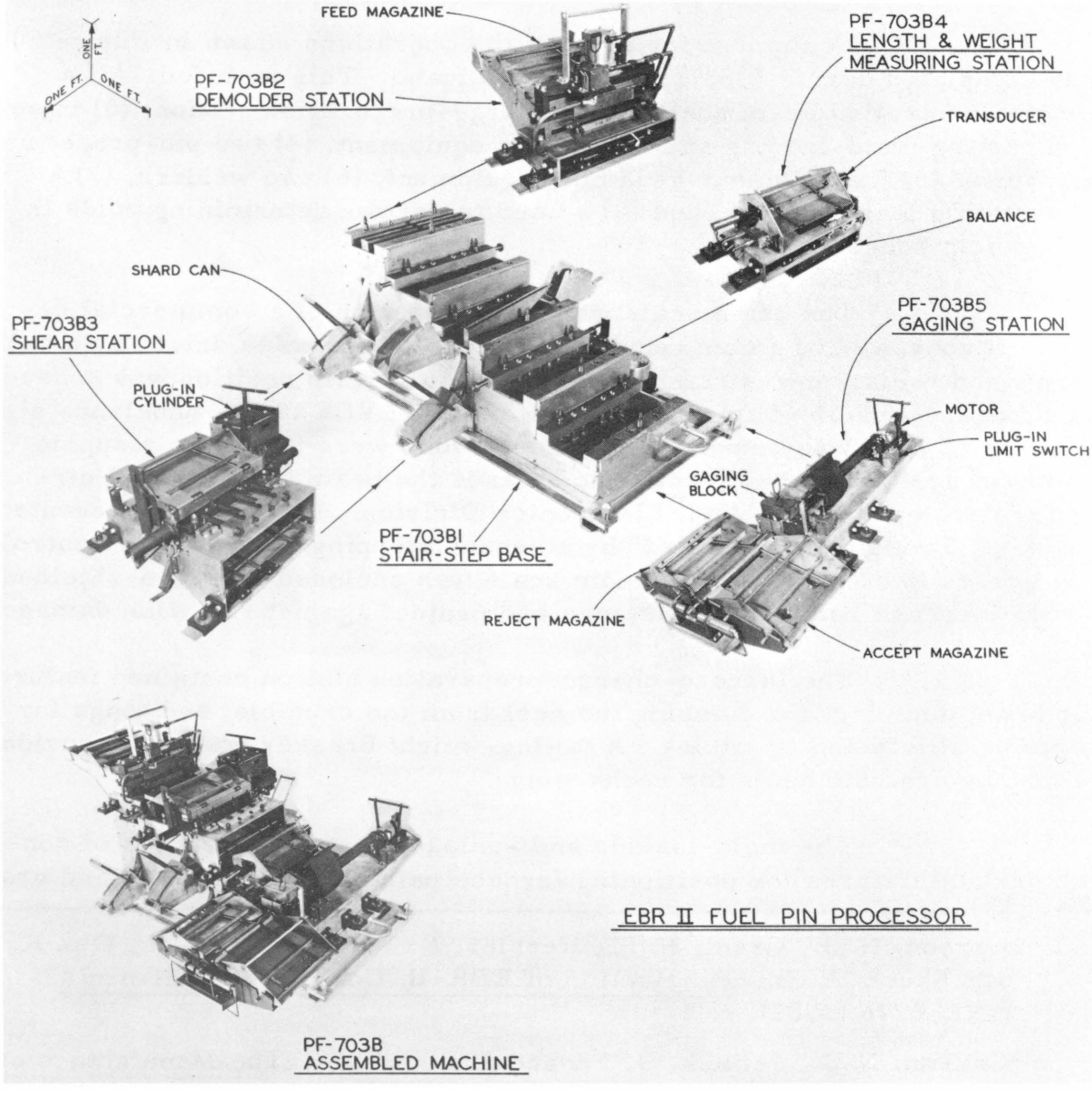

106-7341

with the pin-process machines as they were received from the vendors. About 1600 hr were expended in aligning, securing, and modifying components.

Master-slave manipulators were not originally available for the Argon Cell. For this reason, the welders incorporated a restrainer feeding and loading mechanism, as shown in Figure 32. Because of the necessarily tight fit between the plug section of the restrainer and the jacket and the need for very accurate alignment, this mechanism gave considerable trouble. Welding was accomplished by discharging a bank of capacitors across a gap between the restrainer and a tungsten electrode. The arc is started by a high-frequency ionizing current. This method was perfected and fully tested during Core-I production. Field modification of the welding machines is described later (see Sect. A-5).

Figure 32. Welding Machine with Restrainer Feeder and Loader

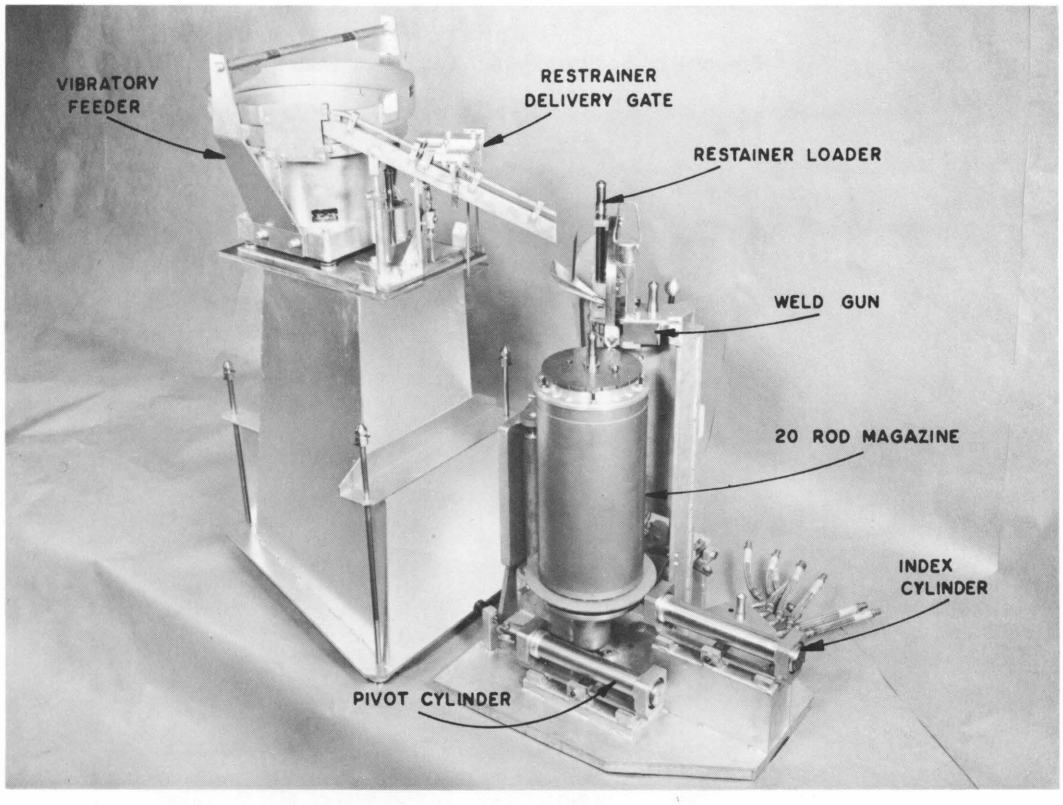

350-497

Pressure leak detection is accomplished by enclosing the top weld of the fuel rod in a close-fitting chamber and injecting into the chamber a metered quantity of helium at 800 to 1000 psi. Pressure decay is measured by a transducer and plotted versus time by a strip-chart recorder. The rate of pressure decay, shape of the curve, and ultimate pressure all yield information on leaks in the welds. The method worked rapidly and reliably with nonradioactive specimens, with neoprene rubber seals, and piezoelectric transducers in the test heads. Radiation-resistant rubbers and strain-gage pressure transducers, coupled with the long

pneumatic lines, have made the remote-controlled equipment considerably less satisfactory. A five-station leak detector was supplied for the Fuel Cycle Facility. To date three stations have worked reasonably well under remote-controlled conditions.

Figure 33 shows the "hot rod" bond tester. Two types of defects in the sodium bond are indicated without discrimination by a cold-rod eddy current bond tester: gas bubbles and shrinkage voids. Gas bubbles larger than 1.6-mm diameter are cause for rejection of a fuel rod. Shrinkage voids, if not gas filled, disappear on melting and are of no consequence. The EBR-II bond tester was designed to scan the fuel rods at 175°C with the sodium molten. It consists of a heated fifty-rod magazine, an indexing mechanism, a fuel-rod elevator and sensing coil. Heating elements are provided to heat the rod as it is lifted through the coil by the elevator. Only minor adjustments were required to make the bond testers function mechanically before shipment.

Figure 33. Sodium Bonder and Level Tester

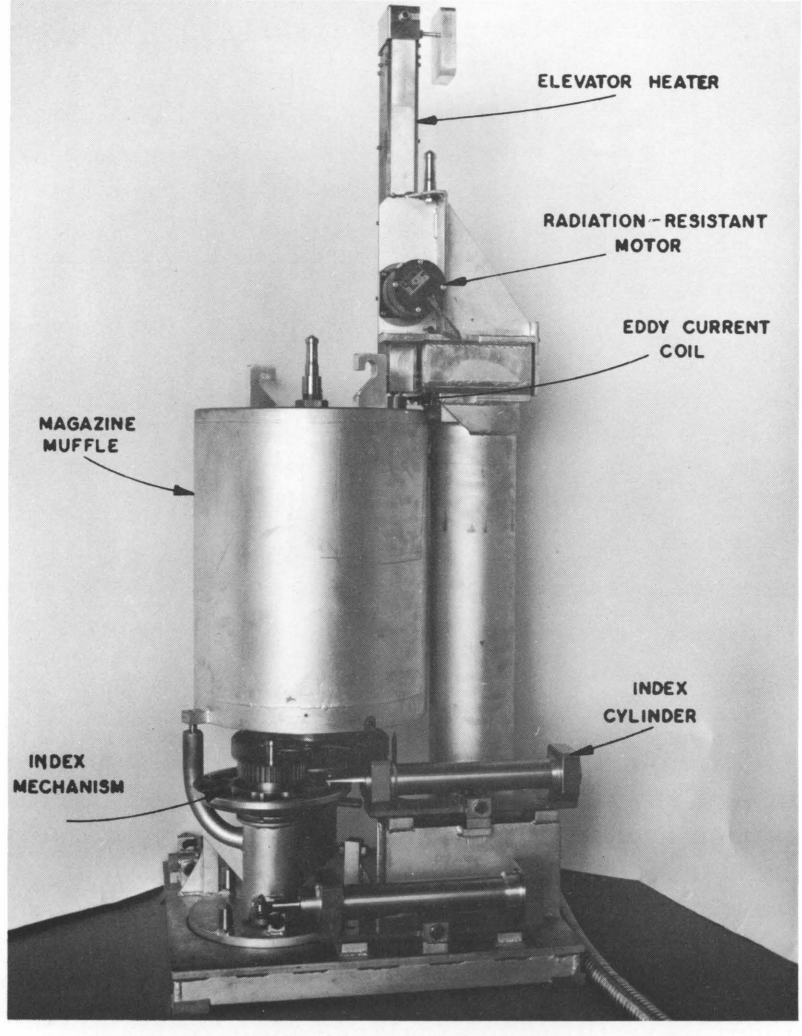

350-516

As of December 1963, three major items are still under construction. The fuel-element-assembly machine and the fuel-element gage and tensile tester are scheduled for delivery in January 1964.

b. Installation and Operational Testing of Fuel-refabrication Equipment in EBR-II Fuel Cycle Facility (J. E. Ayer, N. J. Carson, H. F. Jelinek, G. J. Pokorny, and A. B. Shuck)

This program includes the supervision of installation and operational testing of the EBR-II fuel-refabrication equipment described in Sect. A-4. Labor for installation of electrical wiring and piping systems was supplied by J. F. Pritchard and Company from January 1962 until termination of their contract in December 1962. Installation of the process machines in the Argon and Air Cells was done by Idaho Division personnel to familiarize them with the remote assembly and operation of the process equipment. The pneumatic and electrical controls for the refabrication equipment were installed in the Fuel Cycle Facility prior to delivery of the in-cell machinery. For this reason, operational testing could not be completed either in the vendor's plant or at Argonne, Illinois. Major modifications were, therefore, expected during operational testing in the Fuel Cycle Facility.

Work Prior to 1963

The basic wiring and piping systems were largely completed by the contractor during 1962. This work included the installation of argon compressors, piping for control of compressed argon, electropneumatic valve cabinets for control of the refabrication equipment, vacuum pumping systems, a 400-cps power supply, power and instrument wiring, and other work of a construction nature. Completion of this work allowed the installation of the process equipment. Preliminary installation of the injection casting furnaces was made in August of 1962. They were removed from the cell by remote control to demonstrate the feasibility of this operation and to allow necessary modification to improve manipulator handling and operation.

Installation Work during 1963

All of the Argon Cell equipment and most of the Air Cell equipment were installed and operationally tested during 1963. The individual items of equipment are as follows:

(1) Twenty-kilogram Balance

The basic 20-kg balance and electronic control and readout equipment were fitted to a balance table of Idaho Division design. During installation of the balance in the Argon Cell, the balance was

damaged during manipulator installation and several of the structural pivots were broken. The balance was removed from the Argon Cell, repaired, and reinstalled.

(2) Injection Casting Equipment

The injection casting equipment includes the two furnaces, the vacuum-pressure-cooling system, electrical furnace controls, the pallet load and unload station, a charge table, and heel breaker. When this equipment was first installed, some of the components had to be placed by crane. The furnaces were removed from the Argon Cell and pickup trunnions were installed to allow the components to be placed by manipulator.

The furnaces were first tested by making several melts with copper ingots. This allowed the calibration of thermocouples, temperature measurements of critical components, and adjustment to compensate for thermal expansion while an air atmosphere was still in the Argon Cell. After the cell had been filled with an argon atmosphere, it was possible to melt uranium-fissium alloys and set the furnace parameters of pressure rate and temperature. A number of melts were made, some of which yielded more than 95 percent of full-length castings.

The accurate measurement of melt temperature has remained a serious problem. A dipping thermocouple has been installed to supplement the thermocouple in the furnace base, but to date this thermocouple has been only partly successful. The protective tube is rapidly eroded by the liquid metal, and the thermocouple must lift with the crucible during the injection casting cycle.

The pallet load and unload station is essentially a device for positioning the furnace mold holder while loading it with Vycor molds and while unloading the gravid molds. The operation is done by master-slave manipulator. Manipulator accessibility and poor visibility were the principal shortcomings of this station. The components of the station have been remounted on the balance table so that, if items are dropped, they are within the visual range of the operator.

The charge table was found to be reasonably convenient. It was modified to include a billet-turnover tray used to stand the billet on end so that it may be gripped by the billet tongs.

Only minor changes were required in furnace controls. Some additional interlock relays were installed to prevent out-of-sequence furnace operation and possible blowout of the freeze seals while molten. The injection casting equipment is considered presently ready to process irradiated fuel.

(3) Pin-process Machines

Both pin-process machines have been installed in the Argon Cell. They are the most complicated machines in the cell and have required the most time in shakedown. Many problems were caused by misalignment of components and most of these have been corrected. The feeding of short or malformed pins continues to be a problem. The feeder trays were redesigned to improve their function.

Considerable attention was devoted to the data processors used with the pin-process and -inspection machine. Defective digital voltmeters were repaired. Signals from the diameter-measuring transducers did not provide sufficient response on the recorder, and stray alternating current was inductively coupled from power lines, causing signal cancellation and attendant loss in response. The signal leads were isolated from the power leads to correct this condition. One data processor has been modified to actuate an IBM card-punch machine. In trial runs, fuel-pin data have been punched directly on the IBM cards.

(4) Fuel Rod Assembly and Welding

The restrainer feeder and loading operations originally incorporated in the welding machines continued to present difficulties. Alignment of the components was more critical than could be conveniently achieved in remote installation, and malfunctions of the equipment continued to occur. Furthermore, since the tip of the restrainer is submerged in the sodium, the operation had to be performed rapidly while the sodium was still molten from the settling operation.

Restrainer loading was found to be comparatively simple as a manipulator operation with suitable guide fixtures. The fuel-element-assembly station was modified to incorporate one of the settling machines under a master-slave manipulator. The operation consists of loading the sodium-filled jacket tubes into the settler magazine, loading fuel pins into the jacket tubes, melting the sodium, and inserting the restrainers, all of which were done by manipulator with little trouble. The loaded magazine is then transferred to the welder, now a single-function machine, where capacitor-discharge welds are made. These items of equipment are now considered operational.

(5) Leak Detectors

The five-station leak detector has given considerable trouble. First, the Skinner valves installed in the control cabinet would not seal helium at 1100 psig and had to be replaced. Leaks developed in pressure fittings and in the lead-detector heads due to creep of the brass O-ring valves. Hardened steel valves were substituted into leak-detector heads,

which can support the higher compressive forces needed to seal the valve to its pneumatic connection. Two of the five radiation-resistant pressure transducers failed during operation and will have to be replaced. Presently, three of the five leak-detector heads are operational. The electronic readout instrumentation works satisfactorily.

(6) Bond-testing Equipment

The bond-testing equipment is mechanically functional. The eddy-current coils supplied from Illinois were not satisfactory when used in the Fuel Cycle Facility. They were returned for rewinding. Stray inductive current pickup has also proved to be a problem due to the long leads and difficulties in electrical shielding in the cell penetrations. Isolation of the leads and additional shielding has corrected this condition.

By December of 1963, refabrication equipment in the Argon Cell was essentially operational. Figure 34 shows a pin-process machine, injection casting equipment, and, in the background, pyrometallurgical refining furnaces installed in the Argon Cell.

Figure 34. View from FCF Argon Cell Sector IV Showing Pin-process Machine, Injection Casting Machines, and Pyrorefining Equipment

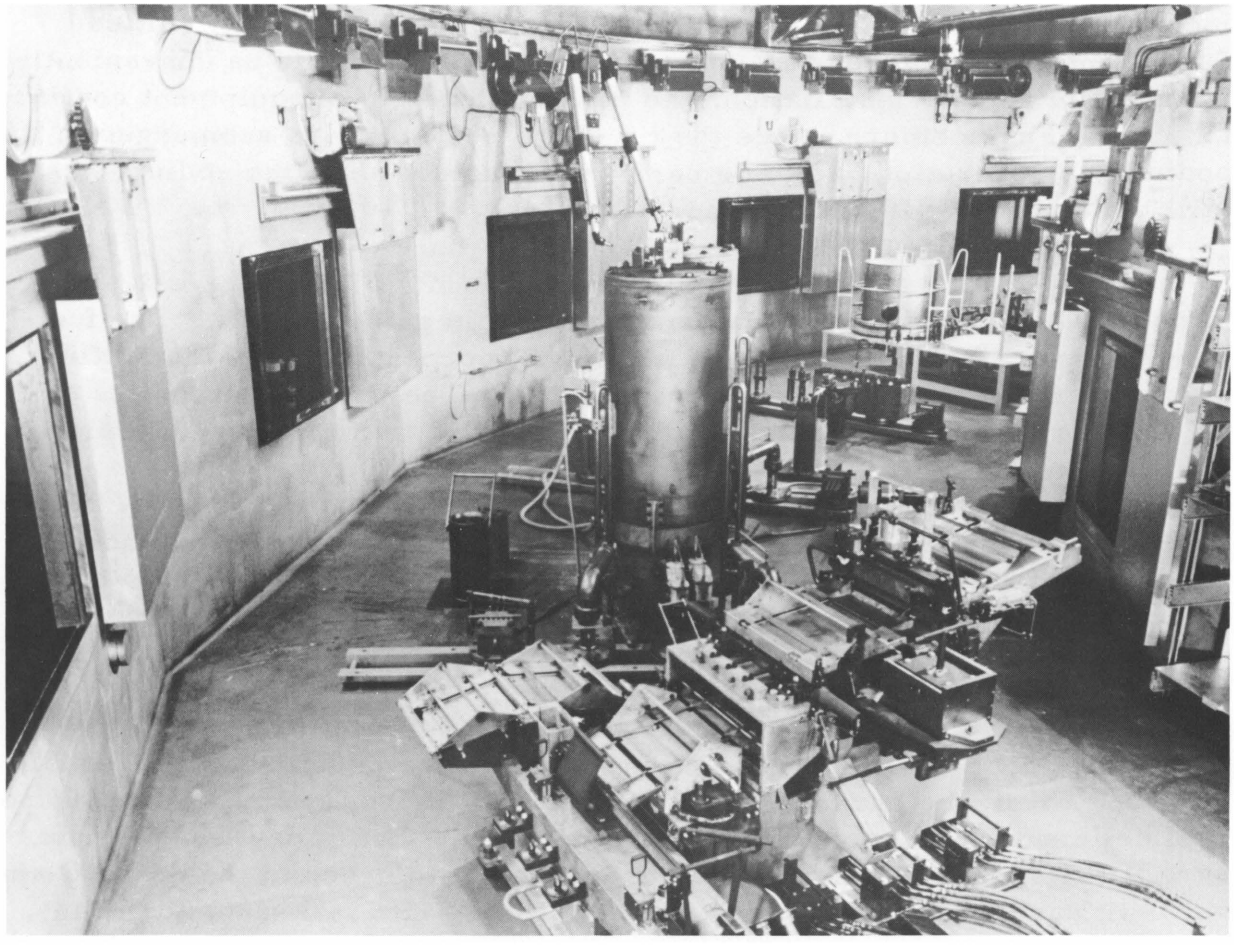

c. Fabrication of EBR-II Test Fuel Elements (A. B. Shuck, E. M. Pilarski, and A. G. Hins)

The primary purpose of this program is to fabricate uranium-plutonium-fissium alloy fuel pins and to jacket them in a variety of refractory metals for irradiation test. Secondary objectives are as follows:

(1) to investigate the casting and fabricating properties of uranium-plutonium-fizzium alloys;

(2) to develop bonding, welding, and inspection procedures for jacketing the fuel pins in Nb-1.0 w/o Zr, Nb-4 w/o V, Hastelloy-X, tungsten-lined Hastelloy-X, vanadium alloys, etc.;

(3) to evaluate the adaptability of EBR-II fabricating process and equipment to U-Pu-Fz alloy fuel and refractory metal jackets.

During development of uranium fuels, it is customary and economical to establish the fabrication procedures and metallurgical properties through use of depleted uranium. Unfortunately, there is no substitute for Pu^{239} that behaves in an identical manner and is low in cost. A somewhat analogous situation exists with refractory-metal hardware which has been in extremely short supply. It was, therefore, desirable to combine process development with the fabrication of useable irradiation-test specimens. The work is still in progress. The following comments are made on results to date.

Injection Casting

A total of eight melts have been injection cast into 352 Vycor-glass molds. The acceptable yield of castings was 288, or 81.8 percent of the molds charged. Individual melts yielded from 53 percent to 97 percent of the molds charged.

EBR-II Core-I-type tooling, materials, and parameters were originally used with fair success. The U-Pu-Fz alloy tends to be more drossy than its uranium counterpart. When yttria (Y_2O_3) was substituted for thoria as a wash for graphite crucibles and Vycor molds, there was an apparent improvement in cleanliness of castings. Prealloying and casting from "strainer" crucibles into an ingot mold also improved the cleanliness of the metal in the later melts.

Three alloys were cast: U-20 w/o Pu-10 w/o Fz, U-15 w/o Pu-10 w/o Fz, and U-10 w/o Pu-10 w/o Fz. The aim composition of the fizzium was 2.80 w/o Zr, 2.75 w/o Mo, 2.95 w/o Ru, 0.50 w/o Rh,

and 1.00 w/o Pd. Incomplete analytic results indicate essentially complete recovery of the fizzium alloys. The analyzed plutonium (4 results) ranged from 96.6 percent to 99.7 percent of the calculated plutonium content. Earlier analyses indicated that the dross tends to be richer in plutonium than the charge.

The fluidity of the alloys appeared to be very good. Once the molds had penetrated the dross crust, 14.25-cm castings were obtained without difficulty. Melt temperature was varied from 1270 to 1375°C. Casting-pressure rise rate was kept at a constant average of 11 psi/sec. Mold temperature varied from 100 to 260°C. Good results were achieved with two U-15 w/o Pu-10 w/o Fz heats cast at 1350°C and with mold temperatures at 100 and 180°C. In both cases the ultimate casting pressure was 25 psia. Yield from these melts was 96.6 percent and 93.3 percent of molds charged. Diametral shrinkage was approximately 1.5 percent for the U-Pu-Fz alloy against 2.0 percent for the U-Fs alloy. Gamma radiography showed internal shrinkage similar to U-Fs alloys.

The castings were sheared to length prior to machining. They are more brittle than U-5 w/o Fz alloy, but are not difficult to handle. Some of the U-20 w/o Pu-10 w/o Fz and U-15 w/o Pu-10 w/o Fz castings broke during mold removal. In some cases, fractures were through dross inclusions or shrinkages.

Although the casting properties of the U-Pu-Fz alloys were somewhat different from those of U-5 w/o Fs, they appear to be adaptable to the present EBR-II fuel cycle.

Refractory-alloy Jacketing

The following jacket tubing and rod stock has been received for jacketing irradiation specimens: Nb-1.0 w/o Zr, Nb-4 w/o V, vanadium, and tungsten-lined Hastelloy-X. The Nb-1.0 w/o Zr, Nb-4 w/o V, and vanadium were required in both stress-relieved and annealed condition. Fully annealed niobium alloys gave some problems in machining and handling because of their extreme softness. Special diamond grinding points were required to remove tungsten from the ends of the Hastelloy tubing.

End plugs were welded in place by TIG welding in a helium-atmosphere glovebox. Vanadium was easily welded, producing an exceptionally clean bead. The niobium alloys required very high amperage. Close fitting chills were required to control grain growth in the tubing. Even with these chills, a great deal of heat is generated in the restrainer. This may cause difficulty and may require redesign of the restrainer to prevent sodium vapor contamination of welds. The fully annealed Nb-1 w/o Zr alloy displayed an unusual local melting pattern in the metal adjacent to the weld bead. The welding of Hastelloy-X required more amperage and higher temperature than stainless steel, but welding characteristics were similar to stainless steel.

The loading of plutonium into clean jackets requires methods similar to "aseptic technique" to prevent contamination of the jackets. The U-Pu-Fz fuel pins are loaded through disposable plastic funnels to prevent contamination of weld joints. Separate tools are used for handling the plutonium alloy.

The glovebox atmosphere containing approximately 30 ppm H_2O and from 200 to 500 ppm O_2 caused oxidation of the niobium and vanadium alloys while sodium bonding at 450°C. A vacuum impact-bonding machine has been designed which will allow vacuum bonding or bonding in a high-purity inert atmosphere. From these limited tests, it appears that the use of refractory metal jackets will present more of a problem in the EBR-II FCF than will the plutonium fuel. New welding and bonding equipment, at least, will be required.

d. Development of Powder-loaded Radiator-type Fuel Elements (J. E. Ayer, A. G. Hins, E. M. Pilarski, and A. B. Shuck)

The primary purpose of this program, started in 1963, is to develop a powder-filled radiator-type fuel element which is adaptable to remote fabrication. It is a long-range program which will have the following secondary objectives:

(1) to develop techniques for producing metal and non-metallic powder, and shot fuels;

(2) to investigate the fundamentals of vibratory fluidization and compaction;

(3) to develop methods for thermally bonding compacted powder fuels;

(4) to develop techniques for determining the thermal characteristics of unbonded and bonded metal powders;

(5) to investigate radiator fuel-element design;

(6) to develop methods for fabricating radiator fuel-element shell;

(7) to fill the radiator shells with compacted particulate fuels;

(8) to bond, weld, and inspect the resulted fuel elements and irradiation test them.

Two methods have been used for the preparation of U-Pu-Fz alloy metal powders. The parameters of vibratory compaction have been explored through use of steel shot and iron carbide grit. Calorimeters

have been modified for study of the thermal characteristics of irregular-shaped shot-filled items. Sodium has been experimentally infused into compacted metal-powder specimens. Welding experiments have been started on miniature shell-and-tube-type radiator specimens.

Production of Metallic Fuel Powder (E. M. Pilarski and D. A. Kraft)

One of the centrifugal casting machines has been modified as shown in Figure 35 to atomize metal powder. The existing furnace shell, conduction-coil assembly, and rotor were used. The powder-collector pan and centrifugal argon separator were mounted on the rotor table. A

Figure 35. Schematic Drawing of Metal Atomizing Furnace

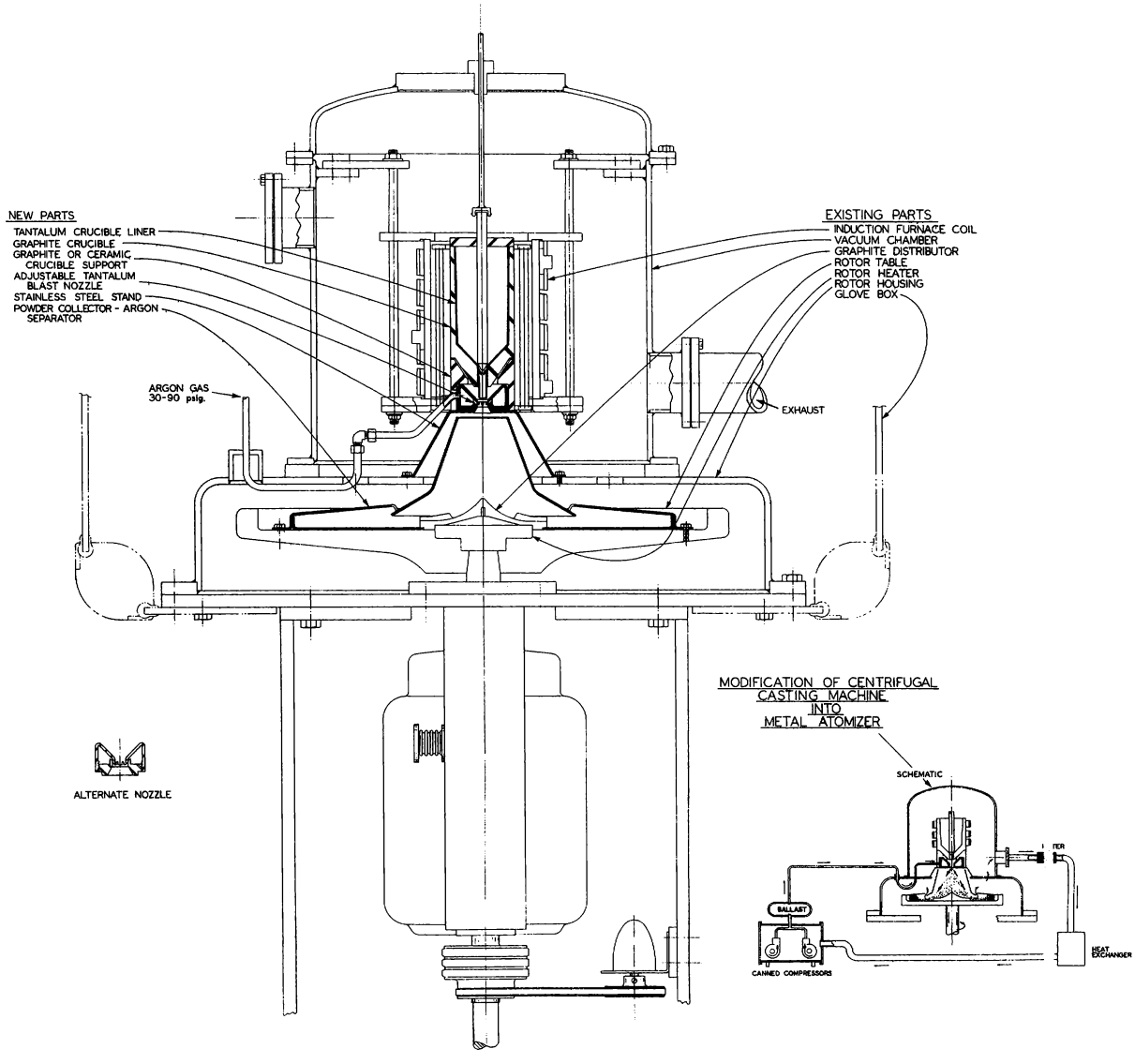

350-444

compressed argon system, consisting of two 175-psig compressors, a compressed-gas receiver, pressure piping to the atomizer furnace, an annular gas nozzle, a sintered stainless steel filter, a heat exchanger, and suction piping to the compressors, was added.

The metal is melted in a yttrium oxide-coated graphite crucible or a tantalum crucible under vacuum. A graphite pintle protrudes from the bottom of the crucible into the annular blast nozzle. This pintle is closed at the bottom and cross drilled to form a number of small openings through which the molten metal runs. Compressed argon gas jets blow across these openings to atomize the metal.

The collector tray and argon separator were designed to separate the powder-gas mixture by centrifugal force. The atomizing gas escapes through annular slots in the argon separator while the atomized powder is collected in the outer rim of the collector tray. The exhaust gas is passed through the sintered stainless steel filter through a gas-to-chilled-water heat exchanger, where it is cooled before being returned to the compressor section.

A series of 12 atomizing melts were made with copper, aluminum-bronze, U-10 w/o Pu-10 w/o Fz, and U-15 w/o Pu-10 w/o Fz. Nozzle configuration and orifice size, manifold, pressure, temperature melt, gas-jet direction, and manifold-to-nozzle distance were found to be quite critical. In the existing setup the distance between the nozzle and the collector is only a few inches. Most of the metal did not remain as separate particles but agglomerated into a spongy irregular mass; Figure 36 shows the results of a typical cast in the collector tray. The metal was an atomized U-10 w/o Pu-10 w/o Fz alloy. The yield of finely divided powder was 28 percent.

Since the yield of powder was somewhat disappointing, the agglomerated metal and the plus 14 mesh particles were pulverized in a laboratory hammer mill, which very effectively reduced the partly fused material to a fine powder. In view of the excellent yield of fine mesh powder from the hammer mill, the procedure was used to pulverize injection cast pin-ends. This, too, was successful. The screen analysis of the powders produced by atomizing, by atomizing and micropulverizing, and by micropulverizing cast materials are shown in Table XXV. Shadow photomicrographs of the atomized and pulverized powders are shown in Figure 37.

Figure 36. Centrifugal Collector with Particulate Fuel in Rim, and Agglomerated Powder at Center

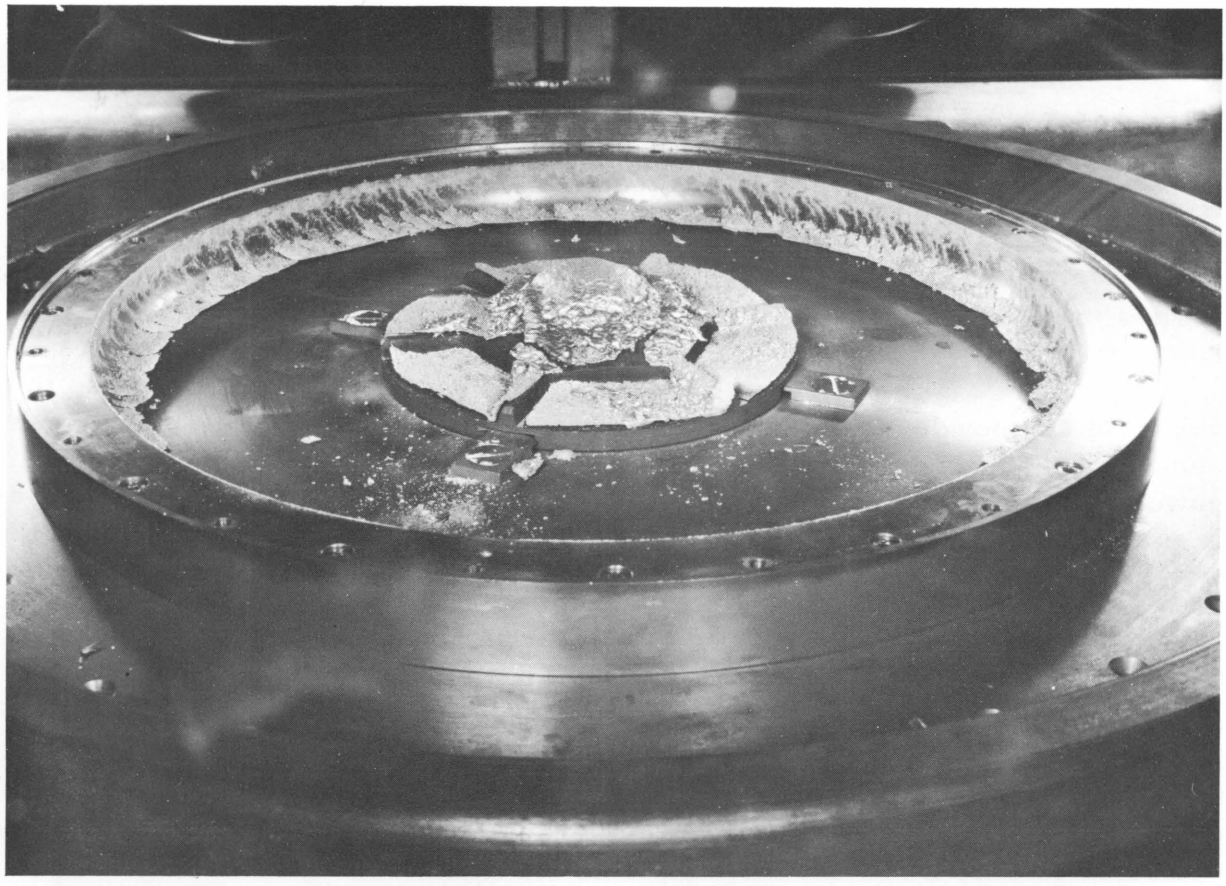

350-538

Table XXV

PARTICLE SIZE DISTRIBUTION OF ATOMIZED, ATOMIZED AND PULVERIZED, AND PULVERIZED U-Pu-Fz ALLOY

NBS Mesh Size	Percent Atomized U-10 w/o Pu-10 w/o Fz	Percent Atomized Pulverized	Percent Pulverized U-15 w/o Pu-10 w/o Fz
14-45	17.8	4.2	1.7
45-200	5.1	56.6	34.3
120-200	1.5	25.0	28.2
200-325	1.6	8.6	28.8
Minus 325	1.7	5.6	12.0

Figure 37. Photomicrographs of Atomized and Pulverized U-Pu-Fz Alloy Fuel

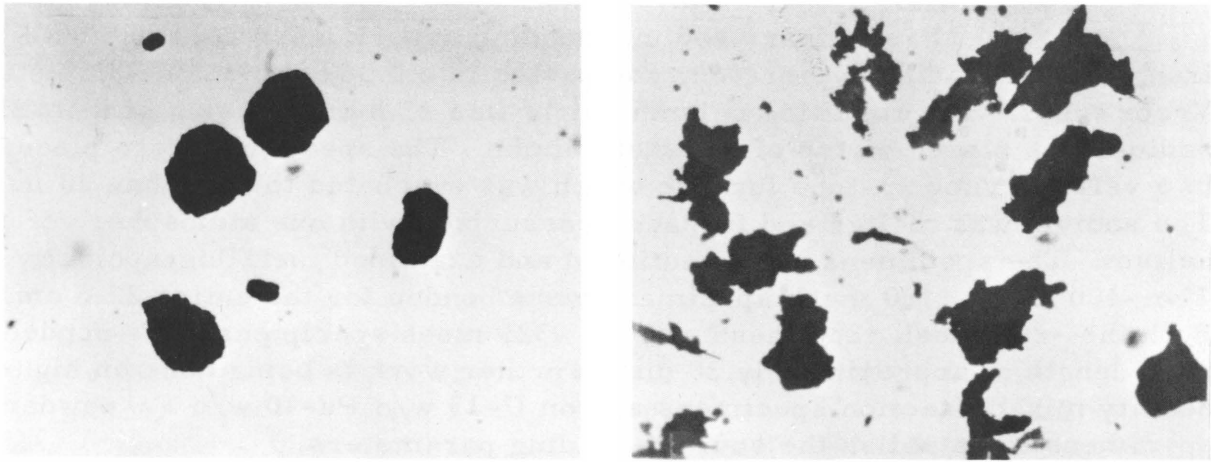

120-200 Mesh

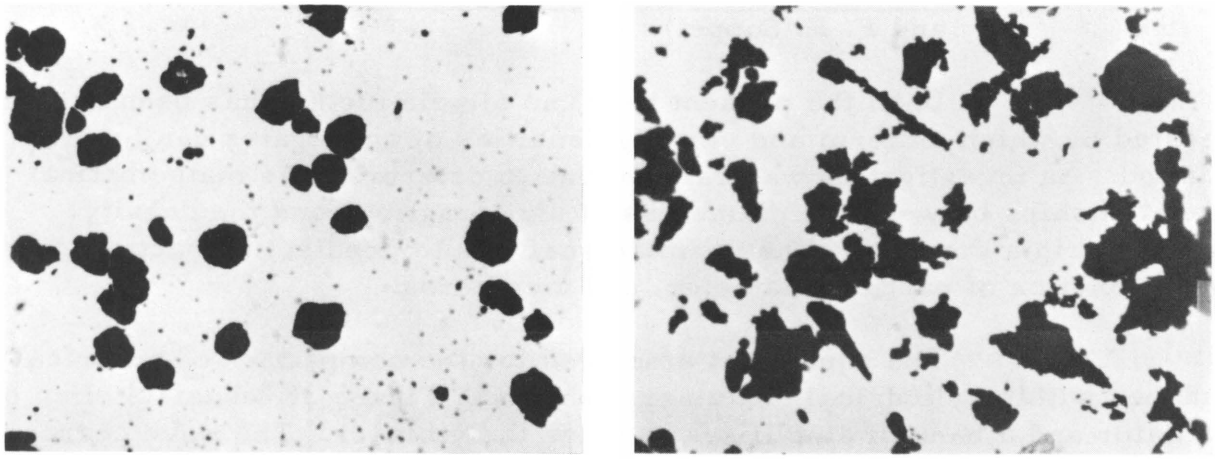

200-325 Mesh

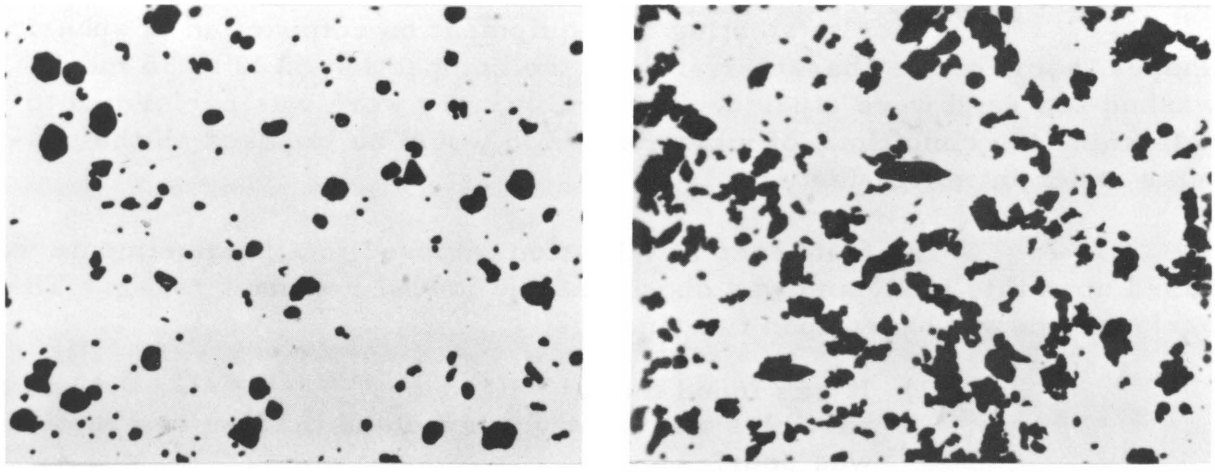

350-35 (A) By Pulverizing -325 Mesh (B) By Atomizing

Powders Produced (Magnification 100X)

Sodium Bonding of Powder-filled Specimens

Preliminary sodium-bonding experiments were run with iron shot that had been vibratory compacted into 0.368-cm-inside-diameter Vycor tubes. The resulting column height was 22.8 cm. A slug of metallic sodium was placed on top of the shot column. The specimens were placed in a vertical vacuum-tube furnace which was evacuated to less than 20 μ. The sodium was melted and furnace pressurized with one atmosphere of helium. The specimens were sectioned and examined metallographically. The -100 mesh +120 mesh specimens were bonded for the entire 22.8 cm. Both the -200 mesh +230 mesh and the -325 mesh specimens were bonded for a length of approximately 20 cm. Further work is being done on high-density mixed-fraction specimens and on U-15 w/o Pu-10 w/o Fz-powder specimens to establish the sodium-bonding parameters.

Vibratory Compaction of Spherical Shapes (J. E. Ayer and F. E. Soppet)

Until the present time, no simple method has been suggested by which uniform and varying densities of aggregates can be predicted. An investigation was carried out to determine the mathematical relationships between the diameters of size fractions and the density achieved in a compact. The ultimate goal was to predict compact density as a function of particle diameter, and vice versa.

The equipment employed for the compaction of spherical shapes within cylindrical containers, shown in Figure 38, consists of an oscillator and a bank of amplifiers to drive the vibrator. The wave characteristics of the vibrating member is transmitted to an oscilloscope by an accelerometer mounted on a platen attached to the vibrator.

Prior to starting the equipment on compaction of spherical shapes, some of the characteristics of the compaction of 20 to 35 mesh washed sea sand were studied. The preliminary work was performed to determine the conditions of vibration which would be imposed on the systems under investigation.

The frequency of vibration imposed in all experiments was based upon this study and was chosen as the lowest resonant region. The performance was based upon two findings:

(1) It was found that at "dissonant" frequencies the bed of particles was slowly stirred and that the compaction was poor.

(2) The lowest resonant region had the higher power efficiency in terms of power input per vibration cycle.

Figure 38. Equipment Used for Experiments Involving Vibratory Compaction

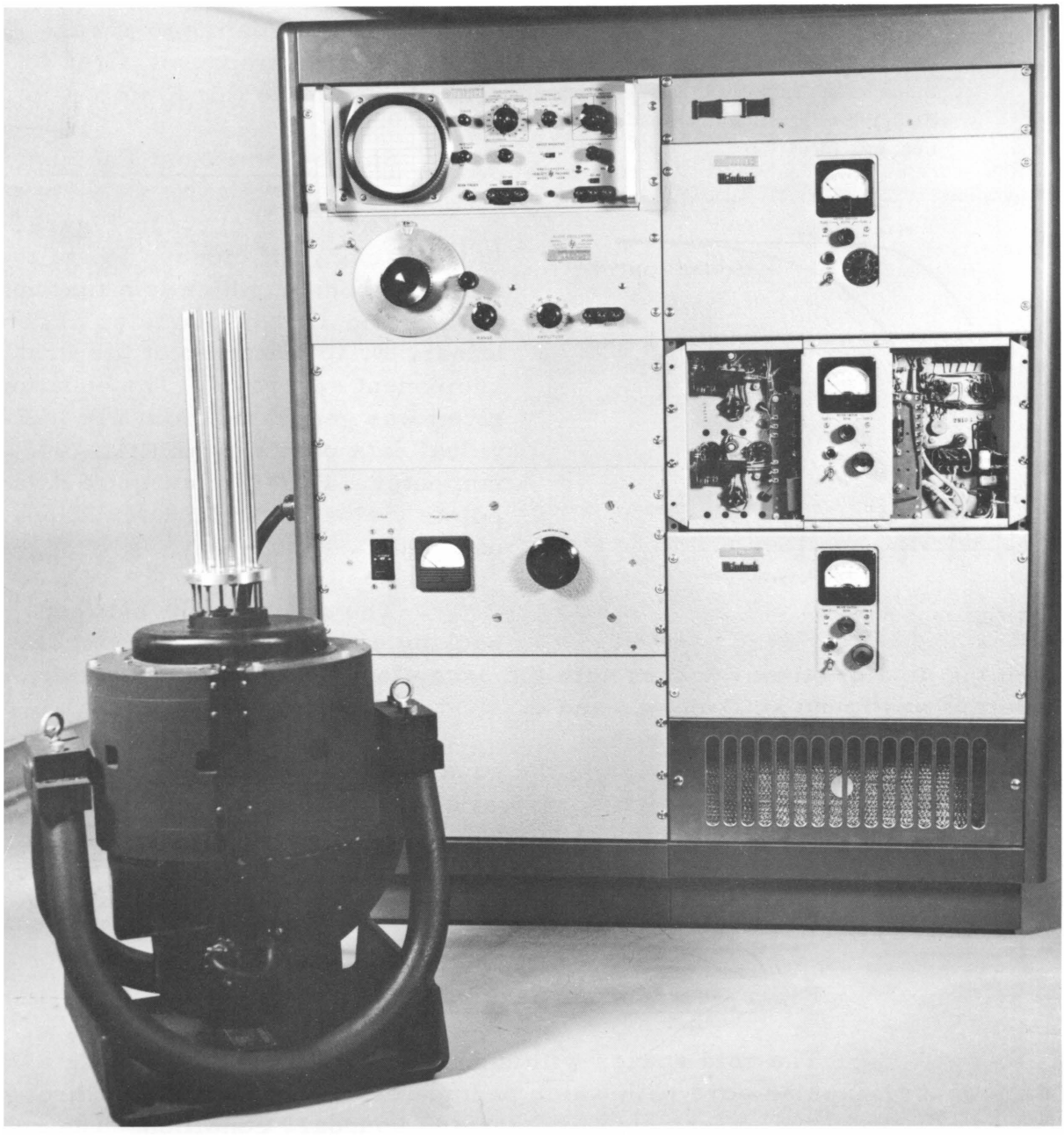

350-464

Because the region of resonance shifts with the mass of the system, each system was checked for changes in the resonance. An investigation of the effect of acceleration and compact density indicated that maximum density was achieved on a plateau of 6 to 12 g's (59 to 113 m/sec/sec).

Steel shot, obtained from a producer of blast-cleaning materials, was selected as the spherical particle. The shot was classified into 12 fractions from -8 +10 mesh to -70 +80 mesh. The pycnometer density of a sample from each classified fraction was made. The average density of the twelve classifications was 7.64 g/cm^3.

The results of the study of compaction of spherical shapes is summarized in Figure 39, in which is graphed void packing efficiency against ratio of diameter of container to first component, first to second, second to third, etc.

Figure 39. Void Packing Efficiency vs Ratio of Diameter of Container to First Fraction (D/d_1), First Fraction to Second Fraction, etc. (d/d)

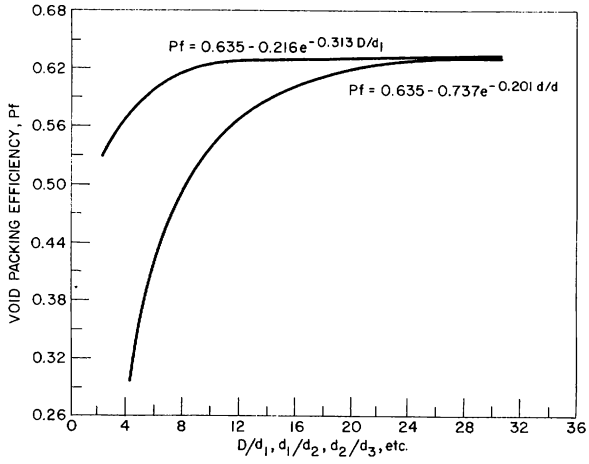

350-612

Single-component Packing

The upper curve in Figure 39 is the packing efficiency, Pf, of the first component, which is a function of the ratio D/d of diameter of container, D, to diameter of the first component sphere, d. The equation given was generated from 219 individual data points by an IBM-7094F computer. The fit of curve to data points yields a standard deviation of 0.010.

The relationship between packing efficiency and D/d agrees with the data of other workers with the exception that no inverse density relation was found at $D/d_1 = 3$ and 4.

The value 0.635 in the equation $Pf = 0.635 - 0.216\, e^{-0.313D/d_1}$ is the limiting density to which spherical bodies will fill a void space. The rate of rise of the curve, which is a function of the exponent, is a measure of the ease with which the void spaces are filled by the material being introduced. The value of the exponent and the constant 0.216 should change with both the shape of the body and the void.

Binary-component Packing

The void spaces within a matrix of packed spheres is a somewhat triangular pore path which permeates, and is continuous through, the entire structure, offering an exaggerated boundary condition. The relationship between the void-packing efficiency and the ratio of diameter of first-to-second component is given by the equation

$$Pf = 0.635 - 0.737\, e^{-0.201 d_1/d_2}.$$

This equation was evolved from 60 data points. The standard deviation of 0.033 is a measure of the fit of data points to the curve. Since the triangular pore path presented to the second fraction is more tortuous and has crevices of converging surfaces, one would expect the curve of packing efficiency to rise more slowly than it does for the case of the first fraction

being packed into a cylindrical void. This point is borne out by the value of the exponent and the multiplier in the equation for the lower curve in Figure 39.

With the aid of the two equations presented, it now becomes possible to calculate the packing efficiency of any multicomponent system of spheres as a function of diameter ratios. If the packing efficiency of spheres within a cylinder is

$$P_{e_1} = 0.635 - 0.216\, e^{-0.313D/d_1}, \tag{1}$$

the void fraction remaining is 1 - (Eq. 1), namely,

$$V_f = 0.365 + 0.216\, e^{-0.313D/d_1}. \tag{2}$$

Since the void packing efficiency P_{e_2} of the second component is

$$P_{e_2} = 0.635 - 0.737\, e^{-0.201d_1/d_2}, \tag{3}$$

the total packing efficiency, P_e (total), is (1) + (2)(3), or

$$P_e(\text{total}) = 0.867 - 0.079\, e^{-0.313D/d_1} - 0.269\, e^{-0.201d_1/d_2} - 0.159\, e^{-0.313D/d_1 - 0.201d_1/d_2}. \tag{4}$$

The value 0.867 is the limiting density for a binary system, which agrees closely with the value 0.860 which was obtained by McGeary[35] by extrapolation of binary systems. The above equation was compared against 60 data points for a two-component system and was found to agree with a standard deviation of 0.013.

Ternary-component Packing

If one accepts the premise that the constant 0.635 in both equations is the limiting density to which spheres will pack into any void, and the value of the multiplier and exponent is determined by the void shape, one must conclude that the equation $0.635 - 0.737\, e^{-0.201D/d}$ will express the void packing efficiency of all spherical matrices. The above reasoning may be extended ad infinitum through multicomponent systems; however, the calculations become somewhat tedious beyond the quaternary. Without leading one through the involved algebra, and dropping terms which have an

---

[35]McGeary, R. K., Mechanical Packing of Spherical Particles, J. Am. Cer. Soc. 44, (10) 513-22 (1961).

insignificant effect on the packing efficiency, the following equation may be developed for the ternary system,

$$Pf = 0.951 - 0.029\, e^{-0.313D/d_1} - 0.098\, (e^{-0.201d_1/d_2} + e^{-0.201d_2/d_3})$$

$$-0.198\, e^{-0.201[(d_1/d_2)+(d_2/d_3)]}.$$

In the ternary system the limiting density is 0.951 as determined by this method, which may be compared with the value 0.395 proposed by McGeary.[35] The average difference between the calculated density and that achieved by experiment was 0.014.

Conclusions

The importance of the findings reported lies chiefly in the ability to predict achievable densities by a purely mathematical method. The obviation of graphical solutions or extrapolations greatly reduces the labor and inaccuracies involved in reaching desired densities in compacted bodies. The procedures employed led to very regular packing densities which were repeatable to within 0.015 for systems up to the ternary

The range of the systems studied is presented in Table XXVI which compares the various component systems with achievable packing efficiencies and the component limitations of each.

Table XXVI

PACKING EFFICIENCY AND LIMITATIONS OF SPHERICAL SYSTEM

Number of Components	Packing Efficiency		Size Limitations
	Minimum	Maximum	
One	0.550	0.635	$D/d, \geq 3$
Two	0.720	0.867	$D/d, \geq 3$; $d_1/d_2 \geq 5$
Three	0.840	0.951	$D/d, \geq 3$; $d_1/d_2 = d_2/d_3 \geq 5$

Development of Radiator-shell-fabricating Methods
(A. G. Hins and J. R. Summers)

A preliminary investigation was made to determine whether TIG welding procedures can be used to fabricate 61- and 91-tube "radiator" sections. Because of its availability, standard EBR-II Type 304 stainless steel fuel-element tubing, measuring 0.443 cm in OD with a 0.023-cm wall thickness, was used. The outer shells were made from sections of EBR-II hexagonal tubing measuring 58.2 cm for outside flats and having a 0.1-cm wall thickness. The tube sheets were machined from 0.32-cm stainless steel plate. After drilling the 61 or 91 hexagonally spaced holes, a piloted shell mill was used to undercut the area around each hole, leaving an

upstanding rim. This rim was approximately 0.07 cm high and 0.035 cm thick. The holes were drilled to a slip fit with the tubes. The milling operation reduced the rim diameter slightly, making a tight fit with the tubes.

A welding positioner was constructed. Two "universal" milling indexing tables were superimposed "piggy-back" on a base plate. The TIG welding gun was mounted on a post and arm over the approximate center of the indexing tables. A rack and pinion was provided to position the gun vertically. Each indexing table was provided with graduated horizontal x and y motions, and a vertical-axis rotary motion controlled by a gear and worm. The rotary motion on the lower table was driven by a DC motor with variable speed control.

The radiator assembly was fixtured to the upper table. With the rotary drive in slow operation, the x and y motions were adjusted until the welding electrode traced the rim of the center tube. The lower table x and y motions were now locked, and a TIG weld was made on the center tube upon completion of the first weld. The x and y motions of the upper table were moved to index the rim of a second tube under the gun. Since the x and y motions of the lower table were not disturbed, rotation of the lower table caused the weld gun to follow a circle of the same diameter at the new position. A new weld was made and the process was repeated for each tube position. The results of this procedure are shown in Figure 40.

Figure 40. Shell-and-tube Radiator Specimen

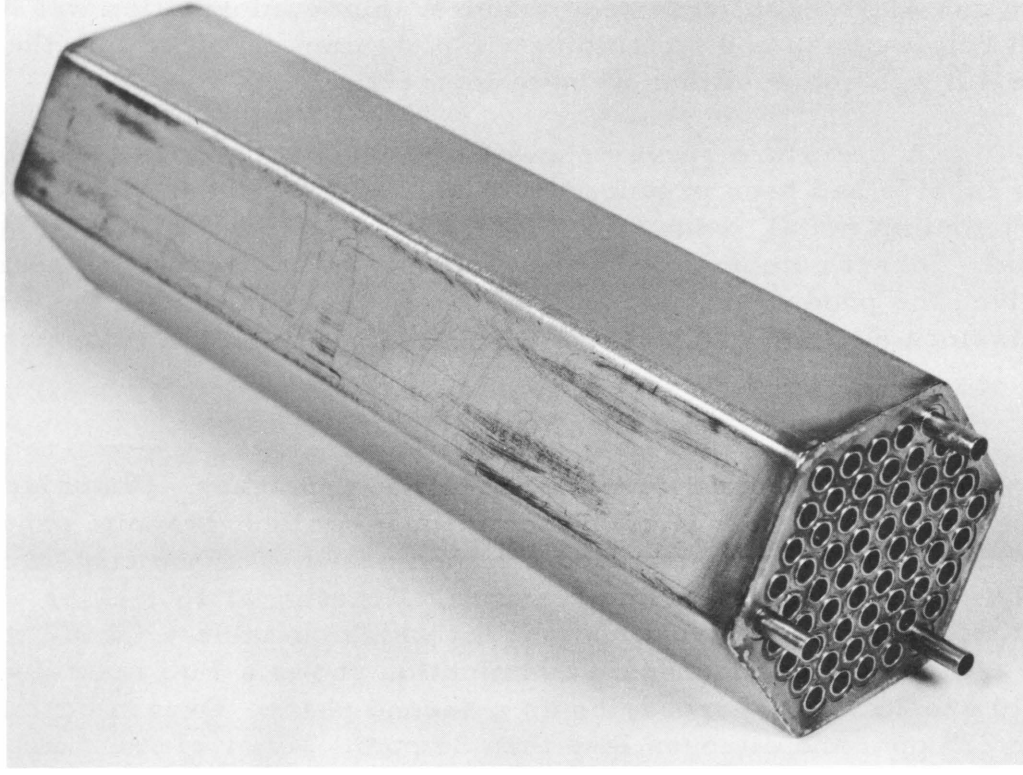

350-463

5. Production of PuC and (U·Pu)C, and Fabrication of Carbide Fuel Element Specimens (W. G. Tope)

Ceramic fuels for nuclear reactor applications are attractive primarily for their high-temperature properties. Oxide fuels are capable of attaining a high burnup at elevated operating temperatures, but have an extremely low thermal conductivity. Carbide fuels have a better thermal conductivity, but somewhat lower melting points. The literature contains little information upon the physical properties and irradiation behavior of carbide fuels. A program was initiated in 1961 to investigate the methods of preparation and of fabrication.

Stoichiometric uranium monocarbide, containing 4.8 w/o carbon, melts at 2400°C. Plutonium monocarbide is hypostoichiometric, containing about 4.4 w/o carbon, and decomposes peritectically at 1650 C into plutonium sesquicarbide plus liquid. The two monocarbides form solid solutions throughout the whole range of uranium composition, but when approaching 100% PuC with a single-phase microstructure, the carbon decreases from 4.8 w/o toward 4.4 w/o. Most nuclear reactor fuels would contain less than 60% PuC and the carbon deviation would be of little consequence.

Uranium carbide is commercially available, but neither plutonium carbide nor solid-solution carbides are available. Thus, the first objectives of the program were to develop methods to produce plutonium carbide and solid-solution mixed carbides. Since information was needed on both single-phase and stoichiometric plutonium carbide, both the 4.4 w/o and the 4.8 w/o compositions were of interest.

A literature survey showed that laboratory-size batches of plutonium carbide had been produced by pressing and sintering, and arc melting. Plutonium metal, oxide, and hydride had been used as the starting material. Direct combination of the elements by arc melting appeared to have given the product of best quality. Direct combination of the elements by resistance heating was selected for investigation and development.

Production of PuC

A process was developed for 300-g batches. Plutonium button stock is charged into a 3.8-cm-diameter, thin-walled, graphite crucible liner and reacted near the peritectic temperature. Carbon content is controlled by reaction time and temperature. Reacting at 1600°C for 45 min consistently gave a homogeneous product which contains 4.3 ± 0.2 w/o carbon by analysis. Metallographic examination shows a PuC matrix with about 10% to 15% Pu_2C_3 appearing as a second phase. Oxygen contamination is near 225 ppm and nitrogen less than 25 ppm. Minor element impurities total between 600 ppm and 1200 ppm.

One-kilogram batches have been produced in 5-cm-diameter crucibles. Reacting at 1600°C for 90 min gives a product with 4.8 w/o carbon and at 1575°C gives a product with 4.4 w/o carbon. There is a tendency for the larger batches to have a small carbon-rich core which analyzes about 0.3 w/o higher than other samples from the batch. Remelting in a tantalum crucible results in a more homogeneous product. The product button is separated by machining the excess graphite. Recovery of the plutonium in the form of carbide is 85% for the one-kilogram batches.

Additional graphite-contaminated carbide can be separated from the turnings. This material is recovered by charging (with additional plutonium) into a tantalum crucible, reacting at 1600°C, and fusible-plug casting by raising the temperature to 1950°C. A tantalum mold is used, and overall recovery is above 95%. The ingot is readily removed from the mold. Figure 41 shows the tantalum melting crucible and cover, graphite muffle, tantalum mold used for remelting and a one-kilogram remelted ingot.

Figure 41. Tantalum Crucible, Cover and Mold, Graphite Muffle and PuC Casting

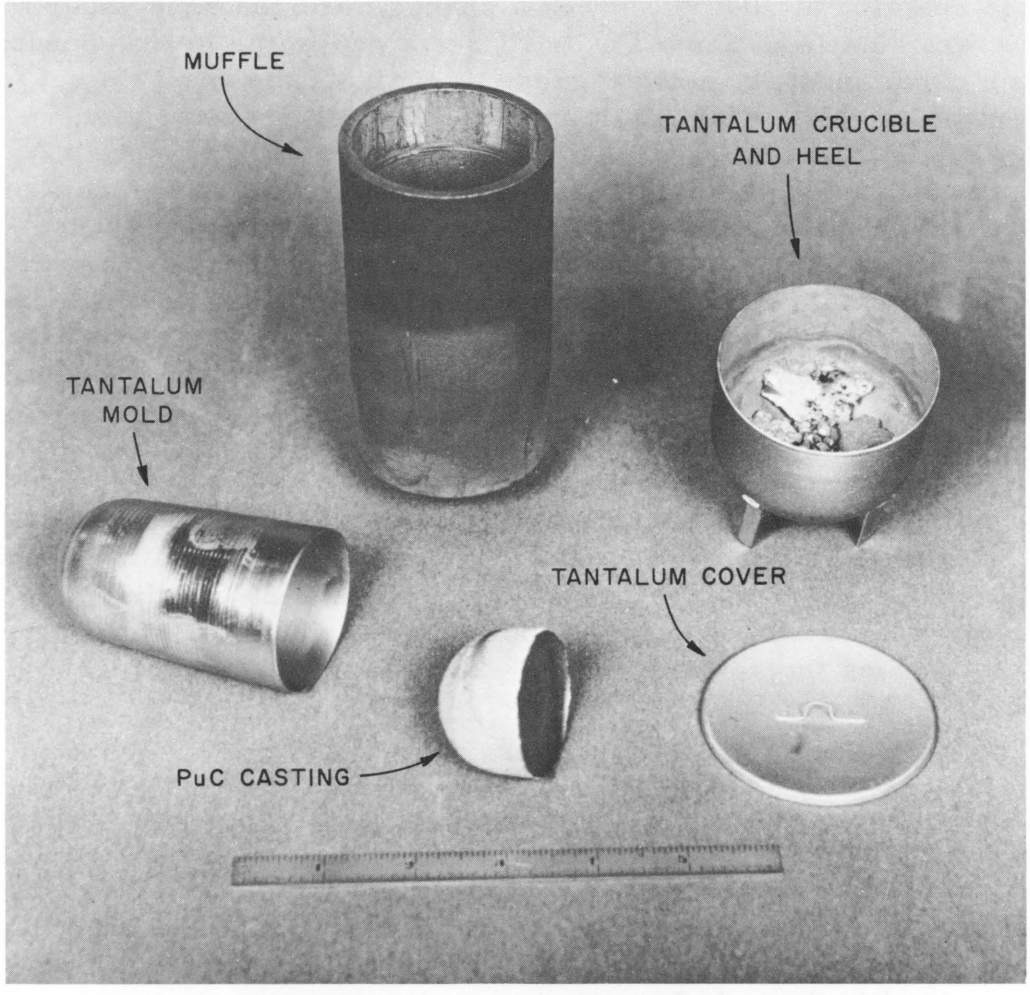

350-602

Solid-solution (U·Pu)C

Two methods are currently being studied to produce solid-solution (U·Pu)C carbides: (1) carburization of (U·Pu) alloy, and (2) combination of the individually produced carbides. Both melting and diffusion techniques are being studied. The compositions of present interest range from $(U_{0.9}Pu_{0.1})C$ to $(U_{0.5}Pu_{0.5})C$.

The $U_{0.8}Pu_{0.2}$ alloy is rapidly attacked even by a protective atmosphere containing less than 500 ppm O_2 and 50 ppm moisture. The maximum carburization which has been achieved is 3.8 w/o C on material reacted at 2000°C. Microscopic examination is difficult because of the extreme reactivity of the material. Additional experimentation is necessary before the method can be properly evaluated.

Attempts have been made to diffuse plutonium carbide into uranium carbide with use of equal amounts of 80/325 mesh powders. Reacting at 1900°C for 10 min showed most of the UC particles to be encased in PuC. Further reaction at 2000°C showed a shaded diffusion zone under metallographic examination. Some PuC still remained in the grain boundaries. Further experiments are in progress to evaluate the variables of temperature, time, particle size, and plutonium carbide concentration.

Various specimens are necessary for measurements of physical properties and irradiation testing. Two methods have been successfully used to fabricate irradiation-test specimens: casting and vibratory compaction. Plutonium carbide has been remelted in a tantalum crucible and cast into tantalum-coated graphite sleeve molds. Castings measuring 0.90 cm in diameter and greater than 5 cm in length have been made in this manner.

Vibratory compaction has been used to produce twenty 5-cm-long specimens of 0.366-cm, 0.4-cm, and 0.65-cm diameter. Compaction of 80% density was achieved by use of three size fractions in the following proportions: 60 w/o coarse, 20 w/o medium, and 20 w/o fine. The diameter of the coarse size should be about 1/5 the diameter of the tube For 0.4-cm-ID tubes the ratio is 60 w/o -20 +40 mesh, 20 w/o -120 +200 mesh, and 20 w/o -320 mesh.

Originally, considerable difficulty was experienced in producing alpha-free closure welds. The problem was overcome by using a protective Teflon (or nylon) insert when filling the specimen jacket and compacting within a closed protective tube. Both PuC and 80 w/o UC-20 w/o PuC specimens have been fabricated. The hardware and equipment used to produce these specimens are shown in Figure 42. Preliminary irradiation results are discussed in Sect. A-3-a.

Figure 42. Vibratory-compaction Driver, Jackets, Loading Funnels, Protective Tubes, Ground PuC, and Loaded Specimen

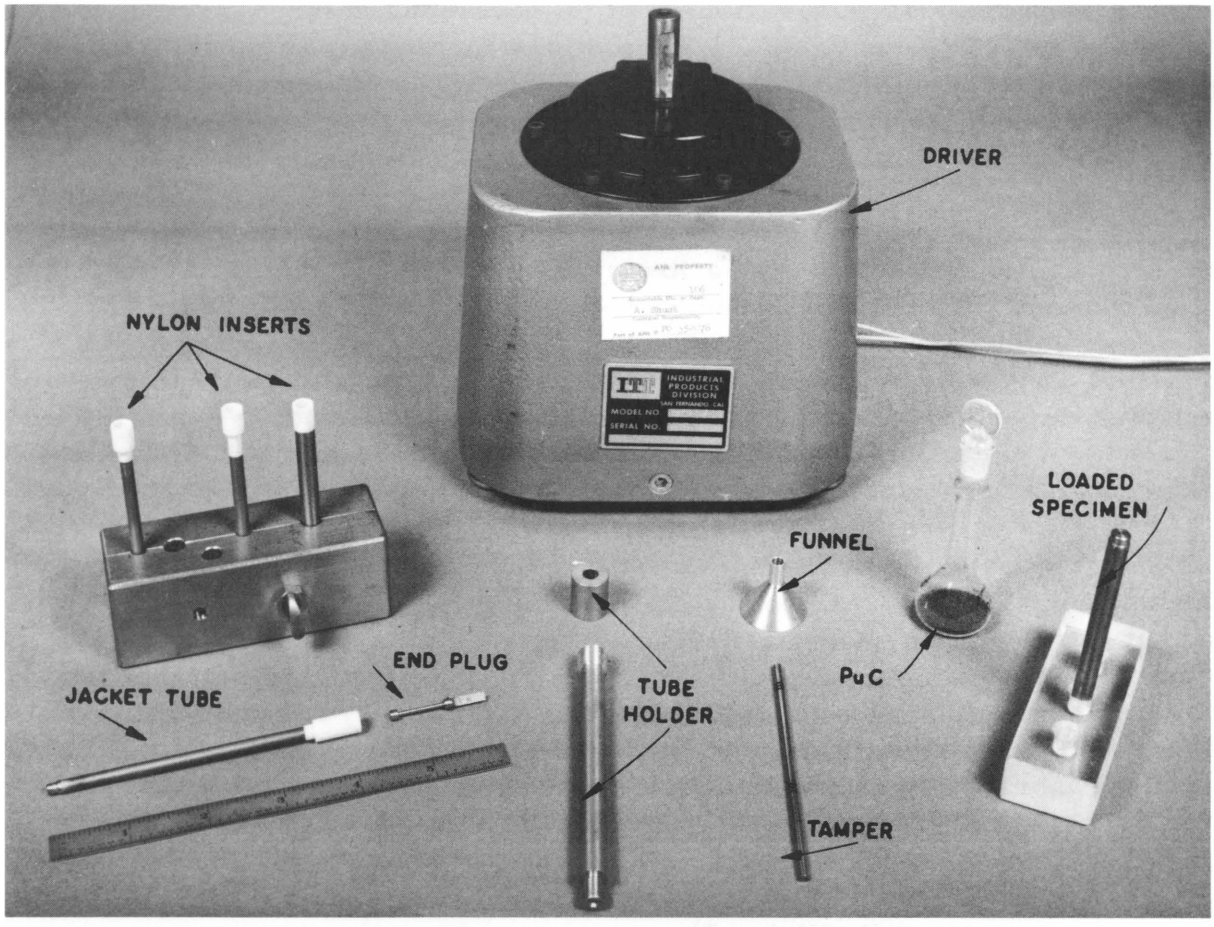

350-535

PuC, (U·Pu)C Program

The development work on PuC production is essentially complete. A few specimens are yet to be fabricated for irradiation and measurement of physical properties. Approximately 12 kg of PuC have been made, of which 9.8 kg are still available. Nearly all of this will be used in making (U·Pu)C. We currently have orders for approximately 200 (U·Pu)C specimens and EBR-II fuel rods to be made with varying enrichments. Fifteen kg of 93% enriched UC and 10 kg of normal UC have been ordered from Kerr-McGee Company for combination with our PuC.

Experiments are also under way on the production of particulate carbide permeated with a liquid metal bond. Work has been programmed on vibratory compaction and/or pressing of PuC to a controlled density and partial sintering to produce a porous fuel. Various inert materials will be tested to prevent (and also to promote) complete sintering and also to enhance physical and mechanical properties of the carbide.

Particle shape and size control will prove very important in an economic process for production of vibratory-compacted PuC fuel. Controlled particle-size generation must be developed if large quantities of fines are not to be recycled. Spheroidizing methods may be desirable for producing fuel elements of controlled density.

6. Fast Reactor Jacket Development

Fast reactor fuel jacketing or cladding must meet stringent requirements. It should have a low cross section for neutron absorption, good thermal conductivity, good high-temperature strength under irradiation (for retention of fission products), and resistance to dimensional changes or distortion. It should also be compatible with the fuel and coolant, and depending upon the specific application, meet other explicit demands. Of equal importance, the material should be easily fabricable and ultimately commercially available.

Because of these requirements, the Foundry and Fabrication Group found it necessary to investigate many facets of the refractory-metal jacket development program during the past year. The work included, but was not necessarily restricted to, tubing procurement and price analysis, development and evaluation of fabrication techniques, annealing studies, alloy development and scale-up, and a review of the problems associated with the fabrication of duplex tubing. The fruits of some of these efforts are described briefly in the sections that follow.

a. Tubing Procurement and Price Analysis (W. R. Burr, Jr., and R. Hiskes*)

In addition to the procurement of refractory metals and alloys for general fabrication development studies, tubing was purchased and delivered to the Engineering Irradiation Group for in-pile experiments and evaluation. Procurement attempts revealed that aside from the pure metals, two tantalum-base alloys, and three niobium-base alloys, no other small-diameter thin-walled tubing was available on a firm quotation basis. The commercially available small-diameter thin-walled tubing materials are indicated in Table XXVII, along with the prospects of availability in 1964. Procurement on a "best effort" basis has been abandoned because of the high quoted prices and poor yields of acceptable tubing.

Nb-1 w/o Zr, V, and Ta-10 w/o W tubing was procured during the reporting period. An order for small-diameter thin-walled TZM (Mo-0.5 w/o Ti-0.08 w/o Zr) tubing was cancelled by the vendor because of the lack of suitable annealing facilities. All of the tubing was of satisfactory quality when nondestructively tested at ANL, except for the Ta-10 w/o W. This latter tubing was of poor quality due to the use of defective tube blanks for secondary fabrication.

*Student aide during summer of 1963.

Table XXVII

AVAILABILITY AND FABRICABILITY OF COMMERCIALLY PRODUCED REFRACTORY METALS AND ALLOYS

Alloy (Numerals Represent Weight Percent, w/o)	Fabricability[a] of SDTWT			Commercial Availability at End of 1963	Prospects of Commercial Availability during 1964
	ANL	Others	Expected		
Niobium Group					
Pure Nb	VE	VE	-	Yes	-
Nb-1 Zr (D-11) (Also FS-80, Cb-751 etc.)	VE	VE	-	Yes	-
Nb-5 Zr (D-14)	E	VE	-	Yes	-
Nb-33 Ta-1 Zr (FS-82)	E	-	-	Yes	-
Nb-4 V (B-33)	ME	-	-	Yes	-
Nb-10 Ti-5 Zr (D-36)	E	VE	-	No	Good
Nb-5 V-5 Mo-1 Zr (B-66)	D	D	-	No	Good
Nb-10 W-1 Zr-0.1 C (D-43)	ME	ME	-	No	Excellent
Nb-28 Ta-10 W-0.9 Zr (FS-85)	-	-	ME	No	Poor
Nb-10 W-10 Hf (C-129)	-	-	-	No	Poor
Nb-10 Hf-1 Ti-0.5 Zr (C-103)	-	-	E	No	Good
Nb-10 Ti-10 Mo-0.1 C (D-31)	-	-	D	No	Poor
Nb-15 W-5 Mo-1 Zr (F-48)	-	-	D	No	Poor
Nb-10 W-2.5 Zr (Cb-752)	ME	ME	-	No	Good
Nb-10 W-10 Ta (S-291)	ME	ME	-	No	Good
Vanadium Group					
Pure V	VE	VE	-	Yes	-
Several V alloys are under investigation but none have been made commercially available during 1963.					
Tantalum Group					
Pure Ta	ME	VE	-	Yes	-
Ta-10 W	ME	E	-	Yes	-
Ta-8 W-2 Hf (T-111)	ME	E	-	Yes	-
Ta-9.6 W-2.4 Hf-0.01 C (T-222)	-	-	ME	No	Good
Ta-30 Nb-7.5 V	-	-	D	No	Poor
Ta-10 W-1 Zr	-	-	ME	No	Good
Molybdenum Group					
Pure Mo	ME	ME	-	Yes	-
Mo-0.5 Ti	D	ME	-	No	Poor
Mo-0.5 Ti-0.08 Zr (TZM)	D	ME	-	No	Poor
Mo-30 W	D	D	-	No	Poor
Mo-1.25 Ti-0.15 Zr-0.15 C (TZC)	-	-	D	No	Poor
Tungsten Group					
Pure W	-	D	-	Yes	-
W-25 Re	-	D	-	Yes	-
W-3 Mo	Commercial availability not established				
W-30 Re-5 Mo	Commercial availability not established				
W-10 Ta	Commercial availability not established				

[a] Fabricability of small-diameter thin-walled tubing is based upon secondary fabrication (redraw). Primary fabrication, extrusion, forging, etc., are not evaluated in this table.

The classifications are: VE - very easy, E - easy, ME - moderately easy, and D - difficult.

A survey is in progress to evaluate current prices of 304 stainless steel, Hastelloy-X, and refractory-metal tubing with regard to probable costs of complete reactor core loadings. Prices for various tube sizes and quantities of 304 SS and Hastelloy-X were obtained rather easily, although the prices for seamless Hastelloy-X tubing represents one supplier only. A total of fourteen firms supposedly able to supply refractory metal tubing have been contacted. Only six have been heard from to date. Three firms are unable to supply such tubing. Preliminary price data for the refractory metals, stainless steel, and Hastelloy-X are given in Table XXVIII. Refractory metal prices can be considered realistic for the date of the quotation but cannot be construed as the actual price for a firm order, or a price that will be quoted six months hence. Suppliers are too numerous in some metals, too few in others. As the market is developed,

prices obviously can be expected to change. Even 304 stainless steel prices cannot be considered firm over a long period of time.

Table XXVIII

QUOTED PRICES FOR FAST REACTOR TUBING MATERIALS

Tubing Material ( ) No. of Quoting Firms	Tubing Costs ($/m)[a]					
	0.40-cm ID x 0.04-cm Wall			0.95-cm ID x 0.09-cm Wall		
	30.5 m	305 m	3,050 m	30.5 m	305 m	3,050 m
Seamless 304 SS (Many)	2.16	1.41	1.31	4.36	2.89	2.70
Welded 304 SS (2)	-	-	-	-	1.34[b]	1.08[b]
Seamless Hastelloy-X (1)	-	4.03	3.64	-	-	-
Welded Hastelloy-X (2)	-	-	-	9.15[b]	5.94[b]	5.25[b]
Cb (3)	21.32 to 28.60	11.18 to 28.60	9.35 to 28.60	63.99 to 85.61	59.04 to 84.69	55.10 to 8 .66
Cb-1 Zr (2)	23.29 to 23.88	15.15 to 20.40	12.53 to 20.37	76.36 to 94.14	66.12 to 93.22	62.98 to 9 .18
Ta (4)	27.88 to 33.29	20.93 to 32.54	18.53 to 32.54	96.76 to 149.57	96.95 to 139.07	90.53 to 1 7.92
Ta-10 W (1)	49.53	39.95	32.14	191.88	180.40	167.12
Mo (1)	25.62	25.62	25.62	47.00	47.00	47.00

[a] Multiply $/m by 0.3 to get approximate $/ft.

[b] 0.953-cm ID x 0.071-cm wall.

b. Secondary Fabrication Techniques (J. E. Flinn, Jr., and R. M. Mayfield)

Small-diameter thin-walled tubing of various refractory metals and alloys has been required during the reporting period for continuing evaluation studies. A 0.396-cm (0.156-in.)-ID x 0.038-cm (0.015-in.)-wall tube size has been typical, but other sizes have also been fabricated. The evaluation tubing was produced by secondary fabrication methods developed to assure a high-quality product. The alloys included were generally those listed in Table XXVII under the column headed by "ANL."

Because of the lack of extruded tube products, the starting material in the desired size range usually consisted of drilled tube blanks. Certain of the blanks were then ironed by swaging and drawing on a nondeformable mandrel to produce the D/t (diameter-to-wall thickness ratio desired for subsequent operations. Ductile core drawing (including powder or partial powder fills) followed the ironing operation. (The selection of core material will depend upon the alloy being fabricated and the D/t ratio of the tube prior to core insertion.) The core materials consisted primarily of copper with or without a powder annulus of Al_2O_3 or sugar. In some instances sugar alone was used as the filler material.

Once the ID-support material was in place, the tube was pointed by swaging, followed by drawing down to near finished size. The reduction per pass varied, but in general ranged from 10-20% per pass. Total reductions were usually 60% or less. Copper cores, with or without Al_2O_3, were removed by swaging. If sugar was used, it was removed by melting. Cores were removed near the finished size, and the tube then was either sunk a slight amount or ironed slightly over a nondeformable mandrel to the desired size. Vacuum anneals (at 0.05 μ or better) were incorporated

where needed. Nondestructive testing, including ultrasonics, eddy current and radiography, was utilized after each major fabrication step. For further details of these processing techniques, including results and problem areas, reference should be made to a recent publication.[36]

c. Isochronal Annealing Studies of Refractory Metals (J. E. Flinn, Jr.)

Annealing studies have been carried out during the reporting period to provide critical information needed for the secondary fabrication of many of the refractory metals and alloys. Fabrication operations can be brought to an abrupt halt if reasonably precise recrystallization and stress-relieving temperatures (as well as times) have not been determined for the alloy being processed.

Table XXIX summarizes selected data obtained from niobium and tantalum alloys. The values are based on hardness measurements which are in the process of being confirmed by metallographic examination. All alloys investigated were cold rolled to reductions of 20, 40, 60, and 80%, except that Nb-39 w/o V-1 w/o Ti had reductions of 25, 50, and 80%. The anneals were carried out in vacuums of 10^{-5} torr or better for 2 hr at temperature.

Table XXIX

RECRYSTALLIZATION AND STRESS-RELIEVING TEMPERATURES[a] OF SELECTED Nb AND Ta ALLOYS

Nominal Composition (Numerals indicate w/o)	Stress-relieving Temperature, °C[b]	Recrystallization Temperature, °C[b]	Interstitial Analysis (ppm)
Nb-1 Zr (Square wire) Heat No. 1592	750	1150	$H_2 < 30$, $O_2 < 60$, N_2-160, C-67
Nb-1 Zr (Round) Heat No. 10-4430	850	1250	$H_2 < 1$, O_2-97 N_2-151, C-271
Nb-5 Zr (D-14)	<600[c]	1250	$H_2 < 50$, O_2-177 N_2-45, C-44
Nb-10 Ti-5 Zr (D-36)	<600[c]	950	H_2-6, O_2-249 N_2-20, C-24[d]
Nb-39 V-1 Ti	<600[c]	950	H_2-4, O_2-270 N_2-130, C-260[d]
Ta-8 W-2 Hf (T-111)	950	1500	O_2-18, N_2-20, C-28[d]
Ta-10 W	800	1500	O_2-30, $N_2 < 10$, $C < 10$[d]

[a]Based on DPH hardness measurement.
[b]Time at temperature - 2 hr.
[c]Temperatures below 600°C not investigated.
[d]Billet analysis.

---

[36]Flinn, J. E., Jr., and Mayfield, R. M., Evaluation of New Fabrication Techniques for High Quality Refractory Metal Tubing. Technical Conference on Applied Aspects of Refractory Metals (AIME), December 9-10, 1963, Los Angeles, California. To be published in proceedings.

The annealing behaviors of Nb-5 w/o Zr (D-14) and Ta-10 w/o W are shown in Figures 43 through 45. An increase in hardness is noted in Figure 43 for the Nb-5 w/o Zr material after the full recrystallization temperature had been surpassed. A similar behavior has been reported for Nb-1 w/o Zr and was attributed to the solution of interstitial compound phases.[37]

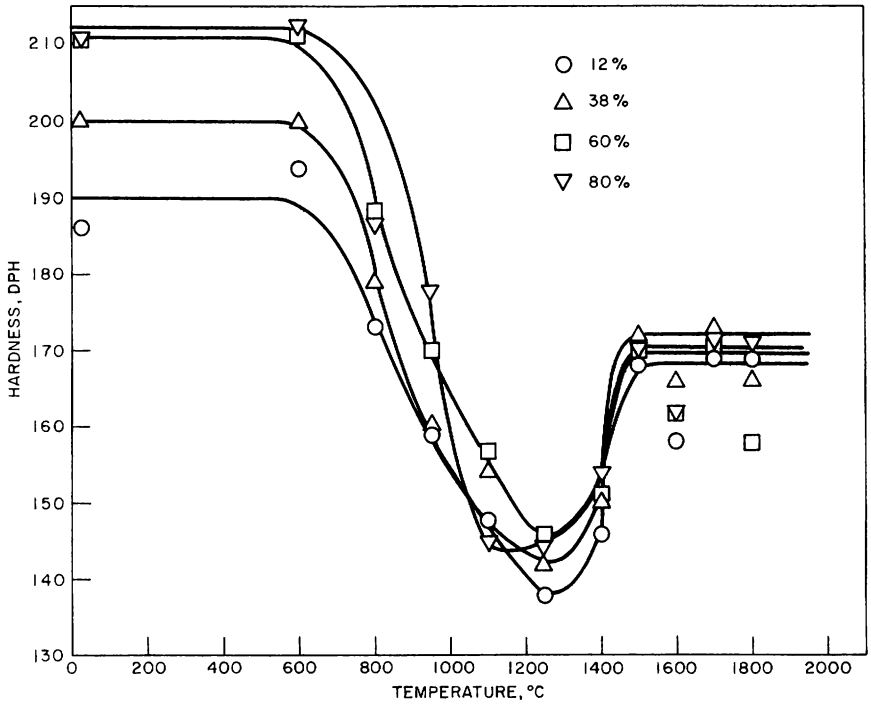

Figure 4

Isochronal Annealing Behavior of Nb-5 w/o Zr (D-14) before Repolishing

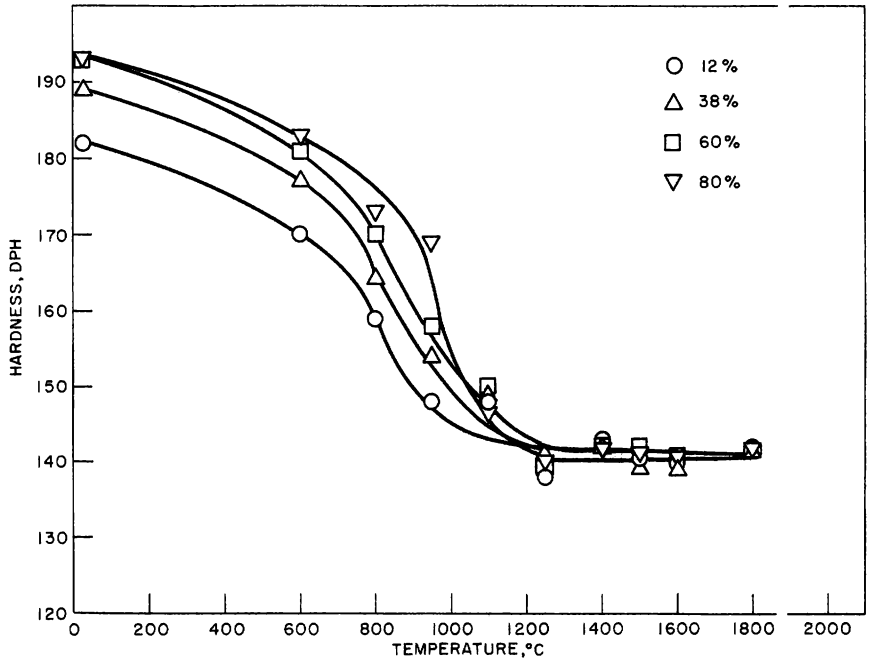

Figure 44

Isochronal Annealing Behavior of Nb-5 w/o Zr (D-14) after Repolishing

[37]Chang, W. H., A Study of the Influence of Heat Treatment on Microstructure and Properties of Refractory Alloys, DM-60-779, Contract AF33(616)-7125, Quarterly Report No. 3, November 960.

Figure 45. Isochronal Annealing Behavior of Ta-10 w/o W

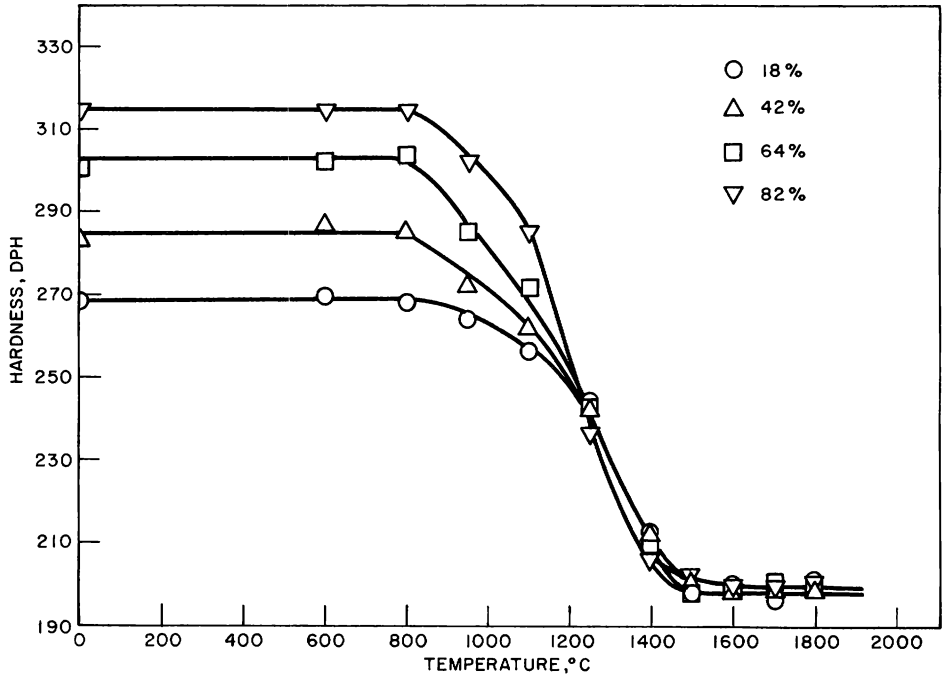

The hardness versus temperature curves of Figure 44 were obtained from the same specimens used in Figure 43. Each specimen was reground and polished to assure sufficient removal of any possible contamination layer that might have formed during annealing. Under these conditions of specimen preparation there is no evidence of a hardness increase at temperatures above that required for complete recrystallization, i.e., above 1300°C. The increase in hardness at elevated temperatures for the Nb-5 w/o Zr indicated in Figure 43 must therefore be pseudo in nature, representing a surface effect rather than the true effects occurring in the interior of the test specimen. Repolishing even had an effect on the as-worked hardness values, but to a considerably lesser degree than for the specimens annealed at the higher temperatures.

All of the alloys listed in Table XXIX exhibited a rise in hardness with the higher annealing temperatures until sufficient surface and subsurface contamination had been removed to reveal the true annealing behavior. The true annealing behaviors were similar to behaviors of the Nb-5 w/o Zr and the Ta-10 w/o W shown in Figures 44 and 45, respectively.

It is entirely possible that a hardness increase could occur by virtue of age-hardening effects, interstitial solutioning, etc., but this did not seem to be the case for the temperature or alloy parameters of this particular investigation.

d. Evaluation of Alloy Fabricability (F. J. Karasek)

The alloy-development phase of the overall fast reactor jacket development program has been concerned with small-scale alloying, arc casting, and rolling of a variety of refractory alloys that were not commercially available. The alloy button melts, while small, were generally large enough to provide 0.81-mm (0.032-in.)-thick corrosion coupons, as well as a knowledge of the rolling parameters.

The alloys that have received attention during the year are generally of the solid-solution type, devoid of intentional additions of dispersion and/or precipitation hardening elements. Strength at elevated temperatures is desired, but not at the sacrifice of fabricability. Although fabricability of refractory metals into bar, sheet, and structural shapes has been intensively studied, fabrication of these same materials into small-diameter thin-walled tubing has not received a great deal of attention. Tubing fabricability should receive major emphasis in selection of candidate tubing materials for the fast reactor program.

The alloys studied were consolidated from precleaned materials. The arc-melting procedures were such that a homogeneous product would be assured. Most of the alloys were jacketed in either mild steel or 304 SS to prevent contamination during hot rolling. The rolling practice was quite similar to that reported for foil production.[38]

The results of the alloy-fabricability study are summarized in Table XXX. The most fabricable binary alloys were Nb-10 w/o Ti, V-10 and 20 w/o Ti (TV-10 and TV-20), and the more easily workable ternaries were Nb-9 w/o Ti-3 w/o Mo, Nb-18 w/o Ti-4 w/o V and Nb-15 w/o Ti-6 w/o V, based on the methods and temperatures employed. Regarding the V-Ti alloys, interstitial analyses of the 0.81-mm-thick coupon stock yielded values averaging 850 ppm O_2 and 500 ppm C for TV-10, and 800 ppm O_2 and 450 ppm C for the TV-20 alloy.

The ease of workability of these alloys (TV-10 and 20) confirms earlier results reported by Smith,[39] even though different fabrication techniques were employed. Further, the interstitial contents of the final product were not reported in this ANL-sponsored work that was conducted at Armour Research. Based on the reported analysis of the starting material, however, the impurity level can be assumed to have been reasonably close to the values reported above.

---

[38]Karasek, F. J., Techniques for the Fabrication of Ultra Thin Metallic Foils, Nuclear Science and Engineering, 17, 365-370 (Nov 1963).

[39]Smith, K. F., and Van Thyne, R. J., Selected Properties of Vanadium Alloys for Reactor Application, ANL-5661 (May 1957).

Table XXX

FABRICABILITY EVALUATION OF SELECTED Nb, V, AND Zr ALLOYS
(Not commercially available)

Alloy Composition (Numerals indicate w/o)	Hardness As Cast	Hot Rolling Temp (°C)	Hardness after Hot Breakdown	Cold Reduction	Hardness after Cold Reduction	Remarks
Nb-5 Mo[a]	NA[b]	1000	NA	~25%	93 R_B	Some difficulty in cold working.
Nb-5 Mo[a]	NA	850	NA	10% initially 30% after anneal	20-24 R_C	1125°C anneal dropped hardness to 91 R_B.
Nb-10 Ti[a]	74-80 R_B	850	75-77 R_B	40% anneal then 50%	95 R_B	Works well.
Nb-10 V	20-21 R_C	950	20-23 R_C	Not attempted		(d)
Nb-20 V	28-31 R_C	1000 to 1150	-	-	-	(c)
Nb-39 V-1 Ti	25-27 R_C	1000 to 1150	-	-	-	(c)
Nb-9 Ti-8 V	96 R_B	850 to 1150	-	-	-	(c)
Nb-9 Ti-3 Mo[a]	75-79 R_B	850	92 R_B	60%	98 R_B	Works well.
Nb-15 Ti-6 V	87-90 R_B	950	87-91 R_B	50%	26-28 R_C	To be annealed prior to further cold working. Works well.
Nb-18 Ti-4 V[a]	85-90 R_B	650	90 R_B	68%	22-25 R_C	Works well.
V-10 Ti (TV-10)[a]	NA	850 (Air)	NA	50%	95 R_B	Works well.
V-20 Ti (TV-20)[a]	NA	850-900 (Air)	NA	50%	27 R_C	Works well.
V-40 Ti	24-26 R_C	1050	20-24 R_C	Not attempted	-	(d)
V-5 Mo	94 R_B	950	88 R_B	-	-	Unable to cold work without cracking.
V-50 Mo	28-36 R_C	1050 to 1150	-	-	-	(c)
V-20 Nb-5 Ti	30 R_C	1000 to 1150	-	-	-	(c)
65 V-35 Nb (AS-514)	28 R_C	850 to 1150	-	-	-	(c)
56 Zr-28 V-16 Ti (AS-537)	41-43 R_C	1000	43 R_C	-	-	(c) 1125°C anneal dropped hardness to 35 R_C.

(a) Alloy coupons supplied to Engineering Corrosion Group for evaluation of compatibility with sodium.
(b) Not available.
(c) Breakdown by hot rolling unsuccessful at temperatures indicated (Furnace limitation: 1150°C).
(d) Further hot rolling at higher temperature or high-temperature anneal required.

Corrosion coupons also have been fabricated from various commercially available materials: pure Nb, Nb-1 w/o Zr (D-11), Nb-5 w/o Zr (D-14), and Nb-10 w/o Ti-5 w/o Zr (D-36). The workability of these Nb-base alloys had already been established, and no difficulties were experienced. The coupons have been delivered to the Engineering Corrosion Group for Na compatibility studies.

e. V-10 w/o Ti and V-20 w/o Ti Alloy Scale-up (W. R. Burt, Jr., R. D. McGowan, R. A. Beatty, W. C. Kramer, F. J. Karasek, and R. M. Mayfield)

The V-10 w/o Ti (TV-10) and V-20 w/o Ti (TV-20) alloys were scaled up to 3.8-cm (1.5-in.)-diameter ingots and extruded to bar stock for studies of mechanical properties, compatibility with fuel and coolant, as well as a more thorough study of fabrication parameters.

The decision to scale-up these alloys was predicated upon the following facts: (1) the cross section of both vanadium and titanium is favored for fast reactor applications, (2) initial evaluations of fabricability were encouraging, (3) the existing niobium alloys were not encouraging from the standpoint of compatibility with sodium, and (4) the materials could not be purchased commercially within a reasonable amount of time. From the availability standpoint, the vanadium field is rather barren (see Table XXVII, p. 87).

Consolidation by Melting

The charge materials for melting consisted of vanadium chips (400 ppm O_2, 500 ppm C, 200 ppm N_2, and 40 ppm H_2) procured from the Union Carbide Metals Co. and titanium plate (250 ppm O_2, 100 ppm C, 20 ppm N_2, and 10 ppm H_2) purchased from the Chicago Development Corporation. The vanadium chips were consolidated into a 6.85-cm (2.8-in.)-diameter ingot by nonconsumable arc melting, followed by remelting into a 3.81-cm (1.5-in.)-diameter ingot in the electron beam (EB) furnace. The vanadium ingots were wrapped with titanium sheet and drip melted into alloy ingots in the EB furnace. To promote homogeneity, the TV-10 alloy was double melted and the TV-20 alloy triple melted. Analyses showed the ingots to be rich in titanium at the extreme bottom and depleted in titanium at the extreme top due to the alloy-electrode design and subsequent rod "melt-off" characteristics of the electron beam. The main body of the ingots showed fair homogeneity, although further improvement will be required.

The ingots were scalped to a 3.41-cm (1.34-in.) diameter to remove all surface defects. Ultrasonic inspection of the ingots revealed no internal defects. Following inspection, the ingots were machined into extrusion billets approximately 16.2 cm (6.375 in.) in length.

Extrusion of Ingot Stock

The machined alloy billets were canned in 304 SS for extrusion. The overall dimensions of the canned extrusion billet were 4.95 cm (1.95 in.) in diameter by about 19.1 cm (7.5 in.) long. The billets were induction heated to 1110°C, soaked at temperature for 5 min, and extruded at 14.2 cm/sec (5.6 in./sec) through a 1.865-cm (0.734-in.)-diameter die corresponding to a 7.7:1 reduction ratio. The average running extrusion pressures measured 4,200 kg/cm^2 (59,800 psi) for TV-10 and 4,400 kg/cm^2 (62,700 psi) for TV-20, in contrast with 3,660 kg/cm^2 (52,000 psi) for a 304 stainless steel billet extruded at the same temperature.

X-radiography of the extruded composite bars revealed that the TV core materials were nonuniform in diameter and showed a

rippled appearance. After decanning, the cores were found to have deep, full-length longitudinal striations, possibly caused by the large as-cast grain size.

Product Evaluation

The results of interstitial analyses based upon samples taken from the lead, middle, and tail ends of both extrusions are reported in Table XXXI.

Table XXXI

RESULTS OF INTERSTITIAL ANALYSES ON EXTRUDED BAR STOCK OF TV-10 AND TV-20 ALLOYS

Alloy	Element	Analytical Results (ppm)		
		Lead	Middle	Tail
TV-10	O[a]	300	300	400
	C	365	326	322
	N	320	360	382
TV-20	O[a]	700	600	600
	C	352	408	316
	N	372	288	324

[a]Oxygen results converted from w/o.

The higher oxygen content of TV-20 was traced to an annealing of the titanium alloy stock prior to EB melting. No analysis was made of the annealed product, but the evidence is strong that the vacuum annealing was not carefully controlled.

Metallographic examinations were made on transverse and longitudinal samples taken from the lead, middle, and tail ends of each extrusion. The rods were uniform in structure along their length, with the typical "as-extruded" structure shown in Figure 46. Both alloys exhibited a fine grain size, approximately 90% recrystallized. Bands oriented in the extrusion direction were evident in the microstructure, with few grains existing within these bands. Also evident in the longitudinal direction were long dark stringers of a fine, discontinuous network of particles.

Measurements of the diamond pyramid hardness of the extruded rods gave the results shown in Table XXXII. The hardness increase along the length of TV-10 is most likely associated with a gradual increase in titanium content from 8.6 w/o at the lead end to 10.3 w/o at the tail end. [For comparison, 304 stainless steel extruded at 1100°C measured 137-139 DPH (74 R_B).]

Figure 46. As-extruded Microstructure of Titanium-Vanadium Alloys; a) V-10 w/o Ti, b) V-20 w/o Ti

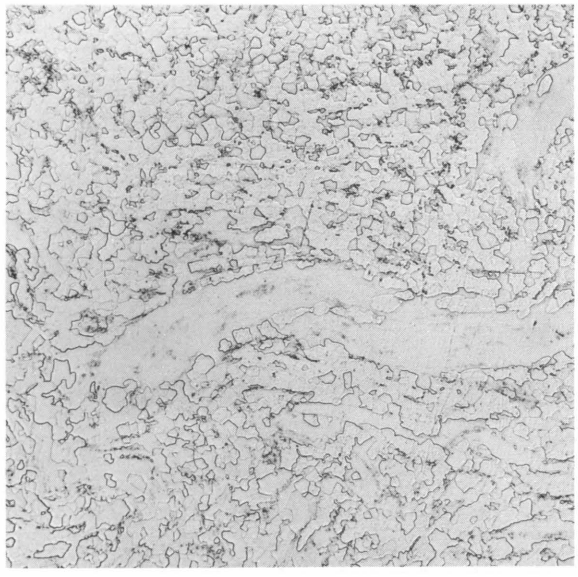

Micro 37632 Transverse ~130X

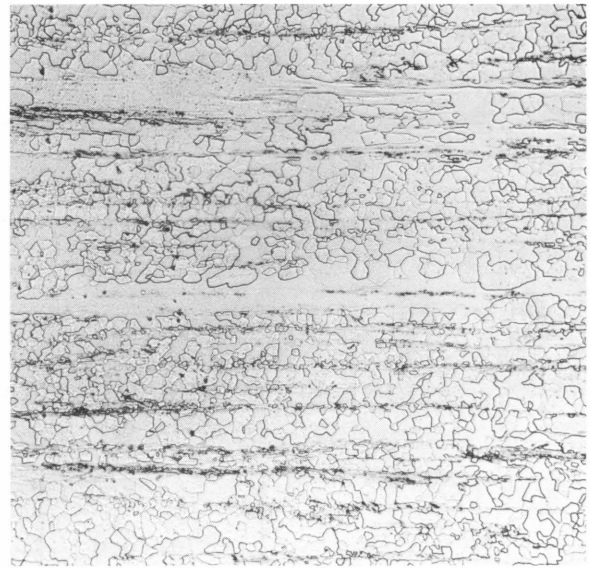

Micro 37633 Longitudinal ~130X

(a) TV-10

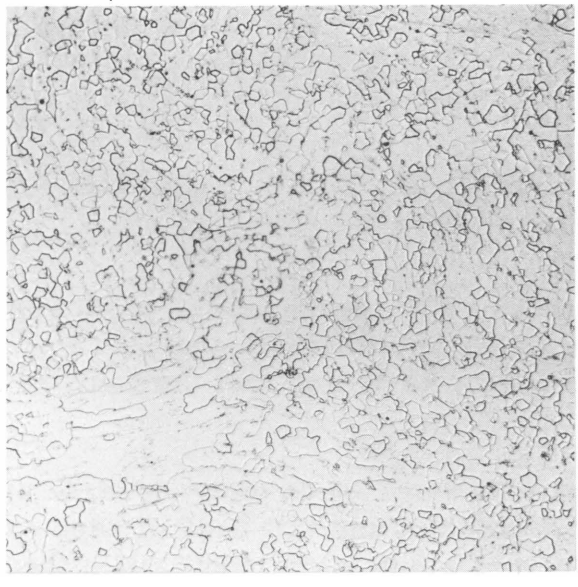

Micro 37635 Transverse ~130X

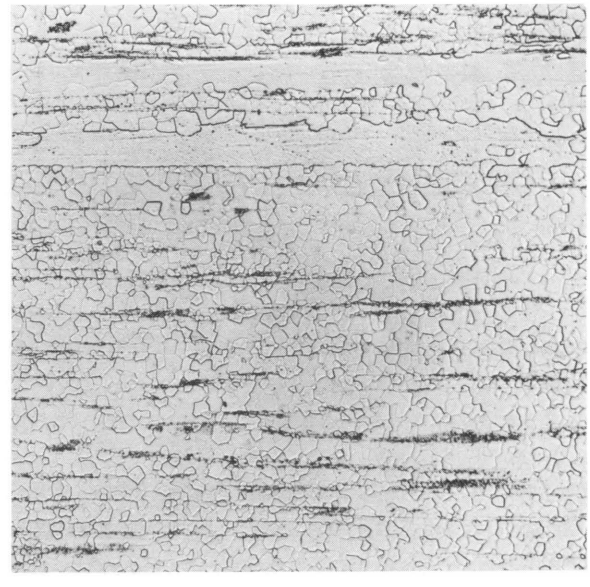

Micro 37636 Longitudinal ~130X

(b) TV-20

Etchant: 5% HF and 2% $AgNO_3$

In an effort to determine if the as-extruded alloys were in a "dead-soft" condition and essentially fully recrystallized, extruded material was heat treated in vacuum for 1 hr from 800 to 1200°C in 100° increments. Hardness measurements after heat treatment are reported in Table XXXIII.

Table XXXII

AS-EXTRUDED HARDNESS VALUES FOR THE
TV-10 AND TV-20 ALLOYS

Section	DPH Hardness (10 kg load)							
	TV-10				TV-20			
	Transverse		Longitudinal		Transverse		Longitudinal	
	DPH	R_B	DPH	R_B	DPH	R_B	DPH	R_B
Lead end	170	(86)	172	(86)	232	(98)	235	(98)
Middle	181	(88)	186	(89)	233	(98)	233	(98)
Tail end	187	(89)	199	(92)	236	(98)	233	(98)

Table XXXIII

HARDNESS CHANGES IN TV-10 AND TV-20 ALLOYS
AS A RESULT OF HEAT TREATMENT

Specimen Condition	DPH (10-kg load) and R_B Hardness							
	TV-10				TV-20			
	Transverse		Longitudinal		Transverse		Longitudinal	
	DPH	R_B	DPH	R_B	DPH	R_B	DPH	R_B
As extruded	187	(89)	199	(92)	236	(98)	233	(98)
1 hr @ 800°C	169	(85)	172	(86)	207	(93)	212	(94)
1 hr @ 900°C	160	(83)	164	(84)	206	(93)	213	(94)
1 hr @ 1000°C	167	(85)	173	(86)	216	(95)	222	(96)
1 hr @ 1100°C	163	(84)	161	(83)	216	(95)	227	(97)
1 hr @ 1200°C	173	(86)	182	(88)	222	(96)	233	(98)

In TV-10, the microstructure revealed a slight amount of grain coarsening at 1000°C, whereas at 1100°C small grains appeared at grain boundaries and additional grain growth was quite evident. A few grains were also visible in the long stringers of discontinuous particles. Heating at 1200°C resulted in marked grain growth, and the grains in the long stringers became larger, more profuse, and outlined by the particles. There also was evidence of particles appearing within the original grains.

Similar effects were observed with the heat-treated TV-20 alloy. Slight softening occurred, but the heat-treated hardness increased with increasing temperature. Very slight grain coarsening occurred at 1000°C, whereas at 1100°C further growth was evident, together with small grains appearing at grain boundaries and in the stringers. Particles also were visible within the grains after the 1100°C treatment, similar to that

seen in TV-10 after the 1200°C treatment. Heat treating the TV-20 alloy at 1200°C resulted in further grain growth and profuse amounts of particles present within the grains. The increase in hardness with increase in heat-treat temperature may be attributed to the increased amount of particles formed.

Isochronal annealing studies of the TV alloys are under way, as well as of unalloyed vanadium, to determine stress-relieving and recrystallization behavior as a function of cold work. Small TV arc melts are being prepared covering a range of oxygen and titanium contents in order to determine compatibility with sodium and fabricability as a function of composition.

Additional TV material is being prepared on a larger scale with improved homogeneity to provide stock for extrusion studies which, in turn, will yield controlled material for evaluation purposes by other laboratory groups. Tubing fabrication will receive considerable emphasis once this new material is available for processing.

f. Duplex Tubing (W. R. Burt, Jr., and J. E. Flinn, Jr.)

A duplex tube consisting of stainless steel or Hastelloy-X on the exterior of a refractory metal tube (or liner) may offer a possible simultaneous solution to the corrosion problem that has been experienced in certain refractory metals after exposure to 650°C sodium containing 100-200 ppm oxygen and to the problem of compatibility of the fuel.

Three methods of obtaining such a tube are currently being investigated: (1) coextrusion followed by secondary fabrication, (2) codrawing of two tubes with or without a diffusion-bonding annealing treatment, and (3) plasma-spraying 304 SS on the OD of a suitable refractory metal tube.

Coextrusion

The initial work consisted of extruding a vanadium rod canned in 304 SS at 1200°C. Ultrasonic examination indicated a sound bond between the 304 SS and vanadium core. The outer surface was cleaned and a hole was drilled in the vanadium core to form a duplex tube, 1.268 cm (0.499 in.) in OD and 0.873 cm (0.344 in.) in ID. The wall consisted of equal thicknesses of stainless steel and vanadium. The tube was ironed on a non-deformable mandrel to a 1.029-cm (0.405-in.) OD and a 0.850-cm (0.335-in.) ID. Ultrasonic inspection at this point showed only 50% of the 304 SS/V interface to be bonded. The tube was vacuum annealed at 850°C, ironed to a 0.923-cm (0.362-in.) OD and 0.729-cm (0.312-in.) ID, and reannealed. A copper ductile core was inserted in the tube and the composite assembly drawn to a tube size of 0.572-cm (0.225-in.) OD x 0.485-cm (0.191-in.) ID. The copper core was removed and after annealing, the duplex tube was sunk

to a final size of 0.442-cm (0.174-in.) ID and 0.047-cm (0.018-in.) wall thickness. Characteristics of the bond are being evaluated by nondestructive testing.

To provide additional material, a 5.08-cm (2-in.)-diameter 304 SS/V duplex billet was extruded at 1200°C by conventional mandrel techniques at a 19.3:1 reduction ratio. Radiography and metallography showed no apparent nonbond areas. The vanadium portion of the tube showed a duplex structure of recrystallized grains with fine bands of unrecrystallized material aligned parallel to the extrusion direction. Following a nondestructive examination for bond quality and defects, the tubing will be processed to small-diameter thin-walled tubing.

Extrusion of niobium granules in a 304 SS billet to form a 304 SS/Nb duplex tube resulted in a poor quality extruded tube not acceptable for further fabrication. The niobium granules were not compacted uniformly during extrusion, thereby resulting in a rippled tube over a majority of the extruded length. Small areas of acceptable tubing indicated that the technique may be feasible. Further work will be done with a new billet design incorporating a precompaction prior to actual extrusion.

An attempt to extrude a 304 SS/Nb-4 w/o V duplex tube at 1100°C and a 18:1 reduction ratio was unsuccessful, for the press stalled before extrusion was initiated.

Codrawing

Although it is desirable to have a metallurgical bond in duplex tubing, the possibility that a good mechanical bond will be acceptable has not been eliminated. In an effort to obtain a mechanically bonded duplex tube, 304 SS and Hastelloy-X tubing have been codrawn over Nb-1 w/o Zr, Nb-5 w/o Zr, and Nb-33 w/o Ta-1 w/o Zr. Drawing reductions were between 30 and 40%. The tubing is near finished size and is being evaluated for bonding and defects by nondestructive testing.

Some of the codrawn tubing will be annealed at relatively high temperatures in order to obtain a diffusion layer between the two materials. Earlier work has shown that anneals at approximately 1200°C will result in a diffusion layer of about 0.0025 mm (0.0001 in.).

Plasma-sprayed Coatings

To prevent exposure of the outer surface of a refractory-metal cladding to contamination in unpure sodium at moderate temperatures, the feasibility of spraying 304 SS on that surface for protection is being investigated. Nb-1 w/o Zr bars with a plasma-sprayed surface layer have been corrosion tested in sodium with apparent corrosion of the base

materials. Two Nb-1 w/o Zr tubes with a plasma-sprayed, 0.012-cm (0.005-in.)-thick 304 SS surface has been delivered to the Engineering Irradiation Group for "in-pile" irradiation capsule testing.

7. Fabrication of U-Mo Alloys for Blanket Rod Stock

(H. C. Katiyar,* R. A. Beatty, and R. M. Mayfield)

An evaluation of U-Mo alloys, whose production has been described elsewhere,[40] as a possible high-temperature fast reactor blanket material has necessitated development of suitable fabrication techniques for alloys containing up to 14 w/o molybdenum. Fabrication parameters for the alloys of lower molybdenum content have been fairly well established. Starting material for fabrication consisted of 7.6-cm (3-in.)-diameter ingots produced by vacuum induction melting and casting.

Rod rolling, extrusion, and recasting of a U-14 w/o Mo alloy were evaluated as methods for producing bar stock for machining to .04-cm- and 0.80-cm-diameter blanket slugs. As-cast material whose microstructure is shown in Figure 47a was fabricated. The dendritic structure is a probable reason for the erratic nature of the fabrication results. A homogenization heat treatment of 20 hr at 1000°C resulted in the microstructure shown in Figure 47b. Heat treating for 8 hr at 1000°C produced a similar structure. Fabrication experiments will be repeated using homogenized cast material. Hopefully, the material will be more amenable to fabrication and result in better quality material.

The results of fabrication studies of as-cast U-14 w/o Mo are discussed below.

Rolling

U-14 w/o Mo bars, 2.54 cm in diameter, were hot rolled both bare and with 0.63-cm-thick Zircaloy-2 jackets. Bare material was rolled out of chloride salt at temperatures ranging from 950 to 1030°C. All rolled material was characterized by deep circumferential cracks along the total length of the bar. Jacketed material was rolled at temperatures ranging from 950 to 1170°C. It appears that 1000-1100°C is the best rolling temperature, for the U-Mo alloy exhibited cracking at 950°C and possible hot shortness above 1100°C. This latter behavior may be due to the nonhomogeneous cast material. At 1000-1100°C, the as-cast material could be reduced 10-15% per pass. Nose bursts and end tears were often evident.

---

*INSE Participant.

[40] Loveland, C. W., and Owen, J. E., Production of Molybdenum-Uranium and Zirconium-Uranium Alloys, Union Carbide Nuclear Co. KY-348 (Aug 1960).

Figure 47a. Microstructure of As-cast U-14 w/o Mo

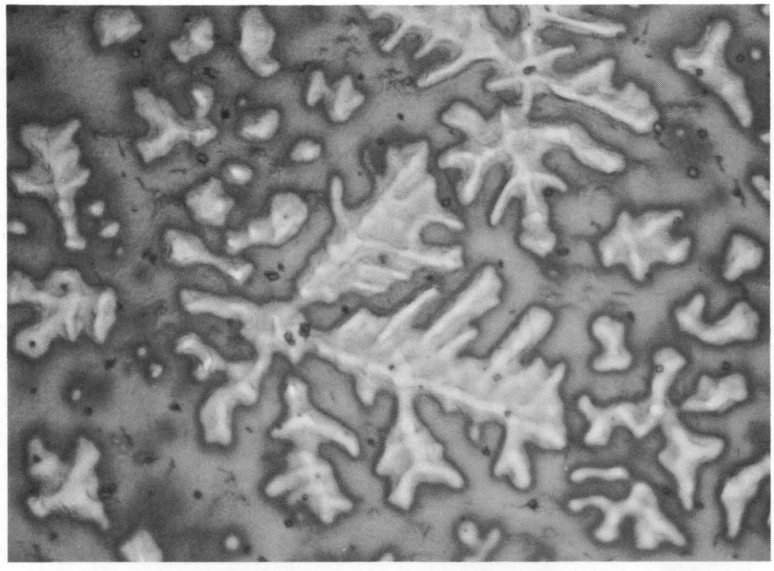

Micro 38021 250X

Etchant: (1) 1/2 nitric acid - 2 citric acid - 97.5 water; electrolytic
(2) Phosphoric acid electrolytic for film removal

Figure 47b. Microstructure of Cast U-14 w/o Mo after a Homogenization Heat Treatment of 20 hr at 1000°C

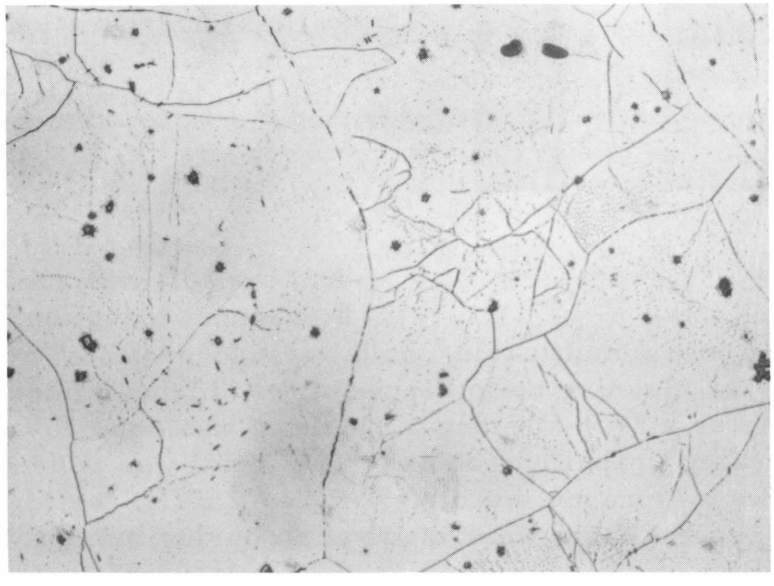

Micro 38020 250X

Etchant: Same as above

Extrusion

Both Zircaloy-2-jacketed and bare U-14 w/o Mo billets were extruded on a 150-ton vertical extrusion press at a speed of 2.54 cm/sec. Extrusion ratios ranged from 4.0 to 5.3:1, and extrusion temperatures were varied between 725 and 1000°C. Billets extruded at 1000°C were relatively uniform in diameter, but exhibited severe circumferential cracking or checking. The severity of this cracking decreased with decreasing extrusion temperatures. However, as the temperature was lowered, deep longitudinal striations and a nonuniform diameter resulted. This can be seen in Figure 48, showing U-14 w/o Mo extruded bare at three different temperatures. The use of a Zircaloy cladding on the billets did not eliminate the cracking or striations and led to further variance in the extruded diameters due to the relative softness of Zircaloy compared with U-Mo at the extrusion temperatures employed. The use of a stronger jacket material as well as incorporation of a homogenizing heat treat for as-cast material should improve extrusion results.

Figure 48. Surface Appearance of U-14 w/o Mo Extruded Bare at: (a) 1000°C, (b) 870°C, (c) 750°C

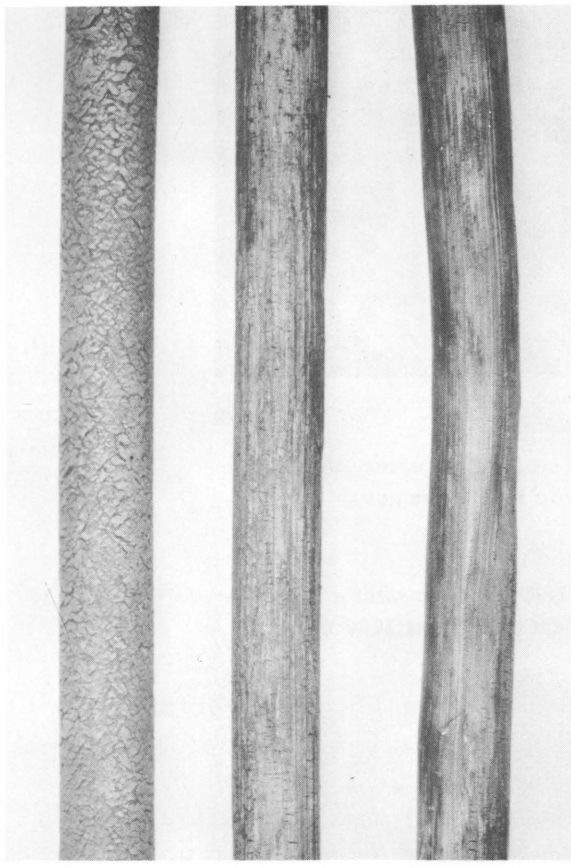

Macro 37282 1X
(a) (b) (c)

Casting

Casting U-14 w/o Mo into 1.27-cm-diameter x 30-cm-long bars by vacuum induction melting and bottom pouring into a multicavity mold was successful. These castings were suitable for cleaning up to the required finished dimensions of 1.04-cm diameter x 27.9-cm length. Melting was done in a "Korundal" (80% Al_2O_3)-coated graphite crucible. The metal was poured into a graphite mold with a flame-sprayed mullite ($3\ Al_2O_3 \cdot 2\ SiO_2$) coating on the mold cavities. Successful casts were made at a pouring temperature of 1750°C.

8. Fabrication Development for FARET Test Fuel Elements for Physics Experiments (J. H. Handwerk and A. J. Carrea*)

The fuel design of the test core of the FARET reactor requires a ceramic piece in the form of a cylinder, 6.90 cm in length and 1.27 cm in

*Resident Research Associate, Comision Nacional de Energia' Atomica, Argentina.

diameter, which has a central longitudinal hole and 12 surface projections. Six of these projections are on the diametrical surface of the cylinder to space the fuel cylinder centrally in the jacketing tube. Three projections are on each end of the fuel cylinder to space the fuel pellets lengthwise in the fuel tube. The central hole is a thermocouple well; however, for out-of-pile testing the fuel pellet design was modified to use the central hole for a resistance heater. Three additional holes equally spaced around the central hole were incorporated in the design, and these holes were to be used for thermocouple instrumentation.

The test core fuel is to be either UO_2-PuO_2 or UC-PuC. Since UO_2 is a more convenient material to use, fabrication development was started with this material. The fuel pellet could be formed either by extrusion or isostatic pressing. To expedite the fabrication of samples, the extrusion process was selected.

UO_2 was mixed with 4 w/o glycerine, 2 w/o methyl cellulose, and 12.15 w/o water. This mixture was extruded over a core bridge and through a fluted die to form rods having the necessary four holes and three flutes the full length of the rod. The rods were dried, sectioned, and flutes machined to form the surface projections on the diameter and ends. After machining the specimens were sintered in hydrogen for 4 hr at 1700°C. Sintered densities of the specimens varied from 10.3 to 10.6 gm/cc (90-95% of theoretical density). Specimens were neutron radiographed and tested with a dye penetrant for cracks and voids prior to assembly in the test tubes.

Initial out-of-pile heating tests resulted in the fracturing of all test specimens. Thermal stresses can be estimated by the Timoshenko formula[41] if uniform heat distribution and steady-state conditions can be assumed. Table XXXIV compares the three ceramic fuel materials on which more information is available. From these data and some conservative assumptions for safety coefficients, it appears that a linear heat flux of 10 to 12 W/cm applied to high-density UO_2 would produce considerable fracturing of the UO_2 pellets. Based on the present design of the fuel pellet, the out-of-pile heating tests appear to confirm this estimate.

From the data in Table XXXIV it appears that UC would withstand a linear heat flux in excess of 30 W/cm which is anticipated in the FARET test core. Test specimens of UC were, therefore, prepared by first crushing arc-melted UC buttons to a particle size of $<44\ \mu$. This powder was preformed in a steel die, and the resulting cylindrical blanks were sintered in vacuum at 1650°C. The blanks were machined to size on the outer surfaces, and a central hole was drilled in each pellet. During machining many

---

[41] Carter, J. C., Temperature and Stress Distribution in Spheres, Rods, Tubes, and Plates, ANL-4690 (Sept 1951).

of the pellets developed fissures; however, sufficient pellets were selected, and, when tested, appeared to withstand a heat flux of about 30 W/cm. Based on these encouraging results, additional UC samples are being fabricated in addition to less complex specimens of UO_2.

Table XXXIV

ESTIMATED MAXIMUM PERMISSIBLE FUEL HEAT FLUXES FOR FARET DESIGN

	UO_2[a]	UC[b]	UN[c]
Estimated Sintering Density, Percent of Theoretical	95	90	80
Temperature Operation, 800°C			
q_v, W/cm^3	5.6[a]	47	30
q_l, W/cm	33[a]	205	400
ΔT, °C	72	70	60
Temperature Operation, 1000°C			
q_v, W/cm^3		27	
q_l, W/cm		115	
ΔT, °C		40	
Temperature Operation, 1200°C			
q_v, W/cm^3	3.8[a]	deformed	15
q_l, W/cm	21[a]	plastically	300
ΔT, °C	72	-	45

q_v = Volume heat generation. q_l = Linear heat flux.
ΔT = Maximum temperature drop along the radius.

(a) Values of mechanical and physical properties taken from Uranium Dioxide. Properties and Nuclear Applications, edited by J. Belle, Naval Reactors, Division of Reactor Development, U.S.A.E.C. The thermal conductivity value at 800°C is the one used for FARET calculations and also the most optimistic one. A more conservative value reduces the linear heat flux by a third. The fracture stress, $\sigma_t = \sigma_2$ = 13,000 psi, is 50 to 100% higher than the values obtained on extruded samples of the design proposed for FARET.

(b and c) Values from K. M. Taylor and C. H. McMurtry, Synthesis and Fabrication of Refractory Uranium Compounds, Contract No. At-(40-1)-2558, The Carborundum Company, ORO-400 (Feb 1961).

9. Nondestructive Tests of Experimental Fast Reactor Components

a. Electromagnetic Tests of Tubing for Fast Reactor Development (C. J. Renken)

Electromagnetic test methods have been applied to the testing of various types of tubing of interest in the fast reactor development program. Among the materials which have been encountered are: Hastelloy-X, Nb-1 w/o Zr, 304 SS, D-43, Nb-5 w/o Zr, Ta-10 w/o W, Ta, Nb-10 w/o Ti-1 w/o Zr, and Nb-33 w/o Ta-1 w/o Zr, as well as various combinations of duplex tubing, and both Hastelloy-X and 304 SS with coatings of vapor-deposited tungsten on the inner circumference. Tubing was tested in a wide variety of diameters and wall thicknesses. Alloys which were the subject of tubing fabrication development were often tested in a range of sizes corresponding to various steps in the fabrication process. In general, tubes of 0.508-mm and thinner wall thickness were tested by electromagnetic methods, whereas those with a thickness of 0.508 mm and over were tested by ultrasonic methods.

Electromagnetic test methods are most efficiently applied to the rapid inspection of large quantities of tubes of a particular type. The utilization of this method for tests on a wide variety of alloys, diameters and wall thicknesses is inherently an inefficient process because of the time involved in setting up test equipment for each separate test problem, and because so many standards are necessary in order to provide test results which are relatively quantitative. Unfortunately, it has been found necessary to test tubes with either an electromagnetic or ultrasonic method in addition to radiography because quite often fine cracks cannot be detected by the latter method, particularly if they follow a curved path with respect to the tube radius. An example is shown in Figure 49.

Figure 49. A Microphotograph of a Transverse Section of Ta-10 w/o W Tubing, of 3.96-mm ID and 0.38-mm Wall, Showing a Crack Emanating from the Inside Surface

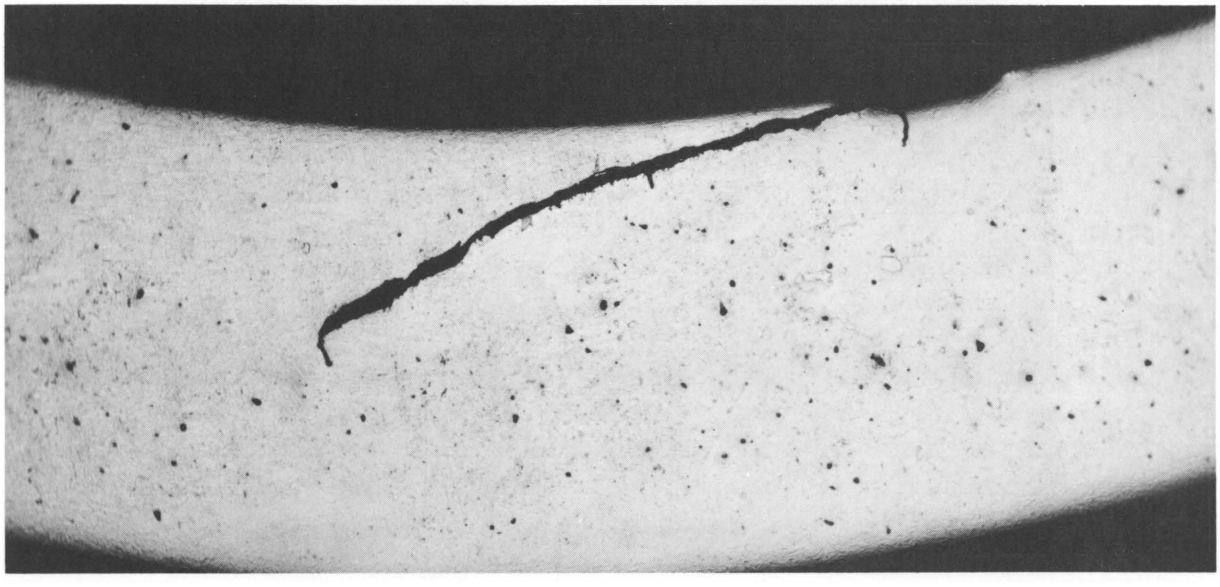

Micro 36975 150X

Tubing made from refractory alloys presents no special problems for electromagnetic inspection methods. Duplex tubes are very difficult to test, however, unless a very uniform bond between the tubes has been achieved. Electromagnetic tests of stainless steel or Hastelloy-X tubes with vapor-deposited tungsten on the inner surface have not been satisfactory because of the variations which occur in the strictly mechanical bond between the two metals.

b. Ultrasonic Tests on Tubing for Fast Reactor Development (R. H. Selner)

In the past year, ultrasonics has been applied to the inspection of a wide variety of components being developed for fast reactor applications. As many of these materials have not been inspected at Argonne previously, considerable effort was necessary to understand and interpret ultrasonic indications. Considerable experience has been acquired in the testing of tungsten, vanadium, molybdenum, titanium, niobium, and stainless steel. An example of a defect detected by ultrasonics which would have been very difficult to discover by other testing methods is shown in Figure 50.

Figure 50. Crack Detected in 406 SS Welded Tubing by an Ultrasonic Technique

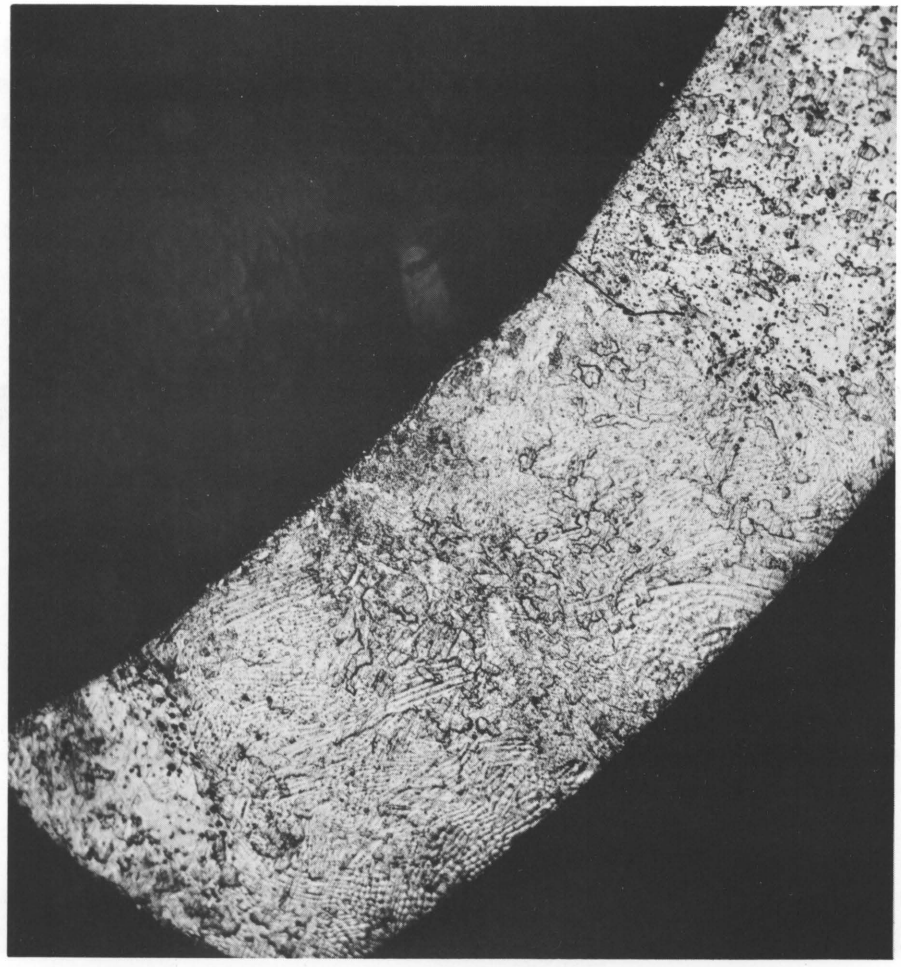

Micro 36578 50X

c. Radiography of Tubing for Fast Reactor Development (N. P. Lapinski)

Numerous radiographs were made of tubing used or produced for general fast reactor development. Most of the tubing radiographed appeared to be of good quality; however, some defects were noted in a few lots, the highest rejection rate appearing in 0.38-mm-wall Hastelloy-X and stainless steel. The defects in this tubing were generally of the same type, appearing on the inner wall, with depths of approximately 0.025 mm to 0.10 mm.

In addition to the radiography of ordinary tubing, radiographs were made of tungsten-coated Hastelloy-X and stainless steel tubing. Radiographs of this tubing serve a twofold purpose, namely, to approximate the amount of tungsten deposited on the wall of the tubing, and to show if any imperfections appear in the tungsten deposit. The amount of tungsten deposit is approximated by radiographing the tubing along with known thicknesses of tungsten foils and a tube of the same dimensions as that of the precoated tubing. After film processing, density measurements are made at various points on the coated tubing and compared with density measurements taken of the tungsten foils and precoated tube.

Some of the imperfections which appear in the tubing are shown in Figure 51, which shows a flaking condition which was very prevalent in one lot of Hastelloy-X tubing.

Figure 51. Reproduction of Radiograph Showing Flaking of the Tungsten Deposit in Hastelloy-X Tubing

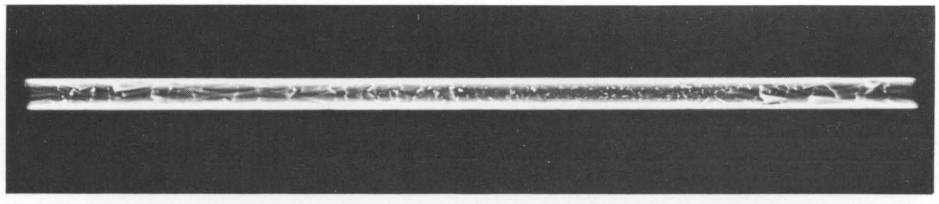

Micro 38059

d. Inspection of EBR-II Core-I Jacket Tubing (C. J. Renken)

Type 304 stainless steel tubing of 3.96-mm ID and 0.229-mm wall is to be used for reloading the EBR-II. A total of 3720 of 1.8-m-long tubes were tested this year. A reject rate of 19% occurred. A 10% localized reduction in wall thickness for any reason will normally cause the rejection of a tube, but many of the rejects in this case were caused by the existence of an electrically conductive brittle deposit on the tube inner surface. Analysis showed that the deposit contained about the same percentage of iron, nickel, and chromium as does ordinary 304 stainless steel. The deposit tended to occur in layers from 0.002 mm to

0.01 mm thick over areas up to 90° of the tube circumference and 12 mm along the axis. Since the deposit was brittle and very weak, there was a possibility that it would interfere with the sodium bond. Accordingly, tubing from this order was not used.

Sometime later a pilot quantity of new tubing arrived from the fabricator. Testing stopped after 40% of the initial 397 m had been rejected, mostly because of nonmetallic inclusions in the tube walls.

Full-scale inspection was resumed upon the arrival of a third order of tubing. Of the first 2251 tubes inspected, 15.2% were rejected. Evaluation of the defects detected indicated that many were radial cracks in the weld interface of up to 90% of the tube wall. This type of defect is potentially so serious that it is doubtful if any of this third order of tubing will be used.

A pulsed-field differential test system was used in these tests up until about mid-year. This equipment was then replaced by a pulsed-field system with a coaxial mask-aperture assembly, since careful correlation of the test results from both systems had shown that the mask-aperture system provided better resolution and also required much less maintenance. Tube axial velocity for all of these tests was 3.6 m/min.

B. Development and Fabrication of BORAX-V Superheat Fuel Elements

1. Fabrication of BORAX-V Superheat Fuel Elements

The fabrication of BORAX-V superheat fuel elements has proceeded on three fronts: (1) and (2) evaluation and assembly of the 304L and 406 stainless clad fuel plates, and (3) fabrication development associated with superheat elements of advanced design. Progress made during the year in each of these areas is outlined below.

a. Evaluation and Assembly of Type 304L Stainless Steel Plates (W. C. Kramer)

The present superheat fuel for BORAX-V consists of plates containing a dispersion of UO_2 in 304B stainless steel clad with 304L stainless steel. Atomics International fabricated the plates. Evaluation and assembly of the fuel plates into elements was done at ANL.

During the year, fabrication of the required 35 superheat fuel elements was completed. Details of the operations, and evaluation are found in a final report[42] and in earlier Metallurgy Division annual reports.[43,44]

b. Evaluation and Assembly of Type 406 Stainless Steel Plates (W. C. Kramer and R. M. Mayfield)

The testing of two instrumented, 406 stainless steel-clad fuel elements in BORAX-V is intended to establish the acceptability of 406 stainless steel for this type of nuclear superheat application. The choice of 406 stainless steel was made primarily on the basis of superior corrosion resistance exhibited during testing under simulated reactor steam conditions. Atomics International has fabricated fifty 406 stainless steel-clad fuel plates from which the two fuel elements are to be assembled.

Inspection of the fuel plates has been completed. Three plates were rejected because of inadequate side cladding. In addition to the nondestructive inspection techniques, several samples from end cladding coupons furnished by the vendor were polished and etched for clad-to-clad bond examination. Some bond-line inclusions were found, as seen in Figure 52, but they were not continuous and were therefore considered acceptable.

---

[42] Kramer, W. C., and Bean, C. H., Fabrication of UO_2-Stainless Steel Dispersion Fuel for BORAX-V Nuclear Superheat, ANL-6649 (Dec 1963).

[43] Annual Report for 1961, Metallurgy Division, ANL-6516, p. 82.

[44] Annual Report for 1962, Metallurgy Division, ANL-6677, p. 69.

Figure 52. Longitudinal Sections through the 406 Stainless Steel End Cladding of a Depleted Superheat Fuel Plate Showing Bond-line Inclusions

Micro 36101 Etchant: 5 v/o Chromic Acid; 95 v/o H_2O 100X

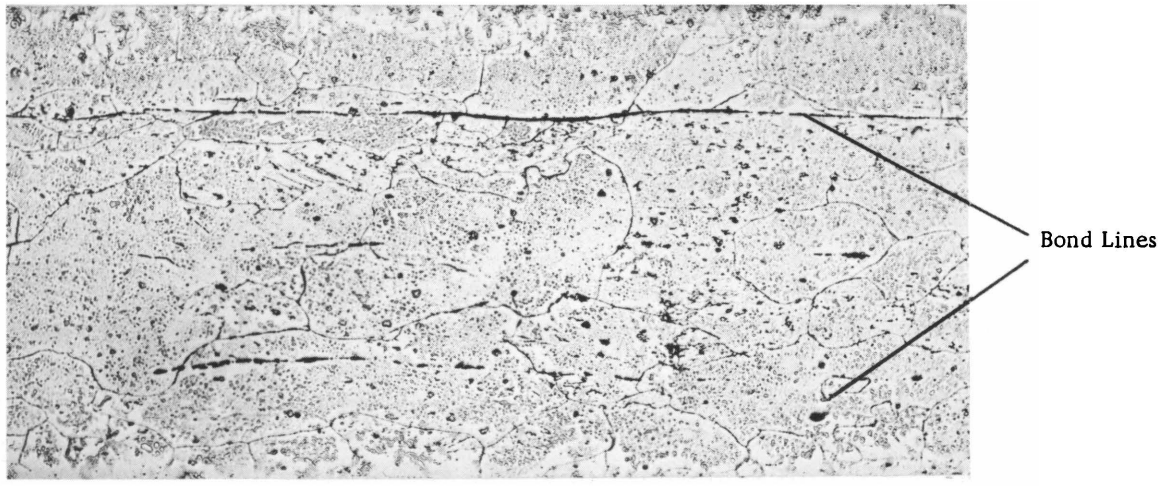

Micro 37339 Etchant: 50 v/o HNO_3; 50 v/o H_2O 100X

Brazing of the 406 stainless steel fuel subassemblies cannot be satisfactorily accomplished unless the formation of oxides on the fuel plate surfaces is prevented.[45] Application of a thin nickel plate [less than 0.0015 cm (0.0006 in.) thick] to a descaled 406 stainless steel plate will prevent oxidation and permit successful vacuum furnace brazing with Coast Metals 60 (20 w/o Cr, 10 w/o Si, 3 w/o Fe, balance Ni), Premabraze 128 (72 w/o Au, 22 w/o Ni, 6 w/o Cr), or Nioro (82 w/o Au, 18 w/o Ni). Sections of specimens brazed with Coast Metals 60 and Premabraze 128 have been tested in oxygenated steam at 650°C and 42.2 kg/cm^2 for 68.7 days. No significant corrosive attack was found. A section of the specimen brazed with Nioro is now being corrosion tested under similar conditions.

[45] Annual Report for 1962, Metallurgy Division, ANL-6677, p. 78.

A full-scale dummy fuel subassembly has been vacuum furnace brazed at 1160°C with Coast Metals 60. The 406 stainless steel dummy fuel plates, spacer wires, and side strips were nickel plated prior to assembly. Flow and wetting of the braze alloy was satisfactory, but the resulting grain size was large, indicating a probable loss in ductility. Premabraze also has produced a satisfactory braze at 1050°C on small 406 stainless steel plate specimens, but the grain size was not perceptibly smaller. Specimens brazed with Nioro up to 990°C have not exhibited grain growth, but penetration of the Nioro into the grain boundaries of the 406 stainless steel base metal has been extensive. The depth of penetration appeared to be approximately 0.025 cm (0.010 in.) after the 990°C, 45-min brazing operation. [NOTE: The fuel plate cladding thickness is nominally 0.020 cm (0.008 in.).] A dummy fuel subassembly brazed with Nioro at 980°C for 15 min exhibited brittleness at the brazed joints, whereas the nonbrazed material remained ductile. Plate samples of 406 stainless steel with chromium and copper platings are being prepared for brazing with Nioro in an attempt to minimize braze penetration.

Lap-joint tensile specimens are being prepared with Coast Metals 60, Premabraze 128, and Nioro braze materials. It is expected that the property data obtained from such tests will aid in the selection of an acceptable alloy for brazing 406 stainless steel-clad fuel subassemblies.

c. Advanced Superheat Fuel Elements (W. C. Kramer and R. M. Mayfield)

A program was originated in January 1963 to cover the development of stainless steel superheat cladding materials and investigations of techniques for the fabrication of two advanced superheat fuel design concepts. Progress in both areas of the work is outlined in the following sections.

Cladding Development

Type 406 stainless steel has been found to exhibit a rapidly decreasing rate of corrosion in both oxygenated and deoxygenated steam at 650°C and 42 kg/cm^2 (600 psi), and the corrosion rate is not significantly dependent upon the surface condition of the material.[46] The fabrication technology for this material is not well established. One of the main problems that has been encountered is the large grain growth and loss in ductility that occur upon exposure to temperatures of approximately 1000°C or higher.

[46]Ruther, W. E., and Greenberg, S., Corrosion of Steels and Nickel Alloys in Superheat Steam, Journal of Electro-Chemical Society (to be published).

Six arc-cast alloys, containing varying amounts of aluminum and yttrium were made in an effort to (1) determine the effect of aluminum content on the corrosion rate, and (2) to control deleterious grain growth at elevated temperatures. Samples of as-cast material were hot rolled to 0.08-cm (0.030-in.) sheet. The sheet specimens were corrosion tested for one week in oxygenated steam at 650°C and 42.2 kg/cm^2 (600 psi), with the results shown in Table XXXV.

Table XXXV

CORROSION RATES OF SEVERAL 400 SERIES STAINLESS STEEL IN OXYGENATED STEAM AT 650°C AND 42.2 kg/cm^2 (600 psi)

Base Alloy and Nominal Aluminum Content (w/o)	Addition (w/o)	Weight Loss after One-week Exposure (mg/cm^2)
406 SS (3.25-4.50)	None	4.3
406 SS "	0.5 Ti + 1 Y	4.2
405 SS (0.1-0.3)	0.5 Ti + 1 Y + 3 Al	6.3
405 SS "	0.5 Ti + 1 Y + 2 Al	10.7
405 SS "	0.5 Ti + 1 Y + 1 Al	16.6
405 SS "	0.5 Ti + 1 Y	21.7

The increase in corrosion resistance with increasing aluminum content is clearly evident from Table XXXV. The modified 406 stainless steel (with added titanium and yttrium) had a weight loss essentially the same as that of the 406 stainless steel control specimen. (The 4.2-mg/cm^2 weight loss reported for this sample of 406 stainless steel is somewhat higher than weight losses previously reported for other 406 stainless steel samples tested under similar conditions. Possibly this is due to differences in fabrication histories.) The grain structures in specimens from arc-cast buttons of 406 stainless steel and modified 406 stainless steel are shown in Figures 53 and 54. The dendritic structure of the modified 406 stainless steel is quite different from that of the large-grained 406 stainless steel. Some of the modified 406 stainless steel arc-cast buttons were fabricated into 0.25-cm (0.010-in.) sheet by hot rolling at 950 to 1050°C and cold rolling approximately 50% to the final size. The rolled material was annealed at 1000°C. The annealed grain size was rather large. Resistance seam weld studies showed that the weld consisted of the dendritic structure characteristic of the arc-cast button shown in Figure 53. No transition structure between the weld and parent metal was observed.

Figure 53. Grain Structure of Arc-cast 406 Stainless Steel

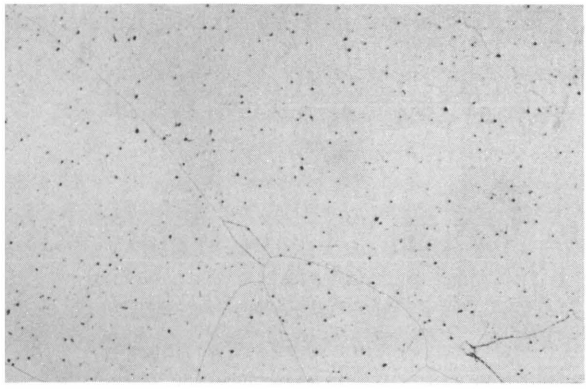

Micro 36969 100X

Etchant: 50 v/o HNO_3, 50 v/o H_2O (electrolytic)

Figure 54. Arc-cast Structure of 406 Stainless Steel Modified by Additions of Yttrium (1 w/o) and Titanium (0.5 w/o)

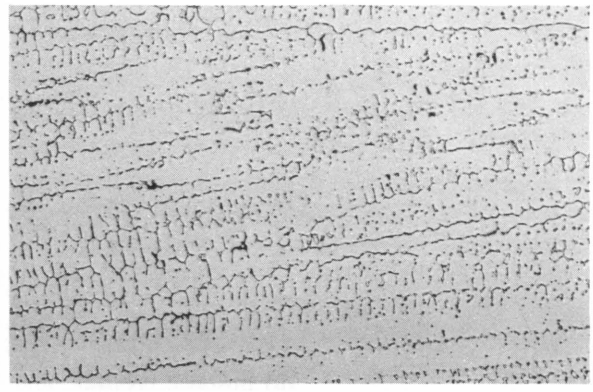

Micro 36968 100X

Etchant: 50 v/o HNO_3, 50 v/o H_2O (electrolytic)

An arc-cast ingot of modified 406 stainless steel (containing 1 w/o Y) will be made to provide billet material for extrusion. Extruded material will be used for limited studies of mechanical properties, weldability, and fabricability. Hopefully, the addition of yttrium will provide a material retaining a fine grain size even after a high-temperature treatment, similar to the findings reported by General Electric on additions of yttrium to an Fe-Cr-Al alloy.[47]

Incoloy 800 (30-35 w/o Ni, 19-23 w/o Cr, balance Fe) has been reported to have a lower corrosion rate in superheated steam than 406 stainless steel.[48,49] Experience at ANL has shown that the corrosion rate is actually dependent upon the surface preparation of the material.[46] At this time, however, Incoloy 800 is the most favorable alternative to 406 stainless steel for cladding superheat fuel. Techniques for welding and fabricating this material are not expected to present any extraordinary problems.

Fabrication Development

The development of techniques for fabricating the "spherical pellet" superheat fuel has been carried out by the ANL Central Shops. The approach taken was to encapsulate a UO_2 ball with hemispherical cladding

[47] Collins, J. F., and McGurty, J. A., High Temperature Cladding Alloys, XDCL 60-8-40 (August 8, 1960), pp. 25-28.

[48] Gaul, G. G., Out-of-pile Superheat Cladding Tests, Proceedings of the Nuclear Superheat Meeting - No. 8, COO-267 (March 20-22, 1963), pp. 11-15.

[49] Pessl, H. J., Effects of Exposure to Superheater-Oxygenated Steam of 550°C (1022°F) and 1000 to 3000 psi Pressure upon Iron and Nickel Base Alloys, Proceedings of the Nuclear Superheat Meeting - No. 8, COO-267 (March 20-22, 1963), p. 16.

shells and apply a circumferential weld at the mating seam. Little difficulty was encountered in cold-forming hemispherical shells of either 406 stainless steel or Incoloy 800. In the case of the 406 stainless steel, however, it was necessary to use a two-step forming operation, with intermediate annealing to prevent cracking. Resistance and electron beam butt weldments could be made with both materials. Weld joints on 406 stainless steel made by either means, however, can be expected to show large grain size and poor ductility.

Development of the "pea-in-a-pod" fuel rod concept was approached in three ways, as illustrated in Figure 55, namely, (a) swaging, (b) isostatic pressing, and (c) swaging followed by isostatic pressing.

Figure 55. Sections of Mockup "Pea-In-Pod" Fuel Rods Produced by (a) Swaging, (b) Isostatic Pressing, and (c) Swaging Followed by Isostatic Pressing

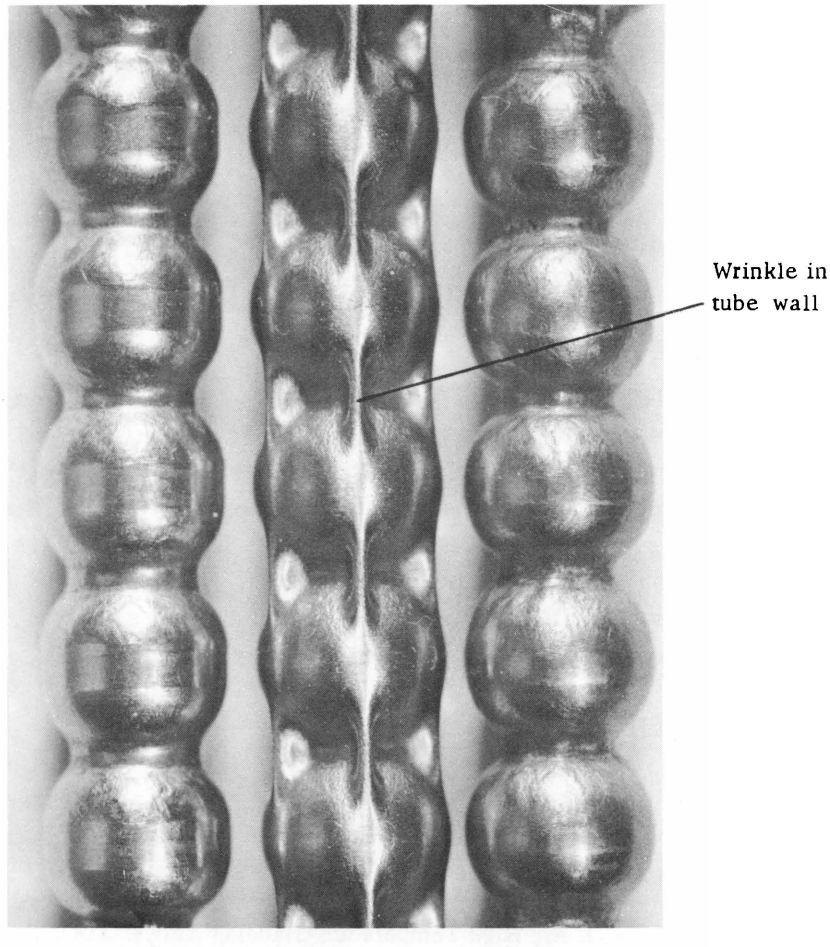

Several lengths of 406 stainless steel tubing filled with chrome alloy steel balls were isostatically pressed at 1,400 kg/cm^2 (20,000 psi). Although the tubing was adequately formed around the balls, wrinkles or folds formed in the tubing between balls. By predenting the tubing, it was possible to keep wrinkles aligned longitudinally along the rod length. Incipient ID cracks appear at the apex of such folds in the tubing walls. No evidence of cladding cracks was found at other locations.

Several swage-formed specimens were fabricated by the Torrington Company, Torrington, Connecticut. Using a single-cavity die, the metal flowed sufficiently to prevent wrinkles forming in the tubing between balls. Although the tubing did not crack during forming, thinning of the wall occurred at points between the maximum and minimum rod diameters as the die pressed the tubing against the balls. Although the die was reworked to alleviate the pressure causing this wall thinning, the greatest reduction which could be achieved by swaging with the existing dies was from 0.82 cm (0.321 in.) at the maximum diameter to 0.56 cm (0.220 in.) at the minimum diameter (between balls).

One of the specimens produced by the Torrington Co. was annealed and isostatically pressed at 1,400 kg/cm^2 (20,000 psi) in an attempt to further reduce the between-ball diameter. By a combination of these two forming methods, a rod was produced having a minimum diameter of 0.47 cm (0.185 in.). Although the reference reduced diameter of 0.44 cm (0.172 in.) was still not achieved, some refinement of methods (e.g., redesigned swaging dies and/or optimized pressure) could result in achievement of the desired rod dimensions.

Techniques for the production of high-density UO_2 spheres to be used for either the "spherical pellet" or "pea-in-a-pod" rod concept have been under investigation. The best spheres produced were uniformly spherical except for a 0.25-cm (0.10-in.) flat circumferential band formed by die pressing. Ball milling did not successfully remove the band from the UO_2 spheres. A grinding method could, perhaps, be adapted for this purpose.

Present Program Status

Air-flow pressure-drop tests recently reported by the Idaho Division[50] on fuel mockups representing both of the above concepts have shown that pressure drops through elements incorporating these fuel designs are excessive. Accordingly, fabrication development on both concepts has been terminated. Limited studies of cladding materials having improved corrosion resistance for superheater applications that are now in progress will be carried to completion.

---

[50] Reactor Development Program Progress Report, ANL-6801 (October 1963), p. 5.

d. Inspection of BORAX-V Superheater Plates, Drive Components, and Fuel Rods (R. H. Selner)

Fifty BORAX-V superheater fuel plates clad with 406 stainless steel were ultrasonically inspected for bond integrity. Details and results of earlier inspections of 304 stainless steel-clad plates appeared in the 1962 Annual Report.[51] One plate, FCE-8, was rejected. Indications from the defect area in this plate were typical of those observed in areas of large UO_2 particle concentration in 304 stainless steel plates.

[51] Annual Report for 1962, Metallurgy Division, ANL-6677, pp. 79-81.

C. Plutonium Recycle Fuel Elements and Control Rods

1. Plutonium Recycle Fuel Fabrication (C. H. Bean and F. D. McCuaig)

The Plutonium Recycle Program is a joint Argonne-Hanford program to obtain data which will be useful for the utilization of plutonium as a fuel in light water, thermal systems. Experiments will be performed in EBWR, the reactor serving as a boiling water irradiation facility.

Physics studies have indicated that the most desirable fuel loading for the reactor is a three-zone loading with the plutonium fuel in the central zone. This zone will contain 36 test fuel elements of plutonium. An intermediate shim zone will contain 60 elements fueled with enriched uranium. The outer blanket zone will consist of 58 natural uranium elements.

All fuel elements contain 36 fuel rods in a square lattice. The fuel is contained in 0.945-cm-ID by 0.064-cm-wall Zircaloy-2 tubing. The composition of the central plutonium fuel is 1.5 w/o PuO_2-98.5 w/o $U^{238}O_2$. The shim fuel is UO_2 enriched with 6 w/o U^{235}. The shim fuel also contains a burnable poison, 0.158 w/o Eu_2O_3 and 0.0288 w/o Sm_2O_3, to extend the life of the fuel and limit the range of excess reactivity present over the period of irradiation. The blanket fuel is natural UO_2. Both the enriched and natural uranium fuel are referred to as the Plutonium Recycle Driver Fuel.

The 36 fuel rods in each fuel element are supported and positioned by support grids and spaced by a center spacer grid. The fuel rods are contained within and fastened to a square Zircaloy-2 fuel element can with a 0.157-cm ($\frac{1}{16}$-in.) nominal wall thickness. A stainless steel end fitting completes the fuel element. With the exception of the oxide composition, this core is identical with the original EBWR Core-2 reference design.[52]

Plutonium-bearing fuel rods for the Plutonium Recycle Experiment are being fabricated by General Electric, Hanford. These will be assembled into fuel elements at ANL. All driver fuel, components for assembly of plutonium fuel elements, and components for future replacement of 28 driver shim elements are being procured by ANL.

Hanford has completed procurement of fuel rod components. Zircaloy-2 tubing fabricated at Harvey Aluminum for Hanford was inspected by Hanford. Comparison of nondestructive testing procedures for optimum inspection of this tubing was a joint effort between Hanford and ANL.

---

[52] Avery, R., and Kelber, C. N., Physics Analysis of Proposals for EBWR Core 2, ANL-6306 (April 1961).

Hanford is preparing all PuO_2 fuel by the Dynapak process. This is a high-temperature, high-pressure impacting process which produces a uniform dispersion of PuO_2 in UO_2. Dynapaked material is being crushed, screened, and loaded into the fuel tubes by vibratory compaction. This process is being used for all plutonium fuel in place of the incremental loading and vibratory compaction which was originally proposed. Plutonium fuel rods are now being loaded for the critical tests which are to be performed at Hanford.

Specifications were prepared by the Laboratory for procurement of the driver fuel and all components needed to assemble the plutonium fuel elements and one future shim replacement loading. Contract No. 31-109-38-1622 was awarded to United Nuclear Corporation for this procurement. During the course of contract negotiation, some questions were raised regarding the degree of homogeneity which could be maintained for the rare earth oxide in UO_2 in the shim elements.

United Nuclear Corporation's Chemical Division does not have facilities for preparation of the rare earth oxide and UO_2 by coprecipitation. Attempts to blend small quantities of rare earth oxide with ceramic-grade UO_2 by mechanical mixing of dry powders showed that a wider distribution of rare earth was obtained in the UO_2 than was desired. Further evaluation samples prepared as a master blend of high-fired rare earth oxides and UO_2, blended with ceramic-grade UO_2, resulted in a distribution of the rare earth oxide within the desired homogeneity.

The following companies have been awarded subcontracts by United Nuclear Corporation:

(a) Harvey Aluminum Company for Zircaloy-2 tubing;

(b) Wah Chang Corporation for Zircaloy-2 rod and strip stock;

(c) Hartford Machine Screw for machined end plugs;

(d) Bristol Spring and Manufacturing Company for compression springs;

(e) Superior Tube Company, Nuclear Products Division for fuel element can fabrication and center spacer grid;

(f) Kelly Industries for end fittings;

(g) Ragin Precision Industries for support grids;

(h) Whitehead Metals for special rivets and screws.

Present production schedules call for delivery of all fuel and hardware before the end of the second quarter of FY 1965.

2. Plutonium Recycle Control Rods (C. H. Bean)

A new set of control rods will be fabricated to replace eight existing control rods in the EBWR reactor. The existing control rods have riveted transition sections between the boron-stainless absorber section and the Zircaloy-2 follower section. A number of Inconel rivets in these transition sections have failed in service. It has been determined that a shear stress exists in these rivets due to differential expansion between the Zircaloy and the stainless steel.

Replacement control rods for EBWR have been redesigned to eliminate the mechanical riveted transition section. This new design incorporates a tongue-and-groove joint which will eliminate the stress due to differential thermal expansion of these two materials.

Along with the change in mechanical design, the new control rods will contain highly enriched (~90%) B^{10} in place of natural boron, although the total boron content will remain at 2 w/o. The use of enriched rather than natural boron will provide some additional rod worth arising from increased epithermal absorptions.

A total of eight control rods containing boron are required. One central oscillator rod with hafnium as the absorber material will be replaced with a new hafnium rod.

Specifications have been prepared for all boron-stainless steel required for control rod fabrication. The boron-stainless steel is being procured from a commercial supplier. The boron-stainless steel for the eight boron rods and the hafnium for the oscillator rod will be furnished by the Laboratory to a commercial supplier who will fabricate the control rods.

D. Development of Alloy Fuels and Jacket Materials

1. The Constitution of the Th-Pu and the Thorium-rich Th-U-Pu Alloys (B. Blumenthal)

Thorium-uranium-plutonium alloys are potential high-temperature nuclear fuels. A study of the ternary thorium-plutonium-uranium phase diagram was undertaken to find the compositions of useful alloys.

Of the three binary boundary systems, the phase diagrams of the thorium-uranium alloys[53-57] and the uranium-plutonium alloys[58] are well known. For the purpose of this report it is good enough to assume that the solubility of thorium in the uranium-plutonium alloys is negligibly small. On the other hand, it is important to mention that α and β uranium have only a very small solubility in thorium so that the useful alloys of this binary system are two-phase alloys consisting, at room temperature, of α-thorium and α-uranium.

There exist two phase diagrams of the binary thorium-plutonium alloys, one by Poole, Williamson, and Marples[59] which is in agreement with the one published by Schonfeld,[60] and the other one by Bochvar et al.[61] For brevity's sake we shall call them the US-UK and

---

[53]Carlson, O. N., Some Studies of the Uranium-Thorium-Zirconium Alloy System, AECD-3200 (1950).

[54]Bentle, G. G., A Physical Metallurgical Study of Thorium-rich Thorium-Uranium Alloys, NAA-SR-2069 (1958).

[55]Murray, J. R., United Kingdom, Unpublished information reported by Rough, F. A., and Bauer, A. A., in Constitutional Diagrams of Uranium and Thorium Alloys, Addison-Wesley Publishing Company, Reading, Massachusetts (1958).

[56]Bauer, A. A., Rough, F. A., and Dickerson, R. F., An Investigation of Uranium Solid Solubility in Thorium, BMI-1188 (1957).

[57]Wilson, W. B., Austin, A. E., and Schwartz, C. M., The Solid Solubility of Uranium in Thorium and the Allotropic Transformation in Thorium-Uranium Alloys, BMI-1111 (1956).

[58]Ellinger, F. H., Elliot, R. O., and Cramer, E. M., The Plutonium-Uranium System, J. Nucl. Materials 3, 233-243 (1959).

[59]Poole, D. M., Williamson, G. K., and Marples, J. A. C., Preliminary Investigation of the Plutonium-Thorium System, J. Inst. Met., 86, 172-176 (1957/58).

[60]Schonfeld, F. W., "Plutonium Phase Diagrams Studied at Los Alamos," Chap. XXII in The Metal Plutonium, Ed. by Coffinberry, A. S., and Miner, W. N., The University of Chicago Press (1961).

[61]Bochvar, A. A., Konobeevsky, S. T., Kutaitsew, V. I., Menshikova, I. S., and Chebotarev, N. T., The Interaction between Plutonium and Other Metals in Connection with Their Arrangement in Mendeleev's Periodic Table, Proc. 2nd Intnl. Conf. on Peaceful Uses of Atomic Energy, Geneva Switzerland, 6, 184-193 (1958).

Russian phase diagrams. The two diagrams differ considerably on the thorium side. The US-UK diagram shows a maximum solubility of plutonium in α thorium of 48.5 a/o at 615°C. The Russian diagram shows the same solubility limit to be 28 a/o. The thorium beta phase is not shown in the US-UK version, whereas the Russians show the beta field to dip deep to the low temperature of 600°C where the phase decomposes eutectoidally to alpha thorium and Th_2Pu.

A major effort of the phase diagram work during the report period was directed towards an evaluation of the extent of the alpha-thorium phase field. Since the US-UK work was based mainly on metallographic and X-ray diffraction work and gave no indication of the presence of the beta phase at low temperatures, we did not expect much evidence from the metallographic and X-ray diffraction work which we too used to determine the alpha-thorium phase boundaries of the ternary system. After an initial metallographic investigation of binary alloys with from 0 to 60% plutonium in intervals of 10%, we made two series of ternary alloys with 2 and 4% uranium, also in intervals of 10%. The arc-melted alloys made from high-purity materials were heat-treated at 700 and 900°C, and water quenched. The metallographic work seemed to confirm the US-UK phase diagram. Beyond 50 a/o plutonium at 700°C and 43 a/o at 900°C a liquid phase was observed at the grain boundaries of the α grains. After solidification, this phase was found to be δ plutonium, in agreement with Poole.[59] The addition of uranium to the binary thorium-plutonium alloys greatly restricted the solubility of plutonium in thorium. Debye-Scherrer patterns of heat-treated and stress-relieved needles, made with Cu-Kα radiation, gave lattice parameters whose plot versus composition for 700 and 900°C (see Figures 56 and 57) resulted in solubility limits in fair agreement with those shown in the US-UK diagram.

Figure 56. Lattice Parameters of α-Thorium Phase. (The high-temperature phases are indicated.)

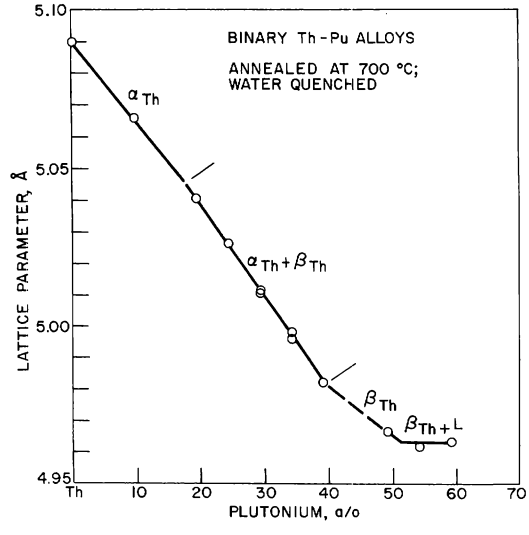

Figure 57. Lattice Parameters of α-Thorium Phase of Th-Pu Alloys. (The high-temperature phases are indicated.)

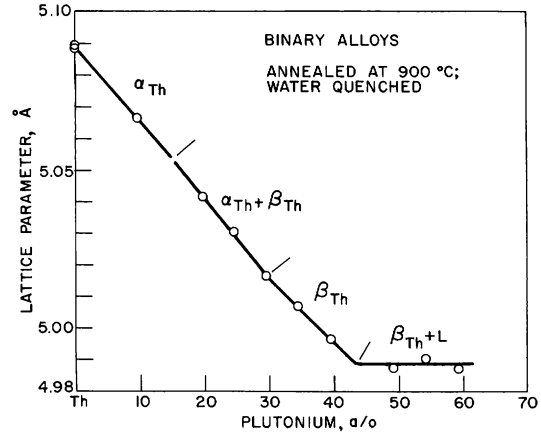

106-7631

When the lattice parameters of the ternary alloys were determined, the lattice parameter versus composition plots (Figures 58 to 61) showed substantial deviations from the course that one might expect from ternary alloys where an alpha solid solution is in equilibrium with a liquid. The presence of discontinuities, which subsequently were observed also in the binary system (here the effect is much weaker), could only be explained by the assumption that the beta phase is indeed present at 700 and 900°C in the binary and ternary alloys.

Figure 58. Lattice Parameters of α-Thorium Phase of Th-2 a/o U-Pu Alloys. (The high-temperature phases are indicated.)

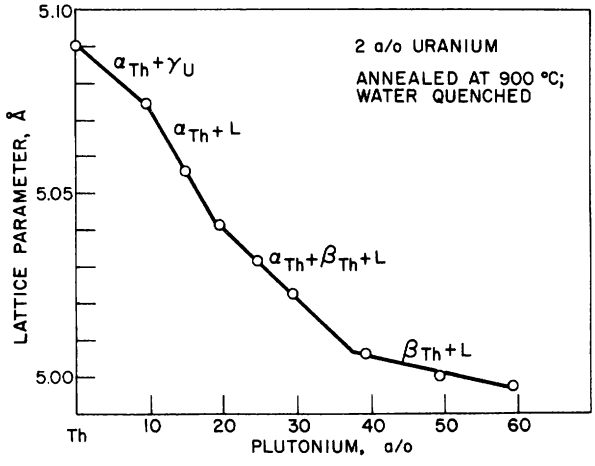

106-7639

Figure 59. Lattice Parameters of α-Thorium Phase of Th-4 a/o U-Pu Alloys. (The high-temperature phases are indicated.)

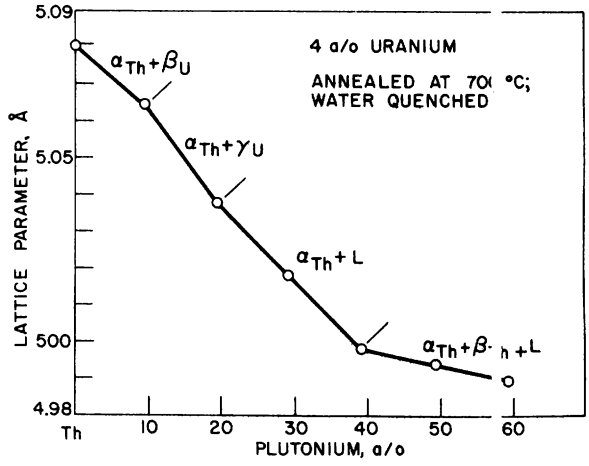

106-7633

Figure 60. Lattice Parameters of α-Thorium Phase of Th-2 a/o U-Pu Alloys. (The high-temperature phases are indicated.)

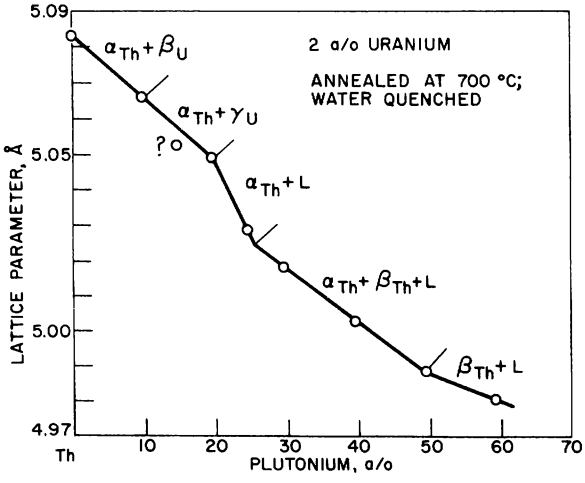

106-7632

Figure 61. Lattice Parameters of α-Thorium Phase of Th-4 a/o U-Pu Alloys. (The high-temperature phases are indicated.)

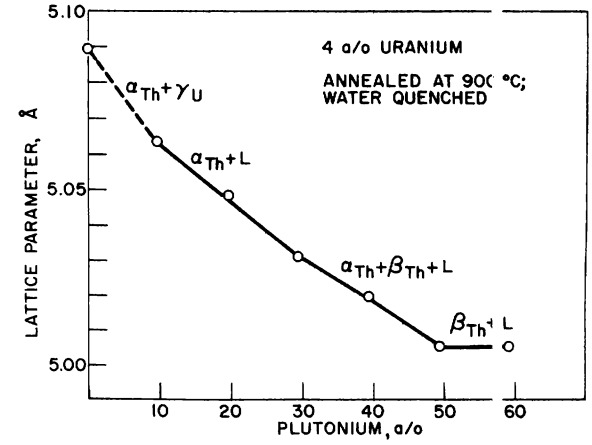

106-7634

The evidence is an indirect one. At 700 and 900°C the α, $\alpha + \beta$, and β-phase thorium alloys dissolve equilibrium quantities of plutonium. Upon quenching to room temperature, the beta phase is transformed to alpha. It is not possible to suppress this transformation. At room temperature, the entire alloy series contains only alpha thorium and, beyond the solubility limits, δ plutonium. The alpha phase has in solution those quantities of plutonium that were in equilibrium in the beta phase at 700 and 900°C. In such a way the room-temperature lattice parameters of the alpha phase do reflect the extent of the α, $\alpha + \beta$, and β thorium fields at the high temperature.

Figure 62

a. A Phase Diagram

b. The Room-temperature Lattice Parameters of the α Phase when the β Phase is not Retained upon Quenching from Temperature T

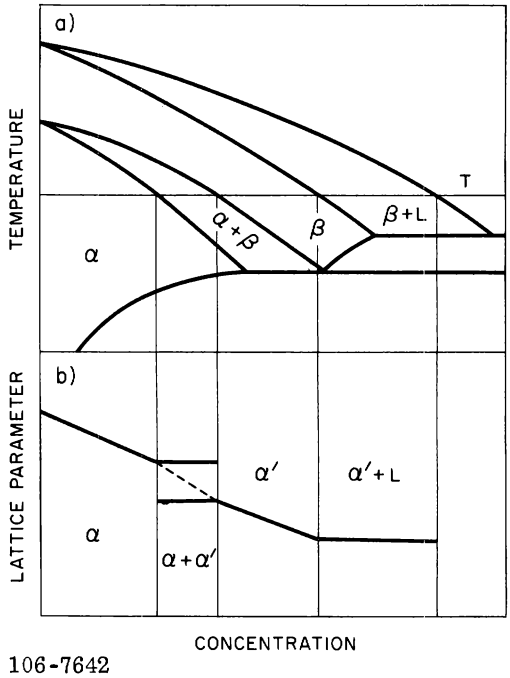

106-7642

A schematic phase diagram and its relationship with the room-temperature lattice parameters after quenching is shown in Figure 62a and b. The $\alpha + \beta$ phase field is characterized by a mixture of two alpha phases of constant lattice parameters; since these two lattice parameters differ very little, a continuous transition from one end of the range to the other, as shown by the dotted line, will actually be observed. Within the β field itself the lattice parameters are changing continuously, but the slope of the line of lattice parameter versus concentration may differ from the slope of the line for the α phase. Equivalent observations have been made in the ternary system.

In such a way it was possible to evaluate the lattice-parameter measurements for the ternary alloys, as shown in the ternary phase diagrams of Figures 63 and 64. Metallographic evidence concerning the first appearance of the liquid phase at rather low plutonium concentrations supported these results. As an example, a series of micrographs is shown in Figure 65a to d. Similarly, we arrived at the preliminary binary phase diagram of Figure 66 from the lattice-parameter measurements of Figures 56 and 57.

The effect of the beta phase on the lattice parameter of α thorium in ternary alloys is a very strong one, as shown in Figures 58 to 61, whereas the effect in the binary system is a rather weak one. The effect in the binary system can easily escape observation if the effect in the ternary system is not known. We have made a considerable effort to interpret the data in some other way, but to date the interpretation given in Figures 63 and 64 appears to be the most plausible one. Still, the results should be considered preliminary at this stage of the research.

Figure 63. Thorium-Plutonium-Uranium Phase Diagram (Preliminary) at 700°C

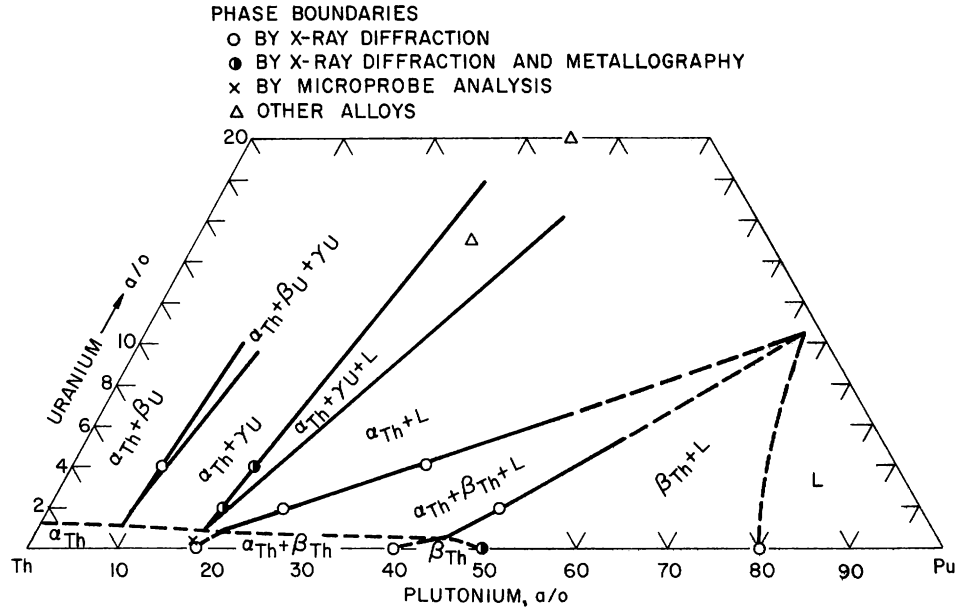

106-7644

Figure 64. Thorium-Plutonium-Uranium Phase Diagram (Preliminary) at 900°C

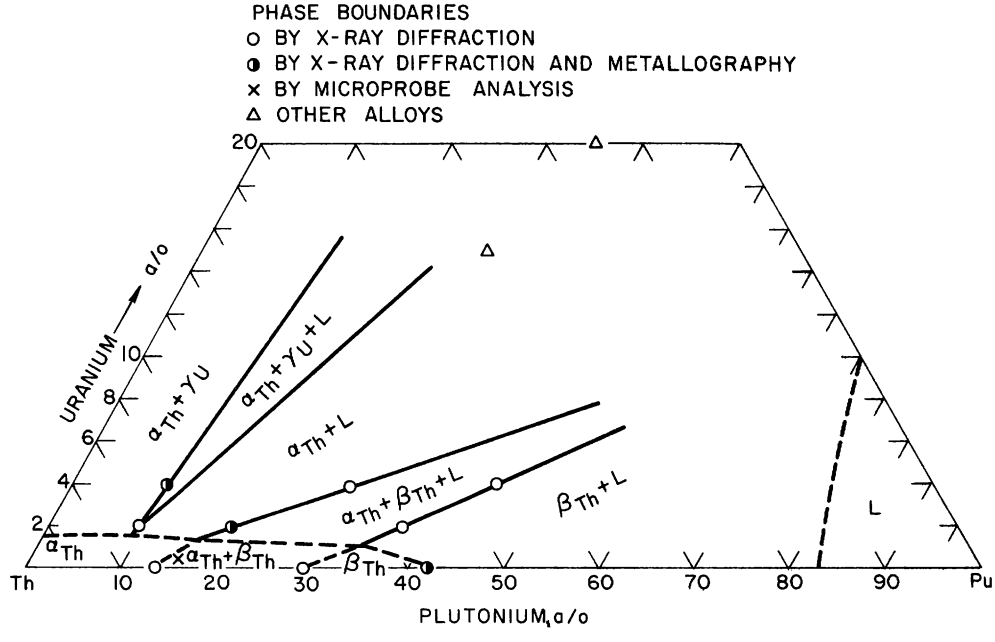

106-7643

Figure 65. Thorium-Uranium-Plutonium Alloys Annealed for 3 Weeks at 700°C and Water Quenched. All specimens electro-etched with phosphoric acid. A liquid phase is seen in micrographs (c) and (d).

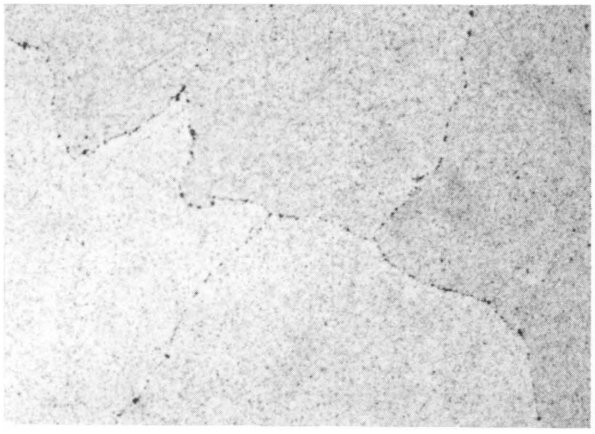

Micro 36599 (a) 200X

Th-4 w/o U

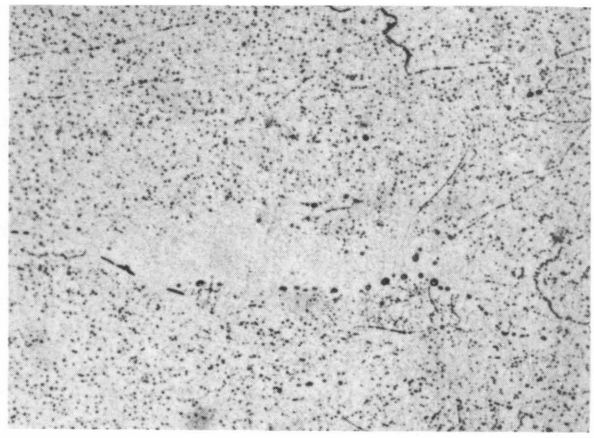

Micro 36600 (b) 200X

Th-4 w/o U-10 w/o Pu

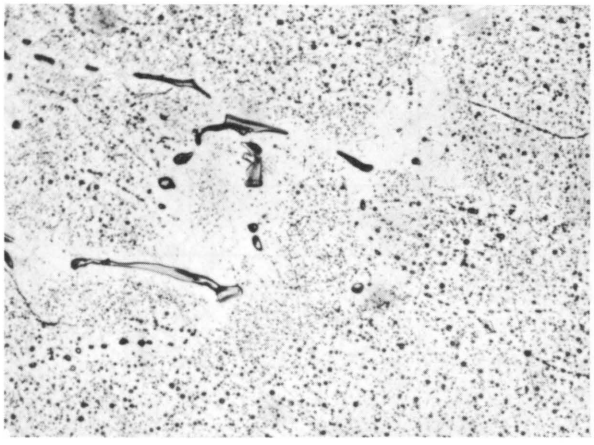

Micro 36601 (c) 200X

Th-4 w/o U-20 w/o Pu

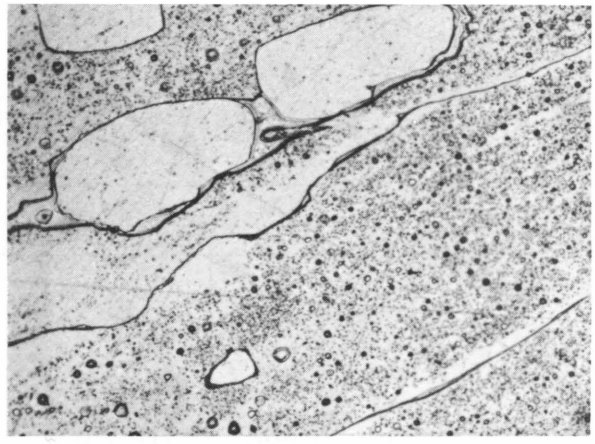

Micro 36602 (d) 200X

Th-4 w/o U-30 w/o Pu

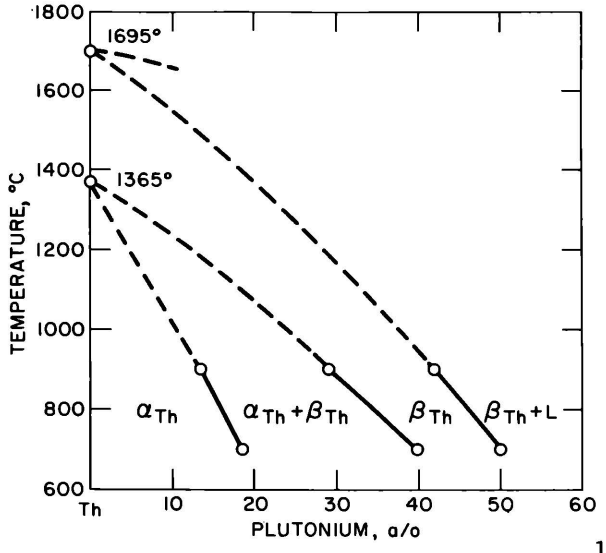

106-7640

Figure 66

Portion of Binary Thorium-Plutonium Phase Diagram Showing the β Phase between 700 and 900°C

2. Impurity Levels in High-purity Thorium and Its Alloys with U and Pu (B. Blumenthal)

The alloys used for the phase-diagram study reported in the preceding section were made from crystal-bar thorium and high-purity uranium and plutonium. Complete analyses of the alloys were made by the ANL Chemistry Division. Table XXXVI gives the analysis of the thorium.

Table XXXVI

ANALYSIS OF CRYSTAL-BAR THORIUM (B794)
(Data in ppm)

Chemical Analysis				Spectrochemical Analysis*	
H	2			Al	7
C	7			B	1
N	5			Fe	30
O	45			Ti	0.5
Si	10			Y	2
				Zr	10
Limits of Spectrochemical Detection					
Ag	1	Co	1	Li	0.005
Al	1	Cr	0.5	Mg	1
B	1	Cu	5	Mn	0.1
Ba	0.2	Ga	0.5	Mo	0.5
Be	0.002	Hf	0.5	Na	1
Bi	2	Fe	5	Ni	1
Ca	2	K	2	Pb	1
Cd	2	La	0.2	Rb	0.5
Sb	20				
Sn	2				
Sr	0.005				
Ti	0.2				
V	0.5				
Y	0.02				
Zn	2				
Zr	0.2				

*All other elements below limits of spectrochemical detection.

The hafnium and boron content of this material were suspected to be high. However, activation analysis showed the hafnium content to be 0.5 ppm ±30%. A boron determination by spectrochemical analysis gave a boron content of 1 ppm correct within a factor of 2. Thus, on the atomic scale, the most important impurities in crystal-bar thorium are oxygen and hydrogen 650 apm (atoms per million) and 460 apm, respectively. Carbon with 140 apm, iron with 130 apm, and nitrogen and silicon with about 80 apm are of lesser importance.

The same general picture is obtained from the analyses of ternary alloys of which the series with 4% uranium is a good example of current melting practice (see Table XXXVII).

Table XXXVII

ANALYSES OF A SERIES OF
THORIUM-URANIUM-PLUTONIUM ALLOYS

Alloy No.	Nominal Composition (w/o)			Important Impurities (ppm)				
	Th	U	Pu	H	C	N	O	Si
B791	96	4	0	6	40	27	49	9
B801	86	4	10	12	35	39	39	4
B802	76	4	20	24	30	31	52	9
B803	66	4	30	7	41	35	31	17
B804	56	4	40	5	27	31	15	30
B805	46	4	50	12	23	21	13	3
B806	36	4	60	0.3	4	31	53	13

It should be noted that the hydrogen content of some of the alloys is disturbingly high, and we have as yet no sure way of controlling this impurity.

3. The Lattice Parameter of High-purity Thorium (B. Blumenthal)

In the process of evaluating the lattice-parameter measurements of the binary and ternary alloys, we have investigated the effect of heat treatment on the lattice spacing of high-purity crystal-bar thorium and found an increase in the lattice spacing with time and temperature of heat treatment. This is shown in Table XXXVIII. The observed changes

Table XXXVIII

LATTICE SPACINGS OF CRYSTAL-BAR THORIUM (B794)
BEFORE AND AFTER HEAT TREATMENT

Film No.	Lattice Parameter a_0, Å at 25°C	Heat Treatment		
		Temp (°C)	Time (hr)	Cooling
54B	5.0840	As Received		
66B	5.0842	700	2	Furnace cooled
67B	5.0848	700	2	Oil quenched
80B	5.0855	900	2	Furnace cooled
79B	5.0857	900	2	Oil quenched

are not likely to be caused by contamination during heat treatment, since the heat treatment was made with bulk material which was protected by a tantalum foil wrapper and sealed under vacuum in Vycor tubes. Needle specimens were prepared by grinding after the heat treatment. The specimens were stress relieved under the same protective conditions. The lowest value, 5.0840 Å, is in excellent agreement with the best literature values: Evans and Raynor[62] 5.0740 KX = 5.0844 Å, and James and Straumanis[63] 5.0843 Å. The theoretical density is 11.728 g/cm^3.

4. Properties of Thorium-Uranium-Plutonium Alloys
(B. Blumenthal)

When the work on the properties of the thorium-uranium-plutonium alloys was started, we had no knowledge of the constitution of the ternary alloys. We are now in a better position to determine which alloys are most likely to give satisfactory metallurgical properties for fast reactor application. Superimposed on the metallurgical conditions are the nuclear requirements as outlined by D. Okrent,[64] which may further restrict the number of acceptable alloy compositions. The ternary phase diagrams of Figures 63 and 64 show the range of alloy compositions which do not contain a liquid phase at the temperatures of 700 and 900°C.

Alloys with a high plutonium content are restricted to a narrow band of alloys of very low uranium content (probably less than 1 a/o paralleling the binary thorium-plutonium alloys. On the other hand, an alloy with 20 a/o uranium allows a 15 a/o plutonium content and is still solid at 900°C, and one with 20 a/o uranium and 25 a/o plutonium is still solid at 700°C. Therefore, the alloy containing 20 a/o plutonium and 20 a/o uranium, which is now being encapsulated for irradiation and which was selected and prepared at an early stage of the research, should give useful information on irradiation stability at 700°C.

Density measurements of three series of alloys with 0, 2, and 4 w/o uranium and up to 60 w/o plutonium were made by the hydrostatic weighing method with monobromobenzene as the liquid. The factors influencing the precision of the density measurements in gloveboxes were investigated. The most important factor was found to be differences between the temperatures of the glovebox atmosphere and the liquid surrounding the specimen during weighing.

---

[62]Evans, D. S., and Raynor, G. V., The Lattice Spacing of Thorium with Reference to Contamination, J. Nucl. Materials 3, 281-288 (1959).

[63]James, W. J., and Straumanis, M. E., Lattice Parameter and Coefficient of Thermal Expansion of Thorium, Acta Cryst. 9, 376-379 (1956).

[64]Okrent, D., "Nuclear Considerations in the Selection of Materials for Fast Power Reactors," Nuclear Metallurgy, Vol. IX, pp. 1-56 (1963), Materials for Sodium Cooled Reactors, Ed. Kelman, L. R. and Greenberg, S., IMD Special Report No. 12, The Metallurgical Society of A.I.M.E.

A revised formula taking into account these temperature differences was derived. For a substitution-type balance the density equation corrected for temperature variation is

$$\rho_s = \frac{M_f}{M_k} \{\rho_{\ell'}[1 + \alpha(t' - t)]\} + \rho_a, \quad (1)$$

whereas the uncorrected equation is

$$\rho_s = \frac{M_f}{M_h} (\rho_\ell - \rho_a) + \rho_a, \quad (2)$$

where

ρ_s is the density of the specimen at the temperature t of the glovebox atmosphere,

M_f the weight at temperature t removed to restore equilibrium when the specimen at the same temperature is placed on the balance pan,

M_k the weight at temperature t required to restore equilibrium when the specimen at temperature t' is immersed in the liquid at temperature t',

M_h the weight at temperature t required to restore equilibrium when the specimen at the same temperature is immersed in the liquid also at the same temperature,

$\rho_{\ell'}$ the density of the liquid at temperature t',

ρ_ℓ the density of the liquid at temperature t,

ρ_a the density of the glovebox atmosphere,

α the volume coefficient of expansion of the specimen.

Upon comparing equation (1) with equation (2), we see that only the volume change of the specimen and the true density of the liquid enter the density formula when the temperature of the liquid differs from that of the surrounding atmosphere. This is of particular importance in glovebox work during which temperature variations are large enough to become significant and while working with plutonium and its alloys where self-heating may create difficulties. When the corrected density formula is applied, an accuracy of better than ± 0.005 g/cm^3 is obtained.

This method was applied to the three series of alloys mentioned above. The results of these measurements are shown in Figures 67, 68, and 69, in which the specific volume is plotted versus composition. Generally, the data reflect the effect of the constitution on the specific volume,

particularly the presence of the beta phase at the temperatures at which the alloys were heat treated and water quenched. The data support the conclusions, based on the lattice-parameter measurements, that the observed lattice parameters do represent the structural changes caused by the beta phase. The effect is not caused by contamination during heat treatment, since it occurs in the bulk material as well as in the small needles with which X-ray diffraction measurements were made.

Figure 67. Specific Volume of Binary Thorium-Plutonium Alloys Quenched from 700 and 900°C

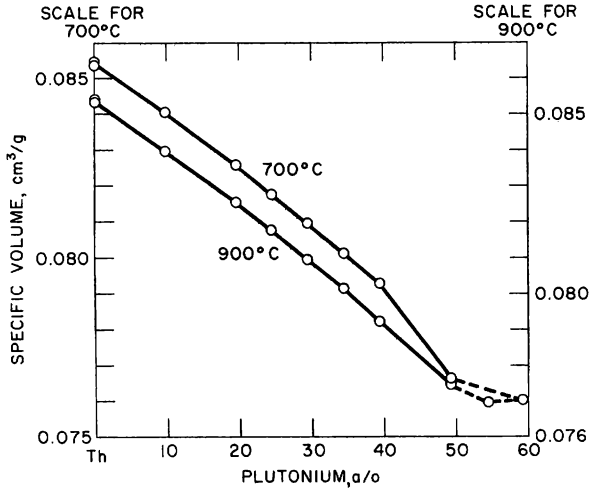

106-7637

Figure 68. Specific Volume of Ternary Thorium-2 a/o Uranium-Plutonium Alloys Quenched from 700 and 900°C

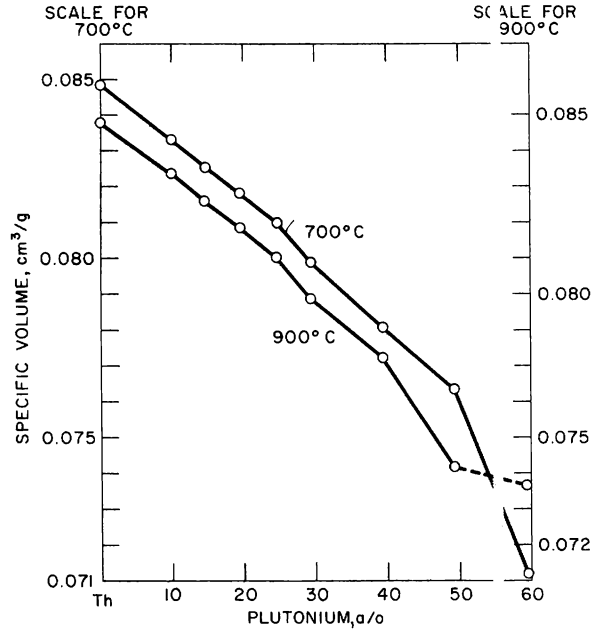

106-7638

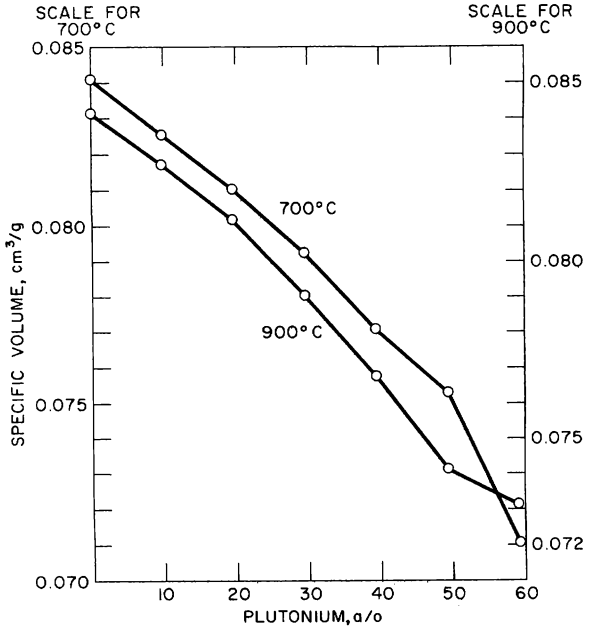

106-7636

Figure 69

Specific Volume of Ternary Thorium-4 a/o Uranium-Plutonium Alloys Quenched from 700 and 900°C

5. High-temperature Mechanical Properties of Refractory Metals (F. L. Yaggee and E. R. Gilbert)

The refractory metals vanadium, niobium, molybdenum, tantalum, and tungsten, and their alloys, are of considerable interest for medium- and high-temperature reactor applications. As a group, they are superior to iron, nickel, and chromium alloys (e.g., Hastelloy-X, stainless steels, Inconel, Fe-2.25 w/o Cr-1 w/o Mo) in their compatibility with uranium and plutonium-containing fuels up to 800°C. Their high melting points (>1850°C) and high-temperature strength retention make them logical candidates for service at much higher temperatures as fuel cladding and structural members.

A survey of the literature dealing with refractory metals reveals an abundance of information about high-temperature mechanical properties, which, in most cases, is confined to short-time tensile data obtained under conditions of uniaxial loading. Creep and long-time stress-rupture data are very scarce, as are data for tubular members biaxially loaded by an internal pressure. Surprisingly little of the available data are directly applicable to reactor systems without questionable extrapolations and/or interpolations of temperature and test conditions. In addition, serious omissions in the definition of test variables (e.g., strain rate and test environment) and description of material purity in regard to interstitial contaminant levels[65,66] and prior thermomechanical history limit the usefulness of other data. Yet, it is an experimentally documented fact that a detailed record of all these variables is indispensable to the accurate interpretation of the test results.

Since the bulk of the data on these materials was obtained from aerospace programs, direct and unqualified applicability to specific reactor temperature and environmental conditions can hardly be expected. Furthermore, it is reasonable to assume that a fair portion of these data were obtained with experimental quantities of alloys of unknown purity and were primarily intended to fill a void where no property data previously existed. Finally, the inadequacies of many mechanical extensometer systems at these high temperatures encourage the common, but objectionable, practice of equating crosshead displacement to specimen strain, further adding to the confusion of reported data.

Since much of the reported data about mechanical properties are not usually accompanied by the detailed background information necessary for determining applicability in specific service conditions, it is desirable, if not mandatory, to recheck the data. Toward this end test equipment is being set up with temperature and vacuum capabilities of 500-3000°C and 10^{-6} to 10^{-8} torr, respectively.

---

[65] Bartlett, E. E., and Schmidt, F. F., Review of Recent Developments in the Technology of Columbium and Tantalum, DMIC Memorandum 130 (Oct 10, 1961).

[66] McCoy, H. E., and Douglas, D. A., Effect of Various Gaseous Contaminants on the Strength and Formability of Columbium, Columbium Metallurgy, Interscience Publishers, Vol. 10, p. 85 (1961).

Some determinations of uniaxial tensile properties have been made with V-10 w/o Ti, V-20 w/o Ti, and Nb-1 w/o Zr alloys. These are presented in Table XXXIX. A difference in the plastic flow behavior was observed between the V-Ti alloys and the Nb-Zr alloy. The V-Ti alloys were deformed with uniform elongation, whereas the Nb-1 w/o Zr alloy was deformed primarily within a localized length of the gage section. As a result, the total elongation was greater for the V-Ti alloys. The strain at which the ultimate tensile strength occurred was also greater for the V-Ti alloys. It is possible that this difference in plastic behavior may be due to strain hardening which occurs in the V-Ti alloys to a greater extent than in the Nb-1 w/o Zr alloy. The V-Ti alloys were in a recrystallized condition, whereas the Nb-1 w/o Zr was in the stress-relieved condition. Tests will be conducted on recrystallized Nb-1 w/o Zr to determine if this difference in behavior is a characteristic of the alloy or condition. Chemical analyses are not yet available on specimens tested.

Table XXXIX

UNIAXIAL TENSILE PROPERTIES OF Nb-1 w/o Zr AND VANADIUM-TITANIUM ALLOYS

Alloy	Temp (°C)	Ultimate Tensile Strength ($kg\ mm^{-2}$)	0.002 Offset Yield Strength ($kg\ mm^{-2}$)	Elongation[a] (%)	Reduction of Area (%)	Elastic Modulus ($10^3\ kg\ mm^{-2}$)	Engineering Strain at Ultimate Tensile Strength (%)
Nb-1 w/o Zr, Stress Relieved 1 hr at 850°C	Room	53.2	47.4	28	90	12.4	7.3
	640	43.4	42.0	19	93	8.4	1.9
	650	48.2	44.2	19	87	12.4	1.9
	800	36.2	34.6	24	83	12.4	1.3
	850	36.2	34.4[b]	14	87	(c)	-
	950	35.9	34.8[b]	15	90	(c)	-
V-10 w/o Ti, Extruded at 1110°C, Recrystallized Structure	Room	48.4	37.2	38	62	23.9	16.4
	Room	50.6	39.5	38	61	14.3	17.3
	650[d]	49.9	45.0[b]	34	53	(c)	15.2
	750	37.3	27.1	42	69	8.1	10.7
V-20 w/o Ti, Extruded at 1110°C, Recrystallized Structure	Room	70.3	62.6	34	56	17.7	16.7
	Room	70.6	64.2	36	56	18.4	20.2
	650	66.2	45.8	37	44	12.0	15.6
	750	46.3	38.3	36	56	14.3	7.0
	800	41.5	35.9	48	50	9.6	5.0

Threaded bar specimens with 6.35-mm (0.250-in.) diameter and 3.18-cm (1.25-in.) reduced section.
Tests conducted in vacuum of 2×10^{-5} mm Hg.
Tests conducted with crosshead speed of 8.3×10^{-4} cm/sec (0.02 in./min).
[a]Measured as change in 2.54-cm (1-in.) gage length after completion of test.
[b]Measured from crosshead travel and may not correspond to true 0.002 offset yield strength.
[c]Not measured in absence of extensometer.
[d]Specimen surface oxidized during testing because of air leak in vacuum furnace.

Some preliminary measurements were made on the creep of the Nb-1 w/o Zr alloy. A test conducted at 550°C and a stress of 37.2 $kg\ mm^{-2}$ resulted in a minimum creep rate of less than $1 \times 10^{-7}\ sec^{-1}$. Increasing the stress to 38.7 $kg\ mm^{-2}$ caused the specimen to deform very rapidly and resulted in immediate failure.

E. Development of Ceramic Fuels and High Absorbing Materials

1. Preparation and Properties of Uranium and Plutonium Monocarbides

a. Preparation and Fabrication of Uranium and Plutonium Carbides (O. L. Kruger)

Sintering studies were made on PuC and UC-PuC solid solutions in an effort to fabricate these materials into fuel pellets. Material for both studies was made by fusing pieces of Pu and C, or Pu, U, and C, in an arc furnace. This method of preparation was chosen because it was best for making high-purity carbides with low oxygen content. A good starting material was essential for these studies in order to determine the extent of oxygen contamination introduced by various methods of powder preparation. These powders were handled in an inert atmosphere of nitrogen gas with approximately 500 ppm combined impurities of oxygen and water vapor.

The sintered density of plutonium monocarbide was studied as a function of binder addition and particle size. Pellets with a density of 93% theoretical were pressed and sintered from powder with a particle size of less than 44 μ. These pellets were pressed at 5.6 metric tons/cm^2 from powder coated with 0.5 w/o Carbowax binder. The density as a function of sintering temperature in vacuum is shown in Figure 70 for pellets made from various powders. Reduction of the particle size from less than 44 μ to less than 15 μ did not aid densification. The optimum sintering temperatures of the <74 and <44 μ powders were 1400 and 1350°C, respectively, for a time of 2 hr. Reduction of the particle size to <15 μ lowered the optimum sintering temperature to 1250°C for the same length of time.

Figure 70. Densities of Pellets Made from PuC Powder with Various Particle Sizes after Sintering in Vacuum for 2 hr at Increasing Temperatures

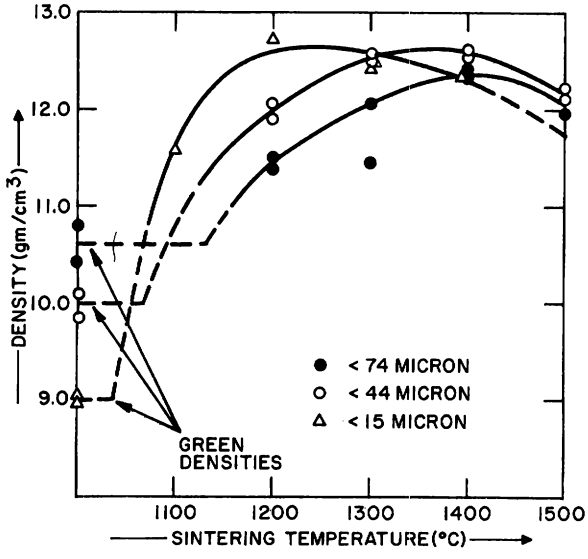

106-7542

Binder additions of more than 0.5 w/o caused a decrease in density and an increase in the carbon content of pellets made from <44 μ powder. The carbon content increased from 46.5 a/o carbon in the arc-melted material to as high as 50 a/o carbon in the sintered pellets when

0.5 w/o binder was used with the <15 μ powder. This substantial carbon pickup clearly shows that control of the carbon content would be extremely difficult in pellets made from fine powder coated with binder.

Figure 71. Change in Green and Sintered Densities with Forming Pressure for Pellets Made from PuC Powder with a Particle Size of <15 microns

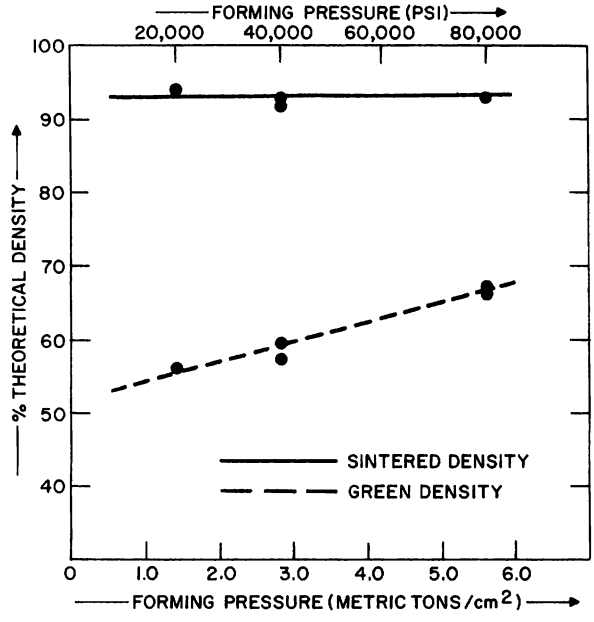

106-7541

The change in green and sintered densities of the pellets with forming pressure is shown in Figure 71. These pellets were made from <15 μ powder coated with 0.5 w/o binder. Increasing the forming pressures from 1.4 to 5.6 metric tons/cm^2 increased the green density, but there was no corresponding increase in the sintered density, which remained constant at about 93% of theoretical. Similarily, a change in forming pressure from 3.5 to 5.6 metric tons/cm^2 produced no increase in the sintered density of pellets made from powder with a particle size of <44 μ.

The sintered pellets were examined by ceramographic and X-ray diffraction techniques, and chemically analyzed for carbon and oxygen contents. Most of the pellets contained from 1.5 to 3.5 a/o oxygen. An oxide phase was present in all pellets which had combined carbon and oxygen contents of more than 50 a/o, whereas pellets with combined carbon and oxygen contents of less than 48.5 a/o contained no oxide phase.

These data indicate that a Pu(C, O) phase region exists in the Pu-C-O ternary system. This region appears to have an extensive solubility for oxygen. Compositions with combined carbon and oxygen contents of more than 50 a/o appear to be in a three-phase region between Pu(C, O), Pu_2C_3, and oxide. One boundary of this three-phase triangle was very close to the plutonium-carbon side of the ternary diagram.

There was a slight, almost uniform, loss in weight of the pellets up to the optimum sintering temperature of 1250°C for the <5 μ powder and 1350°C for the <74 and <44 μ powders, as shown in Figure 72. Above these temperatures the weight loss was high and appeared to be responsible for the decrease in densities with increasing sintering temperature.

Figure 72. Weight Loss of Pellets Made from PuC Powder with Various Particle Sizes after Vacuum Sintering for 2 hr at Increasing Temperatures

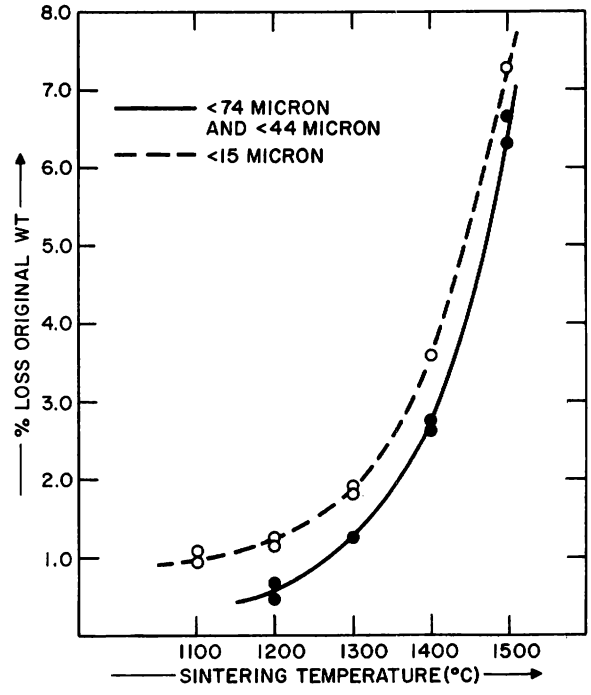

106-7544

Measurements of the melting point of PuC in a vacuum were inconsistent because of the rapid vaporization of material at temperatures near the melting point with a corresponding increase in carbon content. In some cases no melting point was observed for specimens heated in vacuum to above 1800°C. PuC heated in an argon atmosphere at atmospheric pressure had a melting point of 1665 ± 20°C, which was very close to the literature value of 1654 ± 20°C.[67]

Sintering studies were also made of solid solutions of UC with about 20% PuC. These studies indicate that the solid solution was considerably more difficult to sinter than either PuC or UC alone. Pellets made from powder with a particle size of <44 μ were vacuum sintered to a density of 85% theoretical at 1750°C. Powders of <15 μ particle size showed a great deal of outgassing when heated above 1200°C, which indicated the presence of oxygen in the UC-PuC powder. The highest density achieved with vacuum sintering at 1600°C was about 80% theoretical. Use of a flowing argon atmosphere for sintering of this powder at 1600°C increased the density to 86% theoretical.

b. Heat Capacity of Plutonium Monocarbide (O. L. Kruger and H. Savage)

The heat content of PuC above 298°K was measured with an isothermal drop calorimeter. The specimen was prepared by arc-melting the elements into a button and then drop-casting the button into a rod-shaped specimen. Since PuC has a defect structure with some vacancies at the carbon lattice sites, a composition of 46.5 a/o C was selected as being the closest to single-phase PuC. Ceramographic examination of the sample showed that no phases other than PuC were present.

---

[67] Mulford, R. N. R., Ellinger, F. H., Hendrix, G. S., and Albrecht, E. D., "The Plutonium-Carbon System," in Plutonium 1960 (Cleaver-Hume Press Ltd., London, 1961) 301.

The observed changes in enthalpy with increasing temperature are shown in Figure 73. No discontinuities were observed in this curve, which was described by the equation

$$H_T - H_{298} = -5035 + 13.08T + 5.718 \times 10^{-4}T^2 + 3.232 \times 10^5 T^{-} , \quad (1)$$

calculated by the method of least squares after correction of the data for the self-heating of plutonium. The magnitude of the self-heating correction was in the range 0.3 to 3.3 percent of the enthalpy values and was greater at low temperatures. The first derivative of the enthalpy equation gave the heat capacity equation:

$$C_p = 13.08 + 11.44 \times 10^{-4}T - 3.232 \times 10^5 T^{-2} \quad (2)$$

Values of $H_T - H_{298}$, C_p, and $S_T - S_{298}$ at temperature intervals of 100°K are listed in Table XL. These quantities were calculated to a temperature of 1900°K, which was 50°K below the melting point of PuC.[64]

Figure 73. Heat Content of PuC above 298°K

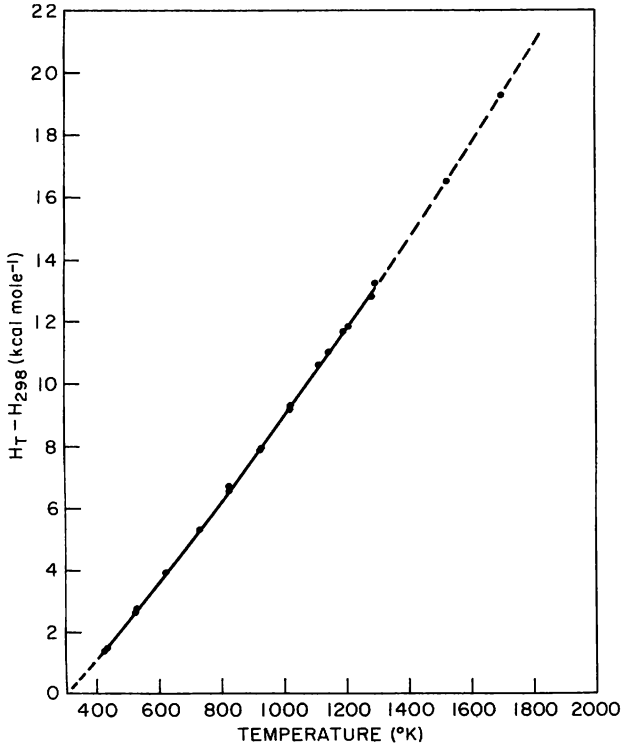

106-7622 Revised

The curve of C_p as a function of temperature is shown in Figure 74. The agreed[68] C_p curve for UC is shown for comparison. From 500 to 1200°K the PuC curve parallels the agreed curve for UC with a 0.8-cal mole^{-1} °K^{-1} displacement below the UC curve. Below 500°K the C_p values obtained from equation (2) decreased rapidly in an apparently unrealistic manner. In the absence of low-temperature data for PuC it was assumed that the curves for UC and PuC remained parallel below 500°K. Graphical extrapolation gave a C_p value of 11.3 cal mole^{-1} °K^{-1} for PuC at 298°K.

The PuC phase is known to have solubility for carbon from about 42.5 to 48.5 a/o. There is a corresponding expansion of the PuC lattice up to about 48.5 a/o

[68] The Uranium-Carbon and Plutonium-Carbon Systems. A Thermochemical Assessment. Technical Report Series No. 14, (International Atomic Energy Agency, Vienna, 1963).

Table XL

MOLAR THERMODYNAMIC PROPERTIES
OF PLUTONIUM MONOCARBIDE*

Temperature (°K)	$H_T - H_{298}$, cal mole^{-1}	C_p, cal mole^{-1} °K^{-1}	$S_T - S_{298}$, cal mole^{-1} °K^{-1}
400	1097	11.52	3.16
500	2296	12.36	5.83
600	3559	12.87	8.13
700	4865	13.22	10.15
800	6201	13.49	11.94
900	7562	13.71	13.52
1000	8943	13.90	15.01
1100	10342	14.07	16.34
1200	11757	14.23	17.57
1300	13188	14.38	18.68
1400	14633	14.51	19.77
1500	16091	14.66	20.57
1600	17564	14.78	21.94
1700	19049	14.92	22.61
1800	20547	15.04	23.47
1900	22057	15.16	24.30

*Last digit retained for comparison purposes only.

Figure 74. Heat Capacity of PuC and UC as a Function of Temperature

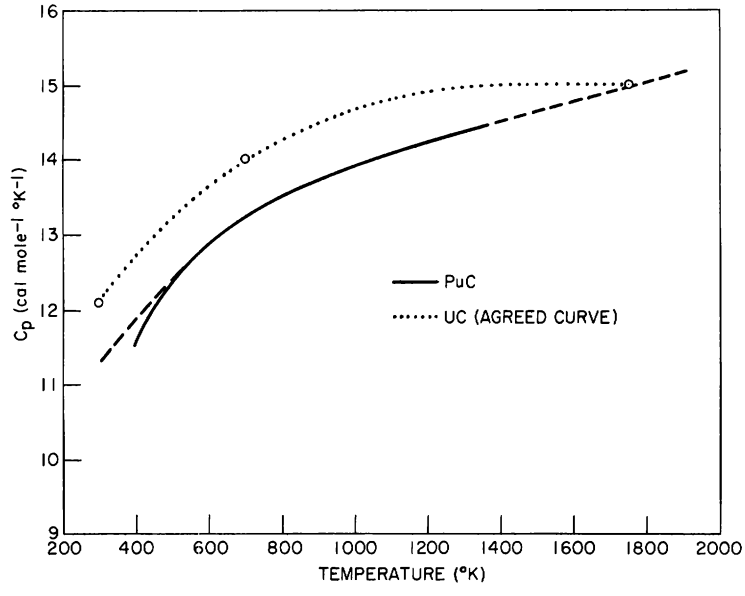

106-7621

carbon with the addition of carbon atoms to the vacant lattice sites.[69] Consequently, the C_p curve for PuC containing 46.5 a/o carbon may be below the curve for stoichiometric PuC because of the defect PuC structure. The increase in heat capacity that might be expected for a stoichiometric PuC phase with all of its carbon lattice sites filled was calculated by use of the Neumann-Kopp rule for a temperature of 700°K. With heat capacities of plutonium and carbon of 9.0[70] and 4.4[71] cal $mole^{-1}$ $°K^{-1}$, respectively, the heat capacity of stoichiometric PuC was 13.4 cal $mole^{-1}$ $°K^{-1}$. The defect PuC had a calculated heat capacity of 12.8 cal $mole^{-1}$ $°K^{-1}$. This increase of 0.6 cal $mole^{-1}$ $°K^{-1}$ in going from a defect to stoichiometric structure is very close to the 0.8 cal $mole^{-1}$ $°K^{-1}$ difference between the PuC and UC heat capacity curves.

This difference between the heat capacity curves of PuC and UC could be related to similar behavior observed in the heat capacities of the actinide dioxides. Osborne and Westrum[72] found that the room temperature heat capacities of ThO_2, UO_2, and NpO_2 increase with atomic number of the cation. From their entropy calculations they concluded that the isomorphous actinide dioxides above thorium in atomic number should have increasing entropies in accordance with the magnetic contribution of their cations. The magnetic contribution would increase with atomic number to give a predicted value for the entropy of PuO_2 of about 19.7 cal $mole^{-1}$ $°K^{-1}$ at 298°K. Sandenaw[73] measured the heat capacity of PuO_2 below 320°K and obtained a value for the entropy of 16.30 cal $mole^{-1}$ $°K^{-1}$ at 298°K. The value was considerably lower than predicted and was near the ThO_2 entropy value of 15.59 cal $mole^{-1}$ $°K^{-1}$ for the same temperature. This relationship between the heat capacity curves of the actinide dioxides may also be observed in the heat capacity curves of the actinide carbides. On this basis at 298°K the heat capacity of PuC would be below the value for UC, and then ThC would have a value near the one for PuC.

---

[69]Kruger, O. L., Phase Studies on Arc-melted Plutonium-Carbon Alloys Near the Monocarbide Composition, J. Am. Ceram. Soc., 46(2), 80 (1963).

[70]Loasby, R. G., Discussion in Plutonium 1960 (Cleaver-Hume Press Ltd., London, 1961).

[71]Kelley, K. K., Contributions to the Data on Theoretical Metallurgy, XIII. High Temperature Heat Content, Heat Capacity and Entropy Data for the Elements and Inorganic Compounds, Bur. Mines Bull., 584, 47 (1960).

[72]Osborne, D. W., and Westrum, E. F., Jr., Heat Capacity of Thorium Dioxide from 10 to 305°K. The Heat Capacity Anomalies in Uranium Dioxide and Neptunium Dioxide, J. Chem. Phys., 21, (1) 1884 (1953).

[73]Sandenaw, T. A., Heat Capacity of Plutonium Dioxide below 325°K, J. Nucl. Mat., 10(3) 16 (1963).

2. Preparation and Properties of Uranium, Thorium, and Plutonium Sulphides

a. Uranium Sulphide (P. D. Shalek, R. J. Dunworth, and J. T. Dusek)

The monosulphides of uranium, thorium, and plutonium are being investigated to ascertain their potential as nuclear fuels. Uranium and thorium sulphide were prepared by reacting H_2S gas with the finely divided metal. These materials have been found to have high melting points and large thermal expansion coefficients.[74]

The thermal conductivity was measured with a sintered specimen, 2 cm in diameter and 8 cm in length, with a central longitudinal hole of 0.3 cm, by paste molding. Uranium monosulphide having a particle size of $<37\ \mu$ was mixed with a binder to form a thick paste, which was charged to an aluminum mold and vibrated until solid. The formed piece was dried and then sintered in vacuum at 1850°C for 2 hr.

The specimen contained approximately 2.3 w/o of UOS and had sintered to 97.0% of theoretical density. The material in the specimen had a slightly contracted lattice parameter of 5.4871 Å, which would indicate that some foreign anions were in solid solution.

The thermal conductivity, measured to 1000°C in a previously described apparatus,[75] was found to increase with increasing temperature. The data are listed in Table XLI. The total thermal conductivity followed an equation of the type

$$K_{tot} = 0.060 + \frac{5.9}{T} + 2.44\,(10^{-8})\,T\sigma,$$

where the first two terms represent the phonon conductivity (K_p) and the last term, the electron conductivity $K_{(el)}$. The equation represents the data reasonably well between 0 and 1000°C.

b. Plutonium Sulphide (O. L. Kruger and J. B. Moser)

The reaction of plutonium metal with appropriate gases to form PuS and PuN was studied in apparatus, whose arrangement of the piping and glovebox connections is shown diagrammatically in Figure 75. A molybdenum reaction chamber was placed inside a stainless steel vessel

---

[74] Shalek, P. D., Preparation and Properties of Uranium and Thorium Monosulfides, J. Am. Ceram. Soc., 46(4) 155 (1963).

[75] Dunworth, R. J., Thermal Conductivity Apparatus, Annual Report for 1961, Metallurgy Division, ANL-6516, p. 403.

lined with molybdenum. This design was used to prevent the hot hydrogen sulphide gas from coming in contact with stainless steel. All tubing from the gas cylinders to the reaction chamber and vacuum pump was made of stainless steel. The tubing was connected through either O-ring seals or compression fittings. The entire gas system was checked with a helium leak-detector and found to be leak-tight.

Table XLI

CONDUCTIVITIES OF URANIUM MONOSULPHIDE

Temp (°C)	σ, $ohm^{-1}\ cm^{-1}$	K_{el}, W/(cm °C)	K_p, W/(cm °C)	K_{tot} W/(cm °C)
0	4440	0.0296	0.0814	0.1110
100	4150	0.0378	0.0758	0.1136
200	3950	0.0456	0.0729	0.1185
300	3820	0.0534	0.0717	0.1251
400	3730	0.0613	0.0727	0.1340
500	3660	0.0691	0.0744	0.1435
600	3620	0.0772	0.0751	0.1523
700	3610	0.0857	0.0740	0.1597
800	3610	0.0946	0.0705	0.1651
900	3640	0.1040	0.0645	0.1685
1000	3730	0.1160	0.0548	0.1703

σ - electrical conductivity
K_{el} - electrical contribution to thermal conductivity
K_p - phonon contribution to thermal conductivity
K_{tot} - thermal conductivity data

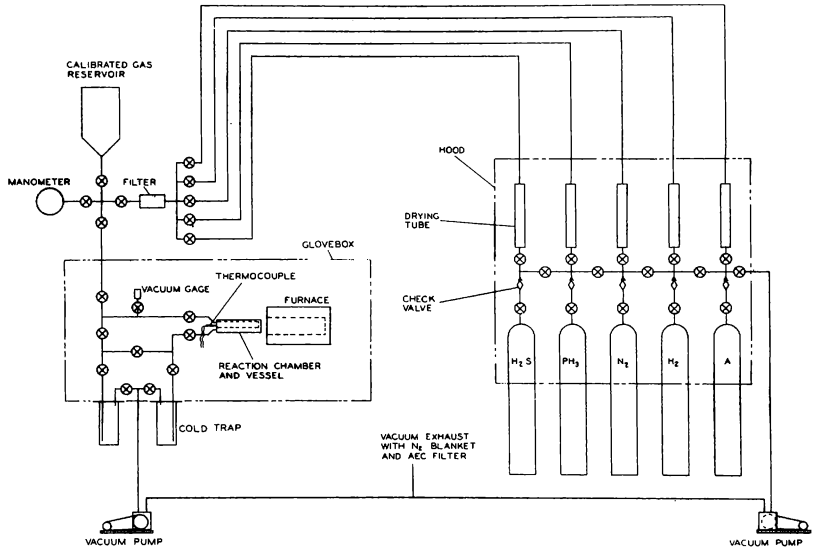

Figure 75
Plutonium-Gas Reaction Apparatus

Macro 38034

A calibrated gas reservoir and manometer were used to measure the amounts of gases needed for the preparation of the compounds. The gas line was filtered outside the glovebox to prevent plutonium from back diffusing into the piping system. Cold traps were incorporated into the system to cycle the H_2S gas by alternately freezing and pumping on each trap. During this process any hydrogen gas produced by the reaction of the gases with plutonium to form the sulphide was pumped off. The remaining gas pressure was then measured on the manometer to determine the extent of the reaction.

Pieces of plutonium metal were placed in the reaction chamber, and the apparatus was purged several times with argon gas. The plutonium was reacted with hydrogen gas at a temperature of about 200°C to form $PuH_{2.0}$-$PuH_{2.7}$. Unlike the uranium compound, the hydride did not break up into a fine powder by alternately hydriding and dehydriding; therefore, the pieces of plutonium hydride were removed from the reaction chamber, crushed to a fine powder, and replaced in the chamber. After again purging the entire system with argon gas, the powder was dehydrided under vacuum at 420°C. Complete decomposition of the hydride powder was never achieved. X-ray diffraction powder patterns always showed strong lines of the $PuH_{2.0}$-$PuH_{2.7}$ phase. To activate the powder further before reaction it was again hydrided at 200°C and then dehydrided at 400°C.

This powder was reacted with H_2S to make the sulphide, or with nitrogen to make PuN. For the sulphide the reaction was studied over a temperature range from 400 to 580°C. The best product obtained was from reaction at 400°C for 16 hr with H_2S gas at a pressure slightly below atmospheric. This reaction yielded Pu_2S_3 which had strong but diffuse lines on its X-ray photograms. Homogenization of the Pu_2S_3 powder at 1500°C in vacuum gave a powder composed of the PuS and Pu_2S_3 phases in equilibrium with a very small amount of an oxysulphide phase. All lines on the X-ray diffraction patterns were sharp, and doublets were easily identified. As with uranium sulphide, further heat treatment of the powder at 1750°C for 3 hr produced a sintered body. Sintering probably occurred through a liquid phase which was formed when the plutonium sulphide-oxysulphide eutectic temperature was exceeded. X-ray photograms of this material were identical with the ones made from the powder.

In a similar manner, plutonium nitride was prepared without difficulty by reacting plutonium hydride with nitrogen gas at atmospheric pressure for 16 hr at 230°C.

3. Preparation and Properties of Uranium, Thorium, and Plutonium Phosphides

a. Uranium and Thorium Phosphides (Y. Baskin and J. F. Dusek)

Uranium monophosphide was initially prepared by the reaction in vacuum of finely divided uranium with red amorphous phosphorus. The reaction was highly exothermic and resulted in the formation of a sub-stoichiometric UP clinker with a lattice constant of 5.57 Å. The greatest disadvantage of this method was the difficulty in obtaining a high-purity product. Oxygen contents of 1.1%, corresponding to about 9% of UO_2, represented the lowest values obtained with the powdered materials used. UO_2 was present as a grain boundary phase. Departure from stoichiometry was deduced from lattice-constant data and was caused by partial dissociation of UP at the high temperatures attained during the exothermic reaction (above 2500°C). Dissociation was suppressed by carrying out the reaction in a stainless steel autoclave.

A more satisfactory method of preparation was to react phosphine gas (PH_3) with finely divided uranium derived from the hydride. Reaction temperatures were varied between 280 and 720°C, and P/U ratios from 0.98 to 1.30, with only minor effects on the final material. However, smoothest operation and highest yields resulted when the reaction was carried out at 385°C with a P/U ratio slightly greater than one. X-ray diffraction analysis of the black, reacted material revealed the presence of only U_3P_4, although uranium was undoubtedly present in a very finely divided state.

The material was calcined at 1400°C in vacuum to homogenize it and drive off excess phosphorus, converting it into UP. The calcined material gave a very sharp X-ray pattern. A listing of some of the properties of the powder is given in Table XLII. The lattice constant, 5.589 Å, appeared to correspond to that of stoichiometric UP, since this was the value for UP in equilibrium with U_3P_4. Powders that were calcined at 1400°C were not hygroscopic. Material having an average particle size of 2.7 μ exhibited a 0.05% weight gain after a 5-week exposure to the atmosphere at room temperature. After 100 hr at 110°C, similar material showed a 0.15% weight gain.

Table XLII

PROPERTIES OF UP POWDER CALCINED AT 1400°C

Color	Dark gray	Oxygen Content	0.18-0.29%
Lattice Constant	5.589 ± 0.001 Å	UO_2 Content	0.4-1.5%
Theoretical Density	10.23 g/cc	Oxidation Resistance	Good
Pycnometric Density	9.77 g/cc	Hydration Resistance	Good
Particle Size	1.7-3.8 μ		

There are three compounds in the uranium-phosphorus system: UP_2, U_3P_4, and UP. The two higher phosphides are unstable at elevated temperatures, particularly UP_2, which decomposes rapidly in vacuum above 700°C. U_3P_4 decomposes at somewhat higher temperatures in vacuum (about 1150°C) to form UP and phosphorus vapor. UP, however, is quite stable, and has a melting point of 2540°C measured under a hydrogen atmosphere.

Uranium monophosphide is a gray, metallic-appearing, brittle compound with the hardness of glass. It has the rock salt-type crystal structure typical of other uranium compounds, such as UC, UN, and US.

UP has a room-temperature electrical resistivity of about 325 microhm-cm. On the basis of resistivity measurements performed between 78°K and room temperature, UP appears to have a positive, linear coefficient of resistivity with a value of 0.35 microhm-cm/°C. This indicates the presence of electrons in the conduction band.

Preliminary sintering curves for pellets pressed from fine, calcined UP powder are shown in Figure 76. Fabrication and heating temperatures were the only two variables. Increasing the forming pressure from 1406 to 2812 kg/cm^2 resulted in an increase in fired density of from 3 to 5% for all sintering temperatures used. Both the sintered density versus temperature curves showed discontinuities between 1700 and 1800°C. The curves steepen considerably in this temperature range, again becoming more shallow at higher sintering temperatures. No explanations are currently offered for the presence of the discontinuity. No significant increase in density occurred when sintering was carried out above 2000°C, since further shrinkage was offset by vaporization losses.

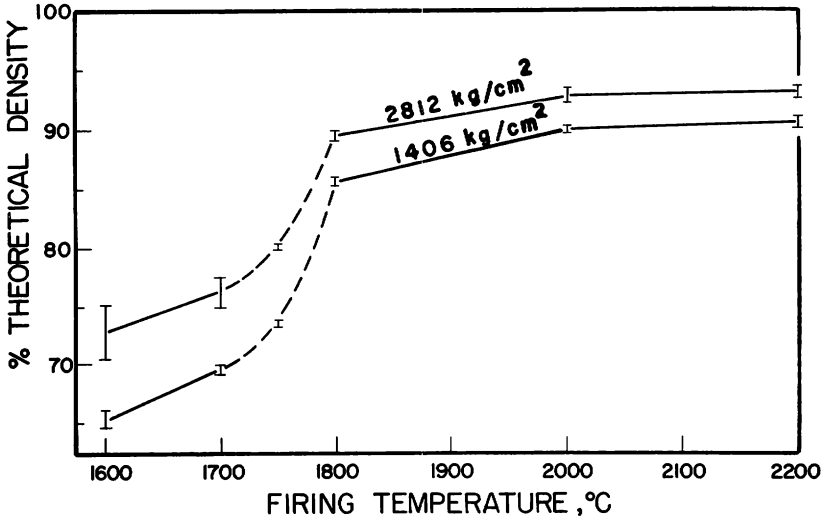

Figure 76

Bulk Density of UP Pellets vs Firing Temperature (Fired in Vacuum for 1 Hour).

Macro 38037

UP pellets appeared to be susceptible to formation of surface crazing, particularly when heated to only 1600°C. Crazing was minimized by using pressures of 2812 kg/cm^2 and higher. In all cases surface cracks were virtually healed after heating to 2000°C. Experiments are underway to determine the cause of cracking.

Densities of the order of 92-93% of the theoretical value were achieved by use of forming pressures of 2812 kg/cm^2 and heating at 2000°C for one hour. Figure 77 shows a photomicrograph of a sample sintered to a density of 9.4 g/cc, or 92% of the theoretical density. The small amounts of UO_2 represent the only other phase present.

Figure 77. Photomicrograph of UP Pellet Fired at 2000°C in Vacuum. Matrix is UP, Medium Gray Phase is UO_2, and Black Areas are Pores.

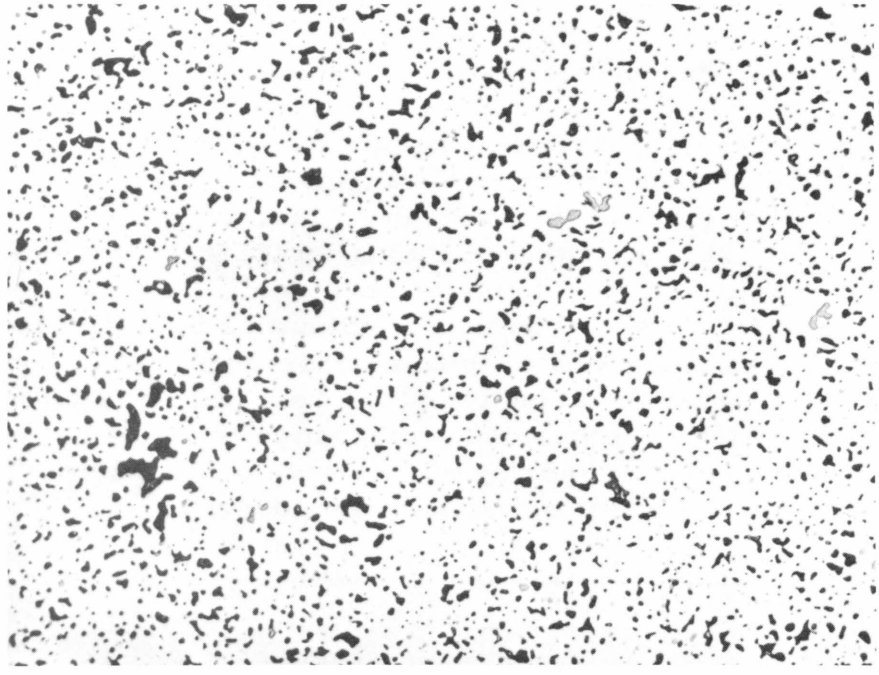

Micro 36398

Determination of the thermal conductivity is currently in progress. A specimen was prepared by paste molding. UP having a particle size of $<37\ \mu$ was mixed with a binder solution of stearic acid and acryloid in carbon tetrachloride to form a thick paste. This paste was slowly added to an aluminum mold, and the mold was vibrated until the paste became sufficiently firm to be removed from the mold and dried. The formed specimen was isostatically pressed at 3.86 metric tons/cm^2, and following this treatment was found to have a density of 75% of theoretical. The specimen was sintered in vacuum at 1900°C for 3 hr, and this heat treatment was found to increase the density from 75 to 86% of

theoretical. The rough surfaces of the specimen were removed by surface grinding, and a center hole was drilled.

Preliminary vaporization studies made with a mass spectrometer were conducted by R. J. Ackermann of the Chemistry Division with UP containing 1% oxygen. UO and some UO_2 were the major gaseous species coming off between 1500 and 2000°C. Above 2000°C the oxide gases diminished, and elemental P and then U became very prominent. In contrast with US, no sign of the compound UP was noted among the gaseous species. These observations corroborated results of weight-loss experiments with fairly pure UP, which indicated that weight losses only became significant above 2000°C and that phosphorus was first selectively lost from the UP structure. Chemical analysis of samples heated to high temperatures showed lower oxygen contents than originally, indicating that UP vaporizes more slowly than UO_2.

Single crystals of UP grew along the cooler portions of crucibles during heating of samples above 2000°C. The crystals exhibited good euhedral shapes and averaged 0.2 mm in size. On the basis of single-crystal X-ray studies, such crystals were of good quality. However, they were somewhat substoichiometric as a result of formation at these elevated temperatures.

UP reacts with metallic uranium to form an anion-deficient structure. Up to 5% uranium can be absorbed at 1600°C, producing 5% of anion vacancies. The unit cell contracts with departure of the composition from stoichiometry. Stoichiometric UP has a lattice constant of 5.589 Å, whereas $UP_{0.95}$ has a value of 5.582 Å. The fully stoichiometric structure does not appear capable of accommodating excess phosphorus. Below 1200°C in vacuum or at higher temperatures under high phosphorus pressures, U_3P_4 coexists with UP when the P/U ratio exceeds unity.

The lattice constant of UP has also been observed to shrink as a result of heating in vacuum at temperatures above 1500°C. This was attributed to irreversible loss of phosphorus at elevated temperatures. Departure from stoichiometry increased with rising temperature, indicating that the UP rock salt structure can tolerate more vacancies concomitant with greater phosphorus loss. Based on preliminary results and assuming a linear lattice constant-composition relationship, an equilibrium composition of about $UP_{0.90}$ exists at the melting point (2540°C). Attempts will be made to determine the melting point of stoichiometric UP.

UP was readily arc-melted, but the compound showed considerable weight losses at the melting temperature due to its dissociation. Losses of about 7% occurred after the material was molten for 4 min. Uranium reflections were detected in X-ray photographs of the melted material, and substantial amounts of phosphorus were seen to be condensed on the cooler positions of the apparatus.

UP and UO_2 were compatible even above the melting point of the former. No evidence was found for the existence of a uranium oxyphosphide compound, either at low or high temperatures. X-ray analysis of compositions across the UP-UO_2 system showed that neither structure was affected by the presence of the other during heating at 2000°C. The lattice constants of both compounds remained unchanged across the entire compositional range. Work is in progress to determine the composition and temperature of the eutectic presumed to occur in the system.

Resistance to tarnishing and the relatively nonpyrophoric nature of UP were observed early in the study. Coarse UP powder could be ground in air without igniting, and polished specimens maintained a bright metallic appearance at room temperature. This behavior differed markedly from that of other uranium compounds having the same crystal structure; these were quite susceptible to oxidation and generally ignited during grinding. From a thermodynamic standpoint UP should behave similarly.

Ignition studies, conducted in a DTA apparatus and employing a dynamic flow of oxygen, confirmed the difference in oxidation behavior between UP and the compounds UC, UN, US and UAs. The contrast is vividly illustrated in Figure 78.

Figure 78. Representative DTA Thermograms for UC, UN, UP, US, and UAs in Dynamic Oxygen at 1 atm. Powdered samples were passed through a 200 mesh screen, diluted with an equal weight of Al_2O_3, and heated at 10°C/min.

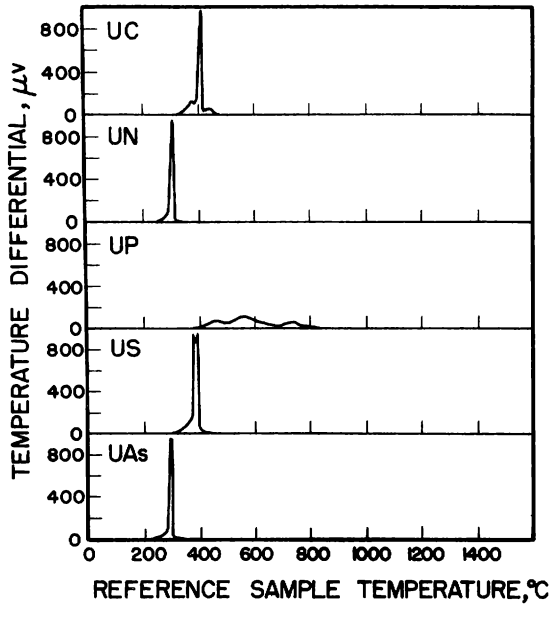

Macro 38036

UP exhibited several broad exothermic peaks over the range 400-750°C, as opposed to sharp peaks produced by the other compounds, which occurred between 290 and 420°C. Moreover, the solid residues of the other four compounds, after firing to 1000°C, consisted exclusively of U_3O_8. On firing to 1000°C, the oxidation residue of UP consisted primarily of $(UO_2)_2P_2O_7$; small amounts of U_2O_8 were present. Evidently, the difference in oxidation behavior between UP and the four other uranium compounds was a kinetic one and was related to the formation of an oxidation product which coated the grains and retarded oxygen attack. Of the five compounds investigated, only UP has an anion that oxidizes to a nongaseous compound at moderate temperatures and which in turn reacts with uranium oxides.

The course of oxidation of UP can be followed in Figure 79, which is a representative DTA thermogram along with a listing of crystalline phases observed in samples heated to different temperatures. The first peak at 460°C represents oxidation of the finer fraction of the UP to form UO_2 of an unknown oxidation state and amorphous P_2O_5. Although not detectable by X rays, the presence of amorphous P_2O_5 is unequivocal, since crystalline uranium phosphates form at higher temperatures. Formation of moderate amounts of UP_2 on heating of UP in oxygen is quite unusual. Apparently, during the early stages of oxidation of UP, oxygen atoms are preferentially bonded to uranium atoms. In the process phosphorus atoms are ejected from the rock salt structure, reacting with UP to form UP_2 and some U_3P_4. Similar formation of U_2N_3 has been observed during oxidation of UN.[76] Formation of UP_2 at the expense of UP, and its persistence at 600°C in the DTA run after all the UP has been consumed, appears to establish its greater oxidation resistance compared with the monophosphide.

Figure 79. DTA Thermogram for UP in Dynamic Oxygen at 1 atm. Pellet sintered at 1800°C was ball milled, diluted with an equal weight of Al_2O_3, and heated at 5°C/min.

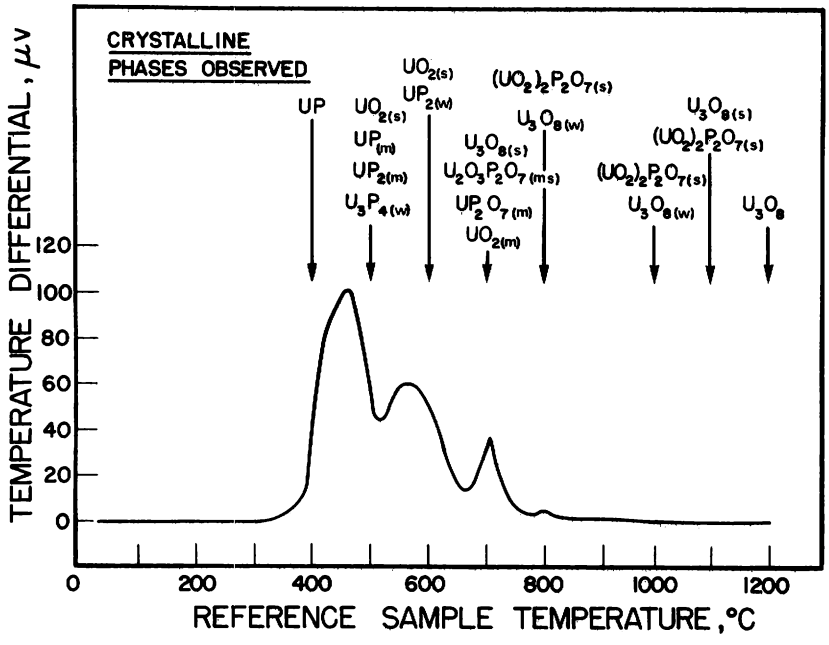

Macro 38038

Oxidation of the coarser UP fraction produced the second peak at 560°C. Interestingly enough, the temperature of the second peak coincided with the melting point of P_2O_5. This is probably not coincidental as oxygen diffusion rates through P_2O_5 may accelerate rapidly at or near its melting point.

---

[76]Dell, R. M., Harwell, personal communication.

The third peak at 700°C resulted primarily from oxidation of UO_{2+x} to U_3O_8. Formation of the two uranium phosphates, UP_2O_7 and $U_2O_3P_2O_7$, may also have contributed to the exothermic reaction. Above 700°C the liquid P_2O_5 no longer delayed oxidation of the UO_2 phase to U_3O_8, which occurred concurrently with formation of the uranium phosphates.

Reaction of U_3O_8 with P_2O_5 and UP_2O_7, and oxidation of $U_2O_3P_2O_7$ resulted in the formation of $(UO_2)_2P_2O_7$ at 800°C, producing the small exotherm. Presence of small quantities of U_3O_8 indicates that some P_2O_5 volatilized during heating to 800°C. Heating above 1100°C resulted in decomposition of the phosphate to give U_3O_8.

Particle size of the UP affected the shape of the DTA thermogram. This is not unexpected since specific surface area is known to influence exothermic peak intensities and the temperatures at which peaks occur. Decreasing the particle size resulted in an augmentation of the peak at about 460°C at the expense of the one at 560°C (see Figure 79). Ignition of very fine calcined UP powder yielded a different thermogram from that of Figure 79, but one similar to those for UC, UN, US, and UAs. The exothermic peak at 440°C was very sharp and strong, whereas the peaks at 560 and 700°C were relatively weak.

Static oxidation studies conducted in air yielded results similar to those obtained with the DTA; however, as temperatures were increased stepwise very slowly, reactions took place at lower temperatures than in the DTA apparatus. X-ray examination of powders at various stages of oxidation provided interesting insights on the structural changes occurring in UP during the process. The UP structure showed signs of degradation with an oxygen pickup of 2%. High-angle X-ray reflections became diffuse, and the lattice showed a small expansion. These two phenomena may be related to the occurrence of interstitial oxygen atoms, which resulted in both an enlarged and strained UP lattice. This trend continued with increased oxygen pickup until about 6%, at which point UO_2 first appeared. UP_2 was also present throughout the early stages of oxidation and persisted after total consumption of the UP.

Thorium monophosphide was prepared by reaction of phosphine gas with finely divided thorium obtained from the hydride. Comminution of thorium was more difficult and generally required more hydriding cycles. Reaction with phosphine was carried out at 550°C and proceeded smoothly. X-ray diffraction of the black reacted material revealed the presence of Th_3P_4 as the major phase, with some ThP, ThO_2, and thorium hydride as minor phases. The material was calcined in vacuum at 1300°C to homogenize it and drive off excess phosphorus. The calcined material was dark blue and yielded a very sharp X-ray powder pattern. The lattice constant of 5.83 Å corresponded to the literature value for the compound. The X-ray powder pattern showed only small amounts of ThO_2 contamination, corresponding to about 0.3% of oxygen.

b. Plutonium Phosphide (J. B. Moser and O. K. Kruger)

Plutonium phosphide was prepared by the reaction of plutonium metal with phosphorus in a tantalum-lined stainless steel pressure vessel. Constant external pressure during the heating and cooling cycles was maintained by means of spring loading.

The apparatus used, shown in Figure 80, consists of a bench vise which holds a C-clamp to which a platform is welded for support of the clam-shell furnace and pressure vessel. After this is filled with the reactants, it is held by the C-clamp and the furnace is closed by means of a latch. Figure 81 shows the pressure vessel assembly, which consists of a stainless steel vessel containing a tantalum liner and cap. The vessel is maintained closed and sealed by means of a stainless steel cap pressing against a serrate copper gasket. The screw pressure from the C-clamp is applied through a series of Belleville spring washers insulated from the hot zone of the furnace by transite spacers. A considerable part of the deflection of this type of spring washer will occur at constant load; thus the pressure vessel is permitted to expand thermally against the

Figure 80. Apparatus for Preparation of Plutonium Phosphide

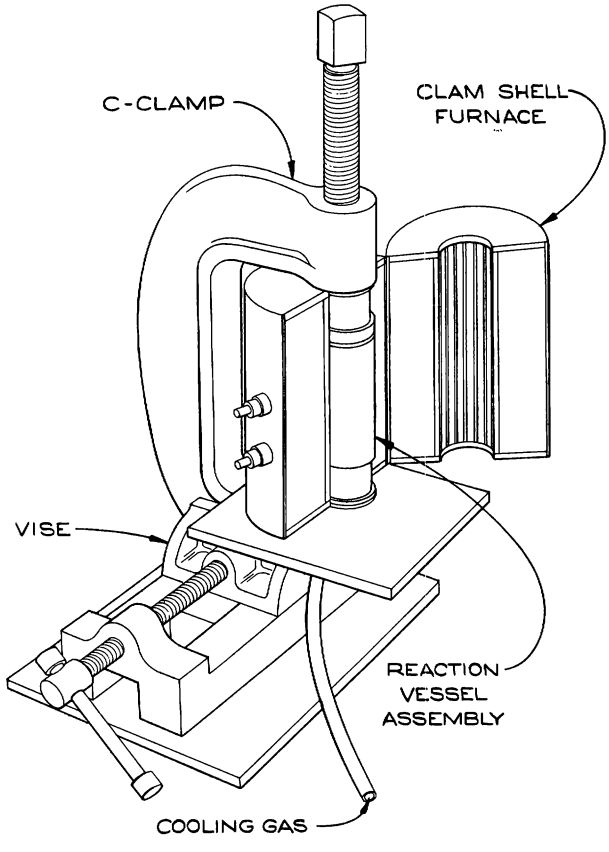

106-7537

Figure 81. Reaction Vessel Assembly

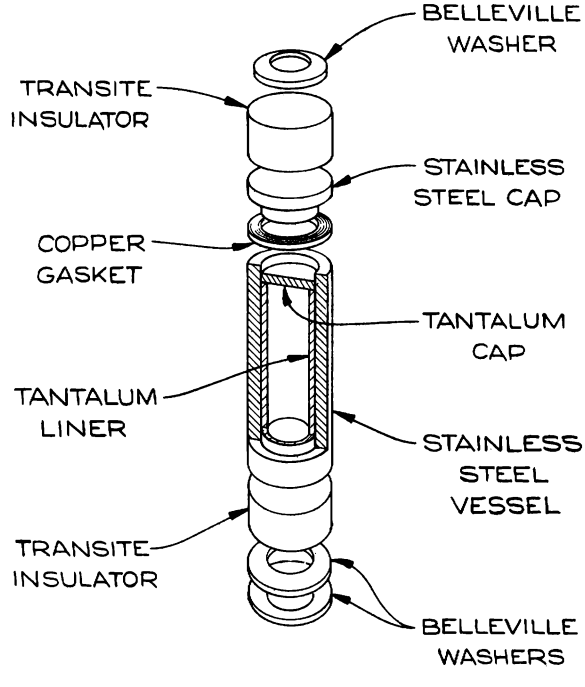

106-7538

C-clamp upon heating without danger of rupture and contract upon cooling without danger of pressure release. On the other hand, a sudden unexpected pressure surge will be relieved safely in this apparatus.

As the glovebox atmosphere consisted of nitrogen with small amounts of water and oxygen, the pressure vessel was purged filled, and sealed in a container full of high-purity argon gas. The vessel was then heated to between 600 and 800°C for one-half to several hours. One hundred to 150 a/o excess phosphorus over the amount needed to produce stoichiometric PuP was used, for the phosphorus vapor reacted with the copper gasket to produce a small amount of copper phosphide, which incidentally, served to seal the reaction vessel tightly. Later this compound was identified by X-ray diffraction as Cu_3P; a green color upon solution indicating the presence of copper ion was also noted. Contamination of the PuP reaction product was suspected but spectrographic analysis revealed only 30 ppm Cu. At the end of each run unreacted red phosphorus was found in the vessel, indicating that the excess amount used was adequate. Upon conclusion of the heat treatment, the furnace was opened and the pressure vessel exposed to a stream of argon gas. A blower cooled it from maximum operating temperature in 30 min to one hour.

The quantity of PuP formed depended on the amount of plutonium used, the maximum temperature that was reached, the length of the heat-up period, and the time held at maximum temperature. The product was identified by X-ray diffraction and the d-spacings found agreed well with those reported by Gorum.[77] It appears that the reaction between plutonium metal and phosphorus is not as strongly exothermic and also differs considerably from the behavior of uranium and phosphorus, which is highly exothermic around 400°C.

This conclusion was reinforced by observations made during the production of PuP and PuS in an arc furnace. As soon as molten metal came in contact with sulphur, PuS was formed in a visibly exothermic reaction and the arc was shut off while the reaction went to completion. However, when PuP was made, the arc had to be maintained throughout the run, long after the plutonium was in the molten state.

Because of the excessive vaporization of the phosphorus, the production of PuP by this method was found to be unrewarding, although promising results were obtained, as indicated in Figure 82, which shows a photomicrograph of arc furnace-produced PuP. The surface is shown in the as-polished condition at 500X. The extensive dark areas consist of PuP surrounded by a small amount of light-colored alpha plutonium at the grain boundaries. This interpretation is borne out by X-ray diffraction and

---

[77]Gorum, A. E., Some Compounds of Plutonium with Metalloid Elements, M.S. Thesis, University of Arizona (1955).

a chemical analysis that yielded 8.5 a/o phosphorus. Stoichiometric PuP contains 11.5 a/o P. The presence of the alpha-plutonium phase may be an indication that the solid solubility of phosphorus in plutonium is quite low.

Figure 82. PuP Produced in the Arc Furnace

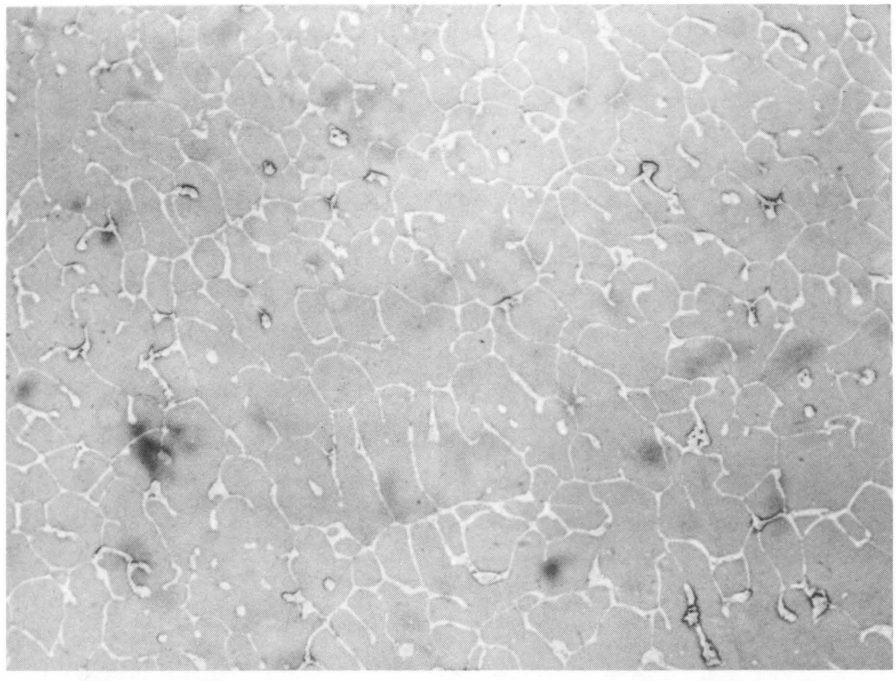

106-7536 As-polished 500X

Massive plutonium pieces of 1 to 5 gm were used to prevent oxidation of the metal in the glovebox atmosphere during preliminary handling; this may account for the relatively low reaction velocity. It was found that if solid pieces of uranium are heated in phosphorus vapor, a surface layer of reaction product forms which acts as a diffusion barrier. This is also likely to occur in the case of PuP. Figure 83 shows a specimen for which the reaction had not gone to completion; the cross section is shown in the as-polished condition at 200X. The darker areas on the outside of the sample consist of the PuP phase; the light, unreacted Pu is shown in the center. The cracks seen in the PuP regions may have been introduced during the polishing operation. The inclusions in the plutonium matrix have not been identified, but appear to consist of PuP fragments breaking loose at the reaction boundary and migrating into the molten plutonium.

Plutonium phosphide will also be made by the reaction of finely divided plutonium with phosphine gas. Phosphine gas, however, is toxic and flammable when exposed to air. Use of this gas with hydrogen in a system containing plutonium could conceivably cause a fire or

explosion at the exhaust of the vacuum pump. A system has been designed and built which will dilute the phosphine-hydrogen gas mixture with nitrogen at the vacuum pump exhaust. This system has been found to be satisfactory for exhausting more than 4 liters of a 50/50 mixture PH_3 and H_2 gas directly into the exhaust system.

Figure 83. Cross Section through Incompletely Reacted Specimen of PuP Taken from Pressure Vessel

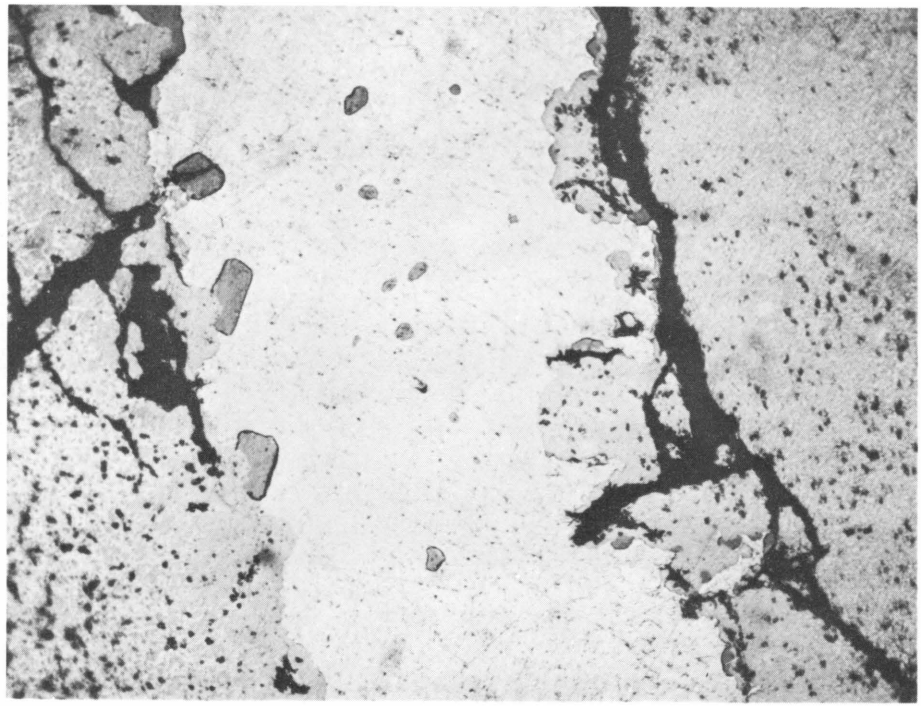

106-7535 As-polished 200X

4. Binary Compound Systems

a. Phase Studies in the System UC-US (G. D. White, P. D. Shalek, and J. T. Dusek)

A study was initiated in the system UC-US to determine phase equilibrium and physical properties of binary compositions. Both compounds have been studied individually,[78,79] and UC is being considered as a fuel for several reactors.

---

[78] Proceedings of the Uranium Carbide Meeting, December 1960, TID-7603.

[79] Shalek, P. D., Preparation and Properties of Uranium and Thorium Monosulphides, J. Am. Ceram. Soc., 46(4), 155-61 (1963).

The UC used was made by reacting uranium and carbon in an arc melting furnace. The granular product was reduced to a particle size of $<15\ \mu$ by crushing and ball milling in argon. Chemical analysis of the powder gave 4.80 w/o carbon and 0.51 w/o oxygen. X-ray diffraction produced only reflections for UC with a unit cell size of 4.960 Å. The US was produced by reacting H_2S with finely divided uranium metal, which was obtained by hydriding metal chips and decomposing the hydride.[78] This material was analyzed to contain 11.76 w/o S, 87.18 w/o U, with a 1.36 w/o insoluble residue which was UO_2. The US was crushed and ball milled to a particle size of $<37\ \mu$.

Specimens for phase-equilibrium studies were prepared by dry mixing the powders and pressing the mixtures into cylindrical pellets with 1 w/o or less of stearic acid binder. All reactions and sintering were done in vacuum (10^{-5}-10^{-6} torr), and temperatures were determined by means of an optical pyrometer. After a period of reaction at temperature, specimens of some compositions were pulverized, repressed, and reacted for an additional length of time to insure that equilibrium had been attained. Specimens were heated for a total of from 3 to 19 hr, depending upon the temperature and composition, and were furnace quenched by suddenly reducing the power to the heating element. Phase determinations were made by ceramographic and X-ray powder diffraction techniques. Unit cell sizes for phases were determined by a Nelson-Riley extrapolation.

The results of specimen equilibration and quenching, as obtained by both X-ray diffraction and ceramographic examination, are shown in Table XLIII. The system contained no intermediate compounds in the temperature range studied, but showed limited solubility of each component in the other, with an intermediate region containing both solid solutions. The change of unit cell sizes of the solid solutions with composition is shown in Figure 84. At 1600°C, US dissolved in UC to produce a maximum unit cell size of 4.981 Å, and at 1700°C of 4.985 Å. The lowered unit cell sizes of specimens heated at 1800°C is attributed to the vaporization of US in vacuum. The saturated solid solution of UC in US had a minimum unit cell size of 5.316 Å for material heated at 1600°C, and there was little change upon heating at 1700°C.

As the amount of UC in solution approached the maximum, the back reflections of the X-ray photographs became progressively more diffuse. This was interpreted as an indication of the large amount of strain in the structure due to the relatively large difference in ion size between carbon and sulphur.

Determinations of melting temperature were made in a hydrogen atmosphere in a tungsten-resistance furnace. Melting was observed visually with an optical pyrometer. A temperature-correction curve was prepared by observing the melting point of materials with

well-established melting points. Fragments of specimens were set on tungsten and heated to their melting temperature in less than 5 min.

Table XLIII

RESULTS OF EQUILIBRATION AND QUENCHING

Composition, m/o UC	Phases Present at			
	1450°C	1600°C	1700°C	1800°C
97.5		UCss*		
96.0	UCss, tr. USss	UCss, tr. USss		UCss
95.0		UCss, USss, tr. UO_2	UCss, USss, tr. UO_2	UCss, tr. UO_2
94.0	UCss, USss	UCss, USss		UCss, tr. USss
90.0		UCss, USss, UO_2	UCss, USss, UO_2	UCss, USss, UO_2
80.0				
70.0				
60.0				
50.0				
40.0		tr. UCss, USss, UO_2	tr. UCss, USss, UO_2	USss, UO_2
30.0		USss, UO_2	USss, UO_2	USss, UO_2
20.0		USss, tr. UO_2	USss, tr. UO_2	USss, tr. UO_2
10.0		USss	USss	USss
5.0		USss	USss	USss

*Solid solution

Figure 84. Unit Cell Sizes of Solid Solutions in UC-US Compositions Quenched from Three Equilibration Temperatures

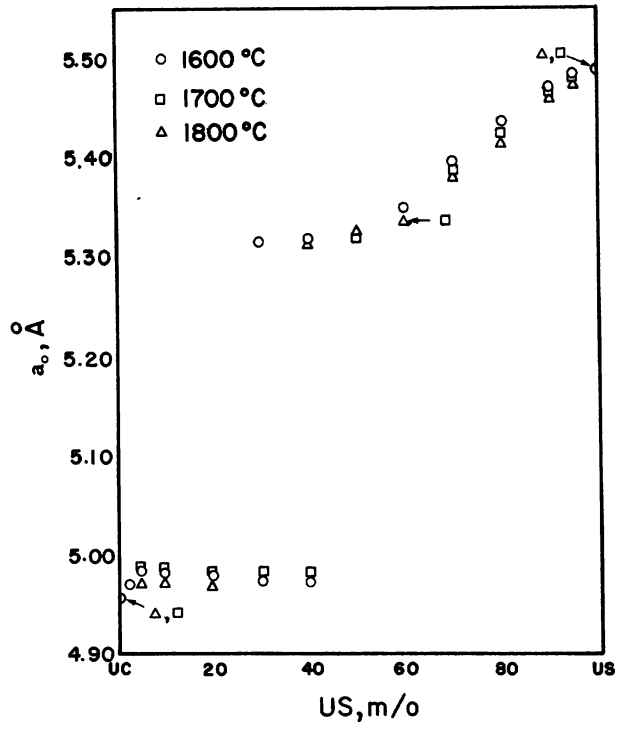

Macro 37575

The determinations indicated a maximum liquidus temperature of 2540°C for the composition 40 m/o UC-60 m/o US, which is also approximately the limit of solubility for UC in US. This temperature is higher than the melting point determined for either US (2460°C) or UC (2410°C). A shallow eutectic was indicated at approximately 90 m/o UC-10 m/o US, and a minimum melting solid solution at approximately 5 m/o UC-95 m/o US.

The effect of small amounts of uranium oxide present in the specimen was thought to be slight. Ceramographic examination indicated reaction only at the surface of the specimens, with a small amount of UO_2 present in the interior as a discrete phase. Weight losses were small for all of the specimens. Based on these data and the melting temperatures, a preliminary phase diagram was prepared (see Figure 85). The limit of solubility of US in UC is a little less than 4 m/o at 1600°C and approximately 4 m/o at 1700°C. Maximum solubility of UC in US is approximately 40 m/o at 1600°C and increases very little at 1700°C. Two saturated solid solutions occur in equilibrium between these phase boundaries.

Figure 85. Preliminary Phase Equilibrium Diagram of the System UC-US

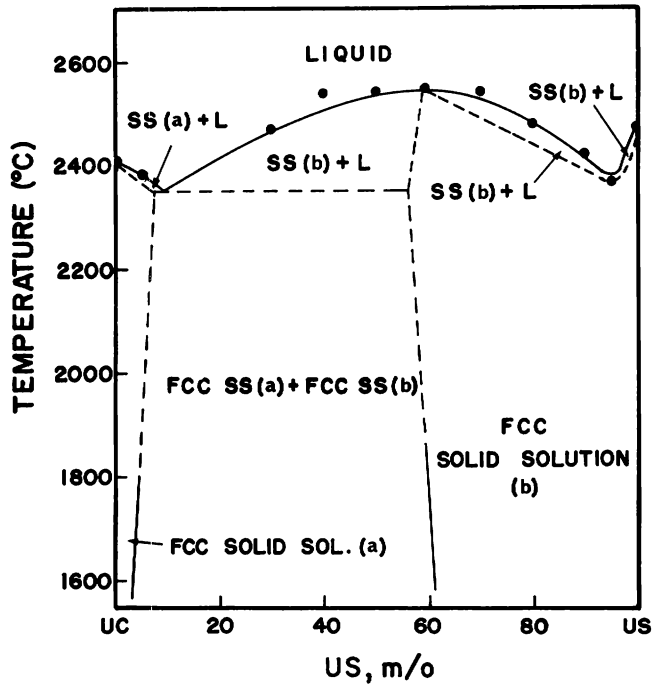

Macro 37576

Specimens 80 mm in length and 20 mm in diameter, having a 2.9 mm central hole, were fabricated for determination of thermal conductivity. Uranium monocarbide and uranium monosulphide were crushed to a particle size of <37 μ. A mixture of 80 w/o UC and 20 w/o US was weighed, and the mixed powders compacted and sintered. The sintered material was crushed to a particle size of <37 μ, and the powder mixed with a binder to form a thick paste. This paste was vibration-compacted in an aluminum mold and allowed to dry. Following drying the formed specimen was sintered in vacuum at 1900°C for 2 hr. The sintered specimen was found to have a density of 72% of theoretical.

b. Phase Studies in System UP-US (Y. Baskin and P. D Shalek)

X-ray diffraction and metallographic analysis revealed that UP and US exhibit complete mutual solubility. This was not surprising in view of the small difference in lattice constants of the two compounds. Lattice constants of compositions at 10% intervals across the system fell on a smooth curve that exhibited a positive deviation from a straight line (Vegard's Law).

Measurements of electrical resistivity at room temperature showed a moderate initial increase in resistivity with incorporation of US in UP. The resistivity values then decreased with larger concentrations of US. Solid solutions toward the US end of the system showed a very sizeable increase in resistivity over that of US, partly as a result of cracking of these sintered samples. The value of electrical resistivity for US was 260 microhm-cm, which may be compared with 325 microhm-cm for UP.

A preliminary phase diagram for the UP-US system is shown in Figure 86. Melting was done in tungsten boats under an atmosphere of hydrogen. The existence of a melting maximum in the system is unusual, although not unique. Chikalla[80] reported a melting maximum in the system UO_2-PuO_2, and Shalek and White[81] have reported one in the system UC-US. A high-temperature ordered structure or compound may exist which would raise the melting point through stronger lattice binding. However, thus far there has been no evidence of superlattice lines or of retention of a high-temperature compound. Annealing of several compositions at 900°C or 1100°C for 30 hr failed to produce visible changes in the

---

[80] Chikalla, T. D., Melting Behavior in the System UO_2-PuO_2, J. Am. Ceram. Soc., 46(7), 323-8 (1963).

[81] Shalek, P. D., and White, G. D., "Studies in the System UC-US," Proceedings of the Symposium on Carbides in Nuclear Energy, MacMillan & Co., Ltd. (in press).

diffraction patterns. Studies will be initiated to find an explanation for this unusual phenomenon.

Figure 86. Preliminary UP-US Phase Diagram

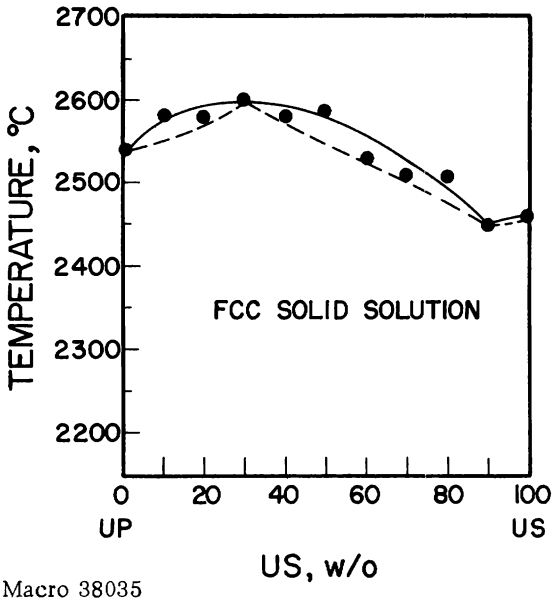

Macro 38035

Samples of the two end members in the UP-US system showed higher sintered densities than those of the intermediate compositions. The drop in density was most prominent toward the US end of the system, partly due to cracking in this compositional range. Cracks showed up again in samples of identical composition during a second run and were attributed to some unknown outgassing reaction. On melting, the cracked samples appeared to exhibit higher vapor losses than samples of UP, US, or the uncracked samples rich in UP.

UP apparently forms an unlimited series of solid solution with isomorphous UAs, which compound has a slightly larger unit cell. Solid solution with UN is very slight and is restricted to a small amount of UN in UP.

Oxidation studies of powdered samples in the UP-US system were made. All samples were heated to 1000°C in dynamic oxygen. As was discussed earlier, US exhibited a sharp exothermic peak at 380°C, whereas UP exhibited several broad peaks, the one at 560°C generally being the largest. Addition of 20% UP in US shifted the exothermic peak to 500°C and made it much broader; addition of 40% US shifted the peak to 560°C. Evidently, incorporation of UP in these amounts is sufficient to retard oxidation by forming an amorphous P_2O_5 coating around the grains. Residues from the DTA runs of all samples, except that of pure US, contained the compound $(UO_2)_2P_2O_7$ in addition to U_3O_8.

5. Rare Earth Oxides (Y. Baskin)

An attempt has been made to stabilize rare earth oxides in perovskite-like compounds (ABO_3) by combining them with other oxides. The two rare earth oxides of interest, Dy_2O_3 and Eu_2O_3, were combined with suitable oxides of cobalt, iron, and nickel.

High-purity Dy_2O_3 and Eu_2O_3 were calcined at 1000°C, and each was mixed with equivalent amounts of reagent-grade Co_3O_4, Fe_2O_3, and NiO, which had been heated to 500°C. The powders were blended in a ball

mill and pressed into pellets. Samples were first heated in air at 1500°C. All of the samples retained their shapes, with the exception of the cobalt-europium oxide, which melted and reacted with the alumina crucible

X-ray analyses showed complete reaction of Fe_2O_3 with both Dy_2O_3 and Eu_2O_3 to form $FeDyO_3$ and $FeEuO_3$. $FeEuO_3$ has been described in the literature, but $FeDyO_3$ has not been reported previously. $CoEuO_3$ formed, but it melted below 1400°C; it also has not been hitherto reported. No sign of reaction was observed between NiO and either of the rare earth oxides or between Co_3O_4 and Dy_2O_3.

Heating at 1200°C did not result in any melting. X-ray analysis showed complete reaction between cobalt oxide and Eu_2O_3 to form $CoEuO_3$. This compound is orthorhombic, has the perovskite structure, and is isomorphous with $FeEuO_3$ and $FeDyO_3$. Incipient reaction occurred between cobalt oxide and Dy_2O_3, but none was observed between NiO and Dy_2O_3 or Eu_2O_3.

DTA studies revealed that the reaction between Fe_2O_3 and Eu_2O_3 was exothermic and occurred at 1200°C. Reaction between cobalt oxide and Eu_2O_3 was also exothermic and took place at 1060°C. The original Co_3O_4 dissociated at 950°C to CoO, which then reacted with Eu_2O_3.

The cubic to monoclinic transformation of Eu_2O_3 at about 1050°C may account for its greater reactivity in comparison with Dy_2O_3; the latter does not undergo a similar change below 1400°C. The greater refractoriness and stability of NiO compared to Co_3O_4 and Fe_2O_3 may account for its lower reactivity.

6. Urania Burnable Poisons (R. J. Beals)

The use of burnable poisons in the shim zone of the plutonium recycle core for EBWR has stimulated interest in the reactions which occur between urania and the several rare earths. Chosen for investigation were compositions containing, in combination with urania, the rare earth oxides ceria, samaria, europia, gadolinia, and dysprosia.

A program to study the effect of the rare earth oxides upon the corrosion resistance of sintered urania compacts was carried out. Compacts composed of 97 w/o UO_2 and 3 w/o rare earth oxide were formed at 3.36 metric tons/cm^2 and sintered at 1700°C for 4 hr in a hydrogen atmosphere. Average geometric sintered densities for the compacts were: uranium-samaria, 10.523 gm/cm^3; urania-europia, 10.486 gm/cm^3; urania-gadolinia, 9.913 gm/cm^3; urania-dysprosia, 10.044 gm/cm^3; and urania, 10.269 gm/cm^3.

The sintered compacts were corrosion tested by the Applied Corrosion Group in both water at 350°C and some in steam at 650°C. Results of these tests are given in Section H-5, p. 195.

The green powder which dusted from the surface of the 100% urania pellet after corrosion testing in 360°C water was analyzed. X-ray analyses of the powder indicated that it was uranium trioxide hemihydrate ($UO_3 \cdot 0.5\ H_2O$). The hemihydrate is the stable form of uranium trioxide.[82] The corrosion product was broken from the surface of the rare earth samples for analysis. X-ray diffraction lines corresponded to U_3O_8 and Eu_2O_3 for the europia-containing material and for U_3O_8 and Sm_2O_3 for the samaria-containing sample. There was no evidence of a hydrated product on the rare earth compacts.

To better understand the behavior of the rare earth-containing compositions, a study of the reactions between the oxides and uranium was carried out. Compacts pressed at 3.36 metric tons/cm^2 were sintered at 1700°C for 4 hr in hydrogen and in argon. The sintered pellets were crushed for chemical and X-ray analysis.

Solid solution of the face-centered cubic fluorite-type structure exists between urania and gadolinia. A strong pattern, with no extraneous diffraction lines, for the solid solution was evident in the hydrogen-sintered samples from 95 m/o UO_2-5 m/o Gd_2O_3 to 30 m/o UO_2-70 m/o Gd_2O_3. At higher gadolinia contents, additional diffraction lines, which correspond neither to urania nor to gadolinia, appeared faintly in the diffraction pattern. These are indicated as UID (unidentified) in Table XLV. In the argon-sintered samples, these lines appeared in the diffraction pattern for samples containing more than 40 m/o Gd_2O_3.

In both the hydrogen- and argon-sintered series, the lattice parameter of the solid solution decreased from the pure urania value of 5.470 Å in a linear fashion to a composition of 60 m/o UO_2-40 m/o Gd_2O_3. The lattice parameters for solid solutions formed under both atmospheres are almost identical, as shown in Figure 87 and Table XLV. A change in the slope of the parameter diminution occurs at this point. The change in parameter for compositions with gadolinia content greater than 40 m/o is considerably less than for compositions of lesser gadolinia content. Again, however, a linear decrease is evident, and the curves extended intersect the ordinate at approximately 5.37 Å for the hydrogen-sintered solutions and at 5.39 Å for the argon-sintered solutions. A lattice parameter of 10.74 Å is reported for gadolinia.[83] The intersection with the ordinate is thus approximately half the value reported for the rare earth.

---

[82] Dawson, J. K., Wait, E., Alcock, K., and Chilton, D. R., Some Aspects of the System Uranium Trioxide-Water, J. Chem. Soc., 1956, 3531-3540.

[83] Curtis, C. E., and Johnson, J. R., Ceramic Properties of Samarium Oxide and Gadolinium Oxide, X-ray Studies of Other Rare Earth Oxides and Some Compounds, J. Am. Ceram. Soc., 40(1) 15-19 (1957).

Table XLV

X-RAY AND CHEMICAL ANALYSES OF URANIA-GADOLINIA SOLID SOLUTIONS

Specimen No.	Analyzed Composition			$GdO_{1.5}$, m/o	Calculated Atomic Ratio		X-ray Analysis of Powder Samples	
	U, w/o	U^{+4}, w/o	Gd, w/o		O/M	O/U	Lattice Parameter as Sintered, Å	Phases Present
HEAT TREATMENT: Hydrogen Atmosphere at 1700°C for 4 Hr								
H95U05Gd	85.06	83.76	2.93	4.97	1.996	2.022	5.4668	FCC
H90U10Gd	81.74	77.67	5.94	9.93	2.020	2.077	5.4578	FCC
H89U20Gd	75.34	66.64	12.27	19.81	1.962	2.076	5.4400	FCC
H70U30Gd	68.14	54.89	18.94	29.66	1.985	2.190	5.4151	FCC
H60U40Gd	60.45	42.59	26.37	39.82	1.954	2.253	5.4010	FCC
H50U50Gd	53.39	30.52	34.52	49.51	1.703	1.901	5.3964	FCC
H40U60Gd	49.50	45.49	37.42	53.42	1.833	2.215	5.3887	FCC
H30U70Gd	35.40	14.28	51.96	69.01	1.649	1.980	5.3889	FCC
H20U80Gd	24.30	14.59	62.19	79.52	1.697	2.460	5.3767	FCC + ID
H10U90Gd	12.75	10.05	74.13	89.82	1.562	2.106	5.3761	FCC + ID
HEAT TREATMENT: Argon Atmosphere at 1700°C for 4 Hr								
A95U05Gd	84.28	82.81	3.76	4.97	1.978	2.010	5.4635	FCC
A90U10Gd	81.37	75.51	6.40	10.67	1.998	2.057	5.4550	FCC
A80U20Gd	75.06	65.96	12.48	20.18	1.973	2.092	5.4389	FCC
A70U30Gd	68.67	54.33	18.66	29.24	1.945	2.128	5.4219	FCC
A60U40Gd	60.60	41.94	25.99	39.42	1.996	2.318	5.4080	FCC
A50U50Gd	53.06	29.45	34.30	49.51	1.791	2.076	5.4026	FCC + ID
A40U60Gd	48.94	23.23	37.00	53.42	1.993	2.557	5.4039	FCC + ID
A30U70Gd	34.94	28.54	52.26	69.41	1.670	2.054	5.4007	FCC + ID
A20U80Gd	24.38	23.11	62.72	79.60	1.608	2.031	5.4004	FCC + ID
A10U90Gd	12.69	12.69	74.23	89.87	1.556	2.054	5.3910	FCC + ID

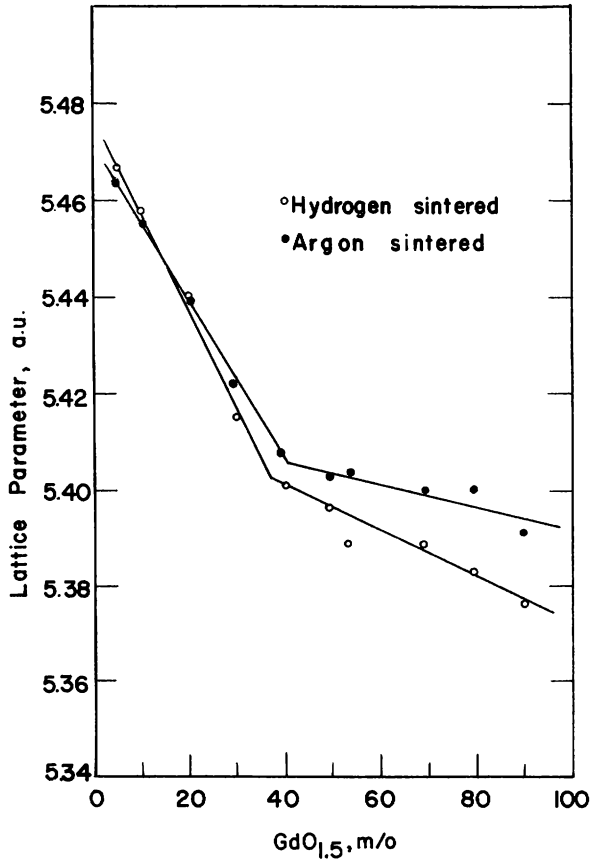

Figure 87

Lattice Parameters for Urania-Gadolinia Solid Solutions

In comparing the anomaly in the lattice parameters with the oxygen-to-metal atom ratio for the compositions, it will be observed that the O/M ratios for compositions from 95 m/o UO_2-5 m/o Gd_2O_3 to 60 m/o UO_2-40 m/o Gd_2O_3 are close to 2.0, whereas the O/M ratios for compositions from 60 m/o UO_2-40 m/o Gd_2O_3 to 10 m/o UO_2-90 m/o Gd_2O_3 are in the range from 1.70 to 1.56 for the hydrogen-sintered solid solutions. A similar decrease in the O/M ratio is noted in the argon-sintered specimens, wherein the ratio decreases from 1.79 to 1.56 as the composition changes from 50 m/o UO_2-50 m/o Gd_2O_3 to 10 m/o UO_2-90 m/o Gd_2O_3. The calculated oxygen-to-uranium values do not show the marked change that the oxygen-to-metal atom ratios show.

The change in the lattice parameters near the oxygen-to-metal atom ratio of approximately 2.0 suggests that different mechanisms may govern the accommodation of oxygen in the cubic fluorite-type structure of these solid solutions. Further analysis will be necessary to establish firmly the reasons for this behavior. It is interesting to note that the lattice parameters of the argon-sintered solid solutions are, for the most part, larger than the parameters for the hydrogen-sintered solutions.

Under investigation are the solid solutions formed between urania and ceria, urania and europia, urania and samaria, and urania and dysprosia. Lattice parameters have been determined for some of these systems, but the absence of the chemical analyses precludes a definitive interpretation of the results.

7. Fueled Glasses (J. H. Handwerk and D. E. White)

For Doppler measurements, a fuel of relatively low density (approximately 70% of theoretical) having essentially a zero expansion up to 1000°C was needed. These general specifications precluded the use of sintered oxide; however, low-density specimens, which were formed by bonding UO_2 grains with a glass, were found to have essentially a zero expansion at 1000°C. In this type of specimen the glass becomes less viscous on heating and allows the UO_2 grain to shift, with the net effect that the size of the specimen is almost constant.

Initially, glass-bonded specimens were prepared from crushed sintered oxide. However, the sizing of the UO_2 grain (250 to 150 μ) was difficult, and a spherical UO_2 produced in a fluidized bed was found to be equally as good. The spherical material as produced was approximately 70 to 80% of theoretical density and was sintered in vacuum at 1750°C to increase the particle density to 95% of theoretical. The dense spheres were mixed with 1 w/o sodium metasilicate and cold pressed into pellets. The pressed pieces were air-dried and then sintered in hydrogen at 1200°C.

Additional experiments are planned that require glass-bonded depleted UO_2, enriched UO_2, PuO_2, and UO_2-PuO_2. Granules of PuO_2 and UO_2-20 w/o PuO_2 have been prepared by cold pressing the materials without a binder. These pressed pieces were crushed, and granules between 375 and 175 μ were removed by screening. The granules were then sintered in an argon atmosphere to achieve high-density particles (90% of theoretical). These dense granules were formed in the prescribed manner, dried, and sintered in vacuum.

Measurements of the thermal expansion of the specimens were made to correlate their behavior with that of the previously measured UO_2. The coefficient of expansion was found to be 10.3×10^{-6} cm/cm-°C for UO_2, 11.6×10^{-6} cm/cm-°C for UO_2-20 w/o PuO_2, and 12.4×10^{-6} cm/cm-°C for PuO_2.

8. Measurements of Thermal Properties (J. B. Moser and O. L. Kruger)

A method to determine the thermal properties of plutonium-bearing ceramic materials considered for use as fuels in nuclear reactors was sought with the following requirements: the size of the specimen to be used is small, the experimental setup must be adaptable for glove box operation, and measurements from room temperature to above 2000°C must be possible. The steady-state methods were thoroughly investigated and found to be unacceptable.

Recently, Parker et al.,[84] reported a method of measuring the thermal diffusivity and heat capacity of small specimens. Measurements on a variety of materials to temperatures as high as 1800°C showed that their calculated values of thermal conductivity were accurate to approximately 5%, which is about the limit of accuracy for this property. The success of their method can best be explained by the fact that the measurement takes place in a very short time (usually less than $\frac{1}{2}$ sec) and during this time all boundary conditions can be satisfied.

The experiment consisted of irradiating the front surface of a thin, small plate with a pulse of thermal energy and recording the resultant rise of surface temperature of the rear surface by a device with a rapid response rate. In practice, a 0.1- to 0.3-cm-thick plate, with a surface area of 1-4 cm^2, is flashed by means of a xenon flashtube or a laser, and the temperature rise of the rear surface picked up by means of a thermocouple or radiation detector. The output of the temperature detector is amplified and shown as a function of time on an oscilloscope screen, which is photographed. From an analysis of the photograph, a diffusion coefficient (α) is obtained, and the thermal conductivity (K) is

[84] Parker, W. J., Jenkins, R. J., Butler, C. P., and Abbott, G. L. Flash Method of Determining Thermal Diffusivity, Heat Capacity and Thermal Conductivity, J. Appl. Phys., 32, 1697 (1961).

found from the expression $K = \alpha DC$, where D is the density and C the heat capacity of the sample.

In the ideal case of a perfectly insulated sample uniformly irradiated with a pulse of thermal energy which is short compared with the time required for heat to flow through the sample, the history of the back surface temperature is given by

$$\frac{T(L,t)}{T_m} = 1 + 2 \sum_{n=1}^{\infty} (-1)^n \exp(-n^2\pi^2\alpha t/L^2) \tag{1}$$

and the specific heat is given by

$$C = Q/DLT_m, \tag{2}$$

where T(L,t) is the instantaneous rise of back surface temperature at time t, T_m is the maximum temperature rise of the back surface, L is the sample thickness, and Q the energy absorbed.

At the time $t_{1/2}$, when $T(L,t) = 0.5\ T_m$, equation (1) reduces to

$$\alpha = 1.38L^2/\pi^2 t_{1/2}, \tag{3}$$

and the thermal diffusivity can be determined from the sample thickness and the time required for the back surface temperature to rise to one-half its final value. This time is obtained from the photograph of the oscilloscope trace.

If a determination of specific heat is needed, an absolute calibration of the vertical displacement axis on the oscilloscope in terms of temperature is required, and a material of known specific heat must be flashed to obtain the energy absorbed (Q). By maintaining identical experimental conditions, the specific heat of an unknown specimen of similar dimensions may be obtained by flashing it at the same energy level and using equation (2).

At higher temperatures, heat losses may become significant.[85] When equation (1) no longer applies, the back surface temperature is given

$$\frac{T(L,t)}{T_m} = 2 \sum_{n=0}^{\infty} \frac{y^2_n}{D_n} \exp(-\alpha y_n^2\, t/L^2), \tag{4}$$

---

[85] Cowan, R. D., Pulse Method of Measuring Thermal Diffusivity at High Temperatures, J. Appl. Phys., 34, 926 (1963).

where y_n and D_n are functions of the heat loss coefficients, which can usually be evaluated. Solutions of equation (4) are available, and thermal diffusivity values can be obtained by measuring $t_{1/2}$ as described before.

A room-temperature experimental setup, shown in Figure 88, was built on an optical bench in order to deal with electrical interference problems and aid in the design of an optical system capable of transferring the energy of the flash to a specimen inside a vacuum furnace. Interference with the measurements is due to the electric and magnetic fields arising from the high voltage and current pulse caused by the discharge of the flashtube in addition to those in the building. A schematic of this arrangement is shown in Figure 89. A 4-turn, quartz, spiral flashtube is operated at a voltage between 3000 to 4000 V from a 250-μf capacitor. This yields a total energy of 1000 to 2000 W-sec per flash, of which a small fraction reaches the specimen.

One of the necessary conditions for the success of the method is a flash duration short compared with the risetime of the rear surface temperature. This was checked experimentally by means of a silicon

Figure 88. General View of Room-temperature Experimental Setup

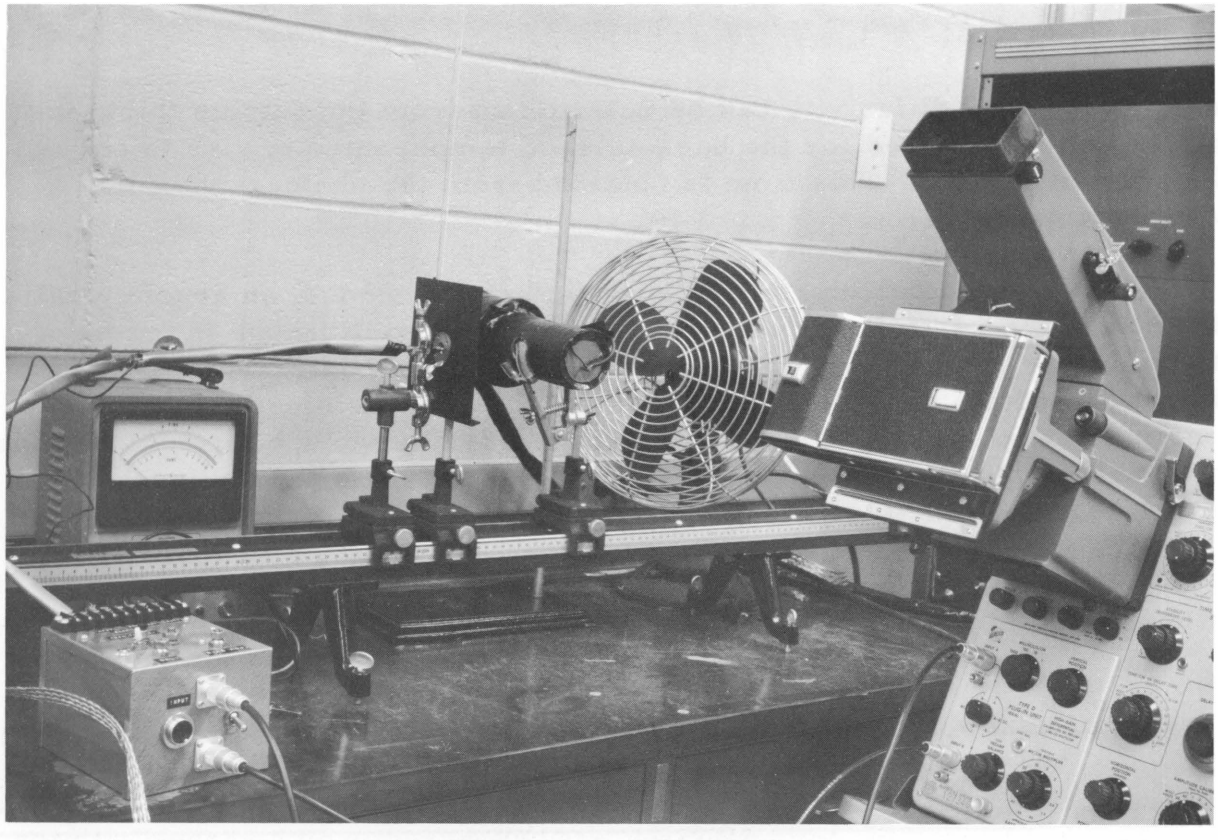

Macro 37921

Figure 89. Schematic of Room-temperature Thermal Diffusivity Apparatus

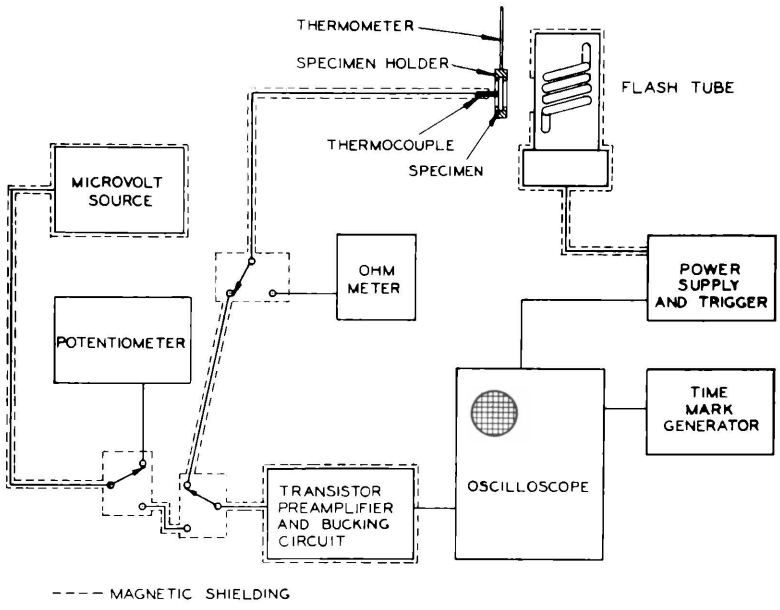

Macro 38032

photo-diode placed behind an iris diaphragm. The output of this photocell was fed into the oscilloscope; a photograph of the voltage pulse is shown in Figure 90.*

Figure 90. Pulse Time of the Flashtube

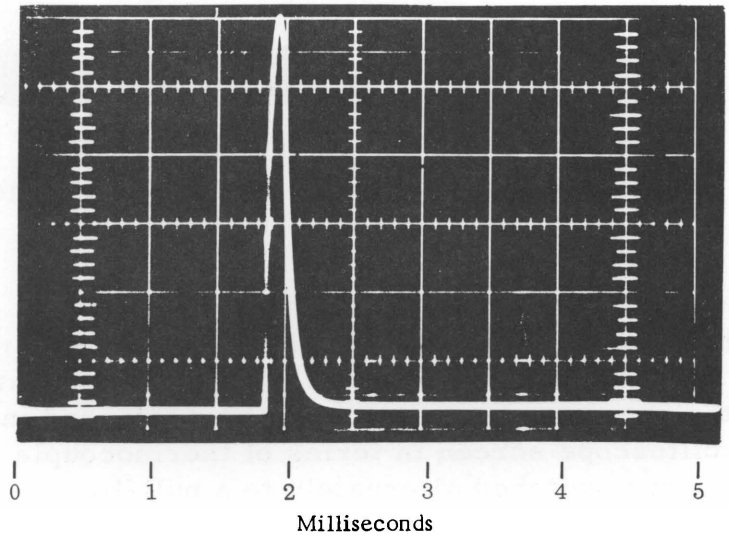

Macro 38057

*A total flash duration of 0.5 ms was measured, which agrees with the value reported by the manufacturer of the flashtube. The irradiation time was generally under 1% of the risetime which is satisfactory.

The front surfaces of the samples were thinly coated with colloidal graphite to increase the amount of energy absorbed and to ensure that the absorptivities of all specimens were identical. To minimize heat losses from the specimen during the time of measurement, care was taken in the design of the sample support. A metal holder with small ceramic inserts at points of contact with the specimen was found to be most suitable. The front surface of the specimen was aligned parallel to the axis of the quartz spiral at a distance of one inch from the envelope of the flashtube. Fine chromel-alumel thermocouple wires were pressed against the back surface, 2 mm apart, so that the electrical circuit was through the sample. For ceramic samples the contact surface was coated with conducting epoxy. Good contact was verified by switching to the ohm-meter in the circuit. A typical oscilloscope trace is shown in Figure 91.

Figure 91. Photographic Trace of Temperature Rise at the Back Surface of an Aluminum Sample

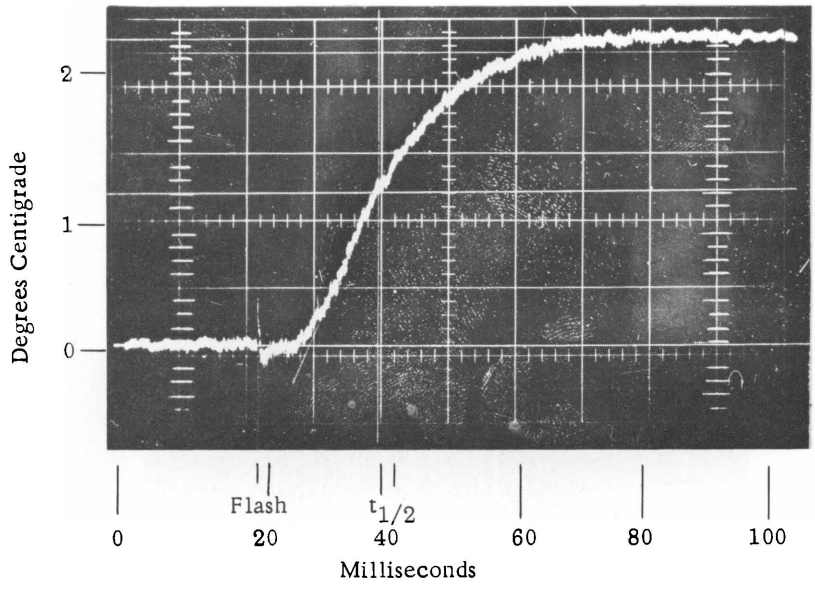

Macro 38056

Although a vacuum-tube voltmeter was used to measure the resistance, the millivolt range was found to be too inaccurate for a determination of the specimen temperature as was intended initially. To calibrate the oscilloscope screen in terms of thermocouple output, a microvolt source was switched alternately to a null-balance potentiometer and the oscilloscope, as indicated on Figure 89. The reason for not using the potentiometer output was that this instrument acted as an antenna, and it was found to be impractical to shield, due to its design and size. A considerable effort had to be devoted to finding suitable shielding. Shielding for the cable leading from the power supply to the flashtube and for the thermocouple wires from the specimen to the preamplifier consisted of copper braid covered with 2 layers of Conetic, an alloy of high magnetic

permeability. The flashtube, preamplifier, and microvolt source were also shielded with 2 layers of Conetic.

The signal voltages obtained from the thermocouple ranged from 40 to 200 μV, indicating a back surface temperature rise of 1-5°C. These EMF were too low to record directly on the oscilloscope, which had a maximum gain of one mV/cm. Several preamplifiers were tested, and a two-transistor battery-operated differential circuit was selected for use in the room-temperature experiments reported here. This amplifier incorporated a bucking circuit and had a gain of 300, a low noise level amounting to 1-2 μV, fast response time, and freedom from drift. Troubles encountered with some preamplifiers included excessive noise, which could only be reduced by external feedback circuits. This, however, cut the frequency response to such low levels that the signal from the thermocouple suffered severe distortion. Other amplifier troubles consisted in lack of stability of the ambient temperature trace and interference from the line-voltage power supply.

The time-base of the oscilloscope was calibrated with a high-precision time-mark generator adjusted to the Bureau of Standards WWV radio signal. As it is necessary to have a baseline on the photograph, an adjustable time-delay generator was used which fired the flashtube shortly after the oscilloscope had been triggered.

Table XLVI lists room-temperature data obtained with common metals.

Table XLVI

ROOM-TEMPERATURE THERMAL PROPERTIES OF SOME COMMON METALS

Material	Thermal Diffusivity α($cm^2\ sec^{-1}$)	Specific Heat C(cal $gm^{-1}\ °C^{-1}$)	Thermal Conductivity** K = αDC (cal $cm^{-1}\ sec^{-1}\ °C^{-1}$)
Iron	0.203	0.107*	0.17
Aluminum	0.928	0.215	0.54
Copper	1.12	0.095	0.95
Nickel	0.173	0.103	0.15

*Specific heat of Armco Iron was used to obtain the other C values.

**Thermal conductivities obtained in this research are within 5% of the best literature values.

9. Thermogravimetric Studies (E. D. Lynch)

One type of equipment required for materials evaluation studies is the thermogravimetric balance. This provides the ability to determine weight changes associated with reactions as a function of temperature, time, and environment. In the materials study programs some major applications are evaluation of sintering behavior, oxidation and reduction characteristics, stability in various atmospheres, and volatility studies on materials.

The equipment has been developed in two stages: (1) the development of an apparatus for controlled rate of heating and atmosphere studies to 1550°C, and (2) an apparatus for use to 2500°C in various atmospheres. The equipment for use at lower temperature was designed primarily for oxidation and sintering studies in oxidizing, neutral, or vacuum atmospheres. The high-temperature equipment has been designed for studies of materials stability in vacuum, hydrogen, or neutral atmospheres. At this time the low-temperature equipment has been constructed and is in operation. The high-temperature equipment has been designed and purchased.

The equipment consists of a semimicro, recording, Ainsworth vacuum balance integrated with a platinum-resistance tube furnace and a 10-cm, vacuum system. The furnace is powered through a cam-operated programmer having a capability of providing heating rates from 1 to 25°C/min. The vacuum system is capable of maintaining 1×10^{-5} torr at maximum operating temperature. The recording mechanism indicates weight changes to 0.1 mg directly, and plots sample temperature and weight simultaneously. Chart speeds of from 38 to 152 cm/hr can be selected, depending on the rate of the reaction being studied. Air, oxygen, or inert gases may be used as environment in addition to vacuum.

The weighing and recording mechanisms are the same for the high-temperature unit. The primary difference lies in the furnace installation. For this unit the furnace will be a split-element, tungsten-resistance furnace capable of providing 2500°C in one atmosphere of hydrogen. This furnace will have the capability of operating at 10^{-5} torr at maximum temperature and also with inert gases to 1 atmosphere. Provision for operation in oxygen has not been made due partly to the difficulties encountered and also to the lack of interest in oxygen reactions at these high temperatures.

At present the apparatus has been used to investigate the oxidation and reduction reactions of uranium oxides, oxidation of uranium phosphide, and in the study of removal of organic binders during vacuum sintering of materials.

The thermogravimetric work with uranium oxides was done as an operational check and also to supplement existing information on these materials. In a previous report on oxidation of UO_2,[86] the absence of the $UO_2 \rightarrow U_3O_7$ thermal peak was reported for large-grain-size material.

A thermogravimetric oxidation has been made for a single piece of high-density UO_2 (see Figure 92) and for fine-particle UO_2 (Figure 93). The data correlate with the previously reported thermal data in that there is no measurable weight change in the range of $UO_2 \rightarrow U_3O_7$ oxidation for the high-density, single-particle sample. Fine-grained material shows this oxidation step just prior to the oxidation to U_3O_8. Apparently, the oxidation reaction to form U_3O_7 does not occur at a sufficiently high rate to be detected for the high-density material when heated at the rate of 5°C/min.

Figure 92. Oxidation of Uranium Dioxide (H_2-sintered at 1800°C; 96% theoretical density)

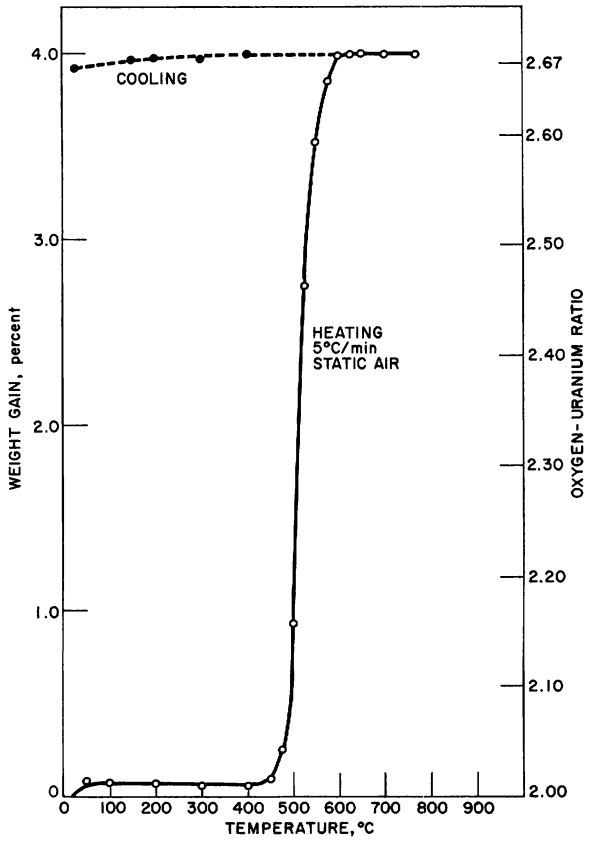

Figure 93. Oxidation of Uranium Dioxide (-325 mesh powder)

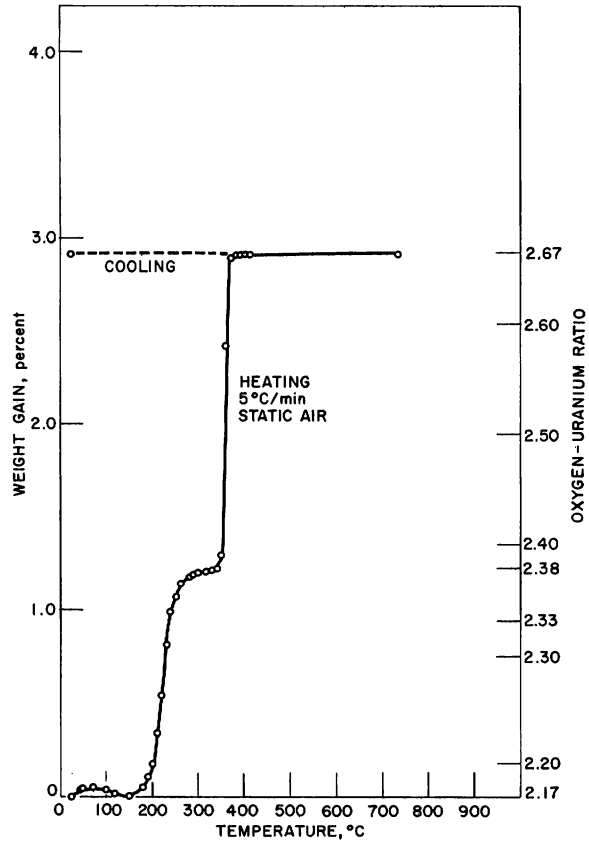

[86] Kolar, D.,* Lynch, E. D., and Handwerk, J. H., Influence of Gas Flow on DTA Curves of UO_2, J. Am. Ceram. Soc., 45(3), 141 (1962).
*Participant, INSE

A determination was made of the rate of reduction of U_3O_8 heated at 1000°C in vacuum, as shown in Figure 94. Fine, powdered (-44 μ) U_3O_8 was heated at a rate of 5°C/min to 1000°C and then held for approximately 1600 min at this temperature. At about 700°C the weight loss from U_3O_8 becomes apparent and appreciable. As calculated from weight loss, the O/U ratio reaches 2.60 at about 900°C. When held at a constant temperature of 1000°C, the weight loss is very rapid to an O/U ratio of about 2.25. The sample was still losing weight slowly when the test was terminated after 1600 min. At this point the calculated ratio of O/U was 2.17.

Figure 94. Weight Loss of U_3O_8 Heated in Vacuum

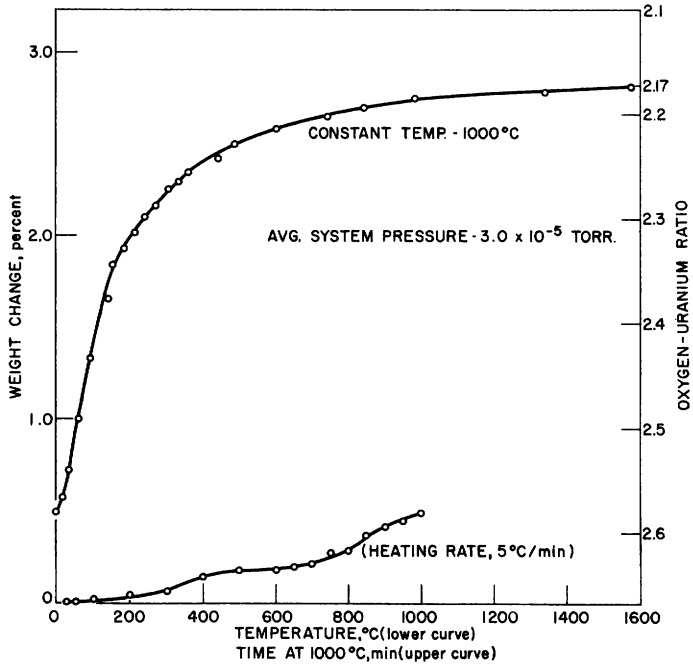

This same material was cooled in vacuum and reheated in air, the oxidation characteristics being those shown in Figure 95. When reoxidized, the material gave no indication of a $UO_{2+x} \rightarrow U_3O_7$ oxidation step. The ultimate oxidation calculated from weight gain was to a O/U ratio of 2.63. This calculation was based on the beginning O/U ratio of 2.17 resulting from the vacuum treatment. The fact that there was no oxidation to U_3O_8 (calculated) may be due to oxidation of the material during the previous cooling. This would result in a higher starting O/U ratio, and the calculated endpoint value would be low by any amount of oxidation that occurred during cooling.

Figure 95. Reoxidation of Uranium Oxide Formed by Vacuum Treatment of U_3O_8

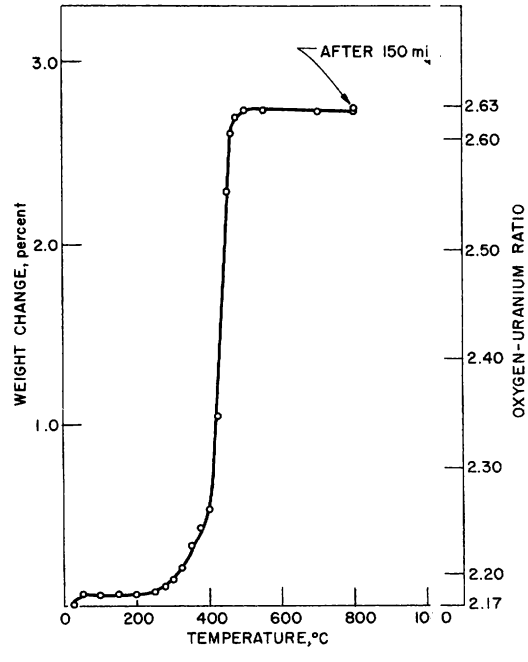

Fabrication procedures for fine-grained ceramics usually require the addition of an organic lubricant or binder. Such materials must be removed during sintering, and their removal must be closely controlled to prevent defects due to gas evolution. In order to determine the temperatures at which binder removal could be safely carried out, thermogravimetric analyses were made

of the most useful binder systems with UO_2 as the material base. The results of these analyses are shown in Figures 96-103.

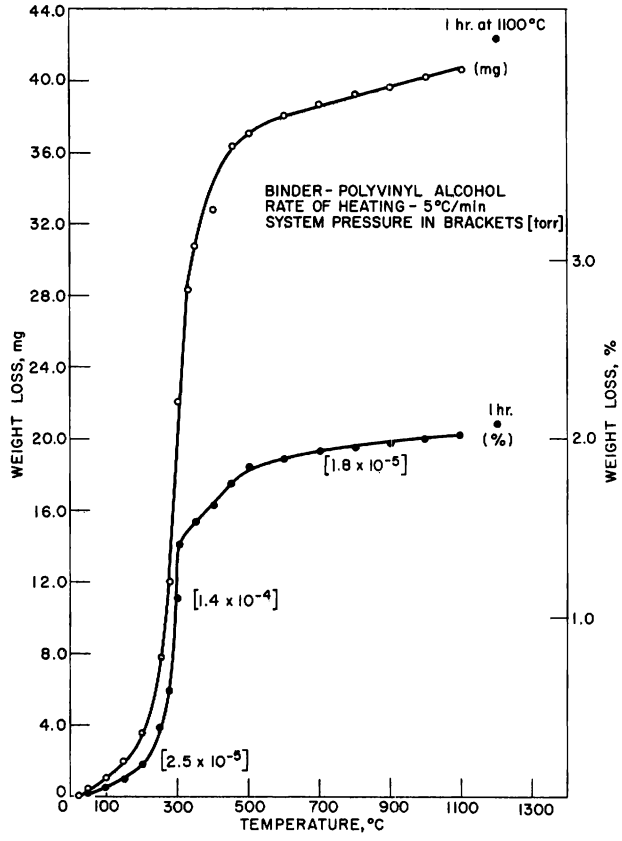

Figure 96

Removal of Binder from Uranium Dioxide

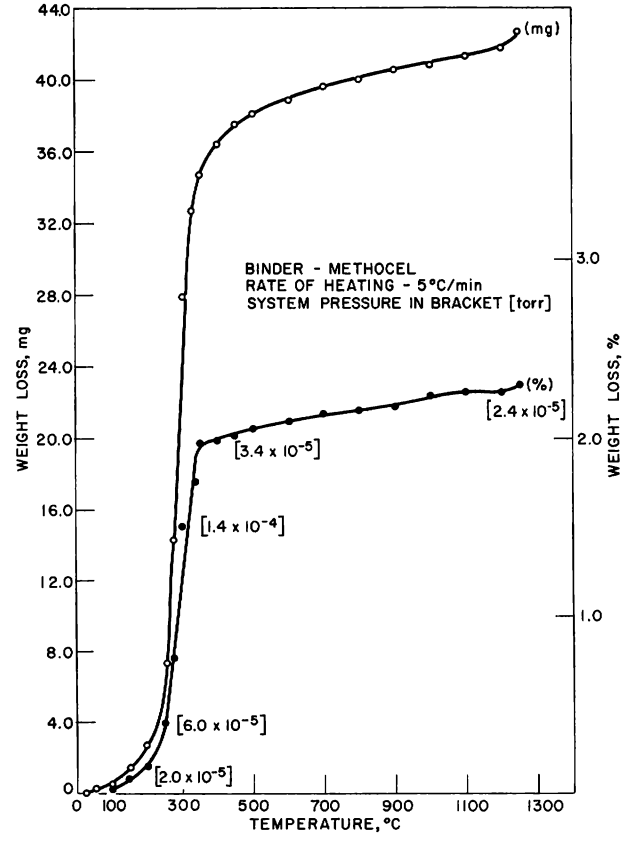

Figure 97

Removal of Binder from Uranium Dioxide

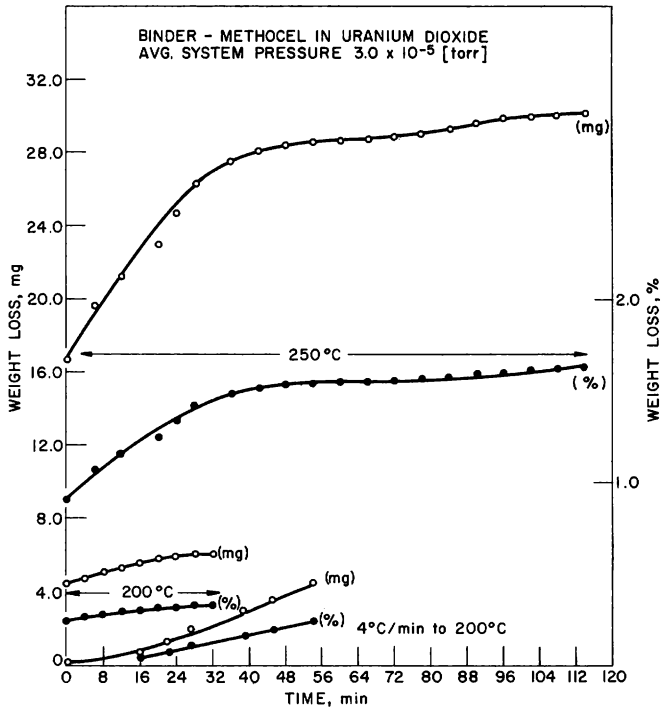

Figure 98

Effect of Temperature on Rate of Binder Removal

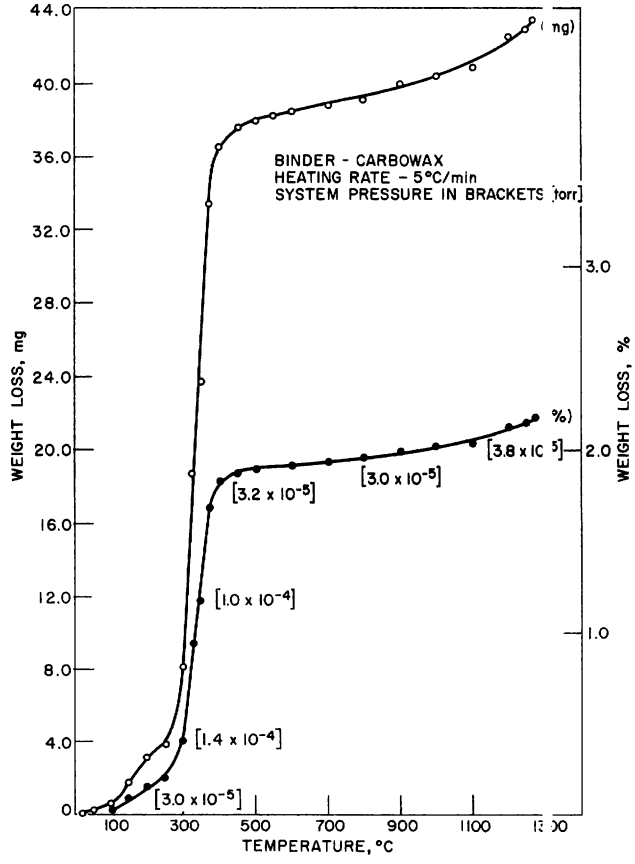

Figure 99

Removal of Binder from Uranium Dioxide

Figure 100. Removal of Binder from Uranium Dioxide

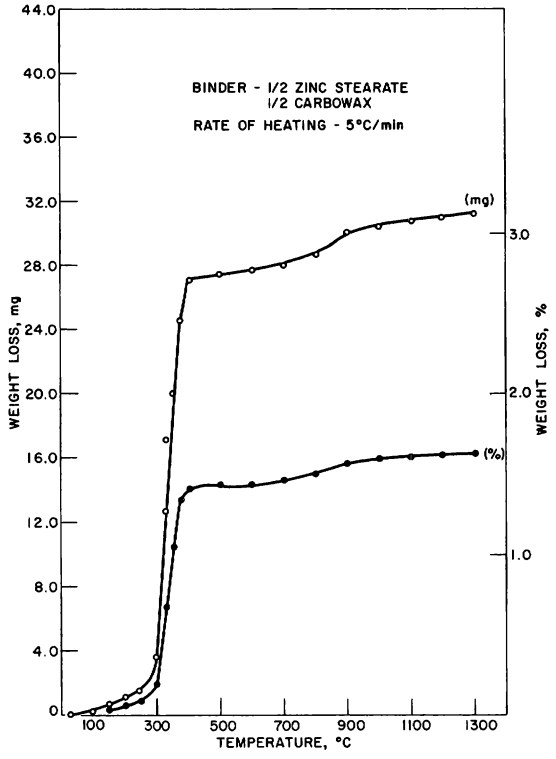

Figure 101. Removal of Binder from Uranium Dioxide

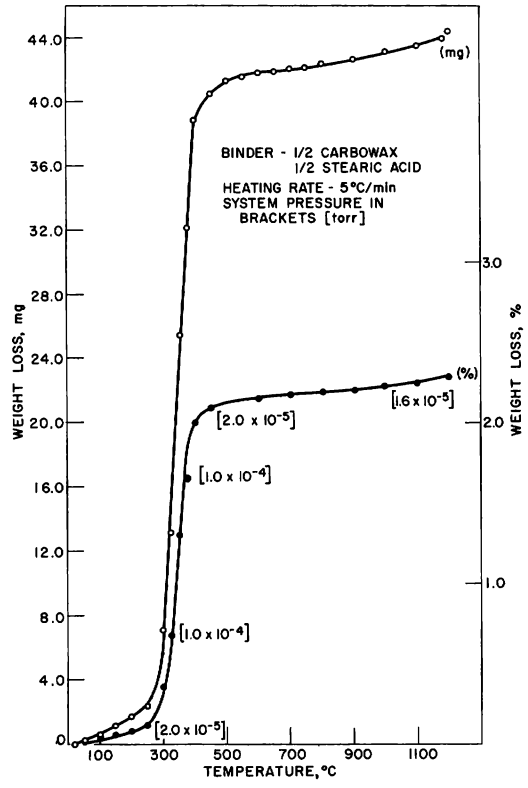

Figure 102. Removal of Binder from Uranium Dioxide

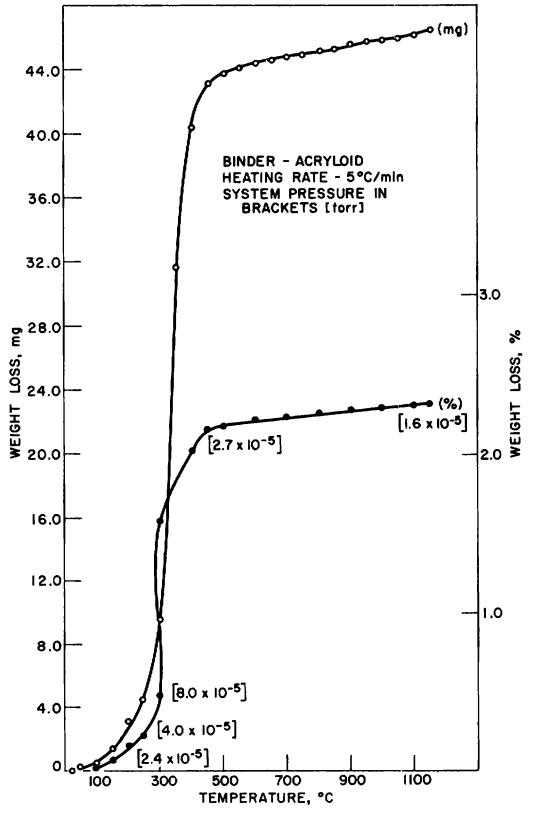

Figure 103. Removal of Binder from Uranium Monophosphide

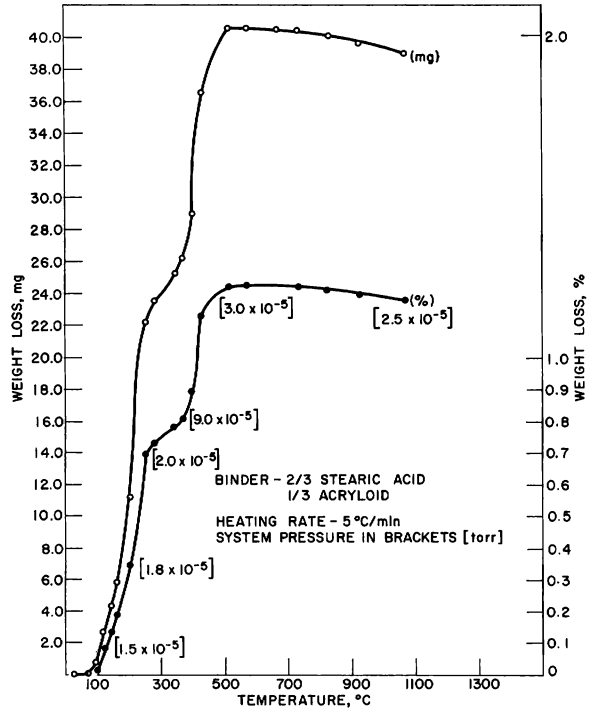

The important data to be taken from the curves, to establish a safe sintering schedule, are the temperature of beginning of rapid weight loss and the temperature where the weight-loss curve flattens. A safe sintering procedure requires either holding the temperature constant until all organics are removed or increasing the temperature slowly through the range of weight loss.

To determine these parameters closely, a rate-of-loss curve at various temperatures in the loss range may be made as shown in Figure 98. As may be seen, for Methocel the practical temperature for binder removal is about 250°C.

Further use of the low-temperature equipment is planned for oxidation and reaction studies of the oxide, phosphide, carbide, and sulphide systems.

F. Experimental Irradiation of Fuel and Control Materials

1. Examination of UO_2 Pellets Irradiated in Collapsed Aluminum Alloy Tubing (L. A. Neimark and R. Carlander)

The examination of ANL-2-13 and ANL-2-16 prototype fuel assemblies containing square and dished-end UO_2 pellets in collapsed wrought aluminum alloy A-288 tubing has continued. The fuel assemblies had been irradiated under boiling conditions in the ANL-2 High Pressure Water Loop, as described previously.[87] Based on uranium isotopic burnup analysis, the average burnup of element ANL-2-13 was 5400 MWd/MT with a peak of 11,100 MWd/MT. The average burnup of ANL-2-16 was 7300 MWd/MT with a peak of 14,800 MWd/MT.

Fission gas releases from two of the three rods in element ANL-2-13 were 0.27 and 0.35% of theoretical. Gas releases from two of the three rods in element ANL-2-16 were 0.09 and 0.12% of theoretical. The average decrease in wall thickness was 0.05 to 0.08 mm (0.002 to 0.003 in.) for the ANL-2-13 assembly, compared with 0.13 to 0.18 mm (0.005 to 0.007 in.) in the ANL-2-16 assembly. Pitting corrosion was quite severe in the ANL-2-16 assembly and penetrated the cladding wall to a maximum depth of 0.46 mm (0.018 in.). A small central void was noted in a rod from the ANL-2-16 assembly, which contained the dished-end UO_2 pellets. This void extended to approximately 38 mm ($1\frac{1}{2}$ in.) from the hot end of the rod. No grain growth or variations in microstructure occurred in any of the rods in either assembly.

2. Irradiation of Dispersion Fuels (C. F. Reinke)

As part of the overall development program of potential fuel materials, a series of dispersions have been irradiated in the ETR. The dispersions, supplied by Nuclear Metals, Inc., consisted of an enriched uranium-containing intermetallic phase dispersed in either a Type 304 stainless steel or 80 Ni-20 Cr alloy matrix. The uranium concentrations in the specimens varied from 18 to 34 w/o.

The results of the preliminary examination of some of the specimens were reported last year.[88] The examination of all the specimens has been completed, and the results are tabulated in Table XLVII, together with pertinent data on the irradiation conditions. The 80 Ni-20 Cr matrix was more resistant to the volume changes accompanying the burnup of uranium and exhibited a rate of volume change of about 0.7% $\Delta V/10^{20}$ fissions/cc for temperatures up to at least 500°C. The Type 304 stainless steel base specimens exhibited a rate of volume change of 1.6 to 2.6% $\Delta V/10^{20}$ fissions/cc for temperatures ranging up to 560°C.

---

[87] Annual Report for 1962, Metallurgy Division, ANL-6677, p. 120.
[88] Ibid., p. 123.

Table XLVII

EFFECTS OF IRRADIATION ON DISPERSION FUELS

Specimen No.	Composition	Fuel Temp, °C	Burnup,(b) Fissions/cc x 10^{-20}	Max(c) Diameter Increase, %	Length Increase, %	%ΔV(d) / Fissions/cc x 10^{-20}
UE-6B	Ni-Cr-18 w/o U	380(a)	1.4	NMC	0.5	0.7
UE-6A	Ni-Cr-18 w/o U	>1200	11.0	Not Measured	Not Measured	3.6
UE-3B	Ni-Cr-29 w/o U	500(a)	1.9	NMC	0.4	0.7
UE-1B	304 SS-27 w/o U	480(a)	1.9	NMC	0.7	1.6
UE-1A	304 SS-27 w/o U	>1100	12.0	Not Measured	Not Measured	3.0
UE-2A	304 SS-33 w/o U	540(a)	2.1	4.9	1.5	2.0
UE-5B	304 SS-34 w/o U	560(a)	2.2	1.6	0.2	2.1
UE-4B	304 SS-29 w/o U	450(a)	1.7	4.2	0.7	2.6

(a) Based on the fission rate necessary to give the analyzed burnup.
(b) Based on mass spectrometric analyses of the uranium isotopes.
(c) NMC means no measurable change.
(d) Based on the assumption of no weight change and calculated from the expression $\% \Delta V = [(\rho_i/\rho_f) - 1] \times 100$, where ρ_i and ρ_f are the initial and final densities, respectively.

Specimens in one of the capsules operated at temperatures significantly higher than anticipated were either partially or totally melted. The remainder of two specimens can be seen in Figure 104. The temperature of both specimens is estimated to have exceeded 1200°C for at least a short time during the course of the irradiation.

Figure 104. Appearance of Dispersion Fuel Specimens

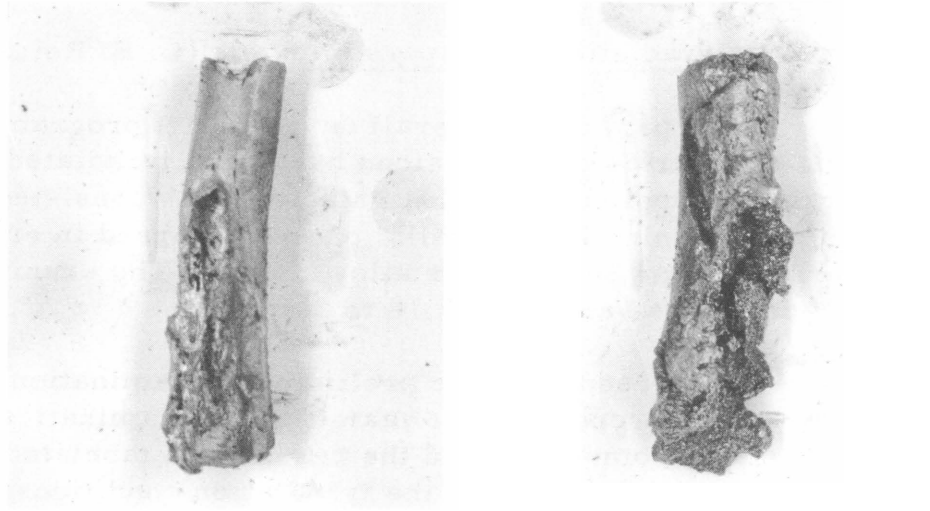

EI-1102 2X EI-1103 2X

Specimen No.	UE-6A	UE-1A
Composition	Ni-Cr-18 w/o U	304 SS-27 w/o U
Max Temperature, °C	>1200	>1100
Burnup, fissions/cc	11 x 10^{20}	12 x 10^{20}
$\%\Delta V/10^{20}$ fissions/cc	~3.6	~3.0

3. Survey Irradiations of Uranium Sulphide (L. A. Neimark and R. Carlander)

Six specimens of 6.42-mm (0.253-in.) diameter, pressed and sintered US pellets clad with 0.30-mm (0.012-in.) Nb-1 w/o Zr alloy with a 0.05-mm (0.002-in.) helium annulus have been examined after irradiation in the MTR reactor. Pellets of both 80 and 90% density were irradiated, with half the specimens having a 2.0-mm (0.080-in.)-diameter axial hole the entire length of the fuel section.

Isotopic burnup analyses indicated burnups ranged from 2.94 to 8.21 x 10^{20} fiss/cc (11,100 to 31,100 MWd/MT). Calculated temperatures of the cladding surface ranged from 400 to 790°C. The irradiation data based on the isotopic analyses are summarized in Table XLVIII.

Table XLVIII

IRRADIATION DATA ON URANIUM SULPHIDE

Specimen No.	Density, % Theor.	Configuration	Burnup		Clad Temp, °C	Cladding Surface, Heat Flux, W/cm^2	Max Dia Increase, mm	Vol Increase, %	Gas Release, % Theor.
			MWd/MT	Fiss/cc x 10^{-20}					
S-1	90	Solid	11,000	2.9	560	250	0.025	0.17	0.05
S-3	90	Cored	14,000	3.8	400	170	0.025	0.38	0.03
S-2	90	Solid	22,000	5.8	640	290	0.025	0.26	0.11
S-4	90	Cored	31,000	8.2	790	360	0.050	0.47	0.21
S-5	80	Solid	22,000	5.3	590	260	0.200	1.0	20.0
S-6	80	Cored	23,000	5.4	540	230	0.050	0.22	1.20

Fission gas release from the 90% dense pellets was a maximum of 0.21%. One 80% dense specimen released 1.20% and the other 20.0%. The difference in gas release is attributed to basically closed porosity in the denser pellets and essentially interconnecting open porosity in the less-dense pellets. The 20% release from the one specimen, S-5, is attributed to an as yet unexplainable temperature transient. This same specimen had a small circumferential bulge at the top of the fuel section.

Metallographic examination of the 90% dense specimens showed no significant changes from unirradiated samples. A Widmanstätten structure of very fine needles, shown in Figure 105, was present in both. These needles tended to disappear toward the center of specimen S-4, which achieved the highest temperature. The needles were only faintly present in a few grains of the finer-grained 80% dense pellets which were originally sintered at 1700°C. The 90% dense pellets were liquid-phase sintered at 1925°C; the 80% dense pellets were not. The composition of the needles is presently unknown.

Sections through the overheated specimen, S-5, showed excessive amounts of a second phase, that has been tentatively identified as UOS. The center of the specimen, shown in Figure 106, contained an irregularly shaped core of very large porosity that was devoid of the

UOS phase. The core was about 35% of the pellet diameter. The equiaxed grain size in this region was 0.08 mm, compared with 0.05 mm for the rest of the specimen and the unirradiated material.

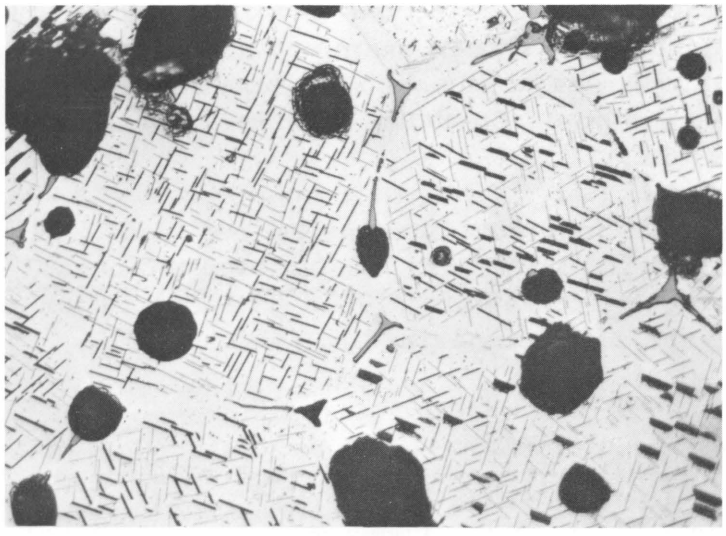

EI-1798 300X

Figure 105

Needle Structure in Unirradiated 90% Dense US. Gray grain-boundary phase is UOS.

Figure 106. Center Area of High Porosity in 80% Dense US in Specimen S-5

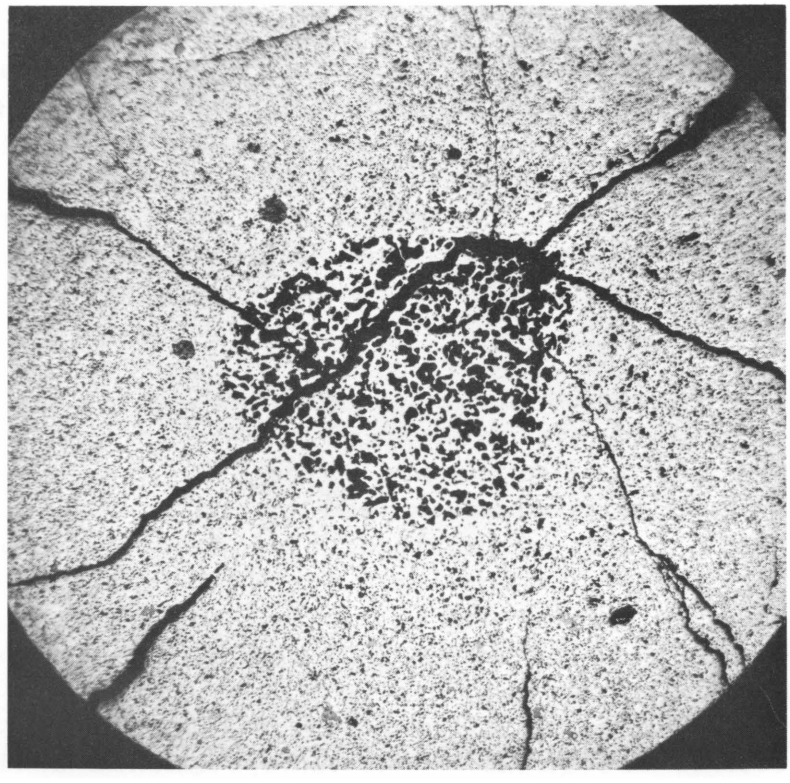

EI-1799 22X

A longitudinal section through the bulge in this specimen (see Figure 107) showed that the bulge was immediately adjacent to a central cavity. The cavity was surrounded by an area of high porosity, some columnar grains of US, and massive areas of UOS. The porous area is believed to connect with the porous center core found in lower regions of the fuel. A tantalum spring at the top of the fuel, used to keep the pellets from separating, was half gone, and the half remaining showed strong evidence of reaction with the sulphide. Particles believed to be melted tantalum were also found in areas of UOS at the base of the cavity and the periphery of the pellet.

Figure 107. Cavity at Top of Fuel Column Adjacent to Bulge in Cladding of Specimen S-5

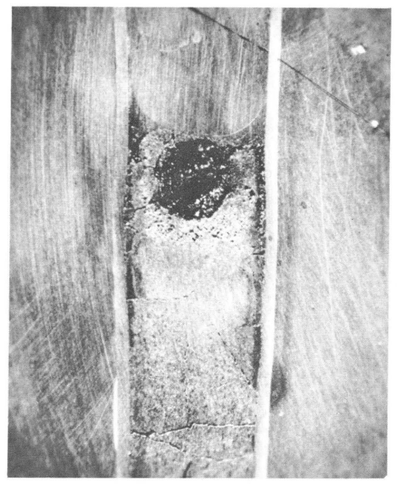

EI-1429 4X

A temperature transient is the suggested cause of the center core and the melting at the top. The lack of significant grain growth or sintering in areas adjacent to the core is the primary evidence for this belief. The immediate cause of melting and formation of the cavity at the top would be the inability of the helium gas space to dissipate the heat generated during the transient. The top fuel pellet was in immediate contact with the gas space. Since considerable fission gas was released, the transient did not occur early in the irradiation period. Specimen S-6, irradiated under almost identical conditions of heat generation and cladding temperature in the same reactor position, showed none of the adverse conditions found in S-5. The only difference was the 2.0-mm-diameter axial hole in S-6.

4. Irradiation of Control Rod Materials (C. F. Reinke)

a. Silver-Indium-Cadmium Alloys

Specimens of 80 w/o Ag-15 w/o In-5 w/o Cd alloy plated with 0.025 mm of nickel or 0.025 mm each of copper plus nickel have been examined after irradiation to an integrated unperturbed exposure of 2.3×10^{21} nvt thermal. The results of pre- and postirradiation tensile and hardness tests were reported in last year's annual report.[89] Chemical analyses which were underway at that time have been completed, and the results are listed in Figure 108, together with a comparison of microstructures of all the types of specimens tested. One specimen from each capsule was analyzed chemically for the quantity of silver, indium, and

[89] Annual Report for 1962, Metallurgy Division, ANL-6677, pp. 127-130.

Figure 108. Comparison of Pre- and Postirradiation Microstructures on Ag-15 w/o In-5 w/o Cd Alloys. All photos are bright field at 250X magnification.

Spec. Desig.	CR6A	CR6B	CR6C&D	PCR4E
Unirradiated	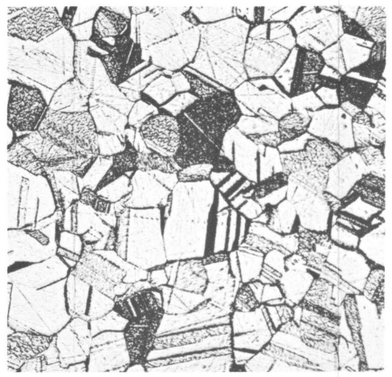	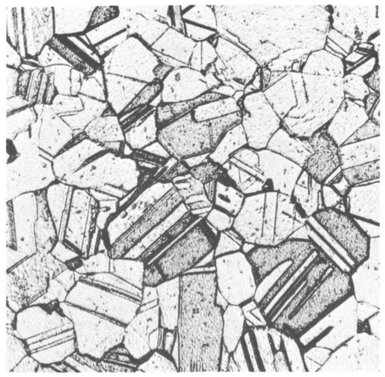	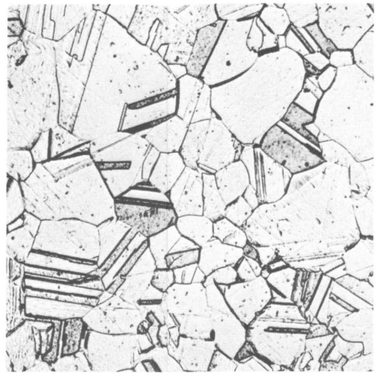	
	EI-1473	EI-1476	EI-1479	EI-1485
Composition in w/o	80.55 Ag-14.83 In-4.62 Cd	80.47 Ag-14.86 In-4.67 Cd	80.08 Ag-14.82 In-5.10 Cd	80.23 Ag-15.11 In-4.66 Cd
Irradiated	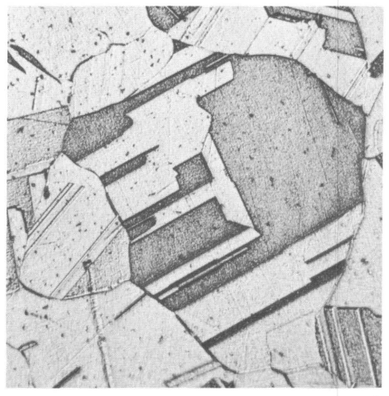	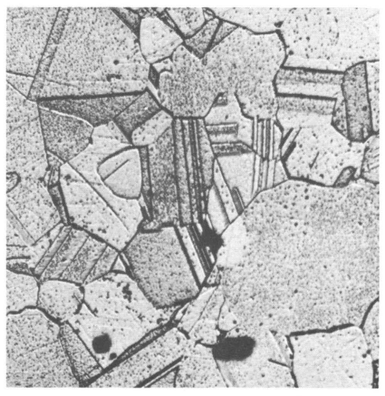	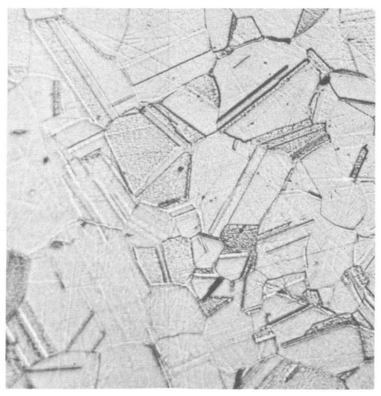	
	EI-1510	EI-1523	EI-1528	EI-1519
Composition in w/o	78.82 Ag-14.76 In-6.35 Cd-0.08 Sn	78.36 Ag-13.36 In-6.79 Cd-1.49 Sn	78.65 Ag-14.25 In-6.53 Cd-0.57 Sn	79.23 Ag-14.56 In-5.66 Cd-0.55 Sn

Spec. Desig.	PCR4E
Unirradiated	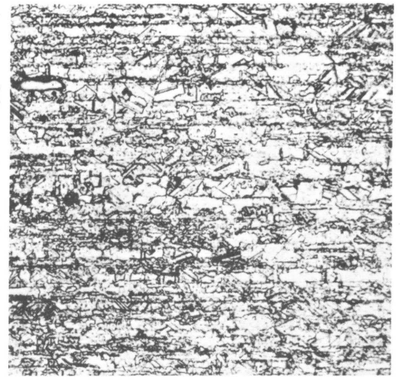
	EI-1488
Composition in w/o	80.75 Ag-15.16 In-4.09 Cd
Irradiated	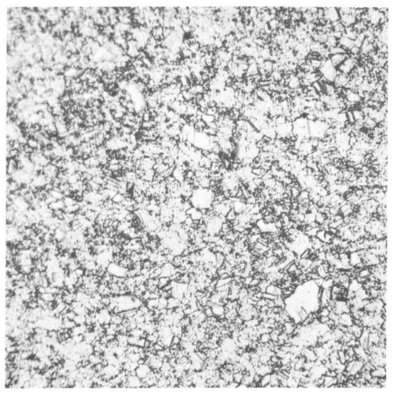
	EI-1516
Composition in w/o	78.36 Ag-14.72 In-6.48 Cd-0.44 Sn

cadmium present. The amount of tin was obtained by difference, noting the fact that the atom fraction of indium before irradiation is equal to the sum of the atom fractions of indium and tin after irradiation.

b. Cobalt-Dy_2O_3 Dispersions

A possible approach toward decreasing the cost of reactor control rods is to use a rod whose economic worth at the end of its life is greater than its original cost. Cobalt-base control rods may meet this criterion because of the production of cobalt-60 during their use. To evaluate their potential, five capsules containing sintered pellets of 30 w/o dysprosium oxide dispersed in cobalt have been irradiated. The specimens were compacted by powder metallurgy techniques and sintered at 1300°C. No reaction was detected between the Dy_2O_3 and the cobalt. X-ray diffraction analyses and metallographic examinations indicated that the cobalt was present as fine-grained alpha cobalt (hexagonal).

The initial two capsules in this series, ANL-51-1 and ANL-51-2, have been returned for postirradiation evaluation. The capsules were irradiated to integrated effective thermal neutron fluxes of 3.3×10^{20} nvt and 4.4×10^{20} nvt, respectively, at temperatures of approximately 300°C. Measurements indicated that the pellets were dimensionally stable and that no changes had occurred. Metallographic examinations of representative pellets indicated that no reaction had occurred between the Dy_2O_3 particles and the cobalt matrix.

The results of postirradiation compression tests conducted at room temperature are tabulated in Table XLIX and compared with unirradiated values. The ultimate compressive strength and percent decrease in length have decreased with increasing neutron exposure for all the specimens except specimen 51-2-5. The reason for the anomalous behavior of this specimen is unknown.

One pellet from each capsule was analyzed for production of cobalt-60. The specific activities of pellets from ANL-51-1 and ANL-51-2 were found to be 13.8 and 18.3 C/gm, respectively. The value of the cobalt-60 present in each capsule far exceeds the original cost of the cobalt and dysprosium oxide. The values of the cobalt-60 in ANL-51-1 and ANL-51-2 were $190 and $260, respectively, compared with a cost of about $1 for the cobalt and dysprosium oxide present.

5. Operation of Instrumented Capsules at the MTR (C. C. Crothers)

The development of an instrumented, temperature-controlled capsule for use at the MTR has been continued. The capsule design employs a gas annulus containing a flowing mixture of nitrogen and helium as a means of temperature control. Since the thermal conductivity of nitrogen is

only about one-fifth that of helium, the thermal resistance across the gas annulus may be controlled by varying the ratio of nitrogen and helium in the gas mixture. By controlling the thermal resistance across the gas annulus the fuel temperature may be controlled.

Table XLIX

COMPARISON OF ROOM-TEMPERATURE PRE- AND POSTIRRADIATION COMPRESSIVE STRENGTH OF Co-30 w/o Dy_2O_3 PELLETS IRRADIATED AT 300°C

Specimen	Integrated Effective Thermal Neutron Flux, nvt x 10^{-20}	Ultimate Compressive Strength, kg/cm^2	% Total Decrease in Length at Fracture
Unirradiated	-	7520 to 7878	19.4
51-1-1	3.3	6100	7.6
51-1-2	3.3	5300	16.2
51-1-3	3.3	5000	13.8
51-1-4	3.3	5580	16.9
51-1-7	3.3	5270	13.8
51-1-8	3.3	5600	16.4
51-2-1	4.4	4700	10.4
51-2-2	4.4	4470	14.4
51-2-3	4.4	4590	12.0
51-2-5	4.4	8020	17.6

The advantages of this capsule have been demonstrated in several extended in-pile fuel irradiations. A temperature control range of 200 to 300°C is possible, the auxiliary equipment necessary for the operation of the capsule is economical and simple, and any type of fuel-bearing material may be irradiated in the capsule. Although the thermal neutron flux for a specific position in the MTR may have been determined with reasonable accuracy for a particular cycle, these values may vary appreciably from cycle to cycle. The effective neutron flux supplied to the capsule depends greatly upon the reactor core loading. It is for this reason that a wide range of temperature control is important.

The first of these capsules was inserted in the MTR in October 1962 and contained a full-length EBR-II fuel pin. Because of operational errors, the capsule was overheated during the initial startup period. Although the results of the experiment were compromised, the capsule was operated successfully for eight reactor cycles to gain operational data.

Three other capsules of this type are under irradiation at the MTR. One of these, inserted in March 1963, contains three EBR-II fuel pins.

The experiment has operated satisfactorily during the entire irradiation period and is expected to be completed by March of 1964.

The second capsule, containing six fuel specimens mounted vertically in the capsule, was inserted in the reactor in June 1963 and has operated satisfactorily. The fuel specimens contain PuC and UC-20 w/o PuC. The experiment will be completed in approximately two years or when a fuel burnup of 10 a/o (maximum) is achieved.

A third capsule of this type, inserted in the reactor in August 1963, contains a single EBR-II fuel pin. The experiment will be completed by April 1964.

The consoles and auxiliary equipment for use with these capsule experiments are functionally identical and completely interchangeable. Three of the consoles are in use and two are being constructed for use with subsequent experiments. Although the controlling gas flow systems for these capsules are manually operated, little attention is required to maintain any desired temperature in the control range. Operators normally check the experiments once every 8 hr. With this attention the temperature may be held to within ±10°C. An automatic control system for the capsules has been designed. At least one of these systems should be in service in about 2 months.

Our experience thus far with this type of capsule has indicated that it is ideal for most fuel irradiations requiring temperature control and instrumentation. However, because of the relatively large temperature drop across the gas annulus, this type of capsule would be undesirable for fuel irradiations in which a rapid rate of burnup is important.

6. Measurement of Neutron Exposure for Radiation-damage Experiments (A. D. Rossin)

In order to determine the amount of fast neutron exposure for an irradiation experiment, and to report it in a meaningful way useful for design purposes, the spectrum shape, flux intensity and time, and the relative effectiveness of neutrons of different energies must be known. In practice, each of these quantities can be evaluated, but the accuracy is limited by present knowledge of cross sections and the damage mechanism itself. Simplifying assumptions are needed in order to compute fluxes and spectra. Thus, even though some uncertainty is bound to be present in the results, a logical procedure can be devised yielding results which are as good as the input data available.

In a previous paper,[90] a model was developed in which the relative importance of a neutron to cause damage was proportional to its energy

[90] Rossin, A. D., Radiation Damage in Steel; Considerations Based on the Effect of Neutron Spectra, Nuclear Science and Engineering, 9 (2), 137 (Feb 1961).

and its scattering cross section. This model was applied to various calculated reactor spectra. The results showed that neutrons of energies down to 1/10 MeV and below contribute significantly to damage production, and that dosimetry methods commonly in use can give results in error by factors of 2 or 3 in exposure.

A series of irradiation experiments was performed to test the energy-dependent model. Since the question of embrittlement of steel by reactor irradiation was of paramount interest, sets of multinotch Izod impact specimens of A212-B carbon steel were irradiated.[91] Three reactor environments were used; temperatures were maintained between 100° and 145°C in all three, but the fast-neutron spectra were significantly different. The reactor spectra were calculated by multigroup reactor theory, and the absolute magnitudes of the fluxes were determined by detector foils.[92] Relative exposures between samples were verified by counting Mn^{54} activity in chips of the steel taken from the actual specimens. Although the cross section for the reaction Fe^{54} (n,p) Mn^{54} ($T_{1/2}$ = 314 d) is not well known, the reaction is still very useful for obtaining relative exposures.[93]

The energy-dependent model is then applied to each spectrum to determine the exposure rates. A unit was developed for use with this model. It is simply called RDU (Radiation Damage Unit). 10^{18} RDU of any fast-neutron spectrum will create the same amount of damage as 10^{18} unmoderated fission neutrons. The RDU for iron as a function of neutron energy is shown in Figure 109. The curve was constructed as indicated in reference 90 but was later revised as explained in reference 94.

Figure 109. Multigroup Format Quarter-lethargy Unit Intervals

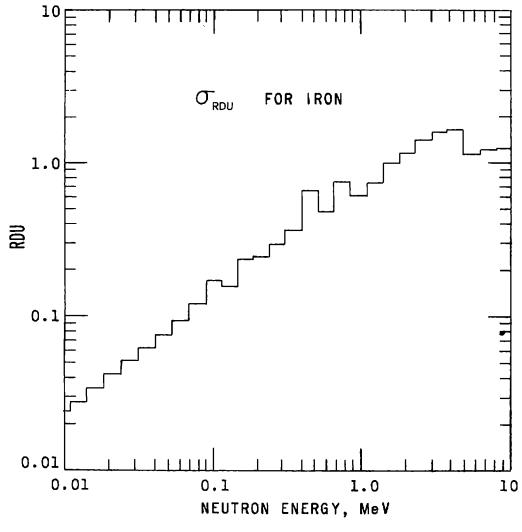

112-3541

The experiment consisted of computing the integrated RDU exposures of specimens in each of the three reactors. The results of mechanical tests were then plotted on one set of coordinates. If the model is correct, all the points should fall on one line. The actual data are shown for each system in Figure 110.

[91] Rossin, A. D., Significance of Neutron Spectrum on Radiation Effects Studies, ASTM-STP-341, pp. 115-132 (1963).

[92] Rossin, A. D., and Armani, R. J., Fast Neutron Dosimetry for Radiation Damage Studies, IAEA SM 36/86, V. II, pp. 293-304 (1963).

[93] Rossin, A. D., A Monitoring Technique for Radiation Damage Experiments, IAEA Disc. V. I pp. 515-519 (1963).

[94] Reactor Development Program Progress Report, ANL-6739, p. 35 (May 1963).

Here the shift in the upward brittle-ductile transition temperature is used to indicate the amount of radiation embrittlement. It is evident by the slopes that the same mechanism is involved in each case, and that discrepancies of the order of ±20% remain. Considering the inherent scatter of impact test data, some temperature differences, and differences of almost a factor of 100 in flux rate between the CP-5 dummy and the EBR-I, the model appears to give reasonable results. The different neutron spectra employed do not differ as drastically as one might wish in order to cover all possibilities. They do show, however, that careful and accurate dosimetry is essential if results of radiation damage experiments are to be compared.

Figure 110. Transition Temperature Shift vs RDU Exposure in Three Reactor Spectra

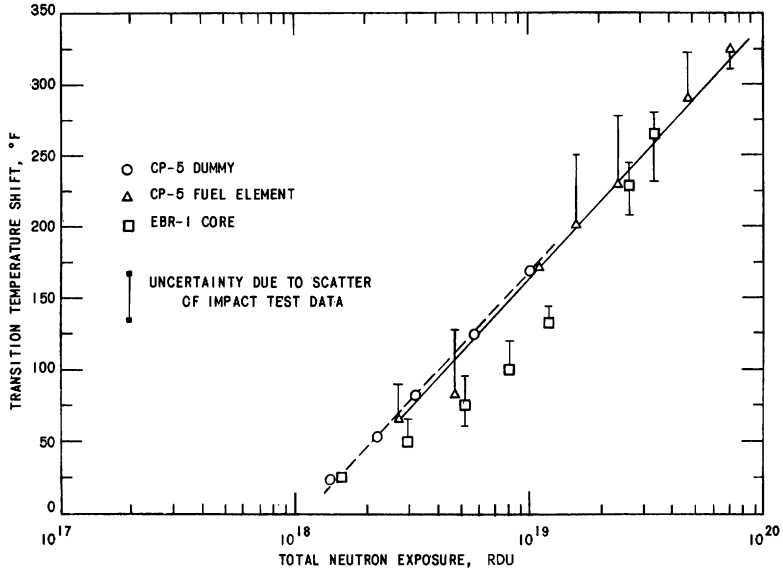

112-3540

As a result of this work, a dosimetry procedure has been developed which is logical and as accurate as its input data permit. Its accuracy can be improved as new data become available. The method employs (1) computation of fast-neutron spectral shape by multigroup reactor theory, (2) fixing magnitudes or flux rates by threshold-type detecting foils, and (3) applying a damage model based on neutron energy to give quantitative values of neutron exposure.

An example of a practical extension of this approach is the determination of the neutron flux in a new cryogenic irradiation facility at CP-5. The spectrum at the center of the facility with the reactor at 4.6 MW is shown in Figure 111. The dashed histogram is a newly computed RDU function for copper. In the facility the instantaneous foil activation rates are:

$S^{32}(n,p)P^{32}$ = 5.01×10^{10} activations/sec
$Ni^{58}(n,p)Co^{58}$ = 7.26×10^{10} activations/sec
$Fe^{54}(n,p)Mn^{54}$ = 4.75×10^{10} activations/sec
U^{238}(fission) = 1.94×10^{11} fissions/sec.

The damage production rates are:

RDU (copper) = 9.78×10^{12} RDU (Cu/sec)
RDU (iron) = 9.20×10^{12} RDU (Fe/sec).

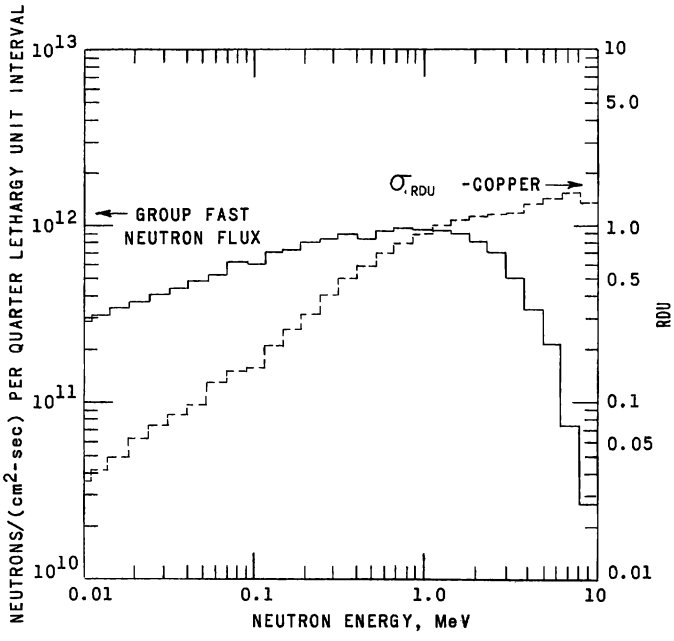

Figure 111
Neutron Spectrum of Cryostat in CP-5 Reactor, Location VT-53; Reactor Power = 4.6 MW

7. Development of Metallographic Techniques for Irradiated Plutonium Fuels (R. Carlander)

The modification of a conventional glovebox for the metallographic processing of irradiated plutonium-bearing fuel alloys is approximately 95% complete. A tent of PVC manipulator bootery has been developed, and a complete exhaust system is presently being assembled. The atmosphere will consist of tank nitrogen fed at a rate of 0.1 cfm. The tolerable oxygen level has been met at 1% with operating pressures of between 2.5 to 5 mm w.c.

The metallographic operations of polishing, etching, cleaning, and examination will be performed within the enclosure. The sectioning, mounting, and initial grinding will continue to be performed in an inert atmosphere enclosure developed by the Remote Control Division.

8. Neutron Radiographic Installation (W. N. Beck)

A neutron shield enclosure was fabricated with which neutron radiographs of encapsulated, irradiated fuel specimens could be taken.

This nondestructive inspection procedure permits the removal of a complete irradiation capsule experiment from the CP-5 reactor, radiographing the specimens within the capsule, and then returning the experiment to the irradiation facility if so desired. In order to accomplish this, a portable shield enclosure with a cassette discharge and recharge magazine was designed and fabricated. This enclosure was fitted to a horizontal neutron beam hole, 6H1 of the Juggernaut reactor. Handling of the experiment to and from the CP-5 reactor is by a fuel transfer cask originally modified for pinhole radiography and further modified to handle a complete 3.3-m experiment.

The inspection technique makes use of a potential radioactive screen to detect the neutron imaging beam after it has passed through the inspection object. The screen, which then contains the radioactive image, is made visible by allowing it to decay in close contact with photographic film. Contrast resolution of the system is 0.25 mm (0.01 in.) or better. Contrast sensitivity is in the order of 1 to 2 percent.

A photograph of the installation, adjacent to the Juggernaut reactor, is shown in Figure 112.

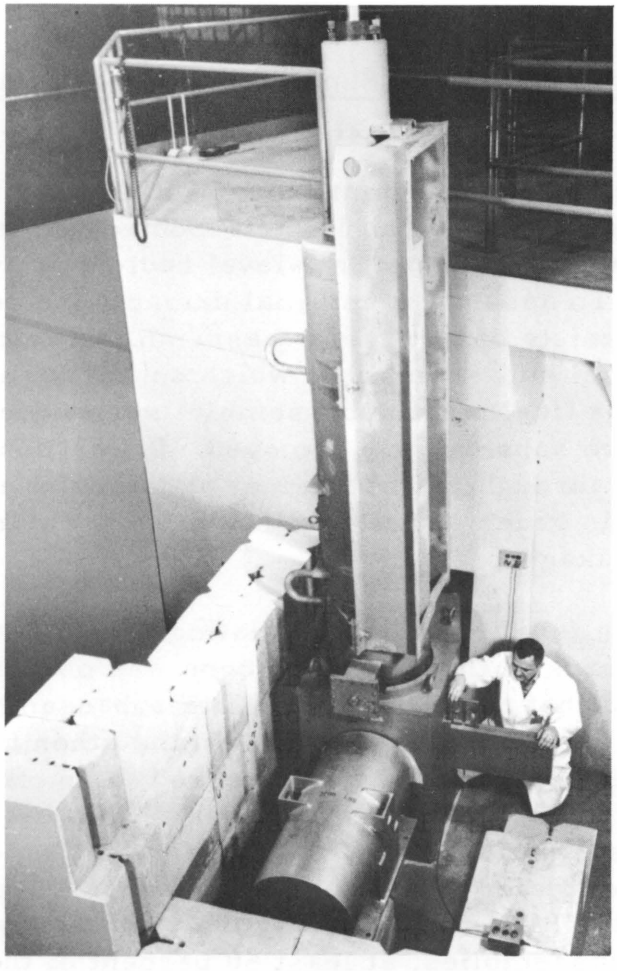

106-7338

Figure 112

Neutron Radiographic Equipment in Position at the Juggernaut Reactor

G. Examination of Full-scale Reactor Fuel Elements

1. Evaluation of EBWR Fuel Element after 100-MW Run (R. Carlander)

Postirradiation disassembly and examination of EBWR fuel element ET-11 have been initiated in order to maintain a check on the irradiation behavior of the Zircaloy-2 clad, U-5 w/o Zr-1.5 w/o Nb fuel elements. The fuel plates are of the thin type, 5.4 mm thick, and have been irradiated to an estimated maximum burnup of 0.40 a/o. The channel gaps were measured at 76.2-mm intervals; the average value for the gap varied from 10.3 to 11.6 mm, which may be compared with the reference value of 11.1 mm.

The maximum increase in the thickness of the plates prior to descaling was found to be 0.76 mm. There was no discernible swelling pattern in the plates since the thickness values probably represent areas in which varying amounts of scale have been removed. Additional thickness measurements are planned after descaling operations. Gamma scan measurements, chemical analysis, and metallographic examination remain to be performed.

2. Examination of Damaged BORAX-V Superheater Fuel Element (J. H. Kittel)

An irradiated superheated fuel element from BORAX-V is being destructively examined with the assistance of the Remote Control Division. This element was found to be the main source of low-level radioactivity detected in the superheated steam. To assess the internal damage, the central section of the assembly, which consists of five fuel subassemblies, was cut out. Further cuts separated the fuel subassemblies, which consist of a brazed assembly of four fuel plates (fuel plate subassembly) surrounded by an insulating can. These cans were subsequently removed. In addition, a number of lateral cuts were made through two of the fuel plate subassemblies. Further cuts will be made in order to find the location and nature of the source of fission product leakage.

External damage in the form of bulged insulating cans, bowed fuel-plate subassemblies, and a crack in the transition cone was observed. After disassembly it was observed that two of the fuel-plate subassemblies were buckled, nearly blocking the steam-flow passages. In the other three, a number of individual fuel plates were bent and two appeared to be torn.

In all of the fuel subassemblies, there was partial welding of the lower ends of the two outer fuel plates to the surrounding insulating can (see Figure 113). The fusion evidently occurred during faulty repair welding at the reactor site. In two subassemblies, at least 50 percent of the circumference of the insulating cans were firmly welded to the adjacent

fuel plates. In the other subassemblies there were a number of short welded areas. In the two firmly fused subassemblies, all four fuel plates were buckled. In the subassemblies with short welded areas, buckling occurred only in the individual fuel plate adjacent to the fused area.

Figure 113. Lower End of Damaged BORAX-V Superheater Fuel Assembly

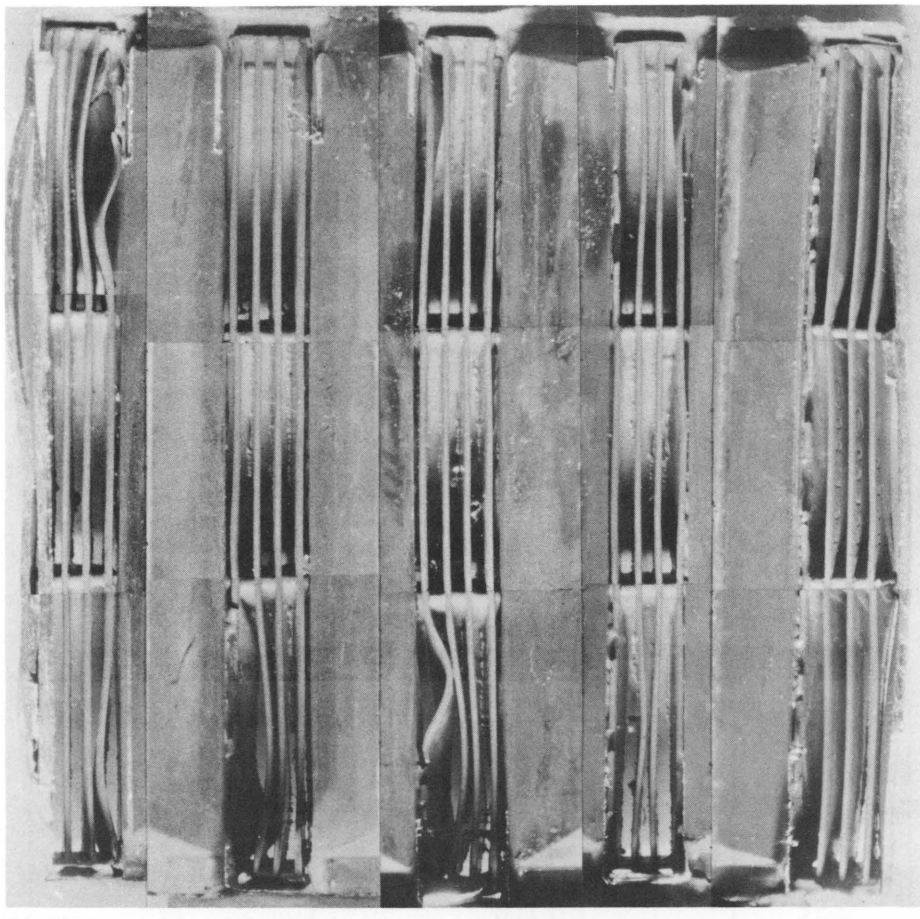

106-7611

In the design of the BORAX-V superheater fuel element, the lower end of each fuel-plate subassembly is free to move with respect to its insulating can to allow for thermal expansion. In the case of the present superheater fuel element, the observed welding of the free ends of the fuel plates to the insulating can prevented this motion. It is believed that the differential thermal expansion and contraction during reactor operation was sufficient to cause the observed damage. For example, the bulges in the insulating cans could result from the stretching of the cans upon heating and subsequent buckling of the cans upon cooling.

The locations where fission products were released from the subassembly have not all been identified. Metallographic examinations to date, however, indicate that one of the torn areas resulted in exposed fuel.

H. Development of Corrosion-resistant Jacketing and Structural Materials

1. Aluminum Alloys for High-temperature Water Service
(W. E. Ruther, J. E. Draley, and S. Greenberg)

The use of corrosion-resistant aluminum alloys as cladding for "free standing" uranium oxide pellet fuel in power reactors may require greater high-temperature creep strength than can be obtained with wrought products. For this reason the corrosion resistance of aluminum alloy powder products has been investigated during the past three years.[95]

The powder products supplied by Herenguel and Lelong at Trefimetaux, Service des Etudes et Fabrications Nucleaires, have been the most satisfactory of those tested. Their behavior, under static conditions (refreshed system) in high-purity water at 290°C is given in Table L.

Table L

AQUEOUS CORROSION OF TREFIMETAUX POWDER PRODUCTS AT 290°C

(Static Conditions)

Time, days	Defilmed Metal Loss, mg/cm^2	Average Penetration, μ
189	11.0	40
189	9.2	33
189	10.3	37
189	11.4	41
251	11.6	41
251	11.7	42
251	11.3	40
293	12.3	44
293	12.0	43
293	12.5	45

Unfortunately, the dynamic (5.5-m/sec flow rate) corrosion resistance at 315°C was not as satisfactory. The metal-loss data were limited by the small number of specimens available. The corrosion behavior of these specimens is compared with that of one of the better wrought alloys (exposed in the same equipment) in Figure 114. These powder products suffer considerably more corrosive attack in this environment than does the wrought alloy.

[95] Draley, J. E., Ruther, W. E., and Greenberg, S., Corrosion Experience with Aluminum Powder Products, ANL-6785 (Oct 1963).

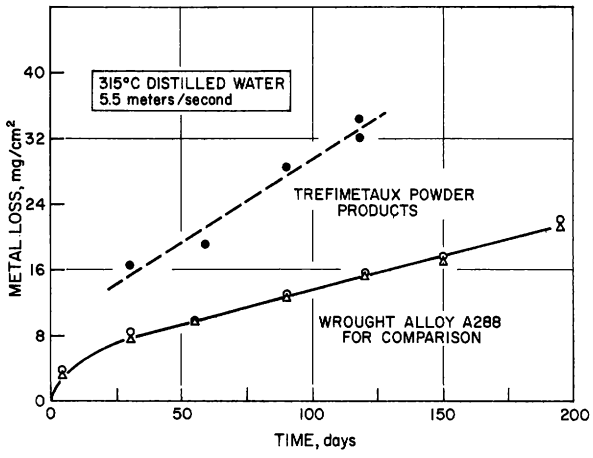

Figure 114

Corrosion of Trefimetaux Specimens in Flowing Water

2. Zirconium Alloys for Use in Superheated Steam (S. Greenberg and C. A. Youngdahl)

The behavior in steam of corrosion-resistant zirconium alloys has been investigated from the points of view of a) the effect of alloy composition and metallurgical pre-treatment on corrosion rate, and b) material embrittlement during corrosion as a result of absorption of oxygen and hydrogen. The alloys, containing small percentages of nickel, iron, and copper, were tested in 42.2-kg/cm^2 (600-psig) steam at 540°C and 650°C.

a. Corrosion Behavior at 540°C and 42.2 kg/cm^2

In comparison with pure zirconium and the Zircaloys, many binary and ternary alloys containing small (approximately 1 to 4 w/o total alloy content) additions of nickel, iron, copper, and chromium are relatively resistant to steam at 540°C and 42.2 kg/cm^2 (600 psig). The long-term weight-gain rates of most of the resistant alloys are comparable under similar conditions of exposure, although there are differences in total amounts of weight gained and surface complexion after corrosion. Of the wrought materials tested, the hot-rolled Zr-1.1 w/o Cu-1.2 w/o Fe alloy ranks highest in every respect for which data are available, followed by hot-rolled Zr-3 w/o Ni-0.5 w/o Fe. These in turn are followed by a group of materials which includes copper-iron and nickel-iron alloys of lower total alloy content, as well as zirconium alloys developed elsewhere. The presence of these additives in the 1 w/o range provides substantial protection, and further improvement is obtained in the cases of the particular compositions noted.

However, the weight-gain rates of certain as-cast zirconium alloy samples, e.g., Zr-4 a/o Cu and Zr-4 a/o Ni, were lower than those of the best wrought materials. Other materials were less resistant in the as-cast than in the hot-rolled state. Marked effects of quenching and aging on the corrosion behavior of hot-rolled samples of the more resistant alloys were also observed. These results suggested that microstructure as well

as composition significantly affected the corrosion behavior. This conclusion was reinforced as the corrosion resistance of quenched samples decreased with time of exposure and the microstructure was observed after test to have been modified toward the less resistant form, i.e., the aged structure. Thus, it appears that further effort to optimize and stabilize the microstructure could result in improved alloys for use in steam at 540°C.

The most resistant wrought alloys exhibit metal-loss rates of about 64-92 μ (2.5-3.6 mils) per year (for exposure times of about 10 months). If these rates did not markedly increase with time, the more resistant alloys might be suitable for several years service in a superheated steam environment in which metal temperatures did not exceed 540°C. This tentative conclusion is based solely on metal-loss considerations. The effect of the corrosion film on fuel element heat transfer, the effect of nonadherent corrosion product on other components of the system, and the effect of the steam environment on the mechanical properties of the alloy are also of prime concern in considerations of serviceability of the alloy.

Only the latter effect has been investigated. Hardness tests indicated no serious metal embrittlement as a result of exposures of 300 days, and microhardness surveys showed the depth of surface hardening to be relatively small (e.g., the surface hardness was within 10 DPH units of the bulk hardness value of 250 at a distance of 60 μ or less from the surface of 0.25-cm-thick samples).

b. Corrosion Behavior at 650°C and 42.2 kg/cm^2

The corrosion-resistant Zr-Ni-Fe and Zr-Cu-Fe alloys have been tested extensively at 650°C in 42.2 kg/cm^2 steam for up to 90 days. The appearances of samples after test were similar to those of samples exposed at 540°C. The weight-gain rates were somewhat higher (total weight gains were about 8 mg/cm^2 after 60 days). Steam flow rates of up to 91.5 m/sec (300 ft/sec) and additions of oxygen or oxygen-hydrogen gas mixtures to the steam did not significantly affect the corrosion behavior.

The absorption of corrosion product hydrogen by samples was found to be markedly less at 650 than at 540°C. The results of an experiment in which samples were transferred from 540°C to 650°C indicated that this behavior was probably not a metal-environment hydrogen equilibrium phenomenon. Subsequent electrical experiments suggested the possibility that temperature-sensitive electrical properties of the surface determined the rate of absorption of hydrogen.

Oxygen absorption by these alloys in 650°C steam was more serious than at 540°C. The more resistant alloys absorbed little oxygen in the bulk metal, but surface embrittlement and cracking of the metal was observed, and the depth of hardening was excessive (e.g., the hardness was 400 DPH or greater to a depth of about 140 μ for a 3.2-mm-thick sample exposed 88 days; bulk hardness was 190 DPH). It is interesting to note that the

thickness of the affected layer correlated qualitatively with absorption of oxygen by bulk metal, but not with weight-gain rate for the less-resistant materials. This observation indicates that the rate of oxygen diffusion through the metal is not directly related to the corrosion (weight-gain) rate.

It is thought that rates of diffusion of oxygen as well as the effects of oxygen absorption, may be reduced by further alloy modification. Approaches toward this objective are under study. Theoretical considerations indicate that modifications which result in lower rates of oxygen diffusion should simultaneously result in alloys which are both stronger and less susceptible to the detrimental effects of aging on corrosion resistance.

3. Corrosion of Stainless Steels and Nickel-base Alloys in Superheated Steam (W. E. Ruther, R. Schlueter, R. H. Lee, and D. J. Dorman)

The effort to find (or develop) a suitable corrosion-resistant alloy for use as fuel cladding for nuclear superheat fuel elements has continued. Type 304 and Type 406 stainless steels have been tested most frequently because of their proposed use in the BORAX-V reactor.

The corrosion behavior of the "18-8" stainless steels and some nickel alloys in superheated steam was found to be dependent on the surface preparation. Those treatments which left a severely cold-worked surface resulted in reduced corrosion attack in subsequent exposure to steam as compared with annealed metal surfaces.

The corrosion rate of electropolished annealed Type 304 stainless steel in oxygenated (30 ppm) steam rose rapidly as the temperature increased from 540 to 650°C. At 600 and 650°C the measured rate decreased with increasing time during 80-day static tests. The corrosion appeared more linear with time in dynamic tests at 650°C (~7 $mg/dm^2/day$). In these tests there appeared to be no effect of velocity (30-91 m/sec) or of oxygen and hydrogen content on the corrosion rate. Flaking and loss of the outer corrosion coating was severe in the dynamic tests.

The corrosion rate of Type 406 was too small to be precisely measured in all of the tests, static and dynamic, in which it was simultaneously exposed with Type 304. A coating equivalent to about 2×10^{-4} cm metal penetration was formed on the initial exposure of 406. No flaking of the outer coating was evident in 80-day tests.

The corrosion attack of the 400 series steels in static oxygenated steam went down with increasing chromium content, particularly above about 13 w/o Cr. Both Type 430 (16 w/o Cr) and 446 (25 w/o Cr) exhibited greater short-term corrosion resistance than Type 304 to steam at 650°C and 42 kg/cm^2.

The high nickel alloys, particularly Inconel 625, were also more corrosion resistant than Type 304 in short static and dynamic tests in steam at 650°C and 42 kg/cm^2.

4. Aqueous Corrosion of TD Nickel (R. H. Lee, C. A. Youngdahl, and S. Greenberg)

TD nickel is a relatively new material developed by duPont. Improved high-temperature mechanical properties are obtained by the dispersion of 2 v/o ThO_2 (as submicron particles) in a pure nickel matrix. Although TD nickel would not be considered for use as a fuel element cladding or nuclear reactor structural material, it is considered of interest to learn the effect of the process on the corrosion behavior of the base material. Conceivably, dispersants other than thoria, as well as other base materials, may prove to be adaptable to this process. Accordingly, a brief investigation was undertaken to compare the corrosion behavior of TD nickel with that of pure nickel in water and superheated steam enviornments.

a. Corrosion in Water

A comparison of the corrosion resistance of TD nickel with that of commercially pure nickel in 360°C, static, degassed, distilled water revealed no appreciable difference between the two materials. After 104 days both samples had formed soft, loose films over lustrous, dark, adherent films. The oxide on the TD nickel appeared to be more uniform. The total weight gain at 104 days was 0.38 mg/cm^2, compared with 0.33 mg/cm^2 for the commercially pure nickel.

b. Corrosion in Superheated Steam

Samples of TD nickel and high-purity (< 99.9% Ni) nickel were exposed under static (refreshed autoclave equipment) conditions to oxygenated (30 ppm oxygen) superheated steam at 650°C and 42 kg/cm^2 (600 psi). Results for degreased samples were summarized in Figure 115.

Figure 115. Corrosion of Degreased Nickel Sheet in Oxygenated (30 ppm) Steam at 650°C and 600 psi

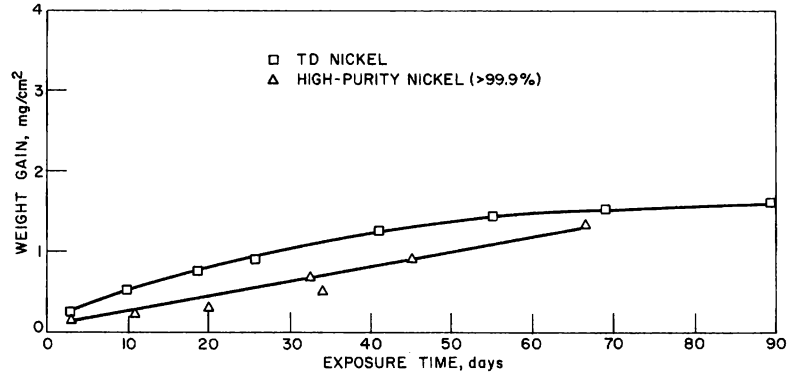

Since the corrosion product was uniform and adherent, weight-gain data are a valid indication of corrosion behavior. There were small differences in corrosion behavior associated with differences in surface preparation.

Vacuum annealing at 1000°C for 30 min affected neither the microstructure nor corrosion behavior of the TD nickel in 650°C steam. No recrystallization occurred in TD nickel after 89.4 days in steam at 650°C. As would be expected, severely cold-worked pure nickel was fully recrystallized after 2.9 days at the same conditions.

The electrical resistivities of corrosion product films, measured under test conditions of temperature and environment, were identical (within about 5%, the limit of sensitivity of the measurements) for the two materials.

The results indicate that the corrosion resistance of TD nickel in degassed pure water at 360°C and oxygenated superheated steam at 650°C is comparable with that of pure nickel.

5. Corrosion of Ceramic Materials (R. H. Lee, R. R. Schlueter, and C. A. Youngdahl)

Uranium oxide containing small percentages of certain rare earth oxides are of potential interest as fuel materials containing burnable poisons. It is of importance to know the behavior of such materials if they should inadvertently become exposed to a water or a steam environment.

Accordingly, disk samples (0.64 cm high by 0.86 cm in diameter), containing 3 w/o of the rare earth oxides (as well as pure UO_2 to serve as a basis for comparison), were fabricated by the Engineering Ceramics Group (see Sect. E-6, p. 158) and subjected to short exposures in high-temperature water and superheated steam.

a. Corrosion in Water at 360°C

The corrosion products were loose and friable, and there was some spalling of all samples, particularly of the pure UO_2. There was also noticeable swelling of the UO_2. Two groups of samples were tested. The first group was tested for 2.8 days, removed for evaluation, and replaced with the second (nominally identical) group which was tested for 5.75 days. The weight changes (subject to errors caused by spalling) are given in Table LI.

Table LI

WEIGHT CHANGES OBSERVED AFTER EXPOSURES OF URANIUM OXIDE PELLETS TO WATER AT 360°C

Material	Weight Change, mg/cm^2			
	Deoxygenated		Oxygenated (30 ppm Oxygen)	
	2.8 Days	5.75 Days[a]	2.8 Days	5.75 Days
UO_2-3 w/o Gd_2O_3	+2.2	+9.5	+15.6	+13.6
UO_2-3 w/o Dy_2O_3	+0.6	+7.3	-0.7	-6.7
UO_2-3 w/o Eu_2O_3	-7.7	+1.7	+6.9	-7.4
UO_2-3 w/o Sm_2O_3	-15.1	+1.4	-71.9	-99.2
UO_2	-107.1	-24.7	-338.8	-426.1

[a] Autoclave leakage occurred. Test environment was steam for last (unknown) fraction of exposure.

b. Corrosion in Steam

This test was conducted at 650°C and 42 kg/cm^2 under static conditions in the refreshed autoclave system. Steam was generated from high-purity distilled water. Oxygen was added to produce a concentration of 30 ppm in the inlet steam. The samples were relatively resistant during the first few days; no disintegration or cracking was observed on removal at 2.7 days. However, oxygen uptake was appreciable during this time. The oxygen concentration was reduced to less than 10 ppm in the effluent at the beginning of the test, gradually rising to 18 ppm after 10 days. The condition of the samples after 10 days was as follows:

Wholly or largely disintegrated (order of decreasing resistance)	Intact except for minor spalling (order of decreasing resistance)	
	UO_2-3 w/o Eu_2O_3	edge cracking
UO_2-3 w/o Gd_2O_3	UO_2-3 w/o Sm_2O_3	scattered cracking and swelling
UO_2-3 w/o Dy_2O_3	UO_2	severe cracking and swelling

No general statement can be made concerning the effect of the additions of rare earth oxides. It is clear, however, that depending upon conditions, one or another of the rare earth oxides appears to increase the resistance of UO_2 to water or steam environments.

6. Light Alloy Suitable for Use with Mercury at Elevated Temperatures (J. Y. N. Wang and W. D. McFall)

Work in this field during 1963 has been concentrated in the area of inhibition. It appears that this phase of the work may be of general theoretical interest and practical importance. The details of the program have been published.[96,97]

Long-term exposure of titanium* to nickel-inhibited mercury in isothermal static systems at 538°C (1000°F) for 30, 60 and 90 days resulted in consistent sample weight gains with time of exposure (5.20, 7.81, and 8.90 mg/cm^2, respectively). Figure 116 illustrates the surface layers after 30, 60, and 90 days of exposure. The first two samples showed a continuous single phase. Two distinct layers are formed after 90 days. No interface attack under these layers was detected. Spectrographic analysis indicates that these layers are primarily composed of nickel and titanium along with a small amount of mercury. Efforts to identify the compound by X-ray diffraction techniques were not successful.

A thermal convection loop made of 1.27-cm (0.5-in.)-ID quartz tubing was used to study the effect of nickel inhibition in a dynamic system with a thermal gradient. Pure nickel, in an amount calculated to give a concentration of about 700 ppm, was inserted in a cold branch of the loop. This location was chosen to limit the concentration of dissolved nickel to the solubility at the temperature of the coldest point in the system and to insure a continuous supply of inhibitor.

The loop was operated at a maximum temperature of 454°C in the hot leg and a minimum temperature of 320°C in the cold leg for a period of 90 days. The average flow rate was about 5.3 cm/sec (10.5 ft/min).

Visual examination of the exposed titanium samples indicated that no gross corrosion had occurred. Metallographic examination of hot-leg samples showed the formation of a uniform protective layer 8 μ thick. A weight gain of 1.86 mg/cm^2 was recorded. The small weight gain (0.42 mg/cm^2) and even surface on cold-leg samples implied little or no corrosion at 353°C (average cold-leg temperature). Spectrochemical analysis revealed that there was very little nickel deposition on cold-leg samples. However, nickel concentration on the surface of hot-leg samples was heavy. It is planned to examine sample surfaces by X-ray diffraction techniques and to analyse the mercury chemically.

---

* Crystal bar titanium arc melted and rolled.

[96] Wang, J. Y. N., Titanium and Titanium Alloys in Mercury. Some Observations on Corrosion and Inhibition, Nuclear Science and Engineering, 18, 1 (Jan 1964).

[97] Wang, J. Y. N., The Effect of Metallic Additives to Mercury on the Corrosion of Titanium. To be presented at Twentieth Annual NACE Conference, March 1964. [Invited paper-title published in Materials Protection, 2(11), 83 (Nov 1963).]

Figure 116. Protective Layers Developed on Titanium Exposed to Nickel Containing Mercury at 538°C. (Kroll's Reagent)

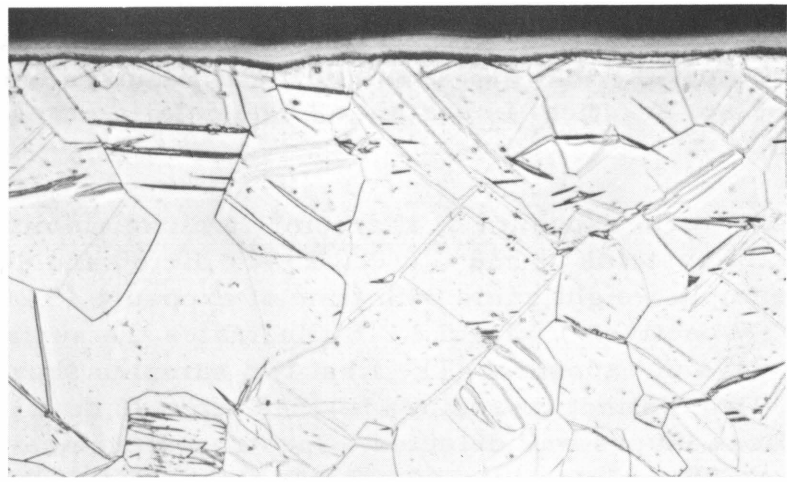

Micro 37004 30 Days 250X

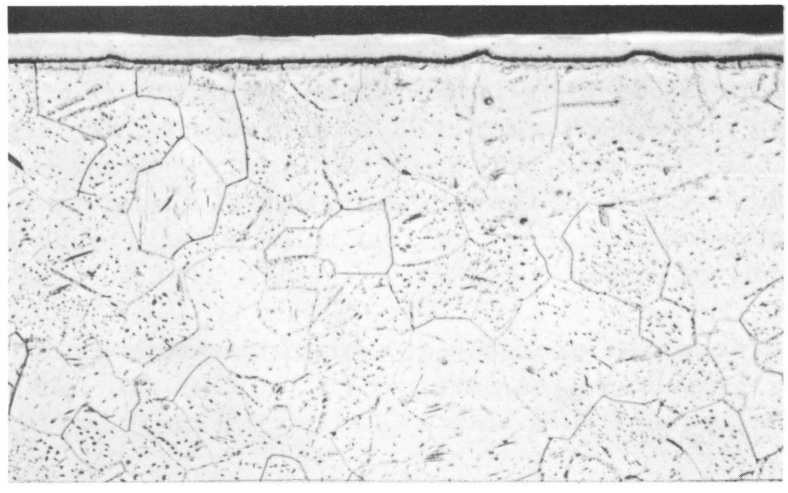

Micro 37000 60 Days 250X

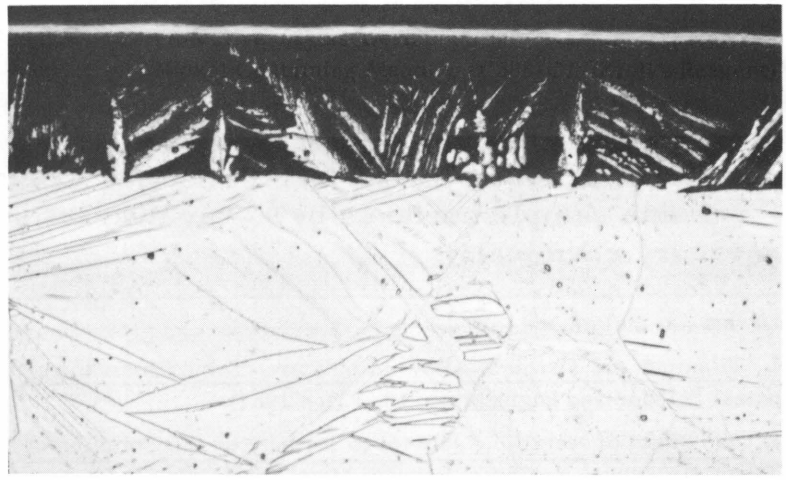

Micro 37002 90 Days 250X

The phenomenon of thermal mass transfer to the hot zone is new and unexpected. Relatively little study has been made of the mechanisms of the inhibiting process. On the basis of the limited information accumulated, it may be that the thermal mass transfer observed here consisted of the dissolution of the soluble inhibitor, transfer by diffusion and convection through the system to the surface of the solid, and subsequent interdiffusion. The temperatures at which the phenomenon occurs may be quite critical.

7. Cathodic Protection of Refractory Alloys in Oxygen-containing Sodium (C. A. Youngdahl, V. C. P. Morfopoulos* and S. Greenberg)

The performance of many reactor structural materials in liquid metal at elevated temperatures is limited by corrosion. The presence of dissolved oxygen in the liquid metal appears to influence the degree of attack on refractory metals, although the mechanisms are not well understood. If it is assumed that a step in the process includes diffusion of negative oxygen ions, it follows that a cathodic protection approach may be a means of reducing the attack. That dissolved oxygen behaves as a negative ion in such an environment is documented in the literature.[98] That cathodic protection may be realized at such temperatures in a gaseous environment was recently confirmed.[99]

Exploration of the feasibility of protection in oxygenated sodium (in the range of saturation) at 500, 600, and 700°C is in progress. Sample materials have included Zircaloy-2, Zr-1 w/o Cu-1 w/o Fe, unalloyed zirconium, and unalloyed niobium. Current densities at the sodium-sample interface have ranged from 1 to 1000 mA/cm^2. Sample-evaluation methods have included visual appearance, weight change, hardness change, and metallographic inspection. Cell resistance and voltage-current data have also been obtained.

The results of the initial work, although largely qualitative, are encouraging. With Zircaloy-2 at 500°C a degree of protection at current densities above 100 mA/cm^2 was indicated by hardness data. At 600°C Zr-1 w/o Cu-1 w/o Fe showed a small weight gain at a current density of 2.5 mA/cm^2 applied after an initial delay to permit film formation, whereas an unpolarized specimen in the same test lost weight. Unalloyed zirconium at 500°C appeared to be protected at current densities above 450 mA/cm^2, judging by visual inspection. At 700°C there was some tendency toward lower weight gains (compared with unpolarized samples) at current densities approaching $1A/cm^2$. Niobium samples at 500 and 600°C lost weight with or

*Temporary employee - graduate student at Columbia University.

[98] Nevzorov, B. A., The Nature of Oxygen in Liquid Sodium, AEC-tr-5412 (June 1962).

[99] La Combe, C. P., High Temperature Gas Corrosion, presented at Second Int. Cong. on Metallic Corrosion (March 1963).

without applied current (1 A/cm^2), but the approach continues to be of interest on the basis of surface appearance and cell voltage versus current data.

Investigation of the technique is continuing with further attention to the range of low current densities and with samples on which a surface film has been permitted to develop and remain.

I. Development of Fabrication Methods

Research and development effort was devoted to a variety of fabrication operations during the year.

The major emphasis centered on the fabrication of refractory-metal, small-diameter, thin-walled tubing - an integrated tubing technology, covering consolidation by arc and electron beam melting, primary breakdown by extrusion, and secondary fabrication into the finished product. New and perhaps novel fabrication techniques, as well as the more conventional methods, were tested and evaluated in an attempt to gain new knowledge. Such knowledge is needed to assure a high quality and economical processing of the required tubing from a wide range of starting materials.

Foil fabrication received further attention, with lesser effort being devoted to the fabrication of Zircaloy tubing, superconducting tubing composites, and to the processing of high-strength aluminum tubing products. The details pertaining to all of the above-mentioned developments are highlighted in the sections that follow.

1. Integrated Fabrication Technology for Small-diameter, Thin-walled Tubing

a. Consolidation Methods (R. D. McGowan and W. C. Kramer)

An arc furnace and electron beam furnace are available for use in converting particulate or solid refractory metals and alloys into ingots suitable for fabrication.

The electron beam furnace shown in Figure 117 has a maximum power level of 60 kW utilizing a 3-A beam current and a 20,000-V accelerating potential. As seen in the schematic diagram shown in Figure 118, the unit consists of two chambers - a gun chamber and a melting chamber - each with its own evacuation system. The chambers are isolated except for a 2.54-cm-diameter aperture for passage of the collimated electron beam. This degree of isolation minimizes passage of gaseous contaminants from the melting chamber to the gun, thereby increasing gun life.

The furnace-evacuation system maintains vacuums of 10^{-5} to 10^{-6} torr during melting, thus providing a means for expulsion of volatile, gaseous, and low-melting elements from molten metals. Purification of high-melting point materials is a prime advantage of this type of furnace.

Melting is performed in water-cooled copper molds ranging in size from 3.8 to 11.7 cm in diameter with a maximum ingot length of 59 cm. As charge materials in the form of chips or a solid rod are fed into the beam, the solidified ingot is gradually retracted in a manner analogous to a continuous casting operation.

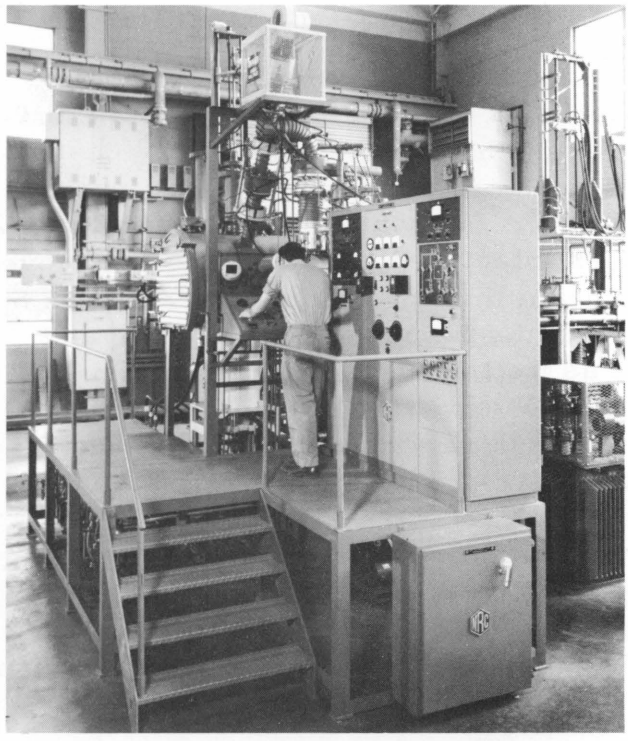

106-7335

Figure 117

60-kW Electron Beam Melting Furnace

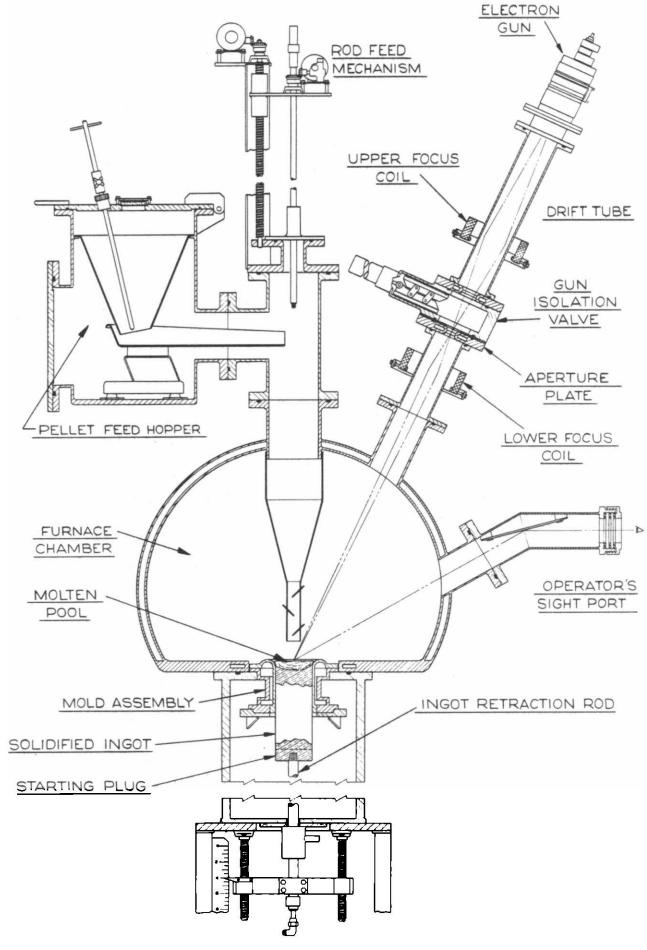

106-7362

Figure 118

60-kW Electron Beam Melting Furnace

To date, one niobium ingot has been made, with the balance of castings being vanadium and V-Ti alloys. Purification of the niobium material in a single melt operation resulted in reducing the interstitial element content from 1.27% in the sinter bar charge to 0.115% in the cast ingot. Results for vanadium, while not as impressive, show a beneficial purification by melting. Typical results on EB melting of vanadium are given in Table LII.

Table LII

PURIFICATION OF VANADIUM BY ELECTRON BEAM MELTING

Element	Interstitial Content, ppm		
	Charge	Single EB Melt	Double EB Melt
C	400	230	130
O_2	1300	1070	820
N_2	390	340	380
H_2	54	13	18
Total	2144	1653	1348

In providing ingot materials for fabrication, continued effort will be placed on evaluating factors affecting purification and alloying during electron beam melting.

Although purification is not an attribute of arc melting, this technique generally produces an ingot possessing a better surface quality and a finer grain size, making it more attractive from a yield and fabricability standpoint. The arc furnace shown in Figure 119 can be used either for consumable or nonconsumable melting. A parallel bank of welding generators provides a maximum of 5400 A and a continuous rating of 4200 A for melting. The evacuation system maintains vacuums as low as 10^{-3} torr during consumable melting. During nonconsumable melting, the melting chamber is maintained at 250 torr of argon gas to sustain the arc. Mold sizes range from 2.8 cm in diameter by 27.9 cm long to 14.5 cm in diameter by 45.7 cm long. The molds are wrapped with a magnetic stirring coil to promote arc stability and ingot quality.

To date, 7.1-cm-diameter ingots of V, Ti, and Ti-50 w/o Zr have been made by the nonconsumable technique from vanadium chips, and titanium and zirconium sponge materials. Oxygen contents of the ingots increased from approximately 0.04% in the charge material to 0.05% in the casting.

Figure 119. NRC Model 2721A Vacuum Arc Furnace

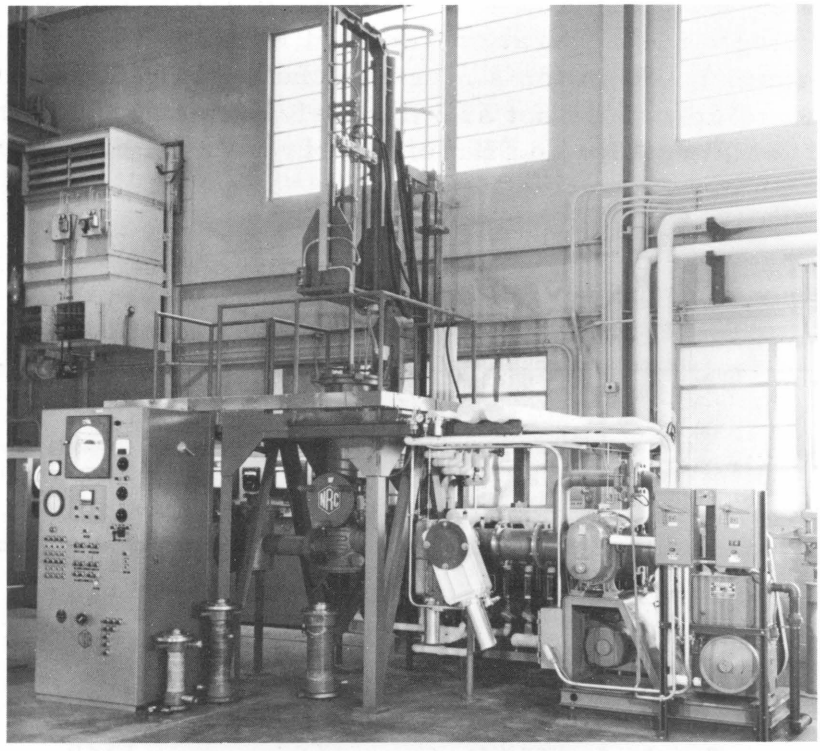

106-7045

Techniques for consumable electrode preparation are being investigated. If bar stock is not available, chips or powder must be consolidated into a bar with sufficient strength for handling and adequate density to provide the required current flow for melting. Isostatic pressing is feasible, although elaborate particulate containment is usually required to assure an adequate product. Sintering of the pressed material may be required in order to achieve adequate electrical properties. An alternate "boat melting" technique is under investigation wherein a horizontal copper trough is filled with particulate matter - even small chunks sheared from plate - which is fused by a traversing welding electrode. The fused bar then serves as the consumable electrode.

b. Extrusion Development (W. R. Burt, Jr.)

Two techniques have been used for the extrusion of high-strength refractory metal and alloy tubing. Both methods involve the use of a deformable core inside a refractory-metal sleeve rather than conventional extrusion over a nondeformable mandrel. One technique also incorporates a powder-filled annulus between the sleeve and deformable core to aid in core removal after extrusion. A detailed description of the process has been given elsewhere.[100]

[100] Burt, W. R., Jr, and Mayfield, R. M., Techniques for Extrusion of Small Diameter Refractory Metal Tube Blanks, Technical Conference on Applied Aspects of Refractory Metals, (AIME), December 9-10, 1963, Los Angeles, California. To be published in Proceedings.

The benefits from the technique include elimination of small-diameter conventional mandrels and associated problems during high-temperature extrusion, elimination of ID lubrication and conditioning after extrusion, and avoidance of possible ID contamination during billet heating and extrusion. Also, since the refractory metal sleeve comprises only about 20% of the billet cross section, the overall billet extrusion constant is materially less than for a billet comprised totally of the refractory metal. This allows a higher reduction ratio and/or a lower extrusion temperature. For example, tungsten sleeves are currently extruded at 1100°C with the use of a molybdenum core and 304 SS outer jacket.

The ability to extrude at relatively low temperature eliminates two serious problems that occur in high-temperature extrusion: (1) inadequate die performance and (2) inadequate high-temperature lubrication. Current ANL practice incorporates ordinary hot-work tool steel dies without ceramic coatings. Characteristically, two extrusions per die are obtained before the die becomes sufficiently plated with metal to require reworking. No serious die wash has been encountered. Similarly, lubrication normally consists of a MoS_2-graphite-oil mixture. Glass lubrication and its associated problems of "rub-in" and reaction with the billet material have been avoided.

To date, successful extrusions of molybdenum, Mo-0.5 Ti, Mo-30 W, TZM (Mo-0.5 w/o Ti-0.08 w/o Zr), and pure tungsten tubing have been achieved. All have been extruded at 1150°C or lower by use of the deformable-core technique.

c. Secondary Fabrication Development

Current Techniques (J. E. Flinn, Jr.)

The need for high-quality, small-diameter, thin-walled tubing (approximately 0.396 cm in ID by 0.038-cm wall thickness) and the lack of commercial availability of many of the refractory metals in this tubing size have led to a general evaluation of commercial tube-fabrication practices and the development of alternative methods.

Figure 120 represents typical dimensional changes encountered during tubing fabrication by various reduction techniques. The terms length ratio, λ, and OD reduction ratio, R, correspond to changes in length, ℓ/ℓ_0, and the ratio of die area reduction, D_0^2/D^2, respectively. The reference diagonal, $\lambda = R$, corresponds to dimensional changes observed in bar drawing. Commercial tube drawing includes ironing (wall thinning with constant ID), sinking (OD reduction with no ID support), and plug and mandrel drawing (combining both ironing and sinking). The latter methods reduce both the ID and wall thickness in a single draft, as shown by the exemplary draw mill schedule in Figure 120.

Figure 120. The Effects of Various Drawing Methods upon the Deformation Behavior of Tubing

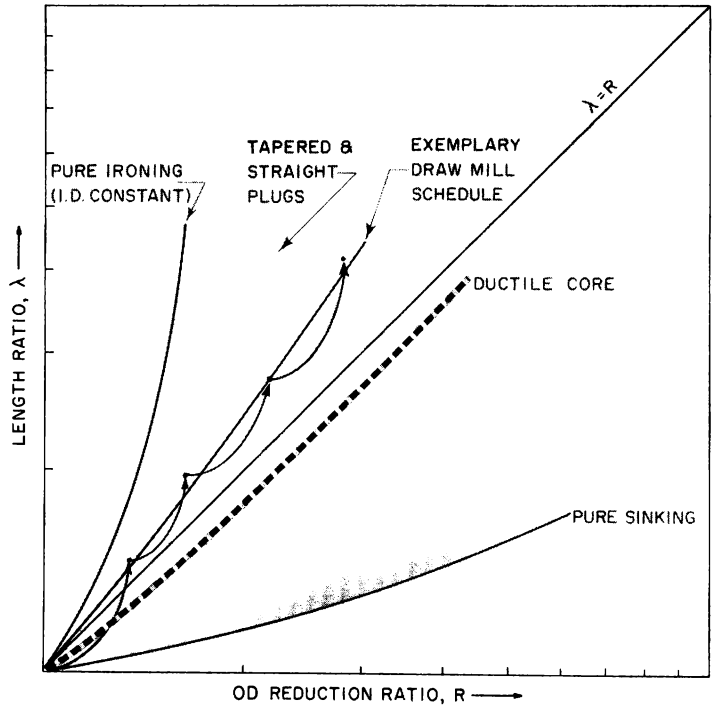

106-7379

The alternative techniques are based on the need (1) for support of the tube ID during reduction to prevent the creation and/or propagation of defects and (2) to minimize tooling inventory for fabricating a large variety of materials and sizes.

The ID support can be provided by using a ductile core, powder core, or a combination of both. In Figure 120, reduction characteristics for the ductile core are shown below the reference diagonal. Powder cores with or without a ductile core generally exhibit reduction characteristics which lie between the ductile core and pure sinking limits, with the deviation from the diagonal being dependent upon the type of powder and the clearance between the tube and core material. Sinking occurs until the tube becomes "seated" upon the core material, whence the assembly reduces as a rod and constructs a line parallel to the reference diagonal. By selecting the proper technique, the D/t (diameter to wall thickness) ratio can be controlled to either remain essentially constant or to undergo a desired change.

Families of curves, such as that shown for Ta-10 w/o W in Figure 121, have been generated for several refractory alloys to validate initial results obtained with copper and stainless steel and to provide data for selecting techniques for different materials or variable starting sizes of tube blanks.

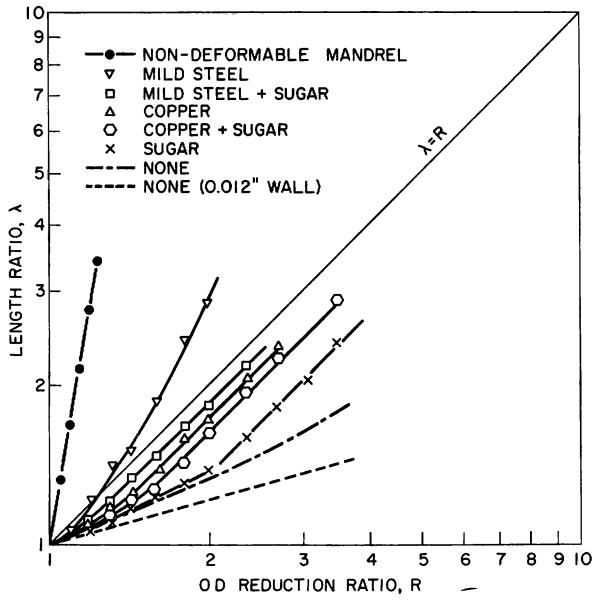

106-7373

Figure 121

Effect of Fill Materials upon the Deformation of Ta-10 w/o W Tubes during Drawing (D_0 = 0.360 in., t_0 = 0.025 in.)

These techniques have been evaluated.[101] Further work is being carried out to compare these methods with commercial practice and to evaluate their merits for large-scale tubing production. Most of the present work has been with V, Nb, and Ta and their alloys. The knowledge gained will be applied to tubing materials requiring warm working such as molybdenum, tungsten, and their alloys.

New Methods - Drawing of Tubes with Fluid Cores
(R. A. Beatty and R. M. Mayfield)

After having investigated the effect of ductile cores and particulate cores on the deformation behavior of tubing during drawing, the next logical avenue of approach would appear to be an appraisal of the benefits (or drawbacks) of a fluid core. [The deformation behavior of tubing with no core support (sinking) is currently under investigation, as reported elsewhere in this section.]

Within a certain range of D/t ratio values, generally above 3, the internal volume of a tube decreases with increased sinking (no ID support). If an incompressible fluid is sealed under pressure within the tube, little or no volume decrease can occur when the tube is drawn. Theoretically the tube should behave as a bar or in a manner analogous to ductile core drawing as mentioned above. The calculations below will indicate more clearly why such a reaction might be anticipated.

---

[101] Flinn, J. E., Jr., and Mayfield, R. M., Evaluation of New Fabrication Techniques for High Quality Refractory Metal Tubing, Technical Conference on Applied Aspects of Refractory Metals (AIME) December 9-10, 1963, Los Angeles, California. To be published in Proceedings.

Assuming the volume (V) of the solid metal of a tube remains constant, the volume (v) of the tube interior (central hole) and its change during drawing are computed as follows:

$$v_n = (\pi D_n^2 L_n/4) - V = (\pi D_n^2 L_n/4) - [\pi(D_0^2 - d_0^2) L_0/4];$$

$$k = v_n/v_0 = (D_n^2 L_n - [D_0^2 - d_0^2] L_0)/d_0^2 L_0.$$

Substitution of λ for the length ratio L_n/L_0 gives

$$k = v_n/v_0 = \lambda(D_n/d_0)^2 - (D_0/d_0^2) + 1. \quad (1)$$

Expressing k in terms of d_0, d_n, and λ, one finds that

$$k = (d_n/d_0)^2 \lambda, \quad (2)$$

where k = the volume ratio, and 0 and n are suffixes denoting initial and instantaneous conditions. [k is usually determined from equation (1), since easily measured dimensions are involved.]

When k = 1 there is no change of v during drawing. This condition is approached in a tube with a deformable core, so that the relations $D_n:D_{n-1} = t_n:t_{n-1}$, etc., are approximately met. In tube sinking, $k < 1$ and the ratio decreases progressively. With a tube containing a pressurized fluid, k would be made to approach 1. Rupture of sound tubes should not occur during drawing, since $k > 1$ is unrealistic unless the internal pressure is excessive.

The advantages of such a processing technique are tempting. The problem of core removal would be eliminated. After final drawing the tip of the tube would be cut off and the fluid core poured out.

In order to evaluate this premise, several tests of fluid-core drawing with aluminum, copper, and Zr-2 tubes have been conducted. Although the results are incomplete and preliminary in nature, they certainly present interesting implications. The technique involves filling tubes with oil or water, pressurizing and sealing the tube, followed by drawing through successive dies without releasing the pressure.

In the case of aluminum, a 100-cm-long 2S Al tube, of 0.635-cm (0.250-in.) OD by 0.151-cm (0.062-in.) wall (D/t of 4.1), was pressurized with oil to 560 kg/cm^2 (~8,000 psi) and drawn in four passes to a diameter of 0.485 cm (0.191 in.) a 43% OD reduction. The final D/t of 4.2 clearly indicates that no sinking occurred in drawing over the fluid core. An aluminum tube having the same dimensions before drawing produced a D/t of 2.4 when sunk to the same final diameter.

Hard-drawn copper tubes of 0.635-cm (0.250-in.) OD with a D/t of 8.1 were filled with water and the ends sealed without pressurizing. Sufficient pressure had built up after about three-quarters of the tube length had passed through a 0.99-cm die to maintain a constant D/t ratio in the balance of the tube length. Rough rechecks of a similar fluid-core tube indicated that a 1055-kg/cm^2 (15,000-psi) internal pressure was generated on drawing without completely eliminating sinking.

Zr-2 tubes with a 0.759-cm (0.299-in.) OD and a D/t ratio of 14.2 were pressurized by means of oil to approximately 560 kg/cm^2 (8,000 psi) and drawn through two (2) dies to a 0.683-cm (0.269-in.) diameter (~20% OD reduction) with the D/t ratio remaining constant over the whole tube length.

The behavior of the ID surface during fluid-core drawing has not been fully analyzed, but indications are that a matte finish is obtained, similar to that resulting from sinking operations. In either case there is no nondeformable core to smooth the inner surface.

Aside from ease in core removal, a pressure test is an integral part of the processing operation - if serious defects exist, the tube very likely will rupture. Further, a predetermined D/t value may be attainable through regulation and control of the internal pressure.

Application of this technique to stronger materials such as SS and certain refractory metals is planned.

Method Analysis (R. M. Mayfield and N. H. Polakowski*)

Bulk reduction by drawing on a ductile core does not seem to present fundamental difficulties, irrespective of whether the operation is conducted at ambient temperatures (as with Nb, Ta, V, and most of their alloys) or at elevated temperatures (as with Mo, W, and alloys). However, since even the highest drawing temperatures envisaged do not exceed 500-550°C, the disposable ductile core will be work hardened in each case, and its retained ductility may be too small to permit direct elongation and extraction. Since annealing for core softening must generally be conducted at temperatures above 550°C, the difference between thermal dilation of the core (as with low carbon steel of 304 SS) and the usually lesser expansion of the tube may develop significant tensile hoop stresses in the latter. The higher the working (drawing) temperature compared with that needed for core softening, the lower will be the stress attributable to this cause. Unfortunately, this temperature-stress advantage may be offset by the high elastic moduli of molybdenum and especially of tungsten. This leads to the interesting conclusion that optimum working temperatures for easy core removal might well be above the ductile-brittle transition range. With further

* Illinois Institute of Technology, Consultant to ANL Metallurgy Division.

development, the fluid-core technique may be applicable to drawing at elevated temperatures. If such is the case, some of the above-mentioned difficulties might be overcome.

For numerous applications the sound but fine grainy character of the ID surface that can result from the use of a ductile core (and perhaps also with a fluid core) should prove acceptable. Nevertheless, as stated previously[102] and recently confirmed,[103] some kind of final sizing by drawing over a fixed plug or mandrel would be required in certain cases to achieve a high-grade finish and close dimensional tolerances.

Plug drawing down to small sizes of the order of 0.25-cm OD has not been successfully practiced, but appears feasible if the plug and anchor rod are made as a single, continuous solid piece. Despite the difficulty with ID lubrication, plug drawing has the obvious and important virtue that the need for separating the tube and the mandrel does not arise, as in the case of mandrel drawing. Neither procedure is foolproof, even when employed at ambient temperature, on account of seizing and galling tendencies of some metals. These difficulties are compounded at higher temperatures, and the feasibility of plug drawing under these conditions must yet be proven.

Extraction (stripping) of nondeformable mandrels is a routine operation in commercial fabrication of ductile metal tubing. When applied to some of the refractory metals, both stripping and the related straightening procedure are recognized as major problems. Mandrel removal by warm reeling naturally will be tried, although warm swaging and shot blasting are possible alternatives. Spheroidizing the steel mandrel followed by plastic stretching-out has also some potential, and the loss of a relatively cheap mandrel in this manner may still be justifiable in terms of economics. Indeed, from the point of view of possible injury to a low-ductility tube, the last two procedures appear to be safer than either reeling or swaging.

2. High-temperature Reactor Jacket Fabrication

The development of techniques for fabricating small-diameter tungsten and tungsten-alloy tubing began in late June 1963. The objectives of this effort are to (1) study the fabrication parameters (both primary and secondary) associated with the production of high-quality tubing in diameters of less than 3.18 mm (0.125 in.), (2) produce limited quantities of high-quality tubing for evaluation studies, and (3) indicate areas where cost reductions can be made to reduce the current price of tungsten tubing.

---

[102] Annual Report for 1962, Metallurgy Division, ANL-6677, p. 161.

[103] Hunt, J. G. et al., Development of a Fabrication Process for Seamless Tungsten Tubing. NMI-1260 (Oct 17, 1963), p. 39.

a. Primary Fabrication (W. R. Burt, Jr.)

Efforts to date have consisted of extruding various tungsten starting materials into tube blanks suitable for secondary fabrication. Results on the extrusion of tungsten tube blanks will not be discussed at length as a progress report covering the specific details is forthcoming.[104] Briefly, tube blanks have been successfully extruded from vapor-deposited tungsten tubing, pressed and sintered tungsten-powder sleeves, and pre-extruded tube blanks as starting materials. All billets were extruded with a deformable core inside the tungsten sleeve rather than by extrusion over a non-deformable mandrel, which is the conventional technique. This eliminates problems associated with the use of small-diameter mandrels in high-temperature extrusion and protects the ID of the tungsten tube from atmospheric contamination during heating and extrusion. In addition, lower extrusion pressures and temperatures are realized than when extruding a billet totally comprised of tungsten. To date, the billet design, similar to that developed at Nuclear Metals Inc., incorporates a molybdenum core, a tungsten sleeve, and a 304 stainless steel outer jacket, the latter for protection against contamination and better lubrication during extrusion. Billets are generally extruded at 1100°C.

In addition to extrusion of preformed sleeves, high-purity tungsten granules have been directly compacted and extruded into tubing in a single operation with a molybdenum billet containing an annular space filled with the loose tungsten granules. A thin outer shell of molybdenum at the tail end of the billet initially collapses to allow a back plug to compress the tungsten granules prior to the billet actually extruding through the die. The billets were extruded at 1500 to 1660°C, although lower temperatures will be explored. Reduction ratios were about 4:1. The resultant tungsten tubing was fully densified and bonded, although a circumferential crack occurred near the core. This technique will be explored further through use of larger billets and a faster extrusion press to minimize heat loss in the billet during transfer and extrusion.

Figure 122 shows the results of extruding the various starting materials of tungsten. The "snake skin" appearance of the tungsten-granule extrusion is due to the large size of the tungsten granules and the relatively low reduction ratio.

b. Secondary Fabrication (J. E. Flinn, Jr.)

Little effort can be devoted to the secondary fabrication of these materials until hot swaging dies and other warm-working equipment has been received. Such procedures and equipment are necessary to work tungsten above its ductile-brittle transition temperature, which is generally above room temperature.

---

[104] Burt, W. R., Jr., Katiyar, H. C., and Mayfield, R. M., Development of Techniques for Fabrication of Small Diameter, Thin Wall Tungsten Tubing, ANL-6806 (to be published).

Figure 122. As-extruded Surface Quality of Extruded Tungsten Tubes

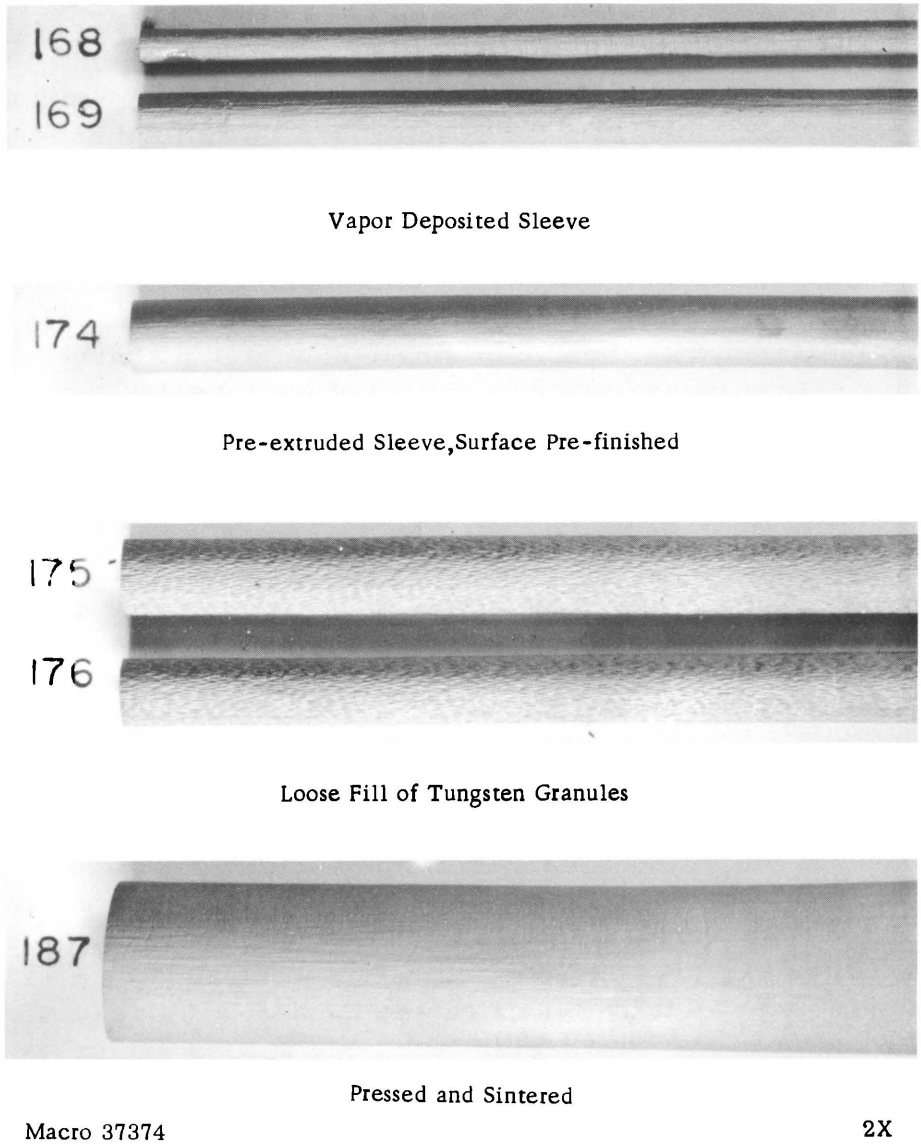

Despite the lack of certain required tooling, secondary fabrication has included the swaging and drawing of pure molybdenum and TZM (Mo-0.5 w/o Ti-0.08 w/o Zr) tube blanks as forerunners for the more difficult tungsten materials. Most of this preliminary work has been done with pure molybdenum. Tubing with a stainless steel core - with or without an annulus of Al_2O_3 - has been drawn from approximately 1.588 cm (0.625 in.) to 0.2615 cm (0.103 in.) at temperatures of 300 and 600°C with no intermediate anneals. The quality of the tubing is currently being evaluated.

3. The Effect of Die Sinking on the Quality of Zircaloy Tubing (R. A. Beatty)

Zirconium and/or Zircaloy tube fabrication has received only limited attention during the past year. For all practical purposes the

Zr-2 tubing program has been closed out due to the pressure of other activities and the fact that industry can now handle zirconium tubing in a manner that assures a high-quality final product.

A brief series of experiments have been conducted to determine the ability of Zr-2 tubing to withstand die sinking without generating ID defects or excessive ID surface roughening. It is known that excessive sinking of Zr-2 can lead to serious ID problems,[105] but it was not known whether this behavior was a function of starting tube quality or an inherent characteristic of Zr-2 per se. At least partial answers were obtained from the series of tests conducted.

The tubing used in the tests was fully annealed and free of defects. Two 60-cm-long tubes, of 7.59-mm (0.299-in.) OD and 0.533-mm (0.021-in.) wall, were sunk various amounts, with results as summarized in Table LIII.

Table LIII

EFFECT OF DIE SINKING ON THE QUALITY OF Zr-2 TUBES

Schedule Code	Reduction and Annealing Schedule(a)	Pass Number				
		1	2	3	4	5
A	Approx 10% reduction/pass; no anneals.					
	% Total reduction	12	19	29	36	42
	Wall defects(b)	NDD(d)	NDD	NDD	<10%	-(e)
	ID surface quality(c)	1	2	3	3	4
B	Approx 30% reduction/pass; anneal after pass 3.					
	% Total reduction	28	45	62	72	80
	Wall defects	NDD	NDD	NDD	>20%	-
	ID surface quality	2	4	5	6	6
C	Approx 10% reduction/pass; anneal after pass 3.					
	% Total reduction	12	19	29	36	42
	Wall defects	NDD	NDD	NDD	<10%	-
	ID surface quality	1	2	3	3	4
D	Approx 30% reduction/pass; anneal after each pass.					
	% Total reduction	28	45	62	72	80
	Wall defects	NDD	10%	-	-	-
	ID surface quality	2	4	-	-	-

(a) 675°C anneal for 1 hr.
(b) % of wall thickness.
(c) Arbitrary scale based on starting quality 0. 0 = approx 20-30 rms. 6 = approx 120 rms.
(d) No defects detected.
(e) In process.

[105] Bean, C. H., and Polakowski, N. H., Fabrication of Defect Free Small Diameter Zirconium Alloy Tubing, ANS Transactions, Vol. 5, No. 1, June 1962, p. 247.

The results of these limited tests indicate that the first pass of even a light reduction may affect the ID surface quality of the tube. This effect becomes more pronounced with heavier drafts. In either case the roughening increases with the number of passes.

The Zr-2 tubes can be sunk as much as 30% without the generation of detectable defects or propagation of possible existing defects that were not apparent in the original tubes. The first draft following an anneal produced detectable defects. This phenomenon that occurs on the first pass following an anneal will require further study.

The information gained from this brief investigation will be further studied and the results applied to general tubing technology, involving other refractory materials.

4. Fabrication of Thorium-Uranium Fuel Materials (W. R. Burt, Jr. and W. C. Kramer)

Thorium-uranium alloys have shown excellent resistance to high-temperature swelling under irradiation. Further, alloys containing up to 20 w/o U irradiated to total atom burnups of at least 5 percent retained surface smoothness.[106] To evaluate the Th-20 w/o U alloy further, additional samples were prepared by extrusion and machining to yield a fabricated structure for comparison with material tested in the as-cast condition. Extrusion temperatures were chosen to represent a low-temperature (500°C) uranium α-phase extrusion and a high-temperature (850°C) uranium γ-phase extrusion.

The Th-20 w/o U (fully enriched) specimens prepared for irradiation testing ranged from 0.356 to 0.366 cm (0.140 to 0.144 in.) in diameter and were 5.08 or 33.0 cm (2.00 or 13.00 in.) in length. Thorium-20 w/o uranium castings were made in a Vycor tube vacuum induction furnace. Metal was charged into a thoria crucible and bottom poured into a 2.22-cm (7/8-in.)-diameter, graphite split mold, internally coated with mullite. A pressure of 1 μ or less was maintained through the melting period, and pouring temperatures ranged from 1770 to 1830°C.

Extrusion billets measuring 1.9 cm (0.748 in.) in diameter and ranging in length from 5.72 to 6.03 cm (2-1/4 to 2-3/8 in.) were machined from the castings. The billets were jacketed in copper prior to extrusion. The copper served to protect the Th-U billets from contamination during heating and to prevent galling between the billet and die during extrusion. The jacketed billets were heated in air to 500°C and extruded on the 50-ton vertical extrusion press at a 25.5:1 reduction ratio and at a ram speed of 2.54 cm/sec (1 in./sec). This represented extrusion in the uranium α-phase

---

[106] Kittel, J. H., Horak, J. A., Murphy, W. F., and Paine, S. H., Effects of Irradiation on Thorium and Thorium-Uranium Alloys, ANL-5674, p. 33 (April 1963).

region. All billets extruded satisfactorily with the running extrusion pressure averaging 10,900 kg/cm^2 (153,00 psi), corresponding to an extrusion constant of 3,360 kg/cm^2 (47,000 psi).

Following radiography, excess copper nose and tail pieces were cropped off and the copper jacket removed by pickling in nitric acid. The dejacketed Th-U rods then were centerless ground to the final diameters and machined into irradiation samples 5.08 to 33.0 cm (2.00 to 13.00 in.) in length.

Metallographic examination of extruded material showed fine stringers of uranium elongated in the extrusion direction in a matrix of thorium. The thickness of the uranium stringers was approximately 2.5×10^{-3} mm (100 μ).

Additional samples are being prepared from billets extruded at 850°C, representing a uranium γ-phase extrusion. The billets extruded successfully are in the process of being dejacketed prior to machining to final size.

5. Fabrication of ZPR-VI Danger Coefficient Specimens (A. G. Hins and E. M. Pilarski)

A process and tooling was developed to make double-jacketed plates for use in ZPR-VI. These consist of plutonium-1.25 w/o aluminum alloy plates measuring 4.23 cm x 4.55 cm x 0.45 cm and 6.80 cm x 4.55 cm x 0.45 cm. The corners of the plates were radiused 0.64 cm. The plates were cast to specified dimensions in copper book molds, one of which is shown in Figure 123. The only machining required was to mill the sprue and a light filing of the parting line.

Figure 123. Multiple-cavity Copper Molds for ZPR-VI Plate Specimens (Dimensions in in.)

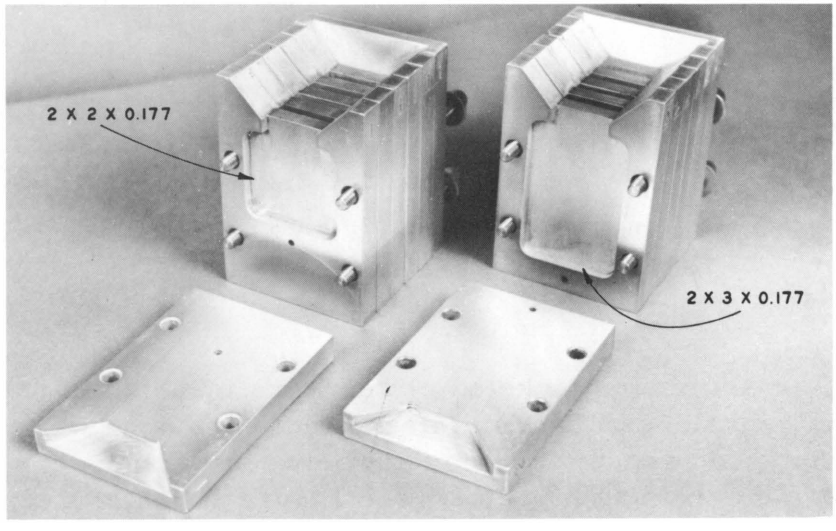

350-596

The specimens were clad in aluminum half-cans. These were drawn to size from 0.4-mm-thick type-1100 aluminum sheet by means of a 12-ton hydraulic press. The dies were made of Masonite die stock. The punch was of brass. The excess flash was trimmed from the half-cans. They were degreased, lightly etched with NaOH, rinsed through an acid stop, alcohol washed, and acetone dried. Each can was inspected for evidence of thinning or tearing at the corners.

The jacketing steps are illustrated in Figure 124. The half-cans and plutonium alloy plates were transferred to the welding hood line. A vacuum "lifter" was used to place the plutonium plate in the lower half-can, and the upper half-can was carefully positioned to avoid contaminating the welding edges. The assembly was clamped between formed copper chill blocks which ironed the half-cans down tightly against the core and clamped the welding edges with a projection of about 0.4 mm for welding. Aluminum pads were provided on each end of the joint for arc starting and run off. Self-fusion TIG welds were made on each of the four edges of the aluminum can. The welds were visually inspected and leak detected by the vacuum bubble test method.

Figure 124. Steps in Jacketing ZPR-VI Plate Specimen

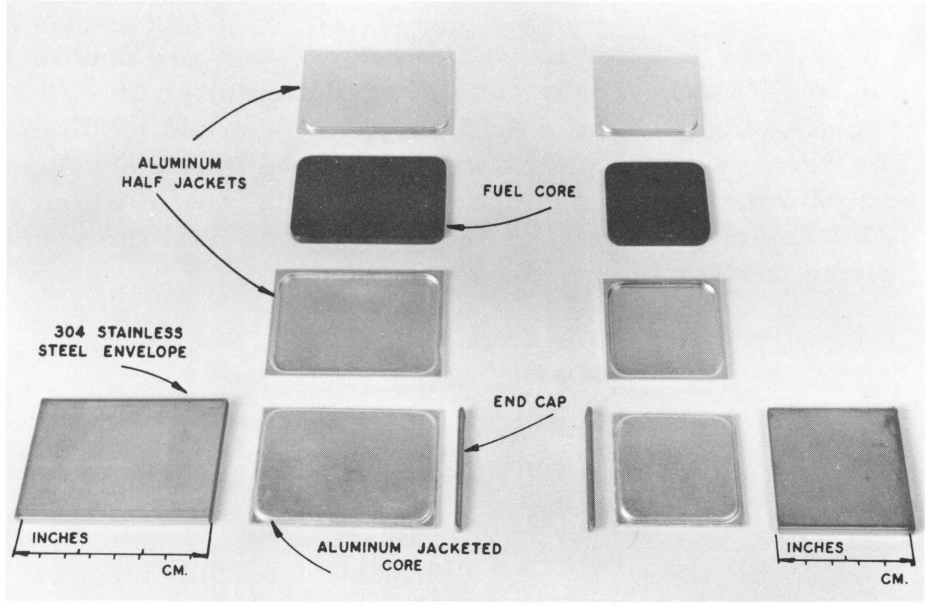

2 in. x 3 in. Fuel Plate Assembly 2 in. x 2 in. Fuel Plate Assembly

350-608

The aluminum-jacketed plates were inserted in prefabricated stainless steel envelopes. The stainless steel envelopes were welded under a partial vacuum to assure close contact between the envelope and the specimens. A vacuum-welding machine, (see Figure 125) was developed to

accomplish this. The plug was inserted and the ends of the plug tack welded to the envelope. The assembly was clamped between chill blocks in the welding machine. Weld starter and run-out blocks were clamped on either end of the envelope. The weld chamber was then closed and repeatedly evacuated and filled with a helium-argon welding mixture. Welding was accomplished at approximately 5 psia by two passes, one along each edge between plug and envelope. Welding conditions were 10 A, 20 V, 6 in./min.

Figure 125. Fuel Plate Welding Machine

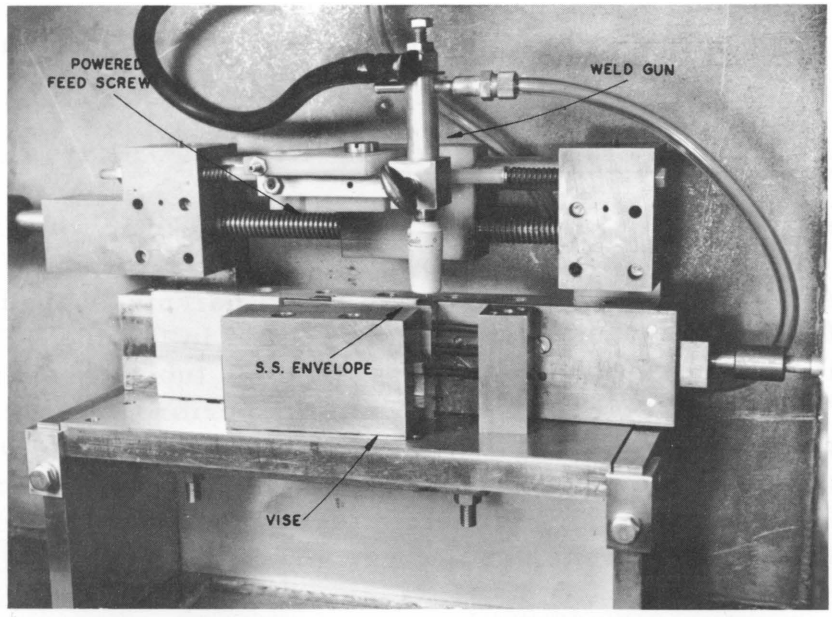

350-613

6. Fabrication of Ultra-thin Metallic Foils (F. J. Karasek)

The demands for metallic foils have continued throughout the year. The procedures employed for general foil fabrication have been reported elsewhere.[107] By means of the basic techniques, numerous materials have now been rolled to calculated foil thicknesses of 1 to 2 μ. Natural titanium was recently rolled down to a thickness of 0.35 μ (1.4×10^{-5} in.).

Beryllium was fabricated into foils in a range of thicknesses for use with the Compton Mass Spectrometer. The raw material was commercially rolled beryllium sheet of 1.5-mm thickness. The sheet was jacketed in mild steel and rolled at 800°C to a thickness of 0.4 mm. After the final pass the assembly was reheated and slow cooled. After cooling, the beryllium was removed from the sheath, cut into several sections, and etched in a 50 v/o H_3PO_4-50 v/o H_2O. The beryllium sections were then individually jacketed in 16 gage 304 SS and rolled at 400°C, with reductions of 5% per

107 Karasek, F. J., Techniques for the Fabrication of Ultra-Thin Metallic Foils, Nuclear Science and Engineering, 17, 365-370 (Nov 1963).

pass, to a total reduction of 50%. The assemblies were then annealed at 800°C for 20 min and slow cooled. The SS jacket was removed and the foil was again etched and rejacketed in SS. This procedure was repeated until foils ranging in thickness from 0.15 to 0.03 mm had been produced.

Other undertakings have included the formation of compounds such as Mg_3Sn for use in studies of the Mössbauer Effect; the roll bonding of uranium to copper and/or zirconium for high-level irradiation-test specimens; preliminary developments for the rolling of samarium foils. The conversion of rare earth oxides to metal cannot be accomplished with existing equipment. A specially designed furnace will be required for the final reduction step.

7. Fabrication of Superconducting Wire (F. J. Karasek)

As reported previously,[108] a limited quantity of Nb-1 w/o Zr-clad, Nb_3Sn-cored wire was drawn down to a diameter of about 0.63 mm (0.025 in.). All attempts to form the wire into a hairpin-shaped loop that was needed for insertion into a test fixture ended in failure. Further testing will await the reduction of the composite-type tubing assembly to smaller diameters. This work will be carried out at Superior Tube with material having a Monel cladding. A finished wire size of 0.25-mm (0.010-in.) diameter, or less, should prove acceptable for the planned test procedures. End fittings have been fabricated, but their effectiveness cannot be evaluated until the finished wire is received and prepared for test.

8. Preparation of High-strength Aluminum Tubing (W. C. Kramer)

A total of six (6) one-inch-diameter billets were prepared from as-atomized and ball milled X8001 aluminum powders and extruded at 450°C, resulting in a reduction of 6.6 to 1. The billets did not blister during heating for extrusion. Tensile results from the extruded stock were as expected, showing an increase in ultimate strength as the particle size decreased.

The interest in fuel cladding from high-strength aluminum powder product has been largely associated with the organic-moderated reactors. The disenchantment in this particular reactor field combined with the increased demands imposed upon the available manpower of the Foundry and Fabrication Group has led to a forced abandonment of the original objectives of this work.[109] Where possible, limited support effort will continue.

---

[108] Annual Report for 1962, Metallurgy Division, ANL-6677, p. 174.

[109] Annual Report for 1962, Metallurgy Division, ANL-6677, p. 170.

J. Development of Nondestructive Testing Methods

1. Ultrasonic Imaging (H. Berger)

A system for obtaining a television presentation of ultrasonic radiation images has been placed in operation. The essential elements of the imaging system are shown in Figure 126. The camera tube, which is the heart of the system, is shown in greater detail in Figure 127.

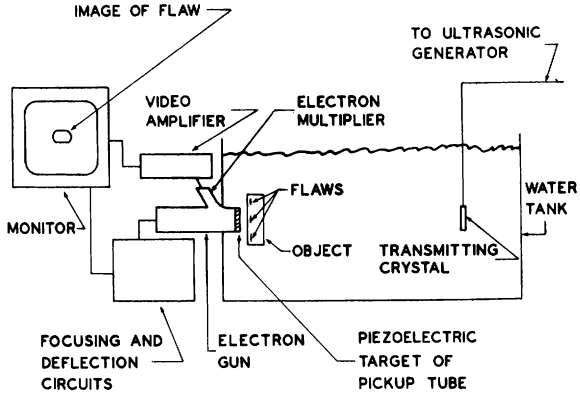

Macro 35431

Figure 126

The Diagram Shows the Essential Elements of the Television Ultrasonic Image System

As now arranged the useful diameter of the 2-Mc piezoelectric target of the pickup tube is approximately 4.5 cm.

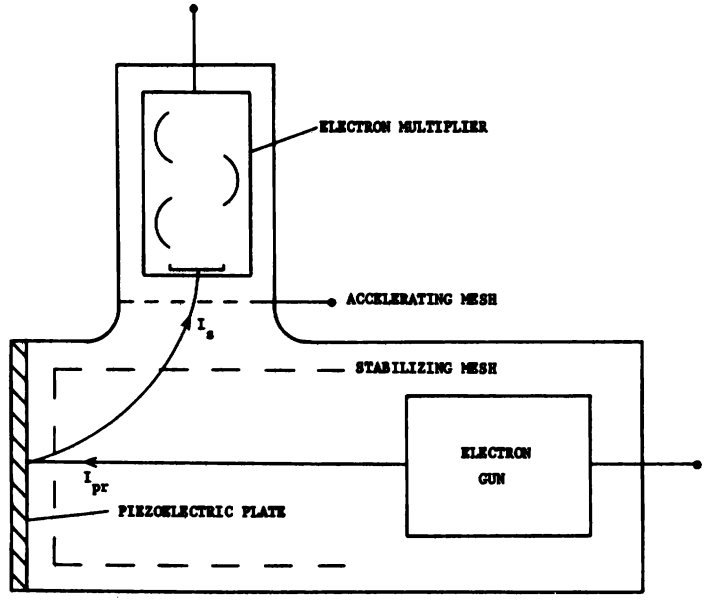

Macro 35495

Figure 127

Schematic Diagram Showing Ultrasonic Camera Tube Used in the Imaging System

In operation, a uniform, continuous ultrasonic radiation beam, obtained by working at a large distance from the ultrasonic transmitting transducer in order to eliminate near-field nonuniformities in the beam pattern, is directed through the test object and then to the camera tube

detector. The detected signal is processed by conventional closed-circuit television methods to yield a televised image of the ultrasonic radiation reaching the detector. The scanning system used is the American standard, 525 lines interlaced, 30 frames/sec.

Referring to Figure 127, the operation of the camera tube to detect ultrasound depends on the voltage developed across the piezoelectric target and faceplate of the tube as ultrasound strikes it. This voltage, which varies from point to point on the piezoelectric target in proportion to the ultrasonic intensity at any point, modulates the secondary electron beam generated on the target surface by the scanning beam from the electron gun. The secondary electron beam, containing the modulation caused by the ultrasonic image, is collected and amplified within the tube by the accelerating mesh and the electron multiplier. Amplification of this weak signal within the tube produces a large signal in which interfering pickup from the fields produced by the ultrasonic generator can be more easily eliminated [110]

A continuously pumped, demountable camera tube system employing a barium titanate target operating at approximately 2 Mc has been used for most of the evaluation studies of this system to date. However, some studies have been made with sealed ultrasonic camera tubes having quartz targets.[111] These tubes, also operated at 2 Mc, yielded ultrasonic images similar to those obtained with barium titanate in the demountable camera system. The results comparing these detecting systems tended to confirm previously reported information[110] that quartz piezoelectric targets respond to ultrasonic intensities lower than those required by barium titanate, but that resolution properties do not appear to be quite as good as those found with barium titanate.

Evaluation studies made thus far on these systems have involved flat samples of various thicknesses. The samples have contained through holes, flat-bottomed holes, and the latter type of samples with a bonded cover plate, thereby yielding a sample containing a metal-air interface of known size. Results of the resolution investigation with such samples indicate that flaws as small as 0.75 mm in diameter can be detected and that reasonable correlation of flaw size and image size can be obtained for flaw sizes of the order of a mm or more in diameter. The limiting size of the flaw for good image-size correlation appears to be set by the larger of either the wavelength of the ultrasound or the thickness of the detecting transducer In the case of barium titanate or quartz operating at 2 Mc, the approximate thickness of 1 mm for the detector appears to be the limitation.

---

[110] Jacobs, J. E., Berger, H., and Collis, W. J., An Investigation of the Limitations to the Maximum Attainable Sensitivity in Acoustical Image Converters, IEEE Trans. on Ultrasonic Engineering, UE-10, 83-88 (Sept 1963).

[111] Jacobs, J. E., To Develop a System for Employing Ultrasonic Imaging Techniques for Nondestructive Testing, TID-19009 (June 1963).

By means of direct shadowing methods, as illustrated in Figure 126, the image obtained correlates well with object flaw size for flaw sizes beyond the limitation just indicated, for flaw-detector distances up to approximately 4 cm. In most cases, as this flaw-detector distance is increased further, the apparent image size increases and degrades in sharpness.

A similar depth-of-focus limitation is obtained with the use of lens systems. Although the total thickness of flat material which can be inspected by direct shadowing methods to yield good correlation between flaw size and image size may be limited to about 8 cm, this restriction does not apply to the lens-system technique. In this case, the position of good focus can be readily moved to any area within the inspection material. Nevertheless, most of the present effort has been concerned with the direct shadowing method and thin material.

For relatively thin, flat material this inspection method does appear to be capable of detecting flaws difficult to detect by other methods. Recently reported comparisons[112] between this imaging method, a two-transducer mechanical scan ultrasonic technique,[113] and X-radiography have clearly shown this capability for small inclusions in metals.

Further studies planned for this system include additional investigations concerning the angular positioning of the sample with the ultrasonic beam. Recent work in this area indicates that flat samples should be angled 15 to 20 degrees from the perpendicular to the ultrasonic beam direction for the clearest visual indication of a flaw. Although one reason for this is the elimination of standing-wave patterns, further studies of angular positioning may indicate other causes and may lead to a determination of optimum angular positioning.

Further plans also call for studies involving samples having configurations other than flat, restricted aperture work and investigations of transducer materials other than quartz and barium titanate.

2. Correlation of the Sound Transmission Properties, Heat Transfer Properties and Strength of a Bond (R. A. di Novi)

The acceptance or rejection of a bonded element which has been tested by ultrasonic methods has been made on the basis of the ability of the bond to transmit or reflect ultrasonic energy, with only occasional reference to destructive evaluation of the bond. The criteria for acceptance are often

---

[112] Jacobs, J. E., Berger, H., and Collis, W. J., An Evaluation of an Ultrasonic Inspection System Employing Television Techniques, to be published.

[113] McGonnagle, W. J., and Beck, W. N., An Ultrasonic Scanning and Recording System, Proc. ASTM, 56 1415 (1956).

poorly defined, as the tests do not provide any information about the serviceability of the element, i.e., its strength or its thermal properties, because it is not known what correlation, if any, exists between these service properties and the ultrasonic transmission properties. To make ultrasonic bond tests more significant, such a correlation is being sought.

To determine the thermal properties of bonded elements, the thermal pulse method for measuring thermal diffusivity and thermal conductivity developed by Parker et al.,[114] is being utilized. The front surface of specimens are uniformly irradiated by a very short pulse ($\geq$600 μsec) of radiant energy supplied by a xenon flash tube. The temperature history of the back surface is continuously monitored by feeding the output of the back-surface temperature into a differential amplifying system and then into an oscilloscope. This oscilloscope trace can then be photographed. The flash tube and oscilloscope are triggered together, but there is in the former circuit a variable time delay which insures that the early portion of the back-surface temperature curve is completely visible on the scope. Figure 128 is a typical photographic trace of the temperature rise at the rear surface.

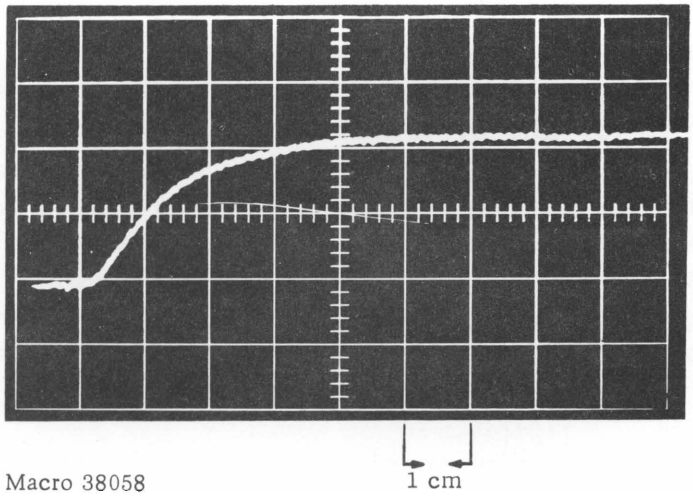

Macro 38058

Figure 128

Typical Photographic Trace of the Temperature Rise at the Rear Surface

Trigger transient and reference base line are at left. (Abscissa, 10 ms/cm; ordinate, approximately 2.5°/cm).

Upon completion of the flash tube apparatus, the system was checked by measuring the thermal diffusivities α of several known metals. Results are given in Table LIV.

The reproducibility of the system was found to be within 3%. Parker estimates the accuracy of the system as 10%.

The method requires thin specimens (1-2 mm for metals), and the first set of bonded specimens consisted of two 0.063-cm-thick pieces of copper joined with a solder braze. Values of the diffusivity ranged from

---

[114] Parker, W. J., Jenkins, R. J., Butler, C. P., and Abbott, G. L., Flash Method of Determining Thermal Diffusivity, Heat Capacity and Thermal Conductivity, J. Appl. Phys. 32, 1679 (1961).

1.11 cm^2/sec for solid copper to 0.063 cm^2/sec for specimens separated by a very narrow air gap; the most uniformly well-bonded specimen that could be made gave values from 0.849 to 0.919 cm^2/sec. Tests upon the other 12 specimens in this set are in progress, and for these specimens values of the diffusivity are found to vary within the above range with the region of the specimen that the thermocouple contacts. The method is proving itself to be very sensitive to bond variations over small regions (1-2 mm).

Table LIV

RESULTS OF MEASUREMENTS OF THERMAL DIFFUSIVITY

Specimen	$\alpha(cm^2/sec)$	$\alpha(cm^2/sec^*)$	% of Difference
Brass	0.337	0.339	-0.6
Al (2S)	0.872	0.860	+1.4
Steel (1018)	0.1647	-	-
Cadmium	0.450	0.467	-3.6
Copper	1.11	1.14	-2.6

*Values taken from Handbook of Physics.

Present activities include the measuring of the thermal conductivities of these specimens and the extension of the method to roll-bonded specimens.

In preparation for the ultrasonic tests, the recording system was modified to use Alfax recording paper. A two-dimensional one-to-one map of the bonded area can be made; the intensity of the recorded trace is proportional to the amount of transmitted ultrasonic energy. Thus, the dark and light areas on this map will directly indicate the good or bad regions of the bond.

3. Ultrasonic Instrument and Transducer Development
(R. H. Selner)

The development of reliable and efficient transducer probes is part of a program designed to improve and expand the capabilities of the ultrasonic method of nondestructive testing. Such effort is desirable for two reasons. First, commercial probes often have been unreliable and inconsistent. Second, the ability to fabricate special function probes would prove extremely helpful in solving many difficult inspection problems.

Initially, efforts were concentrated on developing an operational pilot model which was economical, rugged, and relatively simple to fabricate. After several probes had been successfully built and tested, emphasis was shifted to such parameters of probe design as crystal backing and material.

Early probe models utilized tungsten-loaded epoxy of the same mixture suggested by Washington.[115] This mixture produces the shortest pulse length and therefore is ideally suited for inspections requiring the utmost in resolution. In later models, Fiberglas-loaded epoxy replaced the tungsten mixture, as it could be processed faster and easier. Pulse lengths of both mixtures are comparable.

Quartz, the traditional piezoelectric material for ultrasonic probes, is being replaced more and more by the ceramic materials of lead zirconate-titanate and lead metaniobate, which have higher sensitivity. Because of this higher sensitivity, most of the transducer probes will be constructed with ceramic crystals. So far, Clevite's PZT-4 and PZT-5 crystals, and lead metaniobate crystals from Branson have been utilized.

In order to analyze the transducers made under this program and also to provide a guide for use in future endeavors, an optical Schlieren system is being set up.

4. Neutron Imaging (H. Berger)

The neutron radiographic facility at Juggernaut reactor has been employed for a variety of inspection problems. In addition to the increased use of this beam for the inspection of radioactive, irradiated reactor fuel capsules, as previously reported,[116,117] the beam has been used for the inspection of reactor control materials and a variety of heavy metal objects.

In a recent study of neutron radiography,[118] it was shown that the use of neutron radiography to inspect natural uranium, lead, and bismuth was attractive because exposure times were lower than those required by most normal X-radiographic methods and because there were no serious radiographic effects caused by fast neutrons or gamma radiation in the thermal neutron beam, or by prompt radiation emitted from the inspection material. In the case of tungsten and steel some effects of prompt radiation emitted from the inspection material were noticed. This tended to reduce exposure times for heavier sections, but also resulted in decreased sensitivity to small changes in object thickness because of lowered

---

[115] Washington, A. B. G., The Design of Piezo-Electric Ultrasonic Probes, TRG Report 17 (C), United Kingdom Atomic Energy Authority (1961).

[116] Annual Report for 1962, Metallurgy Division, ANL-6677, pp. 133-134 and 185-186.

[117] Berger, H., and Beck, W. N., Neutron Radiographic Inspection of Radioactive Irradiated Reactor Fuel Specimens, Nuc. Sci. and Eng. 15 411-414 (1963).

[118] Berger, H., and Kraska, I. R., Neutron Radiographic Inspection of Heavy Metals and Hydrogenous Materials, Materials Evaluation, to be published.

contrast. These problems can be eliminated by employing transfer exposure methods in which the film used to record the final image is exposed, not to the neutron imaging beam, but to a transfer screen containing a radioactive image of the transmitted beam. However, in this case there is also a limiting material thickness which can be usefully inspected, because the radioactivity of the detecting transfer screen eventually becomes saturated as the exposure times required for the thicker sections approach several half-lives. These limiting thicknesses in a neutron intensity of 1×10^7 n/cm^2-sec, together with the use of dysprosium metal screens transferred to a medium-speed X-ray film, such as Type AA, were about 6 cm for tungsten and 7.5 cm for steel. These limits could be extended by the use of higher neutron intensities, faster films, or longer development times.

The characteristics of the neutron beam facility itself have been studied[119] in an attempt to improve its application use. The studies included intensity determinations for thermal and epithermal neutrons and gamma radiation, and a study of the influence of beam divergence on radiographic resolution.

The results of this beam investigation indicated that the more useful beam configurations involved a beam collimated to a rectangular opening 6.25 x 10 cm, and employing an extra thickness of graphite moderator at the reactor fuel end of the beam tube. Two different graphite thicknesses appeared particularly useful. With a graphite plug, 37.5 cm in thickness, the collimated beam yielded a total neutron intensity of 1.5×10^7 n/cm^2-sec with a cadmium ratio of 3.6 and a gamma intensity of 42 r/hr. For inspections which can be made with a less thermalized beam, such as for the inspection of most heavy metals, a graphite plug thickness of 12.5 cm yielded a collimated beam total intensity of 4.5×10^7 n/cm^2-sec, a cadmium ratio of 2.4, and a gamma intensity of 110 r/hr.

Each of these beam configurations yields a beam having a thermal neutron to gamma intensity ratio approaching 10^6 neutrons/cm^2/mr, as shown in Figure 129. These data indicate that with the use of these collimated beam configurations a square-centimeter detector would receive approximately 9×10^5 thermal neutrons for each milliroentgen of gamma radiation. This ratio is such that a normal photographic neutron-detection technique would respond much more to the neutrons in the beam than it would to the gamma radiation. Watts[120] has shown that the normally used direct-exposure methods require 10^4 to 10^5 n/cm^2 exposure to equal the

---

[119] Berger, H., Characteristics of a Thermal Neutron Beam for Neutron Radiography, International J. Appl. Radiation and Isotopes (to be published).

[120] Watts, H. V., Research on Neutron Interactions in Matter as Related to Image Formation, ARF-1164-27 (1962).

detector response to 1 mr of cobalt-60 gamma radiation. Work at this Laboratory substantiates this result.[121] Therefore, photographic detection methods in which film is exposed to this neutron imaging beam can be successfully used with little danger that a superimposed gamma image will complicate interpretation.

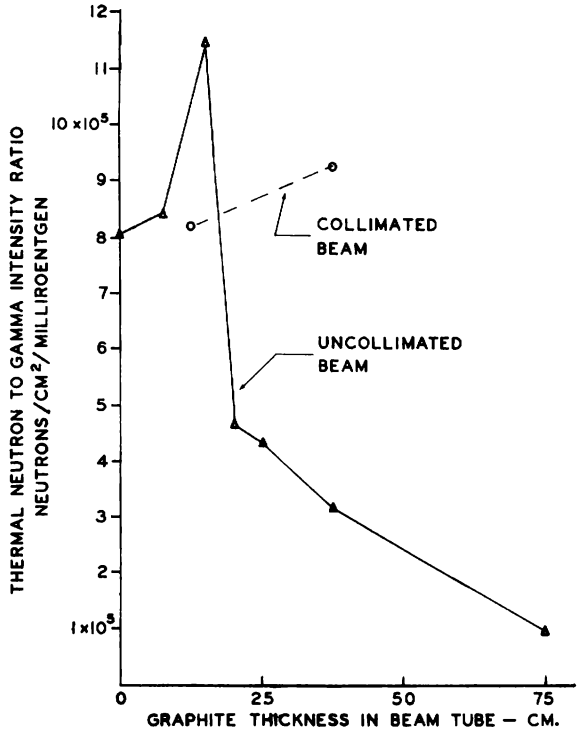

Macro 37915

Figure 129

The ratio of the thermal neutron intensity (n/cm^2-sec) divided by the gamma-radiation intensity (mr/sec) at the reactor face is plotted against extra graphite in the beam tube for the uncollimated beam, and for two collimated beam configurations for the neutron radiographic facility at Juggernaut reactor (reactor power level used was 200 kW).

The best result, yielding the highest ratio and, therefore, the greatest neutron intensity for a given gamma intensity, is 11.4 x 10^5 n/cm^2 per mr for 12.5 cm of graphite added in the uncollimated beam. Both collimated beams studied yielded ratios about 9 x 10^5 n/cm^2 per mr.

Further efforts on this neutron radiographic study are expected to be devoted primarily to application studies and inspection uses.

5. Application of Infrared Radiation to Nondestructive Testing (R. B. Perry)

Infrared detectors may be divided into two general classifications: thermal detectors which make use of the heating effect of infrared radiation, and photodetectors which make use of the quantum photoelectric effects. One detector of each type is being studied for possible application to nondestructive testing problems. The thermal detector, Radelin thermographic phosphor, may be mixed with a special lacquer and applied to the surface of the test object which is illuminated with ultraviolet light. The luminescence of the phosphor is quenched when heat is applied.

The temperature at which the phosphor quenches varies from 35 to 80°C, depending on the intensity of the ultraviolet light. When applied

[121] Berger, H., and McGonnagle, W. J., Progress Report on Neutron Radiography, ANL-6279 (1962).

to a sodium-bonded fuel pin the sodium level and a number of small voids could be seen as dark areas when a heat gun was passed over the sample.

The indium antimonide photoelectric magnetic detector is sensitive in the wavelength region from approximately 1 to 7.5 μ. The relative response is unity to 5 μ and is down 50% at 6.9 μ. With the detector at room temperature it is sensitive to radiation from objects with temperatures as low as body temperature.

An infrared scanning camera has been designed around the indium antimonide detector. The basic components of the system are the optical head, preamplifier, amplifier, oscilloscope, oscilloscope camera, and a lathe. The optical head contains the detector, a mechanical chopper, a spherical mirror optical system, and a motor-driven scanning mirror. The amplified signal from the detector is used to modulate the intensity of the oscilloscope beam. The horizontal sweep of the oscilloscope trace is synchronized with the scanning mirror in the optical head. The optical system is mounted on the carriage of a lathe. The vertical position of the oscilloscope beam is synchronized with the motion of the lathe carriage. A 10 x 10-cm area can be scanned in 90 sec, producing an infrared picture or surface-temperature map. Applications for the instrument and the temperature resolution are still being studied.

6. Development of a Pulsed-field Reflection System (C. J. Renken)

Electromagnetic inspection systems built around devices termed mask-aperture assemblies have been under development at Argonne for several years as part of an effort to increase the effectiveness of the eddy current test method. The mask-aperture assemblies are devices which restrict the induction field to small cross-sectional areas in order to produce a relatively limited system of currents in the test specimen. A well-defined system of currents allows an increase in both the resolution and sensitivity of the test system. The mask-aperture assemblies which were developed prior to this year were analogous to point probes in conventional eddy current test equipment.

A new type of mask-aperture assembly has now been developed, which is analogous to the encircling coil of conventional equipment. This device, called a coaxial mask-aperture assembly, is intended for the inspection of small-diameter, thin-walled tubing. It has been successfully employed with tubing down to 1.27-mm OD. Because of the very large signal derived from a coaxial mask-aperture assembly, the associated electronic equipment is very simple and practically drift-free.

The development of the pulsed systems has now progressed to the point where they have completely replaced the dual-frequency sinusoidal equipment formerly used for various test purposes. The advantages of the

pulsed-field electromagnetic test systems are particularly important under the conditions encountered in the nuclear field, which call for high sensitivity, reliability and resolution, and do not emphasize high inspection speeds.

7. Measurement of Elastic Properties of Materials as a Function of Temperature (R. G. Peterson)

A new project has been started to measure the elastic properties of refractory metals at elevated temperatures. The equipment to be used is that described in the 1962 Annual Report.[122] Work done so far has been to study the various materials of interest from the standpoints of fabricability, corrosion, and radiation effects, and to learn what has been previously found out regarding their elastic properties. Material will soon be ordered, some from outside suppliers, some from within our own facility. The vacuum furnace which will be used for this work has been standing idle for the past year and a half, and it is necessary to get it back in condition.

[122] Annual Report for 1962, Metallurgy Division, ANL-6677, p. 80.

PART II

BASIC METALLURGY

A. Metallurgy of Uranium

1. High-purity Metal (L. T. Lloyd)

Requests for high-purity uranium metal are continuing to be filled from existing inventory. During the past year, approximately 3 kg of metal were consumed by our own research programs. About 2.3 kg were distributed as follows: to the ANL Chemical Engineering Division for studies on compounds; to Northwestern University for oxidation studies; to Nuclear Metals for alloy studies; and to the University of California at Los Angeles for studies on the effects of pressure on the allotropic transformations.

2. Elastic Moduli of Single Crystals of Alpha Uranium (E. S. Fisher)

Measurements of the elastic moduli of single crystals of alpha uranium at elevated temperatures (above 300°K) have been resumed during the past year after an interruption about two years ago to complete measurements at low temperatures. The apparatus and techniques for that determination have been described previously (see Metallurgy Division Annual Report, 1961, ANL-6516). In Figures 130 and 131 are summarized all measurements to date for each of the stiffness moduli which are required to evaluate the nine principal elastic moduli. The data obtained during the past year are: the c_{11} measurements have been extended to 893°K; c_{22} has

Figure 130. Variation of the Compressional Stiffness Moduli of Alpha Uranium with Temperature

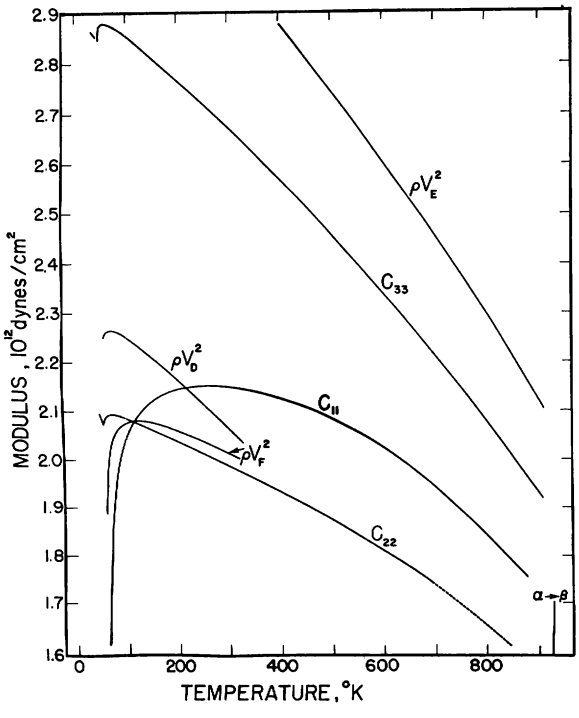

Macro 38109

Figure 131. Variation of the Shear Stiffness Moduli of Alpha Uranium with Temperature

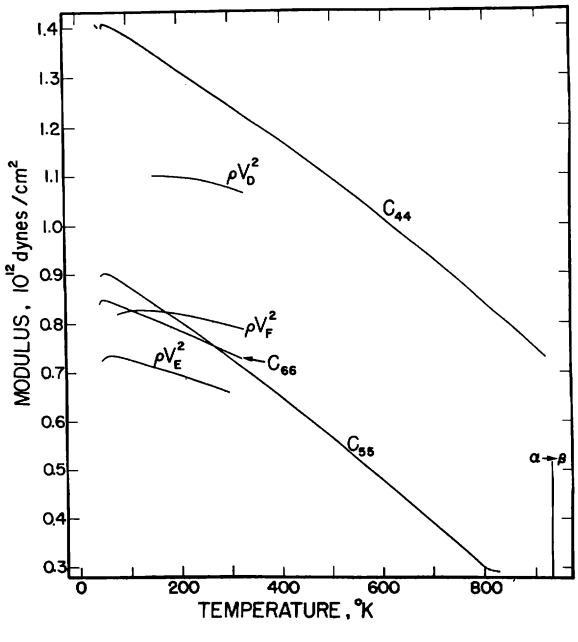

Macro 38029

been measured up to 848°K, but the data above 698°K are doubtful and will bear repeating; c_{33} and ρV_E^2 are now known to 923°K; among the shear moduli, measurements have been completed on c_{44} to 918°K, and on c_{55} to 820°K, but the data for c_{55} which indicate a relatively sharp change in curvature at about 800°K are suspect and will require confirmation.

The data permit some inferences to be drawn regarding the $\alpha \rightarrow \beta$ structural change in uranium by comparing the temperature dependence of its elastic moduli with those in zirconium and other h.c.p. metals. The h.c.p. metals in which diffusionless phase transformations occur (h.c.p. → b.c.c.) have been found to have characteristically one shear modulus with a large temperature dependence, with a relatively small temperature dependence for the other principal elastic moduli (see Sect. C of Part II of this report). Figure 132 is a comparison of the fractional changes in the moduli of uranium and zirconium. The ordinate is the ratio of the modulus, M, at a given temperature, divided by the maximum value of the respective modulus, M_{max}.

Figure 132. Fractional Changes of the Elastic Moduli for Uranium and Zirconium as Functions of Temperature

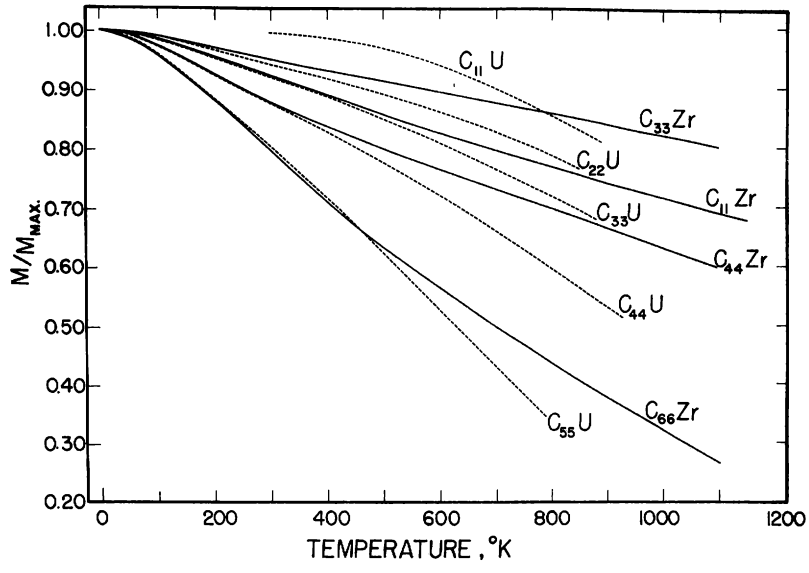

Macro 38030

Uranium has this chief characteristic of the h.c.p. metals with diffusionless transformations, namely, a very large temperature dependence in the c_{55} shear modulus which decreases by 65% over a 800°K range in contrast with a 40% decrease for the c_{44} shear modulus, but it differs from zirconium in that the c_{44} and c_{33} also have a relatively large temperature dependence compared with the respective moduli in zirconium. One may infer from this that whereas the driving force for the h.c.p. → b.c.c. martensitic transformation can be interpreted in terms of the lattice vibrations corresponding to a single shear mode, the $\alpha \rightarrow \beta$ phase transformation

in uranium seems also to involve a weakening of the nearest-neighbor interatomic bonds. Further studies on the effects of temperature on the linear compressibilities should provide a greater insight into these changes in bond stabilities. Work along these lines is continuing. Our immediate objective is to measure the temperature dependence of c_{13}, c_{12}, and c_{66}, which are needed for the compressibility evaluations.

3. Crystallographic Structure of Alpha Uranium (M. H. Mueller, C. S. Barrett,* L. Heaton, and R. L. Hitterman)

Publication:

C. S. Barrett,* M. H. Mueller, and R. L. Hitterman, Crystal Structure Variations in Alpha Uranium at Low Temperatures, Phys. Rev. 129 625 (1963).

The results to date of the investigation of alpha uranium at low temperatures have been presented in the published article above and in the last Annual Report.[123] This study has indicated that: (1) the atom position parameter, y, decreases to a minimum at 43°K and then rises rapidly on further cooling; (2) the cell dimensions a_0 and b_0 decrease to a minimum at this same temperature and then rapidly increase; the c_0 dimension contracts on cooling to 43°K and decreases even more rapidly below this temperature; and (3) neutron diffraction studies have indicated the existence of additional reflections at the lower temperatures, which may be due to a magnetic arrangement. In order to investigate this later observation we have: (1) prepared a germanium monochromator to eliminate the $\lambda/2$ component as described in Sect. G1, Part II, of this report; (2) changed the θ-2θ gear arrangement for more easy alignment of the single crystal; (3) made special holders for attaching the uranium single crystal to the Hoffman crystal, and (4) made provision for raising on the counter tube above the horizontal on Neutron Spectrometer II. This later modification has been completed, which permits the detector tube to be tilted approximately 60° from the horizontal. When this is used in conjunction with the uranium crystal in the cryostat, it will be possible to obtain 3-dimensional intensity data from a relatively large number of reflections at the low temperatures. This is especially important since preliminary results have indicated that considerable intensity change is observed in some of the normal nuclear reflections, as well as the appearance of some intensity at positions corresponding to fractional indices.

---

*Consultant to the Metallurgy Division. The University of Chicago.

[123] Annual Report for 1962, Metallurgy Division, ANL-6677, p. 204.

B. Metallurgy of Plutonium

1. Preparation of High-purity Metal (G. B. O'Keeffe and L. T. Lloyd)

The preparation of high-purity plutonium to provide material for our research programs has continued during the past year, along with some development work to improve the process and the quality of the metal. One hundred and six deposits of electrorefined metal have been made in a KCl-LiCl-PuF_4 salt bath. The deposits were melted under a NaCl-KCl salt mixture into 34 "buttons," and these in turn were melted under vacuum into 20 "consolidation melts." A gross weight of 2.6 kg of refined metal was obtained from 3.3 kg of anode stock. After cropping and sampling for chemical and spectrographic analyses, 2.1 kg of usable metal remained. Our own research programs consumed 1.0 kg, and 0.1 kg has been supplied to other ANL divisions. Analytical data for some of the melts are given in Table LV.

Table LV

ANALYSES OF HIGH-PURITY PLUTONIUM[a]

Material	Chemical Analyses							Spectrographic Analyses[b]									Remarks
	Am[c]	C	H	N	O	Si	U	Al	Cr	Fe	Ga	Li	Mg	Mn	Mo	Ni	
Anode Stocks																	
3-858	408	1893	360	362	166	568	178	313	791	389	190	3	9	22	25	1133	Went into CM32, CM33, CM34, CM35, CM36 CM37, CM38
3-895	436	1370	552	812	469	34	59	179	70	173	<0.3	<3.5	<9	22	<1	21	Went into CM38, CM39, CM40, CM41, CM42 CM43
Cell VIII (Buttons M86 through M90)																	
CM26T	19	1833	792	380	136	111	54	179	232	259	347	1.74	<19	13	<5	494	MgO crucible. Held 1.75 hr at 1073°K and
CM26B	19	1551	648	414	378	267	47	179	232	216	347	3	<19	13	<5	494	19.25 hr at 813°K
CM28	25	2034	144	155	45	111	34	44	37	64	3	34	<9	2	<1	32	MgO crucible. Held 2.7 hr at 1073°K and 16 hr at 833°K
Cell IX (Buttons M91 through M101)																	
CM29	10	1168	216	345	75	120	38	35	23	43	6	0.34	<19	1	<2	32	MgO crucible. Held 3 hr at 1083°K and 15.7 hr at 843°K
CM31	20	322	384	1192	45	60	13	17	4	43	<1	0.69	<9	<1	<1	8	MgO crucible. Held 21.1 hr at 863°K
CM32T	28	604	288	328	30	94	15	17	37	43	1	0.69	<9	2	<1	20	MgO crucible
CM32B	30	181	384	345	75	206	16	17	37	43	1	0.34	<9	2	<1	20	Held 17.5 hr at 863°K
CM34	47	362	288	276	60	172	26	44	93	173	3	0.15	<9	4	<1	82	MgO crucible. Held 14.8 hr at 883°K
Cell X (Buttons M102 through M119)																	
CM36T	5	584	192	466	30	86	32	89	232	129	24	0.15	<19	2	<1	164	Ta crucible
CM36B	7	463	120	2867[d]	3130	111	34	89	232	151	20	1.39	99	2	<1	206	Held 15.9 hr at 883°K
CM38	7	1551	1200	570	91	155	61	89	93	86	20	0.15	<9	<1	<1	103	Ta crucible. Held 14.9 hr at 883°K
CM40	15	685	480	138	15	25	48	8	9	22	-	3.5	<9	<1	<1	8	Ta crucible. Held 16.1 hr at 883°K
CM41	10	342	168	380	75	17	44	17	9	43	<1	1	<9	<2	<1	<2	Ta crucible. Held 15.7 hr at 873°K
CM42	29	705	96	190	121	77	57	35	4	43	<1	0.13	<9	<1	<1	<2	MgO crucible. Held 15.9 hr at 883°K
CM45	73	846	600	898	484	8	32	44	37	43	<6	1.39	<9	<1	<1	8	MgO crucible. Held 16.1 hr at 893°K

[a] Values are given for the number of impurity atoms per million atoms. These were calculated from analyses which were expressed as ppm by weight, by assuming each impurity was combined with plutonium alone.

[b] < = less than. Other elements analyzed for, but below limits of spectrographic detection, and their lower limit of detection are: Ag-2, B-22, Ba-0.4, Be-3, Bi-1, Ca-12, Cd-2, Co-4, Cu-4, K-12, La-2, Na-20, Pb-1, Rb-3, Sb-2, Sn-4, Sr-0.003, Ti-3, V-2, Zn-2, Zr-1 and W-2.

[c] Americium content is corrected to average date of electrolysis.

[d] Considered to be a spurious chemical result.

The more important impurity elements continue to be carbon, hydrogen, oxygen, and nitrogen. Among these, hydrogen has been particularly troublesome. Several steps were taken last year to reduce this impurity by minimizing contact of the various materials and products of the processes with water, which was considered to be the major source of the hydrogen (see Annual Report for 1962, Metallurgy Division, ANL-6617).

During this year some additional changes have been incorporated in the operating procedures. Vacuum desiccators have been introduced for storing the purified salts, electrolytic deposits, "buttons," and "consolidation melts." Also, a gas-purification train (anhydrous $CaSO_4$ at room temperature and Zr-50 w/o Ti alloy turnings at 1073°K) was installed into the helium-supply line for the protective atmosphere in the electrolytic cell. In general, the level of hydrogen in the "consolidation melts" has been reduced when compared with metal produced during the previous year (see Table XLIII in ANL-6677), but notwithstanding these precautionary measures, it is still a significant impurity, with a few exceptions (see Table LV). An additional refinement, consisting of purifying the salts by dripping them through a bed of hot titanium chips,[124] is currently being incorporated into the process.

One of the changes in the procedures, introduced near the end of the previous year, in connection with the effort to reduce hydrogen contamination, was to hold the liquid metal at about 1073°K for 1 or 2 hr under vacuum and the solid metal at 773 to 873°K for up to 20 hr. Chemical analytical data for these "consolidation melts" indicated high values for some of the heavier element impurities, namely, aluminum, chromium, iron, and nickel. Spectrographic analyses showed that the "buttons" contained lesser amounts of the above impurities than did the "consolidation melt" that was made from them; this suggested that the contaminates were being leached from the MgO crucibles during vacuum melting. A spectrographic analysis of a random crucible showed the major impurities to be 100 ppm by weight cobalt, copper, and molybdenum, 200 ppm iron, and 800 ppm silicon. Although there was no clear-cut correlation between the impurities in the "consolidation melts" and the MgO crucibles, with the possible exception for iron, another crucible material was tried.

Tantalum is wet by liquid plutonium, but a NaOH-CaF_2 wash provides a suitable barrier between the two metals.[125] Beginning with melt CM36, six "consolidation melts" were made in tantalum crucibles coated internally with this wash. There was no evidence for attack or wetting of the crucible, but all melts were below average in surface quality. Analytical data (see Table LV for some of the results; CM36, CM38, CM40, and CM41) showed in some cases contents of carbon, hydrogen, oxygen, and nitrogen higher than usual. Some of the heavier element impurities in the first three melts were higher than they had been in previous melts, but CM39, CM40, and CM41 contained lesser amounts of aluminum, chromium, iron, and nickel, suggesting that these impurities were not related to the crucible material alone.

Further chemical analysis showed that the levels of the metallic impurities in the "consolidation melts" were related to their levels in the

---

[124]Henrie, T. A., Private communication.

[125]Mullins, L., Private communication.

anode stock. Beginning with CM39 on through CM45, a considerably better anode material (see Table LV, 3-895) was used in place of the anode stock used in previous melts (the analyses for 3-858 are typical). When MgO crucibles were again used for "consolidation melts," starting with CM42, the overall levels of these metallic impurities did not return to those found in melts made from the less-pure anode stock.

Of considerable interest in connection with the use of better grade anode stock was the performance of Cell X. Six of the nine "consolidation melts" were made up of electrolytic deposits from the better anode material. The overall efficiency of this cell was 81.8% (100 x Pu_{out}/Pu_{in}), as compared with efficiencies of 60% to 68% for the other cells in this series. In addition, the largest electrolytically deposited "crystal" of plutonium observed to date (~1 cm x 2 mm x 2 mm) was obtained in one of the runs of the cell with the better anode stock. It is perhaps important to point out that two other refinements in the operating procedures were initiated concurrent with the operation of this cell: 1) purification of the protective helium atmosphere in the cell, and 2) storage of purified salts in vacuum desiccators.

Our lack of success to reduce the content of lighter element impurities (carbon, hydrogen, oxygen, and nitrogen) to consistently low values by the above improvements in the electrolytic process has led to a consideration of other methods for purifying plutonium. The ability to move foreign atoms in a metal when subjected to a DC current and high temperatures has been recognized for some time. The nonmetallic atoms, which can presumably migrate interstitially, show the largest effect, although transport of metal impurities has been observed also.[126] Two such solid-state electrolysis experiments have been performed with plutonium.

In the first experiment, a sheet 7.62 cm long, 0.95 cm wide, and 0.36 mm thick, prepared by rolling impure anode stock, was electrolyzed in a vacuum of 10^{-4} torr with a current of 14 A for 1,317 hr. Attempts to measure the temperature, as a result of the heating by the DC current, were unsuccessful. In light of the conditions employed in the second experiment (see below), it was obvious that the temperature was well below 873°K. Metallographic examination of sections from this specimen showed that the stringer-type inclusions of the original material had become nearly spherical, but there were no clear indications of reductions in the amount of inclusions in any part of the specimen. Chemical and spectrographic analyses of various portions of the specimen did not give conclusive evidence for redistribution or reductions of the impurities.

In a second experiment, a sheet 15.24 cm long, 1.43 cm wide, and 0.51 mm thick, prepared from CM39, was electrolyzed for approximately

[126] Seith, W., and Wever, H., A New Effect in the Electrolytic Transfer in Solid Alloys, Z. Electrochem., 57, 891 (1953).

350 hr with a current of 46 A in a vacuum of 10^{-6} torr. The temperature, measured with a thermocouple, near the center of the specimen was 870°K. Under reduced external illumination, most of the sample had a dull red coloration. Lines separating a smooth surface finish from a matte finish were visible about 2 cm from the water-cooled copper clamps at the ends of the specimen. Presumably these lines delineated the portion of the sample that was heated above the temperature of the $\alpha \rightarrow \beta$ transformation. The lines were still visible after completion of the experiment. No quantitative results for this experiment are available as yet.

2. Metallography (M. D. Odie and L. T. Lloyd)

Effort is being continued to devise standardized and reproducible metallographic procedures for unalloyed alpha plutonium. The mechanical grinding and polishing procedures, which were described in the last Annual Report (ANL-6677), have been adopted as standard techniques. Most of the work during the past year has been concerned with refining the procedures for electropolishing and electroetching to reveal true microstructures and with applying these techniques to samples of interest in connection with other research programs.

Electropolishing: At the time of the last annual report, the electropolishing solution 3B (32 parts by volume orthophosphoric acid, 59 parts ethylene glycol monoethyl ether, and 9 parts distilled water), was reported as showing promise, but difficulties were encountered due to chemical attack of the specimens when they were immersed in the solution without voltage across the cell. This problem has been reduced by the use of a sample and touchwire holder made of Teflon. The specimen is assembled in the holder, the touchwire is placed in contact with the sample, and the voltage is turned on before the assembly is immersed in the solution. When the electropolishing is completed, the assembly is removed from the cell with the potential still on, and the sample is flooded with ethyl alcohol. With this approach, very little chemical attack of the specimen takes place, and the round gray artifacts (see ANL-6677) are no longer a problem.

The voltage-amperage relationship for this solution has been investigated; the amperage increases steadily with voltage. This behavior categorizes the solution as one of high resistance as would be expected from its chemical composition. Thus, the ranges of optimum voltages and current densities are rather small.

The distance from anode to cathode does not seem to be critical, but the voltage must be increased for larger distances. A distance of 3 cm is used normally. If a current density of 0.65 A/cm^2 is employed, structures are obtained like that shown in Figure 133a. The surface of the specimen appears to be slightly etched and the contrast is low between grains and between subgrains. Figures 133b and 133c illustrate structures which were developed with a current density of 0.7 A/cm^2, the optimum value. The grain boundaries are well delineated, and the contrast is improved. With current

densities higher than optimum, the epitaxial film is thicker, the contrast is higher, and the grain boundaries are no longer delineated accurately (see Figure 133d).

Figure 133. Microstructures of Alpha Plutonium As Electrolytically Polished in the 3B Solution at Various Current Densities. Photographs a, b, and d are from a sample slowly cooled by lowering from a furnace at 923°K through a distance of 6 in. at a rate of 1 in./day. Photograph c is from a sample quenched from 648°K into oil. Polarized light illumination.

Micro 35781 250X

a. Electropolished at 0.65 A/cm^2 for 3 min.

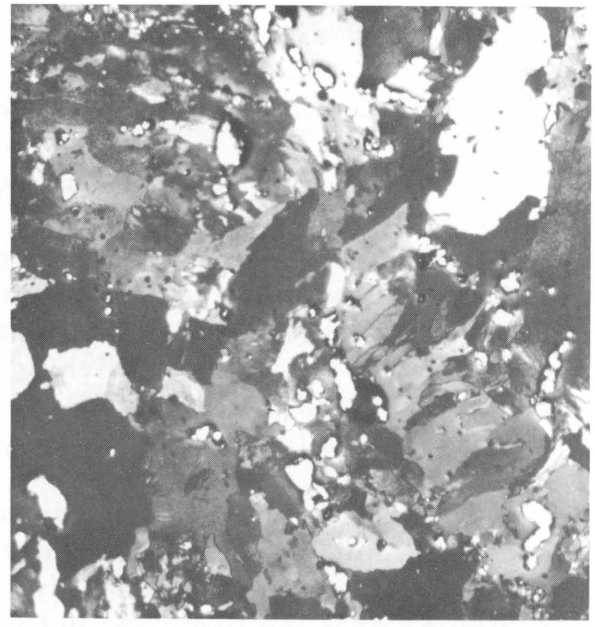

Micro 36174 250X

b. Electropolished at 0.7 A/cm^2 for 3 min.

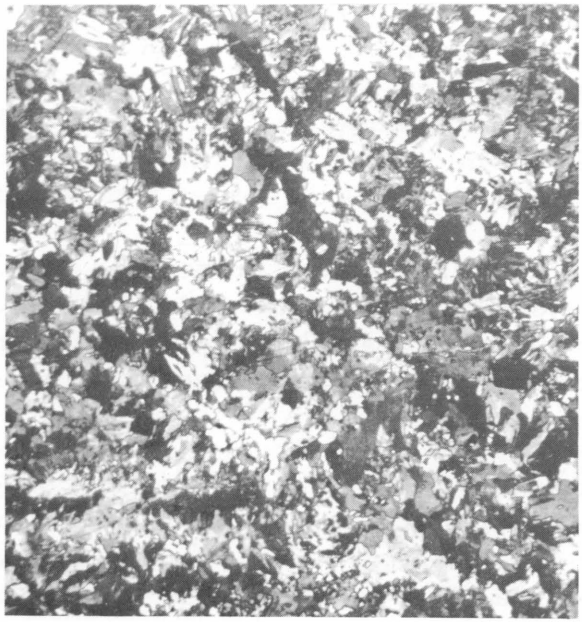

Micro 36311 250X

c. Electropolished at 0.7 A/cm^2 for 3 min.

Micro 35732 100X

d. Electropolished at 1.0 A/cm^2 for 3 min.

Experience has shown that a break-in period (about 2 min) is required before the best electropolishing is obtained with this solution. After about 6 hr of use, the solution no longer yields satisfactory results; the structures look similar to that shown in Figure 133a. Replenishing the bath with freshly prepared solution does not restore its original characteristics. Furthermore, results are unsatisfactory if the unused solution is stored more than 8 weeks in a closed polyethylene bottle.

Electroetching: Some further work has been done with the electroetching solution (5 parts by volume concentrated nitric acid, 20 parts absolute ethyl alcohol, and 50 parts ethylene glycol). Electrolyzing at the optimum current density of 0.052 A/cm^2 for about 2 min reveals grain boundaries due to relief between grain surfaces. Therefore, low-angle boundaries are not sharply defined. The microstructures shown in Figure 134 are typical results for samples etched after mechanical polishing with 1-μ diamond paste. Apparently, an isotropic film is formed by this solution, as the grain structure is not delineated under polarized light. The solution is stable during storage, and it can be replenished with freshly prepared solution without change in its characteristics. There is no evidence of "use-age" or break-in periods. Longer electrolysis or the use of high current densities tend to cause over-etching, especially at sample edges.

3. Recrystallization and Grain Growth in Alpha Plutonium (L. C. Ianniello* and L. T. Lloyd)

Studies of recrystallization and grain growth in alpha plutonium in connection with the problems of preparing single crystals (see below) and polycrystalline samples for other research programs have continued during the past year. Some of the effort has been directed towards attempts at introducing sufficient strain into the lattice to provide a driving force for recrystallization and towards problems that have developed from this work.

Introduction of Strain Energy

Rolling: The attainment of large reductions in thickness (90% or more) by flat rolling high-purity alpha plutonium at room temperature without intermediate heat treatments was reported in the last Annual Report (ANL-6677). Similar fabrications have been repeated many times during the past year. Rolling has been done on a mill with 15.2-cm-diameter rolls which can be heated electrically. The speed of the surface of the rolls (roll speed) could be varied continuously from 15.2 to 1130 cm/min. A typical rolling schedule for accomplishing the large reductions is described below. In all the operations, the direction of rolling for the samples was reversed after each pass.

---

*Presently at Division of Research, AEC, Washington.

Figure 134. Microstructures of a High-purity Plutonium Casting (CM40) after Electrolytic Etching in the Nitric Acid Solution at a Current Density of 0.052 A/cm^2

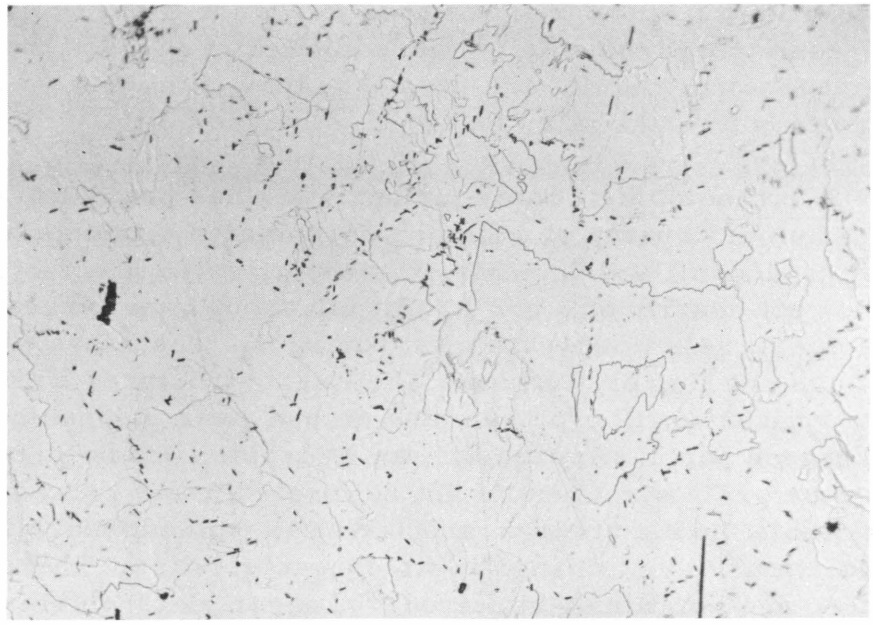

Micro 38220 Bright Field 250X

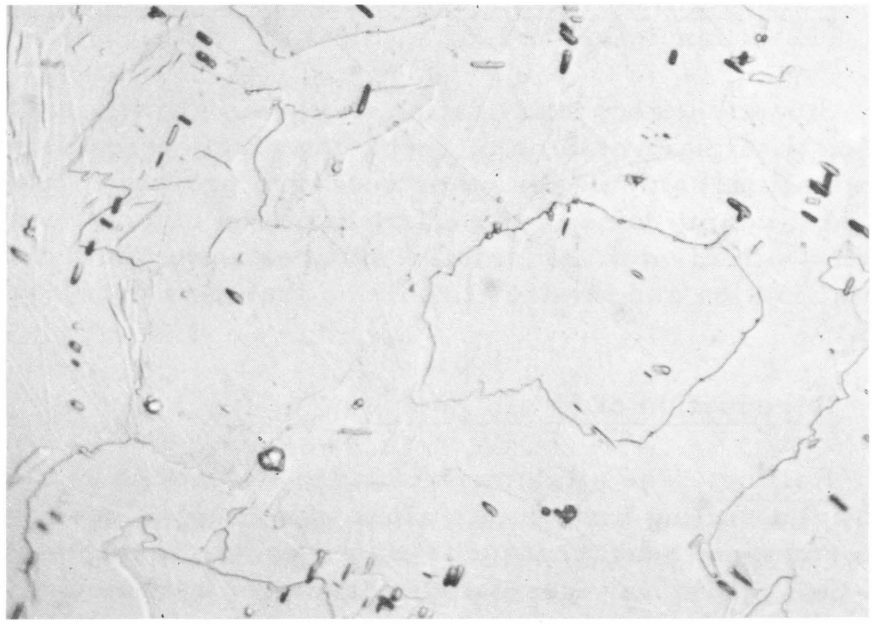

Micro 38221 Bright Field 1000X

A specimen, about 0.20 to 0.27 cm thick, is first rolled in the temperature range of the beta phase. It is preheated in silicon oil at 433°K, and the roll temperature is 433°K also. The material is reduced 15% in thickness by three passes of 5% each, with a roll speed of 91.4 cm/min.

This step serves to break up the as-cast structure while the material is in the very ductile beta phase and, possibly, it also leads to welding shut voids and cracks which are introduced into the structure during the original cooling from the melt.

The electrical supply for the heaters is turned off, and the specimen is rolled while the rolls are cooling. For every drop in temperature of 5°K, the separation between the rolls (roll separation) is decreased by 2.54×10^{-3} cm. The roll speed is reduced to 15.2 cm/min, and rolling is continued until the roll temperature is 323°K. The decrease in roll separation is enough to allow for decreases in the thickness of the specimen due to thermal and transformation contractions, and for decreases in the diameters of the rolls from thermal contraction.

The purpose of rolling during the $\beta \rightarrow \alpha$ transformation is to transform the plutonium in a directional manner so that no voids or cracks would form in the interior of the specimen, or, if they did form, they would be parallel to the plane of the sheet and, hence, would not interfere with further rolling. The plutonium probably cooled faster than the massive rolls so that the surfaces of the sheet were reheated as they hit the rolls. Thus, the center of the sheet would transform first because it was at a lower temperature than the surfaces and because it is under pressure through the forces being applied by the rolls, and the surfaces would transform last.

The specimen is then rolled at room temperature with a roll speed of 15.2 cm/min. Roll separation is reduced 2.54×10^{-3} cm at a time, and the specimen is passed through the rolls about six to ten times, to achieve this reduction in the sheet, before the rolls are lowered again. It is important to keep particles of materials off the surfaces of the rolls and to file off any edge cracks that appeared on the specimen.

Some idea of the importance of carefully controlling the variables indicated above can be gleaned from the results of attempts to roll materials that were subjected to other conditions. With regard to the critical effect of roll speed, when two specimens were given the same preliminary thermal and mechanical treatments, the one that was rolled at 15.2 cm/min was reduced 99% at room temperature, whereas the second, which was rolled at 30.4 cm/min, showed cracking at 37% reduction. This suggests that the rate of straining must be quite low if alpha plutonium is to behave in a ductile manner. A decrease in roll separation by a factor of 4 did not result in a marked difference in the ability to roll the material at room temperature, although the specimen subjected to the larger value did show some cracking at 83% reduction.

The effects of thermal and mechanical histories were investigated for two circumstances. One of two specimens, 0.220 cm thick, which had been previously rolled in the beta phase and during the $\beta \rightarrow \alpha$ transformation, was given an additional anneal at 712°K (delta phase) and cooled

without rolling. It cracked catastrophically after 16% reduction at room temperature, whereas the other specimen was rolled 92%. On the other hand, thinner material, 0.108 cm thick, was rolled over 80% after it had been annealed in the beta phase and cooled to room temperature, but more than the usual difficulty with cracking was encountered.

Ductility and Hardness: Figure 135 shows a specimen of high-purity plutonium (CM22, see Table XLIII in ANL-6677 for chemical analyses) which was rolled 99% at room temperature to a final thickness of 13 μ. The strips, which spell out "Pu," were cut with scissors and bent to illustrate the ductility of the material. From calculations based upon the radius of curvature and the thickness of the sheet, tensile strains of 1.5% to 3.0% were achieved by bending specimens from this and similar sheets.

Figure 135. High-purity Alpha Plutonium Sheet Rolled 99% at Room Temperature to a Final Thickness of 13 μ. Rolling direction is horizontal.

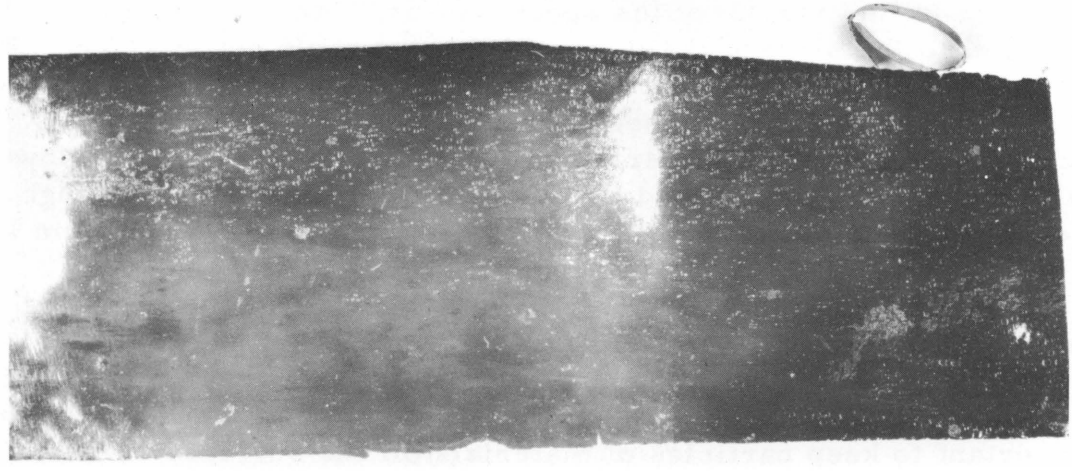

Macro 37070 5.5X

Microhardness measurements for specimens after various reductions at room temperature are given in Table LVI. There is a slight increase in hardness up to approximately a 60% reduction, followed by a decrease for higher reductions.

Table LVI

MICROHARDNESS OF HIGH-PURITY ALPHA-PLUTONIUM SHEET

"Consolidation Melt" Number	Thickness of Sheet before Rolling at Room Temperature (cm)	Location of Surface where Hardness Measurements were Made with Respect to the Rolling Direction (R.D.) and the Rolling Plane (R.P.)		Microhardness* after Various Percent Reductions in Thickness by Rolling at Room Temperature (kg/mm^2)											
		R.D.	R.P.	0	3	6	12	24	44	50	61	75	88	90	92
CM22	0.220	parallel	perpendicular	252	258	263	256	266	-	269	277	252	-	-	235
CM22	0.098	parallel	perpendicular	-	-	-	-	-	265	-	-	-	235	-	-
		perpendicular	perpendicular	-	-	-	-	-	275	-	-	-	233	-	-
		parallel	parallel	-	-	-	-	-	257	-	-	-	241	-	-
CM11	0.178	parallel	perpendicular	227	-	-	-	-	-	234	-	229	-	-	201

*The values in the table are averages of ten hardness measurements. The average standard deviation from four randomly selected sets of values was 8.4 kg/mm^2.

Microstructures and X-ray Patterns: Metallographic examination of specimens after rolling in the beta phase and during the $\beta \rightarrow \alpha$ transformation showed no evidence of voids or cracks in the material. These observations are supported by density measurements, which gave results of 19.75 ± 0.05 g/cc for samples rolled during the $\beta \rightarrow \alpha$ transformation and for samples rolled to various reductions (up to 92%) at room temperature.

Microstructures of specimens rolled to various reductions at room temperature revealed that the grain size decreased with increasing reduction and the grains elongated in the direction of rolling. Specimens from CM22 had a grain size of 10 to 20 μ in diameter before rolling. Only a slight decrease in grain size and very little elongation of the grains was observed up to 50% reduction. Beyond 50%, the grains showed considerable elongation. Finally, the specimen which was reduced 92% had the smallest grain size, 1 to 5 μ, and the grains were elongated only slightly.

Pinhole back-reflection X-ray patterns with Cu K_α radiation from specimens with various reductions confirmed the metallographic observations. The Debye rings for the low reductions were spotty. Increasing the reduction caused the rings to become continuous and broad. At the higher reductions, the rings were still uniform, but they became sharper, and the relative intensities of certain rings were shifted with respect to the same rings for low reductions. The latter observation strongly suggests effects of preferred orientation.

Evidence for preferred orientation was recognized more readily in front-reflection patterns. A specimen reduced 88% had a greater amount of preferred orientation than a specimen reduced 44%, as deduced from the nonuniform intensity of rings as the result of glancing the X-ray beam off the surface of the sheets at angles of 45° to the normal to the sheets. Figure 136 shows a transmission X-ray pattern directly through a specimen that had been rolled 99% to a thickness of 13 μ. The incident beam was Mo K_α radiation at an angle of 45° to the sheet. The evidence for

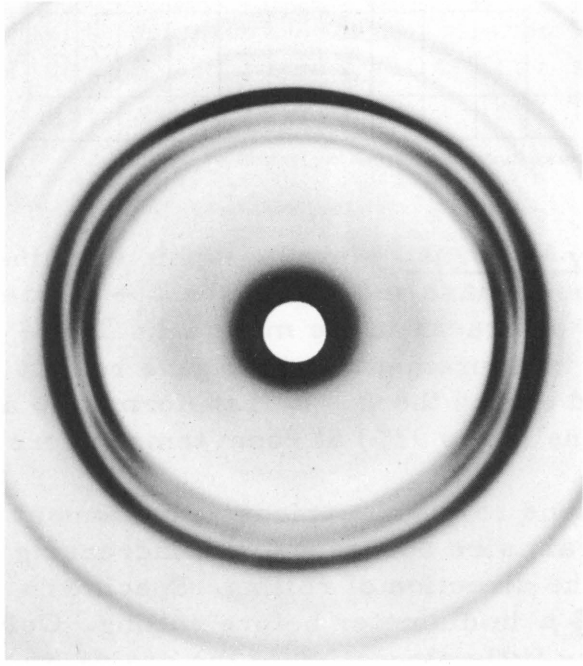

Macro 37309

Figure 136. Transmission X-ray Pattern from a Specimen of High-purity Alpha Plutonium Rolled 99% at Room Temperature to a Final Thickness of 13 μ. Mo K_α radiation, specimen to film distance - 15 cm, X-ray beam inclined 45° to normal to the sheet, rolling direction vertical.

preferred orientation is clearly visible, but the planes responsible for the preferred orientation are not obvious because in each case several different types of planes contribute to the Debye rings.

Discussion: The evidence for preferred orientation as a function of percentage reduction up to 99% strongly suggests that no new strain-free grains, i.e., recrystallized grains, were formed during rolling at room temperature. Some structural change must take place, however, since the diffraction lines sharpen at high reductions and the hardness decreases beyond about 60% reduction. This change is believed to be more in the nature of polygonization than recrystallization.

Since alpha plutonium does not strain harden easily, as may be seen from the results in Table LVI, it would appear that the great sensitivity to strain rate, which was demonstrated by the effect of increasing the roll speed, would be unusual. The two phenomena, however, may be related to the self-damage from radioactive decay products. In other words, the lack of strain hardening may be the result of a recovery mechanism, and if this recovery mechanism is not given sufficient time to operate, such as in a fast strain rate test, further plastic deformation cannot occur. One possible mechanism could be the climb of dislocations which results from the migration of vacancies and interstitial atoms to dislocation jogs. The number of Frenkel defects, which are produced primarily from the alpha decay, can be calculated. This production rate is sufficient to allow a dislocation density of 10^8 per cm^2 to climb one atomic distance in less than one minute. In addition, this mechanism suggests that any process, such as creep or diffusion, which depends in part on the nucleation of vacancies, would have a low activation energy. Some data on the creep of alpha plutonium are available,[127] from which an activation energy of 10.2 kcal/mole was calculated. This compares with

[127] Gardner, H. R., and Mann, I. B., "Mechanical Property and Formability Studies of Unalloyed Plutonium," Plutonium 1960, p. 513, Cleaver-Hume Press Ltd., London (1961).

26 kcal/mole for polycrystalline lead,[128] which, according to empirical relationships between melting point and activation energy, should have a lower activation energy.

Effects of Thermal Treatments

Hardness: In order to assess the effects of thermal treatments within the temperature range of the alpha phase, microhardness measurements have been made of several specimens of the sheet material. Figure 137 shows the variation of microhardness after annealing 7 days at 379°K as a function of percent reduction in thickness. The microhardnesses from specimens which were rolled 88% and annealed at various temperatures for one hour are shown in Figure 138. Finally, Figure 139 shows the microhardness as a function of annealing time at 379°K for specimens rolled 88%. In each case, the black dots represent the average of ten measurements (diamond indentor, square base, 50-gm load); the open circles represent the extreme values. The annealing treatments were performed in a bath of silicon oil that was exposed to the nitrogen atmosphere in the glovebox.

Figure 137. Microhardness of High-purity Alpha Plutonium Sheet as a Function of Percent Reduction in Thickness

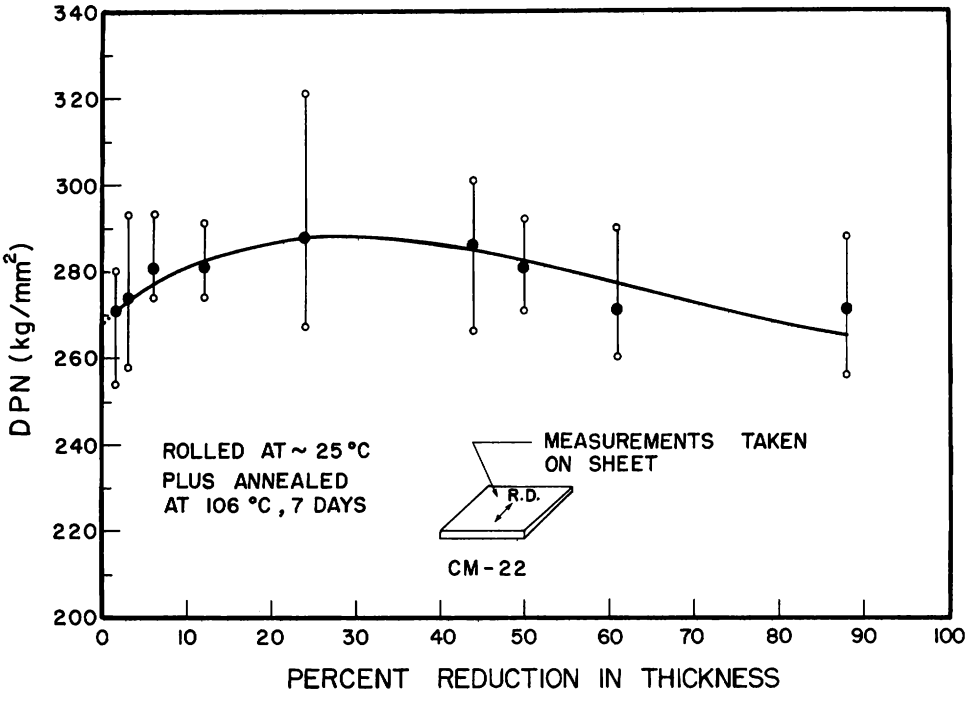

Macro 36713

None of the data show evidence for recrystallization. The microhardnesses after annealing 7 days at 379°K are higher than the respective values for the as-rolled condition (see Table LVI). The explanation

[128] Wiseman, C. D., Sherby, O. D., and Dorn, J. E., Creep of Single Crystals and Polycrystals of Al, Pb and Sn, Trans. AIME 209 57 (1957).

Figure 138. Microhardness of High-purity Alpha Plutonium Sheet as a Function of Annealing Temperature

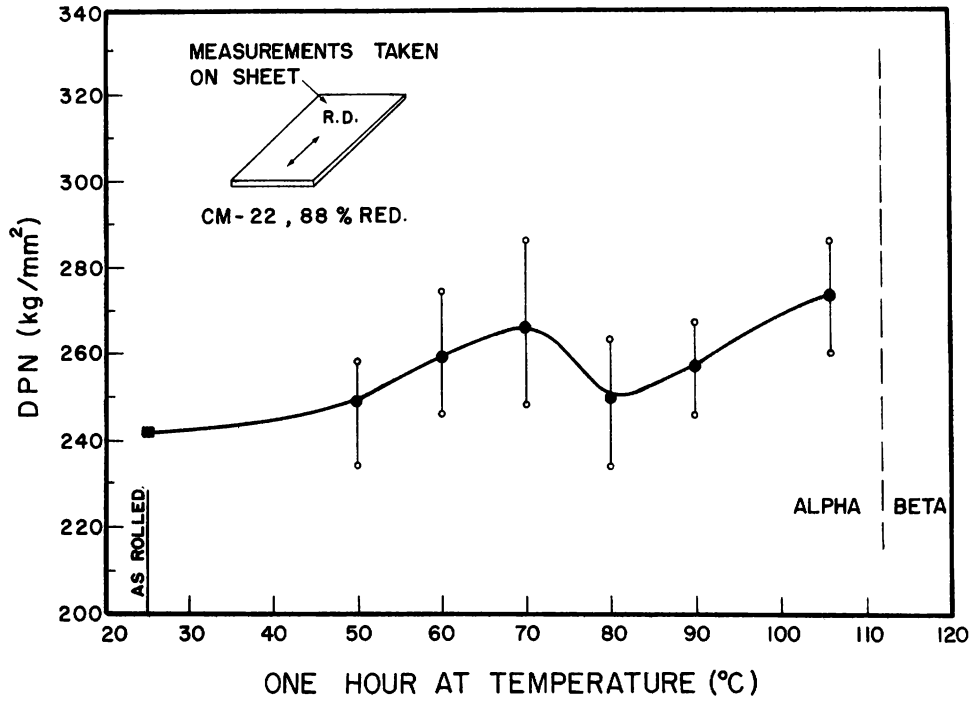

Macro 36711

Figure 139. Microhardness of High-purity Alpha Plutonium Sheet as a Function of Annealing Time

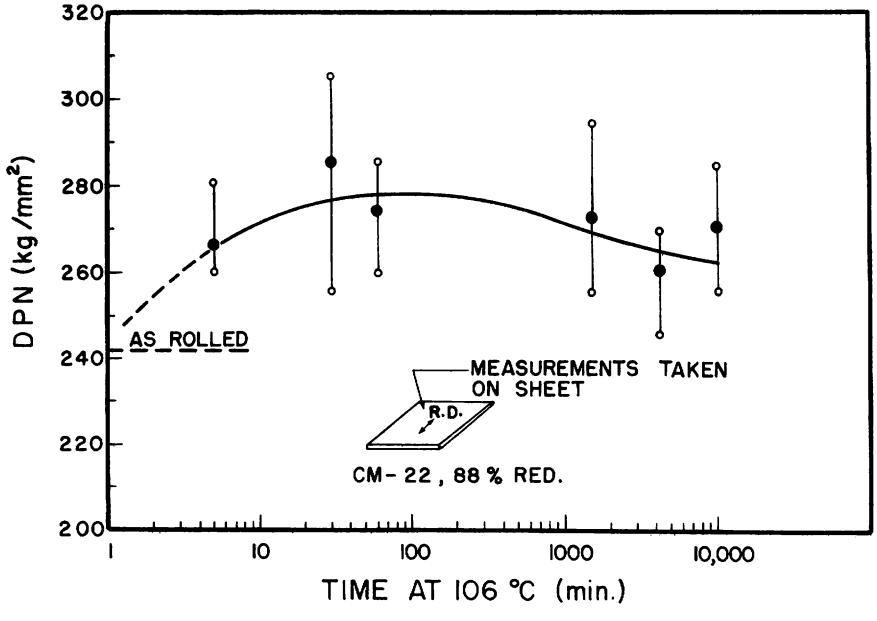

Macro 36714

for this behavior may be contamination from the annealing bath. On the other hand, the increase in hardness with time of annealing (see Figure 139) and with temperature of annealing (see Figure 138) can be rationalized in terms of strain aging, which has been reported previously for alpha plutonium.[129] The same explanation may be valid for the hardness results shown in Figure 137.

X-ray Patterns: To obtain an indication of the change in strain energy with annealing by another method, X-ray line broadening was studied for the same specimens that were used for the microhardness measurements (see above). The results from the samples that were annealed at 379°K for 7 days showed sharpening of the diffraction lines for reductions of 44% through 88%, whereas reductions up to 44% caused little or no change at all. There were no indications of a significant change in grain size. Patterns from specimens which were annealed for various periods of time at 379°K, or for one hour at several lower temperatures, indicated that the annealing process was complete in less than one hour at 379°K and in one hour at 343°K or above.

Since no recrystallization was obvious in any of the above treatments, a higher temperature 393°K, which is 8°K above the equilibrium temperature of the $\alpha \rightleftharpoons \beta$ transformation, was investigated. Specimens from CM22 rolled by various amounts were annealed as follows: 1) 99% reduction - 1/6, 1/3, 2/3, 1-1/2, 2, 4, 8, and 19 hr, 2) 88% reduction - 1/2 hr, and 3) 83% reduction - 1/6, 1/2, 1, and 2 hr.

Before annealing, X-ray patterns of the material rolled 99% showed very little residual strain. The grain size was the smallest among the above samples; also this sample had the thinnest cross section (13 μ thick). The latter two conditions would be expected to favor the initiation of the $\alpha \rightarrow \beta$ transformation, while the absence of large residual strains would be expected to delay recrystallization. No change was found in the X-ray patterns of samples annealed up to 1-1/2 hr. A slight change was observed in the 2-hr sample, and those annealed 4 or more hr showed spotty rings. Surface markings resulting from the $\alpha \rightleftharpoons \beta$ transformation were readily visible on the 8- and 19-hr specimens. The 4-hr specimen had a small number of markings, and the 2-hr specimen was borderline. It was concluded that no more than 5% of the sample was transformed to the beta phase by annealing for 2 hr at 393°K, and that no primary recrystallization was obvious in the samples annealed for 2 hr or less.

The X-ray pattern of the specimen rolled 88% showed broadened lines before annealing. After annealing the pattern showed spotty rings (see Figure 140), which were indicative of a significant increase in grain size and, therefore, of recrystallization.

---

[129] Bronisz, S. E., The Mechanical Properties of Alpha Plutonium in Compression, J. Nucl. Mat. 9 101 (1963).

Figure 140. X-ray Pattern from a Specimen of High-purity Alpha Plutonium Rolled 88% at Room Temperature and Annealed at 393°K for 30 min. Cu K_α radiation, specimen to film distance - 5 cm, X-rays glanced from surface of sheet inclined 45° to the X-ray beam.

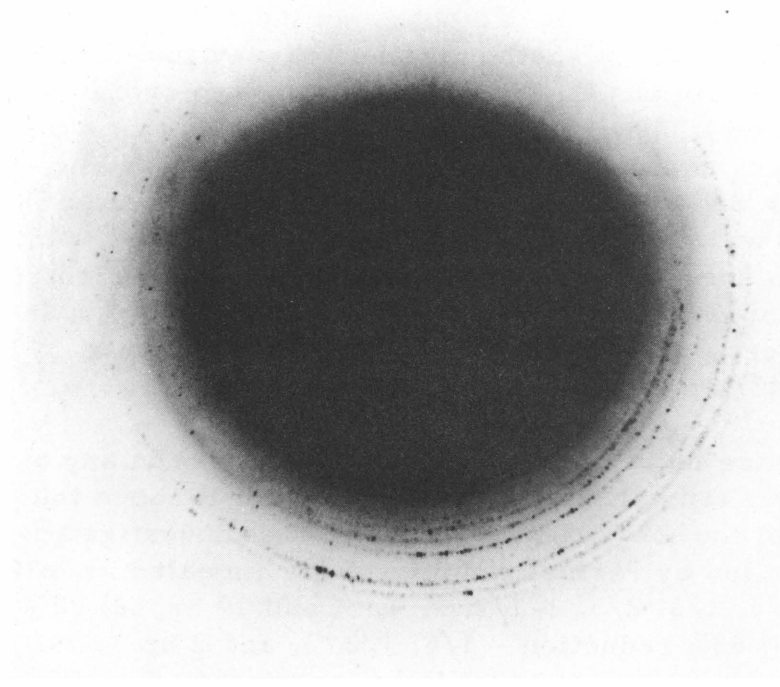

Macro 37307

Annealing of the samples rolled 83% caused sharpening of the X-ray patterns beginning with the 1/6-hr sample, but none of the patterns gave evidence of large grains. Figure 141 shows some microstructures from these samples. The first change was observed after annealing for 1/2 hr. The 2-hr sample gave a fairly regular grain structure with a larger grain size. The corresponding hardness values were:

as rolled - 223 DPN,
annealed 1/2 hr - 242 DPN,
annealed 1 hr - 249 DPN,
and annealed 2 hr - 251 DPN.

Another sample subjected to $\alpha \rightleftharpoons \beta$ transformation gave a hardness of 234 DPN.

It is believed that the changes which occur in grain size and X-ray patterns for samples rolled 83% or 88% and annealed at 393°K for

short times up to 2 hr are the result of primary recrystallization. The recrystallization of the 88% rolled material to a larger grain size than that for the 83% rolled material can be rationalized on the basis that the former material contained less residual strain than the latter, as evidenced by lower hardness in the as-rolled condition.

Figure 141. Microstructures of High-purity Alpha Plutonium Rolled 83% at Room Temperature. Sections are parallel to plane of rolling, electropolished, polarized light illumination, 750X.

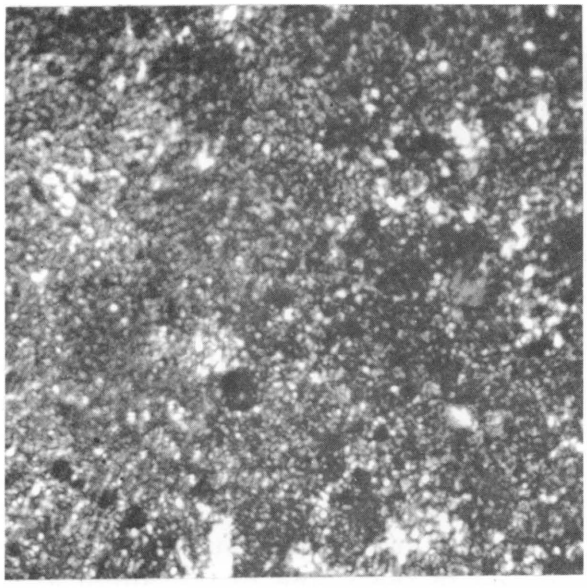

Micro 37207

a. As-rolled

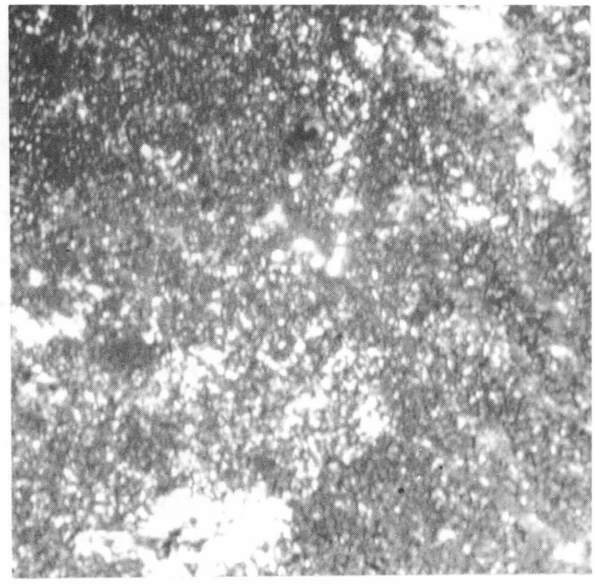

Micro 37209

b. Annealed 1/2 hr at 393°K

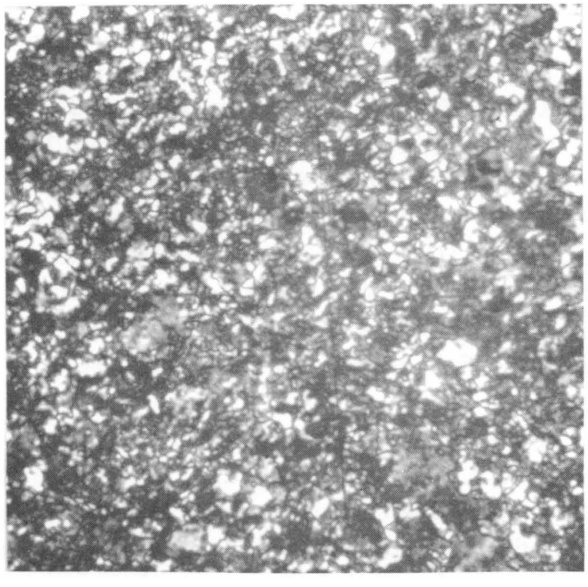

Micro 37211

c. Annealed 1 hr at 393°K

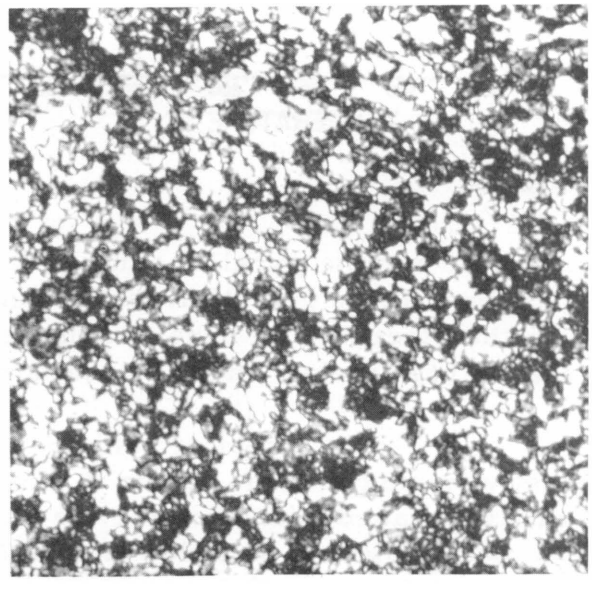

Micro 37212

d. Annealed 2 hr at 393°K

4. Resistivity of Alpha Plutonium (M. B. Brodsky)

An unusual property of alpha plutonium is its variation of electrical resistivity with temperature; there is a maximum value near 100°K and a negative temperature coefficient above 100°K. Since the crystal structure of alpha plutonium is anisotropic, various methods of preparing samples may affect the resistivity. Such effects may be related to the electron scattering processes which might cause the unusual behavior.

Preferred Orientation Effects in Cold-rolled Alpha Plutonium: Development of a technique for rolling alpha plutonium (see above) has permitted a study of the anisotropy of resistivity. Specimens were prepared by rolling in the beta phase to 20% to 40% reduction in thickness, followed by an additional reduction of about 20% during cooling through the beta to alpha transformation. Most of the sheets were then rotated 90° to obtain wide samples from the subsequent alpha rolling (schedule A). In some cases the direction of alpha rolling was the same as the direction of beta rolling (schedule B). Strips were then cut from the sheets, and resistivity measurements were made in the plane of the sheet at various angles to the direction of alpha rolling (R.D.), i.e., parallel, 45°, or perpendicular to the R.D.

Figure 142. Resistivity of Rolled Alpha Plutonium Measured in the Plane of the Sheet

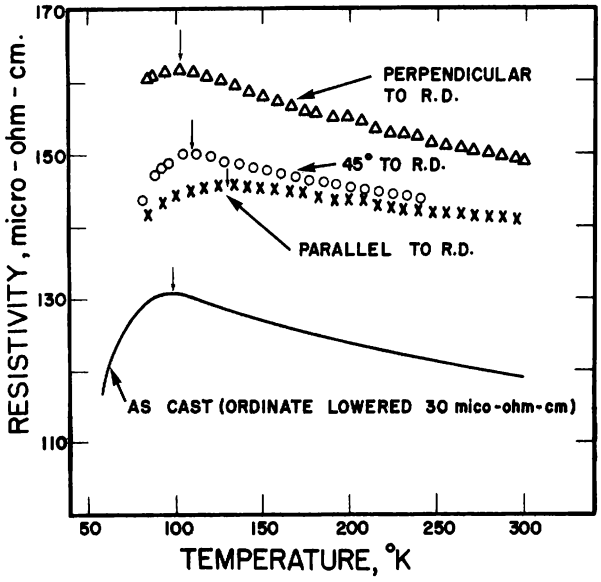

Macro 38271

Figure 142 shows the resistivities of samples between 83 and 300°K which were reduced 84% by alpha rolling (schedule A) It is seen that the temperature coefficient at higher temperatures is less negative for the parallel sample than for the others. Similarly, the temperature of the resistivity maximum is higher for the parallel sample than for the others. The behavior of the perpendicular sample is the same as that of cast metal, and the behavior of the 45° sample is intermediate.

The effect of various reductions on the temperature of the resistivity maximum is shown in Figure 143a. The temperature rises steadily with increased reduction for the parallel samples. It does not change for the perpendicular samples until a 70% reduction is attained. The ratios of the temperatures of the maximum and of the slopes of the resistivity-temperature plots at 190°K are plotted in Figures 143b and 143c, respectively, and they are a measure of anisotropy in the material. These increase

up to 70% reduction and then drop off, as would be expected from the data for $T_{max.}$ The anisotropy is less than 1.0 initially, because some deformation of the alpha-phase material took place during rolling with schedule A before the sample was rotated 90° to the direction of rolling in the beta phase. Figure 143a also shows the effect of rolling with schedule B on the temperature of the resistivity maximum. The only difference due to the methods of rolling seems to be an increase of about 6°K for the temperature of the maximum for rolling with schedule B.

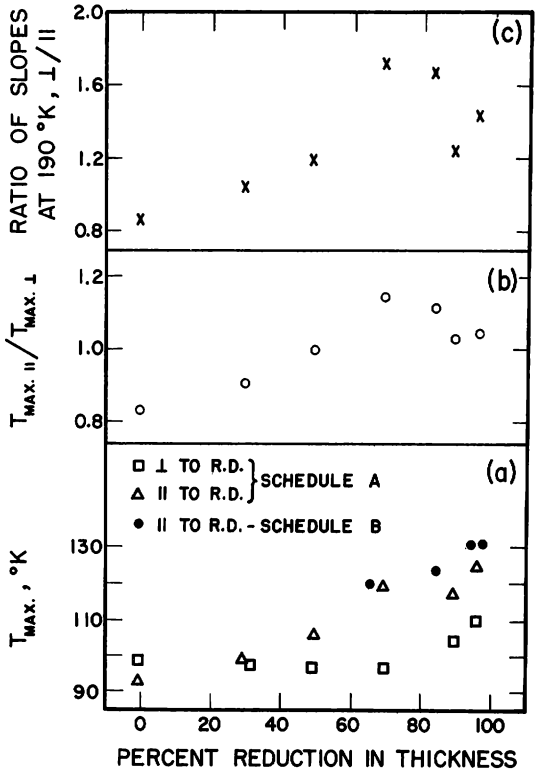

Macro 38272

Figure 143

Effect of the Amount of Reduction in Thickness on: a) the Temperature of the Resistivity Maximum, b) the Ratio of the Temperatures of the Resistivity Maximum Parallel and Perpendicular to the Rolling Direction, and c) the Ratio of the Temperature Coefficients of Resistivity at 190°K

Figure 144 (upper two curves) shows the resistivity in a direction perpendicular to the sheet for metal which was reduced 50% in the alpha phase by rolling with schedule B. The difference between these two curves is probably due to the nature of the electrical contacts; therefore, the absolute values of resistivity for this sample are not significant. These results may be compared with the curves plotted in the lower part of Figure 144 for metal reduced 70% by rolling with schedule A. Both curves for the direction perpendicular to the sheet have a temperature of the resistivity maximum about as high as that for the parallel sample, but the temperature coefficient above this temperature is nearly twice as large as that for cast plutonium.

Thus, it is seen that cold rolling alpha plutonium does cause anisotropy in the resistivity, but even reductions up to 98.5% in thickness do not remove the anomalies in the resistivity in any of the directions which

have been studied. It seems likely that some of the major crystallographic directions are "less anomalous" than others, but that simple "metallic" behavior may not exist for any of the major directions.

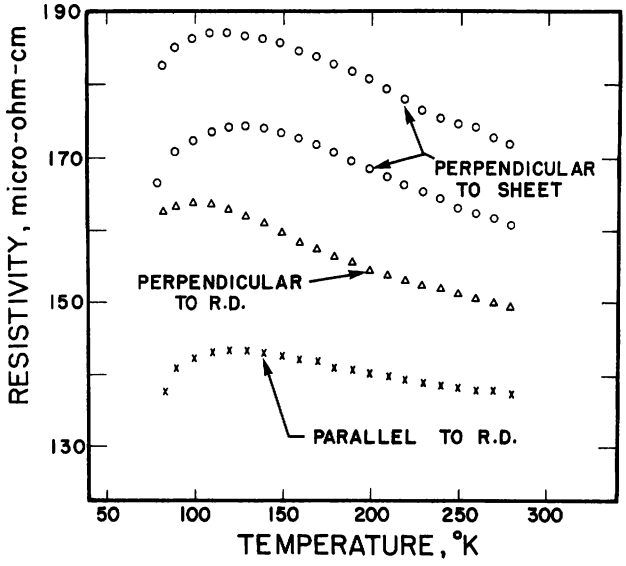

Macro 38273

Figure 144

Resistivity of Rolled Alpha Plutonium Measured through the Sheet as Compared with Measurements in the Rolling Plane of the Sheet

Evidence for Recrystallization from Resistivity Measurements: Recrystallization of alpha plutonium should have an effect on the anisotropy of resistivity in rolled metal. In view of the X-ray and metallographic evidence for recrystallization (see above), an investigation of this was made.

Samples which had been reduced 70% and 97% by rolling with schedule A, were heat treated at 393°K (above the equilibrium temperature for the $\alpha \rightleftharpoons \beta$ transformation), and the resistivity was measured in the plane of the sheet in directions parallel and perpendicular to the R.D. after each half hour of heating. The expectation from the X-ray and metallographic evidence was that the 70% sample would recrystallize after one hour, but the 97% sample would undergo transformation before recrystallization. Unfortunately, the 97% sample for the direction parallel to the R.D. cracked after one hour of heating, but no change in anisotropy had been observed. The anisotropy of the 70% sample in the as-rolled condition was 1.24, and after successive 30-min heat treatments it was 1.18, 1.16, 1.20, and 1.21. It appeared that there was no change after 2 hr at 393°K.

A sample for measurements parallel to the R.D., which was reduced 90%, was given 30-sec heat treatments at increasing temperatures above the equilibrium transformation temperature. No change in resistivity behavior was observed until 408°K was reached, and according to Nelson[130] this treatment would correspond to 8% transformation. Thirty seconds at

[130]Nelson, R. D., Transformation Kinetics of Plutonium, HW-70859 (1961).

418°K (40% transformation) yielded a resistivity-temperature curve very similar to that for the as-cast metal. It seems that resistivity is not a sensitive measure of the recrystallization of alpha plutonium, or that recrystallization under these conditions is limited to reductions greater than 70% and less than 90%.

Magnetic Ordering in Alpha Plutonium: Figure 145 shows the resistivity of rolled alpha plutonium between room temperature and ~4.5°K. Samples CM31-2b2 and CM31-2b5 were reduced 83% by rolling with schedule A, and their resistivities were measured perpendicular and parallel to the R.D., respectively. Sample CM32-Q4C4 was rolled 95% by schedule B and measured parallel to the R.D. The residual resistivity, ρ_0 = 10.2 micro-ohm-cm, is the lowest, and the resistivity ratio $\rho_{273}/\rho_{4.5}$ = 15.3, for CM31-2b5 is the highest, ever reported for plutonium.[131,132] No hysteresis indicative of ordering phenomena was found, which is in agreement with published data.[131,132]

Figure 145. Resistivity of Rolled Alpha Plutonium to the Temperature of Liquid Helium

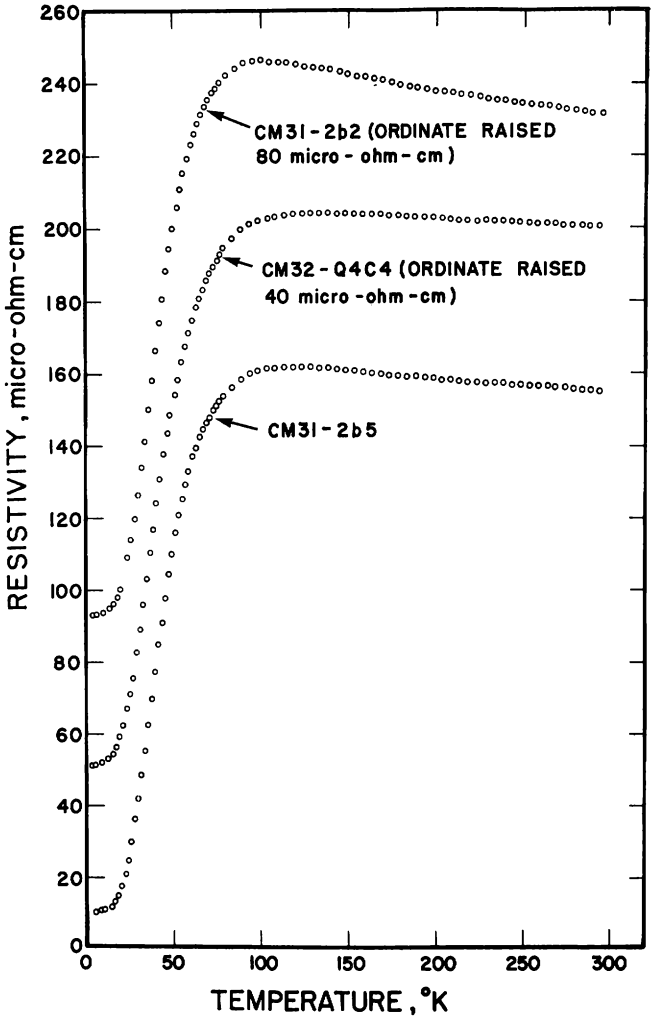

Macro 38274

It had been found that the low-temperature data could be represented by[131]

$$\rho = \rho_0 + BT^n, \qquad (1)$$

where T is the absolute temperature, B is a constant, and values of the constant n were found to be near 2.0. Since the resistivity of alpha manganese may be represented by the same function with n = 2.0, and because of similarities in the shapes of the resistivity curves, it was deduced that the anomalous resistivity of alpha plutonium is due to antiferromagnetic ordering with a Neèl temperature near 100°K.[131] Fits of our data

[131] Lee, J. A., Meadon, G. T., and Mendelssohn, K., The Electrical Resistivity of Plutonium, Neptunium and Some Plutonium Alloys, Cryogenics 1 52 (1961).

[132] Olsen, C. E., and Elliott, R. O., Effects of Impurities and Self-irradiation on the Electrical Resistivity of Alpha-phase Plutonium Below 300°K, J. Phys. Chem. Solids 23 1225 (1962).

in Figure 145 to equation (1) yield values of 3.7 to 3.8 for the exponent, which would seem to refute the analogy to manganese. Furthermore Hall coefficient data of plutonium as a function of field between 88 and 306°K (see Figure 146) showed no deviations from linearity as a function of field strength. The linearity of the data in Figure 146 does not preclude the existence of antiferromagnetic ordering in the temperature range which was studied, but it does represent one more bit of evidence against it.

Figure 146. Hall Voltage for Alpha Plutonium as a Function of Applied Magnetic Field

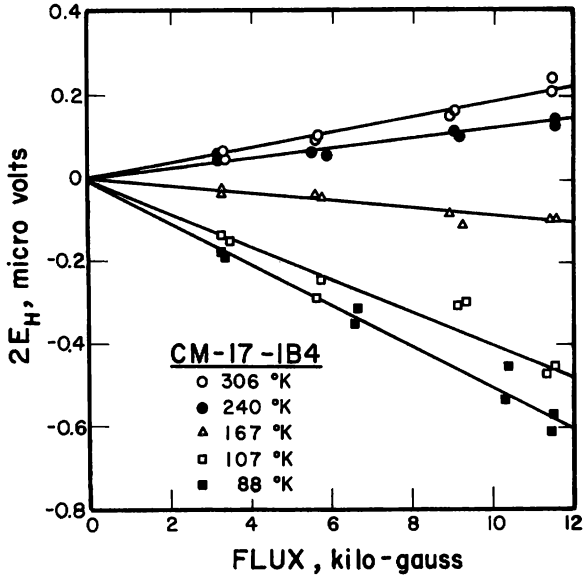

Macro 38275

5. Self-irradiation Damage (L. C. Ianniello* and L. T. Lloyd)

In an effort to determine if the flow stress of plutonium is affected by self-irradiation, some hardness measurements have been made as a function of time. Results presented in the previous Annual Report (ANL-6677) indicated that the hardness of unalloyed plutonium did not increase with time of holding at room temperature. During the past year the studies have been extended to samples held for various periods of time at the temperature of liquid nitrogen (77°K) or liquid helium (4.2°K).

The hardness data from four specimens (which were sections cut from an as-cast ingot, CM20) are presented in Table LVII. The samples were encapsulated in copper and immersed in the respective liquids for the various holding treatments. Hardness measurements were made at room temperature with a square base, diamond indentor, and a 1,000-g load immediately following the treatments.

There does not seem to be any consistent increase in hardness that would indicate an increase in the flow stress. On the contrary, the hardness showed a decrease with holding time in most cases. This could be a result of measuring another area of an anisotropic specimen, or it could be true. A decrease in hardness of quartz and diamond has been observed after irradiation and has been attributed to a rupturing of covalent bonds.[133]

*Presently at Division of Research, AEC, Washington.

[133]Billington, D. S., and Crawford, J. H., Jr., Radiation Damage in Solids, Princeton University Press, Princeton, New Jersey (1961).

Table LVII

HARDNESS OF AS-CAST SPECIMENS FROM CM20 AFTER HOLDING VARIOUS TIMES AT LOW TEMPERATURES

Specimen	Condition	Holding Treatment		DPN Hardness* (kg/mm^2)
		Time (hr)	Temperature (°K)	
1	Initial	-	-	245.4
	1st treatment	24	77	244.8
	2nd treatment	168	77	232.6
	3rd treatment	624	77	231.0
2	Initial	-	-	245.4
	1st treatment	23.2	4.2	222.1
	2nd treatment	17	~300	239.2
	3rd treatment	168	4.2	231.6
	4th treatment	648	77	234.9
3	Initial	-	-	232.0
	1st treatment	429	4.2	238.7
	2nd treatment	45	4.2	234.8
4	Initial			248.9
	1st treatment	24	4.2	237.0
	2nd treatment	45	4.2	249.2

*Hardness measurements were made after collective treatments, i.e., spec. 1-2nd treatment = 24 hr at 77°K + 168 hr at 77°K.

6. Effects of Thermal Cycling (W. J. Stupartiz and A. F. Berndt)

To examine any possible dimensional changes as a result of thermal cycling within the temperature range of the alpha phase, a piece of plutonium was rolled in the beta phase to 0.099 cm and then rolled in the alpha phase to 0.018 cm in order to introduce preferred orientation. Two pieces were cut, one, ~2.7 cm long, parallel to the rolling direction and the other, ~1 cm long, perpendicular to the rolling direction, encapsulated in a piece of copper tubing and cycled 75 times between 373°K (boiling water) and 77°K (boiling nitrogen). Five minutes were allowed for thermal equilibrium at each temperature. No changes greater than the precision of the dimensional measurements were observed.

7. Preparation of Single Crystals of Alpha Plutonium (A. F. Berndt and L. T. Lloyd)

Publications:

Alan F. Berndt and Lowell T. Lloyd, Tabulations of Calculated Crystallographic Data for Alpha Plutonium, ANL-6676 (June 1963).

L. T. Lloyd and L. J. Nowicki, Crystallographic Angles for Alpha Plutonium, J. Nucl. Mat. 10 253-257 (1963).

Experiments designed to produce single crystals of alpha plutonium have continued throughout the year, and a number of approaches have been explored.

Cooling under Pressure: The application of the usual solid-state methods of crystal growth to alpha plutonium is made difficult by the low temperature (~385°K) of the $\alpha \rightleftharpoons \beta$ transition and the existence of five allotropes between the liquid state and the alpha phase. The number of phases can be reduced by the application of pressure.[134] Loasby and Lowe[135] reported that high-density, void-free alpha plutonium can be produced by cooling through the $\beta \rightleftharpoons \alpha$ transformation under a pressure of about 4 kilobars (kb). To confirm this, and to determine the effects of cooling under pressure on grain size, a study of the effects of cooling plutonium under pressure was initiated.

A charge of plutonium was melted in an MgO crucible with a protective covering of molten salt and allowed to solidify by cooling to approximately 773°K. The crucible was then broken and the hot charge was immediately inserted into a steel die lined with vermiculite. The charge was covered with vermiculite and a pressure of about 4 kb was applied (calculated as force per unit area of the piston). All components of the die assembly were pre-heated to 723°K. The plutonium was allowed to cool to room temperature under this applied pressure. The average density of the resulting ingot was 19.595 g/cm^3.

Metallographic examination of this specimen showed numerous voids, concentrated toward the periphery. There were also many inclusions present. The grain size appeared to be larger than that of a sample slowly cooled from the liquid under atmospheric pressure (see Figure 133). This

---

[134] Stephens, D. R., The Phase Diagram of Plutonium, J. Phys. Chem. Solids, 24 1197 (1963).

[135] Loasby, R. G., and Lowe, J. N., "Kinetics of the Beta to Alpha Transformation in Plutonium," Plutonium 1960, p. 3, London, Cleaver-Hume Press (1961).

may be related to the fact that the number of stable allotropic forms decreases with increased pressure.[134] Back-reflection Laue and back-reflection pinhole X-ray patterns indicated the existence of relatively large distorted grains. In view of the contradictory results reported by Loasby and Lowe, this experiment will be repeated using material of higher purity.

Alloying with Neptunium: Alloys of neptunium and plutonium with more than 24 a/o Pu have the structure of alpha plutonium at room temperature, with lattice constants only slightly smaller (≈0.7% at 24 a/o Pu) than those observed for pure alpha plutonium.[136] For compositions between about 39 and 48 a/o Pu, the solid phases that can exist are those whose structures are the same as alpha, beta, and epsilon plutonium, and the temperature of the $\alpha \rightleftharpoons \beta$ transition is raised to about 543°K.[136]

A melt containing 43.4 a/o Pu in neptunium was prepared and cooled at 0.5°K/hr from the liquid to 533°K, held at this temperature for 5 weeks and slowly cooled. Both metallographic and X-ray examination of this specimen confirmed the existence of extremely large grains.

A single-grain particle (about 0.02 x 0.02 x 0.01 mm in size) was fractured from the alloy, mounted for X-ray examination, and oriented by means of oscillation patterns. Rotation and Weissenberg photographs were used to determine the unit cell. It was found to be monoclinic with:

$$a_0 = 6.12 \pm 0.02 \text{ Å},$$
$$b_0 = 4.80 \pm 0.01 \text{ Å},$$
$$c_0 = 10.95 \pm 0.04 \text{ Å},$$
$$\beta = 101.74 \pm 0.23°,$$

which, considering shrinkage due to alloying and experimental error, is the same as that reported by Zachariasen and Ellinger[137] for alpha plutonium. The observed intensities are in good qualitative agreement with those calculated from the reported atomic positions.

Heterogeneous Systems: Several techniques have been explored to grow crystals from heterogeneous systems. As discussed in last year's report, one of these involves the utilization of possible differences in solubility with temperature in alkali metals. Small amounts (<5 a/o) of mercury, thallium, or indium have been added to liquid alkali metals in an attempt to increase the solubility without destroying the favorable phase

---

[136] Mardon, P. G., Pearce, J. H., and Marples, J. A. C., Constitution Studies on the Neptunium-Plutonium Alloy System, J. Less-Common Metals 3 281 (1961).

[137] Zachariasen, W. H., and Ellinger, F., The Crystal Structure of Alpha Plutonium Metal, Acta Cryst. 16 777 (1963).

equilibria. Charges of pure plutonium and of Pu-Tl alloy have been tried. The results to date have not been encouraging, for no concrete evidence has been obtained that the metal dissolved in these solvents. The method is theoretically feasible, but because of extremely low solubilities the time required may be prohibitive.

Plutonium metal can be produced by electrolysis in a suitable electrolyte. If the product is to be the alpha phase, then the electrolyte must be liquid below ~385°K. Fused salts are unattractive electrolytes because, in order to melt below this temperature, they must contain low-melting halides, such as $AlCl_3$, which would be reduced by any plutonium formed,[137A] or they must contain potentially explosive nitrates. Aqueous solvents are also unfavorable because plutonium reacts readily with water.

We have, therefore, carried out some experiments with organic solvents, with various plutonium compounds as the electrolytes. In all cases, a platinum cathode was used, and the anode was a piece of plutonium wrapped in a platinum wire. The deposits were mainly PuO_2. Several deposits, which were obtained from the electrolysis of $PuCl_3$ in ethanol and n-butanol, gave Debye-Scherrer patterns with a number of spots at positions where lines from alpha plutonium should lie, thus suggesting the existence of large-grained particles of alpha plutonium. A Debye-Scherrer pattern from one such particle consisted only of about two dozen spots, all lying at positions corresponding to lines from alpha plutonium, and it possibly may have been a single crystal. Attempts to prove it with a Weissenberg pattern were unsuccessful because the spots became indistinct (probably due to oxidation). This approach does not appear to hold much promise.

The free energies of formation[137A] indicate that alkali metals reduce plutonium chlorides or fluorides to metallic plutonium. If a solvent for both a plutonium halide and an alkali metal could be found, then the reduction could be made to proceed at temperatures below the $\alpha \rightleftharpoons \beta$ transition, and metallic plutonium would be produced, provided there is no reaction with the solvent.

A solution of triphenyl boron in diethyl ether has been found to be a suitable solvent. Lithium dissolved in this solvent to yield a black solution which reacted with plutonium compounds. The Debye-Scherrer patterns from the products have not been completely analyzed as yet because of their complexity. They showed, however, some spottiness almost identical with that obtained from electrolytic residues.

[137A] Glassner, A., The Thermodynamic Properties of the Oxides, Fluorides, and Chlorides to 2500°K, ANL-5750.

8. Mechanism of the Alpha-Beta Transformation (R. G. Peterson, M. Rosen,* and L. T. Lloyd)

Studies on the mechanism of the $\alpha \rightleftharpoons \beta$ transformation by ultrasonic methods have been continued along the following lines: 1) specimens were heated and cooled at slow rates (0.3°K/min) in the temperature range from 196 to 423°K to yield data on the sound velocity as a function of temperature, and 2) specimens were quenched from the beta phase to isothermal holding temperatures within the alpha range to yield data on the sound velocity as a function of holding time, which in turn provided data on the kinetics of the transformation. In both types of experiments, the measured values were the transit times of longitudinal waves, τ, which are related to the velocities, V, by

$$V = L/\tau,$$

where L is the length of the path of the ultrasonic waves.

The velocities of longitudinal waves as a function of temperature for as-cast material (CM29) are plotted in Figure 147. From these data, the fractions of the alpha and beta phases (f_α and f_β, respectively) present in the isothermally treated specimens were determined for various holding times according to the relations

$$f_\alpha = \frac{V - V_\beta}{V_\alpha - V_\beta}$$

Figure 147. Velocity of Longitudinal Waves in Plutonium as a Function of Temperature

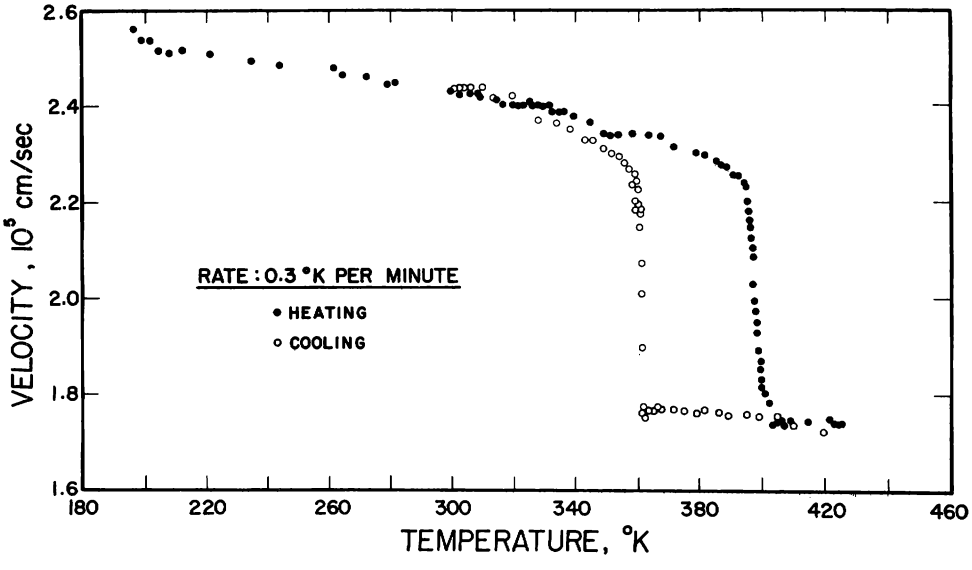

Macro 38315

*Present affiliation, Israel Atomic Energy Commission, formerly Resident Research Associate at ANL.

and

$$f_\beta = \frac{V_\alpha - V}{V_\alpha - V_\beta},$$

where V is the observed velocity for a given holding time, V_α is the velocity for 100% alpha plutonium at the respective temperature, and V_β is the velocity for 100% beta plutonium.

Figure 148 summarizes the results of the isothermal tests. Measurements were obtained on specimens from CM28 at 296, 313, 325, 337, 348, and 361°K, and from CM29 at 199, 223, 253, and 272°K. The TTT diagram should be considered tentative, for additional data are yet to be analyzed. The times required to cool the specimens from 453°K to the temperature of the bath are not known accurately for the samples treated isothermally from 253 to 296°K. Therefore, the times before start of the transformation in this temperature range are not known accurately, but they are probably within a factor of two of the values shown by the dotted line in Figure 148.

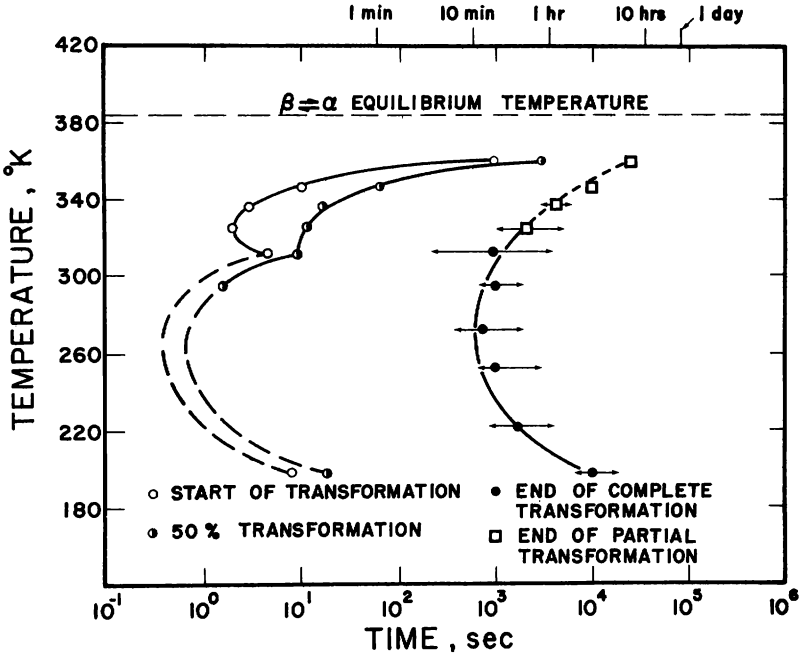

Macro 38316

Figure 148

TTT Diagram of $\beta \rightarrow \alpha$ Transformation in High-purity Plutonium

Figure 149 shows typical microstructures for some of the samples after isothermal treatment to apparent completion of the transformation and return to room temperature. The one transformed at 361°K (see Figure 149a) showed large grains with elongated subgrains, clusters of smaller nearly equiaxed subgrains, and fine grains with high-angle boundaries. Transformation at 325°K (see Figure 149b) yielded smaller grains with elongated subgrains, and a larger proportion of small grains with high-angle boundaries. Almost all of the grains in the sample

transformed at 296°K were nearly equiaxed, with subgrains and with considerable range in size (see Figure 149c). The sample transformed at 199°K had very small grains and an acicular appearance (see Figure 149d).

Figure 149. Microstructures of High-purity Plutonium Subjected to Isothermal $\beta \rightarrow \alpha$ Transformations. Electropolished, polarized light.

Micro 36878 a. Transformed at 361°K 150X

Micro 37058 b. Transformed at 325°K 250X

Micro 36836 c. Transformed at 296°K 250X

Micro 36843 d. Transformed at 199°K 250X

Discussion: Several features of the TTT diagram (Figure 148) are interesting when compared with other information for this phase transformation. The minimum time for the start of the transformation appears

to be smaller by at least a factor of two than that reported by Nelson[130] (~1 sec). This agrees with his observation that purer metal transforms more rapidly at a given temperature. Also, the temperatures of the minimum times for the start of the transformation and for the end of the transformation appear to be higher (~270°K) than those given by Nelson (~253°K).

Another interesting aspect is the location of the curve for 50% transformation. Its relative proximity to the "beginning transformations" curve reflects the shape of plots of longitudinal wave velocities versus the logarithms of the holding times at a given isothermal temperature. For the specimens transformed at 313°K and below, the curves are not sigmoidal. Instead, they show an initial high transformation rate which decreases rapidly thereafter. This behavior led to considerable uncertainty as to the time of completion of the transformation. The arrows shown in the curve for the end of transformation in Figure 148 indicate the limits of uncertainty in this value.

The outstanding feature of the diagram is the double C character. The validity of this is supported by the following considerations: 1) the curve for 50% transformation above 313°K is displaced further to the right from the curve for the beginning of the transformation than it is for samples transformed at 313°K and below; 2) the samples isothermally treated at temperatures above 313°K did not undergo complete transformation. With respect to the first consideration, the location of the curve for 50% transformation above 313°K reflects the nearly sigmoidal shapes of plots of the longitudinal wave velocities versus the logarithms of the holding times.

The incompleteness of transformation in samples held at 325°K and above is evidenced by the fact that the wave velocities for the apparent completion of the transformation did not approach the values for 100% alpha plutonium as determined from the continuous cooling and heating data (see Figure 147). When such partially transformed samples were cooled to room temperature and the surfaces reground to remove the roughening from the phase transformations, the velocities were the same as those obtained at room temperature before treatment, indicating that the samples had completely transformed to alpha plutonium on cooling from the isothermal temperature. In this respect, it should be noted that cold treatment down to 199°K of as-cast specimens and of previously isothermally treated specimens did not change the velocities. Therefore, it must be concluded that the material had transformed completely to the alpha phase once it reached room temperature, regardless of its prior thermal history

Metallographic observations corroborated the fact that samples held at 325°K and above did not transform completely. From the measurements of the wave velocities during the isothermal treatments, the quantities

of untransformed β were 24% and 16% at 361 and 325°K, respectively. These values agree with the apparent volume of small grains in the microstructures of the samples (see Figures 149a and b).

The present results clearly demonstrate that the $\beta \rightarrow \alpha$ transformation in plutonium has a partial athermal character in that at the higher temperatures (325°K and above) the transformation does not go to completion; rather, the amount of transformed material approaches a certain value and further holding time has no effect. Upon subsequent cooling to room temperature the transformation goes to completion. This behavior suggests that the β to α transformation in plutonium might proceed by a martensitic mechanism.

9. The Effects of Pressure on Transformation Behavior
(R. G. Liptai and L. T. Lloyd)

A program has been initiated to study the effects of pressure on transformation behavior in actinide elements. Initial emphasis is on plutonium.

The $\alpha \rightleftharpoons \beta$ transition of plutonium is characterized by an unusually large volume change of about 9%. The equilibrium transition temperature is reported to be near 393°K; however, a hysteresis of about 50°K usually accompanies the transformation. A number of investigators[138-141] have considered quantitatively the temperature hysteresis resulting from stresses caused by volume changes during transformations. On the basis of the elastic theory of a thick-walled sphere under hydrostatic pressure, the following expression was derived[138] for the mean transformation stress, $\bar{p}$:

$$\bar{p} = \frac{1}{2} K \frac{\Delta V}{V} \int_0^{\frac{r_1}{r_2}} \frac{1 - \left(\frac{r_1}{r_2}\right)^3}{1 + 1/2 \left(\frac{r_1}{r_2}\right)^3} d\left(\frac{r_1}{r_2}\right), \qquad (2)$$

---

[138] Honda, K., On the Behavior of Enormously Large Internal Stress Accompanying the Transformation of a Substance, Proc. of Japan Acad. 25 11 (1949), Tokyo, Japan.

[139] Sato, M., and Tino, Y., Zur der inner Spanning in einem Zylindrischen Transformationssysteme, J. Sci. Res. Inst. 44 (1950), Tokyo, Japan.

[140] Honda, K., and Sato, M., "An Interpretation of the Hysteresis Loops in A_3 and A_4 Transformation of Pure Iron," Proc. of 1st World Met. Congress, 1951, p. 707.

[141] Honda, K., and Sato, M., "On the Theory of Transformation Stress," Proc. of the International Symposium on the Reactivity of Solids, Gothenburg, 1952, p. 847.

where K is the bulk modulus, $\Delta V/V$ is the volume change per unit volume upon transformation, and r_1 and r_2 are the inner and outer radii of the two concentric spheres.

The change of the transition temperature ΔT, due to pressure $\overline{p}$ is given by the Clausius-Clapeyron equation:

$$\Delta T = \frac{T\,\overline{p}(\Delta V/V)}{\rho\lambda}, \tag{3}$$

where T is the equilibrium transition temperature, ρ is the density, and λ is the latent heat of transformation.

When equation (2) is applied to plutonium, with a value of 3.91 dynes/cm^2 for K,* the mean internal stress is calculated to be 258,000 psi (~17 kb). In this case, the theoretical situation is unrealistic because plutonium cannot support such a stress. Loasby and Lowe[135] and Nelson[130] have reported that "voids" or microcracks begin to form at 50% transformation of beta to alpha, suggesting that plutonium is only capable of accommodating transformation stresses of the order of those produced at 50% transformation. Again, use of equation (2) indicates that internal stresses of 28,400 psi (~2 kb) are generated at 50% transformation, which would be the maximum stress that the material could support without rupturing. This is in general agreement with reported tensile data. From equation (3), with values of 16.5 x 10^7 dyne-cm/g for λ and of 18.8 gr/cm^2 for ρ,* the total hysteresis (heating and cooling) as a result of internal stresses of 28,400 psi is 44°K, which is in good agreement with the reported value.

The analysis appears to be applicable to the $\alpha \rightleftharpoons \beta$ transformation in plutonium. Further evidence in support of this is the reported observations that pressures of the order of 60,000 psi (~4 kb) eliminate formation of voids during the transition,[130,135] and that the sluggishness of the $\alpha \rightleftharpoons \beta$ transition decreases from its maximum effect at atmospheric pressure to essentially zero at 10 kb. Thus, in considering the $\alpha \rightleftharpoons \beta$ transition in plutonium, where the volume change is large, one must consider the effects of both internally generated and externally applied stresses. Pressure equipment to permit us to study these effects is presently being designed. We are planning a system which will be capable of handling plutonium at pressures up to 80 kb and at temperatures up to its melting point.

*These values of K and ρ are averages of the respective values for alpha and beta plutonium.

10. Electronic Structure of Plutonium (M. B. Brodsky)

Publication:

M. B. Brodsky, Hall Coefficient of Alpha Plutonium, Phys. Rev. 131 137-140 (1963).

Studies of electron transport properties are being made to provide information on the electronic structure of the actinide metals. In the last Annual Report (ANL-6677), data were presented for the Hall coefficient of pure plutonium between 77 and 393°K for the alpha phase and between 353 and 438°K for the beta phase. The above publication discusses the data for the alpha phase in terms of a two-band model and presents a possible band structure to account for the results. This band structure is shown in Figure 150. At temperatures below 190°K (see Figure 150a), the Fermi level is at a higher energy than the top of the 7s band, the 7s band is full, and there is a net electronic conduction and a negative Hall coefficient. As the temperature is increased, thermal excitation broadens the 7s band until the Fermi level is below the top of the band, holes are formed in the 7s band, and there are a net hole conduction and a positive Hall coefficient above 190°K (see Figure 150b).

Figure 150. Proposed Band Structure for Plutonium: a) below 190°K, b) above 190°K

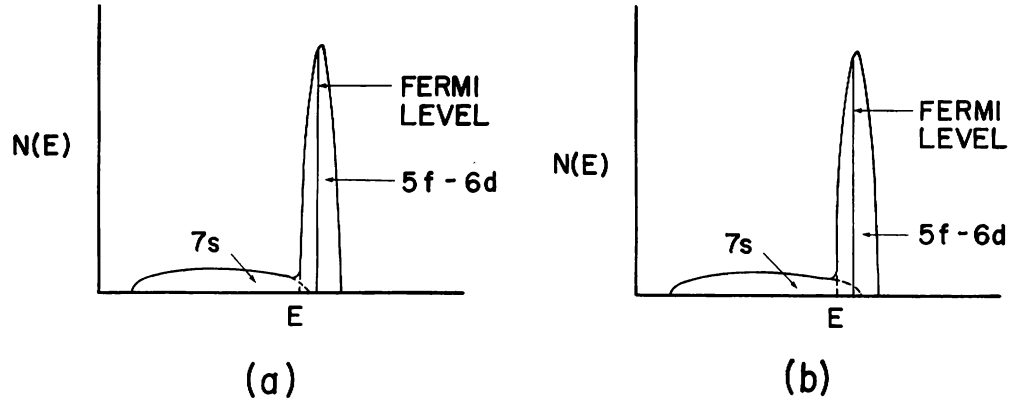

Macro 35803

Solutions for the number of electrons and the number of holes in the two bands at an electron/hole mobility of 0.1 are given in Table LVIII. Also, results are shown for the case of a 6d conduction band. It is seen that a consistent and reasonable set of values may be obtained for the case of the 7s conduction band, but not for a 6d conduction band.

Near the transformation temperature, the number of calculated electron holes is lower in the beta phase than in the alpha phase by about 0.1 hole/atom. If the curve for density of states (see Figure 150) is used

for beta plutonium, the decrease in concentration of holes upon transforming to beta may be accomplished by shifting the Fermi level to a slightly higher energy, but still below the 7s boundary.

Table LVIII

CALCULATED NUMBER OF ELECTRONS AND NUMBER OF HOLES FOR 7s OR 6d CONDUCTION-BAND MODELS

Temperature (°K)	Phase	Sign of Hall Coefficient	7s Conduction Band		6d Conduction Band	
			Number of Electrons[a]	Number of Holes	Number of Electrons	Number of Holes
88	α	-	3.26 5.93	-2.74 -0.07[b]	i[c] i	i i
306	α	+	9.39 6.17	3.39 0.17[b]	4.26 -1.43	6.26 0.57
353	β	+	14.13 6.11	8.13 0.11[b]	i i	i i
438	β	+	15.19 6.10	9.19 0.10[b]	5.10 3.46	7.10 5.46

[a]Note: two solutions are obtained at each temperature.
[b]It is seen that this set of solutions yields reasonable numbers.
[c]Imaginary.

It would seem possible to correlate this change in Fermi level with differences in other properties of the two phases. The thermoelectric power of plutonium drops from +13 to +10 $\mu V/°K$[142] when alpha transforms to beta. This is due to a lower slope of the density-of-states curve at the Fermi surface, as would be the case if the Fermi level is higher in the beta phase. Determinations of the density of states at the Fermi surface are not conclusive.[143] Measurements of specific heat yield 4.5 and 3.6 levels/eV/atom for the alpha and beta phases, respectively; on the other hand, data for the magnetic susceptibility yield 8.7 and 9.1 levels/eV/atom. Although the sign of the change is uncertain, the change is not too drastic, as could be expected from the model proposed above.

A 9-in., iron-core electromagnet has been ordered for use in Hall measurements, magnetoresistivity, etc., of plutonium and other alpha-active materials. The magnet and cryostat will be located under a glovebox and will not come in contact with contaminated materials. Specimens will be loaded into a tube which extends from the bottom of the glovebox into the cryostat. Modifications of the glovebox are 75% complete, and most of the components have been ordered. This assembly should permit measurements from 4.2 to about 1000°K at fields up to 20,000 G.

---

[142]Lee, J. A., and Hall, R. O. A., Some Measurements on the Thermoelectric Power of Plutonium Metal, J. Less-Common Metals 1 356 (1959).

[143]Lord, W. B. H., Some Physical Properties of Plutonium, Met. Rev. 8 277 (1963).

C. Metallurgy of Titanium, Zirconium, and Hafnium

1. Elastic Moduli of Titanium, Zirconium, Hafnium, and Other H.C.P. Metals (E. S. Fisher and C. J. Renken)

Publication:

E. S. Fisher and C. J. Renken, Coupling Cements for Ultrasonic Wave Velocity Measurements at High Temperatures, J. Acoustical Soc. Am. 35 1055 (1963).

Studies of the temperature dependence of elastic moduli of small single crystals by dynamic methods have been handicapped by the lack of satisfactory cements for coupling the crystal to the piezoelectric transducer to support propagation of acoustic waves above temperatures of the order of 600°K. The above paper describes two coupling cements which have been developed over the past two years for both longitudinal and shear wave propagation at relatively high temperatures in vacuo. One, a quasi water glass which is composed of sodium silicate solution, sodium meta-silicate powder ($Na_2SiO_3 \cdot 9H_2O$), and calcium carbonate has been used successfully on titanium and zirconium crystals up to 1155°K. The second, an epoxy phenolic resin, has also been found satisfactory for similar measurements, but only up to 945°K. The latter cement is, however, much less subject to intermittent failure and is consequently to be preferred for studies where temperatures do not exceed 945°K.

The studies of the elastic moduli of single crystals of the h.c.p. phases of titanium and zirconium that were discussed in last year's Annual Report have now been completed for the entire temperature range from 4°K to near the h.c.p. → b.c.c. phase transformations. We have also made some measurements on single crystals of a Hf-7.7 a/o Zr alloy.*

Results: The elastic moduli at 4 and 298°K are given in Table LIX. Some of the values differ from the preliminary results given in ANL-6677 because of refinements in the calculations of the density of the Hf-7.7 a/o Zr crystals at 298°K. The density of 13.248 gm/cc which was used

Table LIX

ELASTIC MODULI OF TITANIUM, ZIRCONIUM, AND A Hf+7.7 a/o Zr ALLOY AT 4 AND 298°K (10^{12} dynes/cm^2)

Metal	Density at 298°K (gm/cm^3)	4°K					298°K				
		c_{11}	c_{33}	c_{44}	c_{66}	c_{13}	c_{11}	c_{33}	c_{44}	c_{66}	c_{13}
Titanium	4.506	1.761	1.905	0.508	0.446	0.683	1.624	1.807	0.467	0.352	0.690
Zirconium	6.505	1.554	1.725	0.363	0.441	0.646	1.434	1.648	0.320	0.353	0.653
Hf + 7.7 a/o Zr	12.727	1.901	2.044	0.600	0.578	0.655	1.811	1.969	0.557	0.520	0.661

*Single crystals of this alloy have been studied in lieu of pure hafnium, which is difficult to obtain. All reference to hafnium in this section applies to this Hf-7.7 a/o Zr alloy.

in the preliminary calculations was based on lattice constants for hafnium containing 2 to 4 a/o Zr[144] and on the atomic weight for free hafnium. The refined density, 12.727 gm/cc, is based on lattice constants obtained at ANL during the past year* and a mean atomic weight for the 7.7 a/o Zr alloy. The lattice constants do not agree with some of the published data if one assumes Vegard's law. A comparison of the published a_0 and c_0 parameters[145-148] and some recent data by J. O. Betterton[149] indicates that the ANL data are consistent with a linear dependence given by the equations

$$a_0(X) = 3.1943 + (X/100)\,(3.2326 - 3.1942), \text{ in Å};$$

$$c_0(X) = 5.0513 + (X/100)\,(5.1473 - 5.0513), \text{ in Å}.$$

The lattice constants predicted by these equations as a function of atomic percent zirconium, X, are plotted in Figure 151, which also includes the

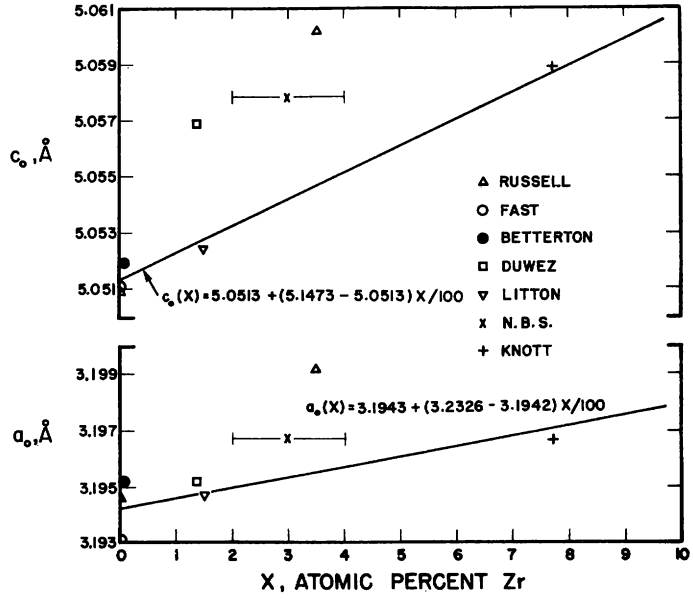

Figure 151

Variation of Lattice Constants of Hafnium-rich Hf-Zr Alloys with Zirconium Concentration

Macro 38162

*The measurements of the lattice constants were made by H. W. Knott.

[144] Swanson, H. E., Fuyat, R. K., and Ugrinic, G. M., Standard X-ray Diffraction Powder Patterns, Nat. Bureau of Standards Circular 539, 3 (1954).

[145] Russell, R. B., On the Zr-Hf System, J. Appl. Phys. 24 232 (1953).

[146] Fast, J. D., The Allotropic Transformation of Hafnium and a Tentative Equilibrium Diagram of the Zr-Hf System, J. Appl. Phys. 23 350 (1952).

[147] Duwez, P., Allotropic Transformation of Hafnium, J. Appl. Phys. 22 1174 (1951).

[148] Litton, F. B., Preparation and Some Properties of Hafnium Metal, J. Electrochem. Soc. 98 488 (1951).

[149] Betterton, J. O., private communication from Oak Ridge Nat. Lab.

reported values of the lattice constants at several concentrations. The lattice constants of pure zirconium used to determine the slopes of the lines are those reported by Swanson and Fuyat.[150]

The effects of temperature on the compressional and shear stiffness moduli are shown in Figures 152 and 153, respectively.* For

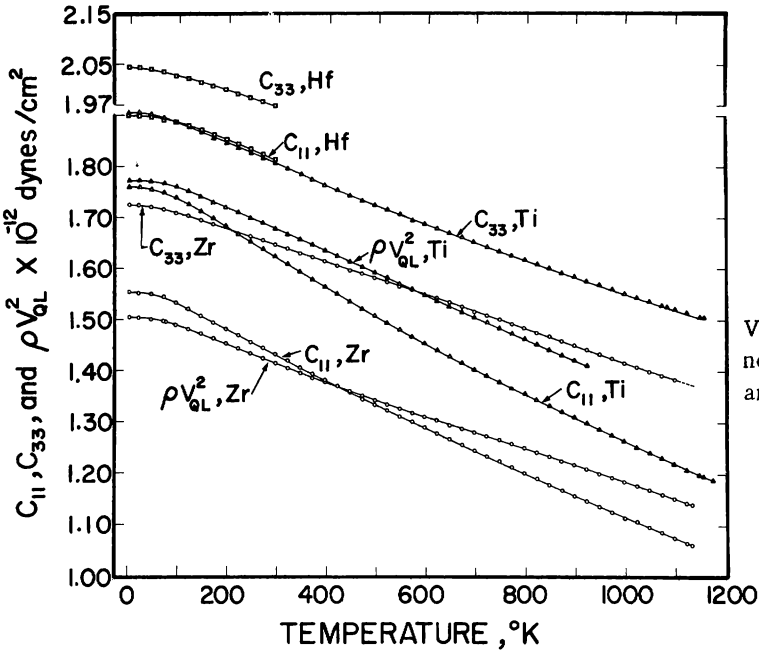

Macro 37860

Figure 152

Variation of the Compressional Stiffness Moduli for Titanium, Zirconium, and Hafnium with Temperature

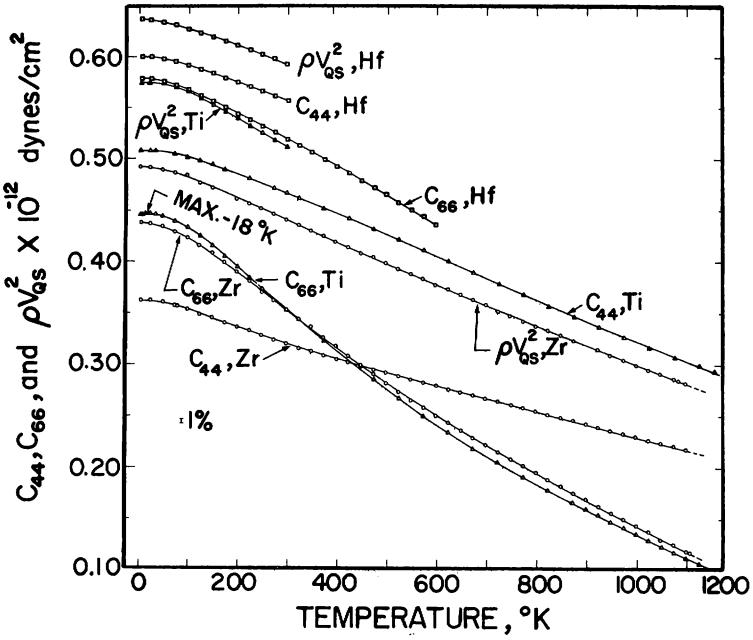

Macro 37859

Figure 153

Variation of the Shear Stiffness Moduli for Titanium, Zirconium, and Hafnium with Temperature

*See Table XLVI of ANL-6677 for the correlation of the moduli with the directions of ultrasonic wave propagation.

[150]Swanson, H. R. and Fuyat, R. K., Standard X-ray Diffraction Powder Patterns, National Bureau of Standards Circular 539, 3 (1953).

titanium the measurements are complete up to the h.c.p. → b.c.c. phase transformation (1155°K), except for the ρV_{QL}^2 values which were extended to 945°K only. For zirconium, only the c_{11} measurements have been completed up to the h.c.p. → b.c.c. phase transformation (1135°K); all the other measurements extend to the 1100°K → 1130°K range, where attenuation of the acoustic energy within the crystals became too excessive for accurate measurements of wave velocities. For hafnium the measurements cover the range from 3°K to 300°K, except for the c_{66} shear modulus, which has been measured up to 625°K.

There are four significant features to note in this set of curves: (1) the remarkable coincidence of c_{66} for zirconium and titanium at all temperatures, (2) the very significant differences between the effects of temperature on the c_{44} and c_{66} shear moduli, (3) the very pronounced positive curvatures in the c_{66} curves for titanium and zirconium above 420°K and (4) the slight, but presumably significant, maximum in the curve of c_{66} for titanium at 18°K.

The effects of temperature upon the c_{12} and c_{13} moduli are shown in the lower part of Figure 154. The c_{13} moduli show no significant variation with temperature; hence, the extrapolations shown by the dashed lines are reasonably justified. The adiabatic linear and volume compressibilities derived from the five stiffness moduli are shown in the top part of Figure 154.

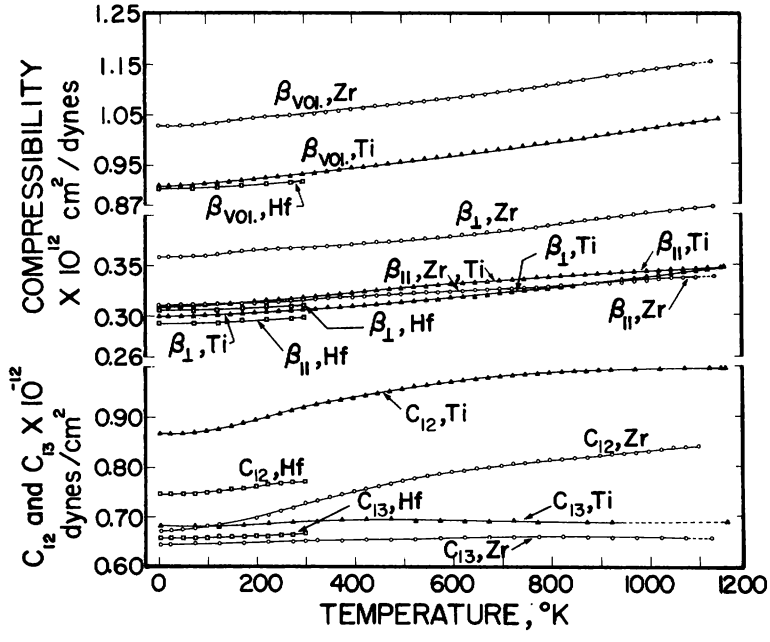

Figure 154
Variation of the Cross-coupling Moduli (lower curves) and the Compressibility Parameters (upper curves) for Titanium, Zirconium, and Hafnium with Temperature

Macro 37858

A comparison of the fractional changes in each of the principal moduli and the bulk moduli (the reciprocal of the volume compressibilities) is given in Figure 155. The ordinate is the value of the modulus, M, , at a

given temperature divided by its value at 4°K, M_O. The fractional changes at the transformation temperatures are remarkably similar for titanium and zirconium. The predominant feature of the plot is the 75% decrease in the c_{66} moduli, compared with a 40% decrease in c_{44} and lesser decreases in the other moduli. The curves for c_{66} and c_{44} for hafnium indicate a similar type of elastic anisotropy.

Figure 155. Fractional Changes in the Stiffness Moduli, M_T, Relative to the Moduli at 4°K, M_O, for Titanium, Zirconium, and Hafnium as Functions of Temperature

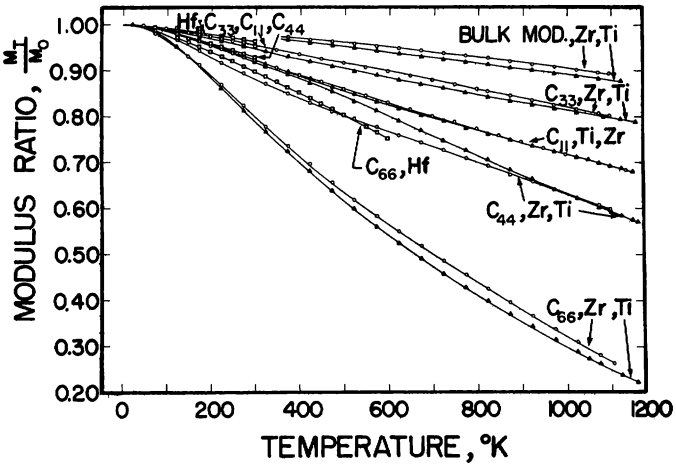

Macro 37861

Figure 156 shows the effects of temperature on three other parameters for titanium and zirconium: the Young's moduli parallel and perpendicular to the [00·1] directions, $E_{\parallel}$ and $E_{\perp}$, respectively, and the anisotropy factor, $A = c_{44}/c_{66}$. The anisotropy factors show a strong positive temperature dependence above 200°K.

Figure 156. Variation of the Directional Young's Moduli, $E_{\parallel}$ and $E_{\perp}$, and the Ratios of the Anisotropy in the Shear Moduli, $A = c_{44}/c_{66}$, for Titanium, Zirconium, and Hafnium with Temperature

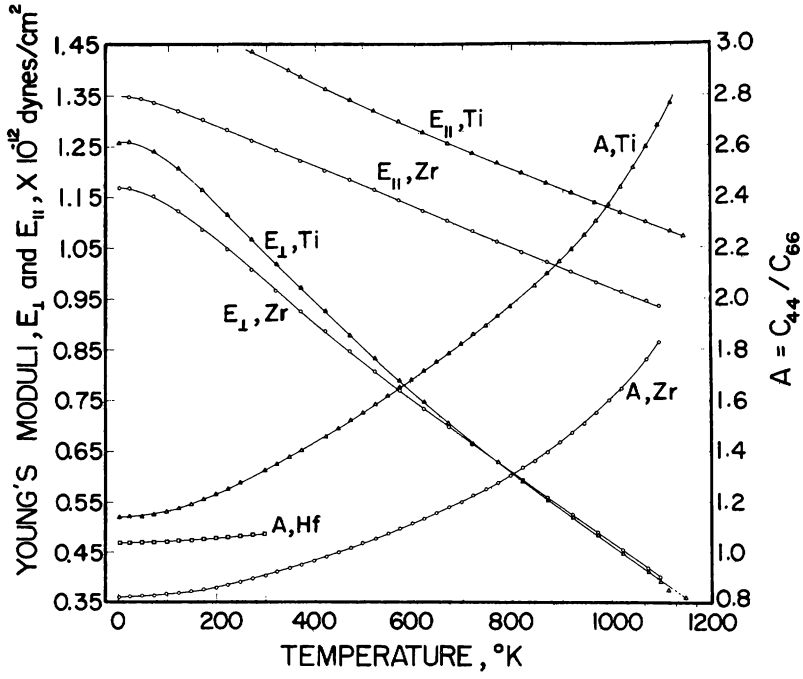

Macro 37857

The Relation of c_{66} to the Shear Mechanism in the Phase Transformations: The possible relationship between the shear mechanism proposed by Burgers[151] for the martensitic h.c.p. → b.c.c. transformations in zirconium and titanium and the large anisotropy in the shear moduli at the transformation temperatures was pointed out in ANL-6677. The scheme of Burgers' shear mechanism is shown in Figure 157, in which the positions of the atoms are projected on the matching planes of the h.c.p. and b.c.c. structures, (00·1) and {110}, respectively. The white circles correspond to atoms of one sublattice in the hexagonal structure and the black circles to the second. Burgers showed that a {10·0}<11·0> shear, with minor dilational adjustments, brings the h.c.p. lattice of zirconium into a b.c.c. arrangement. The ease for this elastic shear to occur is dependent on the c_{66} shear modulus through the strain energy relation, and the small value of c_{66} relative to the moduli of the other principal shear systems strongly supports the Burgers model and also explains the operational preference of this shear system.

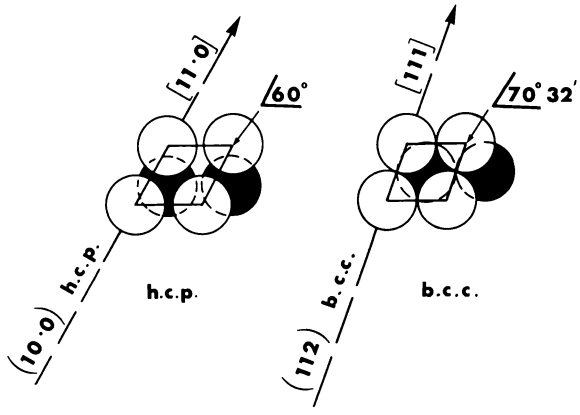

Figure 157

Projections of the atoms on the (00·1) and (110) planes of the h.c.p. and b.c.c. structures which show the changes in interatomic distances and interplanar angles that result from Burgers' scheme for the h.c.p. ⇌ b.c.c. transformation. The white circles correspond to atoms of one sublattice in the h.c.p. structure and the black circles to the second.

Macro 37578

Role of the Temperature Dependence: The very significant differences in the effects of temperature on the two shear moduli, c_{66} and c_{44}, must be interpreted as being primarily a consequence of the crystal structures rather than of any other unique properties of titanium and zirconium. This interpretation is based on a comparison of the present data with similar measurements on other h.c.p. metals, as shown in Table LX. The metals are listed in decreasing order of the c_0/a_0 values at 300°K. The last four columns on the right list the temperature coefficients for the principal shear and compressional moduli, M, at 300°K.

The shear moduli, with few exceptions, are more sensitive to temperature variation than are the c_{11} or c_{33} moduli. The temperature coefficients for c_{66} of titanium and zirconium are significantly higher than in all the other metals. As regards the differences between the coefficients for c_{66} and c_{44}, the trend is quite clear. For c_0/a_0 values above 1.598 (that is, for thallium), the anisotropy is essentially zero (as in cadmium), or c_{44} has the larger temperature dependence (as with zinc, cobalt, and magnesium).

[151]Burgers, W. G., The Process of Transition of the B.C.C. Modification into the H.C.P. Modification of Zr, Physica 1 561 (1934).

For c_0/a_0 values between 1.598 and 1.57, the situation is reversed: c_{66} has the larger temperature dependence.

Table IX

CORRELATION OF c_0/a_0 RATIO FOR H.C.P. METALS WITH OCCURRENCE OF PHASE TRANSFORMATION AND DEPENDENCE UPON TEMPERATURE OF ELASTIC MODULI AT 300°K

Metal	c_0/a_0 at 300°K	a_0 (Å)	Sign of $\frac{\Delta c_0/a_0}{\Delta T}$	Temperature of the h.c.p.→b.c.c. Transformation (°K)	Temperature Coefficients of Elastic Moduli at 300°K $-10^6 \times \left(\frac{1}{M}\frac{\Delta M}{\Delta T}\right)$				References	
					c_{66}	c_{44}	c_{11}	c_{33}	Elastic Moduli	Other Data
Cadmium	1.88	2.973	+	-	867	844	657	409	(159)	(154)
Zinc	1.86	2.660	+	-	538	750	447	278	(160)	(154)
Cobalt	1.623	2.50	+	-	330	412	178	191	(161)	(154)
Magnesium	1.623	3.203	slightly +	-	462	533	300	335	(162)	(154)
Rhenium	1.615	2.76	-	-	-	-	-	-		(156)
Technetium	1.60	2.735	?	?	-	-	-	-		(154)
Thallium	1.598	3.50	+	507	887	231	194	530	(163)	(154)
Scandium	1.594	3.308	+	1608	-	-	-	-		(155)
Zirconium	1.593	3.23	+	1135	1000	523	350	200	*	(152)
Gadolinium	1.590	3.63	+	1535	-	-	-	-		(155)
Titanium	1.587	2.95	+	1155	1000	380	355	203	*	(153)
Lutetium	1.583	3.505	+	1600	-	-	-	-		(155)
Terbium	1.583	3.599	+	1583	-	-	-	-		(155)
Ruthenium	1.582	2.70	+	-	-	-	-	-		(154)
Hafnium	1.581	3.19	+	~2000	476	325	200	150	*	(154)
Osmium	1.579	2.73	slightly +	-	-	-	-	-		(154)
Dysprosium	1.574	3.592	+	1670	-	-	-	-		(155)
Yttrium	1.572	3.645	+	1760	413	333	250	130	(164)	(155)
Thulium	1.572	3.537	+	?	-	-	-	-		(155)
Erbium	1.571	3.559	+	?	-	-	-	-		(155)
Holmium	1.571	3.576	+	1715	-	-	-	-		(155)
Beryllium	1.568	2.281	-	1523	196	184	205	158	(165)	(154,157)
Lithium	1.564	3.086		70	-	-	-	-		(158)

*Present work.

[152]Willens, R. H., A Vacuum X-ray Diffractometer for High Temperature Studies, AFOSR-1839 (1961).

[153]Lloyd, L. T., Thermal Expansion of Alpha Zirconium Single Crystals, ANL-6591 (1963).

[154]Pearson, W. B., Handbook of Lattice Spacings and Structures of Metals, Pergamon Press, New York (1958).

[155]Spedding, F. H., Hanak, J. J., and Daane, A. H., High Temperature Allotropy and Thermal Expansion of the Rare Earth Metals, J. Less-Common Metals 3 110 (1961).

[156]Wasilewski, R. J., Axial Thermal Expansion of Rhenium, Trans. A.I.M.E. 221 1081 (1961).

[157]Martin, A. J., and Moore, A., The Structure of Be, with Particular Reference to Temperatures above 1200°C, J. Less-Common Metals 1 85 (1959).

[158]Barrett, C. S., "Transformations in Pure Metals," in Phase Transformations in Solids, John Wiley Inc., New York (1961).

[159]Garland, C. W., and Silverman, J., Elastic Constants of Cadmium from 4.2 to 300°K, Phys. Rev. 119 1218 (1960).

[160]Alers, G. A., and Neighbours, J. R., Elastic Constants of Zinc between 4.2 and 670°K, J. Phys. Chem. Solids 7 58 (1958).

[161]McSkimin, H. J., Measurements of the Elastic Constants of Single Crystal Cobalt, J. Appl. Phys. 26 406 (1955).

[162]Slutsky, L. J., Garland, C. W., Elastic Constants of Magnesium from 4.2 to 300°K, Phys. Rev. 107 972 (1957).

[163]Ferris, R. W., Shepard, M. L., and Smith, J. F., Elastic Constants of Thallium Single Crystals in the Temperature Range 4.2-300°K, J. Appl. Phys. 34 768 (1963).

[164]Smith, J. F., and Gjevre, J. A., Elastic Constants of Yttrium Single Crystals between 4.2-400°K, J. Appl. Phys. 31 645 (1960). (c_{44} and c_{66} are reversed in this reference.)

[165]Smith, J. F., and Arbogast, C. L., Elastic Constants of Single Crystal Beryllium, J. Appl. Phys. 31 99 (1960).

As regards the data on yttrium, it should be noted that the original reference 164 gave a larger temperature coefficient for c_{44} than for c_{66}. We have now repeated the measurements of the shear moduli using the same crystals as in the original study.* It was found that the orientations of the crystals had been reversed in the original studies. At the same time we have extended the measurements to 900°K, and the results are shown in Figure 158. The absolute values of c_{44} and c_{66} at 298°K are about 0.4% different from the original data. The curves are based on the newer set of values. The two sets of data form reasonably smooth curves between 200 and 400°K. The c_{66} modulus continues to decrease with an almost constant slope, whereas c_{44} shows a positive curvature beginning at approximately 200°K.

*The crystals were loaned to us by Dr. J. Smith of Iowa State College.

Beryllium seems to be the exception with respect to the effects of temperature on the elastic moduli, i.e., they show little change between 4 and 300°K. Beryllium is also the exception with respect to anisotropy in thermal expansion: $(\Delta c_0/a_0)/\Delta T$ is positive for all the metals with $c_0/a_0 < 1.598$, except for beryllium, where it is negative.

Figure 158. Variation of the Shear Stiffness Moduli of Yttrium with Temperature. Values from 300 to 923°K are based on measurements at ANL; below 300°K they are based on results given in reference 164.

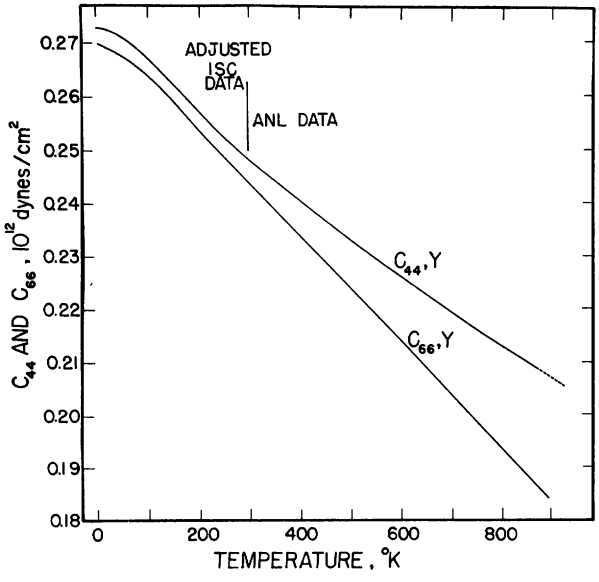

Macro 38028

The fifth column of Table LX shows that h.c.p. → b.c.c. transformations are induced thermally in all the metals listed with $c_0/a_0 < 1.598$, excepting ruthenium and osmium. The latter also are exceptional with respect to the interatomic spacings, as indicated in column 3, which perhaps accounts for the stability of the h.c.p. structures at high temperatures. The situation for thulium and erbium is not known, but the aforegoing correlations indicate that b.c.c. phases could be expected in these metals.

The above considerations lead to the generalization that the anisotropy factor, c_{44}/c_{66}, for metals with h.c.p. crystal structures increases with temperature in those metals which undergo h.c.p. → b.c.c. transformations, and that both phenomena occur only when c_0/a_0 is less than 1.598. The large effect of temperature on c_{66} is an indication of large amplitudes of the thermal vibrations within the basal planes of the h.c.p. structures. With c_0/a_0 much below that corresponding for ideal close packing, it is these modes that are most likely to be excited by thermal energy because of the larger interatomic separations in the basal planes, in contrast with the separations between the sublattices, which are indicated in Figure 157. As the modes with higher frequencies become excited at higher temperatures and give rise to displacements in the [00·1] direction, repulsive forces between the atoms in the different sublattice restrict the thermal displacements which correspond to the c_{66} modulus, and this would then account for the positive curvatures in the curves of elastic moduli versus temperature, the greater thermal expansion of the lattice constant c_0, and other effects of anharmonicity of the lattice vibrations. For example, the pronounced negative curvatures in the curves of electrical resistance versus temperature for titanium and zirconium[166,167]

[166] Wyatt, J. L., Electrical Resistance of Titanium Metal, Trans. A.I.M.E. 197 903 (1953).

[167] Cook, L. A., Castleman, L. S., and Johnson, W. E., Preliminary Report on the Electrical Resistivity of Zirconium, WAPD-25 (1950).

as shown in Figure 159, seem to correspond to the curvatures in the plots of elastic moduli. The temperature at which the electrical resistance deviates from a linear dependence are remarkably coincident with the temperature where deviations are found in the curves for the elastic moduli; in both metals the deviations occur at 420°K. The electrical resistance data may be regarded as further evidence for an effective increase in the overall frequency of vibrations which results from anharmonic interactions.

Figure 159. Ratios of the Electrical Resistivities of Titanium and Zirconium at Temperature T to those at 273°K as a Function of Temperature. The values were obtained from data given in references 166 and 167.

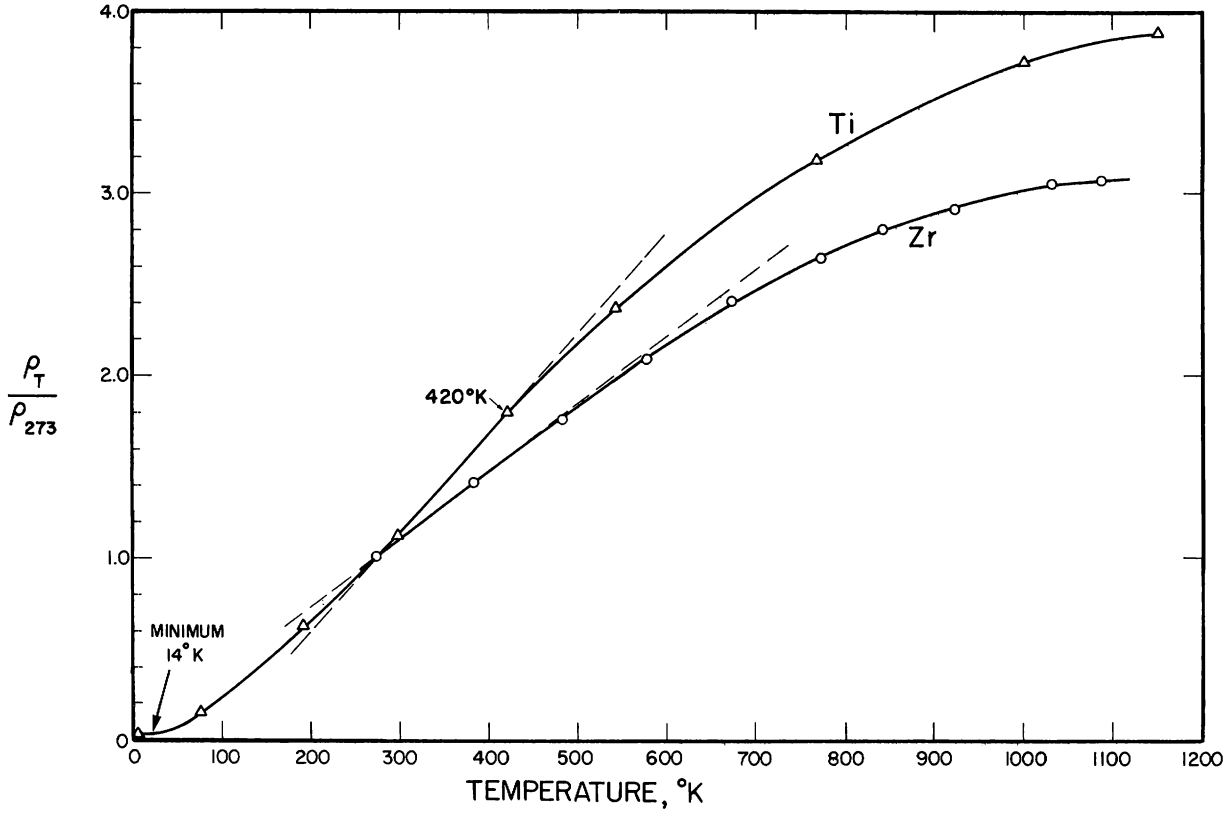

106-7614

Born and Brody's[168] approximate model for the vibrational free energy of a lattice, F, may be applied to evaluating the effects of anharmonicity. According to their model,

$$F = F^h - 3RBkT^2 = F^h - \left(\frac{C_V^{\ell} - C_V^h}{2}\right)T, \qquad (1)$$

where T is the absolute temperature, F^h is the free energy from the quasi-harmonic Debye model, R and k are the gas and Boltzmann constants, B is

[168] Born, M., and Brody, E., Uber die Spezfische Warme Festrkörper bei Hohen Temperaturen (On the Specific Heat of Crystals at High Temperatures), Z. Physik 6 132 (1921).

a function of the coefficients in the expansion of the potential energy of the lattice in terms of powers of the vibrational displacements, and C_V^h is the Debye specific heat at constant volume. The deviation in free energy from the harmonic model can then be evaluated in terms of C_V^ℓ, which is the lattice specific heat at constant volume, and which can be derived from data for the specific heat at constant pressure, C_P, as follows:

$$C_V^\ell = C_V - C_E = \left(\frac{\beta}{\alpha^2 VT + \beta C_P}\right) C_P - C_E, \qquad (2)$$

where β is the adiabatic volume compressibility, α is the instantaneous volume coefficient of expansion, V is the specific volume, C_V is the total specific heat at constant volume, and C_E is the electronic specific heat, which is obtained from γT, where γ is the electronic specific heat coefficient.

Figures 160 and 161 show the results of computing C_V^ℓ for titanium and zirconium, respectively. The C_P data are those of Scott,[169] which were selected from among a number of available sets of measurements because of the higher purity of his specimens and the greater precision of his measurements. The C_E values were obtained from Shimizu's calculations.[170,171] For both titanium and zirconium, C_V^ℓ decreases at

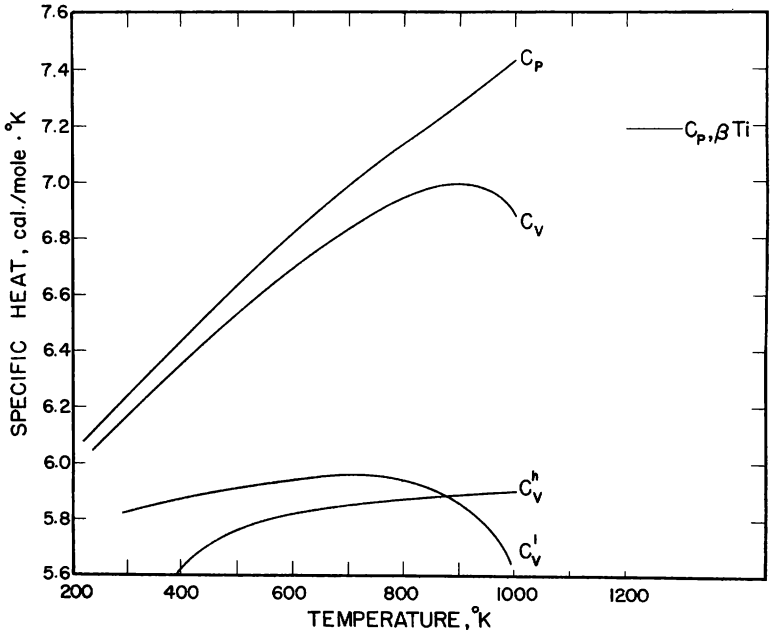

Macro 38374

Figure 160

Dependence of Various Specific Heat Functions for Titanium upon Temperature. The specific heat at constant pressure, C_P, is from the data given in reference 169, the specific heat at constant volume, C_V, was calculated from the data for C_P according to equation (2), C_V^h is the lattice specific heat which was computed from the Debye approximation, and $(C_V - C_E) = C_V^\ell$ is the net lattice specific heat, where C_E, the electronic specific heat, was obtained from Shimizu's calculations.

---

[169] Scott, J. L., A Calorimetric Investigation of Zirconium, Titanium and Zirconium Alloys from 60 to 960°C, ORNL-2328 (1957).

[170] Shimizu, M., Magnetic Susceptibility and Electronic Specific Heat of Transition Metals and Alloys, J. Phys. Soc. Japan 18 1192 (1963).

[171] Shimizu, M., Private communication.

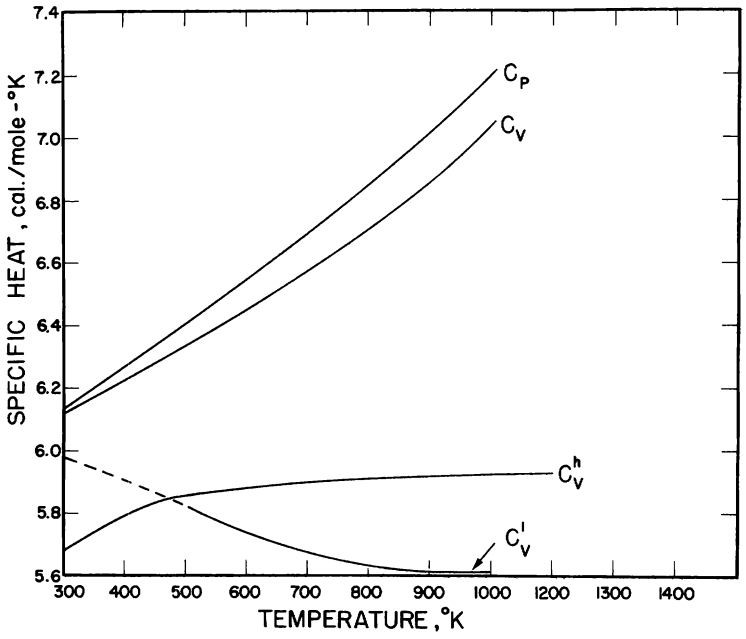

Figure 161

Dependence of Various Specific Heat Functions for Zirconium upon Temperature. The nomenclature is defined in Figure 160.

Macro 38373

the higher temperatures to values less than C_V^h, which indicates that the anharmonicity has the effect of increasing the vibrational free energy of the h.c.p. structures.

Thus there seem to be sufficient grounds for suggesting that the thermodynamic driving force for the martensitic h.c.p. $\rightarrow$ b.c.c. transformations arises from anharmonicity in lattice vibrations. This interpretation, together with Burgers' model for the structural change, and Zener's explanation for the high-temperature stability of the b.c.c. structures,[172] suggests that the transformation can be viewed as a sudden shift in the directions of displacement of thermal vibrations of high amplitude. This view would require that the interatomic distances in the basal planes of the h.c.p. structure suddenly decrease to the close-packed arrangement of the (110) planes of the b.c.c. structure, which is indeed the case, as shown in Figure 157. In the b.c.c. phase, the thermal modes of high amplitude would then presumably correspond to displacements along the $\{110\}\langle 110\rangle$ shear mode (c_{44} shear mode of the h.c.p. phase). To verify the presumed high displacements, or low shear moduli, for the $(110)\langle 110\rangle$ shear mode would require measurement on Ti-Zr alloys, rather than pure components, in order to retain the b.c.c. phase.

In terms of the usual accuracy of such measurements, the noted maximum in the c_{66} modulus for titanium at 18°K would ordinarily not be considered significant, were it not for the fact that other properties also show deviations at this temperature. For example, Hake et al.[173]

---

[172]Zener, C., Elasticity and Anelasticity in Metals, The University of Chicago Press, Chicago (1948).

[173]Hake, R. R., Leslie, D. H., and Berlincourt, T. B., Low Temperature Resistivity Minima in Some Dilute Superconducting Titanium Alloys, Phys. Rev. 127 170 (1962).

recently reported an anomaly in electrical resistivity. They attributed their observations to localized moments of manganese or iron impurities. However, this interpretation is not completely certain,* and further studies would be required to ascertain the suggested correspondence between the electrical resistivity behavior and the c_{66} modulus maximum at this temperature.

Debye Temperature: The Debye temperatures computed from the elastic moduli (θ_E) at 4°K which are given in Table LIX are shown in Table LXI, along with the corresponding values of the Debye temperatures computed from specific heat data (θ_{SH}) by Kneip et al.[174] The θ_{SH} for the Hf + 7.7 a/o Zr alloy was interpolated from a θ_{SH} of 252°K for pure hafnium by assuming a linear dependence on zirconium concentration.** The agreement between θ_E and θ_{SH} is significant in view of the fact that larger differences have been reported for other hexagonal metals; for example, approximately 20°K for magnesium,[162] zinc,[160] and cadmium,[159] and 200°K for beryllium.[175] A theoretical analysis by Blackman[176] suggests that θ_E and θ_{SH} should be equal. Our present data support this view and lead to the conclusion that reported differences in the Debye temperatures are to be ascribed to experimental inaccuracies.

Table LXI

COMPARISON OF DEBYE TEMPERATURES

Metal	Debye Temperatures, °K	
	From Measurements of Elastic Moduli θ_E	From Measurements of Specific Heat θ_{SH}
Titanium	425.65	428 ± 5
Zirconium	295.98	291.7 ± 1.3
Hf + 7.7 a/o Zr	256.29	255.5†

†Interpolated from values for pure hafnium (252 ± 1°K) assuming a linear dependence on concentration of zirconium.

*Private communication.

**This type of dependence has been verified by a private communication from J. Betterton at ORNL.

[174]Kneip, G. D., Betterton, J. O., Jr., and Scarborough, J. A., The Low Temperature Specific Heats of Titanium, Zirconium and Hafnium, Phys. Rev. 130 1687 (1963).

[175]Alers, G. A., and Neighbours, J. R., Note added in proof to reference 160.

[176]Blackman, M., Handbuch der Physik, Vol. VII, Part 1, page 370, Springer-Verlag, Berlin (1955).

2. Effect of Hydrogen on the Plastic Behavior of Zirconium (D. G. Westlake)

Publication:

D. G. Westlake, Initiation and Propagation of Microcracks in Crystals of Zirconium-Hydrogen Alloys, Trans. ASM 56 1-10 (1963).

The studies to determine the mechanisms whereby additions of hydrogen alter the plastic deformation properties of zirconium have continued during the past year. Our earlier work has shown that large precipitates of a zirconium hydride are formed when Zr-H alloys are slowly cooled to room temperature from elevated temperatures at which the hydrogen is in interstitial solution. Upon plastic deformation, these precipitates crack and cause brittle behavior of the alloy even though the metal phase deforms plastically. These results are described in detail in the above publication. In the current phase of the program we have endeavored to quench zirconium-hydrogen alloys, both single and polycrystalline material, rapidly in an effort to retain the hydrogen in supersaturated solution, and to determine the effects of such treatments on the critical resolved shear stress (CRSS) for slip on $\{10\bar{1}0\}$ planes in the temperature range from 77 to 298°K.

The techniques of crystal preparation, hydrogenation, and heat treatment were described in the last Annual Report (ANL-6677). On the basis of optical microscopic observations we were led to believe that up to 0.54 a/o hydrogen could be held in supersaturated solid solution by quenching. Tensile tests of such crystals, however, showed that they were up to 3.5 times stronger at room temperature than unalloyed crystals, and this is more than ten times the strengthening that one would anticipate from solid-solution effects. We therefore proceeded to apply electron microscopic techniques.

Several specimens of zone-refined zirconium and several Zr-0.13 a/o H alloys rapidly quenched from the solution temperature were ground to a thickness of 0.5 mm and chemically polished in a bath of 46.75 v/o H_2O, 46.75 v/o HNO_3, and 6.50 v/o HF (49%) to a thin film suitable for transmission electron microscopy (see Figure 162). Examination of these alloys revealed that there was a finely dispersed precipitate in the zirconium matrix only 2 hr after quenching. Observation of a specimen 6 and 23 hr after quenching showed that some of the needles increased in size during the 17-hr aging at room temperature; a specimen aged 260 days still had a fine dispersion of needles, along with the larger precipitates. Other observations were the following:

1. Most of the precipitates were in the form of needles lying parallel to $\langle 11\bar{2}0 \rangle$ directions.
2. Precipitates formed in the vicinity of some, but not all the dislocations.
3. Dislocations were not essential to the nucleation of precipitates.
4. Nucleation sites were randomly distributed throughout the matrix.

It became apparent from these results that even with low hydrogen concentrations and rapid quenching the observed strengthening, wholly or at least a substantial part of it, is due to precipitation strengthening and the ensuing experimental results and discussion should be viewed as such.

Unalloyed crystals and crystals containing various concentrations of hydrogen up to 0.63 a/o were tested in tension at temperatures between 77 and 298°K. Tests at the extremes in temperature were in liquid nitrogen and in air, and the others were run with the samples immersed in liquid Freon 12.

For the zone-refined crystals that were not alloyed with hydrogen, there was a dependence of the CRSS, τ, upon the absolute temperature, T, which fitted the expression

$$\tau^{2/3} = A - BT^{2/3}, \tag{3}$$

where A and B are constants. There was considerable variation in the values of CRSS (1.0 to 3.7 kg/mm^2 at room temperature), probably due to the differences in their impurity contents. The constant A ranged from 2 to 7 [(kg/mm^2)$^{2/3}$], and B from 0.019 to 0.104 [(kg/mm^2-°C)$^{2/3}$]. Figure 163 shows the data for the crystals that gave the extreme values of A and B (crystals 3 and 16), and the typically good fit of the results to equation (3) (crystals 6 and 14).

Alloying with hydrogen increased the strength, but the temperature dependence of the CRSS still followed equation (3). Typical results are shown in Figure 164. One of the most interesting results is that the value of B decreases with increasing hydrogen concentration. This, too, may be caused by impurities.

Seeger[177] has shown that the value of A in equation (3) is

$$A = \left(\frac{N_z}{Gb}\right)^{1/3} \frac{U_0}{4bx_0}, \tag{4}$$

[177]Seeger, A., "On the Theory of Radiation Damage and Radiation Hardening," Proc. Second UN Intnl. Conf. Peaceful Uses Atomic Energy, Geneva, Switzerland (1958), vol. 6, p. 250.

Figure 162. Transmission Electron Micrographs of a Zr + 0.13 a/o H Alloy Quenched from 573°K, Thinned, and Aged for 108 Days at Room Temperature

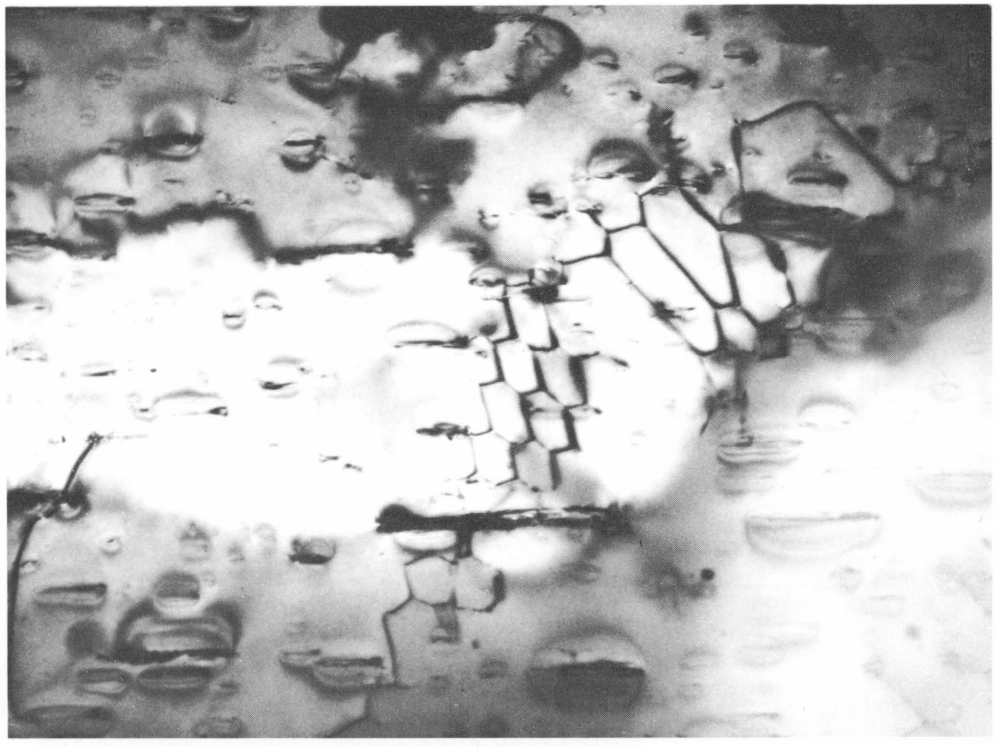

Micro 104132 40000X

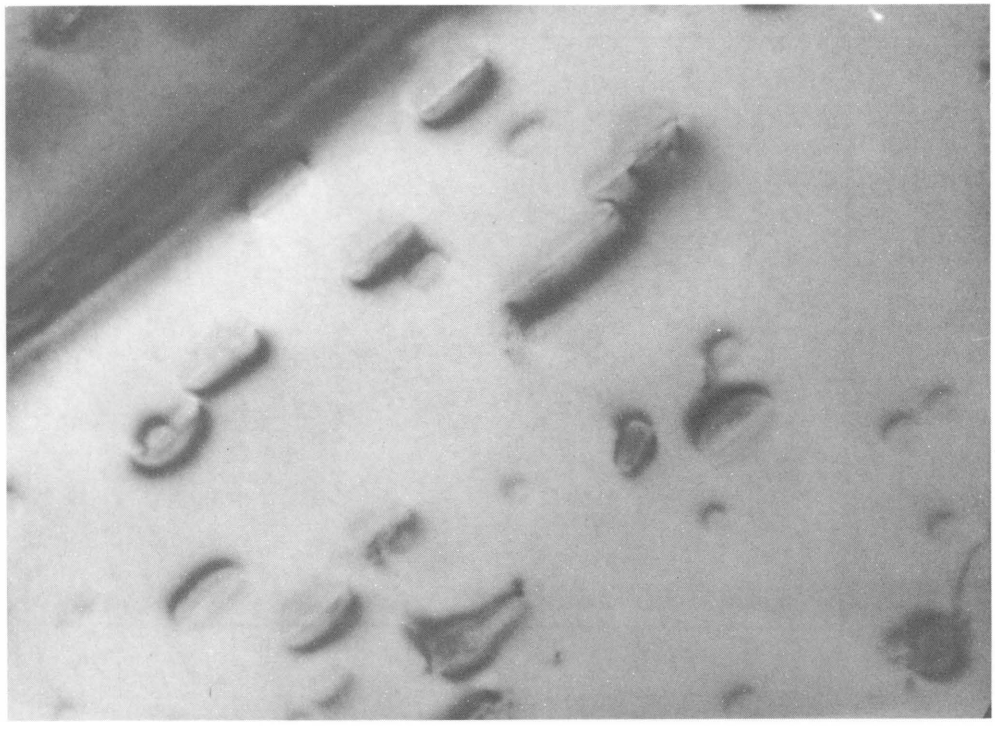

Micro 104137 120000X

Figure 163. Effect of Temperature on the CRSS of Zone-refined Single Crystals of Zirconium that Contained No Hydrogen

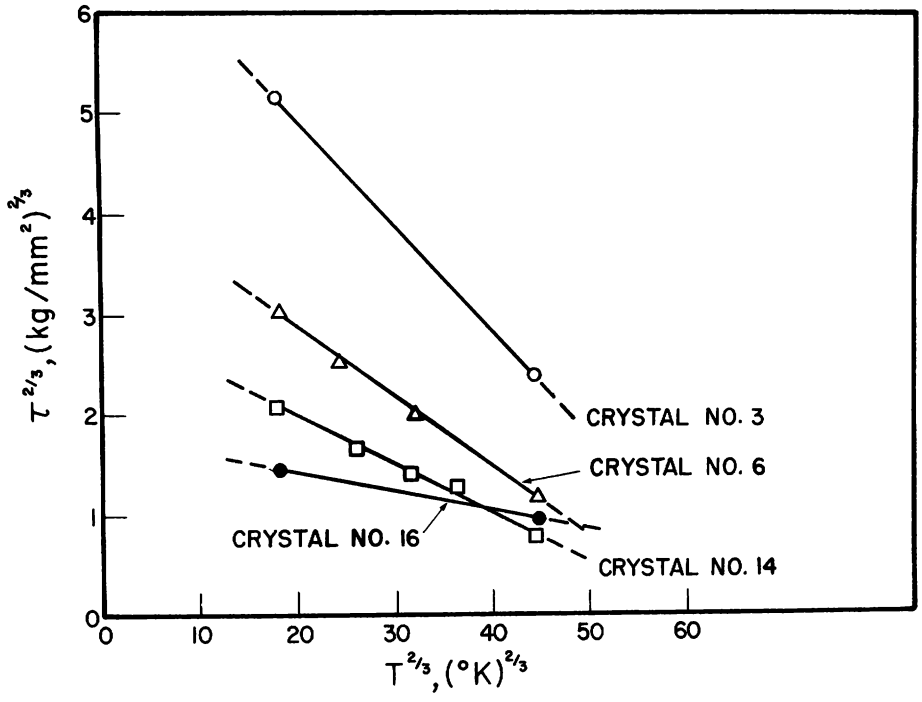

Macro 38159

Figure 164. Effect of Temperature on the CRSS of a Zirconium Crystal with Various Hydrogen Concentrations

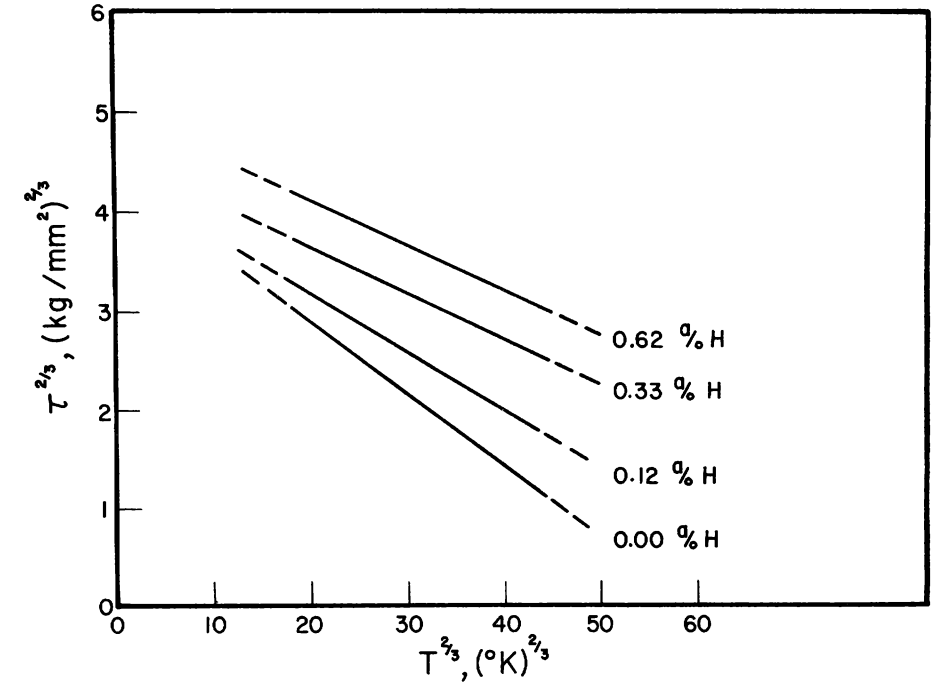

Macro 38157

whereas[178]

$$B = A\left(\frac{3}{2}\frac{k}{U_0}\ln\frac{Nbv_0}{N_z\dot{a}}\right)^{2/3}, \qquad (5)$$

where N_z is the number of obstacles per unit area of the glide plane, G is the shear modulus, b is the Burgers vector of the slip dislocation, U_0 is the thermal energy necessary for a dislocation to overcome an obstacle under zero applied stress, $4x_0$ is the distance traversed in overcoming an obstacle, N is the number of dislocatons per unit volume that are held up by obstacles, v_0 is the frequency with which a dislocation attempts to overcome the obstacles, k is the Boltzmann constant, and $\dot{a}$ is the strain rate.

The expression $(1/N_z)^{1/2}$ would be the distance between particles, d, on a slip plane. Therefore, if one assumes all factors in A to be constant except N_z, A becomes a linear function of $(1/d)^{2/3}$. If the obstacles are atoms or clusters of atoms of interstitial impurities, then d should be inversely proportional to $C_i^{1/2}$, and A should be linear with $C_i^{1/3}$, where C_i is the concentration of the impurities.

Chemical analyses of the samples have not yet been completed, but resistance ratios have been obtained as preliminary indications of the relative levels of impurities. The ratio r_{77}, plotted in Figure 165, is the ratio of the resistances of a hydrogen-free sample at 77°K and 297°K.

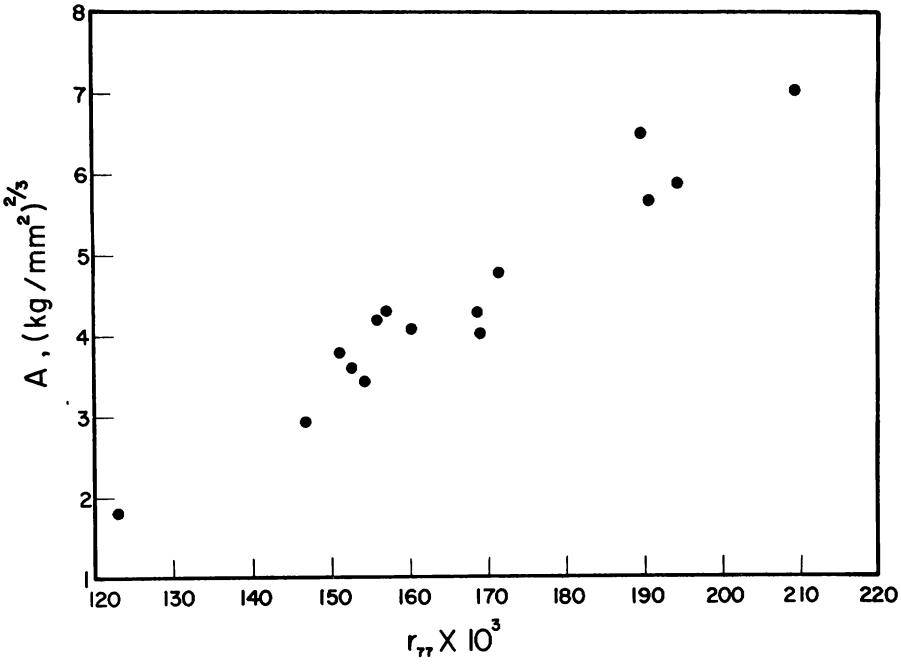

Figure 165

Correlation of Constant A for Zirconium Single Crystals that Contain No Hydrogen with the Resistance Ratio $r_{77} = R_{77°K}/R_{298°K}$.

Macro 38160

[178] Seeger, A., and Essmann, U., "The Mechanism of Radiation-Hardening of F.C.C. Metals by Fast Neutrons," Radiation Damage in Solids, Proc. of the Intern. School of Physics (Enrico Fermi), Sept. 5-24 (1960), p. 717, Academic Press, New York (1962).

Renucci et al.[179] have shown that the resistance ratio for zirconium is virtually equal to the resistivity ratio because the thermal expansion coefficients are small. A correlation between r_{77} and A is evident. When chemical analyses have been obtained, the correlation of the temperature dependence of the CRSS with the concentration of impurities will be examined.

Tensile tests were also made with polycrystalline samples of Kroll zirconium that had been arc-melted, hydrogenated at 900°K, and quenched. Typical results are shown in Figure 166. These results can be rationalized as follows:

Kelly [180] has combined Orowan's[181] equation

$$\tau - \tau_P = 2D/bd$$

and Nabarro's[182] expression for the line tension of the dislocation,

$$D = \frac{Gb^2}{8\pi}\left(1 + \frac{1}{1-\nu}\right)\ln\frac{d}{2b},$$

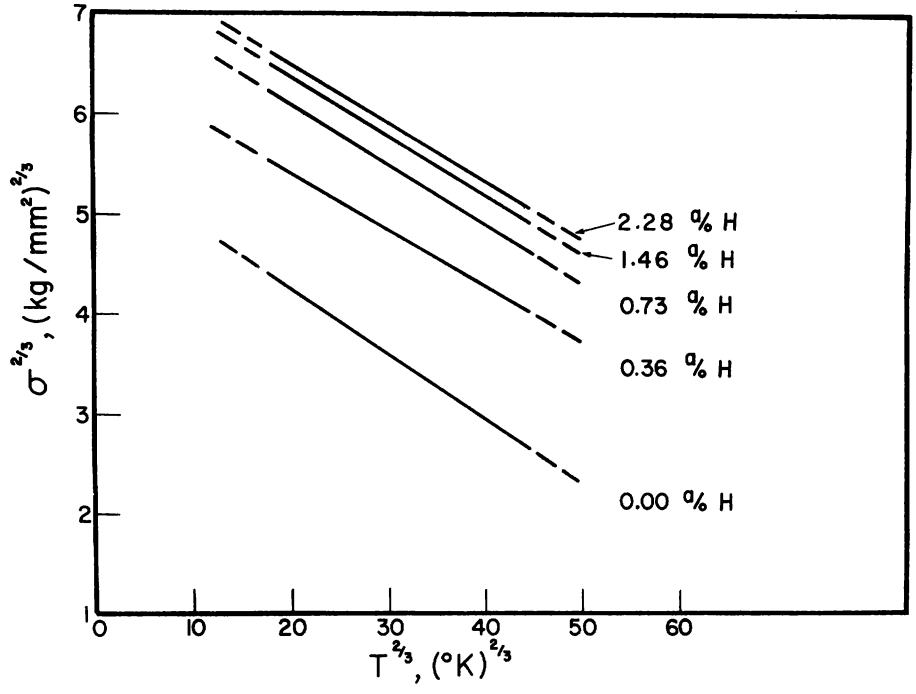

Figure 166
Effect of Temperature on the Yield Stress σ, of Polycrystalline Zr-H Alloys

Macro 38158

[179] Renucci, L., Langeron, J. P., and Lehr, P., Study of the Electrical Resistivity of Zirconium, Mem. Sci. Rev. Metallurg. 58 699 (1961).

[180] Kelly, A., "Theories of Precipitation and Dispersion Hardening," Electron Microscopy and Strength of Crystals, Edited by Thomas, G. and Washburn, J., p. 947. Interscience Publishers, New York (1963).

[181] Orowan, E., "Discussion," Symposium on Internal Stresses in Metals and Alloys, p. 451, Inst. of Metals, London (1948).

[182] Nabarro, F. R. N., The Mathematical Theory of Stationary Dislocations, Advances in Physics 1 269 (1952).

and he has taken account of the effect of size of particles on separation of particles, to obtain

$$\tau - \tau_P = \frac{Gb}{4\pi(d-r)}\left(1 + \frac{1}{1-\nu}\right)\ln\left(\frac{d-r}{2b}\right), \tag{6}$$

where τ is the CRSS of the precipitation-hardened alloy, τ_P is the CRSS of the pure metal, d is the distance between centers of the particles, r is the radius of the particle, and ν is Poisson's ratio. When r is very small, $(\tau - \tau_P)$ should vary linearly with $(1/d)\ln(d/2b)$. If the number of hydride needles varies directly with the concentration of hydrogen, then the distance between particles on a given slip plane would vary inversely with $C^{1/2}$, i.e., $d = K/C^{1/2}$, where C is the concentration of hydrogen and K is a constant of proportionality. Therefore,

$$(\tau - \tau_P) \sim \frac{C^{1/2}}{K}\ln\left(\frac{K}{2bC^{1/2}}\right). \tag{7}$$

From the observations of electron microscopy, it appears that even after aging for 108 days the value of d is of the order of 1000 Å in an alloy which contains 0.13 a/o hydrogen. This leads to an estimate $K \approx 36$ Å. If the relation (7) is written in the form

$$(\tau - \tau_P) \sim \frac{C^{1/2}}{K}\left[\ln\frac{K}{2b} - \ln C^{1/2}\right],$$

and values of K.= 36 Å and b = 3.22 Å are used, it is seen that the $\ln C^{1/2}$ term cannot be ignored for values of C between 0.09 and 2.28 a/o. Thus, a plot of $(\tau - \tau_P)$ vs. $C^{1/2}$ should deviate from linearity over the entire concentration range which has been studied. The deviation from linearity will be enhanced if, at some hydrogen concentration, the number of particles becomes constant and the size of the particles begins to increase with increasing C. Under these conditions, if r is still much smaller than d, then (d-r), and therefore the value of $(\tau - \tau_P)$, would be nearly invariant with C. Figure 167 shows the experimental results for the polycrystalline samples plotted as $(\tau - \tau_P)$ vs. $C^{1/2}$. Values of τ were taken as $1/2\,\sigma$, where σ is the stress on the stress-strain curve where it deviates from a linear relationship. The shape of the curve is that predicted in the foregoing discussion.

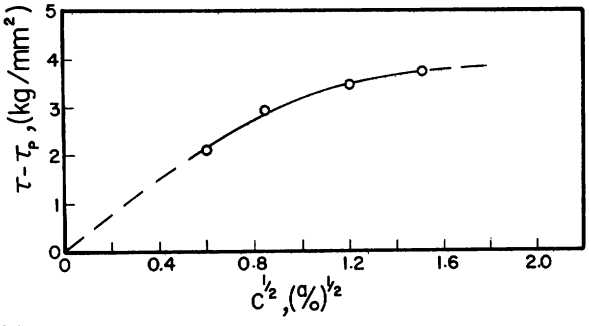

Macro 38161

Figure 167
Incremental Strengthening of Polycrystalline Zirconium by Alloying with Hydrogen

The mechanism whereby dislocations overcome the barriers in hydrogen-free zirconium is thermally activated because the temperature dependence of the CRSS is described by equation (3). The decrease in the constant B with an increase in hydrogen concentration may indicate that the increment of strength due to the hydride needles is described by equation (6). This would mean that the strengthening is not affected by temperature except through the variation of G with T. A more complete analysis of the results will be possible when the chemistry of the samples is known.

Three phenomena which were observed in this study are unexplainable if one accepts that prism planes are the only active slip planes in zirconium.[183] These are: (1) kink bands, (2) wavy slip lines in the hydrogenated samples, and (3) yield points. Baldwin and Reed-Hill[184] have recently detected slip traces attributable to basal glide, so that one can not postulate a double cross-glide mechanism[185,186] for zirconium that can be used to explain all three phenomena.

---

[183] Rapperport, E. G., and Hartley, C. S., Deformation Modes of Zirconium at 77, 575 and 1075°K, Trans. A.I.M.E. 218 869 (1960).

[184] Baldwin, D. H., and Reed-Hill, R. E., "An Evaluation of the Role of Deformation Twinning in the Plastic Deformation of Zirconium," Ninth Quarterly Progress Report, Metallurgical Research Laboratory, University of Florida, Atomic Energy Comm. Contract No. AT(38-1)-252, Nov. 1963 .

[185] Koehher, J. S., The Nature of Work-Hardening, Phys. Rev. 86 52-59 (1952).

[186] Orowan, E., "Dislocations and Mechanical Properties," Dislocations in Metals, p. 69, A.I.M.E., New York, 1954.

D. Diffusion Studies

1. Self-diffusion in Alpha Uranium (S. J. Rothman and R. Bastar)

The results on self-diffusion in the first set of single crystals with mosaic structure were given in the Annual Report for 1961 (ANL-6516). Although this work showed that it was not very likely that the mosaic structure had a large effect on the diffusion, this question was not completely resolved. Further, the temperature dependence of the diffusion coefficients was not measured. Both of these are now being studied.

Another set of mosaic-structured crystals is now being annealed at 927°K. Methods have been devised for using U^{233} as the tracer isotope, which permits the use of more perfect single crystals as samples, and three of these will be annealed together with three of the mosaic-structured crystals to check on the possibility of dislocation diffusion enhancement.

2. Tracer Element Diffusion in Gamma Uranium (S. J. Rothman and N. L. Peterson)

The data presented in the last Annual Report (ANL-6677) left unanswered a number of questions, the reason for the curved plots of logarithm of the diffusion coefficient, D, versus the reciprocal of the absolute temperature, T, being an especially vexing one. It had been suggested[187] that such curved Arrhenius plots could be caused by defects (either excess point defects or dislocations) which might be introduced by plastic deformation due to the volume change during a phase transformation. Since such defects should be removed by a high-temperature anneal, the following experiment was done.

A piece of high-purity uranium, which was attached to a Pt-Pt 10% Rh thermocouple, was annealed at 1371°K for 19.5 hr. The temperature was then lowered to 1082.9°K, Co^{60} was evaporated onto the surface of the sample, and the sample annealed at 1082.9°K for 0.5 hr, cooled and sectioned, and the sections were counted in the usual manner. The penetration plot (Figure 168) yielded a value of D = 1.20×10^{-6} cm^2/sec, which is within 2% of the values for D obtained in a conventional experiment (see Figure 169).

---

[187] Gruzin, P. L., Kuznetsov, E. V., and Kurdyumov, G. V., "Influence of Intra-grain Structure of Austenite on Self-diffusion of Iron," in Problems of Metallography and the Physics of Metals, Fourth Symposium, Edited by Lyubov, B. Y., Moscow, 1955. AEC-tr-2924, p. 343.

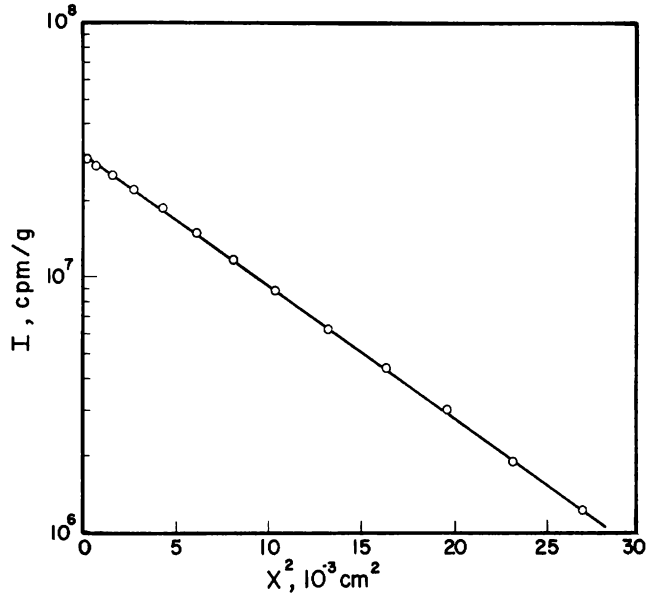

Macro 38147

Figure 168

Penetration Plot for Special Ann al (see text)

Thus, it is very unlikely that excess point or line defects introduced by the beta to gamma phase transformation are responsible for the curved Arrhenius plots, since these defects would anneal out at 1371°K. This experiment has shown that simple defects introduced by a phase transformation[187] do not explain the anomalous diffusion of impurities in gamma uranium, but it has not eliminated defects that do not anneal out at 1371°K as possible causes of the anomalous diffusion. Such defects might well be vacancies associated with, or dislocations locked by, residual or diffusing impurity atoms,[188] and since such defects may not anneal out at 1371°K, the present experiment sheds no light on their role in diffusion in gamma uranium.

The data given in ANL-6677 on impurity diffusion in gamma uranium have been changed in the light of a recent recalibration and correction of the potentiometer used in that work. The values of D are plotted versus the reciprocals of the

Figure 169. Plot of D versus 1/T for the Diffusion of Various Isotopes in Gamma Uranium

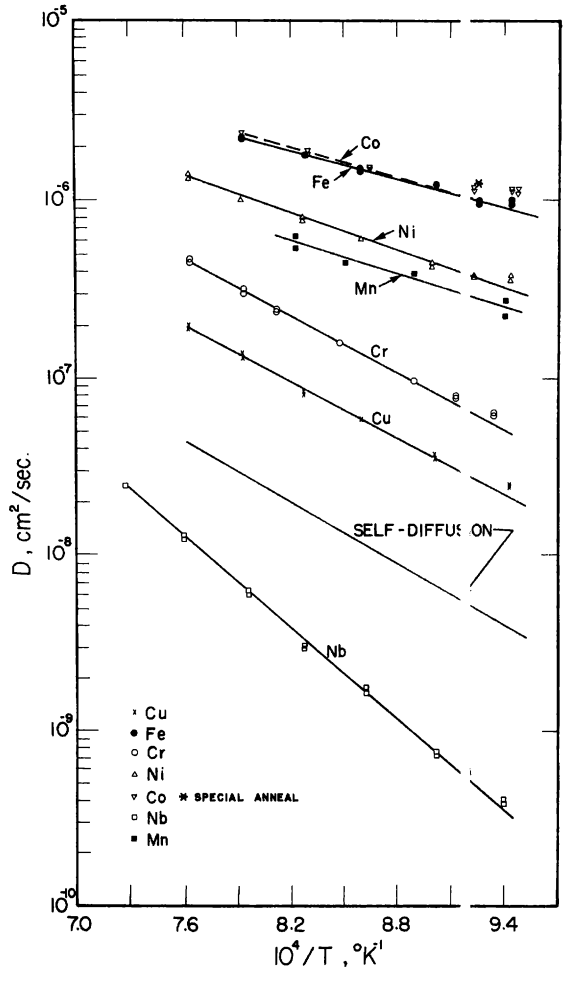

Macro 38145

[188]Kidson, G. V., On the Anomalous Self-diffusion in Zr, Can. J. Phys. 41 1563 (1963).

corrected temperatures in Figure 169, and the corrected activation energies and pre-exponential factors are listed in Table LXII. A final report on this work is in preparation.

Table LXII

PARAMETERS FOR TRACER DIFFUSION IN GAMMA URANIUM

Diffusing Element	Activation Energy (kcal/mole)	D_0 (cm^2/sec)
U	26.5	1.12×10^{-3}
Cr	24.46 ± 0.43	$5.47^{+1.04}_{-0.87} \times 10^{-3}$
Mn	13.88 ± 1.66	$1.81^{+1.95}_{-0.94} \times 10^{-4}$
Fe	12.01 ± 0.34	$2.69^{+0.43}_{-0.37} \times 10^{-4}$
Co	12.57 ± 0.58	$3.51^{+0.95}_{-0.75} \times 10^{-4}$
Ni	15.66 ± 0.35	$5.36^{+0.86}_{-0.74} \times 10^{-4}$
Cu	24.06 ± 0.40	$1.96^{+0.35}_{-0.30} \times 10^{-3}$
Nb	39.65 ± 0.50	$4.87^{+1.18}_{-0.94} \times 10^{-2}$

3. Diffusion of Palladium in Copper, Silver, and Palladium (N. L. Peterson)

Publication:

N. L. Peterson, Diffusion of Palladium in Copper and Silver, Phys. Rev. 132 2471 (1963)

Palladium Diffusion in Silver and Copper: Theoretical considerations and preliminary experimentation on diffusion of tracer amounts of palladium in copper and silver were presented in the 1962 Annual Report (ANL-6677). This work has been completed during the past year, and the results are described in the above publication. Two measurements of the diffusion coefficient, D, were made at each of eight different temperatures for diffusion of Pd^{103} in single crystals of copper and silver. The temperature dependence of D may be represented by

$$D_{Pd \rightarrow Ag} = 9.57^{+1.63}_{-1.37} \exp[-(56{,}752 \pm 300)/RT] \text{ cm}^2/\text{sec},$$

and

$$D_{Pd \rightarrow Cu} = 1.71^{+0.23}_{-0.21} \exp[-(54{,}370 \pm 300)/RT] \text{ cm}^2/\text{sec},$$

where R is the gas constant, T is the temperature in °K, and the errors are standard errors from the least-squares treatment of the data.

The differences in activation energy, ΔQ, between self-diffusion and impurity-diffusion of palladium in silver and copper as calculated from the LeClaire theory[189] are 7.4 and 11.0 kcal/mole, respectively. The corresponding experimental values of ΔQ are 12.6 and 7.3 kcal/mole. One may conclude from this that the electrostatic potential due to an electronegative impurity dissolved in a noble metal cannot be described by the Thomas-Fermi potential.

From Lidiard's theory[190] on the influence of solutes on self-diffusion in metals, one can calculate the correlation factor, f_i, for impurity-diffusion of palladium in silver from the data of Nachtrieb et al.[191] on tracer-diffusion of silver in several Ag-Pd alloys, and the present data on diffusion of palladium in silver. This calculation yields $f_i = 0.96$ and 0.98 at 1203 and 1023°K, respectively. Mullen[192] has shown

$$f_i = 1 - \frac{f_0[D_i/D_s(0)](W_0/K_2)}{(W_1/W_3) + 3.5F},$$

where f_0 is the correlation factor for self-diffusion, D_i is the diffusion coefficient of the impurity in the pure solvent, $D_s(0)$ is the self-diffusion coefficient of the solvent in the pure solvent, W_0 is the rate of exchange of solvent-vacancy when neither the vacancy nor the solvent is a nearest neighbor of the impurity, K_2 is the rate of exchange of solvent-vacancy when only the solvent atom is a nearest neighbor of an impurity, W_1 is the rate of exchange of solvent-vacancy when both the solvent and the vacancy are nearest neighbors of the impurity, W_3 is the rate of exchange of solvent-vacancy when only the vacancy is a nearest neighbor of the impurity, and F is a factor dependent only on W_0/K_2. Using Manning's[193] values of F as a function of W_0/K_2 and the data for the other terms at 1000°K, one finds that W_0/K_2 must be greater than 2.2 for diffusion of palladium in silver. This corresponds to a repulsion between the impurity and a vacancy in the second coordination shell, because the K_2 jump, which would bring the vacancy and impurity together, is less likely than any other jump. The sign of ΔQ and the magnitude of f_i suggest a repulsive

---

[189]LeClaire, A. D., On the Theory of Impurity Diffusion in Metals, Phil. Mag. 7 141 (1962).

[190]Lidiard, A. B., The Influence of Solutes on Self-diffusion in Metals, Phil. Mag 5 1171 (1960).

[191]Nachtrieb, N. H., Petit, J., and Wehrenberg, J., Self-diffusion of Silver in Silver-Palladium Alloys, J. Chem. Phys. 26 106 (1957).

[192]Mullen, J. G., Isotope Effect in Intermetallic Diffusion, Phys. Rev. 121 1649 (1961).

[193]Manning, J. R., Correlation Factors for Impurity-diffusion-fcc Lattice, Phys. Rev. 128 2169 (1962).

interaction between the impurity and a vacancy in the first coordination shell. Recent work by Hamaguchi[194] on quenched-in vacancies in Ag-2% Pd alloys suggests an attractive force between vacancies and palladium ions; our results do not support this view.

Self-diffusion in Palladium: The work on diffusion of Pd^{103} in single crystals of palladium has been completed at eight temperatures (2 more temperature points are planned). The preliminary results may be represented by

$$D = 0.1 \exp(-62{,}000/RT) \text{ cm}^2/\text{sec}.$$

The Isotope Effect in Self-diffusion in Palladium: The initial proposal to measure diffusion of Pd^{103} in single crystals of palladium has been extended to measure the simultaneous diffusion of Pd^{103} and Pd^{112}. The significance of this experiment may best be shown by the following discussion of the relationship between the correlation factor and the isotope effect.

Schoen[195] defined the strength of the isotope effect, E, by the equation

$$E = \frac{(D_b/D_a) - 1}{(m_a/m_b)^{1/2} - 1},$$

where D_a and D_b are the diffusion coefficients of isotopes of the same element with atomic weights m_a and m_b, respectively. Schoen's paper implied that $E = f$, and Tharmalingam and Lidiard[196] have derived this relation theoretically, although its validity is now in doubt. Using Vineyard's formulation of rate theory[197] Mullen[192] showed that in general

$$E = \Delta K f,$$

where ΔK is the fraction of the translational kinetic energy of the activated complex which is possessed by the jumping atom when it is at the height of the potential barrier. Previous experiments on the isotope effect have been done for impurity-diffusion, and ΔK was assumed to be unity in calculating f. In the case of self-diffusion in a pure metal, when

---

[194]Hamaguchi, Y., Quenched-in Vacancies in Solid Solution Alloys, J. Phys. Soc. Japan 16 1692 (1961).

[195]Schoen, A. H., Correlation and the Isotope Effect for Diffusion in Crystalline Solids, Phys. Rev. Letters 1 138 (1958).

[196]Tharmalingam, K., and Lidiard, A. B., Isotope Effect in Vacancy Diffusion, Phil. Mag. 4 899 (1959).

[197]Vineyard, G. H., Frequency Factors and Isotope Effects in Solid-State Rate Processes, J. Phys. and Chem. Solids 3 121 (1957).

the jump frequencies of all the atoms are substantially the same, the correlation factor can be calculated theoretically. Hence an experimental determination of E for self-diffusion will evaluate ΔK.

The experimental techniques developed by Mullen[192] for the determination of E are being used in this experiment. Very thin layers of Pd^{103} and Pd^{112} are deposited on the same surface of a single crystal of palladium. After annealing, the sample is sectioned, and the activity due to each isotope is counted in each section. The solution of the diffusion equation for this geometry of the sample gives

$$\ln C_a/C_b = \text{const.} + [1 - (D_b/D_a)]\, x^2/4D_bt,$$

where x is the distance of the layer from the original interface, C is the activity of the isotope in the layer, and t is the time of the diffusion anneal. By determining D_b first, the quantity $[1 - (D_b/D_a)]$, and hence E, can be obtained from a plot of $\ln D_a/D_b$ versus x^2. By determining D_a/D_b to 0.1%, one obtains ΔK to within 3% for these isotopes. Techniques have been developed for determining C_a/C_b to 0.1%; however, troubles were encountered in trial runs because of impurities in the Pd^{112}. The Pd^{112} was made by an $U(\alpha,f)Pd^{112}$ reaction with 40-MeV α particles, and it is extracted by chemical means from the uranium and other fission fragments. Recently, the Pd^{112} has been purified so that a linear decay curve is obtained over 10 half-lives, and experiments to obtain ΔK are currently in progress.*

The isotope effect for diffusion of palladium in copper and silver will be measured also. Once the value of ΔK for palladium is obtained, f_i will be calculated for diffusion of palladium in copper and silver, and compared with the values obtained from Lidiard's theory and the previous measurements. This should be a good test of the Lidiard theory of the effects of impurity on self-diffusion in metals.

4. The Diffusion of Zinc in, and the Conductivity of, Pure and Zn-doped NaCl Single Crystals** (S. J. Rothman, L. W. Barr,† A. H. Rowe,† and P. G. Selwood†)

The predominant equilibrium point defects in alkali halides are generally considered to be cation and anion vacancies (Schottky defects).[198] The concentration of these defects obeys a mass action law:

*The chemical separation of Pd^{112} has been developed and performed by John Hines of the Chemistry Division.

**This work was done in the Solid State Physics Division, AERE, Harwell, Berks. England, during a year's leave by the first author partially supported by a National Science Foundation Fellowship.

†Solid State Physics Division, AERE, Harwell, Berks. England.

[198]Lidiard, A. B., "Ionic Conductivity" in Handbuch der Physik, edited by S. Flügge, Vol. XX, Part 2, pp. 246-349, Springer-Verlag, Berlin, 1957.

$$c_v a_v = K_s = (c_v^0) = \exp(-G_f/RT)$$

$$= \exp(S_f/R)\exp(-H_f/RT), \tag{1}$$

where c_v and a_v are the atomic fractions of cation and anion vacancies which are unassociated, respectively, K_s is the equilibrium constant, c_v^0 is the concentration of cation vacancies in an absolutely pure crystal, G_f, S_f, and H_f are the Gibbs free energy, entropy, and enthalpy of formation of one mole of Schottky defects, R is the gas constant, and T is the absolute temperature.

If a divalent cation, such as Zn^{++}, is introduced into the NaCl lattice, a cation vacancy also will be introduced to keep the crystal electrically neutral. That is, if c_b is the concentration of Zn^{++},

$$c_b + a_v = c_v. \tag{2}$$

Further, since Zn^{++} has a positive charge and a cation vacancy a negative one, they will be attracted to each other and form associated pairs, i.e., a Zn^{++} ion with a cation vacancy on a nearest neighbor site. The concentration of these pairs, c_p, also obeys a mass action law:

$$\frac{c_p}{(c_v - c_p)(c_b - c_p)} = 12 \exp \frac{G_a}{RT}, \tag{3}$$

where G_a is the free energy of association, and the number 12 arises from the 12 possible orientations of an associated pair.

Since an associated vacancy is not the same species as a free vacancy, equation (1) must be modified to

$$(c_v - c_p)\, a_v = K_s = (c_v^0)^2. \tag{1a}$$

The diffusion of cations in alkali halides takes place by the jump of a cation into a nearest-neighbor vacancy. Therefore the diffusion coefficient of Zn^{++}, D, is proportional to c_p,[198] or

$$D = \frac{1}{3} a^2 w_2 f p, \tag{4}$$

where a is the anion-cation separation, w_2 is the jump frequency of Zn^{++}, f is the correlation factor,[198] and p is the degree of association, which is defined by

$$p \equiv c_p/c_b. \tag{5}$$

When $c_b << c_v^0$, from equations (1) and (2)

$$c_v = c_v^0 + \frac{1}{2} c_b. \tag{6}$$

Since at low concentrations, at which association is negligible, D is proportional to c_v,

$$D = D^0 \left(1 + \frac{c_b}{2c_v^0} \right), \tag{7}$$

where D^0 is the diffusion coefficient at zero concentration of the diffusing isotope.

The temperature dependence of D in a "pure" crystal is given by

$$D = D_0^p \exp (- Q_p/RT), \tag{8}$$

where D_0^p is a pre-exponential multiplier, and Q_p is given by[189]

$$Q_p = \frac{1}{2} H_f - H_A + H_m - C. \tag{9}$$

Here H_m is the activation energy for a w_2 jump, H_A is the enthalpy of association, and

$$C = R \frac{\partial \ln f}{\partial (1/T)}. \tag{10}$$

The temperature dependence of D in a heavily doped crystal is given by

$$D = D_0^s \exp (- Q_s/RT), \tag{11}$$

where D_0^s is a pre-exponential multiplier and

$$Q_s = H_m - C. \tag{12}$$

Conductivity in NaCl is due to the motion of cation vacancies. In a pure crystal, the conductivity, σ, in the intrinsic range, i.e., the temperature range in which $c_v^0 >> c_{bo}$ (the concentration of residual impurities), is given by

$$\sigma = \frac{a^2 e^2}{kT} \exp\left(\frac{S_f}{2R}\right) \exp\left(-\frac{H_f}{2RT}\right) \nu_1 \exp\left(-\frac{H_m^0}{RT}\right), \tag{13}$$

where e is the charge of the electron, k is Boltzmann's constant, H_m^0 is the activation energy, and ν_1 is the frequency factor for the jump of a Na^+ into a neighboring cation vacancy. In the extrinsic region, the temperature range where $c_{bo} >> c_v^0$,

$$\sigma = \frac{a^2e^2}{kT} c_{bo} \nu_1 \exp\left(-\frac{H_m^0}{RT}\right), \tag{14}$$

or in a crystal heavily doped with zinc,

$$\sigma = \frac{a^2e^2}{kT} (c_b - c_p) \nu_1 \exp\left(-\frac{H_m^0}{RT}\right). \tag{15}$$

In a heavily doped crystal, there is another temperature range, below the extrinsic region, in which the conductivity decreases more rapidly due to precipitation of the dopant and consequent disappearance of the vacancies. By finding the temperature at which this region begins as a function of concentration, the solubility of the dopant can be determined.[199]

Equations (9) and (12) through (15) assume that ν_1, H_m^0, and w_2 are independent of concentration.

The preceding formulae show that:

1. From measurements of σ as a function of temperature for "pure" crystals, H_f, H_m^0, and S_f can be determined from equations (13) and (14).

2. With this H_f and the value H_m - C, which is determined from the measurements of D in highly doped crystals, H_a can be found.

3. By measuring D, or σ, as a function of c_b and comparing the experimental curves with the theoretical curves, one can find G_a and c_v^0 by using equations (1a), (2), (3), (4), (13), and (15).

4. By carefully analyzing the penetration plots for the tracer diffusion of zinc in pure or lightly doped crystals, one can find c_v^0 from equation (7). Further, D as a function of c_b can be determined for a whole range of concentrations in one experiment if the crystals are doped to a fairly high concentration of $Zn^{65}Cl_2$ and then annealed in a vacuum to cause out-diffusion of the zinc.

The first of the above measurements has been done for NaCl by several other workers.[200,201] Since the present measurements did not

---

[199]Haven, Y., The Solubility of MgF_2 in Solid LiF, Rec. Trav. Chim. Pays-Bas 69 1505 (1950).

[200]Etzel, H. W., and Maurer, R. J., The Concentration and Mobility of Vacancies in NaCl, J. Chem. Phys. 18 1003 (1950).

[201]Dreyfus, R. W., and Nowick, A. S., Ionic Conductivity of Doped NaCl Crystals, Phys. Rev. 126 1367 (1962).

extend over a wide-enough temperature range, because of low conductivity at low temperatures and creep at high temperatures, the values of other workers for H_f and H_m^0 have been accepted, although the present work shows that c_V^0 is lower than reported by them. The measurements 3, and 4, including out-diffusion of zinc, have been made, but the analyses of σ as a function of c_b and the analyses of the individual penetration plots are not complete yet.

Experimental:

Materials: Harshaw single crystals of NaCl were used, except in two runs, wherein Hilger-Watts crystals, which are less pure, were used. Some of the crystals were doped with zinc by holding them in an atmosphere of reagent-grade $ZnCl_2$ vapor. The homogeneity of the doping was checked by doping some crystals with $Zn^{65}Cl_2$ under similar conditions and was found to be satisfactory. The zinc concentration in the doped crystals was determined polarographically; the estimate of total error, including sampling errors, is 10%.

Diffusion: The thin layer-sectioning method[202] was used. $Zn^{65}Cl_2$ was deposited by evaporation, and the sections were counted in a well-type scintillation counter. The counter efficiency was calibrated with a Zn^{65} source of known strength, so that specific activities in undoped crystals could be converted into mole fractions of $ZnCl_2$. Sectioning was done with a microtome, and distances along the sample were calculated from the chip weights, the crystal area, and the room-temperature density of NaCl. The density was not corrected for temperature or zinc concentration. By moistening the sample surface, chip losses were cut to an average of $<2\%$. Maximum chip loss was 4%. The estimated error in D is 5%,* with an additional error due to a $\pm 4°$ uncertainty in the temperature.

Conductivities were measured with a Wayne-Kerr AC bridge.

Results and Analyses:

Diffusion of Zinc in Pure and Lightly Doped NaCl: For diffusion from a thin layer into a semi-infinite solid, the solution of the diffusion equation is

$$c = \frac{M}{\sqrt{\pi Dt}} \exp\left(-\frac{x^2}{4Dt}\right), \qquad (16)$$

*The estimated error of 5% applies to the crystals for which the penetration plots are straight (vide infra). For curved penetration plots, the error in D is more likely to be 10%.

[202] Tomizuka, D. T., "Diffusion" in Methods of Experimental Physics, edited by Johnson, V. and Lark-Horovitz, K., Vol. 6, pt. A, p. 364. Academic Press, New York (1959).

where c is the concentration of zinc at distance x from the surface, M is the amount of zinc deposited on the surface, and t is the time of the anneal. In other words, a plot of log c versus x^2 should be linear. Penetration plots for pure and lightly doped crystals annealed at temperatures between the conductivity knee and about 1003°K are curved (see Figure 170, curve 1). This is because equation (16) holds only for a diffusion coefficient which is independent of concentration, whereas in this case the diffusion coefficient varies with concentration [see equation (7)], and this variation can be neglected only when $c_V^0 >> c_{Zn}$.* Although a fair diffusion coefficient for $c_V^0 >> c_{Zn}$ can be calculated from the straight-line tail of the penetration plot, it would be more satisfying to solve the differential equation completely and to get an independent value of c_V^0 by fitting the solution to the penetration plots which are determined experimentally. Unfortunately, the solution is difficult because the initial condition is mathematically a Dirac delta function, and, ergo, the Boltzmann transformation[203] cannot be used. Numerical computations are being carried out now with the Pace Analogue Computer,** and preliminary results indicate that D at 912°K is the same as the D calculated from the straight-line portion of the penetration plots, and c_V^0 is about 5×10^{-6}.

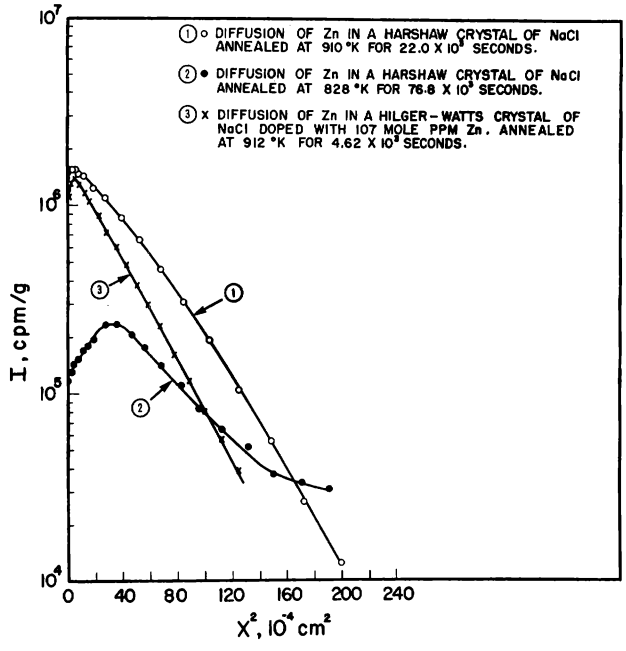

Figure 170

Penetration Plots for the Diffusion of Zinc in NaCl

Macro 38144

*Here c_V^0 means the sum of thermal vacancies and residual impurity vacancies. At T = 900°K, the latter amount to a few percent of the former.

**These calculations are being done at ANL by Messrs. N. F. Morehouse and L. Bryant.

[203]Crank, J., The Mathematics of Diffusion, Oxford University Press, Oxford (1956).

Samples annealed at temperatures below the knee of the conductivity curve had unusual penetration plots (see Figure 170, curve 2), from which no diffusion coefficient could be calculated. There is evidently something besides "honest" diffusion going on here. All penetration plots showed a decrease of activity near the surface due to evaporation of the zinc.

From a plot of the values of D from the straight-line portions of the penetration plots versus 1/T (lower line of Figure 171), the diffusion of zinc in pure NaCl was found to be given by

$$D = 2 \times 10^{-2} \exp\left(-\frac{23{,}800 \text{ cal/mole}}{RT}\right) \text{cm}^2/\text{sec.}$$

Figure 171. Arrhenius Plots for the Diffusion of Zinc in Pure and Heavily Doped NaCl

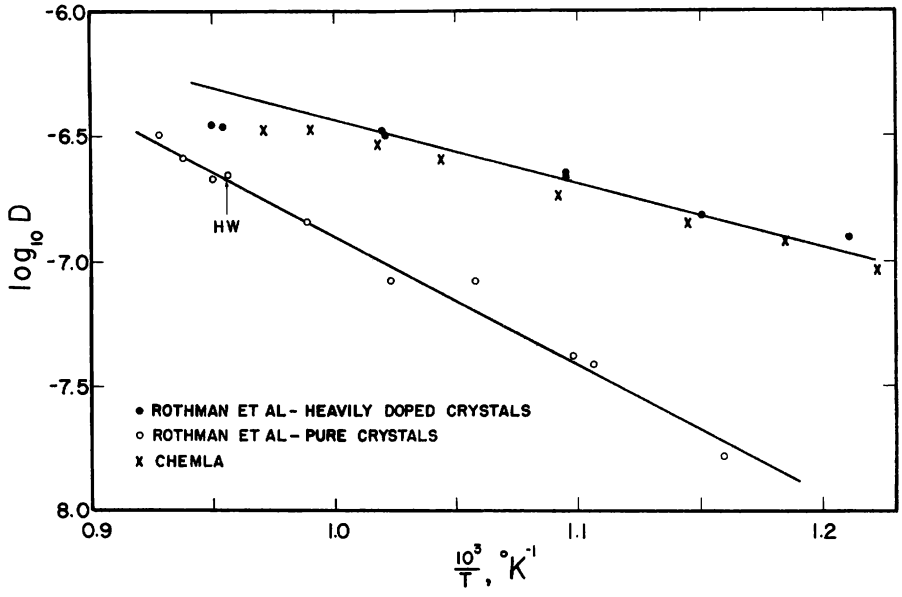

Macro 37704

Diffusion in Heavily Doped NaCl Crystals: Figure 170, curve 3, a typical penetration plot, shows that there are no problems of diffusion coefficients depending upon concentration here. From the upper line of Figure 171,

$$D = 1.4 \times 10^{-4} \exp\left(-\frac{11{,}800 \text{ cal/mole}}{RT}\right) \text{cm}^2/\text{sec.}$$

The pronounced curvature at high temperatures in this plot is probably due to the nonexponential dependence of c_p on 1/T at high c_b (see Figures 172 and 173, or Figure 54 of reference 198).

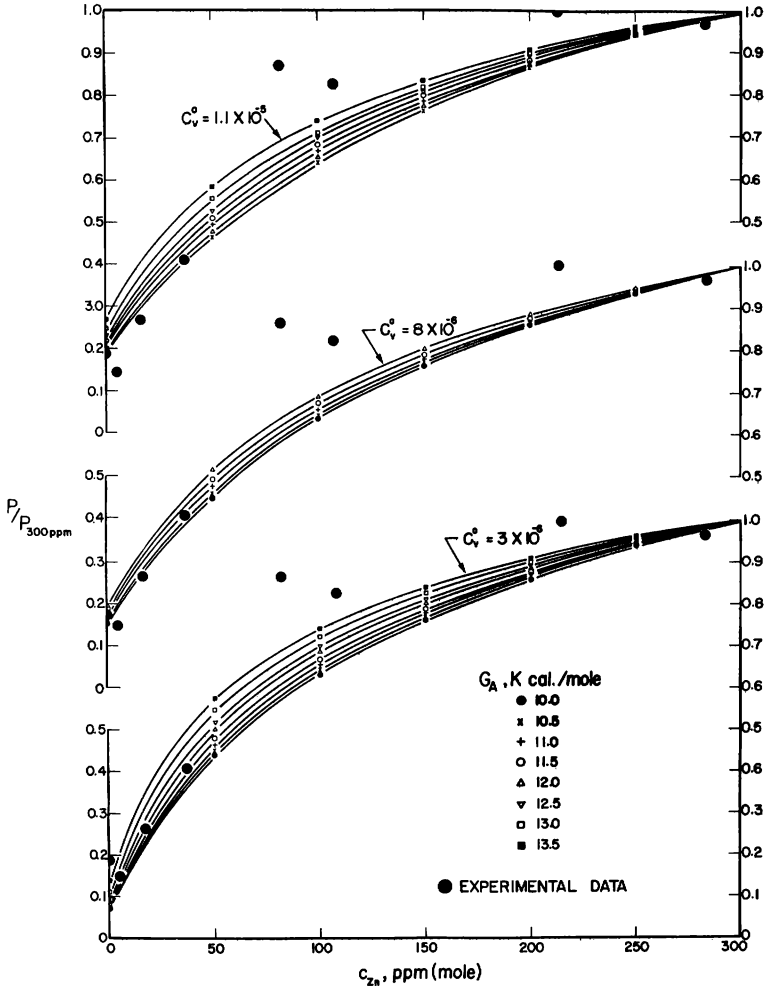

Macro 38146

Figure 172

Plot of p/p_{300} versus c_{Zn} for Diffusion at 912°K, for Different Values of G_a and c_v^0

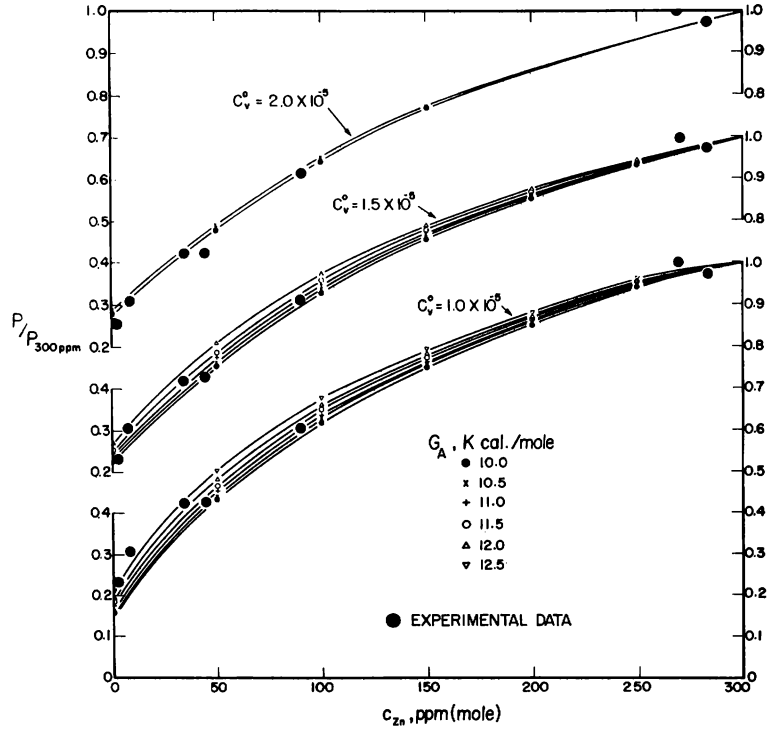

Macro 38143

Figure 173

Plot of p/p_{300} versus c_{Zn} for Diffusion at 976°K, for Different Values of G_a and c_v^0

By means of equations (8), (9), (11), (12), and the value of H_f from reference 200,

$$H_a = 12{,}400 \text{ cal/mole.}$$

Diffusion of Zinc as a Function of Concentration of Zinc Dopant: Figure 172 shows experimental points and theoretical curves of $p/p_{100\,ppm}$ ($\approx D/D_{max}$) for the diffusion of Zn^{65} in pure and doped NaCl at 912°K for different values of G_a and c_v^0. Figure 173 shows the same type of plots, but for diffusion at 976°K. The interactions of unassociated defects,[198] as well as thermal disorder, were included in the calculations.* Three things are notable about these curves:

1. At low c_b the experimental points agree very well with the theoretical curves calculated for $c_v^0 = 8 \times 10^{-6}$ and $G_a = 11.0 \pm 0.5$ kcal/mole at 912°K, and $c_v^0 = 1.5 \times 10^{-5}$ and $G_a = 10.5 \pm 0.5$ kcal/mole at 976°K.

2. Inclusion of thermal disorder in the calculation enables estimation of the value of c_v^0.

3. The experimental points deviate from the theoretical curves at high c_b for diffusion at 912°K.

The first point is gratifying, since the association energy is not in bad agreement with the enthalpy calculated before. Unfortunately, proper enthalpies cannot be calculated because of the inaccuracy of the estimates of G_a. Further, the values of c_v^0 obtained from these curves support the values obtained from the analogue calculations, which are lower than the values given in references 200 and 201.

The third point has not been analyzed yet. The deviation at 50 ppm $< c_b <$ 200 ppm, and perhaps the fact that the D at the highest c_b is lower at both temperatures than the D at the next highest c_b (the difference, ~3%, is within experimental error), may be due to the formation of higher-order, immobile complexes.

Out-diffusion: The results of the out-diffusion run, which is finished, are shown in Figure 174. The diffusion coefficient is measured from such experiments by the Matano method,[203] i.e., constructing tangents and measuring areas, which means that these values of D are not very accurate, especially at c_b near zero. Further, they are not the same thing as a tracer-diffusion coefficient which is measured in a homogeneously doped crystal:[204]

*These calculations were programmed for the IBM 704 by Mrs. Ruth Fu, ANL.

[204]Darken, L. S., Diffusion Mobility, and Their Interrelation through Free Energy in Binary Metallic Systems, Trans. AIME 175 184 (1948).

$$D_{\text{out-diffusion}} = D_{\text{tracer}}\left(1 + \frac{\partial \ln \gamma_{Zn}}{\partial \ln c_{Zn}}\right),$$

where γ is the activity coefficient. The agreement between D obtained this way and the tracer D is not bad, indicating that the thermodynamic factor is not much larger than the experimental error.

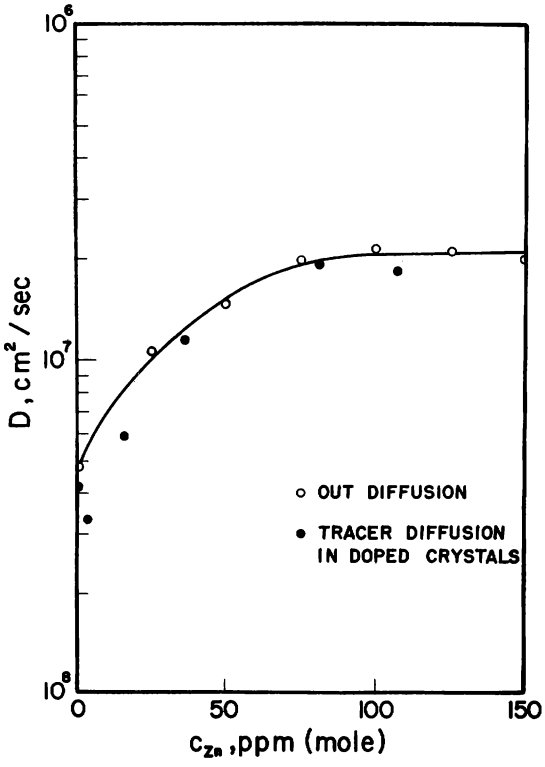

Macro 38148

Figure 174

Plot of D versus c_{Zn} for Diffusion at 912°K

Comparison with the Literature: Two recent papers[205,206] have reported similar studies, and the general trends of the present work agree with theirs. D_{Zn} in NaCl was measured by Chemla,[207] and the results he reported for tracer-diffusion of zinc in NaCl agree with the present results for heavily doped NaCl (see Figure 171, upper curve). This may be due to the presence of large amounts of divalent impurities in Chemla's NaCl (he grew the crystals himself and reported neither analyses nor conductivities), or to his having put on an immense amount of zinc, which is not unlikely since he used an isotope of low specific activity and assayed it with an ordinary Geiger-Mueller counter - an inefficient method for gamma rays.

---

[205] Keneshea, F. J., Jr. and Fredericks, W. J., Diffusion of Lead Ions in KCl, J. Chem. Phys. 33 1952 (1963).

[206] Hanlon, J., Diffusion of Cd in Pure and Cd Doped AgBr, J. Chem. Phys. 32 1492 (1960).

[207] Chemla, M., Diffusion d'Ions Radioactifs dans les Cristaux, Ann. Chim. Phys. 1 959 (1956).

Conclusions:

1. D_{Zn} in pure (Harshaw) single crystals of NaCl is given by

$$D = 2 \times 10^{-2} \exp\left(-\frac{23{,}800 \text{ cal/mole}}{RT}\right) \text{cm}^2/\text{sec.}$$

2. D_{Zn} in NaCl doped with more than 150 molar ppm of Zn is given by

$$D = 1.4 \times 10^{-4} \exp\left(-\frac{11{,}800 \text{ cal/mole}}{RT}\right) \text{cm}^2/\text{sec.}$$

3. The enthalpy of association between Zn^{++} and a cation vacancy in NaCl is about 12.4 kcal/mole.

5. Effect of Magnetic Order on Diffusion (N. L. Peterson)

The theoretical background for this program and the torsion pendulum apparatus for the proposed experiments were discussed in the Annual Reports for the last two years (ANL-6516 and ANL-6677). Preliminary experiments on the internal friction of specimens of a Cu-30 a/o Zn alloy have been conducted during the past year to test the equipment. These measurements yielded a background energy absorption of $Q^{-1} = 2 \times 10^{-4}$, indicating that the problems associated with building vibrations have been overcome. Initial measurements with alloys of Co-20 a/o Mn and Co-40 a/o Mn should begin in the near future.

E. Alloying Properties

1. Occurrence and Structures of Intermediate Phases in Transition Metal Systems (A. E. Dwight, J. B. Darby, Jr., D. J. Lam, and M. V. Nevitt)

Publications:

A. E. Dwight, R. A. Conner, Jr., and J. W. Downey, G Phases Containing Scandium, Nature 197 587 (1963).

J. B. Darby, Jr., L. J. Norton, and J. W. Downey, A Survey of the Binary Systems of Technetium with Group VIII Transition Elements, J. Less-Common Metals 5 397 (1963).

J. B. Darby, Jr., J. W. Downey, and L. J. Norton, Intermediate Phases in the Tantalum-Palladium System, Trans. of the Met. Soc. 227 1028 (1963).

J. B. Darby, Jr., The CsCl-type Ordered Structure in VMn, Trans. of the Met. Soc. 227 1460 (1963).

M. V. Nevitt, Alloy Chemistry of Transition Elements in "Electronic Structure and Alloy Chemistry of Transition Elements," P. A. Beck, Ed., John Wiley and Sons, New York (1963).

Equiatomic Compounds (A. E. Dwight): Table LXIII lists the equiatomic compounds which were studied in 1963. Among them are 14 examples of the Bf (CrB-type) structure. This is an orthorhombic structure with a radius ratio ranging from 1.1 to 1.5. Characteristically, the A partner comes from the Ca, Sc, or Ti group, and the B partner from the Fe, Co, Ni, Al, or Si group. The newly found examples of the Bf structure meet this requirement.

Also in Table LXIII are listed 17 examples of the B27 (FeB-type) structure. Like the Bf structure, the B27 is found in alloys having a large radius ratio (1.18-1.45). The A partner is a member of the Sc or Ti group, and the B partner is of the Ni, Cu, or Si group. The factor which controls the choice between a Bf and B27 structure is as yet unknown.

The study of Bf and B27 structures was extended into ternary systems to examine the miscibility of phases having the same crystal structure and to study the tolerance to substitution of third elements. HfPt and HfNi, both Bf structures, appear to be completely miscible. Two alloys having the B27 structure, ErNi and ErPt, also appear miscible. In contrast, HfNi and GdNi, both Bf structures, have only slight solubility for each other. The limited ternary data now available suggest that

miscibility between two binary Bf (or two B27) compounds may be expected only when the electron-atom ratios of the two binary compounds are nearly identical.

Table LXIII

INTERMETALLIC COMPOUNDS STUDIED IN 1963

A Element(s)*	B Element(s)*	Lattice Parameters				Type	A Element(s)*	B Element(s)*	Lattice Parameters				Type
		a_0 (Å)	b_0 (Å)	c_0 (Å)	c/a				a_0 (Å)	b_0 (Å)	c_0 (Å)	c/a	
Sm	Pt_2	7.662				C15	Dy	Pt[1]	7.118	4.45	5.47		B27
Tb	Pt_2	7.613				C15	Ho	Pt	6.951	4.470	5.532		B27
Ho	Pt_2	7.586				C15	Er	Pt	6.904	4.453	5.512		B27
Tb	Ir_2	7.531				C15	Tm	Pt	6.855	4.446	5.496		B27
Dy	Ir_2	7.517				C15	Lu	Pt	6.810	4.417	5.479		B27
Tm	Ir_2	7.460				C15	Lu_3	Hf_2 Ni_5	3.245				B2
Lu	Ir_2	7.460				C15		Er_2 Pd Ru	3.409				B2
Tb	Os_2	5.31		8.80	1.66	C14		Y_2 Pd Ru	3.444				B2
Ho	Os_2	5.30		8.76	1.65	C14		Tm Ru	3.373				B2
U	Ni Ru	7.227				C15		Tm Au	3.520				B2
U_2	Ni_3 Rh	7.163				C15		Tm Au[2]	3.516				B2
La	Ni	3.907	10.809	4.396		Bf		Sm Rh	3.475				B2
Ce	Ni	3.788	10.556	4.366		Bf		Gd Rh	3.439				B2
Pr	Ni	3.816	10.503	4.354		Bf		Tb Rh	3.418				B2
Nd	Ni	3.803	10.461	4.339		Bf		Ho Rh	3.387				B2
Sm	Ni	3.776	10.358	4.291		Bf		Ho Ir	3.383				B2
Gd	Ni	3.776	10.316	4.244		Bf		Ti Pd	4.562	2.810	4.89		B19
La	Rh	3.986	11.144	4.245		Bf		Ti Pt	4.592	2.761	4.838		B19
Ce	Rh	3.852	10.986	4.152		Bf		V Pt	4.413	2.707	4.747		B19
Pr	Rh	3.905	10.910	4.210		Bf		V Pt[3]	4.42	2.69	4.76		B19
Nd	Rh	3.890	10.839	4.247		Bf		Nb Pt	4.616	2.784	4.976		B19
La	Pt	3.974	11.037	4.558		Bf		Nb Pt[4]	4.611	2.780	4.983		B19
Ce	Pt	3.921	10.920	4.524		Bf		Mo Pt	4.462	2.725	4.951		B19
Zr	Pt	3.409	10.315	4.277		Bf		Mo Pt[3]	4.47	2.74	4.89		B19
Hf	Pt	3.345	10.269	4.288		Bf		V_2 Ir Pt	3.850		3.763	0.977	Ll_0
Y	Ni	7.151	4.124	5.513		B27		V_{10} Ir_3 Pt_7	3.831				Ll_2
Dy	Ni	7.043	4.164	5.451		B27		Nb_2 Ir Pt	3.981				Ll_2
Dy	Ni[1]	6.895	4.319	5.353		B27		Hf_5 Ir_4 Os	3.32		6.23	1.88	B11
Ho	Ni	7.021	4.140	5.435		B27		Hf_{10} Ir_9 Re	3.56		6.12	1.72	B11
Er	Ni	6.991	4.114	5.418		B27		Hf_5 Ir_4 Ru	3.32		6.22	1.87	B11
Tm	Ni	6.959	4.099	5.398		B27	Ti_3	Hf_7 Ir_{10}	3.29		6.08	1.84	B11
Lu	Ni	6.912	4.073	5.366		B27	Sc	Hf_4 Ir_5	3.32		6.22	1.88	B11
Y	Pt	7.009	4.471	5.552		B27	Er	Hf_4 Ir_5	3.34		6.29	1.88	B11
Pr	Pt	7.294	4.560	5.698		B27	Lu	Hf Ir_2	3.36		6.36	1.89	B11
Nd	Pt	7.256	4.551	5.675		B27		Zr_{10} Ir_7 Os_3	3.33		6.31	1.89	B11
Sm	Pt	7.152	4.525	5.626		B27		V Pt_2	3.80	2.74	8.33		$MoPt_2$
Gd	Pt	7.088	4.502	5.590		B27		V Pt_2[3]	3.79	2.72	8.35		$MoPt_2$
Gd	Pt[1]	7.164	4.458	5.575		B27		Er Au_2	3.66		8.98	2.45	C11b
Tb	Pt	7.018	4.494	5.561		B27		Tm Au_2	3.64		8.96	2.46	C11b
Dy	Pt	6.983	4.478	5.544		B27		Lu Au_2	3.62		8.87	2.45	C11b

*The use of a stoichiometric ratio for a ternary alloy does not mean the composition range is restricted to that ratio, but that the indicated tructure and lattice parameters were found at that ratio.

(1)Baenziger, N. C., and Moriarty, J. L., Jr., Acta Cryst. 14 946 (1961).

(2)Chao, C. C., Luo, H. L., and Duwez, P., J. Applied Physics 34 1971 (1963).

(3)Schubert, K., et al., Naturwissenschaften 50 41 (1963).

(4)Giessen, B. C., and Grant, N. J., submitted to AIME (1963).

When HfPt (Bf) and TmPt (B27) are alloyed together, a two-phase mixture results. A ternary B2 (CsCl-type) compound is obtained by alloying HfNi (Bf) with LuNi (B27).

It is tentatively concluded that neither a Bf nor B27 compound can tolerate extensive substitution by a third element except when the third element is very similar in electronic characteristics to a partner of the binary compound. On the other hand, the B2 structure occurs in

many ternary systems and, therefore, must be more tolerant of extensive substitution. The existence of a B2 structure in Er_2RuPd and Y_2RuPd are examples in which palladium and ruthenium synthesize the electron concentration of rhodium, and a structure identical to ErRh and YRh (B2) results.

The existence of an orthorhombic B19 structure was discovered in TiPt, TiPd, and NbPt, and confirmed in VPt and MoPt (see Table LXIII). TiPt and VPt form a continuous solid solution. When half the platinum in VPt is replaced by iridium, a compound with the Ll_0 (CuAu-type) structure is formed at 900°C. In the system $V_{10}Pt_7Ir_3$ has an Ll_2 (Cu_3Au-type) structure after heat treatment at 900°C. The Ll_2 structure was also found in Nb_2IrPt after heat treatment at 900°C.

Eight examples of a tetragonal B11 structure are listed in Table LXIII. The B11 structure is typically formed by a ternary substitution for a portion of either element in $Hf_{50}Ir_{50}$ (structure unknown).

Structure of VMn (J. B. Darby, Jr.): A recent paper on the V-Mn system[208] reports the occurrence of the CsCl-type ordered structure in the alloy $Mn_{47.8}V_{52.2}$ between 725 and 1150°C. The present X-ray investigation was carried out with an alloy having a calculated composition of 49.85 a/o V. When samples were homogenized at 900°C for three weeks, followed by a subsequent anneal at 700°C for six to seven weeks, and then water quenched or furnace cooled, the (100), (111), and (210) Kα superlattice lines were observed in films taken with Cr radiation. An a_0 of 2.904 ± 0.001 Å was determined by a Nelson-Riley extrapolation from a film taken with CuKα radiation.

Laves Phases (A. E. Dwight, J. B. Darby, Jr., and D. J. Lam): The occurrence of Laves phases was investigated in alloys in which the A element is a lanthanide and the B element is from the third long period. This is a continuation of earlier work on the first and second long periods, reported in the 1961 and 1962 Annual Reports. Figure 175 shows the binary and ternary alloys that were investigated. Together with other published data, our results permit us to enclose compositional areas within which a single Laves phase is stable. The area of $MgCu_2$-type stability is larger when the B element is from the third long period than when it is from the second. This difference is due to the fact that platinum forms Laves phases with the lanthanides but palladium does not.

Two ternary Laves phases, UNiRu and U_2Ni_3Rh, demonstrate the conversion of a C14-type phase, UNi_2, to a C15-type by replacement of part of the nickel by an element of lower group number.

---

[208] Waterstrat, R. M., Investigation of the Vanadium-Manganese Alloy System, Trans. of the Met. Soc. 224 240 (1962).

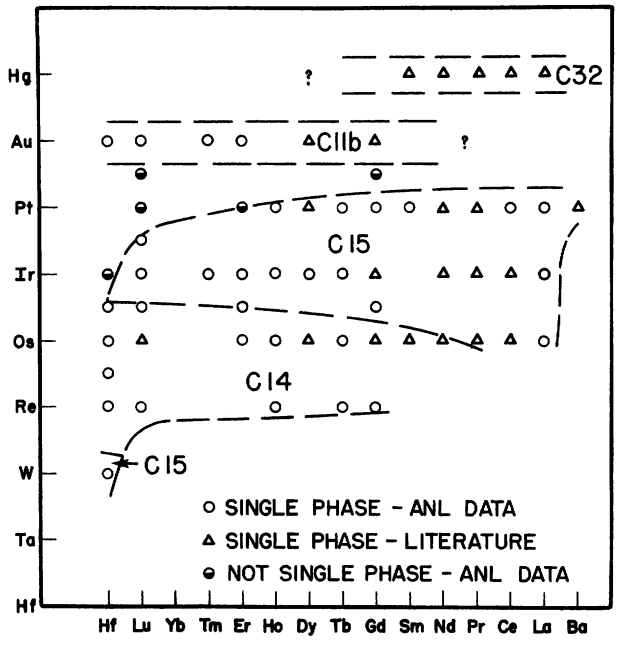

Macro 38153

Figure 175

Areas of Stability of Laves Phases between the Lanthanides as A Elements and B Elements from the Third Long Period

Complete miscibility of the Laves phases listed in Table LXIV has been confirmed by measurements of lattice parameters. Metallographic evidence of coring, as well as the scatter in the X-ray data, suggests that homogenization treatments should be extended to higher temperatures to eliminate segregation in some of the alloys.

Table LXIV

LAVES PHASES FOUND TO HAVE A COMPLETE RANGE OF SOLID SOLUBILITY

System	Isothermal Temperature, °C	Type of Laves Phases
$TaCo_2$-$TiCo_2$	1120	C-15
$TaCo_2$-$ZrCo_2$	900	C-15
$TaCo_2$-$NbCo_2$	1100	C-15
$HfOs_2$-$ZrOs_2$	1200	C-14
$HfRe_2$-$ZrRe_2$	1200	C-14

An investigation of the vertical section UFe_2-UAl_2 in the system U-Al-Fe is continuing. Although a major portion of this section has been established, a component of an apparent three-phase region has not been confirmed by X-ray metallography because it is present at a low volume concentration. Therefore, a portion of an isothermal section of the UFe_2-Al-UAl_2 diagram that should contain this unidentified phase is currently being investigated. In the absence of this information, it is uncertain whether this section is a quasi-binary.

Other systems which have been reported in previous Annual Reports are being examined more thoroughly.

Binary Systems Containing Technetium-99 (J. B. Darby, Jr.): The work on the occurrence and the identity of intermediate phases and solid solutions in binary systems of technetium with the other transition elements has been completed and published, as has a survey on the formation of Laves phases which occur when technetium is alloyed with several of the rare earths. The possibility of Laves phases occurring in the Tc-Th and Tc-U systems is currently being investigated.

A study of the intermediate phases in the systems Tc-Si and Tc-Al has provided the information shown in Table LXV.

Table LXV

STRUCTURES OF THE INTERMEDIATE PHASES IDENTIFIED IN THE Tc-Al AND Tc-Si SYSTEMS

Alloy	Crystal Structure	Structure Type
Tc_2Al	B.C. Tetragonal	C11b
$TcAl_{12}$	B.C.C.	(WAl_{12})
Tc_4Si	B.C.C.	A-2
Tc_3Si	B.C.C. (ordered)	$D8_2$
Tc_5Si_3	Tetragonal	D8m
TcSi	Cubic	B20

2. Thermodynamic Properties (K. M. Myles, A. T. Aldred, and J. B. Darby, Jr.)

Publications:

K. M. Myles, A Study of the Thermodynamic Properties of the Vanadium-Iron Alloy System, ANL-6657 (Feb. 1963).

J. B. Darby, Jr., D. B. Jugle, and O. J. Kleppa,* The Rate of Solution of Some Transition Elements in Liquid Aluminum, Trans. of the Met. Soc. 227 179 (1963).

J. J. Eichholz and J. B. Darby, Jr., Electronic Integrator for Use with a Differential Calorimeter, Rev. Sci. Instr. 34 1274 (1963).

*The University of Chicago. Consultant to Metallurgy Division.

Vapor Pressure Studies of Alloy Systems (K. M. Myles): The vapor pressure of chromium over solid vanadium-chromium alloys has been measured by the torsion-effusion method in the temperature range from 1450 to 1650°K. The chemical activities of chromium were computed from the vapor pressure data. The activities of vanadium were calculated from the activities of chromium by integrating the Gibbs-Duhem relationship. The free energies, entropies, and enthalpies of formation of the alloys have been determined from the activity values. As the activities of chromium and vanadium exhibit small negative deviations from ideality over the entire composition range, as seen in Figure 176; the integral excess free energies found at 1550°K, shown in Figure 177, are negative. The integral excess entropies and enthalpies of formation at 1550°K are also shown in Figure 177.

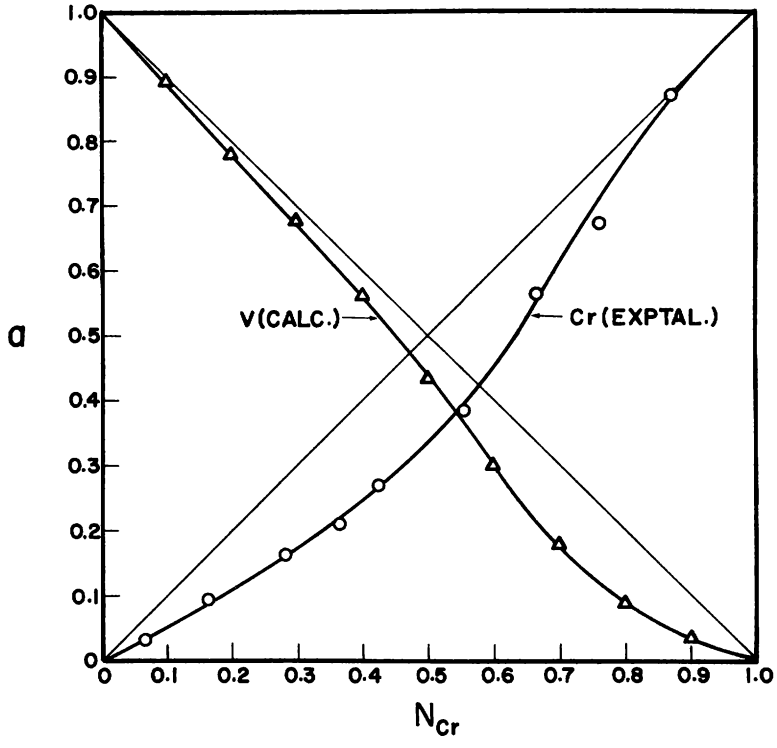

Macro 35792

Figure 176

The Activities of Chromium and Vanadium at 1550°K

Unfortunately, the small experimental uncertainties in the values of the vapor pressures tend to accumulate during the subsequent calculations of the thermodynamic properties. Thus, while the precision of the activities is estimated to be within ±3%, the excess free energies, and especially the excess entropies and enthalpies, are considerably less precise. Hence, the credibility of the excess entropies and enthalpies has been assessed on a theoretical basis in terms of the changes in the configurational, vibrational, and magnetic properties of vanadium and chromium that occur upon alloying. It has been concluded that the alloy system is characterized by negative enthalpies and small, probably negative, excess entropies of formation which are mainly of nonconfigurational origin.

Figure 177. Integral Excess Free Energies, Entropies, and Enthalpies of Formation of Solid Chromium-Vanadium Alloys at 1550°K

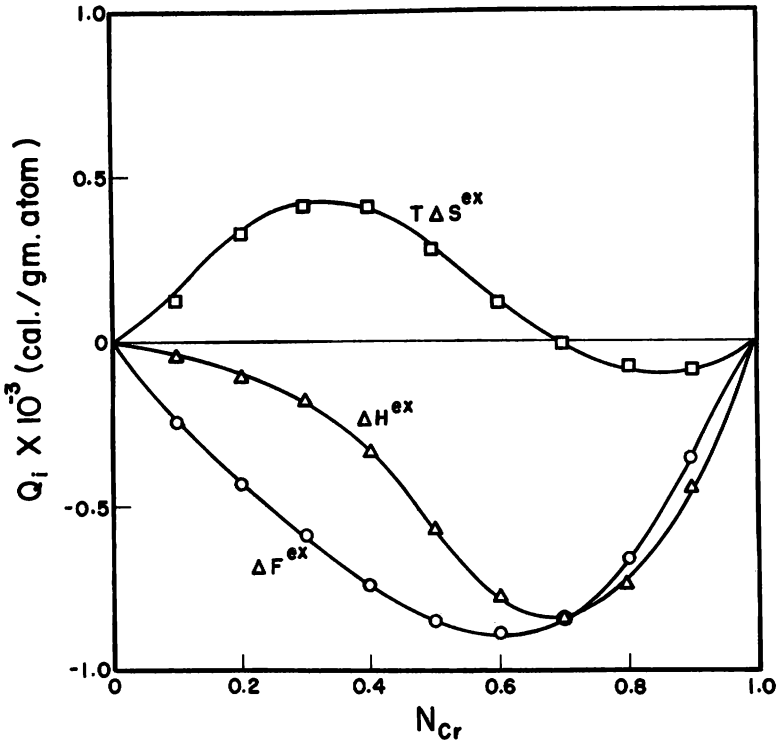

Macro 35791

An attempt has been made to determine the thermodynamic properties of solid vanadium-manganese alloys as a sequel to the studies made with solid vanadium-iron and vanadium-chromium alloys. Unfortunately, at the temperatures where the partial pressure of manganese is approximately 10^{-3} to 10^{-4} mm Hg (the pressure range of the apparatus), it has not been possible to obtain constant pressures within the cells containing the vanadium-rich alloys. The conclusion was reached that at these temperatures the diffusion rate of manganese in the alloys is considerably slower than the effusion rate. It is hoped that further investigation will produce a technique for circumventing this difficulty.

A study of the thermodynamic properties of solid nickel-platinum alloys has been initiated. The experimental effort, directed towards the measurement of the vapor pressure of nickel over the alloys, had proceeded smoothly in the nickel-rich alloys when, unexpectedly, completely implausible results were obtained for the platinum-rich alloys. The data for the latter alloys suggested that some contaminant was entering the effusion cell at the experimental temperatures, thereby creating a torque in opposition to that caused by the effusing nickel vapor. The extent of this counter-torque increased with platinum content. Chemical analyses of platinum samples failed to identify the nature of the contaminant.

Steps to reduce the amount of contaminant have included elimination of all oxide materials from the vacuum system, reduction of the backstreaming from the oil diffusion pumps, a partial bake-out of the vacuum system prior to every experimental run, and the introduction of platinum getters around the effusion cell. It now appears that the effects caused by the contaminant have been reduced to a tolerable limit, but the details of the phenomenon are not understood.

Throughout all of the vapor pressure studies, it has been noted that the pressure when calculated from small rotations of the effusion cell does not, in general, result in an exponential relationship with the reciprocal of the temperature in accordance with the Clausius-Clapeyron equation. This condition is apparently due to the anelastic properties of the tungsten torsion wire. In cases where the deviation from an exponential is negligible or very small, the data can be corrected by an approximation method outlined in ANL-6657. However, no technique has been yet devised to analyze the data when the deviation is large, that is, when the error due to the anelasticity of the wire is of roughly the same magnitude as the rotation of the cell. Since the nickel-tantalum eutectic (the cells are made of tantalum) imposes an upper limit to the temperature to which the nickel-platinum alloys may be heated, the cell rotations are necessarily small and, as a result, subject to error. It is hoped that this problem can be solved in the absence of an analytical technique, in one or more ways.

Various wires drawn from metals with close-packed structures are being tested to determine if the contribution to the rotation of the cell from the anelasticity of the wire can be reduced. Care has to be taken to ensure that the wire has a sufficiently high yield strength to support the weight of the cell. Since the rotation of the cell increases for a given torque as the wire diameter is reduced, thinner tungsten wires are being tested in the anticipation that the ratio of the anelastic contribution to the cell rotation to that from the effusing vapor might be decreased.

High-temperature Heat Capacities of Alloys (K. M. Myles and A. T. Aldred): Analyses of the experimental results of the vapor pressure studies have shown that full elucidation of the thermodynamic characteristics of a given alloy system can only be obtained by utilizing both the free energies, calculated from the vapor pressure studies, and the enthalpies measured in the liquid-metal calorimeter. Unfortunately, since these thermodynamic properties cannot usually be obtained at the same temperature it is also necessary to determine the heat capacity. For this purpose, a high-temperature drop calorimeter has been designed and is being fabricated. In a drop calorimeter the sample, heated to the desired temperature, is dropped into a calorimeter which experiences a rise in temperature relative to its surroundings. The temperature change can be directly related to the heat content of the sample.

The drop calorimeter consists of a chromium-plated copper block surrounded by a large water jacket maintained at a constant temperature. The sample can be heated in the tantalum sheath-type furnace to a temperature of 2000°C. The copper block is shielded from the furnace by two water-cooled copper gates. The rise in the temperature of the copper block is measured by a copper resistance thermometer.

Calorimetry (J. B. Darby, Jr.): The twin "micro" calorimeter has been placed into operation. In the initial attempt to raise the calorimeter above ambient temperature, the thermopile on one of the calorimeters shorted to ground potential as the temperature approached 140°C. When the calorimeter was subsequently disassembled, it was found that thermal expansion of the thermopile elements created sufficient forces to move the junctions within the "locking" mechanism. The thermopiles were secured with greater force, and no further difficulty was experienced.

When heating was resumed, the temperature controls and the circuit for measuring the thermopile output behaved in an erratic manner. The trouble, though evasive, appeared to be stray electrical pick-up. After an extensive procedure of grounding certain components, ungrounding others, insulating instruments from the mounting racks, etc., the electrical noise was virtually eliminated.

At this juncture the two thermopiles were not "twinned" to the degree anticipated. It was found that by varying the power distribution to the heaters, it was possible to essentially eliminate the thermal losses from the calorimeters and to achieve nearly perfect "twinness."

With the emf output from each calorimeter approximately equal in magnitude, the output of the thermopile could be measured on a high sensitivity range. It was then observed that the net differential output of the thermopiles had long- and short-term drifts, the magnitudes of which were at a minimum during night hours. This was reduced by placing the heating elements on regulated and filtered DC power supplies and removing the ground leads from the power supply. At this point the calorimeter was operating satisfactorily at approximately 350°C and preliminary calibration was begun.

The calibration technique consisted of dropping gold samples of a size to produce a net heat liberation of about 20 cal in one of the calorimeters. This procedure was repeated alternately, using one calorimeter and then the other. Although the calibration experiment revealed some deficiencies, to be enumerated below, it verified that the sensitivity of the calorimeter was satisfactory, as indicated by the emf vs. time plot relative to the equilibrium base line.

The specimen-storage and -dispensing mechanism, as well as the stirring linkage, extend into the calorimeters. The initial calibration runs indicated that these auxiliary devices were perturbing the thermal balance between the two calorimeters and the massive metallic block. Since the differential emf generated by the devices was not reproducible and could not be distinguished from that produced by solution experiments, additional modifications were necessary. Study showed that the perturbation introduced by the stirring action was due to mechanical friction and transfer of heat by the movement of the stirring linkage. The friction was eliminated by increasing the clearance in the assembly and changing the materials involved in the sliding contacts. By operating the preheat furnaces, which were installed for heating samples, at the calorimeter temperature, the heat transfer problem was reduced to a minimum. The effects resulting from dispensing samples were eliminated by changing the relative motion of the assembly so that the thermal conduction paths remained constant in the vicinity of the calorimeter.

The twin calorimeter is now operating satisfactorily and final calibration prior to exploratory experiments is now under way.

3. Carbides of the Actinide Elements (M. V. Nevitt)

There have been four contributions to this research program on the NaCl-type monocarbides since preliminary findings were reported in the last Annual Report, ANL-6677:

1. The composition limits and the concentration dependence of the lattice parameter have been determined for the binary phases $\overline{ThC}$,* $\overline{PuC}$, and $\overline{NpC}$.

2. The lattice parameters of the $\overline{(Th,U)C}$ and $\overline{(Th,Pu)C}$ phases have been redetermined after samples were reannealed at higher temperatures.

3. The approximate composition range of $\overline{(Th,Np)C}$ has been explored, and certain other pertinent phase relations have been tentatively established. The lattice parameter of the $\overline{(Th,Np)C}$ phase has been measured.

4. A tentative interpretation of the lattice parameters of the binary monocarbides has been made in terms of the relationship between valence and atomic radius which is characteristic of the actinide series.[209]

*The symbols $\overline{ThC}$, $\overline{NpC}$, $\overline{PuC}$, $\overline{(Th,Np)C}$, etc., are used to denote the phases without implying stoichiometry.

[209] Zachariasen, W. H., in The Metal Plutonium, The University of Chicago Press, Chicago (1961).

The experimental techniques are virtually unchanged from those reported in ANL-6677 except that vacuum annealing furnaces have been employed, which permit homogenizing heat treatments to be performed at temperatures up to 1725°C. Some additional modifications of the normal procedures were required for making alloys containing neptunium, because only a limited quantity of this metal was available. The various compositions were achieved by the systematic dilution of several small master-alloy samples, and the total amount of neptunium consumed in the study has thereby been limited to about 1 g. The successive remelting of the samples has probably led to greater uncertainties in the alloy compositions and greater concentrations of oxygen and nitrogen, but we are unable to give a quantitative estimate of them, as no chemical analyses of neptunium-containing alloys have been made.

ThC. This carbide may be regarded as the reference compound, as it is contained in all of the ternary systems under current study. Samples of the stoichiometric compound have been annealed at 950, 1450, and 1725°C. The lattice parameter after the 950 and 1450°C anneals was 5.3460 Å, in exact agreement with the value of Kempter and Krikorian.[210] The parameter obtained by annealing at 1725°C was smaller, 5.328 Å, but metallographic examination of this sample and others annealed at the same temperature suggests that the decrease is due to inadvertent decarburization which occurred during annealing. Preparations are being made to anneal at the same temperature a new sample which will be packed in granular carbon in a graphite container to inhibit decarburization.

The lattice parameter of the monocarbide phase in Th-C alloys, quenched from 950°C, is plotted in Figure 178 as a function of the carbon concentration. The relation between the parameter and the carbon concentration in the hypostoichiometric region, extending to $ThC_{0.56}$, is not linear; however, in the composition region close to stoichiometry it may be approximated by

$$a_0 = 5.3460 - 0.0676\,[1 - (C/Th)] \qquad (1)$$

UC. The lattice parameter of the carbide in a single-phase alloy is 4.958 Å. Confirming earlier observations, we find that C/U does not deviate from unity by as much as 0.04 in the UC phase, but there is an indication from the X-ray results that there may be a small range of carbon solubility. Specifically, the carbide saturated with carbon (in a U-53 a/o C alloy) has a slightly larger lattice parameter, 4.9604 Å.

---

[210] Kempter, C. P., and Krikorian, N. H., Some Properties of Thorium Monocarbide and Dicarbide, J. Less-Common Metals 4 244 (1962).

Figure 178. The Lattice Parameters of the Monocarbide Phase in the Systems Th-C, Np-C, and Pu-C

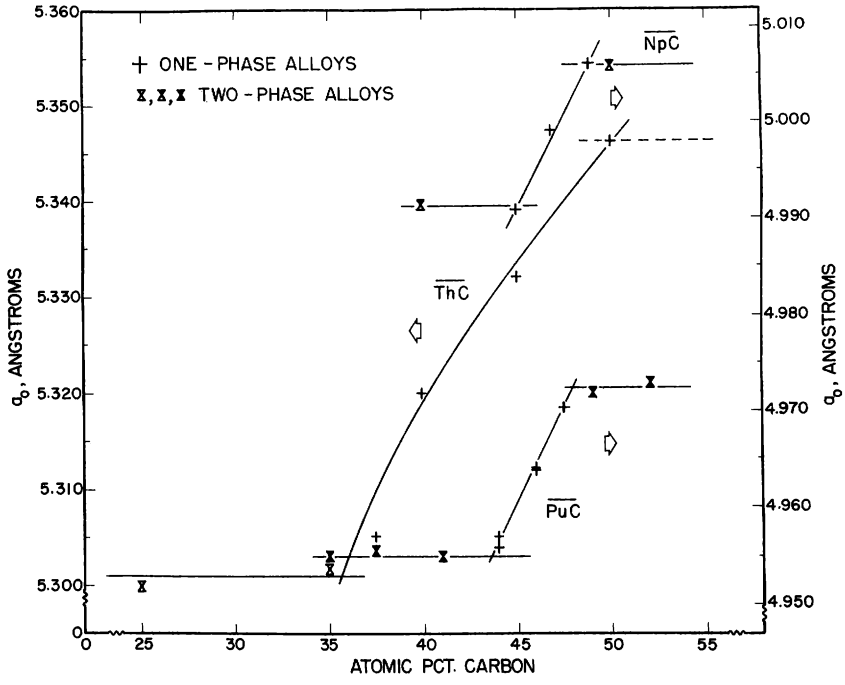

Macro 36653

NpC. Our limited observations with alloys quenched from 950°C indicate that this phase occurs for C/Np between 0.82 and 0.96, and thus does not exist at ideal stoichiometry. The slope of the lattice parameter versus carbon concentration relationship, shown in Figure 178 for alloys quenched from 950°C, may be approximated by the same value that will be given for PuC. For C/Np = 1, it yields a_0 = 5.0101 Å.

PuC. The composition range and the lattice parameter of the monocarbide of plutonium have been previously reported.[211] The parameter varies with carbon concentration (see Figure 178) according to the relation

$$a_0 = 4.9813 - 0.1150[1 - (C/Pu)], \qquad (2)$$

from which the parameter at ideal stoichiometry may be obtained by inspection.

For ThC and PuC, the one-phase/two-phase relationships shown in Figure 178 have been confirmed by optical metallography; the limited size of the samples precluded the use of this technique in NpC.

---

[211] Rosen, S., Nevitt, M. V., and Mitchell, A. W., The Uranium Monocarbide-Plutonium Monocarbide System, J. Nuc. Matls. 9 137 (1963).

Ternary Carbides $\overline{(Th,U)C}$, $\overline{(Th,Np)C}$ and $\overline{(Th,Pu)C}$: The lattice parameters of the solid-solution phases $\overline{(Th,U)C}$ and $\overline{(Th,Pu)C}$, saturated with carbon and quenched from 1430, 1450, or 1725°C, are shown in Figure 179. The compositions are based on chemical analyses. When the 1430 and 1450°C data are compared with the parameters of carbides quenched from 950 and 1050°C (see ANL-6677), it can be seen that annealing at the higher temperatures produces a concentration dependence more closely approaching a linear relationship. Annealing at 1725°C produces consistently lower lattice parameters in $\overline{(Th,U)C}$. Since metallographic examination has revealed that decarburization took place during this anneal, we may conclude that the values measured after this anneal are for phases deficient in carbon. The parameter of $\overline{UC}$ is, of course, essentially unaffected, since this phase has a very narrow range of carbon concentration, and decarburization can only result in the liberation of metallic uranium. $\overline{(Th,U)C}$ and $\overline{(Th,Pu)C}$ samples will be reannealed at 1725°C under conditions which will inhibit decarburization. The desired effect of the annealing, the complete or partial removal of the cored cast structure, was achieved at 1725°C but not at 1450°C.

Figure 179. The Lattice Parameters of Solid Solutions of $\overline{UC}$ and $\overline{PuC}$ in $\overline{ThC}$

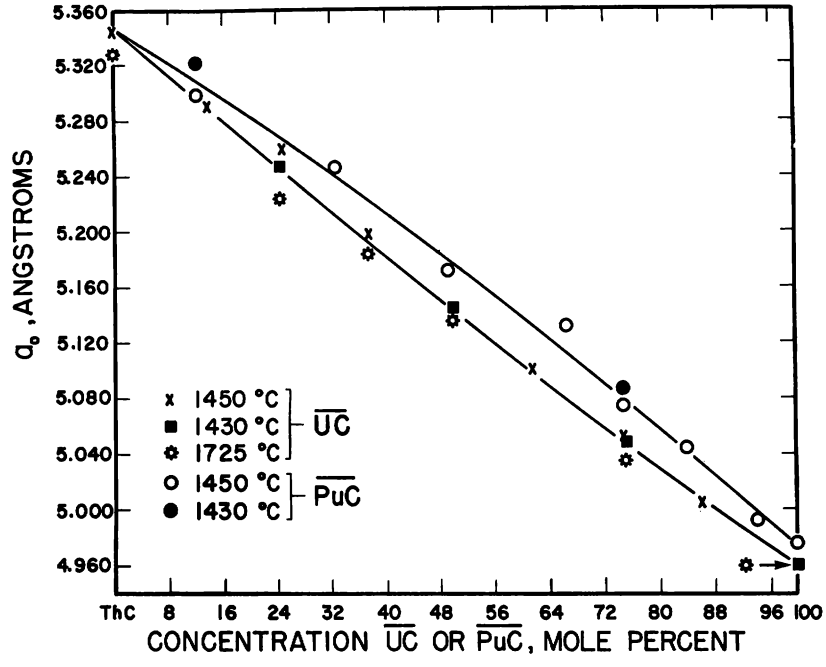

Macro 38155

Figure 180 gives the dimension of the unit cell of $\overline{(Th,Np)C}$ in alloys annealed at 950°C. The considerable scatter in the data results from the uncertainties in composition previously mentioned.

Figure 180. The Lattice Parameter of the Solid Solution of $\overline{NpC}$ in $\overline{ThC}$

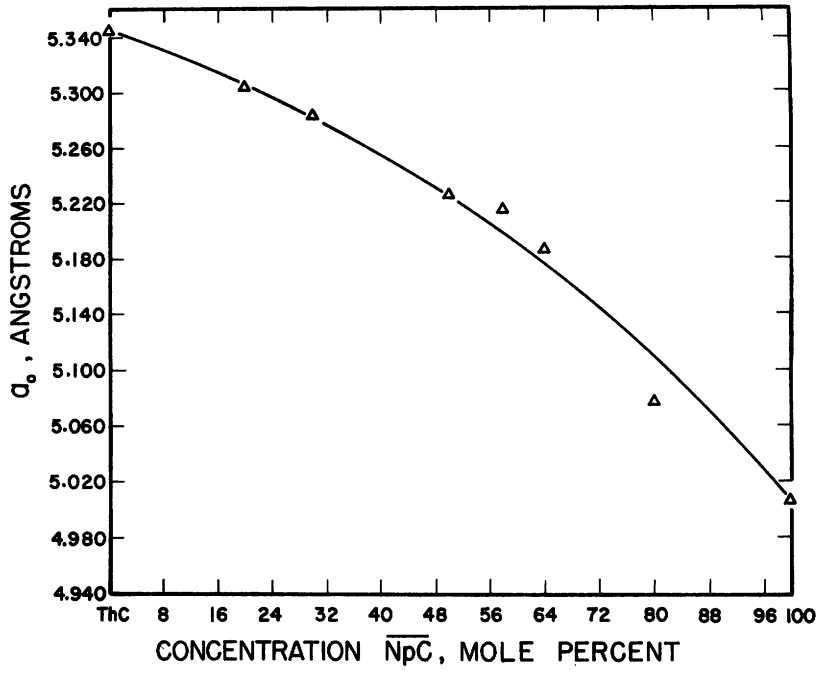

Macro 38154

Figure 181 shows the probable phase relations at 650°C in the system Th-Np-C at carbon concentrations up to 50 a/o. The placement of the phase boundaries is based entirely upon diffraction results, since the alloy samples were not large enough for metallography. The results thus far obtained suggest, but do not prove conclusively, that $\overline{NpC}$ is completely soluble in $\overline{ThC}$.

Figure 181. An Estimate of the Phase Relations for the Th-Np-C System at 650°C

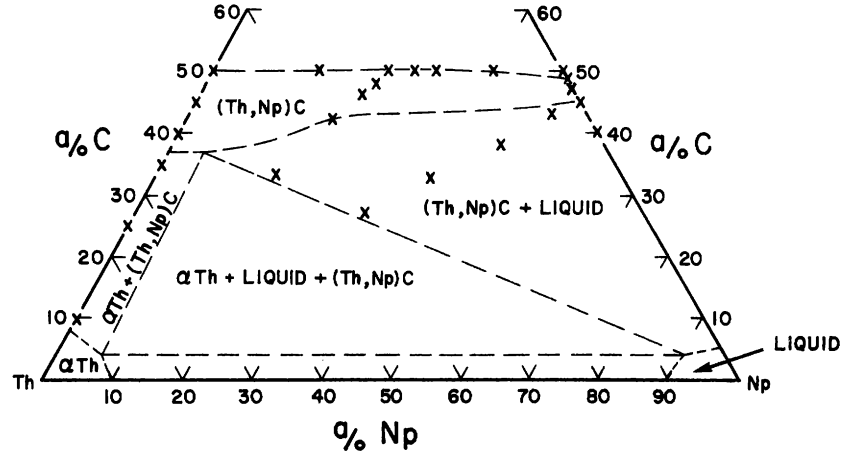

Macro 36655

A sample of composition Np-40 a/o C, annealed for 11 weeks at 400°C and quenched, was found to consist at room temperature of alpha neptunium and the monocarbide. Thus, there is no evidence for the existence of a low-temperature phase analogous to Pu_3C_2.

Discussion: The monocarbide with the NaCl structure is also formed by the fourth column elements Ti, Zr, and Hf, and elements of the fifth column, V, Nb, and Ta. It is reported to be formed by cerium of the lanthanide series. A NaCl-type phase in the Sc-C system has recently been described,[212] but there is some uncertainty regarding its composition.

In seeking an understanding of the factors which control the size of the unit cell, it is useful to consider the complete family of isostructural monocarbides. In Figure 182 the volume of the unit cell, V,* is plotted against the atomic volume of the metallic species, v_M, calculated from the lattice constants of the metals.[213] Except for UC, NpC, and PuC, the data may be fitted by a single smooth curve** which, in fact, does not deviate significantly from the linear relation

$$V = 4v_M + 4v_C, \qquad (3)$$

where the constant term, $4v_C = 23$ Å^3, is four times the atomic volume of carbon.[213] To a rather good approximation, therefore, the cell volume may be reproduced by a simple summing of the volumes of the four metal atoms and the four carbon atoms contained therein.

The failure of UC, NpC, and PuC to conform to the relationship of Figure 182 seems to be due to the use of atomic volumes derived from the cell dimensions of the pure metals. Although the sizes of the atoms in solid uranium, neptunium, and plutonium indicate that the number of electrons in 7s + 6d states (valence electrons) is respectively 6, 6, and 5,[209] their effective sizes in the carbides suggest a smaller number. This is demonstrated in Figure 183 by plotting the cell volume against r_M^3, the cube of the CN12 radius of the metal atom. As expected, the dependence of V closely resembles that in Figure 182. For the three phases under discussion the values of r_M^3 given on the graph are for 3, 4, 5, 6, and 7 electrons distributed in 7s + 6d levels.[209] We infer that the effective atomic sizes of uranium, neptunium, and plutonium correspond to between 4 and 5 electrons per atom, possibly resulting from a mixture of the two configurations. It is noteworthy that the populations of ns + (n - 1)d states in the titanium-group and the vanadium-group elements are also 4 and 5 electrons, respectively.

---

*For phases deficient in carbon the lattice parameter has been extrapolated to C/M = 1.

**The parameter for the phase in the Sc-C system, which also fails to fit the curve, has been omitted, pending a clarification of its composition.

212 Aver-Welsbach, W., and Nowotny, H., Zur Frage des Scandium-carbide, Mh. Chem. 92 198 (1961).

213 Teatum, E., Gschneidner, K. A., Jr., and Waber, J., Compilation of Calculated Data Useful in Predicting Metallurgical Behavior of the Elements in Binary Alloys Systems, LA-2345 (1959).

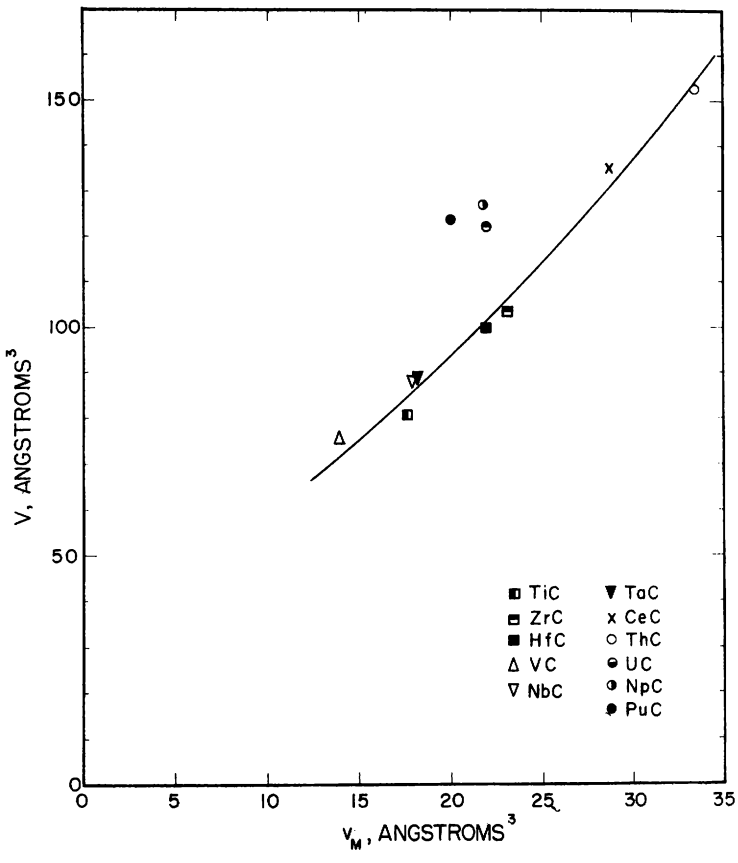

Figure 182

Cell Volume of the NaCl-type Monocarbide as a Function of the Atomic Volume of the Metals Species

Macro 36660

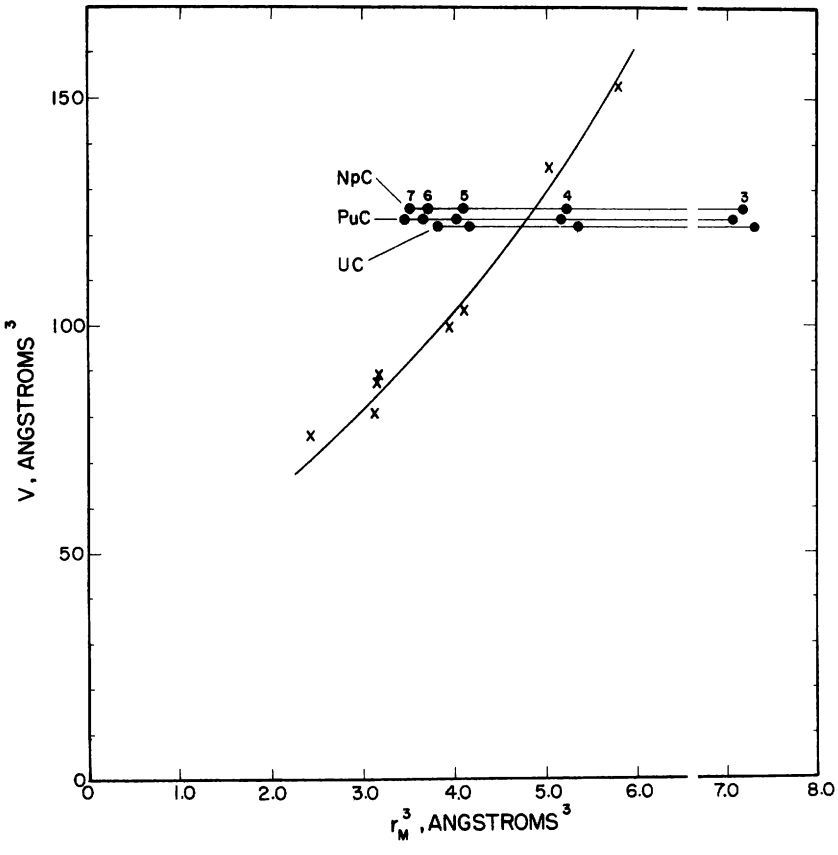

Figure 183

Cell Volume of the NaCl-type Monocarbide as a Function of the Cube of the CN12 Atomic Radius

Macro 36661

As only limited reliability can be placed on the determination of electron configurations from lattice parameters, we plan to start a series of magnetic measurements during the coming year, which, we hope, will clarify the electronic structure of the monocarbides.

4. Magnetization of Iron Alloys (A. T. Aldred and M. V. Nevitt)

Publication:

M. V. Nevitt and A. T. Aldred, Ferromagnetism in V-Fe and Cr-Fe Alloys, J. Appl. Phys. 34 463 (1963).

The modifications to the equipment mentioned in the 1962 Annual Report (ANL-6677, p. 262) consisted of a vacuum interlock to permit rapid changing of specimens at low temperature and an electronic integrator to measure the output of the detector coils. The integrator was necessary for measurements of small effects when the precision of the original ballistic technique was poor.

During 1963 an extensive series of tests were carried out on the integrator. The scatter in the results obtained at liquid helium temperature was much higher than expected. Oscilloscope observations of the signal from the detector coils showed a high noise level. It was initially believed that this was due to pick-up of noise from the magnet, and the control of the magnet current was improved by a factor of 10. However, the signal noise remained. It was finally concluded that the noise was due to vibrations in the coils (which at helium temperatures had very low resistance) caused by translation of the specimen.

At this stage the apparatus was abandoned and a force method of measuring magnetization adopted. This technique involves placing the specimen in a known, constant magnetic field gradient and measuring the force exerted. The new equipment, which has been installed and is now being evaluated, consists of a dual-sensitivity automatic-recording vacuum balance, a new stainless steel cryostat, and a pair of constant-gradient pole caps. In principle, the precision should be about 5 times better than the original set-up and the speed of measurement as fast as the modified version of the original set-up.

5. Measurements of Thermoelectric Power (A. T. Aldred)

Two determinations were made of the absolute thermoelectric power of pure palladium. The results, shown in Figure 184, are in fair agreement with selected[214] values. The average deviation of the experimental points from the selected values and the average reproducibility for the two runs are both about 20%.

[214]Cusack, N., and Kendall, P., The Absolute Scale of Thermoelectric Power at High Temperatures, Proc. Phys. Soc. 72 898 (1958).

Figure 184. Absolute Thermoelectric Powers of Pure Palladium

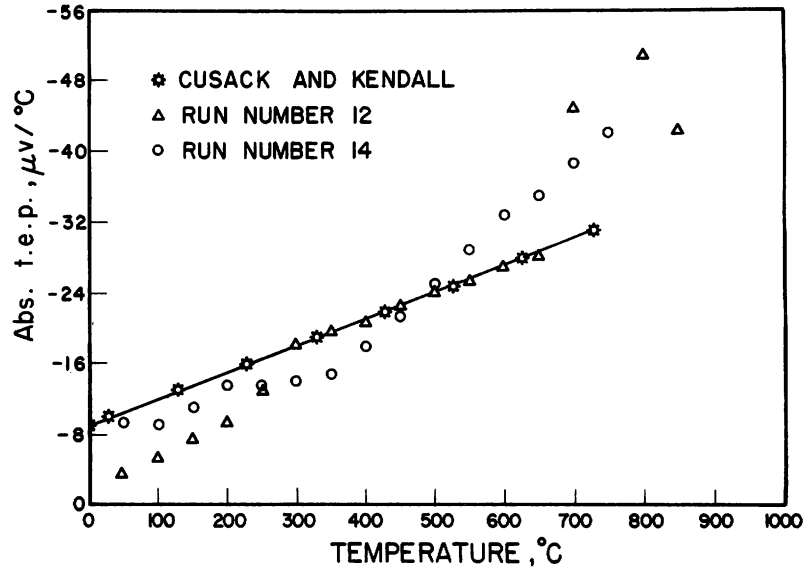

Macro 38150

At high temperatures (that is, above the Debye temperature), the thermoelectric power is essentially due to the scattering of the electrons by lattice vibrations and may be expressed as[215]

$$S = -\frac{1}{3}\frac{\pi^2 k^2 T}{e}\left[\frac{1}{N(E)}\frac{dN(E)}{dE} + \frac{1}{V^2}\frac{dV^2(E)}{dE} + \frac{1}{\tau}\frac{d\tau(E)}{dE}\right]_{(E=\zeta)}, \qquad (1)$$

where k is Boltzmann's constant, T is the absolute temperature, e is the electronic charge, N(E) is the electronic density of states, E is the energy, V is the electron velocity, τ is the relaxation time, and ζ is the energy at the Fermi level.

For free electrons, $N(E) \propto E^{1/2}$, $V \propto E$, and $\tau \propto E^{3/2}$, so that equation (1) becomes

$$S = -\pi^2 k^2 T/e\zeta . \qquad (2)$$

Alternatively, if τ is assumed to be independent of E,[216]

$$S = -\pi^2 k^2 T/2e\zeta . \qquad (3)$$

Now for free electrons, the electronic specific heat, C_{el}, which is the term in the specific heat linear in T, may be written

---

[215]Wilson, A. H., The Theory of Metals, Cambridge University Press, Cambridge (1953).

[216]McDonald, D. K. C., Thermoelectricity: An Introduction to the Principles, J. Wiley & Sons, Inc. New York (1962).

$$C_{el} = \gamma T = \pi^2 k^2 T / 2\zeta. \quad (4)$$

Therefore, the experimentally determined value of γ for palladium[217] may be used to calculate S by either equation (2) or (3). At 700°C, the values of S = -63 μV/deg, calculated by equation (2), and S = -31 μV/deg, calculated by equation (3), may be compared with the selected value[214] of -30 μV/deg and a value of -42 μV/deg determined in the present investigation.

A sample of the experimental data on palladium alloys is given in Table LXVI. The absolute thermoelectric power at 700°C is plotted in Figure 185 as a function of electron concentration for various solutes dissolved in palladium. The electron concentration is taken as the total number of electrons outside the closed shell. It is seen that the addition of any of the transition metal solutes to palladium decreases the numerical value of S, although there is no correlation between, say, the group number of the solute and the magnitude of the decrease.

Table LXVI

ABSOLUTE THERMOELECTRIC POWERS OF PALLADIUM ALLOYS AT 700°C

Solute, a/o	Absolute Thermoelectrical Power, μV/°C
0	-42.0
10 Co	-21.3
20 Co	-12.3
30 Co	-1.6
10 Fe	+2.6
10 Mn	-38.3
20 Mn	-38.9
25 Mn	-28.0
10 Cr	-15.9
20 Cr	-9.0
10 V	+23.5
20 V	-9.6
10 Ta	-2.3
5 U	-1.4
10 U	+7.5

[217] Budworth, D. W., Hoare, F. E., and Preston, J., The Thermal and Magnetic Properties of Some Transition Metal Alloys, Proc. Roy. Soc. A257 250 (1960).

Figure 185. Absolute Thermoelectric Powers of Some Palladium Alloys as a Function of Electron Concentration at 700°C

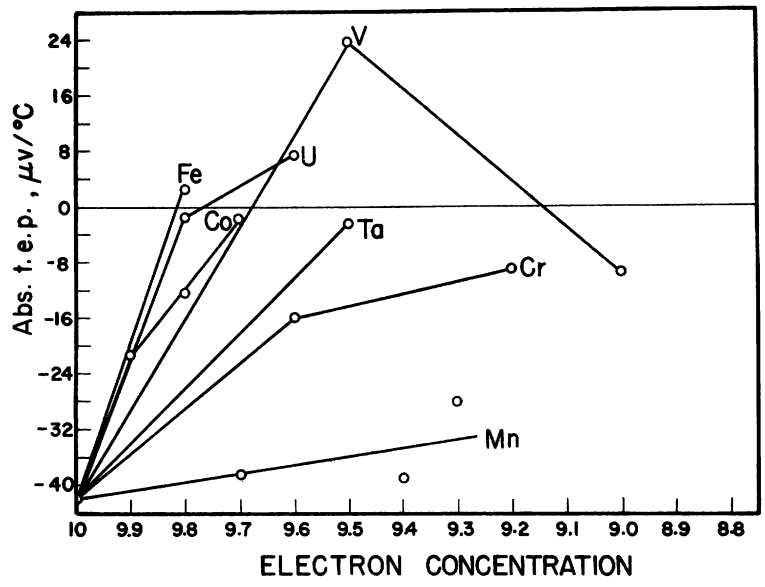

Macro 38151

In the free-electron model,[215] $S \propto C_{el} \propto N(E)$, and so the variation of S with electron concentration should reflect the corresponding variation in N(E) if a rigid-band model is applicable. The usual band model of palladium[218] would imply that S should increase to a numerical maximum on addition of small amounts of transition metal solutes to the left of palladium in the periodic table, and then decrease with larger additions. However, Taylor and Coles[219] have remarked that the $E^{3/2}$ dependence for τ cannot be appropriate in alloys; the relaxation times are in fact controlled mainly by $N_d(E)$, the density of states in the d-band into which the current-carrying s-electrons may be scattered. The term in τ in equation (1) then becomes $-1/N_d(E)\ dN_d(E)/dE$, and the controlling factor in the concentration dependence of S is the variation in $dN_d(E)/dE$, i.e., the slope of the d-band. When palladium is alloyed with an element lying in a column to its left, this term would decrease and then change sign.

The present results are not inconsistent with either model. The initial increase in S predicted by the simpler model has not been observed, but this may be due to the fact that no sufficiently dilute alloys have been examined. Further measurements on such alloys should distinguish between the two models.

---

[218] Mott, N. F., and Jones, H., The Theory of the Properties of Metals and Alloys, Oxford University Press, Oxford (1936).

[219] Taylor, J. C., and Coles, B. R., Phys. Rev. 102 27 (1956).

6. Superconducting Transition Temperatures of Cr_3O-type Ternary Compounds (S. T. Zegler)

Publication:

S. T. Zegler and J. W. Downey, Ternary Cr_3O-type Phases with Vanadium, Trans. AIME 227 1407 (1963).

The publication describes results which were cited in the last Annual Report, ANL-6677.

During 1963, construction of the experimental apparatus for measuring T_c, the superconducting transition temperature, was completed to the point where accurate determinations could be made over the range of temperature from 1.7 to 4.2°K. Procedures are now being devised for calibrating the apparatus for use between 4.2 and 14°K.

The first work involved determining the T_c of a group of solid-solution phases in which Co, Ru, Pd, Os, Ir, Pt, or Au was substituted for part or all of the rhodium in Nb_3Rh. The alloys were prepared from 99.7% pure niobium and other elements of 99.9% purity by arc-melting and casting 3-4-g buttons in an argon-helium atmosphere. They were heat treated in vacuo for 1 week at 1100°C, furnace cooled to 900°C, held 3 weeks at the latter temperature, and water quenched.

X-ray and metallographic studies indicate that at 900°C, cobalt and palladium, respectively, can replace approximately 10 and 30% of the rhodium atoms in Nb_3Rh, whereas ruthenium and platinum can replace about 50% of the rhodium atoms. At the same temperature, complete solubility exists between Nb_3Rh and Nb_3Ir and, although extensive coring is observed metallographically, X-ray data indicate complete solubility between Nb_3Rh and Nb_3Au. No data have yet been obtained on the substitution of osmium for rhodium.

The lattice parameters and transition temperatures are plotted against the intended compositions of the phases in Figure 186. There are only small deviations from a linear relationship between a_0 and alloy composition, except in the case of the $Nb_3Rh_xIr_{1-x}$ alloys, which are thought to have been incompletely homogenized. The substitution of cobalt increases a_0, although the cobalt atom is smaller than the rhodium atom. This behavior is inconsistent with the usual effect of atomic size, as is the fact that palladium, which has an atomic size somewhat smaller than that of platinum, increases a_0 more rapidly than the latter.

Our measurements give 2.52°K as T_c for Nb_3Rh. Except for platinum and gold, the substitutions either decrease T_c or leave it virtually unaffected. The substitution of cobalt for 10% of the rhodium atoms has the most marked effect, decreasing T_c to less that 1.7°K. A similar decrease

in T_c is observed on the substitution of ruthenium for 30 and 50% of the rhodium atoms. Replacement of 30% of the rhodium atoms by either platinum or gold increases T_c to above 4.2°K.

In an effort to determine whether impurities present in the alloys significantly influenced their transition temperatures, a new set of alloys were prepared from 99.9% pure niobium containing no more than 50 ppm* of Fe, Co, and Ni, and 150 ppm of O, N, C, and H. So far, data have been obtained for the substitution of Co, Ru, Pd, and Ir for rhodium in alloys which were heat treated for 1 week at 1400°C, and then given 3 weeks at 1000°C, followed by water quenching. Lattice parameters are in close agreement with those given in Figure 186, and for the $Nb_3Rh_xIr_{1-x}$ alloys a closer adherence to a linear relationship between a_0 and alloy composition is observed. The transition temperatures are within 0.1°K of the earlier values except in the case of $Nb_3Rh_xIr_{1-x}$ alloys, for which they are depressed below 1.7°K by even the smallest substitution of iridium for rhodium. Because of their greater homogeneity, the alloys prepared from the 99.9% pure niobium are believed to indicate more reliably the influence of iridium substitutions.

Figure 186. Lattice Parameters and Superconducting Transition Temperatures vs. Compositions of $Nb_3Rh_xB_{1-x}$, Cr_3O-type Alloys

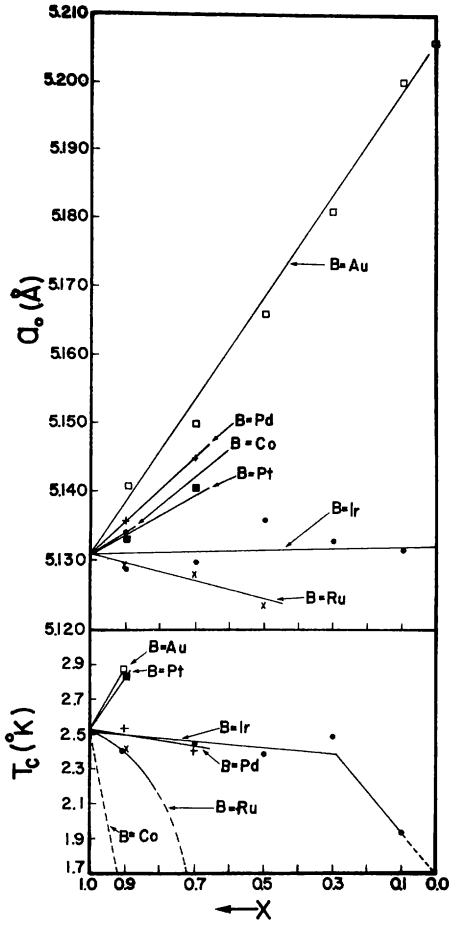

Macro 38156

Measurements of magnetic susceptibility were made at room temperature and at 77°K for most of the alloys prepared from 99.7% pure niobium and containing Co, Ru, Pd, and Ir. For all the ternary alloys paramagnetic susceptibilities are close to that of Nb_3Rh and, like Nb_3Rh, are independent of temperature. At both temperatures, χ values range from 0.7×10^{-6} to 1.1×10^{-6} emu/gm.

According to the relationship provided by the Bardeen-Cooper-Schrieffer theory of superconductivity, given in its approximate form by equation (1), T_c is related to the Debye temperature, θ_D, the energy density of electronic states at the Fermi surface, N(0), and an interaction parameter, V, which measures the average strength of the net interaction between electrons very close to the Fermi surface:

*By weight.

$$T_c \approx \theta_D \exp [-1/N(0)V]. \quad (1)$$

Our reference compound, Nb_3Rh, with six valence electrons per atom, seems to be in a region of the d-band having a low density of states between two peaks. The absence of a temperature dependence of the paramagnetic susceptibility of Nb_3Rh and of the other alloys probably means that the d-band does not have a high curvature in this region. The interaction parameter is not thought to change very much in this region of the d-band, whereas θ_D of Nb_3Rh should be about 300°K, and not altered significantly by alloying. Therefore, if equation (1) is correct, the primary effect of alloying upon T_c should be through a change in the level of filling of the d-band, and those alloy substitutions which do not move the Fermi level far from its position in Nb_3Rh should not have an important effect on T_c. The data obtained thus far seem to confirm the latter prediction. Although there are extensive compositional changes, the electron/atom ratio remains within the relatively narrow range between 5.87 and 6.07. Accordingly, the temperature of the transition to the superconducting state was changed by 0.3°K or less in many cases. The reason for the larger changes in T_c resulting from the substitutions of cobalt or iridium is not yet understood.

F. Nuclear Magnetic Resonance Research and Magnetic Susceptibility

Publications:

D. O. Van Ostenburg, D. J. Lam, H. D. Trapp, and D. W. Pracht, Magnetic Susceptibilities and Knight Shifts in Nb-Tc Alloys, Bull. APS 8 250 (1963). [Abstract].

D. O. Van Ostenburg, D. J. Lam, H. D. Trapp, and D. W. Pracht, Knight Shifts K_V, K_{Tc} and K_{Al} and Magnetic Susceptibilities in the bcc Region of the V-Tc-Al Ternary Alloy System, Bull. APS 8 518 (1963). [Abstract].

D. J. Lam, D. O. Van Ostenburg, and D. W. Pracht, Magnetic Susceptibilities of Mo-Tc Binary Alloys, Presented at the 9th Annual Conference on Magnetism and Magnetic Materials, November (1963) Atlantic City, New Jersey, Paper J7. [Abstract].

D. J. Lam, D. O. Van Ostenburg, M. V. Nevitt, H. D. Trapp, and D. W. Pracht, Magnetic Susceptibilities and Nuclear Magnetic Resonance Measurements in V-Fe Alloys, Phys. Rev. 131 1428 (1963).

D. O. Van Ostenburg, D. J. Lam, H. D. Trapp, and D. W Pracht, Application of NMR to Transition Metals and Their Alloys, 4th O.C.E.A.N.S. Conference, Mellon Institute, Pittsburgh, Pennsylvania (1963).

D. O. Van Ostenburg, D. J. Lam, Masao Shimizu, and Atsushi Katsuki, NMR Magnetic Susceptibility and Electronic Specific Heat of Nb and Mo Metals and Nb-Tc and Nb-Mo Alloys, J. Phys. Soc. Japan, 18, No. 12 (Dec. 1963).

D. O. Van Ostenburg, D. J. Lam, H. D. Trapp, and D. W Pracht, Knight Shifts K_V, K_{Tc} and K_{Al} and Magnetic Susceptibilities in the bcc Region of the V-Tc-Al Ternary Alloy System, Phys. Rev. Letters 11, 352 (1963).

1. Transition Metal Solid Solutions (D. O. Van Ostenburg and D. J. Lam)

Vanadium-Iron: A preliminary account of this system was given in the 1962 Annual Report. In the current work, magnetic susceptibilities and Knight shifts of V^{51} have been measured over the temperature range from 4.2 to 300°K; the nuclear magnetic resonance (NMR) parameters

have been measured from 120 to 300°K and at various external fields. These measurements supplement those made with other V alloys.[220]

The room-temperature susceptibility as a function of composition decreases from pure vanadium to a composition containing around 20 a/o Fe and then increases rapidly with higher iron concentration. The susceptibility of alloys with less than 20 a/o Fe is independent of field up to 11,000 Oe, with a small temperature dependence over the range investigated. Alloys with higher iron content have a temperature dependence which indicates the presence of magnetic moments. The Knight shift of V^{51} shows a maximum in the vicinity of 16 a/o Fe (electron-atom ratio e/a = 5.6), while the line width increases slowly up to 20.2 a/o Fe and then rises rapidly at higher iron contents. The shifts are independent of temperature and field within experimental error. The line widths increase linearly with frequency and are independent of temperature up to about 20 a/o Fe; at higher iron concentration they broaden at low temperatures. The fact that the NMR line width increases rapidly beyond 20 a/o Fe and increases at lower temperatures augments the determination of the composition where magnetic moments first appear. The Knight shifts of V^{51} in the nonmagnetic portion of this alloy system can be interpreted in terms of the contributions from the Fermi contact term, core polarization, and orbital paramagnetism. For further details on this system the reader is referred to the quoted publication.

Vanadium-Niobium Alloys: In certain cases in which vanadium is alloyed with other transition metals, a regularity was found in the data of the V^{51} Knight shift versus electron/atom ratio; that is, when K_V is plotted versus e/a for the alloy systems of vanadium with Cr, Tc, and Fe, respectively, a maximum in K_V occurs near an e/a of 5.6. To gain further insight into this situation a study of the V^{51} and Nb^{93} Knight shifts in the V-Nb binary alloy system has been initiated. This is an alloy series for which the e/a ratio is constant and for which both nuclear species can be observed across the entire composition range; this work is in its early stages.

Vanadium-Technetium-Aluminum Ternary Alloys: In previously reported results for vanadium alloyed with other transition metals[220] of the first and second long periods (e.g., Tc), the constituents appeared to form a common d-band according to measurements of nuclear magnetic resonance and magnetic susceptibility. This deduction came from the fact that the composition dependence of the Knight shift and magnetic susceptibility of these binary alloys depend essentially on the electron/atom ratio rather than on the alloying species. It is said that these elements appear to conform to the rigid-band model.

---

[220] Van Ostenburg, D. O., Lam, D. J., Trapp, H. D., and MacLeod, D. E., Knight Shifts and Magnetic Susceptibilities in V Alloys with Ti, Cr and Tc, Phys. Rev. 128, 1550 (1962).

On the other hand, alloying vanadium with nontransition elements, such as aluminum or silicon, changes the picture. In the 196[illegible] Annual Report (ANL-6677) the binary V-Al system was discussed over the b.c.c. region (up to 40 a/o Al in vanadium). It was found that the V^{51} shift increased only slightly from 0.56% in pure vanadium to 0.58% at 40 a/o Al in vanadium, and that the change was nearly linear with aluminum content. The Al^{27} shift was negative and nearly independent of concentration within experimental error, with a value in the vicinity of -0.03%. This is to be contrasted with the Knight shift of pure aluminum, which is +0.16%. These results lead to the proposal that when aluminum is alloyed with vanadium, the constituents do not form a common conduction band, but that the aluminum nuclei are electronically shielded from the rest of the matrix. To explore further this concept of energy-band compatibility among transition and nontransition elements, a study was made of the b.c.c. region of the ternary V-Tc-Al system. The alloys were prepared by arc-melting requisite amounts of vanadium and technetium and a fixed amount (5 a/o) of pure aluminum.

Again, the magnitude of the shift for aluminum was found to be small. This behavior is similar to that in the binary V-Al system. When compared with the values obtained for the V-Tc binary alloys, the shifts of V^{51} and Tc^{99} show the same magnitude and concentration dependence. As in the binary V-Tc system, the room-temperature magnetic susceptibility decreases with increasing technetium concentration and has a very small temperature dependence. The similar composition dependence of the V^{51} and Tc^{99} shifts in the binary and ternary alloys suggests that the electrons contributing to the shifts of vanadium and technetium enter a common band, while the Al^{27} shift, small in absolute magnitude and nearly independent of alloy composition with or without technetium, indicates that the conduction electrons of aluminum have little or no interaction with those of the transition elements.

Niobium-Technetium and Niobium-Molybdenum Alloys: This work was performed in conjunction with Drs. M. Shimizu and A. Katsuki of Nagoya University, Nagoya, Japan. Magnetic susceptibility and NMR measurements have been made with Nb-Tc alloys. Calculations of the temperature variations of the electronic specific heats and magnetic susceptibilities have been made for niobium, molybdenum, and Nb-Mo alloys through use of the density of states determined from low-temperature specific heat data for 4d transition metals and their alloys. Temperature variations of the electronic specific heats for Nb and Mo metals are explained by the current calculations. Temperature variations of the magnetic susceptibilities of these metals and their alloys are explained by including the temperature-independent orbital paramagnetism and the effects of the negative (for niobium) and the positive (for $Nb_{0.75}Mo_{0.25}$ alloy) molecular fields. The Knight shifts of Nb^{93} and Tc^{99} in Nb-Tc and Nb-Mo alloys are shown to consist of contributions from conduction electrons of s-character, the exchange polarization effect, and

orbital paramagnetism. The main contributions to these shifts appear to arise from the latter term. A more detailed account of this can be found in the publication.

Molybdenum-Technetium Alloys: Magnetic susceptibilities of binary Mo-Tc alloys have been studied. The results and their analysis can be briefly summarized as follows: The room-temperature magnetic susceptibility increases from pure molybdenum (82.5×10^{-6} emu/g-atom) to a small maximum (96.5×10^{-6} emu/g-atom) at the equiatomic composition. Further additions of technetium produce a decrease which reaches a minimum at 70 a/o Tc ($\chi = 87.3 \times 10^{-6}$ emu/g-atom). Beyond this composition there is another increase to the value of 120.8×10^{-6} emu/g-atom for the pure technetium. No Curie or Curie-Weiss type of temperature dependence was observed in any of the alloys in the temperature range from 300°K to the superconducting transition temperature. The present results indicate that the density of states at the Fermi surface increases upon initial addition of technetium to molybdenum and then seems to decrease at technetium contents higher than the equiatomic composition, consistent with low-temperature specific heat coefficients[221] and superconducting transition temperatures[222] in this alloy system.

2. Actinide Metals, Compounds, and Alloys (D. O. Van Ostenburg and M. B. Brodsky)

To date the Pu^{239} NMR line has not been observed. Work will continue as more accurate nuclear magnetic moments are reported and the purity of the samples is improved.

One gram of neptunium oxide was received from Oak Ridge National Laboratory and investigated. The nuclear magnetic moment for Np^{237} is reported to be 5 ± 2.5 nm. A search for the NMR absorption line was made over a range of magnetic moments ranging from 3.39 to 8.82 nm. No resonance was observed. One possible reason is that the line may have been broadened because of the large paramagnetism associated with this compound. Future work will continue when the pure metal is obtained. If the resonance is found, it will provide a means for investigating alpha-plutonium solid solutions, since neptunium is the only element that dissolves to a large extent in alpha plutonium.

The Al^{27} resonance line has recently been observed in the intermetallic compound $PuAl_2$. The spectrum consists of a central line associated with the $-\frac{1}{2} \rightarrow \frac{1}{2}$ transition and four satellites due to transitions

---

[221] Morin, F. J., and Maita, J. P., Specific Heats of Transition Metal Superconductors, Phys. Rev. 129, 1115-1120 (1963).

[222] Compton, V. B., Corenzwit, E., Maita, J. P., Matthias, B. T., and Morin, F. J., Superconductivity of Technetium Alloys and Compounds, Phys. Rev. 123, 1567-1568 (1961).

among the levels associated with the Al^{27} nuclear magnetic quantum numbers $\pm\frac{3}{2}$ and $\pm\frac{5}{2}$. The satellite spacings are such as to yield a quadrupole coupling constant in the vicinity of 3.8 Mc. The central line width is composed of contributions from the second-order quadrupole interaction, the anisotropic Knight shift, the dipolar interaction, etc. The study and analysis currently in progress should separate these contributions. When this information is complete the isostructural compound $NpAl_2$ will be examined and the results compared with that on UAl_2 obtained by another group of investigators.[223] The composite data will be examined with the purpose of proposing possible models for the electronic structure of actinide metals and their compounds.

3. Spin-Lattice Relaxation Measurements (D. J. Lam, D. O Van Ostenburg, and J. J. Spokas*)

Design of a pulsed NMR spectrometer was initiated at the end of 1962. During the past year, construction of the unit has advanced to the point where experiments can now be performed with one frequency.

Since our experiments are mainly concerned with solid solutions and intermetallic compounds, for which the absorption lines are usually broad, intense rf pulses are necessary. They are generated by gated rf high-power amplifiers. The energy contained in the pulses and the time intervals between pulses are controlled by changing the duration of the gate. The rf pulse is applied to the nuclear spin system by means of a transmitter coil, and the nuclear induction signals are picked up by a receiver coil, which is orthogonal to the transmitter coil. The nuclear induction signals are coupled to the receiver and then displayed on an oscilloscope or fed into a box bar integrator.

The unit is designed to operate at four frequencies, 4, 8 13, and 18 Mc/sec with a maximum power output of 50 kW. At present, the unit can be operated at 8 Mc/sec with the intended power output.

A Dewar system has been constructed to provide temperatures from 4 to 300°K, with the specific requirement that samples can be introduced at low temperatures.

The results of tests of the unit at room temperature with V^{51} and Al^{27} in pure metals are in good agreement with published data.

---

*St. Procopius College. Consultant to Metallurgy Division.

[223]Gossard, A. C., Jaccarino, V., and Wernick, J. H., Phys. Rev. 128, 1038 (1962).

G. X-ray and Neutron Diffraction Studies

1. Neutron Diffraction Instrumentation (M. H. Mueller, L. Heaton and S. S. Sidhu)

Publications:

M. H. Mueller, L. Heaton, and S. S. Sidhu, Full Circle Goniostat for Diffraction Intensity Data, Rev. Sci. Instr. 34, 74-76 (1963).

C. S. Barrett,* M. H. Mueller, and L. Heaton, Germanium as a Neutron Monochromator, Rev. Sci. Instr. 34, 847-848 (1963).

Neutron Diffractometer I: The first of the above-indicated articles describes our full-circle goniostat used on Neutron Diffractometer I for obtaining three-dimensional diffraction data. This instrument permits complete 360° motion in both angles ϕ and χ. Electronic angle setting and readout are provided, which facilitates automatic collection of intensity data. A more complete description of its use on Neutron Diffractometer I has been given.**

The necessary electronic equipment for converting the Neutron Diffractometer I to automatic operation has been ordered. This will permit the automatic setting of the ϕ and χ angles of the goniostat described above together with the basic setting 2θ and ω which is a part of the Picker Diffractometer. The input and output will be in the form of punched cards.

The features of this automatic instrument were described by M. H. Mueller, L. Heaton and S. S. Sidhu at the International Union of Crystallography Congress held in Rome, Italy, September 1963, and was presented by one of us (MHM) in a Rapporteured Session devoted to automatic instrumentation.

Neutron Spectrometer II: A brief description was given in the last Annual Report[224] of two modifications made on this instrument: (1) the change to 360 tooth gears for 2θ and θ instead of the 100 tooth gears, and (2) the coupling of the two gears by an electronic pulse system using Slo Syn stepping motors in a 2:1 ratio, thus eliminating a clutching and halving mechanism. Although considerable difficulty has been experienced with

*Consultant to the Metallurgy Division.

**Mueller, M. H. et al., Argonne Dual Neutron Diffractometers Using a Single Primary Beam, ANL-6537 (Nov 1962).

[224] Annual Report for 1962, Metallurgy Division, ANL-6677, p. 301.

the electronic halving system, it is quite reliable at present. A description of this electronic technique has been accepted for publication in Nuclear Materials and Instruments.

In our investigation of the crystal structure of alpha uranium at low temperature, we have previously indicated[225] that it is necessary to use a neutron beam of longer wavelength and also to carefully exclude the $\lambda/2$ component. We have found that a germanium monochromator satisfies both of these objectives. The procedure used in obtaining a good germanium monochromator is described in the second published paper indicated above. It was found that sufficient imperfections could best be introduced in the germanium crystal by a small compression at elevated temperatures. Further details are given in the article.

2. Neutron Coherent Scattering Amplitudes (M. H. Mueller, S. S. Sidhu and L. Heaton)

Since neutron scattering amplitudes can only be determined experimentally, a continuing effort is made to obtain coherent scattering measurements with isotopes as they become available as well as improving previously reported values. The following results were determined in the usual way[226] and were presented orally at the International Conference on Nuclear Physics with Reactor Neutrons. A summary of the scattering data determined or redetermined here at Argonne is included in the Conference Proceedings (ANL-6797). An abbreviated table showing scattering amplitudes only is included below.

Atomic Number	Element or Isotope	b (10^{-12} cm)
12	Mg	0.475
19	K	0.34
	K^{39}	0.37
37	Rb	0.85
	Rb	0.83
40	Zr	0.70
43	Tc^{99}	0.68

During our investigation of the scattering amplitude of magnesium we noted that the results of another investigation[227] indicated that the previous reported value[228] of 0.54×10^{-12} cm is too large. Sabine and

[225] Annual Report for 1962, Metallurgy Division, ANL-6677, p. 209

[226] Sidhu, S. S., Heaton, L., and Mueller, M. H., J. Appl. Phys. 31, 1323 (1959).

[227] Sabine, T. M., and Browne, J. D., Acta Cryst. 16, 834 (1963).

[228] International Tables for X-ray Crystallography, Vol. III, 229 (1962).

Browne[227] have found a value of 0.516 x 10^{-12} cm; however, we believe this to be too large on the basis of three sets of MgO single-crystal measurements plus an independent determination with a powdered magnesium sample together with a standard nickel powder. A value of 0.475 ± 0.005 x 10^{-12} cm has been obtained by least squaring of our data.

3. Crystal Structures of Ti_2Cu, Ti_2Ni, Ti_4Ni_2O, and Ti_4Cu_2O (M. H. Mueller and H. W. Knott)

Publication:

M. H. Mueller and H. W. Knott, The Crystal Structures of Ti_2Cu, Ti_2Ni, Ti_4Ni_2O and Ti_4Cu_2O, Trans. AIME 227, 674-678 (June 1963).

The published article indicated above summarizes the structural investigations of Ti_2Cu, Ti_2Ni, Ti_4Ni_2O, and Ti_4Cu_2O carried out with powder specimens examined by X-ray and neutron diffraction. Lattice constants were determined for all four phases by means of X-ray powder diffraction films. Atom positional parameters of all four phases have been determined from observed neutron intensities. X-ray diffraction calculated intensity data have also been presented for Ti_2Cu to point out the particular suitability of neutron diffraction in spite of the large unit cell size. Interatomic distances have been determined from the positional parameters obtained by neutron diffraction.

4. Structure of Disodium Tetranitritonitrosohydroxyruthenate (III) 2-Hydrate (M. H. Mueller and S. H. Simonsen*)

The determination of the crystal structure of this compound by neutron diffraction has been completed. Results were presented at the International Union of Crystallography Congress held in Rome, Italy, during September 1963. A progress report of the structure was given in the last Annual Report,[229] a more complete description was published as an abstract for the above meeting, and the final paper is now being prepared. We have refined the positional parameters of all 16 atoms together with anisotropic temperature factors for each, and have calculated the resulting rms thermal displacement of each atom.

The structure can be envisioned as consisting mainly of six-fold coordination about three separate atoms, namely, the Ru, Na_1, and Na_2, thus forming three different kinds of octahedra which include almost all of the atoms within the structure. The ruthenium octahedron contains four nitrogens from the NO_2 groups, a nitrogen from the NO group, and an

*Consultant to Metallurgy Division.

[229]Annual Report for 1962, Metallurgy Division, ANL-6677, pp. 304-305.

oxygen from the OH group. Both Na_1 and Na_2 have six oxygens about each, which are from the NO_2 groups, OH groups, or the H_2O. By the use of this description it is evident that these octahedra form an interlocking chain throughout the structure in which there are common atoms or common edges shared between octahedra. Each of the three octahedrons are oriented relatively the same in the unit cell. Four atoms in each are arranged in a near coplanar square in which this plane is perpendicular or nearly so to the mirror plane (or parallel to the b axis). The other two atoms involved in each of the six-fold coordination lie along a line perpendicular to this square plane, thus forming the octahedra.

This octahedral arrangement leaves no octahedrons dangling; rather, they are all tied to each other. The only atoms not included in these octahedra are the hydrogens of the OH groups, the oxygen of the NO group, the hydrogens of the H_2O, and the O_3 and O_6 of the NO_2 group. From the distance involved between the O-H . . . O, it is evident that there is little or no hydrogen bonding. The distances and angles found in the H_2O part of the structure seem reasonable.

5. Structure Determination of Uranyl Nitrate Hexahydrate, $UO_2(NO_3)_2\,6H_2O$ (J. C. Taylor* and M. H. Mueller)

Suitable crystals of this compound have been grown, and the collection of three-dimensional neutron diffraction data are under way. Whereas early X-ray results indicated that the crystal was orthorhombic, space group Cmcm, a later piezoelectric study and two X-ray investigations[230,231] proposed a non-centrosymmetric group $Cmc2_1$. Two recent infrared investigations are in conflict with regard to the ionic or covalent bonding of the NO_3 groups. The results of the first of the above X-ray investigations indicated an ionic compound composed of $[UO_2(H_2O_6)]^{2+}$ and $[NO_3]^-$ ions with the six water molecules in the form of a hexagon around the uranium, whereas later X-ray study has suggested a nonionic structure with the uranium coordinated to two NO_3 groups and two H_2O, with the other four H_2O loosely held. It is planned to use neutron data to resolve the above conflicts as well as to locate the hydrogens, of which there are a number in the structure. A parallel X-ray investigation is to be carried out by Prof. Lynton in British Columbia.

6. Chemical and Magnetic Order in $PtMn_3$ (S. S. Sidhu, K. D. Anderson and D. D. Zauberis)

The susceptibility-temperature measurements[232] of $PtMn_3$ in the range from room temperature to 250°C show an anomaly, which, as shown by X-ray diffraction measurements, does not result from a phase

*Resident Research Associate.

[230]Vdovenko, V. M., Stroganov, E. V., Sakolov, A. P., and Zandin, V. N., Radiokhimiya 2, 24 (1960).

[231]Fleming, J. E., and Lynton, H., Chem. and Industry 79, 1416 (1960).

[232]Wuttig, Manfred, and Read, T. A., University of Illinois, Private Communication, February (1963).

change of the alloy. A neutron and X-ray diffraction study of the chemical and magnetic order in the above temperature range, to explain this anomaly, is being extended to cover a larger temperature range to determine the main characteristic of the magnetic behavior of the alloy and its dependence on the chemical order and disorder.

The crystalline structure of the $PtMn_3$ alloy is face-centered cubic with 4 atoms per unit cell and $a_0 = 3.84$ Å. The structure factor for the disordered state is

$$|F_{hk\ell}| = \left(\frac{b_{Pt} + 3b_{Mn}}{4}\right)\left\{1 + e^{\pi i(h+k)} + e^{\pi i(h+\ell)} + e^{\pi i(k+\ell)}\right\}; \quad (1)$$

for the ordered state, in which, say, platinum is at 0, 0, 0, and 3, and manganese at 1/2, 1/2, 0; 1/2, 0, 1/2; 0, 1/2, 1/2,

$$|F_{hk\ell}| = b_{Pt} + b_{Mn}\left\{e^{\pi i(h+k)} + e^{\pi i(h+\ell)} + e^{\pi i(k+\ell)}\right\}, \quad (2)$$

where b_{Pt} and b_{Mn} are coherent nuclear scattering amplitudes for platinum and manganese, respectively. The above expressions are also applicable to X-ray structure factors in which b_{Pt} and b_{Mn} are replaced by X-ray scattering factors f_{Pt} and f_{Mn}, respectively. Neutron and X-ray structure factors squared are given in Table LXVII.

Table LXVII

STRUCTURE FACTOR SQUARED FOR $PtMn_3$

State	Miller Indices	For X Rays $\lvert F_{hk\ell}\rvert^2$	For Neutrons $\lvert F_{hk\ell}\rvert^2 \times 10^{24}$ cm^2
Disordered	(a) hkℓ all odd or all even	$(f_{Pt} + 3f_{Mn})^2$	0.0237
	(b) hkℓ mixed	0	0
Ordered	(a) hkℓ all odd or all even	$(f_{Pt} + 3f_{Mn})^2$	0.0237
	(b) hkℓ mixed	$(f_{Pt} - f_{Mn})^2$	1.7371

$b_{Pt} = 0.95 \times 10^{-12}$ cm; $b_{Mn} = -0.368 \times 10^{-12}$ cm.

It is apparent from the structure-factor-squared values that, although X-ray diffraction patterns of the disordered and the ordered alloy would give normal reflections for this type of structure, neutron diffraction

patterns would be unique. This is confirmed by the patterns obtained. A neutron diffraction pattern of the ordered alloy consisted mostly of mixed Miller indices reflections. Practically no diffraction peaks were observed for the all odd or all even Miller indices planes. This uniqueness is found in the neutron diffraction patterns of the face-centered cubic nuclear null-matrices in which the atoms making up a null-matrix transform to ordered positions.[233]

The neutron diffraction patterns of the ordered alloy made at room temperature and at 250°C showed that the crystallographic structure of the alloy was the same at both temperatures, but there were marked differences in the relative intensities of (100) and (110) reflections at the two temperatures. These differences are ascribed to superposition of magnetic intensity on nuclear intensity, the magnetic intensity resulting from alignment of magnetic moments at room temperature. The alignment and disalignment of magnetic moments in this temperature range account for the reported anomaly in the susceptibility-temperature curve of the alloy.

A fuller account of the magnetic structure of this alloy and its dependence on the chemical order-disorder in an extended temperature range will be presented elsewhere.

7. The Scattering of Neutrons by Liquid Alloys of Sodium and Cesium (LeRoy Heaton and Clifford W. Tompson*)

Neutron diffraction patterns have been obtained and inverted to atomic radial distribution curves for liquid alloys of sodium and cesium of six different compositions over a temperature range from the alloy melting point to 365°C. The alloys were contained in hermetically sealed cylindrical cells of vanadium, 1 cm in diameter and 5 cm in length. The excellent corrosion resistance of the vanadium to the alloys prevented sample contamination, and the negligible scattering amplitude of vanadium gave no spurious peaks.

The atomic radial distribution curves show nondiscrete first peaks. Although these data do not preclude the existence of weakly bound molecules or clusters with atomic distances nearly the same as distances between neighboring free atoms, the distribution curves do show that no permanent compact molecules exist in the liquid sodium-cesium system. The radial distribution curves of each alloy, except in the vicinity of 80 a/o sodium, have the general shape and behavior exhibited by the

*Summer Research Associate.

[233]Sidhu, S. S., Murthy, N. S. Satya, Campos, F. P., and Zauberis, D. D., Atomic and Magnetic Ordering in MnCo, Nineteenth Annual Pittsburgh Diffraction Conference, November 1-3, 1961.

monatomic elements themselves in that there is a small increase of nearest-neighbor distance and an appreciable decrease in number of nearest neighbors with temperature. Samples of 78.7 a/o sodium and 83.4 a/o sodium gave distribution curves of which the first peaks were broad, though not diffuse, with plateau-like tops at all temperatures.

This work was described at the International Union of Crystallography Congress held in Rome, Italy, September 1963, and was presented by one of us (LH) in a Rapporteured Session devoted to liquid structures.

8. Crystallographic Computer Programs (M. H. Mueller, L. Heaton, and S. H. Simonsen*)

Publication:

M. H. Mueller, Fred Clark, and S. H. Simonsen, Program for the Location of Fourier Peak Centers, ANL-6699 (July 1963).

The computer program described above was written for locating the maxima on Fourier (or Patterson) maps used in crystal structure determinations. It is written in FORTRAN and obtains the peak location and height from 27 surrounding points in the three-dimensional Fourier and from 9 points for a two-dimensional case.

Since the Laboratory has now obtained a CDC 3600 computer, our crystallographic computer programs are being converted so that they can be used with this computer with a free flow of the input and output data. This will require programs for (1) generating a complete set of hkℓ's appropriate for the crystal, together with the angle settings for obtaining the data on the automatic Neutron Diffractometer I; (2) processing the output data; (3) permitting this output data to be used as input for a number of programs, such as least-squares, superposition, and Fourier programs for the analysis of the crystal structures. This will require the rewriting of some programs so as to be suitable for CDC 3600 operation as well as the writing of new programs, both to be carried out in cooperation with the Applied Mathematics Division.

*Consultant to the Metallurgy Division.

H. Corrosion Research (J. E. Draley, S. Mori, R. K. Hart, R. A. Le;ault, D. H. Bradhurst, and W. E. Ruther).

1. Aqueous Corrosion of 1100 Aluminum (S. Mori)

Publications:

a. S. Mori, R. E. Loess, and J. E. Draley, pH Microele:trodes for Use Near Corroding Metal Surfaces, Corrosion 9 165t 168t (1963).

b. J. E. Draley, S. Mori, and R. E. Loess, The Corros on of 1100 Aluminum in Oxygen-saturated Water at 70°C, J. Electrochem. Soc. 110 622-627 (1963).

c. S. Mori, R. E. Loess, and J. E. Draley, An Eddy Cu: rent Gauge for Measuring Aluminum Corrosion, Corrosi(n 19 269t-271t (1963).

Kinetics: Corrosion in oxygen-saturated water at 50°C h as now been shown to vary as the logarithm of time from a few days of ex-posure to the end of a 535-day test. As indicated in Figure 187, this be-havior is quite similar to earlier results obtained at 70°C. In the fig ure, each point during the first several days was determined for an indivi dual sample. Dashed lines for longer times were drawn with the average slope for all specimens which were carried to the end of the test.

Figure 187. Corrosion of 1100 Aluminum in Distilled Water

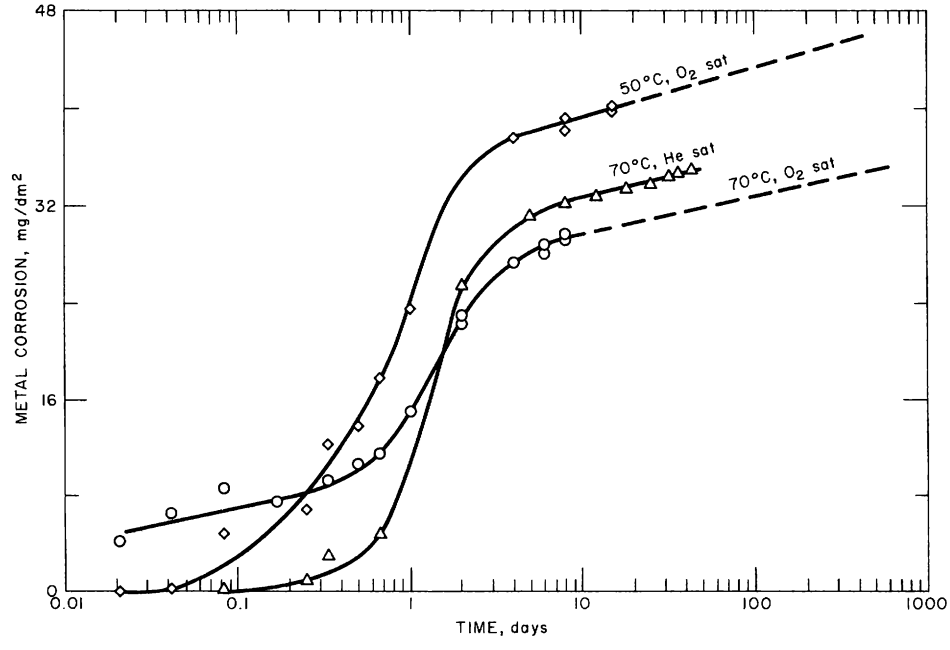

The slopes (rate constants) and logarithmic "intercepts" were calculated for each specimen and averaged for each of the two nomi ially identical tests. The average values are given in Table LXVIII, toge :her

with those for a test run in the same fashion at 70°C. It is notable that the two tests at 50°C were not identical, since intercepts and rate constants were consistently different. The rate constant at 50°C was greater than that at 70°C, but there was no consistent effect of temperature on the intercept.

Table LXVIII

CONSTANTS FOR LOGARITHMIC CORROSION OF 1100 ALUMINUM IN OXYGEN-SATURATED WATER AT 50 and 70°C

Temperature, °C	Slope (mg/dm^2/cycle)	Intercept, Extrapolated to 1 Day (mg/dm^2)	Number of Specimens
50	3.84	32.01	4
	4.20	27.65	4
70	3.13	29.75	5

Data for the initial portions of the corrosion curves in Figure 187 are subject to considerable scatter. It is in this part of the corrosion reaction that there is maximum sensitivity to test conditions. When what were thought to be reasonable precautions had been taken to minimize contamination of the water by reaction products in past work, corrosion was observed to vary as the logarithm of time for the first several hours at 70°C (see publication b above). Results in Figure 187 for the 50°C test, and especially for the helium-saturated test at 70°C, did not show a straight line in the early part of the exposure. For the latter test, contamination was minimized by using only one specimen in the chamber. After the first several days of exposure, it appeared that the oxygen concentration did not significantly influence the corrosion rate at 70°C.

A kinetic expression for the logarithmic corrosion was derived on the basis of periodic repetitive growth and breakdown of protective film (see publication b above). During the year, some effort has been made to estimate the constants basic to the mechanism. No unequivocal method has been found, but approximations can be made simply on the basis of self-consistency. At 70°C, it appears that the film-growth constant is about one-third of the observed corrosion rate constant, and that breakdown of the protective film occurs when it reaches a thickness of the order of 100 Å.

Corrosion Product Lost: Careful calibration of the method of collecting corrosion product lost from specimens has shown that amounts

(at 70°C) reported in previous years have been too small by as much as a factor of two. It is still true that the rate of loss of product does not vary with time in the same way as does the corrosion rate. Also, the rate of loss of product is still considerably less than the rate of corrosion. After 40 days in oxygen-saturated water at 70°C, product is lost about one-third as fast as the metal corrodes.

Since only a small fraction of the product is lost during corrosion, previous estimates of the average composition of the adherent oxide were not significantly in error.

2. Electron Optical Studies of Corrosion Films (R. K. Hart)

Publications:

W. E. Ruther, and R. K. Hart, Influence of Oxygen on High Temperature Aqueous Corrosion of Iron, Corrosion 19 127t-133t (1963).

Film Growth on Pure Aluminum in Steam at 540°C and 600 psi

Structure and Orientation of Corrosion Product Films: Two methods have proved satisfactory to examine in detail the structure and the orientation dependence with respect to the underlying metal of surface films produced on aluminum in the above environment. The first, which was briefly reported in the last Annual Report (ANL-6677), consisted of removing films from corroded metal in a saturated mercuric chloride solution. The stripped films could be viewed directly in the electron microscope and subjected to selected area diffraction (SAD).

The second method was to electrothin corroded specimens from one side while protecting the oxide film of interest with a suitable plastic coating. Composite metal-oxide films, quite suitable for transmission electron microscopy, were prepared in this way. By this method the orientational relationship between the metal and overlying oxide was obtained directly with the aid of selected area diffraction.

From the above experiments only one type of oxide was found to be present. This was γ-Al_2O_3, cubic, A = 7.90 Å (ASTM X-ray card No. 10-425). The reasons for erroneously reporting these films to be corundum (α-Al_2O_3) in earlier publications will be given at a later date. The oxide was found to occur on the surface with four orientations predominant. These were the [001]-zone normal to the surface, [110]-zone normal to the surface, [111]-zone normal to the surface, and randomly oriented "floral" oxide; (110) and (111) were the more commonly observed orientations.

(100) Oxide Surfaces: After short exposures (1 hr), films consisted of many small crystals of about 500-Å diameter. Selected area diffractions from these films consisted of continuous rings with the (440) ring being of abnormally high intensity, indicating that the crystals are fiber textured about the [001] direction. The crystal size in these films increased to about 1500 Å after a 6-hr exposure. For much longer exposures the individual crystals appeared to merge and lose their identity, as shown in Figure 188. The diffraction pattern in Figure 189 is from this type of film. The spots lying on continuous rings indicate that a certain degree of preferred orientation has occurred with the [001]-zone normal to the film surface.

Figure 188. Aluminum Corroded for 30 hr in Steam at 540°C and 600 psi. Oxide Stripped in Saturated $HgCl_2$.

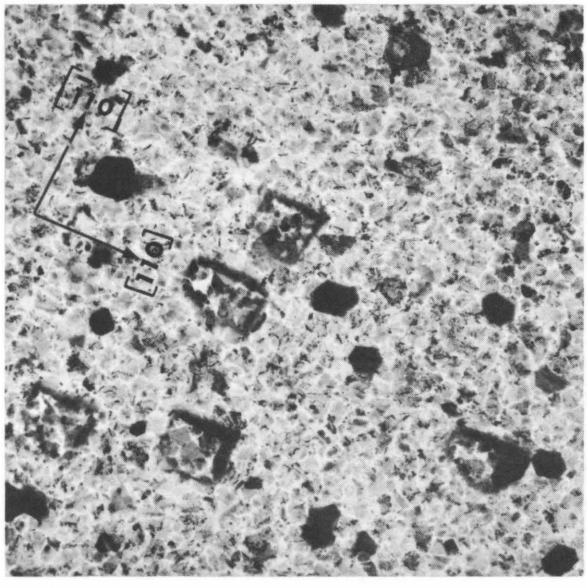

Micro 103199 16,000X

Figure 189. SAD from [001]-Zone Corresponding to Figure 188

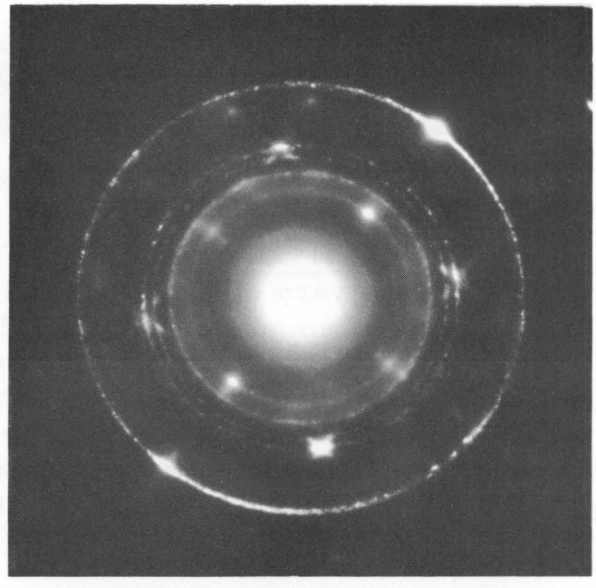

Macro 103817 2X

(110) Oxide Surfaces: These films also exhibited fine-grained structures in their early stages of film growth, the particle size being between 500 and 1000 Å after one hour. These small crystals appeared to be carried on a very thin continuous film, which no doubt contributed to the background on diffraction patterns. These films yielded diffraction patterns which consisted of both rings and spots which showed the films to be partly oriented with the [110]-zone normal to the surface and partly randomly oriented polycrystalline.

After film growth was well established, the film appeared similar to that shown in Figure 190. Here one observes the "fish scale" that has been referred to in previous reports, particularly the topography revealed by replicas. These films were well-oriented, as shown by the diffraction pattern in Figure 191.

Figure 190. Aluminum Corroded for 24 hr in Steam at 540°C and 600 psi. Oxide Stripped in Saturated $HgCl_2$.

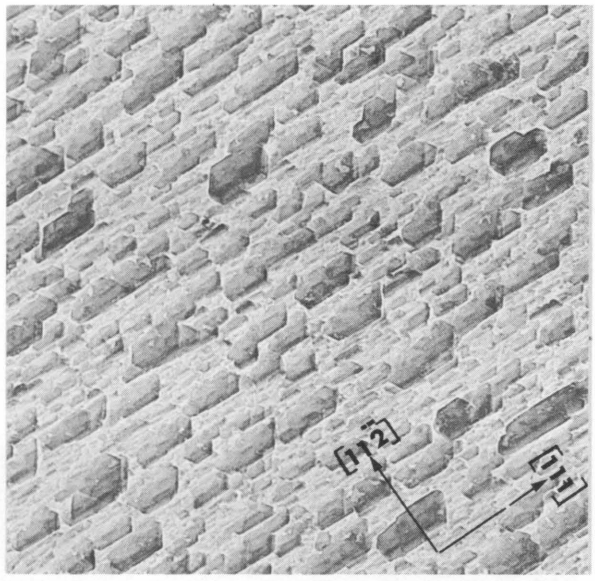

Micro 103284 40000X

Figure 191. SAD from [110]-Zone Corresponding to Figure 190

Macro 103285 2X

(111) Oxide Surfaces: Films oriented with the [111]-zone normal to the surface very closely resembled the (110) films in appearance, as can be seen by comparing Figures 190 and 192. These films again started growth as finely grained crystallites which, after a few hours, gave way entirely to films exhibiting the "fish scale" appearance shown in Figure 192. The shapes of the individual crystals appear as part hexagons; their crystallographic directions, however, differ from those in the (110) films. The diffraction pattern corresponding to Figure 192 is shown in Figure 193.

The diffraction patterns from γ-Al_2O_3 films contain abnormal reflections, as shown in Figure 198. Many of these abnormal reflections also are much stronger in intensity than the normal reflections from the γ-Al_2O_3 lattice. In addition to the abnormal reflections shown in Figure 198, other maxima were observed, often in the form of streaks which are most likely due to stacking disorders in the crystal lattice. These abnormal reflections and maxima were not restricted to patterns from (111) films, but may also be seen in diffraction patterns from films of other orientations.

Randomly Oriented Oxide: In addition to specifically oriented oxide films, occasional areas of film were observed to be randomly oriented. These were easily recognizable in the electron microscope as they appeared to have a "floral" design, seen in Figure 194, and yielded spotty ring patterns, as shown in Figure 195.

Figure 192. Aluminum Corroded for 16 hr in Steam at 540°C and 600 psi. Oxide Stripped in Saturated $HgCl_2$.

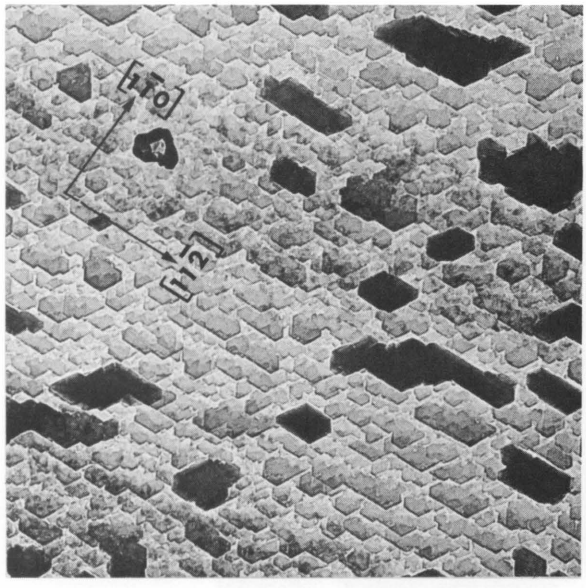

Micro 103497 30000X

Figure 193. SAD from [111]-Zone Corresponding to Figure 192

Macro 103500 2X

Figure 194. Aluminum Corroded for 6 hr in Steam at 540°C and 600 psi. Oxide Stripped in Saturated $HgCl_2$.

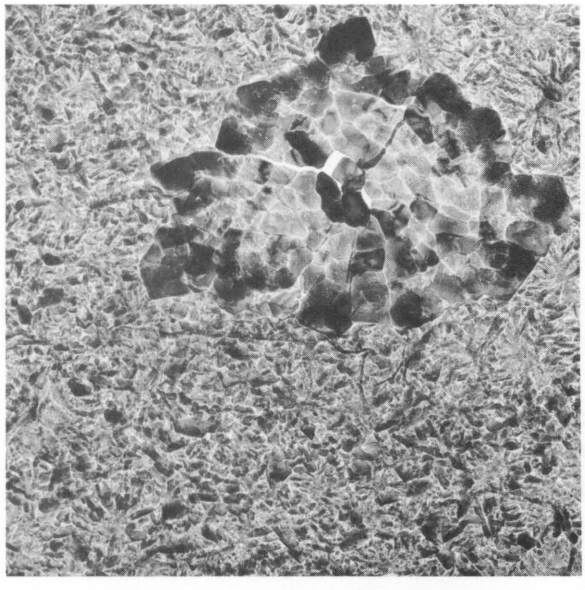

Micro 103420 20000X

Figure 195. SAD Corresponding to Figure 194, Showing Random Growth

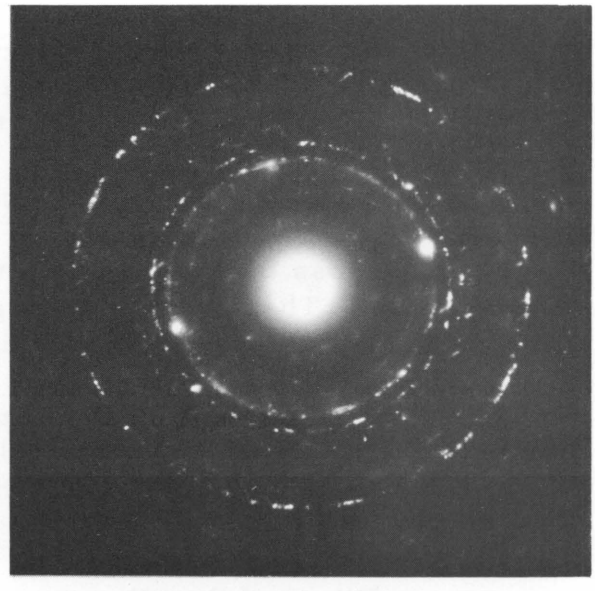

Macro 103274 2X

Occasionally within this "floral" oxide, crystalline conglomerates (shown in Figures 194 and 196) were observed. The occurrence of these features was mainly in this floral-type oxide, although they have

Figure 197. SAD Corresponding to Figure 196, Showing Al (111) and $[1\bar{1}0]$ Parallel to γ-Al_2O_3 (111) and $[1\bar{1}0]$

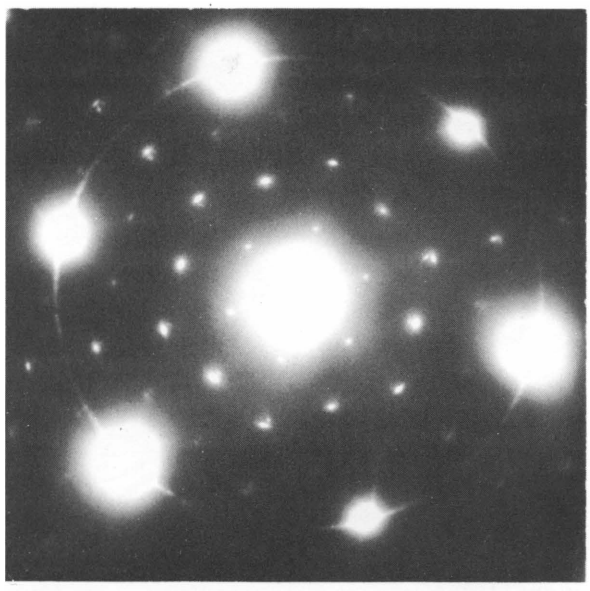

Macro 104313 2X

Figure 198. Indices of Diffraction Pattern of γ-Al_2O_3 Plus Aluminum Shown in Figure 197

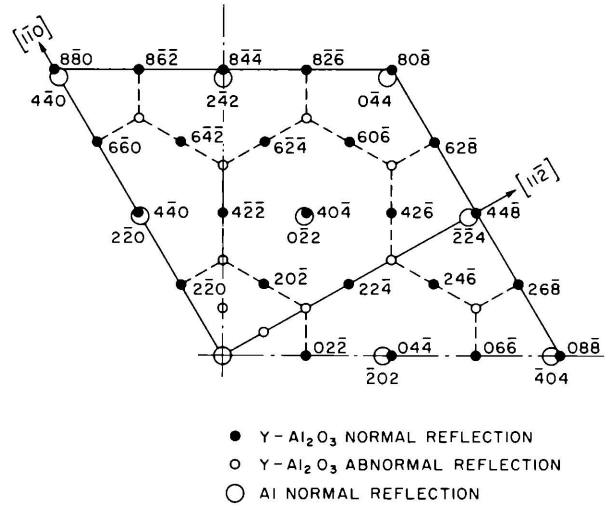

Effects of Pressure on Film Growth: In order to ascertain the pressure dependence of the corrosion of aluminum in steam at 540°C, specimens were corroded at pressures of 40 psi, 600 psi, and 1000 psi, and then subjected to the various examinations described. Each set of specimens was corroded for 24 hr. The general appearance of surface films after corrosion at pressures from 40 psi to 1000 psi is shown in Figures 199, 200, and 201.

One interesting feature of these micrographs is that no outcrops in the form of platelets were formed on specimens corroded at 40 psi, an observation confirmed both by light optical examination and by the more detailed electron optical examination. Platelets were observed in considerable numbers on both 600 psi and 1000 psi specimens, the number formed at 600 psi being the greater. The average number of platelets on 600-psi specimens was $1.3 \times 10^5/cm^2$, and these were scattered fairly uniformly across the surface. The platelets on these specimens were also appreciably larger than those carried by 1000-psi specimens. This can readily be seen by comparing Figures 200 and 201.

Platelets on 1000-psi specimens occurred mainly in clusters at a density of $7 \times 10^4/cm^2$. These clusters of platelets occurred in relatively small areas (as shown in Figure 201) scattered across the surface and showed a morphology different than the surrounding general film.

Figure 199. Aluminum Corroded for 24 hr in Steam at 540°C and 40 psi

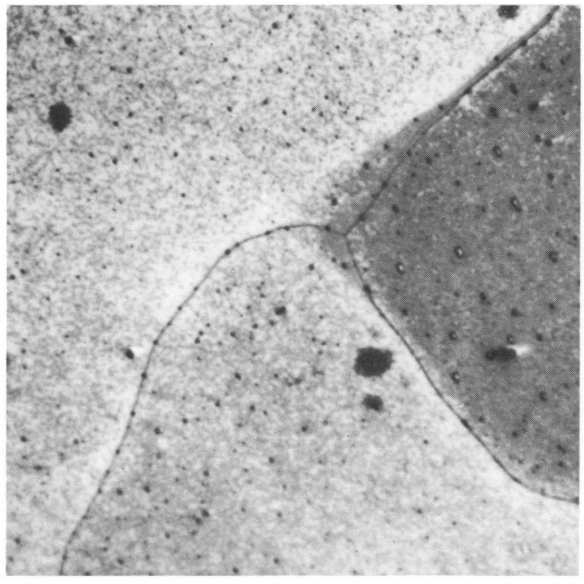

Micro 110714 800X

Figure 200. Aluminum Corroded for 24 hr in Steam at 540°C and 600 psi

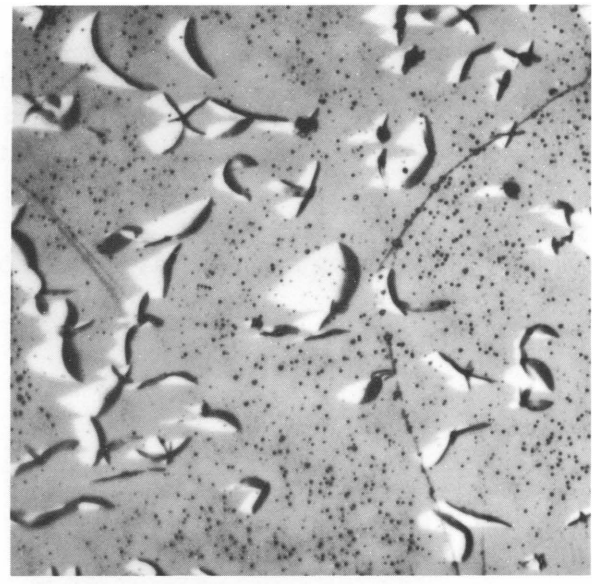

Micro 110704 500X

Figure 201. Aluminum Corroded for 24 hr in Steam at 540°C and 1000 psi

Micro 110708 800X

Detailed electron optical examination showed that 40-psi specimens were almost completely devoid of hexagonally shaped crystallites, which were prevalent on both 600- and 1000-psi specimens. The number present on the latter two types increased rapidly with pressure. These crystallites are seen as small black dots in Figures 200 and 201. The material dotted across the surface on 40-psi specimens (see Figure 199) was found to be small clusters of randomly oriented γ-Al_2O_3 which formed on top of well-oriented film.

Macro observation of corroded specimen surfaces showed that many gas blisters were produced during the corrosion process. There were more of these blisters and of larger dimensions on specimens corroded at the lowest pressure than on specimens corroded at the two higher pressures. Some of the blisters on 40-psi specimens were over a millimeter in diameter. The blister size was observed to decrease with increasing pressure. It is thought that these blisters are caused by the entrapment of hydrogen which is a byproduct of the corrosion reaction.

Some specimens corroded at 1000 psi were found in a partially disintegrated condition upon reopening the autoclaves. The disintegrated areas of these specimens were converted into a white powder product which was subsequently removed and subjected to X-ray analysis. The results showed that both γ-Al_2O_3 and α-Al_2O_3 (corundum) were present in this powder product. In addition, aluminum diffractions were present, and subsequent microscopic examination showed that this powder product contained small particles of aluminum which had resisted corrosion and had been carried away from the bulk metal with the oxide.

The weight gains of specimens corroded at these three pressures were also determined, excluding those specimens which were partially disintegrated in 1000-psi steam. Results showed that films did increase in thickness with increasing pressure, their thickness ranging from 240 Å at 40 psi, through 260 Å at 600 psi, to 310 Å at 1000 psi, all for a 24-hr exposure.

Instrumentation

Three sections of the microprobe analyzer have been redesigned and constructed to improve its operational efficiency. The new units incorporated into the microprobe are a video display system, a vacuum path 2θ scanning spectrometer, and a specimen stage.

Video Display Unit: This unit was designed and constructed by the Electronics Division according to ANL drawing No. EL-D-3613Q. The unit is based on a Tektronix Oscilloscope type RM 561A and can be made to display X-ray scans, X-ray rasters, specimen current scans,

and back-scattered electron scans. The modes of display for the various input signals are standard raster, normal raster, vertical line, horizontal line, and spot.

All that is required to display a particular type of video image on the oscilloscope screen is to set two selector switches at the appropriate settings. Operating in the standard raster mode, the magnification of the final image can be varied from 100 to 2000 diameters with the electron probe beam set at approximately one micron.

Vacuum Path 2θ Scanner: By using a rotary sliding vacuum seal it has been possible to construct a very compact 2θ scanner having a pump-out volume of only a few hundred cubic centimeters and a high-precision drive mechanism. Any angular setting can be reproduced to 0.01°. There are provisions to tune the crystal should this be necessary.

Analyzing crystals for this vacuum 2θ scanner are either of the fixed bent or fixed bent and ground types, and can be readily interchanged with the air path 2θ scanner. The design features allow for the use of variable bent crystals with a minimum of modification to the existing scanner.

A Siemens flow proportional counter has been used for the detector.

Specimen Stage: The new stage has been designed to reduce vibration at the specimen level to a minimum as well as to allow precise and reproducible positioning of a specimen.

Specimen movement is by two micrometers, graduated to 0.0001 in., and 1-in. travel. These operate against plungers which make use of the pressure difference between the vacuum inside the housing and the atmosphere outside.

Four specimens can be loaded simultaneously on a turret which can be rotated with respect to the electron beam axis from outside the vacuum.

The new stage also has a Z-axis control which was lacking in the old stage. This allows one to adjust for differences in specimen height and bring the area under investigation into the right focusing geometry for the X-ray spectrometer.

At the time of writing the microprobe had just been made operational with these units incorporated, and consequently no performance figures are available. No difficulties are expected from the electrical systems, which were thoroughly checked out prior to installation, and it is hoped that the new mechanical stage will reduce vibration to a tolerable level.

3. Mechanism of High-temperature Corrosion of Aluminum Alloys (W. E. Ruther, D. Dorman)

Previous work led to the development of a hypothesis by which the characteristics of the corrosion of aluminum alloys in flowing high-temperature water could be explained.[234] It was assumed that metal corrosion in cracks in the protective film produced soluble corrosion product, and that precipitation within the crack led to plugging (on static exposure), but removal of fresh colloidal precipitate by high-velocity flowing stream prevented such plugging. In the latter case, plugging could be accomplished only by the random settling out of agglomerated colloidal particles.

Efforts have been made to test the validity of the hypothesis. Injected colloids apparently precipitated too rapidly to influence corrosion behavior. The addition of polyvalent ions to the water can be expected to accelerate coagulation of colloidal particles, and thus to influence corrosion rate. If deposition is caused to occur before full passage around the loop, an increase in corrosion rate might be expected to occur. As shown in Figure 202, the addition of magnesium sulfate had this effect at a speed of 5.5 m/sec. In order to allow clear interpretation of the results it will be necessary to examine the results of a current static corrosion test in this environment.

Figure 202. Corrosion of A238 Aluminum Alloy (1 w/o Ni, 0.5 w/o Fe, 0.1 w/o Ti) in Flowing 260°C Solutions

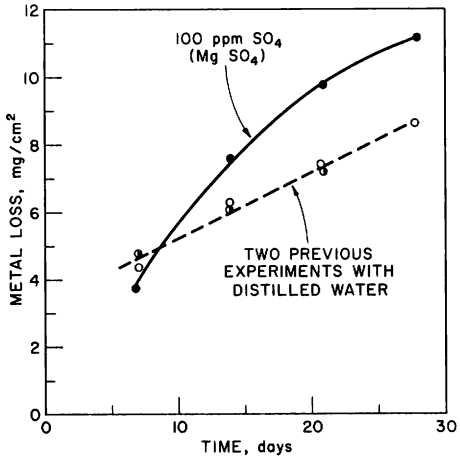

In further work with polyvalent anions, mixtures of acid sodium phosphates have been used. Unfortunately, the decrease in ionization constants for phosphoric acid at elevated temperature caused the formation of a corrosive alkaline solution, thus making it impossible to deduce the effect of the ion.

4. Oxidation Mechanism (D. H. Bradhurst, C. Van Drunen)

In common with many metals, zirconium resists rapid attack by oxidizing media by the formation of a protective oxide film, the properties of which control the rate of the subsequent oxidation reaction. The electrical properties of the oxide film formed on zirconium have been previously studied at ANL by Misch, Iseler, and Van Drunen [see ANL-6434 (1961); also Annual Report for 1960, ANL-6330, pp. 206 et seq.]. They found that a

[234] Draley, J. E., and Ruther, W. E., The Corrosion of Aluminum Alloys in High Temperature Water, Proc. Conf. Corr. Reactor Materials (IAEA), Salzburg, June 4-8 (1962) I 477-498.

measurable emf was developed across the film during growth at elevated temperatures and have interpreted the results in terms of the electrochemical model of oxidation originally put forward by Wagner,[235] and later in simplified form by Hoar and Price.[236] This work is being extended by the use of improved apparatus which allows simultaneous measurements to be made of the weight gain and emf developed during high-temperature oxidation. Polarization experiments are proceeding to determine whether the oxidation rate in dry oxygen can be altered in an analogous manner to that achieved by cathodic or anodic protection in aqueous solution.

The ability of the oxide film to remain free from cracks is important in preserving its protective nature, and in this connection both the nature of the stresses developed in the film, as well as its mechanical strength and deformability, are of interest. There is also some evidence to suggest that grown-in stress may affect the nature of the growth law followed during the initial period of growth. A study of the mechanical properties of the oxide film on zirconium and the nature of the stresses produced during growth has begun in order to evaluate the extent to which these properties influence zirconium oxidation kinetics.

Continuous measurements of emf and weight gain have been made during the oxidation of zirconium samples in dry oxygen at 700°C. A diagram of the modified Ainsworth balance used for the measurements is shown in Figure 203. Contact was made to the oxidizing surface of the sample by surrounding it with lithium-doped nickel oxide powder, and to the zirconium metal by means of a zirconium wire. The presence of the powder did not cause a significant change in the oxidation rate. In addition, the rate appeared to be insensitive to oxygen pressure in the range from 400 mm to one atmosphere. Tests at 400 mm were preferred since at higher pressures turbulence began to produce unsteadiness in the balance readings.

In a typical experiment the emf rises to a value of about one Volt, with the zirconium negative, immediately after admitting oxygen to the system. In some experiments, an initial period was observed in which the emf rose steadily and then suddenly became erratic. One such curve is shown in Figure 204. The reason for the unsteadiness in the emf readings is not known at present, but by analogy with previous work on aluminum [Bradhurst and Leach, Trans. Brit. Ceram. Soc. 62 793 (1963)], sudden changes in emf might be associated with the formation of new cracks in the film. In Figure 204, the weight gain is substantial at

---

[235] See, for example, Hauffe, K., Progress in Metal Physics 4 7 (1961).

[236] Trans. Farad. Soc. 34 867 (1938).

time zero because there was an extended period of thermal equilibration in "vacuum" before measurements were begun.

Figure 203. Apparatus for Simultaneous Measurement of Emf and Weight Gain

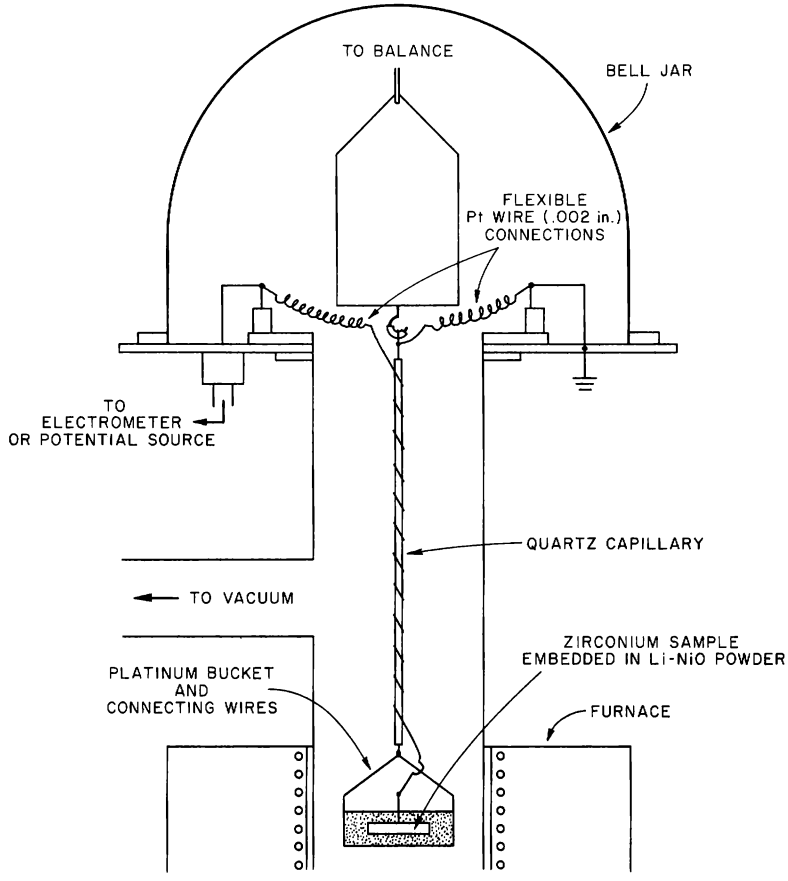

Figure 204. Oxidation of Zirconium at 700°C by Oxygen at a Pressure of 400 mm

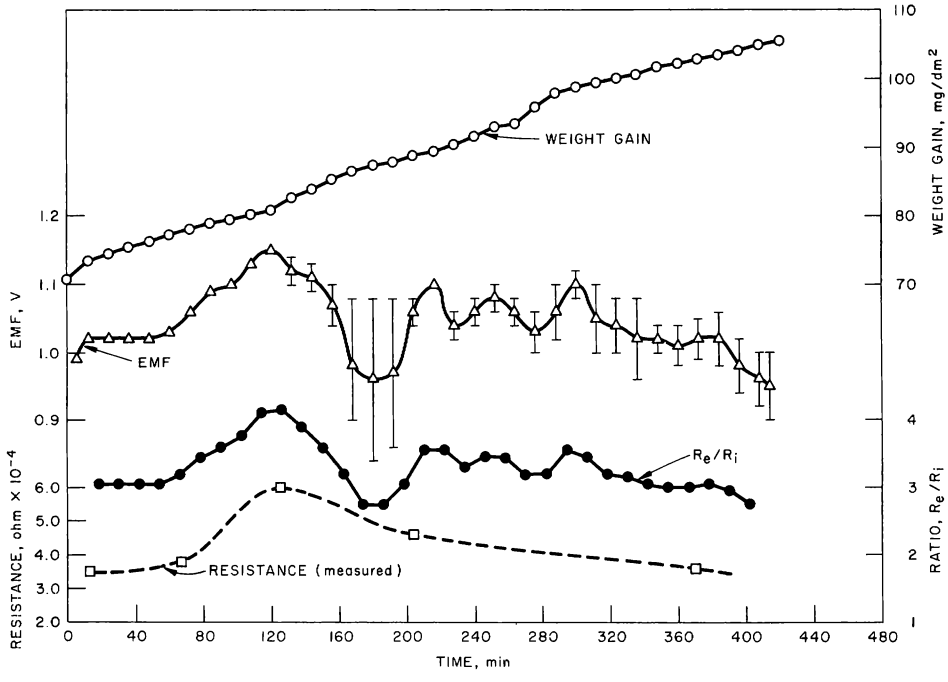

The emf measured in these experiments is thought to correspond to the potential E in equation (1), where E_{oi} is the reversible emf corresponding to the free energy change in converting zirconium into ions in the oxide lattice, i the oxidation current, and R_i the ionic resistance:

$$E_{oi} - E = iR_i. \tag{1}$$

E can also be expressed in terms involving electron transport, as in equation (2):

$$E_{oe} + E = iR_e, \tag{2}$$

where R_e is the electronic resistance of the oxide and E_{oe} represents the free energy change due to solution of oxygen in the zirconium oxide lattice.

Changes in the emf may be seen from Figure 204 to correspond to changes in slope in the weight-gain curve; E falls when the rate increases. By use of the data of Figure 204 and equations (1) and (2), R_e/R_i was found to be approximately 3, suggesting that for this system the electronic properties of the oxide may exert the most important rate-controlling influence. Values of E_{oi} and E_{oe} were estimated from the partial molar free energies of solution of oxygen in ZrO_{2-x} [published by Aronson, J. Electrochem. Soc. 108 312 (1961)] and the free energy of the oxidation reaction.

At longer times of oxidation there was no obvious trend in the emf value. Tests will be continued to determine whether any marked change in emf is detectable during the "transition" in kinetics which occurs at 5000 min and above.

Polarization experiments are in progress to determine whether a change in rate may be brought about by means of an externally applied emf. In preliminary experiments cathodic polarization reduced the oxidation rate at 200 min by about 25%; anodic polarization caused an equivalent rate increase.

Measurements of the stress in zirconium oxide films have been made by observing the direction and extent of bending of a metal strip oxidized on one side. Figure 205 shows the results obtained using two techniques. In the first, flat zirconium strips were initially oxidized on both sides. The oxide on one side was then removed by grinding and the specimen was returned to the temperature of oxidation in vacuum. The radius of curvature of the strip was then measured and the stress in the remaining oxide film calculated. In the second technique, which has so far only been successfully applied as a "blank" experiment (see curve II), the movement of a pointer attached to one end of a zirconium

strip was measured with a traveling microscope. The specimen was mounted on a recording balance for simultaneous measurement of weight gain. Further specimens are being prepared by roll bonding to produce an inert gold surface on one side of the metal strips to enable continuous measurements of stress to be made as the film is formed.

Figure 205. Bending of a Zirconium Strip Due to Oxidation at 700°C in Dry Oxygen

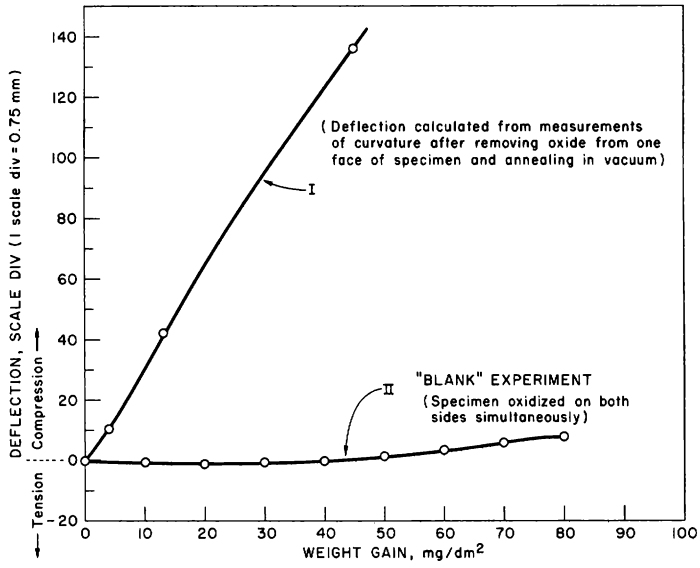

The results in Figure 205 show that the oxide formed at 700°C in oxygen is under compressive stress. Precise calculation of the values of stress is not possible at this time because of the lack of data on the mechanical properties of zirconium at 700°C. Tensile tests are being performed to provide these data. Preliminary calculations based on extrapolated values give stresses of the order of 2×10^4 and 3×10^3 kg/cm^2 for films 1 and 7 μ thick, respectively.

Measurements of the deformability of oxide films on zirconium will be attempted by means of tensile tests on thin oxide covered wires.

5. Polarization Studies of Corroding Aluminum (R. A. Legault, W. Bettin)

This program has recently been reactivated after about a year and a half of decreased activity. Previously published work dealt with the polarization of aluminum in fairly high-purity distilled water (of ~1.4-megohm-cm resistivity).

In order to make it possible to determine whether the impurities present in such water have had significant influence on polarization behavior, a technique has been developed for the routine production

of water approaching theoretical purity. Measurements in this environment have been more difficult because of its high resistance. Changes in measuring circuit and a move into an electrically shielded room are being made to alleviate the problems.

One phase of the experimental program involves essentially instantaneous determination of corrosion rate by means of the "polarization resistance" method described by Stern a few years ago [J. Electrochem. Soc. 104 56 (1957)]. Preliminary measurements with 1100 aluminum in water at 96°C have provided the approximate variation of corrosion rate with time. It is anticipated that further refinements will make it possible to examine the kinetics and to correlate corrosion rates with polarization measurements.

I. Ceramic Materials Research

1. Defect Equilibria of Plutonium Oxides (L. M. Atlas)

Like ZrO_2 and UO_2, the fluorite structure of PuO_2 can tolerate an appreciable departure from stoichiometry. Chikalla, McNeilly, and Skavdahl[237] found that at high temperatures the composition range of this phase extends at least between $PuO_{2.00}$ and $PuO_{1.62}$. Below about 660°C, however, the defect structure transforms into a mixture of fluorite and body-centered cubic phases - the latter (alpha Pu_2O_3) also having a variable composition. The fluorite phase apparently may also exist with an oxygen content as high as $PuO_{2.09}$; Drummond and Welsh,[238] as well as Roberts and his associates,[239] reported the preparation of such a compound by the thermal decomposition of plutonium sulfate.

At present, neither the nature of the defects in nonstoichiometric PuO_2, nor the thermodynamic relations between this phase and oxygen gas are known. Therefore, the major purpose of this program, initiated in March 1963, is to supply information in these two areas mainly through the application of the following procedures.

1. The composition and electrical conductivity of small ceramic specimens will be measured as a function of temperature and the partial pressure of oxygen in a gas mixture. This type of measurement requires that the solid and gas phases reach equilibrium with each other in a reasonable time; hence, such measurements will be made above 1000°C.

2. The emf of the solid-state electrolytic cell

   $$PuO_{2\pm a} \mid ZrO_2 + CaO \mid NiO, Ni \text{ (or } Fe_{0.95}O, Fe)$$

   will be measured as a function of a and temperature. This technique assumes that the cell components are isolated from the surrounding gas; therefore, it is most useful in the temperature region between about 600 and 1100°C

---

[237] Chikalla, T. D., McNeilly, C. E., and Skavdahl, R. E., The Plutonium-Oxygen System, HW-74802 (Sept 1962).

[238] Drummond, J. L., and Welsh, G. A., The Preparation and Properties of Some Plutonium Compounds, Part VI, Plutonium Dioxide, J. Chem. Soc. 1957, 4781.

[239] Roberts, L. E. J., Russell, L. E., Adwick, A. G., Walter, A. J., and Rand, M. H., The Actinide Oxides, Proc. 2nd UN Intl. Conf. on Peaceful Uses of Atomic Energy, Geneva, Switzerland, 28, 215 (1958).

Composition and Conductivity Measurements: The apparatus designed for this program permits the simultaneous measurement of the electrical conductivity and composition of a solid. This is accomplished by suspending a specimen within a closed furnace system whose recirculating gaseous atmosphere can be conveniently sampled and analyzed. The four wires which comprise the suspension system also serve as current and potential leads for both AC and DC conductivity measurements.

The gas system can be switched into either of the two configurations shown in the schematic diagram of Figure 206. In position 1, the stream of gas divides into two parts: one flows through the reference chamber of a thermal conductivity detector, while the other passes over the specimen in the furnace and then through the sample chamber of the detector. This configuration permits the furnace system to be filled with a gas having a known partial pressure of oxygen (e.g., mixtures of H_2 and H_2O). Position 2 is obtained simply by pressing a gas-chromatography switching valve. The two streams of gas continue through the reference and sample chambers of the detector as before, but they are now isolated

Figure 206. Gas System of Defect Equilibria Apparatus
(a) Position 1: Continuous Gas Flow
(b) Position 2: Furnace Loop Isolated

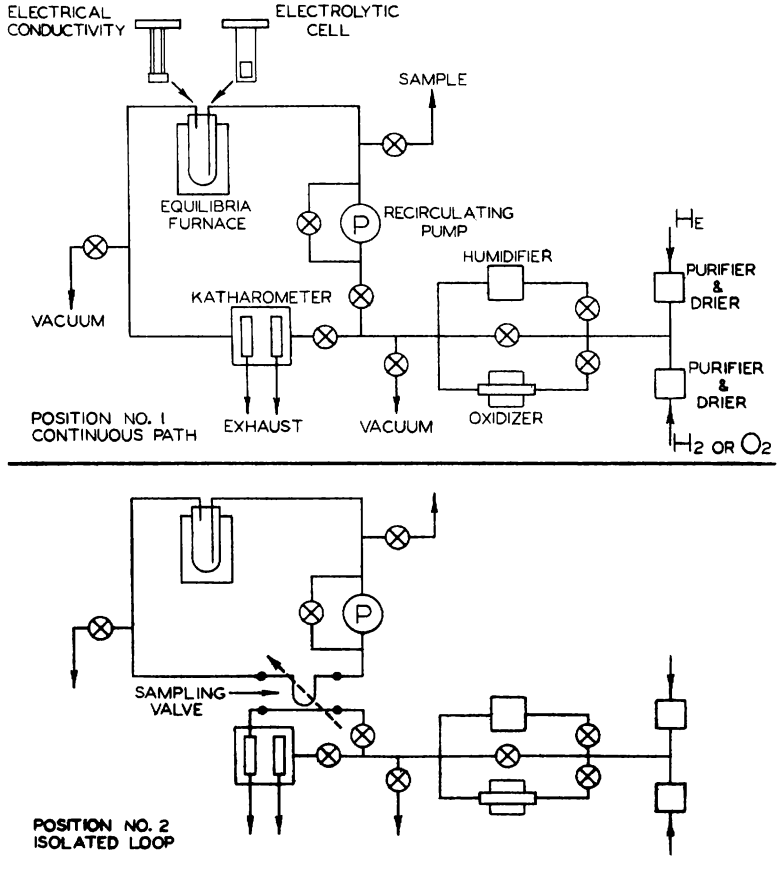

Macro 37866

from the furnace system, which forms a closed recirculating loop. Small samples of gas may be withdrawn from the furnace loop and inserted into the sample carrier gas stream by means of a chromatography sampling valve. In this way, variations of the originally known gas composition flowing over the specimen may be monitored at close intervals while the electrical conductivity is being measured. Now, if all of the changes of gas composition may be ascribed to absorption by, or evolution from, an originally analyzed solid, information is directly provided about the dissociation pressure of $PuO_{2\pm a}$ as a function of x and T. At constant T,

$$\Delta G_1^\circ = - RT \ln p_{O_2}, \tag{1}$$

where ΔG_1° is the standard Gibbs free energy for the reaction

$$\frac{2}{x} PuO_{2\pm a} \rightarrow \frac{2}{x} PuO_{2\pm a-x} + O_2 \tag{2}$$

as x approaches 0.

Measurements of the variation of ΔG_1° with T then give the entropy change for reaction (2) from

$$\Delta S_1 = - \left(\frac{\partial \Delta G_1^\circ}{\partial T} \right)_a , \tag{3}$$

and the enthalpy change from

$$\Delta H = \Delta G_1^\circ + T\Delta S_2. \tag{4}$$

The interaction between the solid and gaseous oxygen may also be written in terms of the creation of structural defects. For the case of PuO_{2-a}, and assuming the defects are only oxygen vacancies (V_O) and that they arise only because of nonstoichiometry,

$$O_{\ell}^{\bar{2}} \rightleftharpoons V_O + 1/2\ O_2 \text{ gas} \tag{5a}$$

(the subscript ℓ denotes ions at regular lattice sites). The vacancies may also produce electrons by dissociation:

$$V_O \rightarrow V_{\dot{O}} + e; \tag{5b}$$

$$V_{\dot{O}} \rightarrow V_{\ddot{O}} + e, \tag{5c}$$

where the dot notation indicates removal of electrons. Application of the law of mass action to reactions 5a-5c gives equilibrium constants which

may be combined (cf. Kröger and Vink[240]) into the following useful relations:

$$[V_O^{\cdot}] = \sigma/C = (K_f K_1)^{1/2}\, p_{O_2}^{-1/4} \tag{6a}$$

and

$$[V_O^{\cdot\cdot}] = \sigma/C = (2K_f K_1 K_2)^{1/3}\, p_{O_2}^{-1/6} \quad , \tag{6b}$$

where σ is the electrical conductivity, and K_f, K_1, and K_2 are the equilibrium constants for the formation and dissociation of V_O according to reactions 5a-5c. The defect concentrations $[V_O^{\cdot}]$ and $[V_O^{\cdot\cdot}]$ are equivalent to a in PuO_{2-a}, and C embodies the molecular weight of the solid (M), its density (ρ), Avogadro's number (A), and the electronic charge e and mobility μ_e:

$$C = \mu_e e A \rho / M. \tag{7}$$

The defects in PuO_{2-a} need not be oxygen vacancies, but may be interstitial plutonium ions (Pu_i). In this case, the analogs of equations (6a) and (6b) become

$$[Pu_i^{\cdot\cdot\cdot\cdot}] = \sigma/C = (3K_f K_1 K_2 K_3)^{1/4}\, p_{O_2}^{-1/4} \tag{8a}$$

and

$$[Pu_i^{\cdot\cdot\cdot\cdot\cdot}] = \sigma/C = (4K_f K_1 K_2 K_3 K_4)^{1/5}\, p_{O_2}^{-1/5} \quad , \tag{8b}$$

where K_f, K_1, K_2, K_3, and K_4 are the equilibrium constants for the formation of interstitial plutonium defects and the dissociation of their first through fourth electrons.

Similarly, PuO_{2+a} may contain either oxygen interstitials (O_i) or plutonium ion vacancies (V_{Pu}). Interstitials should be characterized by p_{O_2} having exponents of +1/4 or +1/6, depending on whether O_i is singly or doubly dissociated. In contrast, cation vacancies should give exponents of +1/4 for $V_{Pu}^{\cdot\cdot\cdot}$ and +1/5 for $V_{Pu}^{\cdot\cdot\cdot\cdot}$. In principle, therefore, it should be possible to differentiate between $V_O^{\cdot\cdot}$ and $Pu_i^{\cdot\cdot\cdot\cdot}$ in PuO_{2-a}, or between $O_i^{\prime\prime}$ and $V_{Pu}^{\cdot\cdot\cdot\cdot}$ in PuO_{2+a}, by measuring the variation of σ or a with p_{O_2} at high temperatures (where complete dissociation is likely to occur). This simple picture may, however, be complicated by other factors such as:

---

[240] Kröger, F. A., and Vink, H. J., "Relations Between the Concentrations of Imperfections in Crystalline Solids," in Solid State Physics, Seitz, F. and Turnbull, D., Eds. 3, 307-435, Academic Press New York (1956).

(a) conduction by electrons in the 5f or 6d levels, i.e., the occurrence of more than one conduction band;

(b) trapping of a significant proportion of the conduction electrons at Pu^{+4} ions in regular lattice sites, i.e., the necessity for considering the equilibrium constant for the reaction $Pu^{+3} \rightleftharpoons Pu^{+4} + e$;

(c) interaction between defects so that their activity coefficients become appreciably less than one.

The preceding arguments assume that p_{O_2} may vary when T is held constant. Changing the temperature ideally alters the equilibrium constants in equations (6a,b) and their analogs:

$$K_{f,1,2,3,4} = K^{\circ}_{f,1,2,3,4} \exp-(E_{f,1,2,3,4}/RT), \tag{9}$$

whereupon equation (6b), for example, becomes

$$[V_{\ddot{O}}] = a = \frac{\sigma}{C} = (1/4\, K_f^{\circ} K_1^{\circ} K_2^{\circ})^{1/3}\, p_{O_2}^{-1/6} \exp-\left(\frac{E_f+E_1+E_2}{3RT}\right). \tag{10}$$

At constant p_{O_2}, therefore, the slope of the straight line obtained by plotting ln σ or ln a against 1/T gives an estimate of the sum of the energies required to form a defect and its dissociation to give electrons.

Electrolytic Cell Measurements: The electrolytic cell constructed for this program has been adapted from Blumenthal's[241] design and, like the electrical conductivity apparatus, is suspended from its own furnace cap (see Fig. 206). The two electrodes consist of small, dense ceramic discs of $PuO_{2\pm a}$ and NiO + Ni (or $Fe_{0.95}O$ + Fe). The electrolyte, following the general practice with oxides, is ZrO_2 with about 15 m/o CaO. Electrical contact with the oxide electrodes is made through platinum discs. To minimize interaction between the PuO_2 and the surrounding gas, the electrode and electrolyte discs are packed into a close-fitting alumina crucible, and surrounded by pure alumina or magnesia grain. By this means it is hoped that a static equilibrium atmosphere will be developed locally around the electrodes, and that this will prevent the $PuO_{2\pm a}$ composition from changing with time.

The emf of the electrolytic cell is measured with a Keithley Model 660 Differential Voltmeter under close to null conditions. The

---

[241] Blumenthal, R. N., A Thermodynamic Study of Non-stoichiometric Alpha-Nb_2O_5 and TiO_2, Ph.D. thesis, Northwestern University (1962).

resulting cell voltages are functions of temperature and of a in $PuO_{2\pm a}$, and at constant T are related to the free energy change of the total cell reaction by

$$\Delta G^{\circ}_{cell} = -nFE = -92.264\ E, \tag{11}$$

where nF is the number of coulombs required to transform 1 mole of $PuO_{2\pm a}$ to $PuO_{2\pm a\pm x}$, and E is in mV. The total cell reaction may also be written in terms of the partial reactions at each electrode:

$$\Delta G^{\circ}_{cell} = -92.264\ E = \Delta G^{\circ}_1 + \Delta G^{\circ}_2, \tag{12}$$

where ΔG°_1 is the free energy change for reaction (2), and ΔG°_2 is for either of the two reactions below:

$$2\ Ni + O_2 \rightarrow 2\ NiO \tag{13a}$$

or

$$1.9\ Fe + O_2 \rightarrow 2\ Fe_{0.95}O. \tag{13b}$$

According to Markin and Bones,[242] who evaluated considerable previous work, ΔG°_2 for the nickel-nickel oxide reaction between 500 and 1100°C is given by

$$\Delta G^{\circ}_2\ (Ni, NiO) = -113,300 + 41.5\ T(°K). \tag{14a}$$

Similarly, Blumenthal and Whitmore[243] have determined that the base energy change for the iron-Wustite reaction between 600 and 1360°C is best given by

$$\Delta G^{\circ}_2\ (Fe, Fe_{0.95}O) = -117,740 + 31.01\ T(°C). \tag{14b}$$

Combination of equation (10) with (12a) or (12b) gives the standard free energy change for reaction (2), i.e., the relative partial molar free energy of oxygen.

$$\Delta G^{\circ}_1 = -92.264\ E\ (mV) + 113,300 - 41.5\ T(°K) \tag{15a}$$

or

$$\Delta G^{\circ}_1 = -92.264\ E' + 117,740 - 31.01\ T(°C). \tag{15b}$$

---

[242] Markin, T. L., and Bones, R. J., The Determination of Changes in Free Energy for Uranium Oxides Using a High Temperature Galvanic Cell, Part I, AERE-R 4042 (1962).

[243] Blumenthal, R. N., and Whitmore, D. H., Electrochemical Measurements of Elevated Temperature Thermodynamic Properties of Certain Iron and Manganese Oxide Mixtures, J. Am. Ceram. Soc., 44 508-512 (1961).

It would be desirable to determine ΔG_1° for many values of a in $PuO_{2\pm a}$. This would ordinarily require either many electrode pellets of different composition, or the repeated removal and re-equilibration of one electrode. In either case, the cell must be cooled and reloaded for each value of a. It has been decided to substitute a somewhat novel procedure for changing the composition of the PuO_2 electrode in situ, by slowly passing an accurately known quantity of electric current through the cell while annealing the pellet to insure homogenization. To simplify this procedure, a Leeds and Northrup Automatic Coulometric Analyzer is used to pass a constant current through the cell despite changes in its internal resistance.

Present Status of the Program: As of the end of 1963, the apparatus, including the gas system, and the electrical conductivity and electrolytic cell caps for the equilibrium furnace have been completed. Figure 207 shows the equilibrium furnace (wound with Pt-10% Rh wire) at the right, with the conductivity head in place. The cell cap is clamped just to the left, next to the press. The rest of the glovebox contains equipment for mixing, milling, pressing, sintering, and grinding - in short, everything needed to fabricate the required PuO_2 ceramic specimens. Most of the rather complicated gas piping system is outside of the glovebox, isolated from the interior by filters. The front panels and flexible entry port have

Figure 207. Arrangement of Equilibrium Furnace and Ceramic Fabrication Line in Glovebox

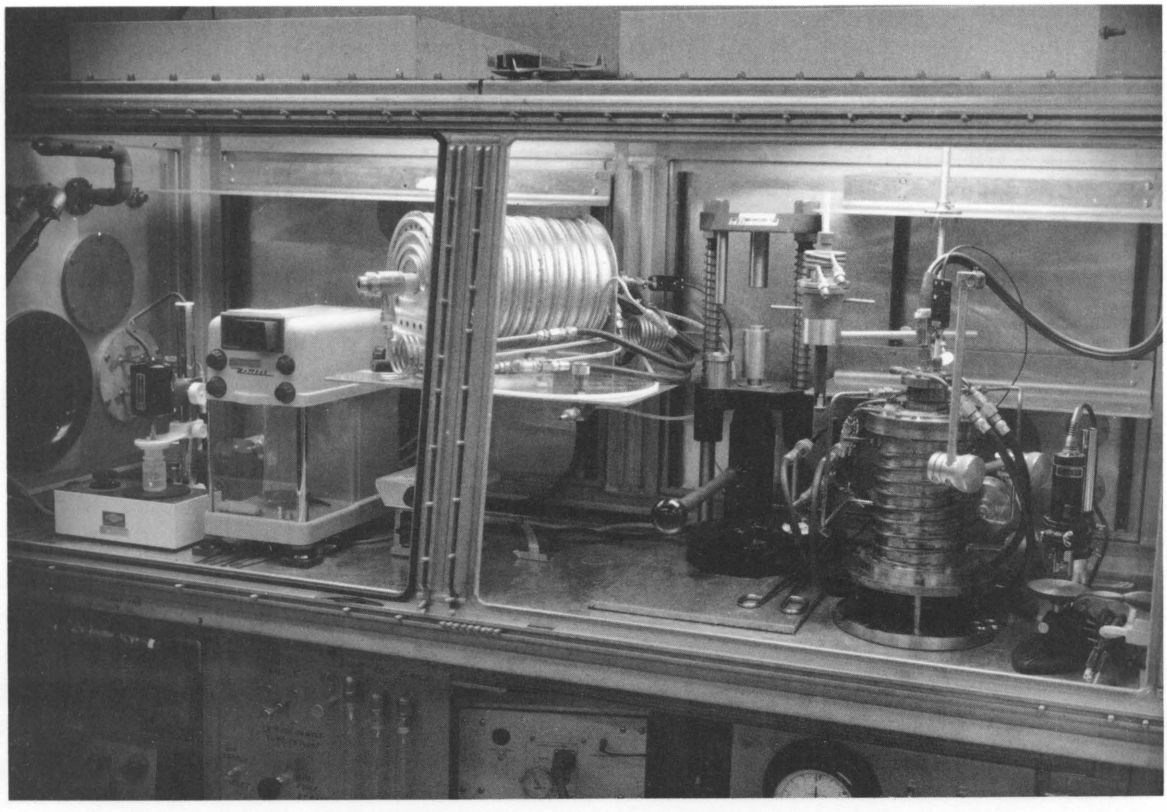

Macro 37671

now been installed on the box, and the apparatus is being calibrated. Present plans are for a few experiments to be conducted with TiO_2 to check out the apparatus, and rutile ceramic specimens have been prepared on the glovebox fabrication line. It is hoped that experiments with PuO_2 will be started in late February or March of 1964. Eventually, these experiments will be broadened in scope to include solid solutions of PuO_2 with UO_2.

2. Effect of Surface Structure upon the Catalytic Activities of Oxides (Milton L. Volpe)

During the past year, apparatus has been built and tested to measure the catalytic activity of single crystals. With the equipment in its present state of development, the rate of decomposition of nitrous oxide ($N_2O \rightarrow N_2 + 1/2\ O_2$) due to one single-crystal wafer of CoO-MgO, having the dimensions 1 cm x 1.5 cm x 0.5 mm, which corresponds to the very small rate of about 0.01 mole % N_2O decomposed per hour (at 350°C) has been measured.

The method is briefly as follows: The catalysis reaction is made to take place in a very small chamber (volume of ~20 ml). The small chamber containing the catalyst is evacuated, and the nitrous oxide then introduced and allowed to react for about an hour. At the end of that time, the nitrous oxide is condensed in a small liquid nitrogen trap. The total pressure of the decomposition products, nitrogen and oxygen, which remain in the gas phase is then measured with a noble-metal thermocouple gage. Because the catalytic activity of the reaction chamber wall was found to be appreciable, the extent of decomposition had also to be measured with the chamber empty. From these measurements, the absolute rate constant, k_a, is calculated,[244] which is a measure of the catalytic activity that is independent of pressure, catalyst surface area, and apparatus volume. The equation relating the observed quantities to

$$k_a = \frac{\frac{2}{3} PV}{tAP_{N_2O}}, \qquad (1)$$

where P is the pressure of the reaction products measured at time t and in a volume V. The symbol P_{N_2O} is the pressure of nitrous oxide, and A is the surface area of the catalyst. The dimensions of k_a are cm/min, with P and P_{N_2O} in torr, V in cm^2, t in min, and A in cm^2.

The apparatus consists of a high vacuum system, an ultra-high vacuum system, and a gas-purifying system. Included in the gas-purifying system is equipment for calibrating the thermocouple gage and measuring

[244] Dell, R. M., Hess, R. A., and Weller, S. W., Catalytic Decomposition of Nitrous Oxide over Magnesium, Second International Catalysis Congress, 1967 (1961).

The nitrous oxide is purified by passing it through a dry ice trap and then condensed in another one in liquid nitrogen. The less condensable gases are then removed by pumping.

The CoO-MgO catalyst wafers were prepared by diffusing powdered cobalt oxide into single crystals of magnesium oxide as described by Zaplatynsky.[245] Microscopic examination and Laue patterns have demonstrated that these crystals were of single orientation although containing mosaic structure. The MgO wafers were prepared by cleaving. A cleaving machine was built which could consistently cleave one-inch-square MgO crystals down to a thickness of 0.5 mm, and occasionally to 0.25 mm. The crystals were carefully polished in phosphoric acid before use.

The work with this equipment thus far has been preliminary to studies on the effect of crystal imperfections on catalysis. The following have been accomplished:

1. An ultra-high vacuum has been achieved consistently in the reaction tube.

2. The feasibility of magnetically moving the catalysts into and out of the reaction chamber has been demonstrated.

3. The method of measuring the pressure of the gases produced by the reaction has been found to be both accurate and precise (within about 3%).

4. It has been found possible to cleave MgO crystals sufficiently thin to permit many of them to be packed into the small reaction chamber. It is estimated that over 80 cm^2 of single-crystal surface could in this way be exposed to the nitrous oxide.

5. Preliminary rate measurements have been made with the empty reaction chamber, with MgO crystals held in a platinum cradle, on platinum, with a fused silica ring, and with CoO-MgO single crystals held in a silica cradle. These catalysts were not subjected to ultra-high vacuum bake-out. Runs using ultra-high vacuum are now in progress.

An idea of the precision with which rate measurements may be made is given in Table LXIX, which lists the results of successive runs that were made with the empty catalyst chamber at 350°C. The catalyst in

---

[245] Zaplatynsky, I., Diffusion of Co^{+2} and Ni^{+2} in Magnesium Oxide, J. Am. Cer. Soc. 45, 28-31 (1962).

this case was the chamber wall itself. The absolute rate constants, calculated from equation 1, are seen to be quite consistent, even though reaction times and nitrous oxide pressures varied considerably.

Table LXIX

CATALYSIS BY CHAMBER WALLS (T = 350°C)

P_{N_2O} (mm)	P(μ)	t(hr)	$k_a \times 10^6$ (cm min^{-1})
125	20	1.42	0.70
60	18	2.50	0.70
60	4.5	0.60	0.77
41.5	17	3.62	0.70

Other runs were made at 359°C, 419°C, and 328°C, and an activation energy of 18.5 kcal/mole was calculated. (It should be noted that if the decomposition had taken place in the gas phase, an activation energy of about 58 kcal/mole[246] would have been observed.)

On the other hand, with magnesium oxide wafers (total surface area = 18 cm^2) held in a platinum wire cradle, consistent results could not be obtained. This was due to interference by the platinum. It appears that platinum is a much better catalyst than MgO, and, in addition, its ability to ad- and absorb oxygen and hydrogen probably made for erratic rate measurements. A silica holder for the MgO crystals is now being made.

Better results were obtained with a single crystal of CoO-MgO (surface area = 4.8 cm^2) held in a silica cradle (surface area 6.8 cm^2); the data are shown in Table LXX. Table LXXI lists equivalent data for a fused silica ring (surface area = 28 cm^2). The rates are given in terms of microns of product per hour (column IV).

Table LXX

CATALYSIS BY CoO-MgO + FUSED SILICA (T = 350°)
(CoO-MgO AREA = 4.8 cm^2; SILICA AREA = 6.8 cm^2)

P_{N_2O} (mm)	P(μ)	t(hr)	μ/hr
64.2	139	2.08	67
64.2	42	1.05	40
64.2	33	1.00	33
64.2	78	3.00	26
58.0	25	1.00	25
58.0	28	1.26	22

[246] Hinshelwood, C. N., and Burk, R. E., The Homogenous Thermal Decomposition of N_2O, Proc. Roy. Soc. (London) A106, 284 (1924).

Table LXXI

CATALYSIS OF N_2O AT A PRESSURE OF 58.0 mm
BY FUSED SILICA RING (T = 350°)
(SURFACE AREA = 28 cm^2)

P (μ)	t (hr)	μ/hr
81	1.53	53
87	3.50	25
55	3.00	18
30	1.72	17
26	1.72	15

It is apparent from these tables that the rate dropped with successive runs and reached a limiting value. The reason for this behavior is still obscure and is being investigated.

From the averages of the last three rates in each of the tables, coupled with the rates in Table LXIX, the absolute rate constants at 350°C for catalysis by CoO-MgO and by silica were obtained:

$$k_a \text{ (CoO-MgO)} = 11.0 \times 10^{-6} \text{ (cm/min)};$$

$$k_a \text{ (Silica)} = 1.2 \times 10^{-6} \text{ (cm/min)}.$$

The value for CoO-MgO is about what would be expected from measurements on powders.[247] On the other hand, the value for silica is about ten times higher than would be predicted from our results on powders. This, coupled with the fact that the activation energy for silica measured in the single-crystal apparatus (16.5 kcal/mole) was considerably less than the value obtained with powders (34 kcal/mole), indicates that large thermal gradients may have existed in the catalyst chamber of the newer apparatus. A search for such temperature gradients will be made and, if found, eliminated.

Work in the immediate future will be concerned not only with improving the precision and accuracy of the rate measurements, but also with reducing the importance of contributions to catalysis by the walls of the reaction chamber. One way in which this last aim could be realized would be by increasing the catalyst surface area by using larger wafers and a greater number of them. Another way would be by cooling the plug and adjacent reaction tube walls during the runs.

---

[247] Hauffe, K., "The Application of the Theory of Semiconductors to Problems of Heterogeneous Catalysis," in Advances in Catalysis, Vol. VII, Edited by Frankenburg, W. G., Komarewsky, V. I., and Rideal, E. K., Academic Press, N. Y. (1955).

3. Irradiation Effects in MgO (Paul F. Stablein)

Publication:

Paul F. Stablein, Dislocation Behavior and the Yield Stress in Neutron-irradiated MgO, J. Appl. Phys. 34 1867 (1963).

Studies of the radiation damage in MgO have been extended during the past year to include damage by deuterons and U^{235} fission fragments. Bombardments were made with 20-MeV deuterons in samples approximately 2 mm thick. After irradiation the crystals were cleaved parallel to the beam direction and small hardness impressions made on the newly cleaved surface. After etching, the outermost dislocation loop size produced by the indentation was measured and plotted as a function of depth in the crystal in the direction of the beam (see Figure 209). The nonirradiated portion where the loop size is largest corresponds to the normal hardness of the MgO crystal. The crystal obviously is much harder in the irradiated region, for which the loop size is smaller. The sharp peak separating the two regions indicates the end of the range where the deuterons stop, and their presence evidently produces a type of interstitial hardening much like that found in metals.

Figure 209. Outermost Dislocation Loop Size Produced at 25-gm DPH Impressions as a Function of Distance from the Bombarded Surface. The MgO single crystal was bombarded with 20-MeV deuterons to a dose of 1.8×10^{16} deuterons/cm^2.

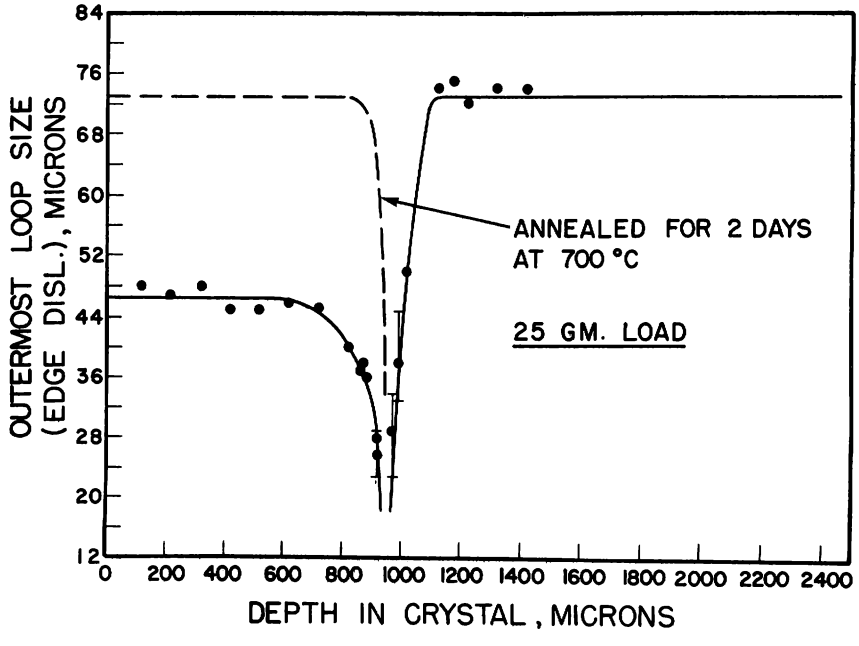

Macro 38170

The damage produced by collisions of high-energy deuterons with lattice atoms anneals out near 400°C, but the deuteron still remains trapped in the crystal. The dashed curve in the same figure shows the result of annealing at 700°C and the hardening caused by the presence of the deuterons. The deuterons migrate to form dislocation loops if the temperature is raised sufficiently (to near 700°C). Eventually they can be redissolved in the lattice.

A calibration curve, which relates the stress to move a dislocation, σ_0, to the outermost loop diameter formed around a hardness impression, has been made from data previously obtained on MgO. From this curve and the hardness data it has been found that the stress σ_0 (see ANL-6677) is only slightly dependent on the deuteron energy as long as it is above threshold.

That dislocation motion is prevented by energetic-particle bombardment is also evidenced from the fission fragment experiments. By vapor depositing U^{235} onto the surface of an MgO crystal and subsequently bombarding the crystal with thermal neutrons, a surface layer about 5 μ deep is created, in which the fission fragments are retained. Previous experimental work (see publication above) has shown that the thermal neutrons would have no effect on dislocation behavior. When a hardness impression is placed on this fragment-bombarded surface, a very small array of dislocation etch-pits is revealed at the surface. However, in the softer area beneath the surface, the loop expands sharply as shown in Figure 210, in which the width of the outermost loop is plotted as a function of distance below the surface in the slip plane. Because the maximum stress occurs at the surface, at the point of initial indenter contact, the nucleation of dislocation loops is not significant, and the variation of the loop width with depth from surface can only be ascribed to the interference of the motion of dislocations.

Figure 210. Surface Hardening Due to Fission Fragments. Outermost dislocation loop size at a single 100-gm DPH impression as a function of distance from the surface. (See text.)

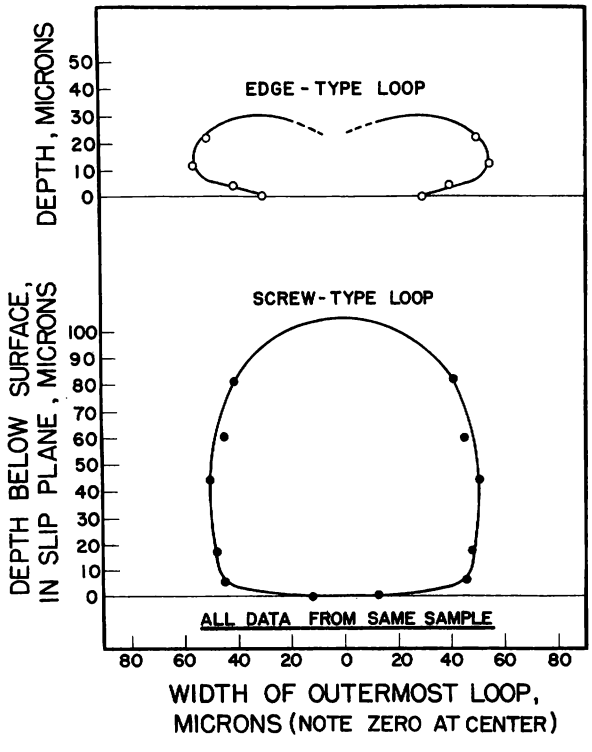

Macro 38171

That dislocations can also absorb radiation-induced defects is evident from Figures 211 and 212. The dislocation distribution at the

surface of the crystal, from which the data of Figure 210 were taken, is shown in Figure 211. At a depth of 4μ (see Figure 212), which is almost the end of the range of the fragments, the etch-pit rows marking edge dislocations have become wavy, instead of straight, as discussed in the last Annual Report (ANL-6677).

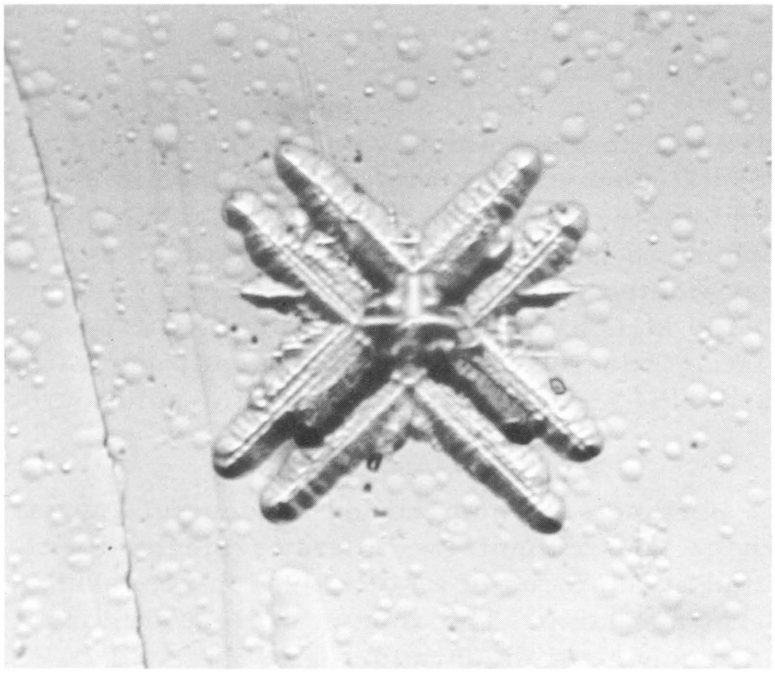

Micro 34432 1000X

Figure 211

(001) Surface of Irradiated (see text) MgO Single Crystal. 100-gm DPH, etched to reveal dislocation distribution.

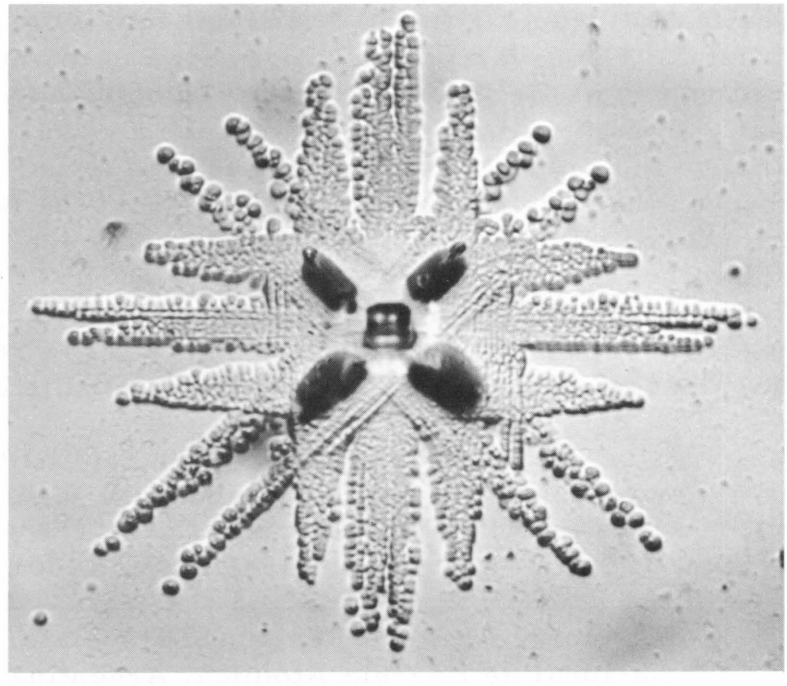

Micro 34435 1000X

Figure 212

Same Impression as Above, after Removal of 4 μ and Re-etching

4. Growth of Single Crystals of Ceramic Oxides (Paul F. Stablein and Carlos Araoz*)

The lack of single crystals of oxides of high perfection, purity, and controlled stoichiometry has been a serious drawback in carrying out basic research with these materials. A program to develop floating-zone melting and crystal-growth techniques for such materials has been initiated through use of an arc-image furnace.

Our first objective was to grow single crystals of CoO, a choice predicted on the suitability of its properties to radiation-damage studies. Among these are its nonstoichiometry,[248] about 3% at the melting point, the ability to cleave, its response to chemical polishing to remove surface damage, and the property that etching reveals dislocations. Also, and perhaps more importantly, CoO and MgO have the same crystal structure (that of NaCl) and are completely miscible, which would permit separation of the effects of radiation hardening from mixed-crystal solid-solution hardening.

To determine the parameters required for successful crystal growth in the arc-image furnace, experiments were first performed with Al_2O_3. The sample was located at the focus of an elliptical mirror which receives its light from a 10-kW arc lamp. The amount of light striking the sample was adjusted by a mechanical diaphragm.

Two techniques have been investigated. In the first, the starting material is a powder which is shaken from a closed hopper and falls vertically through a funnel and small tube onto the molten cap of a seed crystal. The crystal is slowly lowered to maintain the position of the molten cap at the focus, as powder is being added. The second is essentially a zone-melting process in which a rod is fused to a single crystal and, as the crystal is moved through the focus, the molten zone travels through the crystal melting material from the feed rod and freezing it onto the single crystal to lengthen it. A typical zone-melting of Al_2O_3 is shown in Figure 213. The feed rod is shown at the top, the molten zone below it, and part of a grown sapphire single crystal can be seen protruding from the annealing furnace. The latter is required to reduce radiative heat losses, since thermal shock would tend to crack the crystal.

The above techniques were applied to the growth of CoO crystals. By means of the powder method, the feed material was Co_3O_4 reduced in air at the growth temperature to CoO. The seed crystal was a single crystal of MgO. The growth direction was [001], and the atmosphere was

*Formerly Resident Research Associate. Presently at Comision Nacional de Energia Atomica, Argentina.

[248] Carter, R. E., and Richardson, F. D., Trans. AIME 200, 124 (1954).

flowing inert gas. Crystals 0.7 cm in diameter x 13 cm long and 1.1 cm in diameter x 10.5 cm long are the largest crystals grown to-date (see Figure 214). Chemical analysis of one crystal showed a composition of $CoO_{1.03}$ and a total impurity content of 0.5%, about the same as the feed powder.

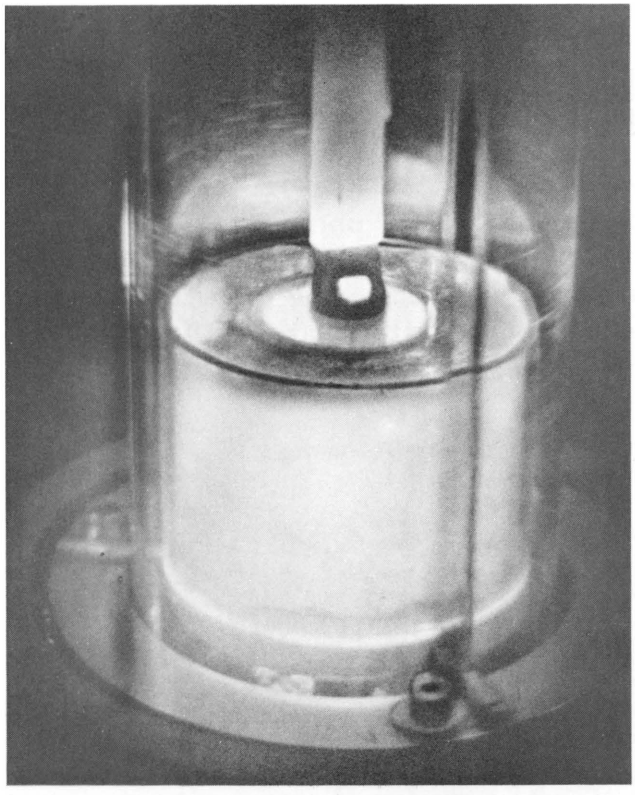

Macro 35719 ~1X

Figure 213

Floating-zone Melting of Sapphire Rod. Rotatable annealing furnace is shown. White spot in center of dark molten zone is reflection of the arc.

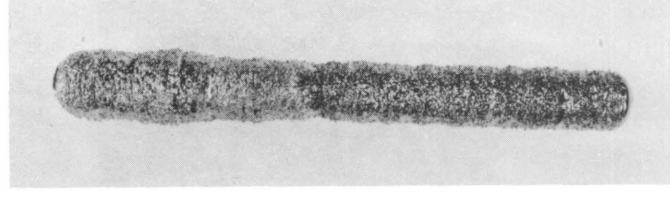

Macro 37587 0.7X

Figure 214

Single Crystal of CoO Grown in Arc-image Furnace

Generally, the crystals are grown in two portions, half one day, then slowly cooled, and finished the second day. The growth rate is 5-10 mm/hr. The maximum diameter that can be attained with CoO is about 2 cm.

The thermal symmetry resulting from continuous rotation of the seed crystal produces crystals which are almost cylindrical, but careful examination reveals that growth in [110] direction is greater than in [100].

The rough, outer layer of all the crystals is polycrystalline to a depth of about 0.5 mm, because some powder falls past the molten cap, strikes the hot side, and sinters there. This can be later removed.

To characterize the properties of these crystals for subsequent irradiation damage studies, the following measurements have been made:

Dislocation density	10^7 cm^{-2}
Slip system	{110} <110>
Yield stress in bending	10.0 kg/mm^2
Cleavage plane	{001}
Hardness	~800 DPH
Electrical resistivity	10^3 ohm-cm

The subgrain size is about 70 μ wide and elongated in the growth direction. An etch-pit structure, showing a dislocation density of about 10^7 cm^{-2}, is shown in Figure 215.

Figure 215. (001) Surface of CoO Single Crystal Showing Dislocation Etch-pit Structure

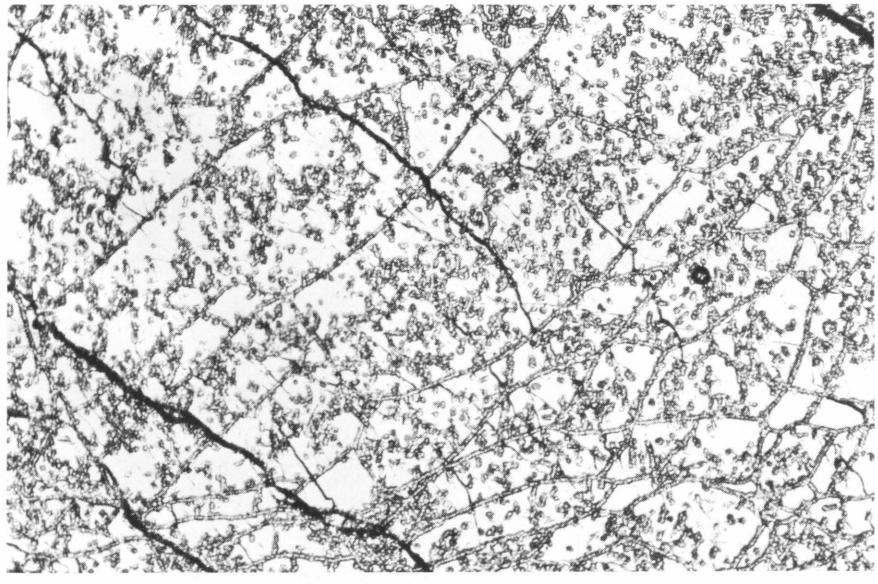

Micro 35888 150X

The large increase in dislocation density, from 10^5 cm^{-2} in the MgO seed crystal to 10^7 cm^{-2} in the grown crystal, is due to the mismatch in the unit cell sizes of the MgO seed and the CoO being grown on it. From the mismatch in unit cells it can be estimated that initially a dislocation density of the order of 10^{11} cm^{-2} would be produced. These dislocations would interact with each other[249] and with the vacancies present at the growth temperature, which would reduce the number significantly. The observed dislocation density is consistent with this interpretation.

---

[249]Matthews, J. W., Phil Mag. 8, 711 (1963).

J. Irradiation Effects

1. Low-temperature Irradiation Facility (T. H. Blewitt)

Publications:

1. T. H. Blewitt, Low-temperature Irradiation Studies, Proceedings of the International School of Physics, E. Fermi, XVIII Corso [Radiation Damage in Solids] pp. 630-716, Academic Press, New York and London (1962). [Not based on ANL work]

2. T. H. Blewitt, R. R. Coltman and C. S. Klabunde, Energy Release in Irradiated Copper and Volume Changes Induced by Radiation in Copper and Aluminum, Proceedings of the International Conference on Crystal Lattice Defects, 1962 Conf., J. Phys. Soc. of Japan, 18, pp. 283-287, Suppl. III (1963). [Not based on ANL work]

A key part in the program of irradiation studies being undertaken at ANL is the low-temperature irradiation facilities being constructed in the CP-5 reactor. Two separate irradiation facilities are being constructed. One is designed to provide a pure thermal-neutron environment (Hole VT-44), and the other to provide a pure fission-neutron environment (Hole VT-53). Both facilities are built to operate at temperatures as low as 4°K. A refrigeration system with a cooling capacity of 60 W at 4°K has been constructed to provide refrigeration for both of these facilities. A valving arrangement makes it possible to refrigerate either of the facilities separately or both simultaneously.

During the past year considerable time was spent in debugging the refrigeration facility. The most serious problem arose with the main compressor. This is a three-stage machine, and difficulties were encountered due to improper alignment of the third stage and improper machining of the piston in the second stage. These errors were remedied, and the compressor is now in operating condition. Additional problems were encountered when leaks opened up in the transfer tubing; these have now been repaired.

The refrigeration facility has been operated on numerous occasions. During May of 1963, liquid helium was successfully introduced into the CP-5 reactor in the Hole 44 facility. These operational periods of the facility demonstrated that it can produce the designed refrigeration capacity of 60 W at 4°K.

The Hole 53 facility (fast-neutron environment) is operational. This facility is located in the reflector region of the graphite reactor. A

fast-flux environment is obtained from the thermal neutrons by means of a uranium converter, which is a cylindrical sleeve, 4 in. in diameter, and contains 600 g of enriched uranium. About half of the thermal neutrons are converted to fission neutrons. A boron carbide thimble that extends from the top of the reactor to the bottom of the radiation facility is utilized to absorb the thermal neutrons which pass through the converter.

The thermal-neutron flux in this facility has been determined by measuring the induced activation in gold foil. The results indicate fewer than 10^8 fission neutrons per cm^2/sec. The fast-neutron flux has been determined by a combination of foil activation and a machine calculation of the neutron spectrum. These results indicate a fission neutron flux of 5×10^{11} neutrons per cm^2/sec. The flux distribution as a function of energy is indicated in Figure 216.* It is interesting to note that the low thermal-neutron flux causes low activation in the samples placed in this facility, and it is therefore possible to remove samples with little or no shielding.

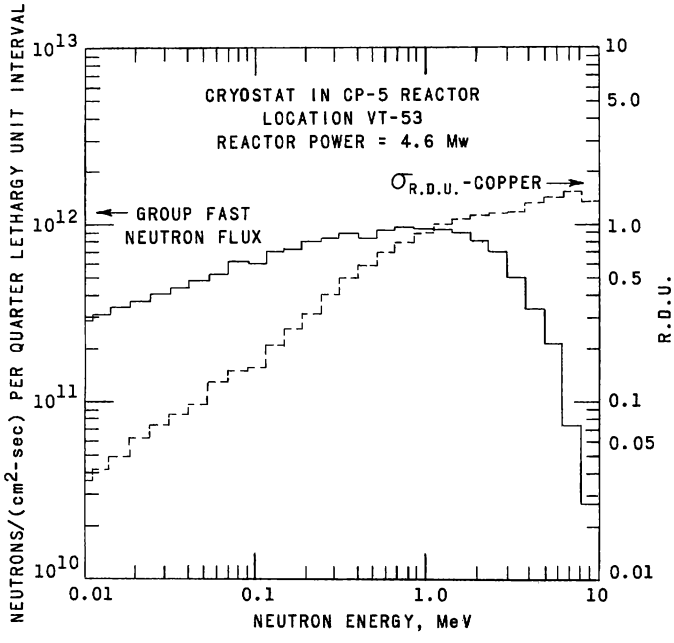

112-3542

Figure 216

Fast-neutron Flux in CP-5 Cryostat and the Damage Cross Section for Copper

The Hole 44 facility is not yet operational. Shortly after the liquid helium had been introduced into this facility, the cryostat had to be removed from the reactor as a result of oxidation of the copper portion of the specimen tube. A replacement cryostat has been constructed, and it is anticipated that the cryostat will be installed in Hole 44 during February 1964.

The new cryostat has been designed with two important modifications. First, the refrigerated radiation shield has been removed from around the irradiated space. This was done in order to eliminate the

*Measurements made by A. D. Rossin.

neutron heating which would exceed the heat load from thermal radiation. The second modification was a provision for gas cooling the sample chamber during those periods when refrigeration was not applied.

2. Radiation Effects in Thin Films (K. L. Merkle)

Publications:

1. K. L. Merkle, Fission-fragment Tracks in Non-metals, Bull. Am. Phys. Soc. 8, 236 (1963). [Abstract]

2. K. L. Merkle, L. R. Singer, and R. K. Hart, Fission-fragment Damage in Gold Films, J. Appl. Phys. 34, pp. 2800-2804 (1963).

Fission Tracks: The basic ideas regarding a model for fission track formation in insulators were outlined in the last Annual Report. According to this model, excited electrons in the vicinity of the path of a fission fragment move in a potential of the form

$$V(r,t) = \begin{cases} e\,\dfrac{r^2}{p(t)^2}\displaystyle\int_{p(t)}^{\infty} n(r,t)\,dr & \text{for} \quad 0 < r < p; \\ 2e\,\ln\dfrac{r}{c}\displaystyle\int_{r}^{\infty} n(r,t)\,dr & \text{for} \quad r > p; \quad c = \dfrac{p}{1.648}, \end{cases} \tag{1}$$

where $n(r,t)$ is the number of excited electrons per unit path length which are at a distance between r and $r + dr$ from the path of the fragment at the time t; $p(t)$ is the radius of the cylinder of ionization, and is equal to the maximum impact parameter p_m initially, which is of the order of 5 Å in a typical insulator. The electrons come into thermal equilibrium with each other in times of the order of 10^{-16} to 10^{-15} sec. The energy transfer to the lattice is mainly by electron-ion collisions.

Preliminary calculations for Al_2O_3 showed that the initial rate of energy transfer to the aluminum ions is 5×10^{13} eV/sec. This shows that displacement of atoms is possible if the time dependence of the potential as described in equation (1) is negligible during times of the order of 10^{-13} sec.

The critical quantity which determines whether or not fission-fragment tracks can occur is $p(t)$. This will increase very rapidly if there is an appreciable concentration of free electrons available or if there is a high probability for tunneling of electrons.

To date no conclusive evidence has been found for fission tracks in graphite, where the band gap $\delta \approx 0$. This is in agreement with our model.

The isolated-particle model which describes the formation of fission-fragment tracks in thin films of isolated metal particles has been refined, and the influence of the substrate on the track formation has been studied.

Heavy Particle Irradiations: Energy Dependence of "Black Spot" Damage in Single Crystalline Metal Films: The damage regions ("black spots") which are produced in single crystalline copper, silver, and gold by energetic knock-ons have been studied by means of transmission electron microscopy. For making quantitative studies of the density of the "black spots," it is necessary to know the thickness of the films. A new method which is based on neutron activation has been devised to determine the average thickness of gold films. Based on the new thickness determinations, we now find $E_T = 3.6 \times 10^4$ eV for the "threshold" energy for the production of "black spots" in gold. This energy which was originally determined from the results from fission-fragment irradiation has now been confirmed by using other heavily-charged particles to produce the energetic knock-ons.

In the Rutherford region one can calculate the total cross section for producing knock-ons with an energy greater than E_T:

$$\sigma = c\left(\frac{1}{T_m E_T} - \frac{1}{T_m^2}\right); \qquad T_m > E_T, \tag{2}$$

where T_m is the maximum energy which can be transferred in a collision and where the constant c depends on the nature of the particle and is given by $c_p = 4.14 \times 10^{-26}$ (MeV^2 cm^2), $c_d = 1.64 \times 10^{-25}$ (MeV^2 cm^2), and $c_\alpha = 2.57 \times 10^{-24}$ (MeV^2 cm^2) for proton, deuteron, and α-irradiation of gold. The number of spots is given by

$$N_s = N_0 \sigma \phi. \tag{3}$$

Introduction of equation (2) into equation (3) yields

$$\sigma_s' = \frac{N_s}{N_0 c \phi} = \frac{1}{T_m}\left(\frac{1}{E_T} - \frac{1}{T_m}\right); \qquad T_m > E_T. \tag{4}$$

In Figure 217 the reduced cross section for the production of spots, σ_s', as determined from irradiations with fission fragments, α-particles, deuterons, and protons, is plotted as a function of T_m. According to equation (4), σ_s' should have a maximum at $T_m = 2\,E_T$ and should

be 0 at $T_m = E_T$. As can be seen from Figure 217, the experimental data do not show this behavior. The maximum is shifted to lower energies, and to the left of the peaks σ_s' falls off more slowly than is indicated by equation (4). This kind of behavior is to be expected if one does not have a sharp "threshold" energy.

Figure 217. Reduced Cross Section for "Black Spot" Formation $\sigma_s' = \sigma_s/c$ in Gold as a Function of the Maximum Primary Knock-on Energy T_m

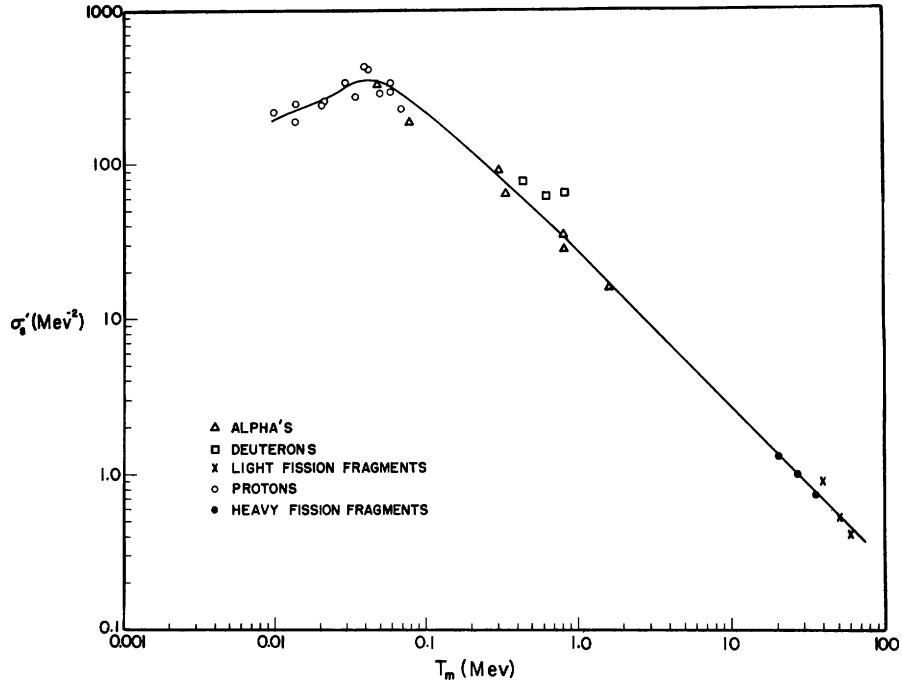

Macro 38233

If the probability for producing a "black spot" by a knock-on atom of energy E is given by W(E), the total reduced cross section for the production of spots is given by

$$\sigma' = \frac{1}{T_m} \int_0^{T_m} \frac{dE}{E^2} W(E). \qquad (5)$$

A computer program is being written to analyze the data that will give us the probability function W(E).

Thin films of silver and copper were also irradiated with charged particles. The results for silver indicate a "threshold" energy of 2.8×10^4 eV, and the results for copper give a "threshold" energy of approximately 5×10^4 eV. This is higher by more than a factor of 10 than the calculated maximum spike energy for copper.[250] We also observe that the

[250] Brinkmann, T. H., Proceedings of the International School of Physics, E. Fermi, XVIII Corso [Radiation Damage in Solids] 830, Academic Press, New York and London (1962).

maximum spot size in copper is much smaller than in gold. Only a small fraction of the spots in copper are larger than 50 Å in diameter. However, a 50-keV copper atom has a range in copper of approximately 250 Å. This indicates that equation (4) is not applicable to the copper data, because there is an upper limit for the spike energy and spike size which lies below the limit of resolution of the electron microscope. Presumably the spots we do see in copper are caused by knock-ons with approximately an energy of 4 to 5 keV, and we see only 1/10 of these events because the size distribution of spots from a 5-keV knock-on has a mean which is smaller than 10 to 15 Å.

Figure 218 shows a film of copper which has been irradiated with 0.7-MeV protons. Some of the defects appear to be triangular dislocation loops (as indicated by arrows in the figure). The differences in the "black spot" damage between copper and gold can be summarized as follows: an energetic knock-on of about 100 keV will produce one "black spot" in gold, whereas in copper a knock-on of this energy will be able to produce several defect regions which do not interact with each other and only part of which are visible in the electron microscope. Observations regarding the dose dependence of fission-fragment damage in gold indicate that the region that is affected by a knock-on is about 200 Å in diameter. In copper, however, the region affected by a spike is expected to be much smaller.

Effects Observed Near the End of the Range: We have performed some experiments with a stack of aluminum foils placed in front of the specimen. The absorber thickness was equal to the mean range of the particles (α or p) in aluminum. Some of the particles that penetrated this absorber came to rest in the gold films. Figure 219 shows the result of an irradiation with protons with the sample held at liquid nitrogen temperature. The large loops visible are thought to be caused by the gas particles coming to rest in the foil and possibly represent gas pockets. As a comparison, Figure 220 shows a film that was irradiated to the same dose, but because the protons did not come to rest in the film, no large loops are observed.

Thick films of approximately 2,000 Å in thickness show a denser network of damage if irradiated under the same conditions as the film in Figure 219. This damage anneals out at 150°C, resulting in a similar arrangement of loops as shown in Figure 219. Further investigations are necessary to determine the nature of these loops that only appear in association with the gas.

Neutron Irradiations: Figures 221, 222, and 223 show films of copper, silver, and gold that have been irradiated in Hole VT-14 of the CP-5 reactor for 8 hr at 50 to 60°C. The fast-neutron dose was 6.2×10^{17} n/cm^2 > 1 MeV. The densities of "black spots" were determined to be 1.9×10^{16} spots/cm^3 in copper; 1.5×10^{16} spots/cm^3 in silver; and 2×10^{16} spots/cm^3 in gold.

Figure 218. Single Crystalline Copper Film of (001) Orientation Irradiated with 5.6×10^{16} protons/cm^2 at a Flux of 2.5×10^{13} protons/cm^2/sec. Note arrows pointing to triangular loops.

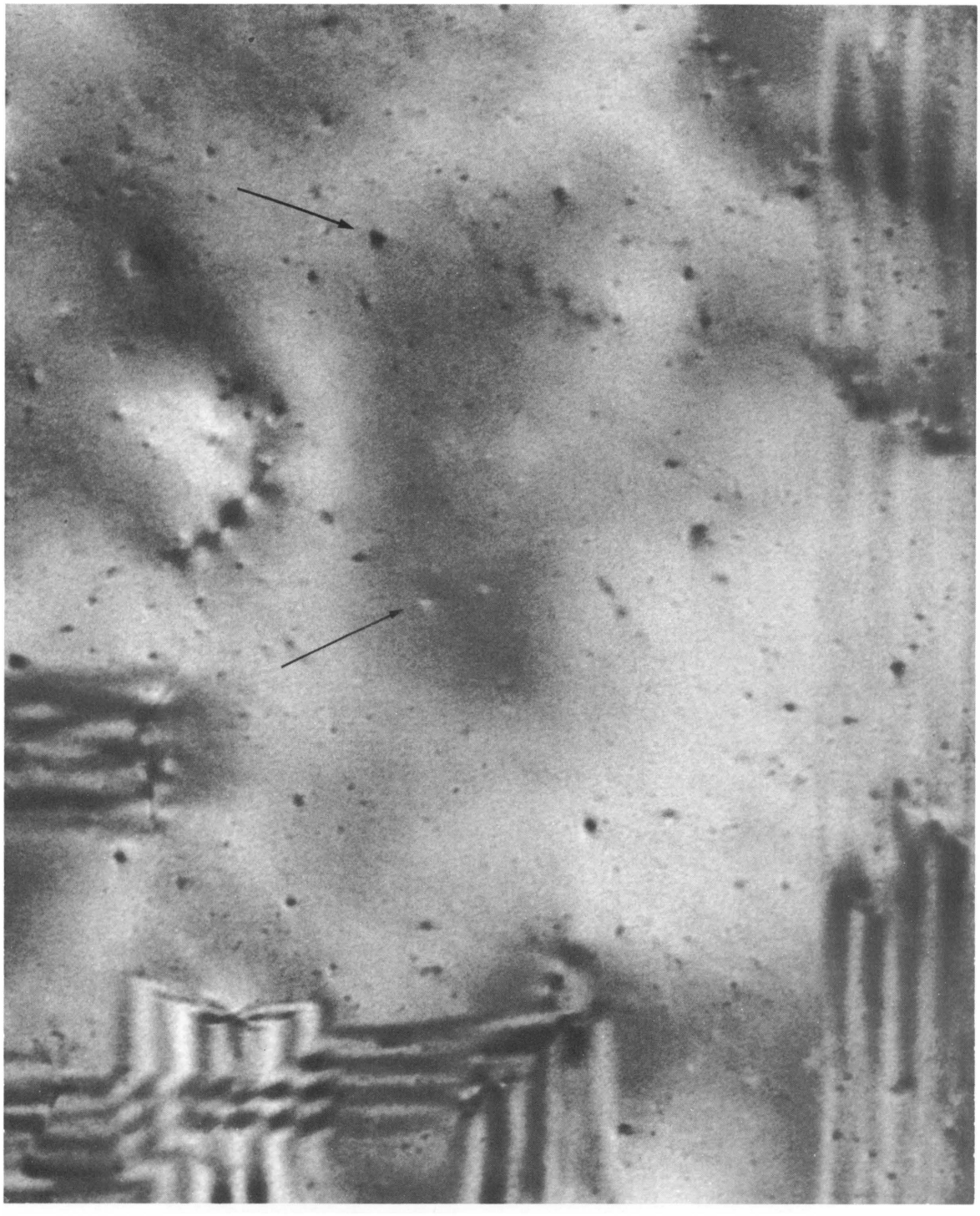

Micro 104,322

500,000X

Figure 219. Single Crystalline Gold Film of (001) Orientation Irradiated with Protons. 3.7 mg/cm^2 aluminum was used to slow down the protons. Energy of incident protons was 1.1 MeV. Dose: 10^{18} p/cm^2. Irradiated at 80^{o}K.

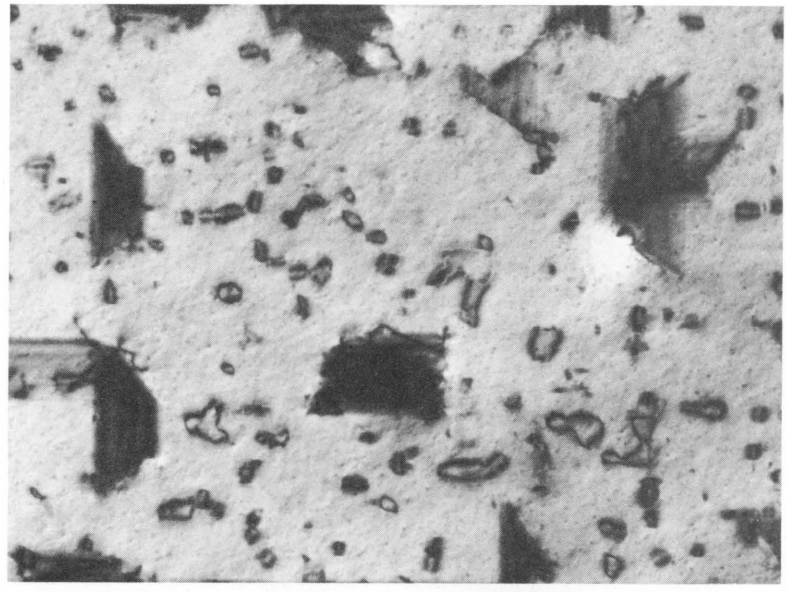

Micro 104,390 160,000X

Figure 220. Single Crystalline Gold Film of (001) Orientation Irradiated under the Same Condition as for Figure 219 without Aluminum Absorber. Energy: 1.6 MeV. Dose: 10^{18} p/cm^2.

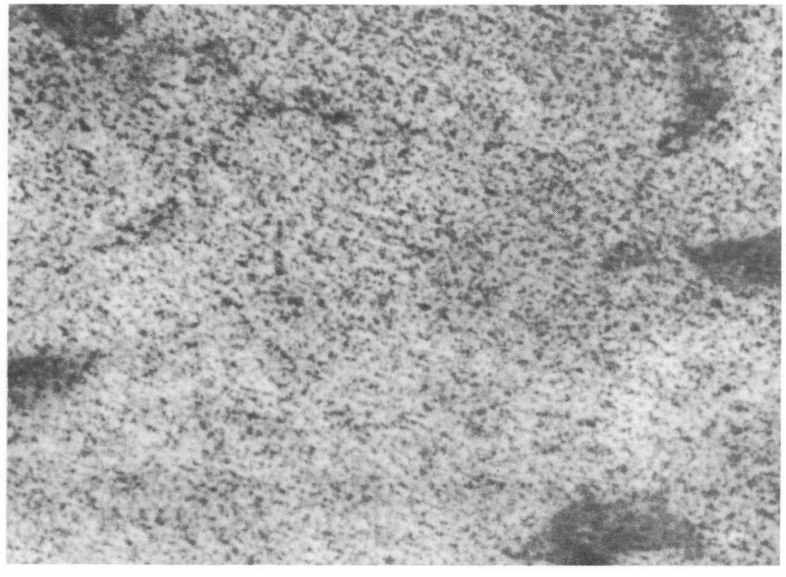

Micro 104,544 160,000X

Figure 221 (Copper) Figure 222 (Silver) Figure 223 (Gold)

Copper, Silver, and Gold Films Irradiated In Vacuo for 8 hr in Hole VT-14 of the CP-5 Reactor. Integrated dose: 6.2×10^{17} n/cm^2 > 1 MeV.

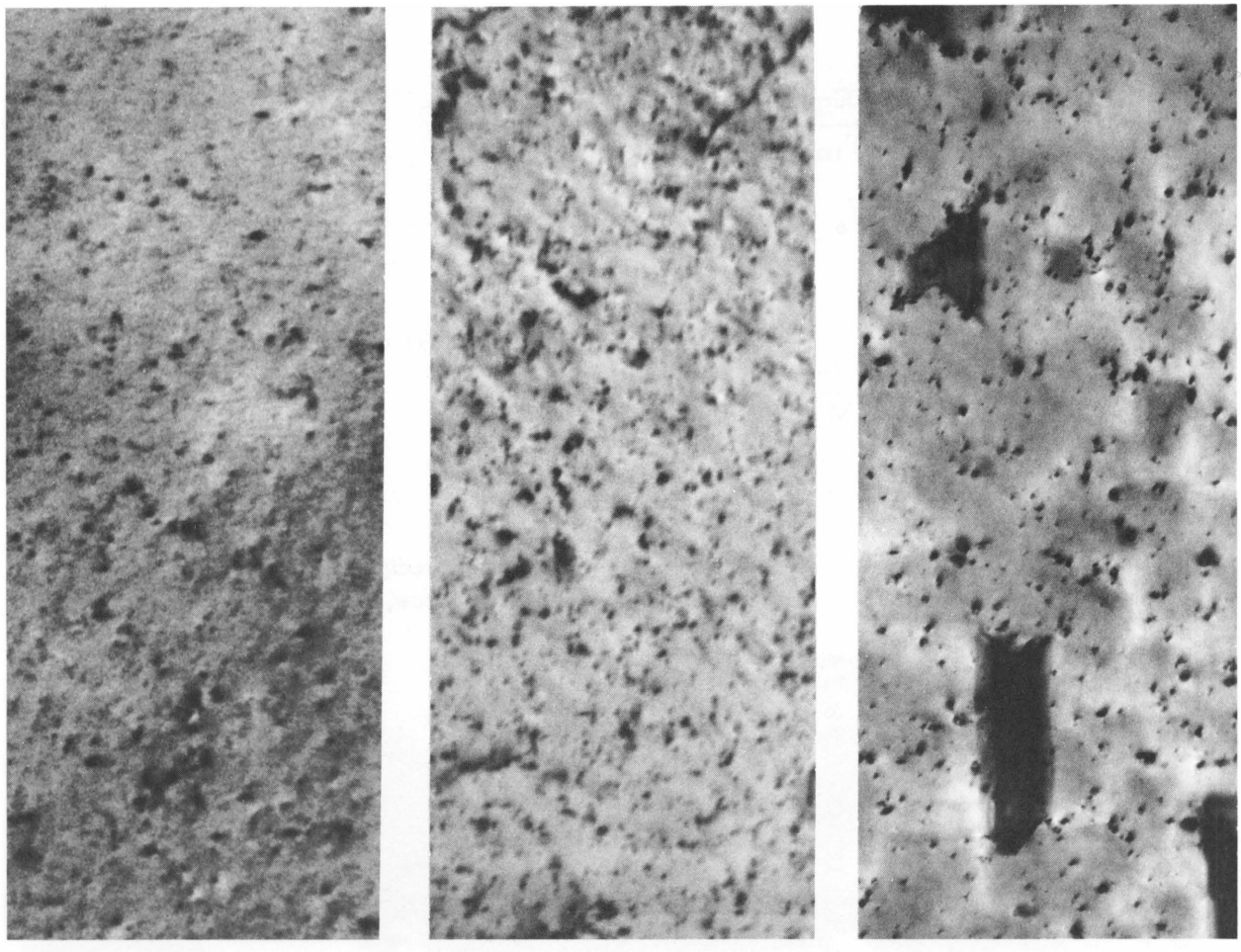

Micro 104,019 160,000X Micro 104,041 160,000X Micro 104,033 160,000X

Figure 224 shows a dark-field micrograph of copper with some defects of anomalous contrast that were identified as vacancy clusters according to Ashby and Brown's method.[251] In contrast to the observations on fission-fragment-irradiated gold, no interstitial clusters were observed. There has been a discrepancy in the literature between the calculated number of defects and the observed number of defects in neutron irradiations. Usually, the calculated number of defects is too high by a factor of 10. At least part of this discrepancy is due to displacement cascades.

We can now compare the results that we obtained from the charged-particle irradiations to the neutron irradiations. A neutron has to have an energy of at least 1.8 MeV to produce a gold primary with energy of 3.6×10^4 eV At these and higher energies there is preferential forward

[251] Ashby, M. F., and Brown, L. M., Phil. Mag. 8, 1083 (1963).

scattering. The angular dependence of the neutron scattering cross sections has therefore to be taken into consideration. The total cross section for the production of a "black spot" by a neutron of energy E is then given by

$$\sigma_s(E) = \int_{1-\frac{2E_T}{T_m}}^{-1} K(E, \cos\theta)\, d\cos\theta. \qquad (6)$$

The number of spots N_s produced per cm^3 and sec is given by

$$N_s = N_0 \int_{E=\frac{E_T(M_1+M_2)^2}{4 M_1 M_2}}^{E=\infty} \int_{1-\frac{2E_T}{T_m}}^{-1} K(E, \cos\theta)\, \phi(E)\, dE d\cos\theta, \qquad (7)$$

where N_0 is the number of atoms per cm^3.

Figure 224. Same Film as in Figure 221, Dark Field. Arrow denotes reciprocal lattice vector. Note that the bright side of the images is in the direction of the arrow, indicating vacancy clusters.

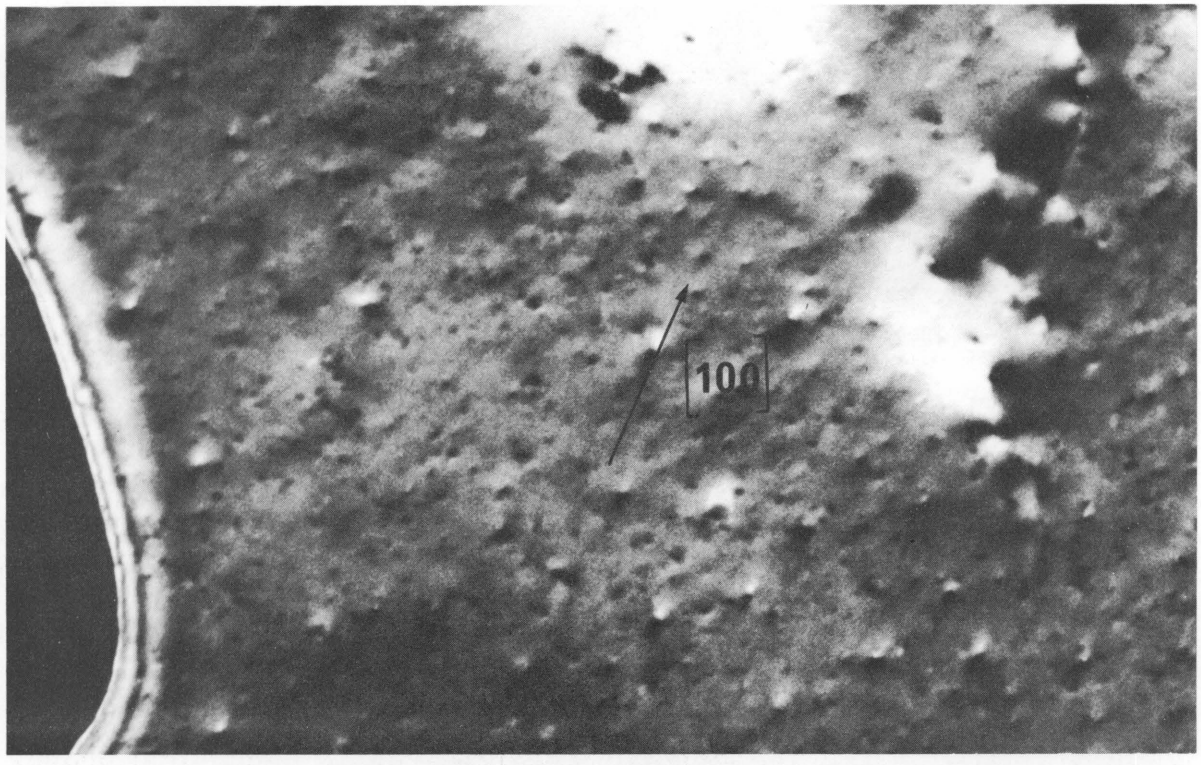

Micro 104,031 240,000X

Unfortunately, only a few measurements of K for gold are available at energies > 1 MeV.[252] With reasonable estimates of K and a

[252] BNL-400, Angular Distributions in Neutron-induced Reactions, Vol. II (1962).

20-group calculation for the neutron spectrum in conjunction with nickel and iron threshold detectors, we find that the observed density of spots in gold is higher by about a factor of 2 than the calculated density. However, we could expect much better agreement if we substitute equation (8) for equation (6) in which a sharp threshold energy is assumed:

$$\sigma_s(E) = \int_1^{-1} W\left(\frac{T_m}{2}\{1 - \cos\theta\}\right) K(E, \cos\theta)\, d\cos\theta. \qquad (8)$$

In equation (8), W is the previously defined probability function for the production of "black spots." Also, the recoils from inelastic collisions should be taken into consideration.

3. Irradiation and Solid-solution Strengthening (T. J. Koppenaal)

Publications:

1. T. J. Koppenaal, Comments on the Rosenfield and Averbach Theory for Initial Yielding in f.c.c. Metals and Alloys, Acta Met., 11, 85 (1963).

2. T. J. Koppenaal, Dislocation Etch Pits in α Cu-Al and α Cu-Zn Alloys, Trans. ASM, 56, 768 (1963).

3. T. J. Koppenaal, The Strain Rate Dependence of the Flow Stress in Neutron Irradiated Copper Single Crystals, Phil. Mag., 8, 1313 (1963).

The Strain-rate Dependence of the Flow Stress in Neutron-irradiated Copper Single Crystals: The influence of neutron irradiation, from dose levels of 1.0×10^{15} to 0.97×10^{19} nvt, on the strain-rate dependence of the flow stress in single crystals of copper has been investigated at 77°K and 300°K. An analysis of the strain-rate dependence, based upon a model suggested by Seeger,[253] indicates that the activation energy for dislocation cutting of the irradiation-induced defects decreases with decreasing temperature and increasing neutron dose. This behavior suggests an inadequacy of Seeger's model. It is, however, possible to explain qualitatively the results based upon variations in the size and density of the irradiation-induced defects.

The Microstrain-yield Stress in Neutron-irradiated Copper Single Crystals: Within the general research area of mechanical properties of neutron-irradiated crystals, the neutron-dose dependence of the yield strength has been investigated by a number of researchers. The

---

[253] Seeger, A. K., Proc. 2nd Inter. Conf. Peaceful Uses Atomic Energy (United Nations: New York) 6, 250 (1958).

principal reason for these continuing studies is primarily due to the fact that the experimental results do not, in general, agree with the predictions of available quantitative theories.

In the present investigation, a study was made of the initial stage of plastic deformation in neutron-irradiated copper single crystals by using electrical-resistance strain gages. The neutron-dose dependence of the stress necessary to produce a plastic strain of 2×10^{-6} has been established. Strain detection was accomplished by use of an electrical-resistance strain gage. The minimum closure failure of the recording pen that could be readily detected was 1 mm of chart, which represented a strain of 2×10^{-6}, with the maximum strain sensitivity being used. The stress necessary to produce this amount of plastic strain is defined as τ_0. Thus, τ_0 is the 2×10^{-6} "yield stress."

The stress τ_0 was measured at 300°K in 23 crystals covering ten different neutron doses, ϕ, levels from 1.6×10^{16} to 0.98×10^{20} nvt (neutrons/cm^2). The results are shown in Figure 225 on a log τ_0 - log ϕ plot. When all of the data points at 300°K were assumed to be on a straight line, a least-squares calculation of the slope showed that

$$\frac{d \log \tau_0}{d \log \phi} = 0.341 \pm 0.010 \qquad (1)$$

Figure 225. The 2×10^{-6} "Yield Stress" τ_0 for Copper Single Crystals vs Neutron Dose ϕ on Log-log Scale. The brackets indicate the spread of the indicated number of data points. Values of the macroscopic flow stress at 300°K (dashed line) are given elsewhere.

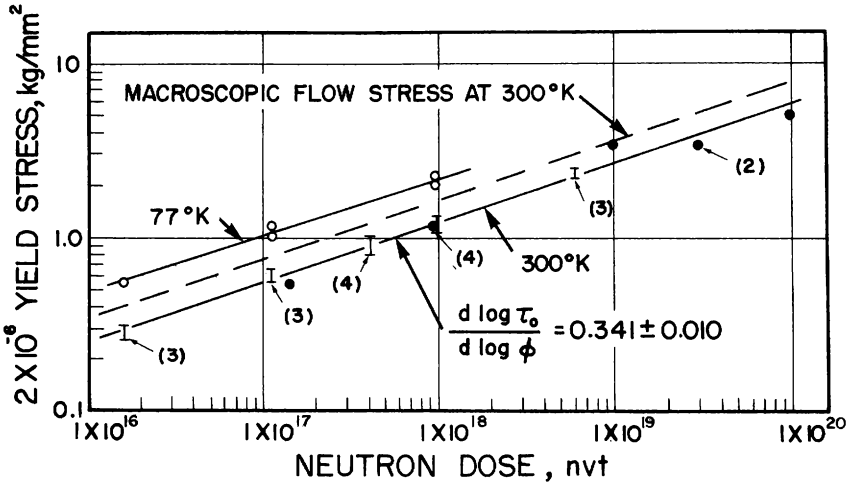

Macro 37572

Figure 225 also shows the behavior of the macroscopic flow stress previously found[254] in neutron-irradiated copper single crystals

[254]Koppenaal, T J., Acta. Met., in the press.

that were grown and irradiated in the same manner. Some of the τ_0 values in Figure 225 were obtained with crystals that were simultaneously irradiated with those of the previous report.[254] In comparing the values of τ_0 and macroscopic flow stress, two important features are evident. First, both properties show virtually the same dose dependence; the slope of the line for the macroscopic flow stress was previously given as 0.34. Second, the τ_0 values are about 75 percent of the macroscopic flow stress.

The stress τ_0 was determined at 77°K for a limited number of crystals, and the results are shown in Figure 225. The slope of the line at 77°K appears to be the same as that at 300°K. In addition, the temperature dependence of τ_0 between 77 and 300°K is about the same as that reported by Blewitt et al.[255] for macroscopic yielding. Figure 226 shows stress-microstrain curves for crystals of identical orientation that were simultaneously irradiated to 1.1×10^{17} nvt and tested at either 77 or 300°K. The ratio of τ_{77}/τ_{300} appears to be independent of strain early in the deformation process.

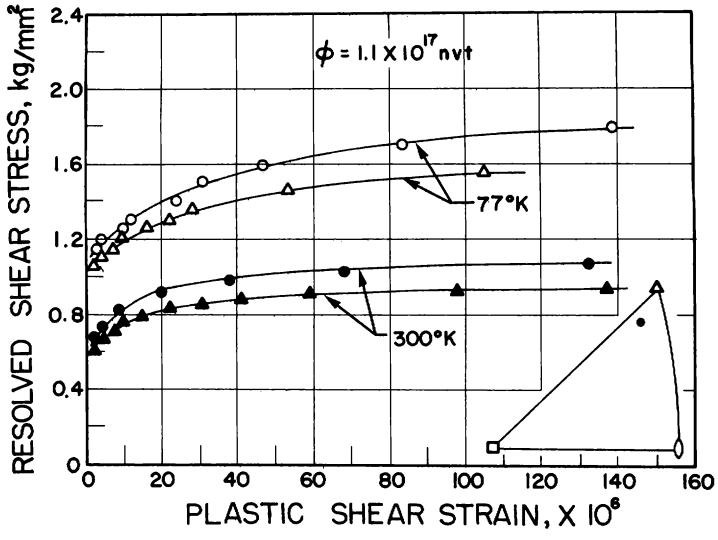

Macro 37571

Figure 226

Stress-microstrain Curves for Neutron-irradiated Copper Single Crystals

Figure 227 shows stress-microstrain curves for copper and copper-alloy crystals containing 0.5 and 14 a/o Al, all of which were simultaneously irradiated to 0.94×10^{18} nvt. Other than the small differences in stress, the general shape of the curves does not appear to be affected by the solutes.

The measurements of τ_0 reported upon here are similar to those by Young[256] in that the initial stage of yielding is being measured, rather than the gross macroscopic yield stress. The interesting feature is

---

[255] Blewitt, T. H., Coltman, R. R., Jamison, R. E., and Redman, J. K., J. Nucl. Matls. 2, 277 (1960).

[256] Young, F. W., Jr., J. Appl. Phys. 33, 3553 (1962).

that both types of measurements show the same dose dependence, namely $\tau \propto \phi^{1/3}$. Diehl et al.[257,258] have found a $\tau \propto \phi^{1/2}$ behavior up to about 2×10^{17} nvt. Study of our data at 1.6×10^{16} and 1.1×10^{17} nvt shows that a $\tau \propto \phi^{1/2}$ behavior could exist between these data points. Our data for $\phi > \sim 10^{17}$ nvt clearly show a $\tau \propto \phi^{1/3}$ behavior. With the results gained here and elsewhere[254-256,259] the cube-root dose dependence of the yielding in neutron irradiated copper single crystals must now be considered as established, at least for $\phi > \sim 10^{17}$ nvt. This behavior may also extend to lower ϕ.

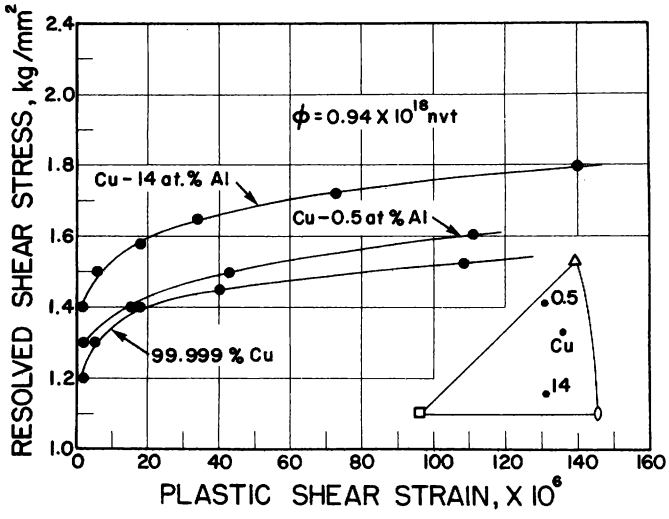

Macro 37573

Figure 227

Stress-microstrain Curves for Copper and Two Alloys Simultaneously Irradiated to 0.94×10^{18} nvt and Tested at 300°K

In Young's[256] determination of the dose dependence of the yield stress with a dislocation etch-pit technique, his "yield stress" is equivalent to a dislocation-generation stress. Since τ_0 shows the same dose dependence as Young's "yield stress," and because τ_0 is reasonably close (~75 percent) to the macroscopic flow stress, an attractive hypothesis appears to be that of associating τ_0 with the dislocation generation stress, e.g., the stress necessary to activate Frank-Read generators. Previous analogies have been made associating τ_0 and the dislocation multiplication stress in annealed crystals.[260-262] The strength of neutron-irradiated α Cu-Al crystals has been previously[254] analyzed on the basis of a dislocation-multiplication mechanism.

We would like to demonstrate initially that our data cannot distinguish between the dislocations being locked in their initial positions

---

[257]Diehl, J., Radiation Damage in Solids, (IAEA: Vienna) 1, 129 (1962).

[258]Diehl, J., Leitz, C., and Shilling, W., Phys. Rev. Letters 4, 236 (1963).

[259]Fischer, J., Z. Naturf., 17A, 603 (1962).

[260]Koppenaal, T. J., Acta Met., 11, 537 (1963).

[261]Hordon, M. J., Acta Met., 10, 999 (1962).

[262]Koppenaal, T. J., Acta Met., 11, 85 (1963).

or the dislocations being moved a small distance before becoming locked. We may express the shear strain γ as

$$\gamma = bLN, \tag{2}$$

where b is the magnitude of the Burgers vector, L the length of travel per dislocation, and N the number of moving dislocations per unit area of glide plane. With the minimum measurable strain of 2×10^{-6} being used, we assume that there are 10^6 moving dislocations per cm^2, and L is then $\sim 10^{-4}$ cm. Thus, even with the relatively high strain sensitivity employed here, we are unable to detect the motion of up to 10^{-4} cm by each of 10^6 dislocations/cm^2. Hence, dislocations could move anywhere from 0 to 10^{-4} cm before running into an obstacle that represents a pinning point. The recent work of Koppenaal and Kuhlmann-Wilsdorf[263] indicates that the obstacles are produced in a random array, rather than mainly on dislocations. The conclusion is therefore made that most of the obstacles acting as pinning points do not lie on the dislocations, but are in the lattice near the vicinity of the dislocations. These obstacles could be the type of zones discussed by Seeger.[253]

Returning to our assumption that τ_0 arises by a dislocation-generation mechanism, we may write

$$\tau_0 = Gb/\pi\ell, \tag{3}$$

where G is the shear modulus and ℓ the length of unpinned dislocation; the factor π arises from assuming that the first generators to become active have unpinned lengths that are π times the average length.

Before proceeding, we should mention an analysis that "appears" to eliminate the dislocation-generation mechanism. Since experimentally $\tau_0 \propto \phi^{1/3}$, equation (3) indicates that ℓ should be proportional to $\phi^{-1/3}$. However, since dislocations move on a plane, and the number of obstacles formed per unit area must be proportional to ϕ, the distance between obstacles on a plane is proportional to $\phi^{-1/2}$ (stated alternatively, the resulting stress should be proportional to $\phi^{1/2}$ and not $\phi^{1/3}$). Thus, while both the dislocation-generation hypothesis, equation (3), and Seeger's[253] obstacle-cutting theory predict a square-root dependence, a cube-root dependence is observed. This difference between the predicted and observed dose dependence remains unexplainable at the present time.

Blewitt et al.[255] gave an empirical equation for the dose dependence of the macroscopic flow stress τ in neutron-irradiated copper single crystals:

$$\tau = A + B\phi^{1/3}, \tag{4}$$

---

[263]Koppenaal, T. J., and Kuhlmann-Wilsdorf, D., submitted to Appl. Phys. Ltrs.

where A was presumed to be the macroscopic flow stress of annealed copper crystals. The experimental results of Blewitt et al.[255] and Koppenaal[254] show that $\frac{d \log \tau}{d \log \phi} = \frac{1}{3}$, but in both cases $\frac{d \log (\tau - A)}{d \log \phi}$ is not $\frac{1}{3}$ at low ϕ if A is the macroscopic flow stress of annealed copper crystals. The same interpretation and conclusion can be given to the results on neutron-irradiated α Cu-Al single crystals,[254] with A associated with the macroscopic flow stress of the annealed alloy crystals. Thus, equation (4) does not accurately describe the dose dependence at low doses.

Koppenaal and Kulhmann-Wilsdorf[263] have shown that when two different types of pinning points are randomly distributed in a lattice, the stress necessary to activate a source, τ, may be expressed as

$$\tau = (\tau_i^2 + \tau_a^2)^{1/2}, \tag{5}$$

where τ_i is the stress necessary to activate a source in the presence of only those pinning points produced by neutron irradiation, and τ_a the generation stress for only those pinning points in annealed crystals. By associating the $B\phi^{1/3}$ term in equation (4) with τ_i, equation (5) yields

$$\frac{d \log (\tau^2 - \tau_a^2)^{1/2}}{d \log \phi} = \frac{1}{3}. \tag{6}$$

For $\tau \gg \tau_a$, equation (6) reduces to the empirical form $\frac{d \log \tau}{d \log \phi} = \frac{1}{3}$. If we take a value of 20 gm/mm^2 for τ_a in equations (5) and (6), this being the dislocation-generation stress in annealed copper single crystals,[256] the data of Blewitt et al.[255] and Koppenaal[254] are in agreement with equation (6). In the present research, the smallest τ observed was ~0.3 kg/mm^2 (for ~10^{16} nvt); since τ_a is only ~0.02 kg/mm^2, a direct confirmation of equations (5) and (6) from the present data is not possible. Our interpretation of equation (5) is that the total number of pinning points in neutron-irradiated copper crystals is the sum of the pinning points due to irradiation and those found in annealed crystals; for the present discussion, the nature of the pinning points in annealed crystals is immaterial.

An attempt was made to explain the previous[254] results of neutron-irradiated α Cu-Al single crystals by means of equations (5) and (6) and the assumption of a dislocation-generation mechanism. In this τ was taken as the flow stress in the irradiated alloy crystals, τ_i the flow stress in copper crystals simultaneously irradiated, and τ_a the dislocation generation stress in the annealed alloys; for reasons given elsewhere,[260] the microstrain yield stress values were used for τ_a. A comparison of the calculated and observed strengths was only slightly encouraging.

A much better analysis was found by associating τ_a with the gross macroscopic flow stress of the annealed crystals. Since the macroscopic flow stress in annealed α Cu-Al crystals has been previously[260,264] explained on a dislocation-cutting mechanism, τ_a in equation (5) would be a cutting stress in this analysis, and τ_i must also be taken as a cutting stress. Note that equation (5), although developed for a generation mechanism,[263] can also be used for a cutting mechanism, since the stress for a cutting mechanism is proportional to the square root of the number of obstacles per unit area. To use equation (5) for a dislocation-generation mechanism, we are summing over all available obstacles that are assumed to be pinning points, and in the cutting mechanism we are summing over all obstacles that are to be sheared. Thus, the yield stress of neutron-irradiated α Cu-Al crystals would be concluded to be an obstacle-cutting mechanism (after Seeger's general theory).

Whether τ in equation (5) is assumed to be a generation or cutting stress, equation (6) is still valid. This observation indicates that an incubation stage must be observed at low doses. Therefore, we do not believe that an incubation stage followed by a $\tau \propto \phi^{1/3}$ behavior is prima facie evidence against the cube-root dependence as others[257,265,266] have assumed.

Since the data appear to support a generation mechanism in one case (pure copper) and cutting in another case (alloys), we believe that these two mechanisms could be represented by essentially the same stress. The stress necessary to generate dislocations could initially be less than the stress necessary to cut obstacles, i.e., the bowing stress τ_b is less than the shearing or frictional stress τ_f. Shortly after generation occurs, the stress against obstacles ahead of the source is no longer τ_b but $n\tau_b$, where n is the number of newly generated dislocations held up at the obstacles. When n is such that $\tau_f < n\tau_b$, the obstacles begin to shear, and a type of catastrophic yielding should occur. The yielding would then be a form of the Johnston-Gilman[267] mechanism and explains the rather large yield points observed in neutron-irradiated copper crystals.[255] We now see that the dislocation-generation mechanism originally operates because of the frictional strengthening of the obstacles. It becomes a question of semantics as to whether one chooses to refer to neutron-irradiation strengthening as either a dislocation multiplication or an obstacle-cutting mechanism.

---

[264]Koppenaal, T. J., and Fine, M. E., Trans. AIME, 224, 347 (1962).

[265]Whapham, A. D., and Makin, M. J., Phil. Mag., 5, 237 (1960).

[266]Makin, M. J., and Minter, F. J., Acta Met., 8, 691 (1960).

[267]Johnston, W. G., and Gilman, J. J., J. Appl. Phys., 30, 129 (1959).

The Effect of Neutron Irradiation on the Strength of α Cu-Al Single Crystals: The phenomenological aspects of solid-solution strengthening and neutron-irradiation strengthening have been established for a number of years. With increasing amounts of either neutron irradiation or solute additions, the following effects are observed in the tensile properties of single crystals:[255,264]

1. The macroscopic flow stress increases.
2. The slip line pattern changes from a homogeneous nature to a heterogeneous nature, with the formation and propagation of a Lüders band.
3. The amount of glide that takes place with little or no work-hardening during the Lüders band passage (sometimes called the "easy-glide" stage) increases.
4. The tensile axis "overshoots," indicating latent hardening on the secondary (conjugate) slip system.
5. The flow stress is more temperature dependent.

Since many of the macroscopic flow properties are the same, the present investigation was undertaken to establish some of the phenomenological aspects of the effect of neutron irradiation on the strength of solid-solution single crystals with hopes of determining the similarities and/or differences in the two strengthening mechanisms. The α Cu-Al alloys were chosen for this investigation.

Values of the flow stress τ defined here as the resolved lower yield point shear stress, obtained at 300°K, are shown in Figure 228 For purposes of convenience, the flow stress is on a logarithmic scale. Through

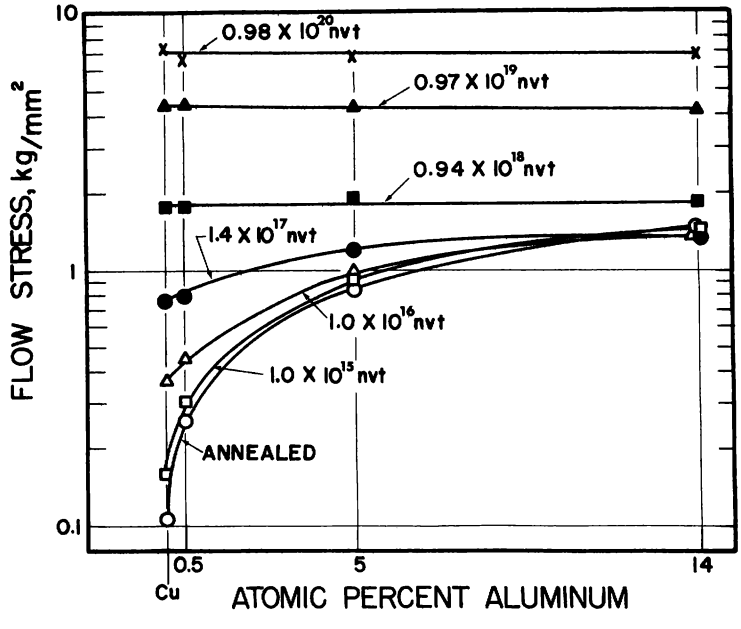

Figure 228

Flow Stress of Neutron-irradiated Cu-Al Crystals vs Aluminum Concentration

Macro 36026

a total dose ϕ of 1.4×10^{17} nvt, copper strengthens more rapidly with ϕ than the solid solutions, and increasing solute additions lead to a smaller amount of strengthening. The data obtained with the 14 a/o Al crystals actually show a small decrease in τ with increasing ϕ; however, this small decrease could be within the experimental error. For $\phi \geq 0.94 \times 10^{18}$ nvt the strength of the crystals is seen to be essentially independent of solute concentration.

Measurements were made to obtain some general information on how the thermally activated flow stress in neutron-irradiated copper crystals varies with solute additions. In one of these measurements, the flow stress was determined at 77°K following approximately 1 percent shear strain at room temperature. This procedure has been previously used in annealed α Cu-Al single crystals, and the flow stress at 77°K determined by this method was found to be in good agreement with direct measurements.[264] Values of $\tau_{77} - \tau_{300}$ (log scale) are shown versus solute concentration in Figure 229. These values are seen to become solute independent at a dose of 0.94×10^{18} nvt, which is the same dose for τ becoming solute independent (see Figure 228). In addition, a saturation effect is seen with the crystals irradiated to 0.98×10^{20} nvt.

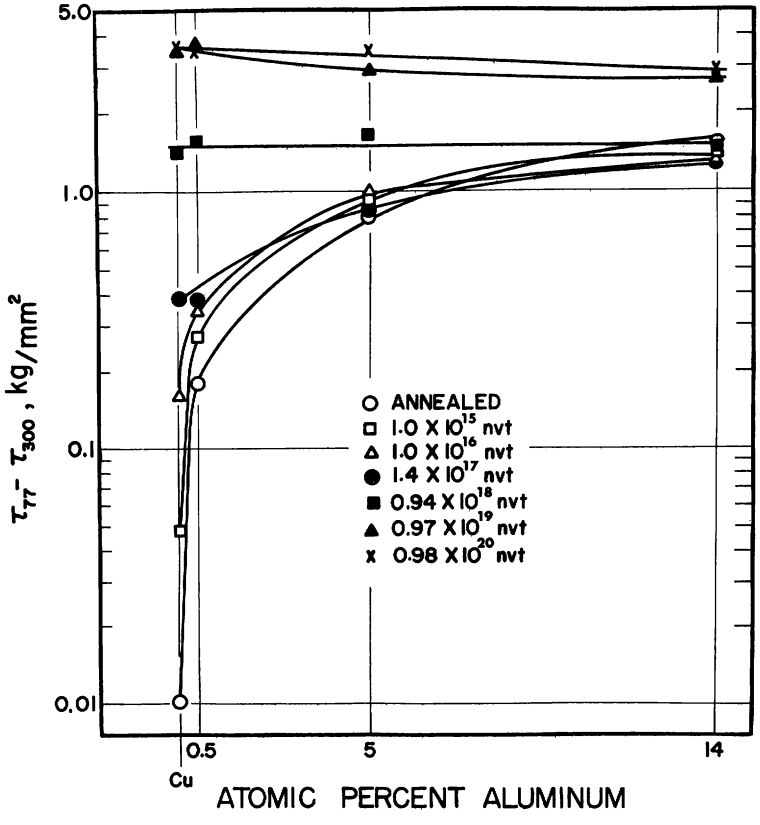

Figure 229

Change in Flow Stress between 77 and 300°K ($\tau_{77} - \tau_{300}$) vs Aluminum Content

Macro 36027

In another measurement for establishing similarities and/or differences in the thermally activated flow stress, the strain-rate dependence of the flow stress was measured at 300°K by increasing the strain

rate from $\dot{\epsilon}_1 = 4.2 \times 10^{15}$ sec^{-1} to $\dot{\epsilon}_2 = 4.2 \times 10^{-4}$ sec^{-1} and measuring the subsequent increase in flow stress, $\tau_{\dot{\epsilon}_2} - \tau_{\dot{\epsilon}_1}$. All measurements were made early in the deformation process, for which $\tau_{\dot{\epsilon}_2} - \tau_{\dot{\epsilon}_1}$ was found to be independent of strain. Qualitatively, the strain-rate dependence of the flow stress varies in a similar manner as does $\tau_{77} - \tau_{300}$, including the saturation effect observed at the highest dose.

Figure 230. Stress-strain Curves for 14 a/o Al Crystals. Each crystal was of the indicated orientation.

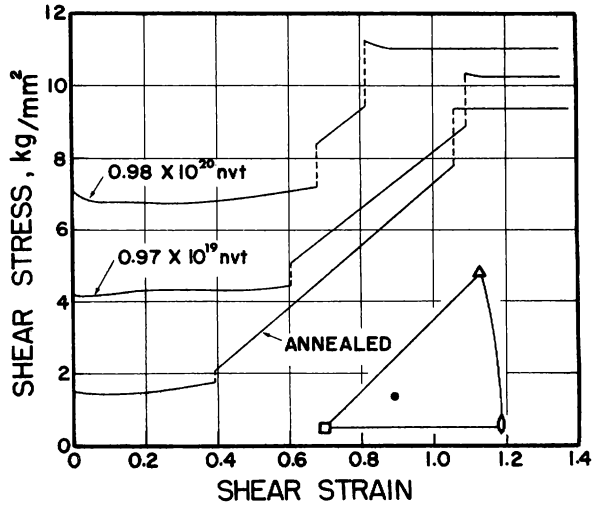

Macro 36225

Shear stress-shear strain curves for Cu-14 a/o Al crystals deformed at 300°K are shown in Figure 230. The discontinuity shown between the first Lüders band extension and the beginning of linear hardening arises from not taking into account a change in cross-sectional area during the Lüders extension,[255] and the discontinuity between linear hardening and the second Lüders band propagation is a result of changing the resolved shear stress from the primary to the conjugate slip system.[255] Stress-strain curves were also determined for the Cu-0.5 and -5 a/o Al crystals as a function of neutron dose $\geq 1.4 \times 10^{17}$ nvt, and the same qualitative features were observed as in Figure 230. For those crystals for which the flow stress was dose dependent, the following behaviors were observed:

1. The amount of strain corresponding to the first Lüders band extension increases with neutron dose.
2. The rate of work-hardening during linear hardening appears to decrease slightly with increasing neutron dose.
3. The stress corresponding to the initiation of the second Lüders band increases with neutron dose, but to a lesser degree than does the stress of the first Lüders band formation.

Since both the gage length and the reduced cross-sectional area varied by 2 to 4 percent in each crystal (due to introducing the reduced cross section by the electropolishing procedure), we do not believe that quantitative comparisons can be made of the above observations.

In the last few years, considerable discussion has arisen by experimental and theoretical researchers over the dose (ϕ) dependence of the strength of neutron-irradiated copper single crystals. Although this

was not one of the objectives of this investigation, it is noteworthy to mention the type of dose dependence that describes the data obtained here. The data in Figure 228 have been replotted on a log τ - log ϕ basis in Figure 231. Assuming that the copper data can be described by a straight line, the slope of the line, $\frac{d \log \tau}{d \log \phi}$, was calculated by the least-squares method, and a value of 0.34 was obtained. This value is in good agreement with the cube-root dependence established by Blewitt et al.[255] and by Young.[256] These two investigations cover the range of about $1.3 \times 10^{13} < \phi < 1.3 \times 10^{20}$ nvt. This dose dependence is not that expected from quantitative theories,[253,266] but the data obtained here and in other investigations clearly establish the cube-root dose dependence. Both Diehl[257] and Makin and Minter[266] tend to disregard the empirical cube-root dependence because of a small incubation period sometimes observed at low dose levels. However, the Cu-14 a/o Al crystals clearly display an incubation stage (see Figure 231).

Figure 231. Flow Stress vs Neutron Dose for Data in Figure 228

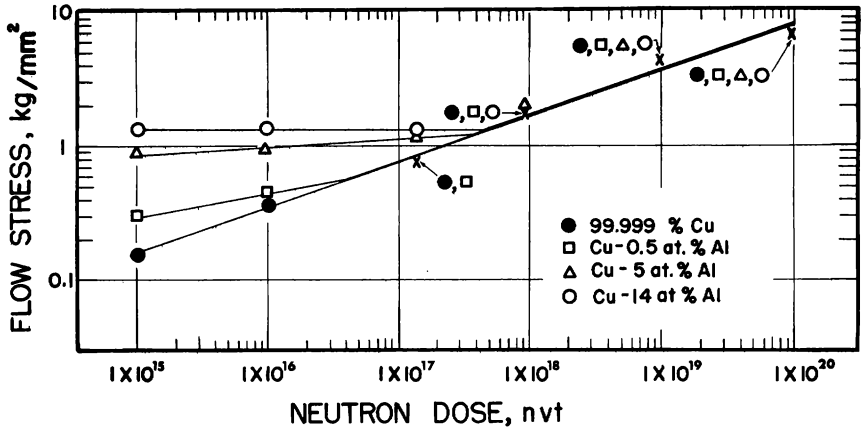

Macro 36223

Wechsler and Kernohan[268-270] have made a rather comprehensive study of resistivity changes during and following neutron irradiation of Cu-15 a/o Al single crystals. During irradiation at ambient temperatures, they observed two processes occurring in this alloy.[268] One process produced a linear increase in resistivity with integrated dose, and the other a diffusion-controlled process that resulted in a rather large decrease in resistivity. Those authors have interpreted this resistivity decrease in terms of irradiation-enhanced local order. This explanation by short-range

---

[268]Wechsler, M. S., and Kernohan, R. H., J. Phys. Chem. Solids, 7, 307 (1958).

[269]Kernohan, R. H., and Wechsler, M. S., J. Phys. Chem. Solids, 18, 175 (1961).

[270]Wechsler, M. S., and Kernohan, R. H., Radiation Damage in Solids, (IAEA: Vienna), II, 81 (1962).

ordering has been quantitatively confirmed with X-ray diffuse scattering measurements by Houska and Averbach[271] and by Borie and Sparks.[272] Houska and Averbach calculated the parameters for short-range order for the first seven nearest-neighbor shells in a furnace-cooled and neutron-irradiated Cu-14.5 a/o Al alloy, and observed that all seven of the parameters increased (in absolute value) after irradiation. The parameter of the first shell changed from -0.137 in the annealed state to -0.206 in the irradiated condition; the latter value indicates that every aluminum is surrounded exclusively by copper atoms in the first shell. The alloy used by Houska and Averbach was irradiated to 2×10^{17} nvt; since the strength of the 14 a/o Al remained unchanged by this irradiation, we conclude that local order does not affect the flow stress of these crystals. The same conclusion was reached in a previous[264] investigation with annealed α Cu-Al single crystals, principally because the composition and temperature dependence of the flow stress for these crystals was not that expected from a theory of short-range-order strengthening. Further support for this conclusion has now been established from the present investigation.

Figure 229 indicates that for dose levels where τ in the alloys is essentially equal to that of copper, the flow stress in the alloys is thermally activated in much the same manner as in the copper crystals. Experiments are in progress to investigate the temperature dependence of τ in the irradiated alloy crystals in significantly greater detail, but thus far it appears that the thermally activated flow stress in neutron-irradiated copper crystals is not affected to a large degree by the presence of solutes.

Since for high dose levels ($\geq 0.04 \times 10^{18}$ nvt) the flow stress, the thermally activated component of the flow stress, and the macroscopic flow characteristics of the alloys are essentially the same as in copper, it appears that the mechanism responsible for neutron-irradiation strengthening in copper is analogous to neutron-irradiation strengthening in the alloys.

Assuming that a lattice contains two types of barriers, one of which has been introduced by solute additions and the other by neutron irradiation, the strength of the lattice will be determined by the strength of each type of barrier and the barrier density. For this discussion the term barrier refers to an obstacle that can interfere with either the generation or motion (or both) of dislocations. From the results of previous investigations, we can gain further information regarding the effect of the barriers for the two strengthening mechanisms. In annealed αCu-Al single crystals a previous study of microstraining, carried out with the use of electrical resistance strain gages, has shown that the flow stress is largely a resistance to dislocation motion.[260] Young[256] has studied

---

[271]Houska, C. R., and Averbach, B. L., J Appl. Phys., 30, 1525 1959).

[272]Borie, B. S., and Sparks, C. J., see reference (270).

the initial stage of deformation in irradiated single crystals of copper by using a dislocation etch-pit technique, and he observes that the macroscopic flow stress is essentially equal to the dislocation generation stress. Thus, the main effect of solute additions is to increase the dislocation motion stress, whereas neutron irradiation increases the dislocation generation stress. This problem of dislocation motion vs. dislocation generation is easily understood with the aid of Figure 232, which shows a schematic representation of stress-microstrain curves for various crystals. In these curves, we are assuming a strain sensitivity of $\sim 10^{-6}$; in the present investigation, this sensitivity was $\sim 10^{-3}$. In Figure 232 the curve for annealed copper is drawn after the general behavior observed by Rosenfield and Averbach,[273] the curve for annealed Cu-14 a/o Al after Koppenaal,[260] and the curves for irradiated copper have been inferred from the dislocation etch-pit studies by Young.[256] In the annealed alloy, plastic deformation begins at a (generation) stress of ~25 percent of the macroscopic flow (motion) stress, but the curves for irradiated copper display a fundamental difference with plastic deformation beginning at a (generation) stress essentially equal to the macroscopic flow stress. With these curves in mind, a reasonable explanation of the data in the present investigation becomes possible. Since neutron irradiation increases the generation stress of copper single crystals, the same general behavior could occur in the alloy crystals. Hence, curve A in Figure 232 is a hypothetical curve for the 14 a/o Al alloy irradiated to 6×10^{16} nvt. The curve has been drawn with the same macroscopic flow stress as the annealed crystals, which has been experimentally established (see Figure 228), and the same microscopic generation stress for copper crystals irradiated to this level. Curve B is another hypothetical curve for $\sim 5 \times 10^{17}$ nvt. At this dose the flow stress of copper, and hence the generation stress, is about the same as the flow (motion) stress in the annealed alloy crystal. Thus, the generation stress due to irradiation is equal to the motion stress due to the solutes. At still a higher dose level, the macroscopic flow stress would be exclusively controlled by the generation stress, as indicated by hypothetical curve C. This general type of

Figure 232. Schematic Representation of the Initial Stage of Plastic Deformation in Various Crystals

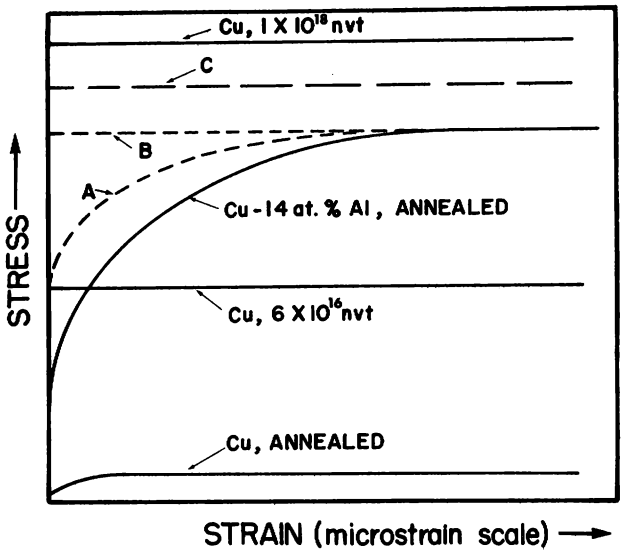

Macro 36024

[273] Rosenfield, A. R., and Averbach, B. L., Acta Met., 8, 624 (1960).

behavior easily accounts for the incubation period noted in the flow stress-dose measurements of the 14 a/o Al crystals, and a similar explanation could be advanced for the incubation stage sometimes observed in copper crystals irradiated to fairly low dose levels.

Figures 228 and 231 indicate that the 0.5 and 5 a/o Al alloys cannot fall into the simplified explanation given above because the τ values for these crystals display a small dose dependence prior to coinciding with the τ values of copper. Note, however, that in the low dose ranges, both the absolute and relative amount of irradiation-induced strengthening in these alloys is less than that of copper. Thus, even in the 0.5 and 5 a/o Al alloys the effects of solid solution and neutron-irradiation strengthening are not simple additive properties.

4. Radiation Effects in Anisotropic Metals (B. A. Loomis)

Publications:

1. B. A. Loomis, Swelling of Uranium, Radiation Damage in Reactor Materials, IAEA, Vienna, 95-107 (1963).

2. B. A. Loomis and D. W. Pracht, Swelling of Uranium on Postirradiation Annealing, J. Nuc. Mat. 10 (4) 346-359 (Dec 1963).

3. B. A. Loomis, Swelling of Aluminum Clad Aluminum - Plutonium Alloys on Postirradiation Annealing, ANL-6651 (Nov 1963).

Swelling of Uranium on Postirradiation Annealing: The effect of grain size and burnup on the swelling of high-purity uranium during postirradiation annealing was investigated. Specimens with an average grain diameter of 17 μ after swaging and subsequent recrystallization, and specimens with an average grain diameter of 90 μ after swaging and subsequent beta heat treatment were prepared for this study. The specimens were irradiated in a constrained condition in the Materials Testing Reactor to either 0.035, 0.17, or 0.35 percent burnup of all atoms. It is estimated that the temperature of the specimens did not exceed 275°C during irradiation.

The irradiated specimens were sealed in evacuated quartz capsules and heated at rates of either 7°C or 100°C per minute to 620°C. After annealing for 75 hr, the specimens were removed from the furnace and allowed to air cool. The density of the annealed specimens was determined by weighing them in air and carbon tetrachloride. The swelling of a specimen is taken as the ratio of the change in density on annealing to the density after irradiation.

The experimental results are presented in Figure 233, and the density decrease is plotted against the burnup. The specimens with an average grain diameter of 17 μ swelled substantially more than those with an average grain diameter of 90 μ at burnups greater than 0.1 percent. At a burnup of 0.035 percent the increase in density was slight in both cases. The rate of heating had no effect.

Figure 233. Swelling of Uranium Irradiated to 0.035, 0.173, or 0.35 a/o Burnup on Annealing 75 hr at 620°C

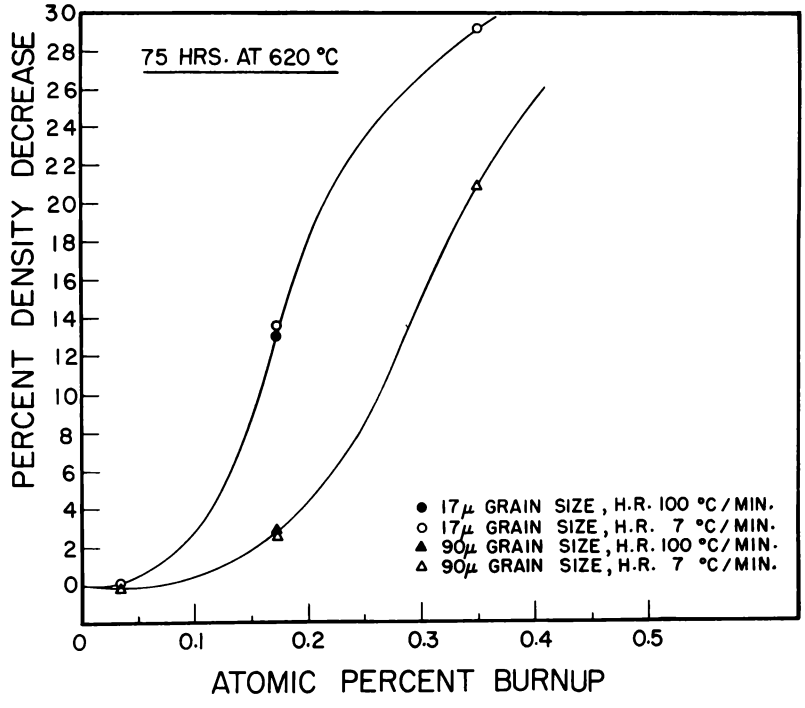

Macro 38163

An interpretation of the observed effects of grain size and burnup must await a detailed examination of the microstructures of the annealed specimens. It should then be possible to assess the importance of recrystallization during annealing, as suggested by Loomis and Pracht.[274] The number of potential recrystallization sites, e. g., grain boundaries and twin-grain boundary intersections, before irradiation should influence the size of the grains formed during postirradiation annealing, and, consequently, the diameter and number of gas-filled bubbles.

A comparison of the results shown in Figure 233 with those previously reported[274] for specimens that were similarly annealed, but

[274] Loomis, B. A., and Pracht, D. W., Swelling of Uranium and Uranium Alloys on Postirradiation Annealing, ANL-6532 (Sept 1962).

the anneals were interrupted five times to cool to room temperature, indicates that the thermal cycles did not appreciably affect the swelling behavior.

Transmission Electron Microscopy and Irradiation Growth of Uranium: Foils of high-purity uranium sufficiently thin for observation by transmission electron microscopy were prepared by electrolytic polishing techniques similar to those previously described by Hudson, Westmacott, and Makin.[275] High-purity material was rolled to 0.001-in. thickness, and then either annealed for 2 hr at 600°C or heated for one hour at 700°C and water quenched. The foils were thinned by electrolytic polishing in an electrolyte (containing 133 cc acetic acid, 25 gm chromium trioxide, and 7 cc water) with a uranium cathode and an open circuit potential of 35 V. An oxide film formed on the foils during thinning, but this could be removed by a short electrolytic polish in an electrolyte (containing 150 cc sulphuric acid, 14 cc water, and 20 cc glycerol) with a stainless steel cathode and an open circuit potential of 20 V. The best results were obtained with this solution when the temperature was maintained at about 5°C.

Transmission electron photomicrographs in the fully annealed condition and in the beta-quenched condition are shown in Figures 234 and 235. Short lengths of dislocations were observed in both foils, with the number of dislocations being higher in the beta-quenched specimens. Twins were also frequently observed in the beta-quenched foils.

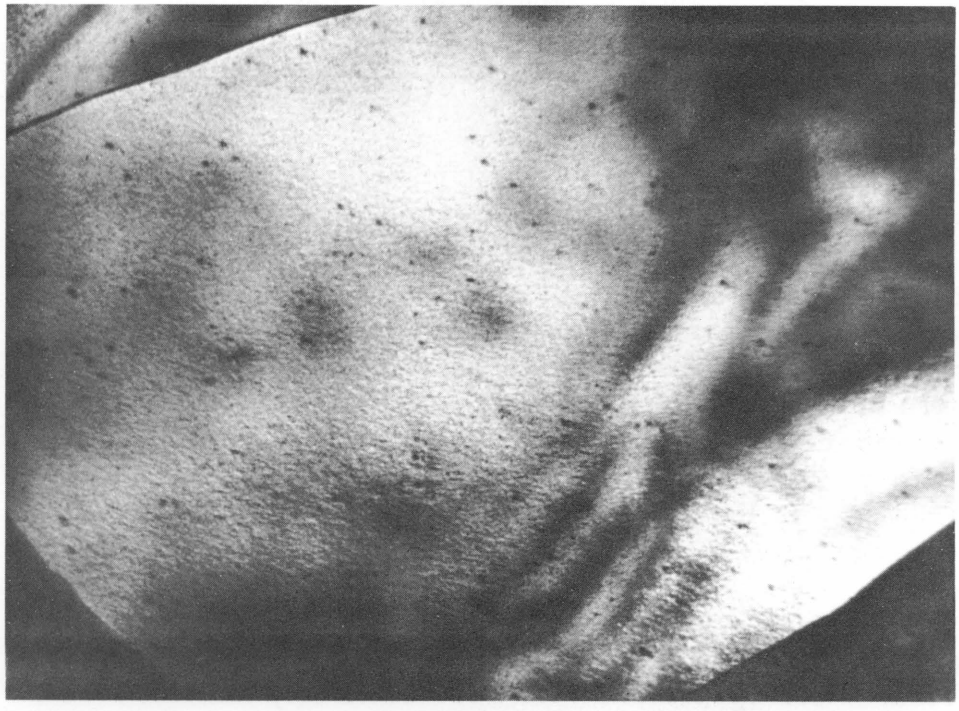

Micro 120,317 22,000X

Figure 234
Transmission Electron Photomicrograph of Uranium in the Annealed Condition

[275]Hudson, B., Westmacott, K. H. and Makin, M. J., Dislocation Loops and Irradiation Growth in Alpha Uranium, AERE-R 3752 (June 1961).

Figure 235. Transmission Electron Photomicrograph of Uranium in the Beta-quenched Condition

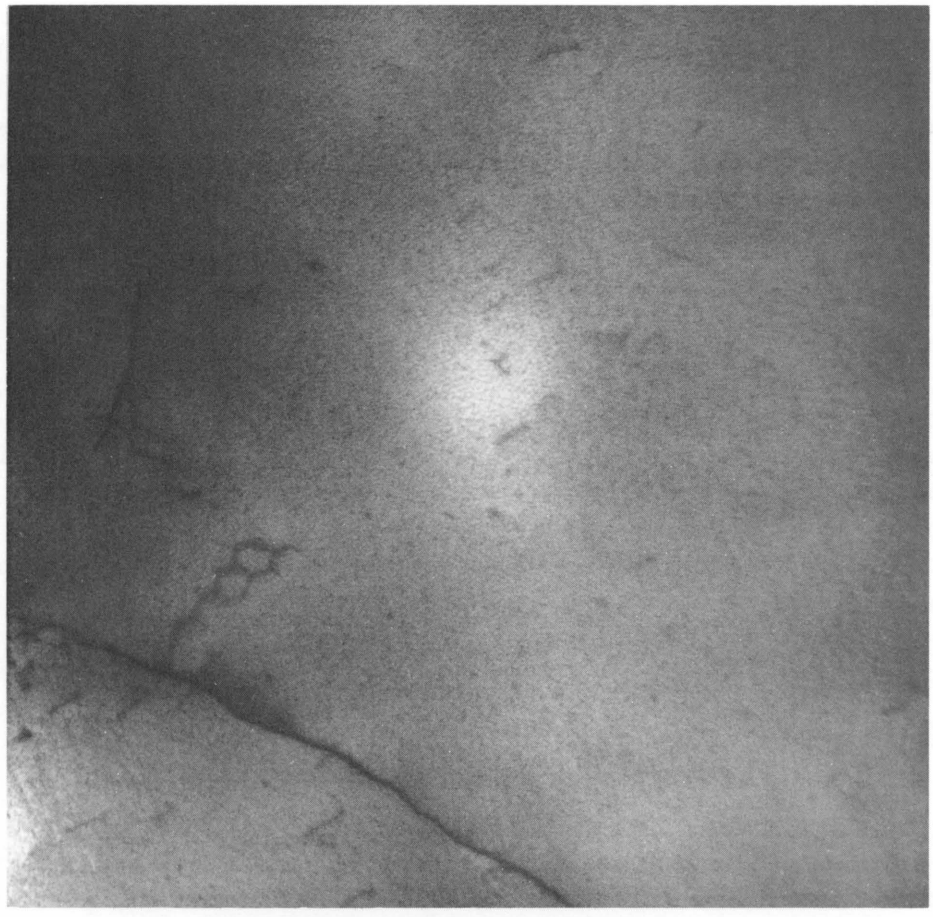

Micro 120,339 22,000X

It is planned to irradiate these foils simultaneously with pseudo-single-crystalline uranium rods which are intended for a study of irradiation-growth phenomena at 4°K. After irradiation the foils will be thinned and examined for irradiation damage. The apparatus for the measurement of the growth of uranium rods during irradiation at 4°K has been calibrated and is awaiting the completion and insertion of the cryostat in Hole V-44 in the low-temperature facility in CP-5.

5. Migration of Pores in Solids (Theoretical) (E. E. Gruber)

In order to understand the phenomenon of swelling in metallic solids due to the formation of fission product gas bubbles, consideration must be given to the problem of bubble growth. Experimental evidence indicates that the bubbles do not grow by migration of gas atoms from the smaller bubbles to the larger ones (that is, by "re-solution"), but that

larger bubbles are formed by coalescence of smaller ones.[276] A research program has therefore been initiated to study the processes of migration and coalescence of pores in solids. The term "pore" is used to include both bubbles and voids, as, for example, voids which may develop during sintering processes or by vacancy precipitation. Although the behavior of bubbles is clearly different from that of voids in some respects (for example, upon coalescence volume is conserved in the case of voids and surface area is conserved in the case of bubbles), they are alike in such features as migration rates.

Dependence of Pore Velocity on Driving Force: We first consider the relationship between the magnitude of a force, f, exerted on an atom situated on the surface of a pore and the speed v of the pore. For simplicity, we assume that the pore remains spherical during migration. This is a rather severe assumption, but no observation of deviation from spherical shapes was mentioned by Barnes and Mazey in connection with their observations of bubble movement in copper foils.[276]

We shall consider the pore sketched in Figure 236, for which the force is directed in the x direction. The flux per unit length on the surface is given by

$$J_S = \nu v = \frac{\nu D_S}{kT} f_s = \frac{\nu D_S f}{kT} \sin \theta, \qquad (1)$$

where ν is the surface density of atoms involved in transport, v is the surface drift speed as defined by the Nernst-Einstein relation,[277] D_S is the surface diffusion coefficient, and $f_s = f \sin \theta$ is the component of f parallel to the surface.

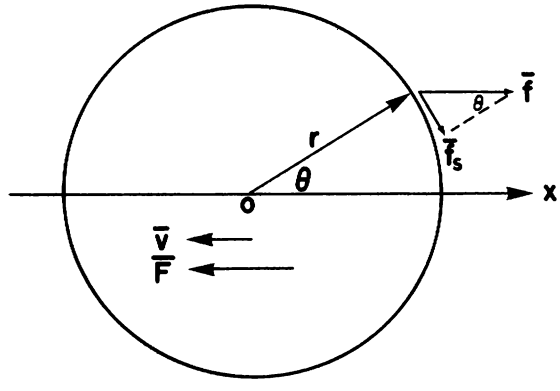

Figure 236

Schematic Representation of Migrating Pore

Macro 38317

[276] Barnes, R. S., and Mazey, D. J., The Migration and Coalescence of Inert Gas Bubbles in Metals, AERE-R 4223 (1963).

[277] Jost, W., Diffusion in Solids, Liquids, Gases, Academic Press, Inc., New York (1952).

The speed with which a surface element D_s moves normal to itself is given by the product of the atomic volume Ω and the divergence of atoms per unit area. Thus, making use of the symmetry about the x axis and considering a strip of width $r\,\Delta\theta$ at $\theta = \theta_0$, the time rate of change of r at $\theta = \theta_0$ is

$$\left(\frac{dr}{dt}\right)_{\theta_0} = \lim_{\Delta\theta \to 0} \frac{2\pi r(\sin\theta_0)J_{\theta_0} - 2\pi r \sin(\theta_0 + \Delta\theta)J_{\theta_0} + (\Delta\theta)\Omega}{2\pi r \sin\theta_0 (r\Delta\theta)},$$

where the numerator represents the net number of atoms which enter the strip and the denominator represents the area of the strip.

Substituting from Eq. (1) for the flux, and simplifying, we obtain

$$\left(\frac{dr}{dt}\right)_{\theta_0} = -\frac{\Omega\nu D_s f}{rkT \sin\theta_0} \lim_{\Delta\theta \to 0}\left\{\frac{\sin^2(\theta + \Delta\theta) - \sin^2\theta}{\Delta\theta}\right\}. \tag{2}$$

Taking the limit of the term in brackets as $\Delta\theta \to 0$, we have by the definition of the derivative

$$\lim_{\Delta\theta \to 0}\left\{\frac{\sin^2(\theta_0 + \Delta\theta) - \sin^2\theta_0}{\Delta\theta}\right\} \equiv \left[\frac{d(\sin^2\theta)}{d\theta}\right]_{\theta = \theta_0} = 2 \sin\theta_0 \cos\theta_0.$$

We thus have

$$\left(\frac{dr}{dt}\right)_{\theta_0} = -\frac{2\Omega\nu D_s f}{rkT} \cos\theta_0, \tag{3}$$

and for $\theta_0 = 0$ this reduces to

$$\left(\frac{dr}{dt}\right)_{\theta_0} = 0 = v = -\frac{2\Omega\nu D_s f}{rkT},$$

or, taking $\Omega\nu = a_0$, the interatomic distance, we obtain finally

$$v = -2a_0 D_s f / rkT. \tag{4}$$

It can be shown that this result is identical with that obtained previously by Greenwood and Speight[278] by an entirely different and somewhat approximate treatment.

---

[278] Greenwood, G. W., and Speight, M. V., An Analysis of the Diffusion of Fission Bubbles and Its Effect on the Behavior of Reactor Fuels, J. Nuc. Matls. 10(2), 140 (1963).

For the case in which a thermal gradient acts as the driving force, the atomic force is given by

$$f = -\frac{dH}{dx}$$

or

$$f = -C_p \frac{dT}{dx}$$

If C_p is taken as approximately equal to C_v as given by the Dulong-Petit law,[279]

$$C_p \cong C_v \cong 3k,$$

we obtain

$$f = -3k \frac{dT}{dx}.$$

Substitution into Eq. (4) gives as the speed of a pore due to a thermal gradient

$$v = \frac{6a_0 D_s}{rT} \frac{dT}{dx} \tag{5}$$

Equations (4) and (5) are consistent with the observations of Barnes and Mazey[276] in that the pore speed is inversely proportional to the bubble radius. The thermal gradient required to give the observed speed of 10^{-5} cm/sec for a bubble of 350-Å radius is about 2×10^5°C/cm, or about 20°C/μ.

Relationship between Force on Pore and Atomic Driving Force: The presence of a force f tends to produce migration of a pore by inducing migration of the atoms on the surface of the pore. It is thus possible to define a force F, which acts on the pore, through the principle of virtual work. Thus, if a pore moves a distance δx, the work done is $\delta W = F\,\delta x$. From the result of the preceding section, the force F acts in the direction opposite to that of the force f.

Consider a small element of area on the surface of a pore. If the pore moves a distance δx, this surface element sweeps out a volume $\delta\tau$, which is equivalent to a number of atoms $\delta\tau/\Omega$. If all atoms in each element $\delta\tau$ are transported to the opposite side of the pore, so that atoms at coordinates x, y, z, are transported to coordinates -x, y, z, the net result is movement of the pore by an amount δx, and the integral over all elements $\delta\tau$ gives the total work δW.

[279] Kittel, C., Introduction to Solid State Physics, John Wiley and Sons, Inc., New York (1956).

Since only the motion parallel to the applied force is involved in the work accomplished by the force f, the work required to transport an atom from (x, y, z) to (-x, y, z) is

$$\delta W = 2fx = 2fr \cos \theta.$$

The number of atoms in a volume element $\delta\tau$ is

$$\frac{\delta\tau}{\Omega} = \frac{1}{\Omega}(2\pi \sin\theta)(r\, d\theta \cos\theta)\delta x,$$

where we have taken the volume element as a ring about the x axis. The total work done is then

$$\delta W = \int_{\theta=0}^{\pi/2} \frac{\delta\tau}{\Omega} 2fr \cos\theta = \frac{2\pi r^2\, \delta x}{\Omega} 2fr \int_0^{\pi/2} \sin\theta \cos^2\theta\, d\theta$$

$$= \frac{4\pi r^3 f\, \delta x}{3\Omega} = F\, \delta x.$$

Recalling that the force on the pore is in the opposite direction to the atomic driving force, we obtain

$$F = -\frac{4\pi r^3}{3\Omega} f = -\frac{4\pi}{3\sqrt{2}}\left(\frac{r}{a_0}\right)^3 f,$$

where we have taken $\Omega = \sqrt{2}\, a_0^3$. Combining this with the earlier result for migration speed, we obtain

$$v = \frac{3}{\sqrt{2}\pi} \frac{D_s}{kT}\left(\frac{a_0}{r}\right)^4 F. \qquad (6)$$

This result differs from that given earlier by Mullins[280] only in the numerical constant. The result quoted by Barnes[276] is

$$v = \frac{1}{8\pi} \frac{D_s}{kT}\left(\frac{a_0}{r}\right)^4 F,$$

where a_0 is the lattice spacing.

Volume Diffusion Coefficient for Pore Migration: We are now in a position to use the preceding results in combination with the Nernst-Einstein relation to define a diffusion coefficient D_b for the pore. From the Nernst-Einstein relation,[277]

---

[280]Mullins, W. S., private communication with R. S. Barnes (see Reference 276).

$$v = (D_b/kT)F. \tag{7}$$

From the preceding results, we have

$$F = -\frac{4\pi}{3\sqrt{2}}\left(\frac{r}{a_0}\right)^3 f$$

and

$$v = -\frac{2a_0 D_s f}{rkT}.$$

Equating the two relations for v, substituting for F in terms of f, and solving for D_b, we obtain

$$D_b = \frac{3}{\sqrt{2}\pi}\left(\frac{a_0}{r}\right)^4 D_s = 0.675\left(\frac{a_0}{r}\right)^4 D_s. \tag{8}$$

This result verifies that obtained by Greenwood and Speight[278] by a different method. The only difference is a factor of $\sqrt{2}$ which arises because Greenwood and Speight took the atomic volume Ω as a_0^3, rather than as $\sqrt{2}\,a_0^3$, which is appropriate for the face-centered cubic structure.

Bubble Coalescence by "Random Walk": Let us consider an approximate treatment of the change in the distribution of bubbles in a solid during post-irradiation annealing. In this treatment, we approximate the distribution f(r,t) of bubbles of radius r as a uniform distribution of bubbles with the radius $\bar{r}$, which is taken as the mean radius of the distribution. Thus $\bar{r}$ is defined by the relation

$$\bar{r} = \frac{\int_0^\infty r\, f(r,t)\, dr}{\int_0^\infty f(r,t)\, dr} = \frac{1}{N(t)}\int_0^\infty r\, f(r,t)\, dr, \tag{9}$$

where N(t) is the total number of bubbles per cm^3 present in the system at time t.

We now consider the rate of coalescence of bubbles of radius $\bar{r}$. The number of collisions of a single bubble, based on a treatment analogous to the kinetic theory of gases, is given by the number of bubbles per unit volume times the volume of a cylinder "swept out" by the bubble in unit time. With the correction factor 4/3 to allow for the fact that other bubbles are also moving,[281] we obtain for the number of collisions in time t

[281] Noyes, A. A., and Sherrill, M. S., A Course of Study in Chemical Principles, MacMillan, New York (1938).

$$n = \pi(2\bar{r})^2 vtN(t)4/3.$$

The time t_1 required for one collision is therefore

$$t_1 = 3/16\pi\bar{r}^2 vN(t).$$

Now the "mean free path," or net distance traveled between collisions, is $\ell = vt_1$, so that

$$\ell = 3/16\pi\bar{r}^2 N(t), \tag{10}$$

But this is just the mean distance traveled in time t_1, which is given by

$$\ell = \sqrt{6D_b t_1}. \tag{11}$$

Thus we obtain for t_1 from Equations (10) and (11)

$$t_1 \cong \frac{1}{524\pi D_b \bar{r}^4 [N(t)]}. \tag{12}$$

Since we are considering the case of post-irradiation annealing, the number of gas atoms per cubic centimeter is constant. If it is assumed that the gas obeys the ideal gas law and that the pressure is balanced by surface tension, the number of atoms per unit volume is given by

$$m = \frac{pV}{kT} = \frac{(2\gamma/r)N(t)(4\pi\bar{r}^3/3)}{kT} = \frac{8\pi\gamma\bar{r}^2 N(t)}{3\,kT},$$

where p is the pressure, V the volume of all bubbles, and γ the surface energy per unit area. Solving for N(t), we obtain

$$N(t) = 3kTm/8\pi\gamma\bar{r}^2. \tag{13}$$

Substituting this result and the result given previously for D_b:

$$D_b = 0.675\left(a_0/\bar{r}\right)^4 D_s,$$

we obtain

$$t_1 = \frac{1}{15.8}\left(\frac{\gamma}{mkT}\right)^2 \frac{\bar{r}^4}{a_0^4 D_s} = \frac{\bar{r}^4}{\alpha}, \tag{14}$$

where

$$\alpha = 15.8\, a_0^4 D_s \left(\frac{mkT}{\gamma}\right)^2.$$

The meaning of the "relaxation time" t_1 is that the number of bubbles that have not suffered collisions is given by

$$f(\bar{r},t) = f(\bar{r},o)\, e^{-t/t_1} = f(\bar{r},o) \exp\left(\frac{-\alpha t}{\bar{r}^4}\right). \tag{15}$$

We obtain the rate of loss of bubbles of radius $\bar{r}$ by differentiation of this equation with respect to time t:

$$\frac{d\, f(\bar{r},t)}{dt} = -\frac{\alpha}{\bar{r}^4} f(\bar{r},t). \tag{16}$$

Now each time two bubbles collide, we assume that they coalesce to form a new bubble of radius

$$r' = \sqrt{\bar{r}^2 + \bar{r}^2} = \sqrt{2}\,\bar{r}.$$

The rate of formation of bubbles of radius r' is therefore

$$\frac{d\, f(r',t)}{dt} = -\frac{1}{2}\frac{d\, f(\bar{r},t)}{dt} = \frac{\alpha}{2\bar{r}^4} f(\bar{r},t). \tag{17}$$

Now let us consider the bubble distribution at time $t' = t + \Delta t$, where Δt is a small increment. Application of equation (9) applied to this situation gives as the new mean radius

$$\bar{r}(t + \Delta t) = \frac{\left[f(\bar{r},t) - \frac{\alpha \Delta t}{\bar{r}^4} f(\bar{r},t)\right]\bar{r} + \left[\frac{\alpha \Delta t}{2\bar{r}^4} f(\bar{r},t)\right]\sqrt{2}\,\bar{r}}{f(\bar{r},t) - \frac{\alpha \Delta t}{\bar{r}^4} f(\bar{r},t) + \frac{\alpha \Delta t}{2\bar{r}^4} f(\bar{r},t)}$$

$$= \frac{1 - \left(1 - \frac{\sqrt{2}}{2}\right)\frac{\alpha \Delta t}{\bar{r}^4}}{1 - \frac{\alpha \Delta t}{2\bar{r}^4}}\,\bar{r}.$$

Since $\frac{1-y}{1-x} \simeq 1 - y + x$ for x and y sufficiently small, we have for sufficiently small Δt

$$\frac{\bar{r}(t + \Delta t) - \bar{r}(t)}{\Delta t} = \frac{\sqrt{2} - 1}{2}\frac{\alpha}{\bar{r}^3}.$$

But this is just the definition of $d\bar{r}/dt$ if we take the limit as Δt tends to zero. Therefore,

$$\frac{d\bar{r}}{dt} = \frac{\sqrt{2} - 1}{2} \frac{\alpha}{\bar{r}^3}. \tag{18}$$

This expression is valid only for r_0 sufficiently large that our assumptions concerning surface tension equilibrium are satisfied. We therefore integrate, between the limits $\bar{r} = \bar{r}_0$ at t_0 and $\bar{r}$ at time t, to obtain

$$\bar{r}^4 = \bar{r}_0^4 + 2\left(\sqrt{2} - 1\right)\alpha\left(t - t_0\right). \tag{19}$$

If we assume that the assumptions are valid for $\bar{r}_0 > 100$ Å, and consider values of $\bar{r}$ in the neighborhood of 1000 Å, it is apparent that $\bar{r}_0^4$ is negligible compared to $\bar{r}^4$. Furthermore, as will be apparent in the following example, the time required to attain a mean radius $\bar{r}_0$ is very short compared with that required to attain a mean radius $\bar{r} \sim 10\,\bar{r}_0$. Equation (19) can therefore be simplified to

$$\bar{r}(t) \cong 1.9\, a_0 \left(mkT/\gamma\right)^{1/2} (D_s t)^{1/4}, \tag{20}$$

where we have substituted the definition of α.

As an example, we consider the time required to achieve a mean bubble radius to 10^{-5} cm in copper at 1000°K after irradiation which introduces 10^{20} helium atoms per cubic centimeter. Taking γ as 1700 ergs/cm^2 and D_s as 10^{-6} cm^2/sec, we obtain t = 10 months. For a larger mean radius, the time increases very rapidly. For example, the time required to achieve a mean radius of one-fourth micron is about 30 yr.

The foregoing treatment indicates that random movement of bubbles is insufficient in itself as a mechanism for swelling in solids due to bubble coalescence. Work is in progress to determine more accurately the effect of coalescence by random movement, by consideration of the entire distribution rather than by consideration of an artificial distribution of bubbles of only one radius. The planned approach is to assume an initial distribution of very small bubbles and to calculate the distribution of bubble sizes at subsequent times by finite-difference methods, by means of the digital computer. The analysis is a generalization of that given here for bubbles of only one size.

It is expected that the mechanism of coalescence by random movement of bubbles cannot predict the amount of swelling observed in most post-irradiation annealing experiments, and that some other mechanism, such as grain-boundary sweeping, migration due to a thermal gradient, or migration due to elastic interaction of stress fields surrounding bubbles, must be considered.

The principal objective of this project is to determine the influence of a driving force on the migration and coalescence of bubbles. Again, the planned approach is to consider the change in some initial distribution due to the presence of a driving force, such as a thermal gradient, by application of finite-difference methods and numerical analysis.

An experimental program is being planned to supplement the analysis of pore migration. Some measurements of swelling of a metal in a thermal gradient after inoculation with helium atoms may be carried out if the analysis indicates that measurements will be fruitful. Another experimental approach being planned is direct observation of bubble migration in a known thermal gradient.

6. The Clustering of Point Defects in Quenched and Irradiated Metals (Theoretical) (R. M. J. Cotterill)

The set of equations governing the clustering of point defects:

$$dC_i/dt = \sum_{m,n} A_{mn} C_m C_n \exp(E_{mn}/kT),$$

can be integrated simultaneously by use of a program that has been written for the ANL analog computer. This program, which is applicable to both pure and impure metals under quenching or irradiation conditions, plots the time variation of each of the C_i, where C_i is the concentration of clusters containing exactly i point defects. The solutions of the above equations are critically dependent upon the values of the E_{mn}, the binding and migration energies. One aim of the calculations is the determination of consistent sets of these energies by comparison of the C_i with experimental values of the same quantities.

The case of a quenched metal similar to copper, silver, or gold has now been solved for a system in which clusters as large as hexavacancies are allowed. The most significant features to emerge from the results thus far are the points of inflection and the maxima which occur in some of the plots of C_i against time during quenching. It is found, for instance, that the divacancy concentration increases during the early part of the quench, but later decreases. This subsequent decrease is due to the formation of trivacancies. The same thing happens to the trivacancy concentration when the quadrivacancy concentration starts to build up. By varying the purity of the metal, the quenching temperature, and the quenching rate the positions and heights of these maxima can be altered.

7. Equilibrium and Transient Configurations of Point-defect Clusters in Metals (Theoretical) (R. M. J. Cotterill*)

This work falls into two main categories: 1) the annealing stages of large clusters of point defects; 2) the formation of small clusters from individual point defects.

A recent paper by De Jong and Koehler[282] includes a discussion of the early stages of growth of stacking-fault tetrahedra in quenched gold. These workers suggested that growth might proceed by the formation of ledges on the stacking-fault faces of the defect. More recently, Kimura et al.[283] considered the two types of ledge which can occur in practice. These are shown in Figures 237(a) and 237(b). Kimura et al. used a qualitative atomistic argument to show that the case shown in Figure 237(a) is energetically more favorable. It might be noted that this is immediately apparent if the two cases are considered in terms of the elementary jogs discussed by Hirsch.[284]

Figure 237. Arrangement of Stacking Faults and Dislocations around (a) a 70.5° Ledge and (b) a 109.5° Ledge

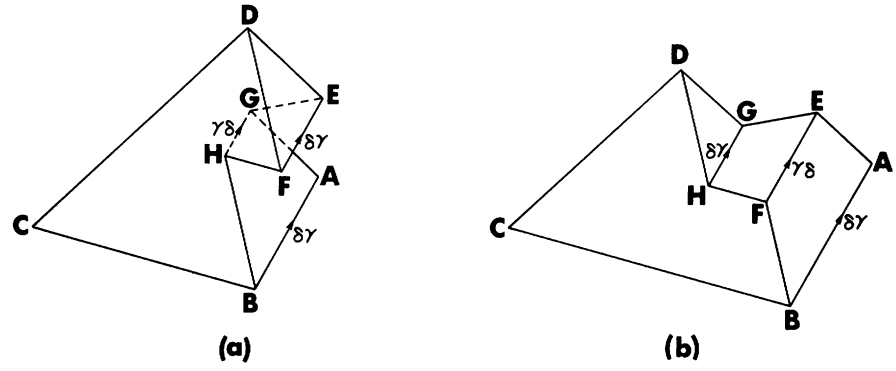

Macro 37864

The step in Figure 237(a) involves acute stacking-fault bends and is equivalent to a one-third vacancy jog, whereas the step in Figure 237(b) involves obtuse stacking-fault bends and is equivalent to a one-third interstitial jog (or two-thirds vacancy jog). Hirsch finds that the latter has a higher energy.

Kimura et al. calculated that the increase in energy as the jog in Figure 237(a) moves away from the corner through a distance of one atomic interval is approximately 0.1 eV. Comparison of this energy with the 0.98-eV energy drop when a vacancy in gold is annihilated was taken

---

*In collaboration with M. Doyama, ANL Solid State Science Division.

[282] De Jong, M., and Koehler, J. S., Phys. Rev. 129 49 (1963).

[283] Kimura, H., Kuhlmann-Wilsdorf, D., and Maddin, R., Appl. Phys. Let. 3 4 (1963).

[284] Hirsch, P. B., Phil. Mag. 7 67 (1962).

as evidence for this mechanism of clustering. Kimura et al. also considered the annealing out of tetrahedra. They noted that the annealing of tetrahedra cannot proceed by the emission of vacancies, such that the growth process is reversed, because the activation energies required would be prohibitively high every time a new ledge is started. They concluded that the dissolution of tetrahedra by the propagation of ledges is unlikely. This conclusion was examined and shown to be erroneous.

As in the case of the formation of tetrahedra, there are two mechanisms to be considered. The one involving the ledge shown in Figure 237(a) has been shown by Kimura et al. to be unfavorable. The one involving the ledge shown in Figure 237(b) would proceed by the steps shown in Figure 238. The first step would be the removal of one of the corners, and the ledge would be formed upon removal of a second vacancy [see Figure 238(b)]. Removal of each subsequent vacancy would be accompanied by the movement of the ledge towards AB by one atomic interval. During this process the stair-rod dislocation CB would attract stair-rod HF and CA would similarly attract GE. In addition, AB would tend to attract EF and repel GH. AB is always closer to EF than GH, however, so there would always be a net attraction of the ledge towards AB. Moreover, this attraction should increase as the distance between the ledge and AB decreases, because the difference between the distances EF-AB and GH-AB would become more noticeable. This suggests that

Figure 238. Dissolution of a Tetrahedron by the Propagation of a 109.5° Ledge

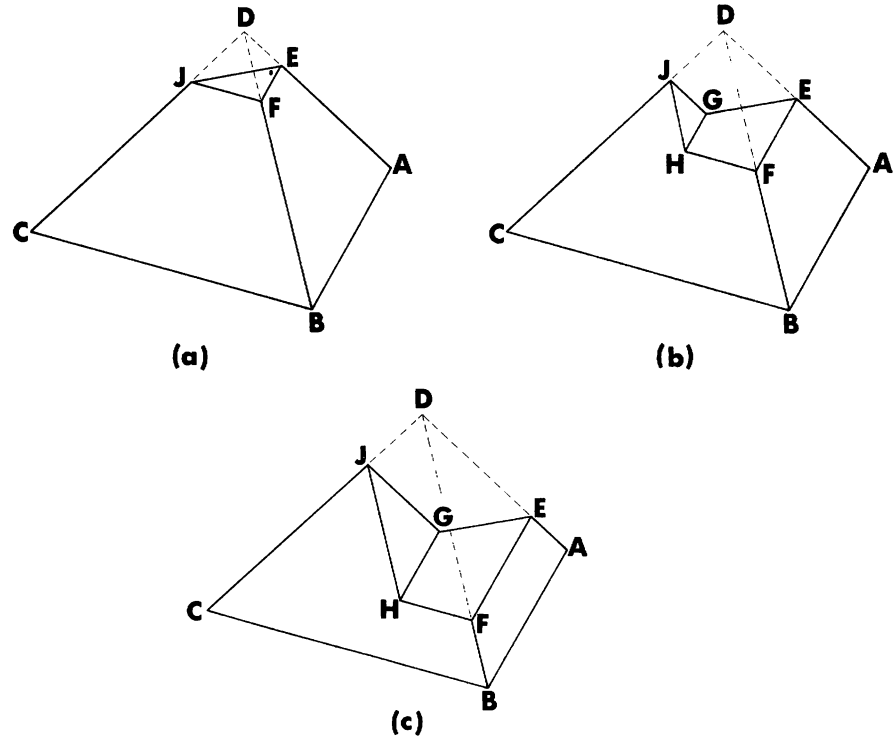

Macro 37865

the rate of emission of vacancies should increase as the ledge approaches AB. It also suggests that emission of vacancies might be easier for very small tetrahedra.

The first step shown in Figure 238(a) involves a decrease of $a^2\sqrt{3}/4$ in the area of stacking fault, a decrease of $3a/\sqrt{2}$ in the length of stair-rod dislocation at acute fault bends, and an increase of $3a/\sqrt{2}$ in length of stair-rod dislocation at obtuse fault bends (a is the lattice parameter). Each subsequent step except the final one involves a decrease of $a^2\sqrt{3}/2$ in fault area, and an increase of $a\sqrt{2}$ in the length of stair-rod dislocation at obtuse fault bends. By means of the formulae quoted by Kimura et al.[283] and an assumption that the energy per unit length of a stair rod at an obtuse fault bend is twice that of a stair rod at an acute fault bend,[284] it is not difficult to show that the first step involves a net energy rise of 0.27 eV and that each of the subsequent steps involves a net energy rise of 0.36 eV. (These figures do not include the energy required to form the vacancy.) It should be noted, however, that this type of calculation may not be applicable to dislocations and faults having atomic dimensions. Moreover, it gives no information as to the heights of the respective energy barriers, and it is these which determine the rate at which the dissolution proceeds. The first step, for instance, requires the movement of an atom towards the corner of the tetrahedron, and this would probably be accompanied by the relaxation of several neighboring atoms.

Damask et al.[285] have considered the movements and relaxations for the case of the tetrahedral trivacancy, which bears some resemblance to the corner of a tetrahedron, and they found that the energy barriers are of the order of several eV. Nevertheless, it is clear that the energy barriers involved in this alternative mechanism will be much lower than the prohibitively high energy involved in the mechanism discussed by Kimura et al.[283]

The completion of annealing after quenching probably corresponds to a situation in which most of the tetrahedra contain ledges of the type shown in Figure 237(a). Upon heating, these ledges should move up towards the corner D, emitting vacancies, until the tetrahedron becomes perfect. It is worth noting that De Jong and Koehler,[282] Meshii and Kauffman,[286] and Cotterill[287] all detected a drop in residual resistivity around 400°C, which might be connected with this effect. (It might also be due to the annealing out of very small tetrahedra, as discussed below.)

---

[285]Damask, A. C., Dienes, G. J., and Weizer, V. G., Phys. Rev. 113 781 (1959).

[286]Meshii, M., and Kauffman, J. W., Phil. Mag. 5 687 (1960).

[287]Cotterill, R. M. J., Phil. Mag. 6 1351 (1961).

At a higher temperature, thermal activation might then overcome the higher-energy barriers involved in the mechanism shown in Figure 238, and the tetrahedra would anneal out. As was noted previously, there may be a size effect in this last process that would make the annealing temperature lower for smaller tetrahedra. Another consequence of this size effect might be a process analogous to that observed by Silcox and Whelan,[288] in which the large dislocation loops in aluminum grow at the expense of the smaller ones. Indeed, Cotterill[289] has observed that in gold quenched from 750°C, the black spot defects, which may be small tetrahedra not resolved as such in the electron microscope, anneal above 350°C and coarsen to produce tetrahedra several hundred Å units wide.

The studies in category 2) involve calculations of the energies of various configurations of point defects in a crystal. The energies are calculated by use of the Morse potential, and allowance was made for the relaxations of many neighboring atoms (sometimes as many as 350) In the case of clusters of vacancies, it is hoped that these studies will indicate the cluster size for which collapse to faulted loops, unfaulted loops or tetrahedra becomes favorable.

8. The Effects of Deuteron Irradiation at 78°K on the Formation of Guinier-Preston Zones. (H. Herman*)

As was reported last year, for the Al-5.3 a/o Zn alloy in the reverted condition, measurements of electrical resistance indicated changes in the kinetics of reaging at 20°C. If it is assumed that the resistivity reflects the reaging process, the results shown in Figure 239 indicate that for doses of less than 9×10^{15} deuterons/cm^2, the reaging process is accelerated in a monotonically increasing manner with neutron dose during the very initial part of the process. It is also interesting to note that the irradiation does not affect the end product in the reaging process. This can be seen from the fact that the maximum of the resistivity curve is unaffected. For doses of 9×10^{15} d/cm^2 and greater, however, it appears that the irradiation does affect the end product of the reaging process. For doses of this magnitude, the resistance does not go through a maximum for half-times up to 10,000 min, whereas in unirradiated material the resistance maxima are observed after about 100 min of aging.

Material preirradiation-aged at 20°C for 10,000 min after reversion exhibited no change in resistance upon further aging at 20°C for times up to 400 min after irradiation to 10^{16} d/cm^2 (see Figure 239, Exp. 5).

---

*Presently at the University of Pennsylvania.

[288] Silcox, J., and Whelan, M. J., Phil. Mag. 5 1 (1960).

[289] Cotterill, R. M. J., Proc. Int. Conf. Cryst. Latt. Def. (1962) J. Phys. Soc. Japan, 18 Suppl. III 48 (1963).

Figure 239. Change in Electrical Resistance vs Reaging Time at 20°C after Irradiation. The specimens were quench-aged at 20°C for one hour and reverted at 200°C for 10 min prior to the irradiation at 78°K. Experiment 8 shows a sample reaged for 10,000 min prior to irradiation.

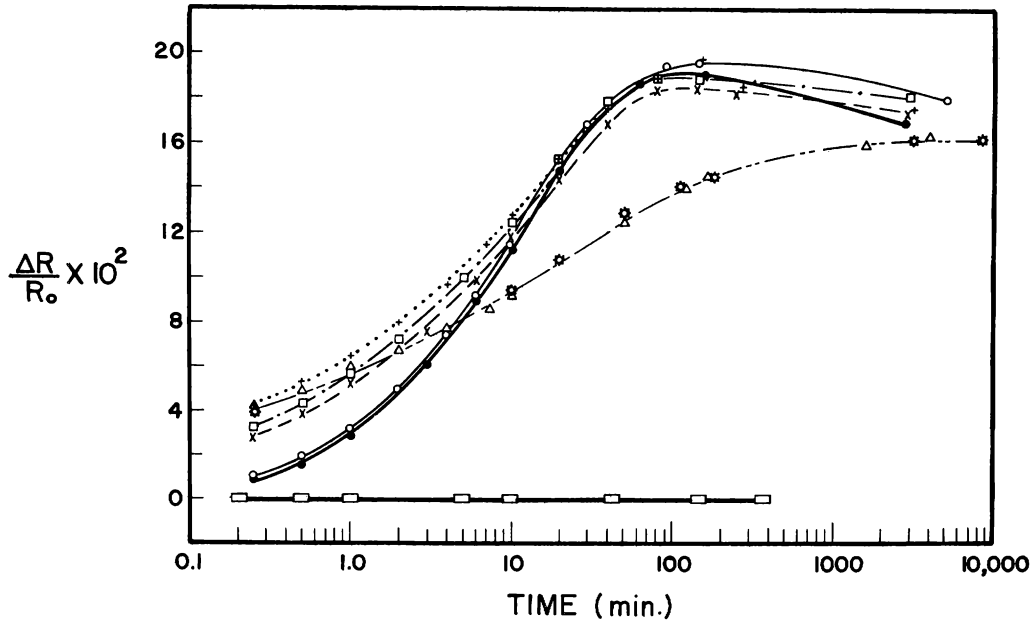

Macro 36707

Exp. 1.	o	Unirradiated.	Exp. 5.	+	1.9×10^{15} d/cm^2.
Exp. 2.	●	Unirradiated.	Exp. 6.	△	9.0×10^{15} d/cm^2.
Exp. 3.	×	0.5×10^{15} d/cm^2.	Exp. 7.	✲	13.3×10^{15} d/cm^2.
Exp. 4.	□	0.9×10^{15} d/cm^2.	Exp. 8.	▭	0.9×10^{15} d/cm^2.

Resistance measurements indicate that irradiation to a dose of 10^{15} d/cm^2 of the as-quenched alloy slightly retards zone formation during the early stages of postirradiation aging at 20°C. As in the case of reverted material, the later stages of aging appear to be unaffected by this amount of irradiation.

Isochronal annealing from -70°C to 190°C indicated that the increase in resistance upon early aging began 20°C lower in material irradiated to 10^{15} d/cm^2 than in unirradiated material. In addition, the resistivity maximum was also displaced 20°C lower in temperature for the irradiated material.

To obtain further information on the nature and sizes of the zones present after normal aging and postirradiation aging, small-angle scattering of X rays was employed. To provide a valid comparison between resistance measurements and the X-ray data, the samples utilized for electrical resistance measurements were also used for the X-ray studies.

A General Electric XRD-5 diffractometer was used with the specimen placed in a holder mounted in a bearing fastened to the base plate at the center of the goniometer. The holder was fixed to the divergent beam slit bracket so that this arrangement eliminated the θ motion of the base plate associated with the counter motion of 2 θ.

An 0.1° small-angle scattering beam slit was employed in conjunction with a 0.2° receiving slit. An adjustable slit was placed at the beam slit to limit vertical divergence. The direct beam intensity and parasitic scattering were limited by employing a copper beam-stop as in the method developed by Kratky.[290]

X rays obtained from a copper tube operating at 35 kV and 23 mA were monochromatized with the use of the balanced-filter technique.[291] A run was first performed with a nickel and an aluminum filter, and then with a cobalt oxide filter; the difference in intensity yielded Cu_{K_α}. The efficiencies of these filters have been previously determined.[292] The filters were matched for Mo_{K_α} to 0.2 percent and for CuK_α to 1.0 percent. Parasitic scattering was determined with the use of a pure aluminum specimen adjusted in thickness to give the same absorption as the alloy specimen (0.0044 in.). This parasitic scattering was subtracted from the scattering curve. Automatic step scanning was employed with a 1000-sec count being made every 0.1° of 2 θ angle with the output registered on a digital printer. The errors in zone size due to counting statistics and variation in X-ray intensity are less than 8 percent.

The small-angle scattering information for four experiments is contained in Figure 240, which is a plot of the logarithm of the scattered X-ray intensity, I_s, as a function of the square of the scattering angle, ϵ, obtained with the equation derived by Guinier:[293]

$$I_s(\epsilon) = Nn^2 I_e \exp\left[-\frac{4\pi^2}{3\lambda^2} R_g^2 \epsilon^2\right], \qquad (1)$$

where

$I_s(\epsilon)$ = Itensity of scattered radiation per unit mass;

N = Number of scattering particles;

n = Difference between the number of electrons contained in the particle and the number of electrons contained in an equal volume of the homogeneous material

---

[290]Kratky, O., Porod, G., and Kahovek, L., Z. Electrochem, 55 53 (1951).

[291]Kirkpatrick, P., Rev. Sci. Instr., 10 186 (1939).

[292]Herman, H., Cohen, J. B., and Fine, M. E., Acta Met., 11 43 (1963).

[293]Guinier, A., Ann. Phy., 12 161 (1939).

I_e = Intensity scattered by an electron at small angles;

λ = The wavelength of incident radiation; 1.54 Å for $Cu_{K\alpha}$

R_g = Radius of gyration of the scattering particles. R_g is the electron density analog of the mass density in mechanics;

ϵ = The scattering angle 2θ expressed in radians.

Figure 240. Small-angle Scattering of X Rays. Counts/second vs $(\epsilon)^2 \times 10^4$.

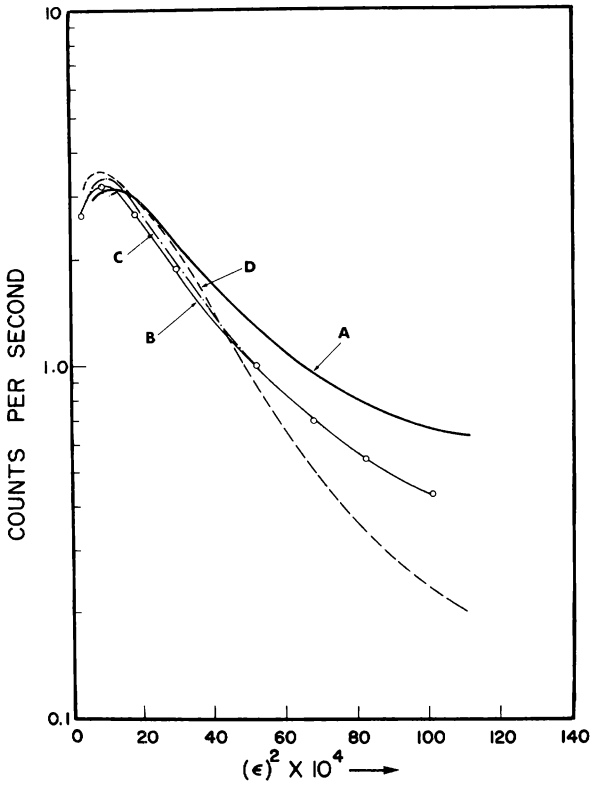

Curve Treatment	I_{max}	$2\theta_{at\ max}$	R(Å)
A. Unirradiated and reaged 1 wk at 20°C.	3.15	2.0	9.0
B. 1×10^{15} d/cm² and reaged 1 wk at 20°C.	3.4	1.75	10.4
C. (a) same as B.	3.2	1.75	9.6
D. 13.3×10^{15} d/cm² and reaged 1 wk at 20°C.	3.6	1.60	11.2

(a) Curve C. is for a specimen irradiated at 20°C.

Macro 36703

The slope of the linear portion of the plot of I_s versus ϵ^2 determines R_g, and the radius R of spherical particles is given by

$$R = \sqrt{5/3}\ R_g. \qquad (2)$$

The size of the largest zones, which give the most contribution to the net scattered intensity, is given by the linear portion of the curve. A reasonable distribution of zone size would give an average zone radius R_{avg} of one-half the radius of these largest zones, R. The range of zone sizes present is indicated by the curvature in the I_s versus ϵ^2 curve above the linear region.

From Figure 240 we can see that the slope of the linear portion of the curves is larger for irradiated material than for unirradiated

material, and the slope increases with increasing deuteron dose. This indicates that the resultant average zone size is larger for material which is irradiated prior to aging, and that the zone size increases with increased dose. Note also that the position of the maximum in the scattered intensity is shifted to smaller angles with increased dose, as is the height of the maximum.

Both the X-ray and resistance information support the idea that point defects play a significant role in the formations of G.P. zones. After reversion at 200°C, the atom fraction of vacancies is approximately 10^{-7}, which is approximately two orders of magnitude lower than after quenching from a solid-solution temperature of 300°C where the atom fraction of vacancies is approximately 10^{-5}. The curve of resistance versus deuteron exposure gives an atom fraction of 10^{-5} vacancy for a dose of 10^{15} d/cm^2. It appears that when the irradiation-induced defect concentration is about the same as the quenched-in vacancy concentration, the interactions among irradiation-induced defects and the thermally generated vacancies actually retard the reaction. When the irradiation-induced defect concentration exceeds the thermally generated vacancy concentration, as occurred for irradiation after reversion, the growth of G.P. zones is enhanced.

For the normal reaging after reversion of the Al-1.7 a/o Cu alloy, an incubation time was observed before the resistance began to increase.[294] Irradiation of two specimens with 10.5-MeV deuterons at 78°K to a dose of 10^{15} d/cm^2 eliminated this incubation time. For the two specimens irradiated, the resistance increased through a small maximum, decreased slightly and then began to increase to a large maximum. The resistance was still increasing after 10,000-min reaging at 20°C.

The results obtained in these experiments suggest the need for further studies on the effects of irradiation in alloy systems where G.P. zones are a normal decomposition product.

9. The Effects of Neutron Irradiation on Precipitation from Supersaturated Solid Solutions (J. A. Horak)

Precipitation from supersaturated solid solutions has been studied extensively for the past 25 yr. Most of the characteristics of the process are well known; however, the basic mechanism of the process has not yet been resolved. In an Al-2 a/o Cu alloy, for example, the clustering of copper atoms to form Guinier-Preston (G.P.) zones occurs at a rate that is 10^7 times more rapid than that calculated from diffusion considerations. The rapid reaction rate is attributed to excess vacancies which are retained on quenching from the solution temperature. Furthermore if after aging at room temperature to produce the G.P. zones, the alloy is

---

[294] Chiou, C., Herman, H., and Fine, M. E., Trans. AIME 218 299 (1960).

reheated, for example, to 478°K, the zones dissolve in about 30 sec. This is known as "reversion." Upon reaging after reversion, an incubation time is observed before zones reappear, which is thought to be due to a deficiency in the concentration of point defects available to participate in G.P. zone formation after reversion.

Neutron irradiation provides a tool to vary and control the concentrations of these point defects, both vacancies and interstitials. By study of the recombination kinetics we hope to shed further light on the role of point defects in the precipitation clustering process. To date we have prepared alloy specimens of Al-Cu, Al-Ag, and Al-Zn for such irradiation studies. The irradiations will be made at 4°K. Subsequently, pulse annealing to sufficiently high temperature will be conducted to attain complete recovery of irradiation-induced electrical resistivity.

10. Low-temperature Alpha-irradiation Accessory for Siemens Electron Microscope (R. M. J. Cotterill)

The modification of the electron microscope to permit observation of specimens near 4°K and to carry out in situ alpha irradiation of such specimens involved the construction of the following items:

1) a new specimen chamber which replaces the old airlock;

2) a liquid helium stage;

3) an alpha-source holder.

All three items have been constructed, and temperatures in the region of 40°K have been reached. Minor modifications of the apparatus are expected to lower the minimum attainable temperature.

Even in its present state, the apparatus can be used for most of the planned irradiation experiments, and one is now in progress. This aims at repeating the experiment described by Cotterill and Jones[295] at lower temperatures in an effort to determine the activation energy for interstitial migration in gold.

---

[295] Cotterill, R. M. J., and Jones, M. W., J. Phys. Soc. Japan, 18 Suppl. III 158 (1963).

APPENDIX A

NEW CONSTRUCTION AND FACILITIES

1. Fuels Technology Center Construction Project, Building 212 (B. J. Koprowski)

Historically, the Metallurgy Division was organized in 1943 as a part of the Metallurgical Laboratory of The University of Chicago. The Division's first location was some makeshift facilities in the North Stands of Stagg Field. In the latter part of 1943, the Division was moved into a part of a building at 6111 South University Avenue, Chicago.

The Argonne National Laboratory was organized in 1946 as a successor to the Metallurgical Laboratory. The present DuPage Site was selected as the new location for the Laboratory and, in 1949, the Metallurgy Division was moved from its location at 6111 South University Avenue into a group of quonset huts in the "East Area."

As the Division's programs increased in scope, additional facilities were acquired, and by 1956 the Division occupied all or parts of twenty different buildings spread throughout the site. To consolidate these activities and, primarily, to expand the facilities and man power for the development of plutonium as a reactor fuel, authorization was obtained for the construction of a central facility.

A prospectus which outlined the preliminary design requirements of the proposed building was completed in April 1957 and used by the Laboratory as a basis for evaluating and selecting the Architect-Engineer. In June 1957 the firm of Singmaster and Breyer was selected for the preparation of a preliminary design concept referred to in Argonne's construction terms as Title I. The original Title I envisaged a metallurgical facility comprised of four zones:

Zone I - Plutonium Physical Metallurgy
Zone II - General Physical Metallurgy
Zone III - General Engineering Metallurgy
Zone IV - Administrative.

After the completion of the preliminary proposal, Zone III was temporarily deleted and the remaining complex became known as Wings A through E. Subsequently, an Alpha-Gamma Hot Laboratory (Wing F) was added. The previously omitted Zone III, known as Wings G and H, was the final addition to the Fuels Technology Center. The design phase of the facility extended from June 1957 until March 1959.

Construction of the Fuels Technology Center began in June 1958, and was completed in May 1961. To expedite the completion of the facility, construction of Wings A through E complex was performed concurrently with the design of Wings F, G, and H. Five major construction contracts were awarded on the basis of competitive bids. Following is information relative to each of the construction contracts, which also correspond chronologically with the various stages of construction:

1. (a) Scope of Work: Site preparation and foundations for Wings A through E

   (b) Contractor: Darin and Armstrong

2. (a) Scope of Work: Construction of upper portion of buildings and extension of utilities for Wings A through E

   (b) Contractor: Malan Construction Co.

3. (a) Scope of Work: Construction of Wing F

   (b) Contractor: Malan Construction Co.

4. (a) Scope of Work: Construction of basic buildings for Wings G and H

   (b) Contractor: Telander Bros. Contractors, Inc.

5. (a) Scope of Work: Erection of structural steel framing for Wings G and H

   (b) Contractor: Chicago Heights Steel Co.

In addition to these five major contracts, purchase orders and minor subcontracts not included in the above were issued throughout the construction period by the Commission for the completion of the work.

The construction of the building was under the direction of the AEC Chicago Operations Office. Engineering inspection was provided by the Architect-Engineer under the supervision of Laboratory personnel.

The first beneficial occupancy of the facility took place on August 12, 1960, with the acceptance of Wing A. The other wings of the facility were officially accepted as follows:

Wing B	- August 17, 1960
Wings C, D, and E	- September 30, 1960
Wing F	- December 15, 1960
Wings G and H	- May 31, 1961

Engineering and planning for the Occupancy Phase of the facility actually began in 1959 and was conducted concurrently with the final stages of construction. By the early part of 1960 sufficient engineering and planning of the Occupancy Phase for Wings A through E had been completed to warrant consideration for the selection of a contractor. Accordingly, the Commission, on April 21, 1960, appointed a Contractor Selection Board. Because of the nature of the work involved and to minimize the time and cost of engineering, the Board decided to solicit bids on the basis of a "cost-plus-fixed fee" contract. Documents consisting of a description and scope of work, a man-power estimate, representative drawings of the type of work to be performed, and a contract in the general form intended to be used were sent to prospective contractors requesting their proposal for accomplishing the work. Based upon a review and evaluation of the various proposals submitted, the Board selected the Phillips-Getschow Company to perform the work. The Occupancy Phase of the work was covered under ANL Contract No. 31-109-38-1255, which went into effect on October 2, 1960. This was in accordance with the responsibility delegated to the Laboratory by the Atomic Energy Commission, Chicago Operations Office, for administering and managing the installation and construction work which was not included in the prime construction contracts being administered by the Commission.

In a broad sense the Occupancy Phase provided for the installation of laboratory furniture and scientific equipment. The detail work performed under this phase of the project included:

1. the design of items such as gloveboxes for plutonium work, remote handling equipment, shielding doors and windows for the Alpha-Gamma Cave, and the design of literally hundreds of special items not commercially available for the type of experimental work to be performed in this facility;

2. the engineering necessary for the installation of equipment ranging from very precise and delicate instruments, such as electron microscopes, to large and heavy equipment, such as rolling mills and extrusion presses;

3. the preparation of specifications and the procurement of new scientific equipment;

4. the administration and supervision of the contractor's work, which included the procurement of all tools and materials necessary to perform the work.

Actual installation work began in November 1960. Generally, installation work began simultaneously in Wings C, D, and E. Some of the first work accomplished was the extension of building utilities and the installation of special utility systems for the plutonium gloveboxes in Wing D.

In January of 1961, the contract with the Phillips-Getschow Company was revised and extended to October 2, 1962, to include the installation of equipment for Wings F, G, and H. Accordingly, installation schedules were revised to permit this work to continue in a manner most compatible with the scientific programs of the Metallurgy Division. Subsequent revisions to the Phillips-Getschow contract extended the term of work to March 29, 1963.

Following are approximate time periods required for the installation of equipment in each Wing of the Building:

Location	Start	Complete
General Building (including Wings A and B)	October 1960	November 1962
Wing C	November 1960	October 1961
Wing D	October 1960	May 1962
Wing E	December 1960	December 1961
Wing F	February 1961	March 1963
Wing G	February 1961	September 1962
Wing H	January 1961	March 1963

A photograph of the completed facility is shown in Figure A-1. Floor plans of the building are shown in Figures A-2, A-3, A-4, and A-5.

Figure A-1. Fuels Technology Center

137-320

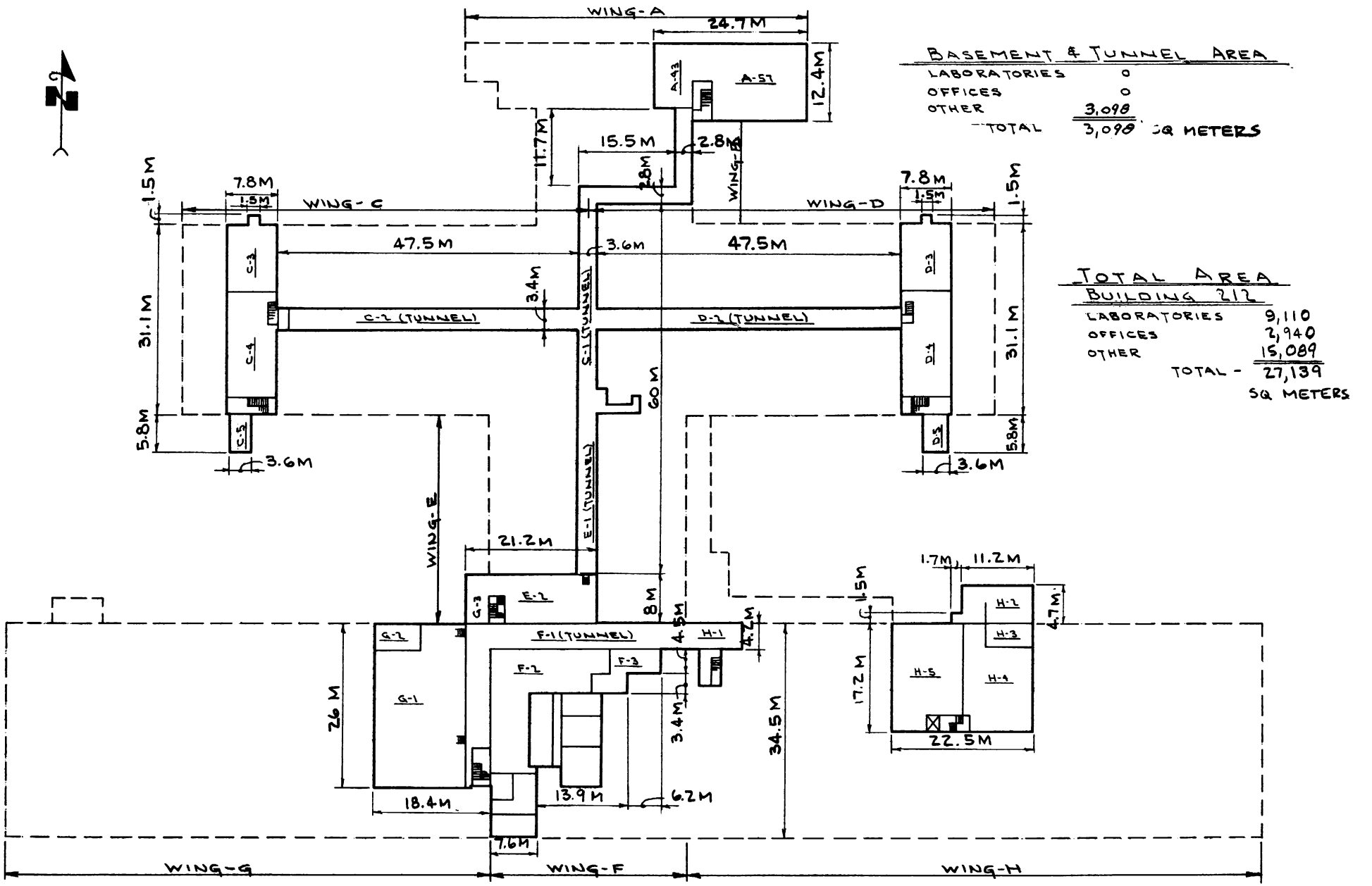

BASEMENT & TUNNEL AREA

LABORATORIES	0
OFFICES	0
OTHER	3,098
TOTAL	3,098 SQ METERS

TOTAL AREA BUILDING 212

LABORATORIES	9,110
OFFICES	2,940
OTHER	15,089
TOTAL -	27,139 SQ METERS

Figure A-2. Basement and Tunnel Plan

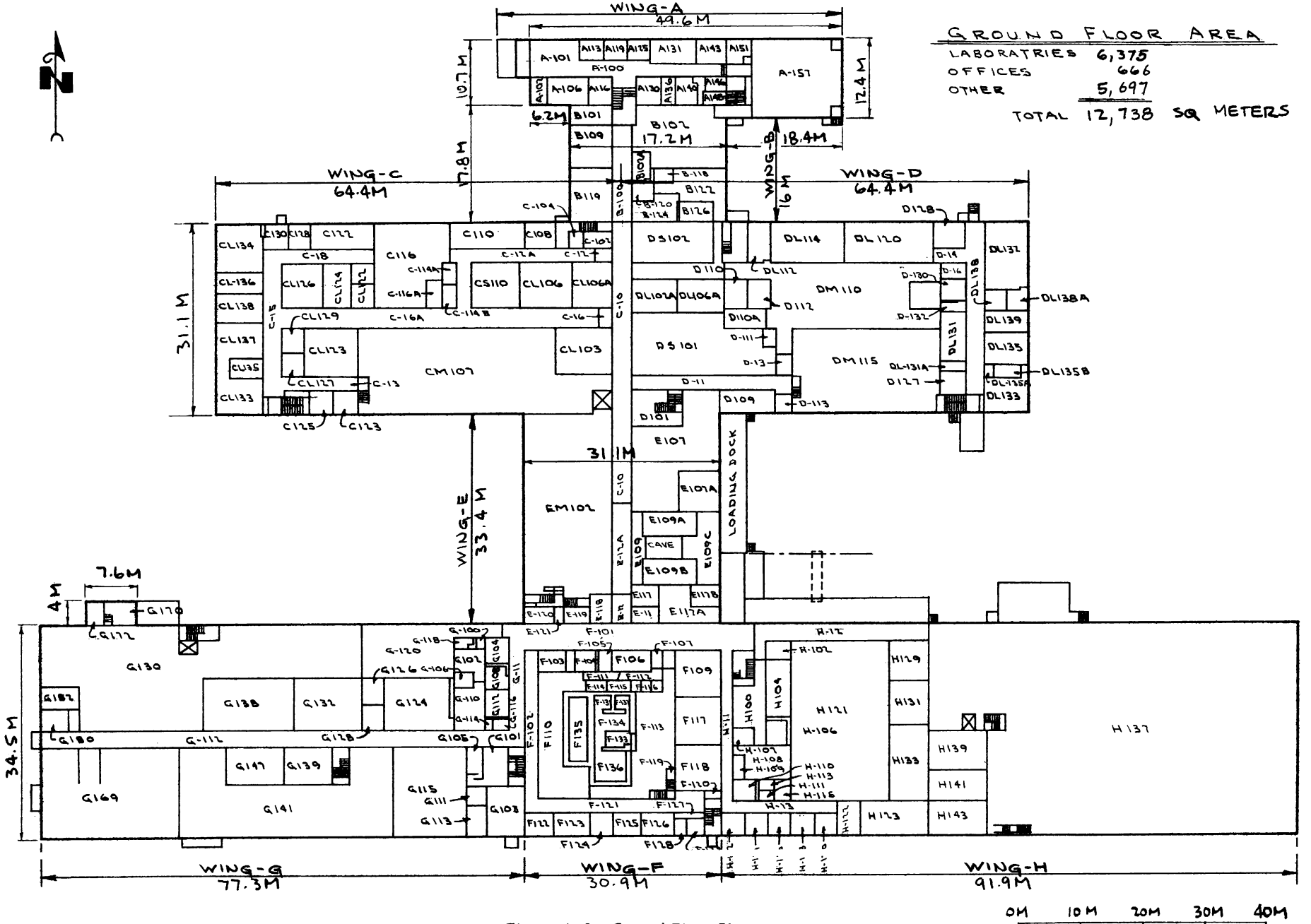

Figure A-3. Ground Floor Plan

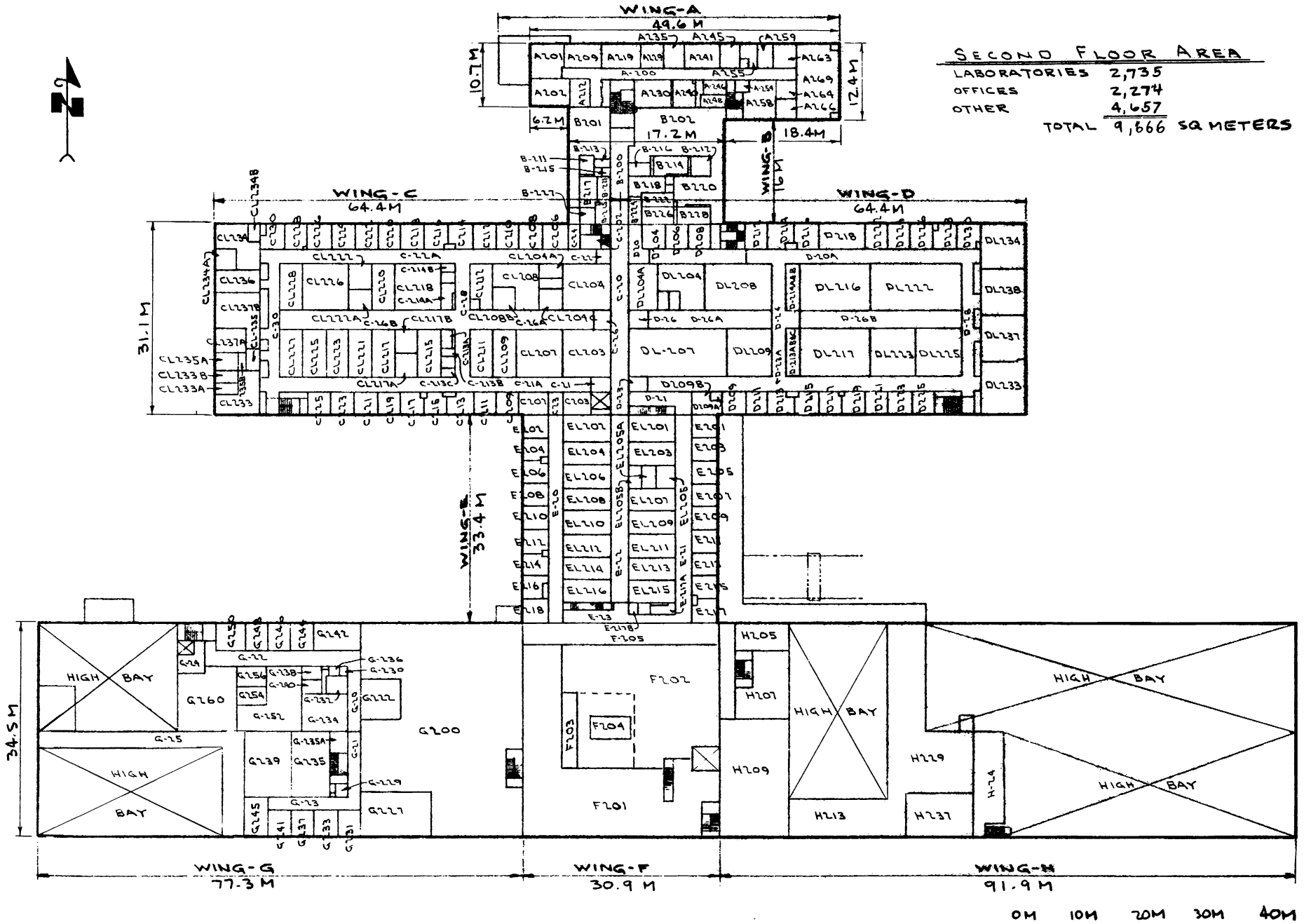

Figure A-4. Second Floor Plan

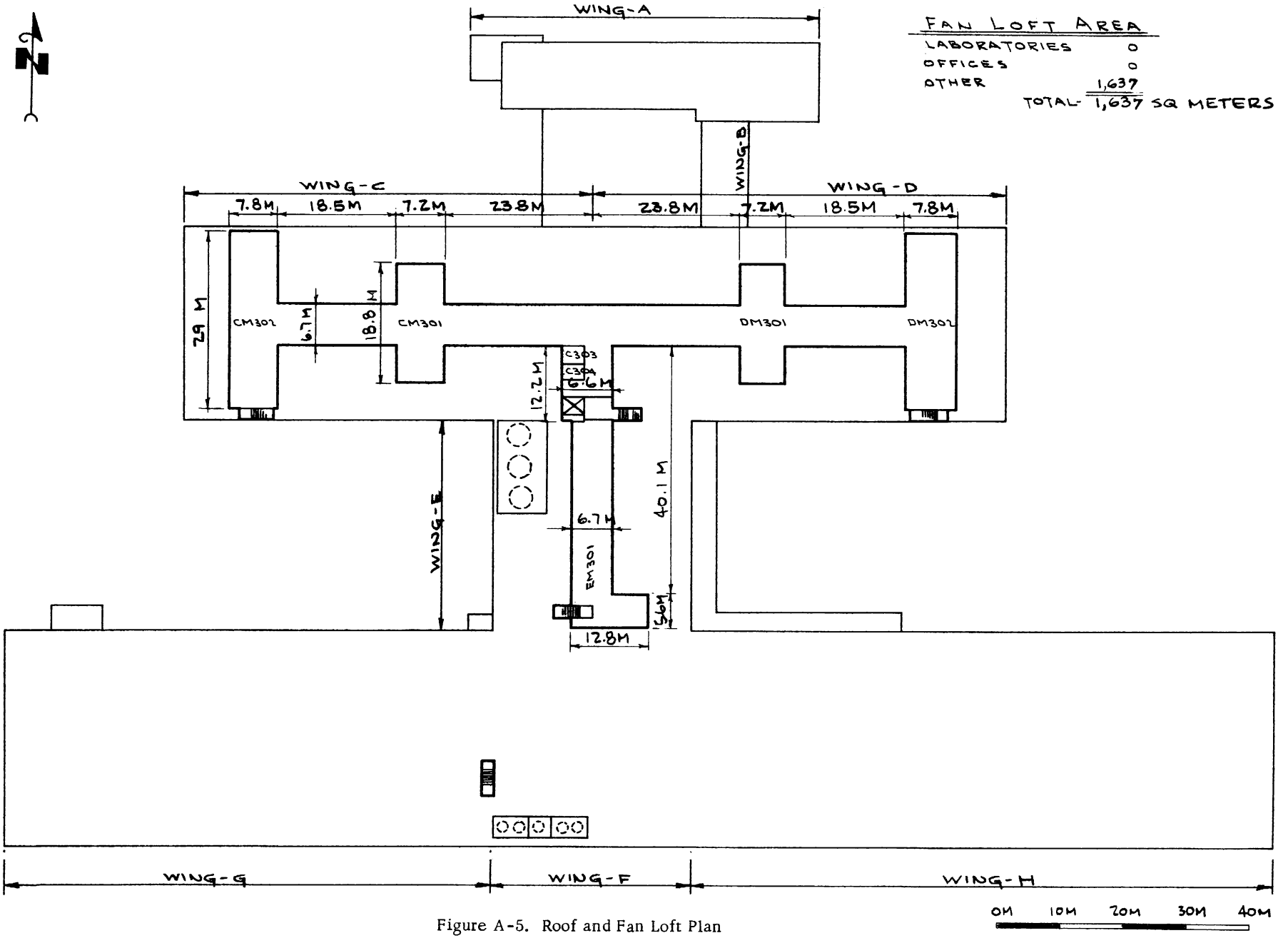

Figure A-5. Roof and Fan Loft Plan

Figure A-6 is a graphic representation of the actual time periods required for each phase of the project and, perhaps, the best illustration of the overlapping schedules for design, construction, and occupancy established to minimize the overall length of time required to complete the facility.

Figure A-6. Fuels Technology Center

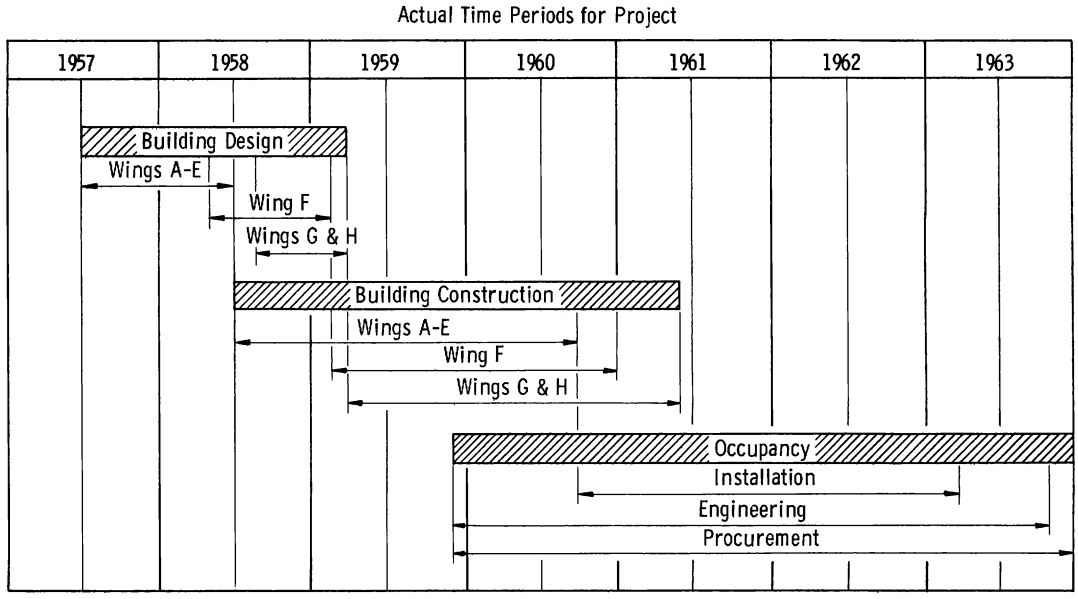

2. Nitrogen-atmosphere System for Gloveboxes (B. J. Koprowski and W. H. Livernash)

The once-through nitrogen atmosphere used for plutonium gloveboxes in Building 212 and described in the Metallurgy Division's Annual Report for 1961 (ANL-6516) has been in constant operation during the past year. The operation of the system has confirmed and in some instances even exceeded the many advantages expected of a low-flow, once-through gas system for extremely leak-tight enclosures.

The flow rate of nitrogen gas through the system for this past year has averaged 5.4 liters/sec. Approximately 100 gloveboxes have been connected to the system for an average flow rate of 0.054 liter/sec per glovebox. Impurities in the gloveboxes resulting from this flow rate vary between 100 and 200 ppm of oxygen and between 200 and 500 ppm of moisture. Several gloveboxes are being purged at higher flow rates (0.24 to 0.38 liter/sec) to maintain lower moisture levels.

All the components in the gas-analysis and pressure-control sections of the system have functioned extremely well. System components have been inspected on a regular schedule, and only a minimal amount of preventive maintenance has been required; this has been done without interrupting the operation of the system.

On two different occasions during the year it was necessary to transfer from the normal liquid nitrogen source of supply to a compressed gas supply. On the first occasion impurities in the liquid nitrogen furnished during one of the deliveries by the vendor exceeded the normal impurity of 20 ppm oxygen in the header. The oxygen analyzer system detected this condition. A tank truck of compressed gas was furnished by the vendor and connected to the system while the liquid nitrogen supply Dewar was isolated and drained of all liquid. The maximum impurity of oxygen in the system resulting from this incident and as indicated by the analyzer system was 1300 ppm. On the second occasion, a leak in a fitting at the air-to-liquid heat exchanger of the supply Dewar necessitated a shutdown of the Dewar system and a transfer to a compressed gas supply for a period of several hours to permit repairs.

Glovebox pressure control has been extremely reliable. Occasionally the building pressure varies between the first and second floor, causing those gloveboxes on the first floor to reach pressures at or above atmospheric. This condition will persist until modifications are made to the building ventilation system.

The overall operation of this system has been very satisfactory. All routine maintenance has been assumed by the Plant Services Department. To date, the safeguards and alarms installed in the system have supplied adequate prior indication of a malfunction to permit repairs to be made without interfering with the experimental work being performed in the gloveboxes.

3. Emergency Exhaust System for Plutonium Laboratories (B. J. Koprowski and W. H. Livernash)

The building ventilation system for plutonium laboratories in Wing D, in addition to satisfying the normal demands for heating and cooling and providing the generally accepted flow pattern of air from areas of least contamination risk to areas of greater contamination risk, has been modified to permit manual control of the air flow rate for each laboratory. This modification has provided an additional safety device that can be used to control the spread of contamination in the event of a "spill."

A very simple procedure, a prerequisite for any safety device, permits the emergency exhaust system to be placed into operation. The components on the control panel for each laboratory are: (1) an electrical switch, (2) a throttle valve, and (3) a pressure gage. By actuating the electrical switch, the supply air is diverted from the laboratory to the corridor, and the electro-pneumatic volume control system in the exhaust air duct is transferred from automatic control to manual control. The position of the damper in the exhaust duct can then be positioned manually by adjustment of the throttle valve, thereby allowing only the

minimal amount of air necessary to maintain the room at a slightly negative pressure with respect to the corridor to flow through the room. Room pressure is indicated on the pressure gage. The air flow through the laboratory can be further diminished by closing openings around the doors with tape, closing louvers in doors and walls or covering the louvers with plastic.

All second floor laboratories in Wing D have been caulked and sealed to ensure leak-tight rooms. During the caulking process it was found that cracks up to 1 cm wide existed at the joint between the concrete block walls and the floor. All such cracks were repaired with resilient caulking materials.

The safety with which experimental work has been performed during this past year has fortunately, averted the need for using this system under emergency conditions. Periodic testing and a few accidental "button-pushing" incidents during the year verified the satisfactory operation of the system.

4. Plutonium Glovebox Alteration and Maintenance Procedure (H. V. Rhude and L. R. Kelman)

A portable housing has been developed which greatly simplifies alterations or maintenance of gloveboxes in which plutonium is used which might release contamination. The housing is shown schematically in Figure A-7 attached to a window opening of a glovebox to permit changing a cracked window. With this housing, alteration and maintenance can be done in the laboratory where the glovebox is used, without hindering research in adjacent gloveboxes. The housing is essentially a very shallow glovebox that can be moved to another glovebox and attached to it by means of tape and a plastic transition piece.

Figure A-7. Portable Housing Used to Change a Cracked Window on a Glovebox

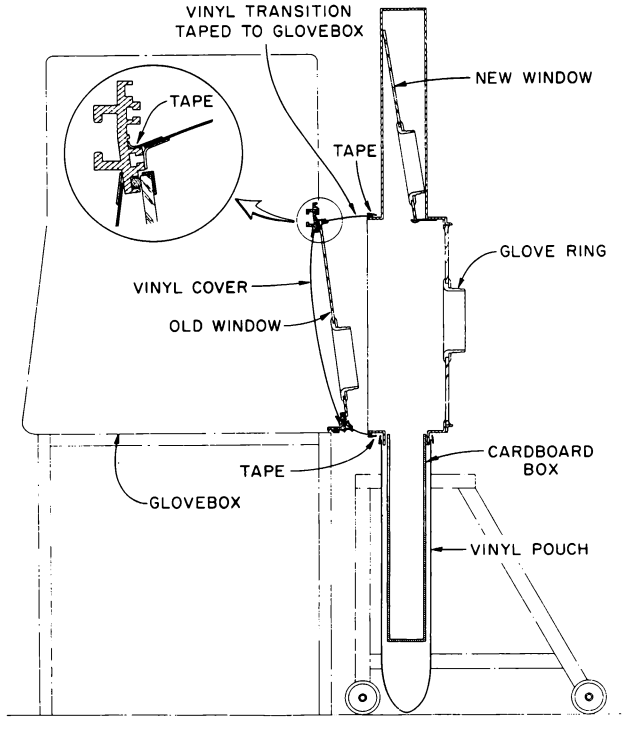

106-7371 Rev.

Although originally developed to change a broken window, the housing has been adapted to other maintenance jobs. With the techniques developed for its use, the housing has been used to introduce or remove equipment through a window opening, to service contaminated equipment attached to a glovebox, to repair or alter contaminated

pipes and ducts, and to prepare contaminated gloveboxes for moving from one building to another.

5. Building 212 Alpha-Gamma Hot Cell (F. L. Brown)

Major construction work on the facility was completed during the year, and procurement and testing of operating equipment proceeded on schedule. The nitrogen gas-filled operating cell was placed in operation before construction work was completed on the service area of the cell. Irradiated cobalt-base control materials and irradiated U-Pu-Fs alloy pins were introduced for decanning, visual examination, photography, and density measurements. The nitrogen atmosphere within the cell eliminated fire hazards. Thus, the decanning of the NaK-filled capsules was a relatively simple operation. Special precautions were taken, however, to prevent the disbursement of excessive amounts of alpha-active particles during these initial operations in order to simplify corrective measures when they became necessary. The transfer of alpha contamination out of the operating cell thus was avoided during the period in which construction work on the service area was still in progress. At the close of the year only minor problems remained to delay operation of the service area in its role as equipment storage facility, repair facility, and source transfer facility. Correction of difficulties to permit full operation of the service area as well as the operating cell is expected early in 1964.

During the year, major installations in the operating cell included the following: gas and electrical utility plugs, a carriage with polar manipulator and hoist, master-slave manipulators, a capsule transfer system (for introduction of irradiated specimens), seal doors for interlocks, source storage hoists, and atmosphere cooling coils.

Associated electrical controls for manipulators, hoists, shield doors, seal doors, and utility receptacles were conveniently located for operation in front of the gas cell. Although simple in operation, the multitude of conductors in the electrical control systems required considerable time to install and check.

Control cables entered the operating cell through overhead utility plugs sealed into access holes with double compression seals. (All penetrations into the operating cell were sealed with double compression seals.) Low-pressure gas piped to the annulus of each double seal permitted monitoring for leakage. Sensitive flow meters indicated relatively large leaks, whereas sensitive pressure meters indicated very small leaks. In either case, leakage into the cell was, primarily, gas from the annulus rather than air, and therefore quite substantial seal leakage could be tolerated without compromising the cell atmosphere.

A number of equipment items for general operation were procured during the year. Included in the list were the following: density balance and hood, a capsule puncture rig, can sealer and opener, dielectric sealer, ultrasonic washer, low-speed abrasive cut-off machine, stereoperiscope and stage, periscope with bench microscope, capsule decanner, power hack saw, and mobile robot. Considerable time was devoted to the development of a handling device to permit removal of in-cell Model A manipulator slave arms with the remote-controlled robot. Although no failures of slave arms were experienced during the year, the robot, in trial runs, operated successfully to remove each of the 8 arms in the operating cell.

Allowances were made, in the design of equipment which would facilitate remote removal from the operating cell, then cleanup, repair, and storage in the service area for future use. The service area was designed to admit personnel in protective suits at fairly frequent intervals (when gamma levels permitted) so that equipment items could be serviced by hand from time to time. Access to the service area was through a series of three showers which were to be used for suit decontamination upon leaving the contaminated cell. Escape of air-borne contamination was to be prevented, during personnel entries, by increasing the flow of air into the cell during the time that the alpha barrier was breached. Inadequately sized exhaust fans and ducts, however, did not permit operation as planned. The structure did not readily lend itself to the construction of an entry interlock. Therefore, the ventilation of the service area has been changed from a static air system to an air purge system. This change not only permitted personnel entry through the showers, as planned, but also eliminated the need for cooling coils and their attendant condensation problems, and eliminated the danger of possible accumulation of inflammable vapors in the previously static environment.

6. Nitrogen Atmosphere for the Alpha-Gamma Hot Cell Facility (B. J. Koprowski and W. H. Livernash)

As a result of the successful operation of the once-through nitrogen atmosphere system used for plutonium gloveboxes in Building 212, a similar system was installed for the alpha-gamma hot cell facility.

The section of the cell provided with a nitrogen atmosphere is a room 9.75 m long, 3.35 m wide and 3.35 m high. This is the main working area of the facility. Adjoining rooms used for transfer operations, storage, and equipment repair are provided with an air ventilation system. Transfer locks, which can be purged with nitrogen gas, isolate the "air side" of the cell facility from the "gas side."

Liquid nitrogen stored in a Dewar of approximately 10,000-liter capacity is the normal source of supply for both the glovebox and the cell-atmosphere systems. On demand, liquid nitrogen is evaporated

through a series of air-to-liquid heat exchangers. The gas phase at the Dewar is maintained at a pressure of 4.2 kg/sq cm. A pipe header distributes the gas from the Dewar system to the glovebox and hot-cell systems.

The principal components of the nitrogen system for the hot cell are: (1) pressure-reducing valves, (2) high-efficiency inlet and outlet filters, (3) activated charcoal traps, (4) pneumatic pressure controls and control valves, and (5) centrifugal exhaust fans. These are all arranged in a parallel system to provide uninterrupted service in the event of a failure or a need of replacement of one of the components.

Nitrogen is normally supplied to the cell at a constant flow rate of 1.4 liters/sec. The pressure in the cell is maintained at about -1.3 cm of water column by the pneumatic control system. Impurities in the cell atmosphere are monitored by a Beckman Model F-3 oxygen analyzer and a Consolidated Electrodynamics electrolytic hygrometer. A sampling system consisting of an alpha detector and a beta-gamma detector has been provided to monitor the exhaust gas to assure that the integrity of the filters and charcoal traps is being maintained. To prevent damage to the facility by accidental pressure excursions beyond the design pressure, a series of pressure relief valves have been installed between the "gas-side" and "air-side" of the facility.

The system has been in operation for approximately three months. The normal flow rate of 1.4 liters/sec provides an atmosphere having impurity levels of 500 to 700 ppm oxygen and of 400 to 600 ppm moisture.

7. Design, Procurement, Installation, and Test of Extrusion Press in Building 350 (G. Burton and A. B. Shuck)

Installation of a 600-ton, hydraulically operated extrusion press and of a 25-ton, hydraulic stretcher-straightener were completed in December 1962. These units were enclosed by a gas-tight glovebox train consisting of storage, extrusion, and stretcher-straightener sections. Services provided adjacent to the press consist of a billet-outgassing furnace, a billet-heating furnace, and a TIG welding station. Dried and purified helium is circulated through the glovebox system.

Start-up and debugging operations, begun in February, 1963, revealed the necessity for extensive modifications. Storage of the press for over one year prior to installation resulted in deterioration of the O-ring seals in the hydraulic system. All seals were replaced. The negative-pressure water-cooling system required repiping. The connections were changed from series to parallel to provide adequate cooling for the billet container, and for the induction furnace bus bars and coil. The air valves and regulators which operate the billet-handling equipment and the hoist turntable were relocated. This was necessary to provide access through glove ports. A new billet-heating induction furnace was designed, built,

installed, and test operated. Alignment difficulties were experienced between the container, billet loader, and billet furnace. These were corrected through modifications to the loader and furnace.

The failure of an extrusion stem during test operation in air prompted the design of protective shields. Sliding double-walled doors were installed inside the glovebox adjacent to the extrusion container. These doors protect the glovebox windows and glove ports from damage in the event of another accidental stem failure.

Instrumentation for indicating and recording extrusion speed, ram location, ram pressure, and billet temperature was installed.

The die stack, billet container, and extrusion stem were redesigned to accommodate a billet measuring 6.25 cm in diameter by 35 cm in length. This new arrangement allows the die and die holder to enter the container. The die stack is heated by conduction from the container. The need for a separate die-heating furnace has been eliminated. The necessity for transferring manually the heated dies from the furnace to the die slide also has been eliminated. Press operation is safer as well as more efficient.

Approximately 80 test billets of copper, brass, aluminum, and steel have been extruded experimentally in air. This work demonstrated press operability and was used to determine the modifications previously delineated.

The glovebox train was filled with helium for the first time in December 1963. Initial difficulty was encountered in sealing the glovebox train. A slight relaxation of the leak-rate requirements was tolerated. Test operation of the press will be continued through gloved access. The gloved operability of the equipment is being demonstrated first with nonfissionable materials. When completely reliable and safe extrusion can be demonstrated, plutonium, thorium, and uranium alloys will be extruded. Fuel components in the geometry of rods and tubes both clad and unclad will be fabricated.

APPENDIX B - PUBLICATIONS AND REPORTS

Publications

Aldred, A. T. and Myles, K. M., Thermodynamics of Vanadium-Chromium Alloys, J. Metals 15 81 (1963). [Abstract]

Barrett, C. S., Mueller, M. H., and Hitterman, R. L., Crystal Structure Variations in Alpha Uranium at Low Temperatures, Phys. Rev. 129 (2) 625-629 (Jan. 15, 1963).

Barrett, C. S., Mueller, M. H., and Heaton, L., Germanium as a Neutron Monochromator, Rev. Sci. Instr. 34 (8) 847-848 (August 1963).

Baskin, Y. and Schell, D. C., Phase Studies in the Binary System MgO-Ta_2O_5, J. Am. Cer. Soc. 46 (4) 174-177 (April 1963).

Baskin, Y., Oxidation Behavior of Uranium Monophosphide, Bull. Am. Cer. Soc. 42 (4) 267 (April 1963). [Abstract]

Baskin, Y., Synthesis and Properties of Uranium Monophosphide, Bull. Am. Cer. Soc. 42 (4) 265 (April 1963). [Abstract]

Baskin, Y., and Prasad, N. S. Krishna, Studies on TTA Complexes with Metal Ions - II. Investigations of Some Tetravalent Complexes in the Solid State, J. Inorg. and Nucl. Chem. 25 (8) 1011-1019 (August 1963).

Beck, W. N., Kittel, J. H., and Carlander, R., Irradiation Behavior of Refractory-Alloy-Clad Plutonium Alloys, Trans. Am. Nucl. Soc. 6 (2) 375-376 (November 1963). [Summary]

Berger, Harold and Beck, W. N., Neutron Radiographic Inspection of Radioactive Irradiated Reactor Fuel Specimens, Nuc. Sci. & Engr. 15 411-414 (April 1963).

Berger, Harold, Resolution Study of Photographic Thermal Neutron Image Detectors, J. Appl. Phys. 34 (4), Part 1, 914-918 (April 1963).

Berger, Harold and Kraska, I. R., An Evaluation of a Fast, Scintillator-Polaroid Film Camera for Neutron Image Detection, Nondestruc. Test'g. XXI (3) 181-182, 184 (May-June 1963).

Berger, Harold, Neutron Radiography - A New Dimension in Radiography, Nondestruc. Testing XXI (6) 369-373 (November-December 1963).

Berger, Harold, The Current Status of Neutron Radiography, PROGRESS IN APPLIED MATERIALS RESEARCH, Vol. 4, 115-148, Haywood of London, London, England (1963).

Berger, Harold, Neutron Radiography: 1962 Progress Report, PROCEEDINGS OF THE SYMPOSIUM ON PHYSICS AND NONDESTRUCTIVE TESTING, held Oct. 2-4, 1962, San Antonio, Texas, sponsored by Southwest Research Institute, 175-197.

Berndt, A.F., Room Temperature Lattice Constants of Alloys of Plutonium in Alpha-Uranium, J. Nucl. Matls. 9 (1) 53-58 (June 1963).

Berndt, A. F., On the Use of a Modified Radial Distribution Analysis for Indexing Powder Patterns, ADVANCES IN X-RAY ANALYSIS [Proc. of 11th Annual Conf. on Application of X-Ray Analysis] Vol. 6, 18-24, Plenum Press, New York, New York (1963).

Beyer, N. S., Berger, Harold, Lapinski, N. P. and Kraska, I. R., A Film Copying Technique for Improving Radiographic Contrast, Nondestruc. Test'g. XXI (4) 230-234 (July-August 1963).

Blewitt, T. H., Coltman, R. R.* and Klabunde, C. S.,* Energy Release in Irradiated Copper, J. Phys. Soc. of Japan 18, Suppl. III [Proc. of Internat'l. Conf. on Crystal Lattice Defects, 1962] 288-289 (1963).

Blewitt, T. H., Coltman, R. R.* and Klabunde, C. S.,* Volume Changes Induced by Radiation in Copper and Aluminum, J. Phys. Soc. of Japan 18, Suppl. III [Proc. of Internat'l. Conf. on Crystal Lattice Defects, 1962] 284-287 (1963).

Blumenthal, B., Book Review: THE METAL PLUTONIUM, J. Nuc. Matls. 7 (1) 220 (1962).

Blumenthal, B., Book Review: PROGRESS IN NUCLEAR ENERGY, [Series V, Vol. 4: Metallurgy of Nuclear Reactor Components], J. Metals 15 (7) 478-479 (July 1963).

Brodsky, M. B. and Carleson, B. G. F., Electrodeposition of Plutonium and Uranium from Molten Salt Solutions of Di-Chlorides, J. Inorg. Nucl. Chem. 24 1675-1681 (December 1962).

Brodsky, M. B., Hall Coefficient of Alpha Plutonium, J. Metals 15 71 (1963). [Abstract]

Brodsky, M. B., Thermoelectric Power of Liquid Lead Alloys, Bull. Am. Phys. Soc. 8 433 (June 1963). [Abstract]

Brodsky, Merwyn, B., Hall Coefficient of Alpha Plutonium, Phys. Rev. 131, 2nd Series (1) 137-140 (July 1963).

*Oak Ridge National Laboratory

Carlander, R. and McGinnis, F. D., Postirradiation Evaluation of EBR-I Mark III Fuel Rods, Trans. Am. Nucl. Soc. 6 (2) 373-374 (November 1963). [Summary]

Darby, J. B., Jr., Jugle, D. B., and Kleppa, O. J., The Rate of Solution of Some Transition Elements in Liquid Aluminum, Trans. AIME 227 179-185 (February 1963).

Darby, J. B., Jr. and Lam, D. J., Alloying Behavior of Technetium-99, J. Metals 15 93 (1963). [Abstract]

Darby, J. B., Jr., Downey, J. W., and Norton, L. J., Intermediate Phases in the Tantalum-Palladium System, Trans. AIME 227 1028-1029 (August 1963).

Darby, J. B., Jr., Norton, L. J., and Downey, J. W., A Survey of the Binary Systems of Technetium with Group VIII Transition Elements J. Less-Common Metals 5 397-402 (October 1963).

Darby, J. B., Jr., The CsCl-Type Ordered Structure in VMn, Trans. AIME 227 1460 (December 1963). [Tech. Note]

Draley, Joseph E., Corrosion of Film-Forming Metals - II, Chem. Engr. 69 152-156 (Nov. 26, 1962).

Draley, J. E., Mori, Shiro, and Loess, R. E., The Corrosion of 1100 Aluminum in Oxygen-Saturated Water at 70°C, J. Electrochem. Soc. 110 (6) 622-627 (June 1963 - Section II).

Dwight, A. E., Conner, R. A., Jr., Downey, J. W., G Phases Containing Scandium, Nature 197 (No. 4867) 587 (February 9, 1963). [Letter to the Editor]

Dwight, A. E., Equiatomic Compounds of the Transition Elements, . . Metals 15 (9) 686 (September 1963). [Abstract]

Eichholz, J. J., and Darby, J. B., Jr., Electronic Integrator for Use with a Differential Calorimeter, Rev. Sci. Instr. 34 (11) 1274-1275 (November 1963). [Tech. Note]

Fisher, E. S., and Renken, C. J., Relationship of Elastic-Shear Moduli to the Phase Transformations in Zirconium, Titanium, and Hafnium, Bull. Amer. Phys. Soc. Series II, Vol. 8, p. 65 (January 23, 963). [Abstract]

Fisher, E. S., and Renken, C. J., Coupling Cements for Ultrasonic-Wave Velocity Measurements at High Temperatures, J. Acoust. Soc. Amer. 35 (7) 1055 (July 1963). [Letter to Editor]

Handwerk, J. H., White, G. D., and Hill, D. C., Ceramic Nuclear Fuels in the System UO_2-ZrO_2-CaO, J. Am. Cer. Soc. 46 (1) 29-32 (January 1963).

Heaton, LeRoy and Tompson, Clifford W., The Scattering of Neutrons by Liquid Alloys of Sodium and Cesium, International Union of Crystallography, Sixth International Congress and Symposia, Rome, Italy, Sept. 9-18, 1963, p. A88 (September 1963). [Abstract]

Heaton, L., Mueller, M. H. and Johanson, E. W., θ-2θ Stepping Motion without Gears, Nuc. Inst. and Methods 24 (4) 411 (October 1963).

Herman, Herbert, Effects of Irradiation on the Formation of Guinier-Preston Zones, J. Metals 15 (9) 722 (September 1963). [Abstract]

Hummel, Harry H., Levenson, Milton, Link, Leonard E., Macherey, Robert E., and Simmons, Wallace R., Using Plutonium in Fast Reactors, Nucleonics 21 (1) 43-47 (January 1963).

Ianniello, L. C. and Berndt, A. F., Observations on the Structure of Rolled Alpha Plutonium, J. Metals 15 74 (1963). [Abstract]

Jacobs, J. E.,* Berger, H., and Collis, W. J.,* An Investigation of the Limitations to the Maximum Attainable Sensitivity in Acoustical Image Converters, IEEE Trans. 10 (2) 83-88 (September 1963).

Karasek, Frank J., Techniques for the Fabrication of Ultra-thin Metallic Foils, Nuc. Sci. & Engr. 17 (3) 365-370 (November 1963).

Kelman, L. R. (Editor) and Greenberg, Sherman (Co-Editor) of IMD Special Report Series No. 12, Vol. IX, A Symposium on Materials for Sodium-Cooled Reactors, 1963 Winter Meeting of the ANS, published by AIME, New York, N. Y. (1963).

Kittel, J. H., Carlander, R., Kruger, O. L., and Lied, R. C., Preliminary Irradiations of PuC and UC-PuC, Ceramic News XI (10) 28 (1962). [Abstract]

Kittel, J. H., Research and Development of Reactor Fuels in ANL, J. Atomic Energy Soc. Japan 5 (8) 693-698 (1963).

Kittel, J. H., Atomic Research Lectures, Atomic Reactor Fuel Research Group; Machine, Apparatus Research Group; JAERI-Memo 1335, 216 pp. Published in Japanese by Japan Atomic Energy Research Institute (1963).

*Northwestern University.

Kittel, J. H., Reinke, C. F., and Horak, J. A., Swelling of Cast Thorium/Uranium Alloys During Irradiation and Postirradiation Annealing, Trans. ANS 6 (2) 372-373 (November 1963). [Summary]

Koppenaal, T. J., Comments on the Rosenfield and Averbach Theory for Initial Yielding in f.c.c. Metals and Alloys, Acta Met. 11 85 (January 1963).

Koppenaal, T. J., Strength of Neutron-Irradiated αCu-Al Single Crystals, Bull. Am. Phys. Soc. 8 197 (March 1963). [Abstract]

Koppenaal, T. J., The Strain Rate Dependence of the Flow Stress in Neutron Irradiated Copper Single Crystals, Philosophical Mag. 8 (92) 1313-1320 (August 1963).

Koppenaal, T. J., Strain Rate Dependence of the Flow Stress in Neutron-Irradiated Copper Single Crystals, J. Metals 15 (9) 675 (September 1963). [Abstract]

Koppenaal, T. J., Effect of Neutron Irradiation on the Strength of αCu-Al Single Crystals, J. Metals 15 (9) 675 (September 1963). [Abstract]

Koppenaal, T. J., Dislocation Etch Pits in αCu-Al and αCu-Zn Alloys, Trans. ASM 56 (3) 768-770 (September 1963).

Kruger, O. L., Preparation and Some Properties of Arc-Cast Plutonium Monocarbide, J. Nuc. Matls. 7 (2) 142-150 (November 1962).

Kruger, Owen L., Phase Studies on Arc-Melted Plutonium-Carbon Alloys Near the Monocarbide Composition, J. Am. Cer. Soc. 46 (2) 80-85 (February 1963).

Kruger, O. L., Sintering Studies on Plutonium Monocarbide, Ceramic News XII (10) 61 (October 1963). [Abstract]

Lam, D. J., Van Ostenburg, D. O., Trapp, H. D., and MacLeod, D. E., Knight Shifts and Magnetic Susceptibilities in V-Fe Alloys, J. Metals 14 (9) 691 (September 1962). [Abstract]

Lam, D. J., Van Ostenburg, D. O., Nevitt, M. V., Trapp, H. D., and Pracht, D. W., Magnetic Susceptibilities and Nuclear Magnetic Resonance Measurements in V-Fe Alloys, Phys. Rev. 131 1428-1433 (August 15, 1963).

Lloyd, L. T., and Nowicki, L. J., Crystallographic Angles for Alpha Plutonium, J. Nucl. Matls. 10 (3) 253-257 (1963). [Letter to Editor]

Loomis, B. A., Swelling of Uranium, RADIATION DAMAGE IN REACTOR MATERIALS, 95-107 IAEA Press, Vienna (1963).

Loomis, B. A., and Pracht, D. W., Swelling of Uranium on Postirradiation Annealing, J. Nucl. Matls. 10 (4) 346-359 (December 1963).

Macherey, R. E., Simmons, W. R., and Noland, R. A., Materials for Argonne National Laboratory Sodium-Cooled Reactors, Trans. ANS 6 (2) 360-361 (November 1963). [Summary]

Macherey, R. E., Simmons, W. R., and Noland, R. A., Materials for Argonne National Laboratory Sodium-Cooled Reactors, IMD Spec. Report Series No. 12, Vol. IX, Nuclear Metallurgy 57-114 (1963).

Merkle, K. L., Fission Tracks in Nonmetals, Bull. Am. Phys. Soc. 8 236 (March 1963). [Abstract]

Merkle, K. L., Singer, L. R., and Hart, R. K., Fission-Fragment Damage in Gold Films, J. Appl. Phys. 34 (9) 2800-2804 (September 1963).

Mori, S., Loess, R. E., and Draley, J. E., pH Microelectrodes for Use Near Corroding Surfaces, Corrosion 19 (5) 165t-168t (May 1963).

Mori, S., Loess, R. E., and Draley, J. E., An Eddy Current Gauge for Measuring Aluminum Corrosion, Corrosion 19 (8) 269t-271t (August 1963).

Moser, J. B., and Kruger, O. L., Preparation and Properties of Plutonium Phosphide (PuP), Ceramic News XII (10) 61 (October 1963). [Abstract]

Mueller, M. H., Heaton, L., and Sidhu, S. S., Full Circle Goniostat for Diffraction Intensity Data, Rev. Sci. Instr. 34 (1) 74-76 (January 1963).

Mueller, M. H., and Knott, H. W., The Crystal Structures of Ti_2Cu, Ti_2Ni, Ti_4Ni_2O, and Ti_4Cu_2O, Trans. AIME 227 674-678 (June 1963).

Mueller, M. H., Heaton, LeRoy, and Sidhu, S. S., Automatic Single-Crystal Neutron Diffractometer, International Union of Crystallography, Sixth International Congress and Symposia, Rome, Italy, Sept. 9-18, 1963, p. A161. [Abstract]

Myles, K. M., and Aldred, A. T., Thermodynamics of Vanadium-Iron Alloys, J. Metals 15 81 (1963). [Abstract]

Neimark, L. A., Kittel, J. H., and Hoenig, C. L., Irradiation of Metal-Fiber Reinforced Thoria-Urania, J. Am. Cer. Soc. 46 219-224 (May 1963).

Neimark, L. A., and Shalek, P. D., The Irradiation Behavior of Uranium Monosulfide, Trans. ANS 6 (2) 372 (November 1963). [Summary]

Nevitt, M. V., and Aldred, A. T., Ferromagnetism in V-Fe and Cr-Fe Alloys, J. Appl. Phys. 34 (3) 463-468 (March 1963).

Nevitt, M. V., and Rosen, Sol, The Monocarbides of Thorium, Uranium, Neptunium, and Plutonium, and Their Solid Solutions, International Union of Crystallography, Sixth International Congress and Symposia, Rome, Italy, Sept. 9-18, 1963, p. A19 (September 1963). [Abstract]

Nevitt, M. V., "Alloy Chemistry of Transition Elements," Electronic Structure and Alloy Chemistry of the Transition Elements, 101-178, Interscience Publishers, New York and London (1963).

Peterson, N. L., Diffusion of Palladium in Copper and Silver, Phys Rev. 132 (6) 2471-2476 (December 15, 1963).

Peterson, Ronald G., and Rosen, Moshe, Study of the α - β Phase Transformation in Plutonium Using Ultrasonics, J. Acoust. Soc. of Amer. 35 (11) 1883 (November 1963). [Abstract]

Polakowski, N. H., and Flinn, J. E., Jr., New Fabrication Procedures for High-Quality Tubing, Proc. Intern. Conf. on Research in Prod'n. Engr., ASME, New York, 1963, 406-410.

Renken, C. J., Theory and Some Applications of Pulsed Current Fields to the Problems of Nondestructive Testing, Nuc. Sci. Abstracts 17 (22) 5007 (1963). [Abstract]

Rhude, Howard V., Fire and Explosion Tests of Plutonium Gloveboxes, Quarterly of the Natl. Fire Protection Assn. 56 (4) 335-341 (April 1963).

Rhude, H. V., and Kelman, L. R., A Simplified Procedure for Alteration and Maintenance of Plutonium Gloveboxes, Trans. ANS 6 (2) 461 (November 1963). [Summary]

Rhude, H. V., and Kelman, L. R., A Simplified Procedure for Alteration and Maintenance of Plutonium Gloveboxes, Proc. of the 11th Conference on Hot Laboratories and Equipment, ANS Winter Meeting, New York, N. Y., Nov. 18-21, 1963, 347-351 (1963).

Rosen, S., Nevitt, M. V., and Mitchell, A. W., The Uranium Monocarbide-Plutonium Monocarbide System, J. Nuc. Matls. 9 (2) 137-142 (July 1963).

Rosen, S., Nevitt, M. V., and Barker, J. J., The U-Pu-C Ternary Phase Diagram Below 50 Atomic Percent Carbon, J. Nuc. Matls. 9 (2) 128-136 (July 1963).

Rosen, S., Nevitt, M. V., and Mitchell, A. W., Metallographic and X-ray Observations of Pu-C Alloys, J. Nuc. Matls. 10 (2) 90-98 (October 1963).

Rossin, A. D., Fast-Neutron Dosimetry for Radiation Damage Studies, NEUTRON DOSIMETRY, Vol. 2, 293-304. Published by the International Atomic Energy Agency, Vienna, (1963).

Rossin, A. D., A Monitoring Technique for Radiation Damage Experiments, NEUTRON DOSIMETRY, Vol. 1, 515-519. Published by the International Atomic Energy Agency, Vienna, (1963).

Rossin, A. D., "Significance of Neutron Spectrum on Radiation Effects Studies," ASTM Spec. Tech. Pubn. No. 341, 1962 Symposium on Radiation Effects and Dosimetry, 115-132 (1963).

Rossin, A. D., Radiation Damage to Steel in Different Reactor Spectra, Trans. ANS 6 (1) 149 (1963). [Summary]

Rossin, A. D., Degradation of Impact Energy of Steel as a Function of Neutron Exposure, Trans. ANS 6 (2) 389-390 (November 1963). [Summary]

Rothman, S. J., and Lloyd, L. T., DISCUSSION: Self-Diffusion in Solid Chromium by W. C. Hagel [Trans. AIME 224-430 (1962)], Trans. AIME 227 265-267 (February 1963).

Ruther, W. E., and Hart, R. K., Influence of Oxygen on High Temperature Aqueous Corrosion of Iron, Corrosion 19 (4) 127t-133t (April 1963).

Ruther, W. E., and Greenberg, S., Corrosion of Stainless Steels in Superheated Steam, J. Electrochem. Soc. 110 (8) 177C (August 1963).

Schumar, James F., Book Review: The Metal Plutonium, Nuc. Sci. & Engr. 15 104-105 (1963).

Schumar, J. F., Development of a Nonmetallic Fuel Element, ANL Reviews 1 (1) 17-19 (September 1963).

Shalek, P. D., Preparation and Properties of Uranium and Thorium Monosulfides, J. Am. Cer. Soc. 46 (4) 155-161 (April 1963).

Shalek, P. D., and Handwerk, J. H., "Refractory Sulphides of Uranium and Thorium," SPECIAL CERAMICS 1962, Proceedings of a Symposium held by the British Ceramic Research Association, July 1962, Academic Press, London and New York (1963), 1-10.

Sidhu, S. S., Neutron and X-ray Diffraction Studies on Nonstoichiometric Metal Hydrides, Structure de la Matiere XXIII (11-12) 906 (1962). [Abstract]

Sidhu, S. S., Murthy, N. S. Satya, Campos, F. P., and Zauberis, D. D., "Neutron and X-ray Diffraction Studies of Nonstoichiometric Metal Hydrides," Nonstoichiometric Compounds, Advances in Chem. Series 39, 87-98. Pub'd. by Am. Chem. Soc., Washington, D C. (1963).

Sidhu, S. S., and Zauberis, D. D., Neutron and X-ray Diffraction Study of LiRh, Pittsburgh Diffraction Conference Abstracts 21 11 (1963).

Sidhu, S. S., and Campos, F. P., Carbon Positions in Titanium-Zirconium Null-Matrix by Neutron Diffraction, Pittsburgh Diffraction Conference Abstracts 21 10 (1963).

Simonsen, S. H., and Mueller, M. H., The Crystal Structure of Disodium Tetranitritonitrosohydroxyruthenate (III) Dihydrate by Neutron Diffraction, International Union of Crystallography, Sixth International Congress and Symposia, Rome, Italy, September 9-18, 1963, p. A34 (September 1963). [Abstract]

Smith, Karl F., Facts About Solid State Devices, Metal Prog. 83 (5) 138-155 (May 1963).

Stablein, Paul F., Dislocation Behavior and the Yield Stress in Neutron-Irradiated MgO, J. Appl. Phys. 34 (7) 1867-1871 (July 1963).

Stablein, P. F., and Araoz, Carlos, Technique for Fusion Bonding Ceramics, Rev. Sci. Instr. 34 (11) 1275-1276 (November 1963). [Tech. Note]

Van Ostenburg, D. O., Lam, D. J., Trapp, H. D., and Pracht, D. W., Application of NMR to Transition Metals and Their Alloys, CONF-54-1 (January 31, 1963).

Van Ostenburg, D. O., Lam, D. J., Trapp, H. D., and Pracht, D. W., Magnetic Susceptibilities and Knight Shifts in the Nb-Tc Alloys, Bull. Am. Phys. Soc. 8 250 (March 1963). [Abstract]

Van Ostenburg, D. O., Lam, D. J., Trapp, H. D., and Pracht, D. W., Knight Shifts K_V, K_{Tc}, and K_{Al}, and Magnetic Susceptibilities in the bcc Region of the V-Tc-Al Ternary Alloy System, Phys. Rev. Letters 11 (8) 352-354 (October 15, 1963).

Van Ostenburg, D. O., Lam, D. J., Trapp, H. D., and Pracht, D. W., Knight Shifts in K_V, K_{Tc}, and K_{Al}, and Magnetic Susceptibilities in the bcc Region of the V-Tc-Al Alloy System, Bull. Am. Phys. Soc., Series II 8 (7) 518 (October 18, 1963). [Abstract]

Van Ostenburg, D. O., Lam, D. J., Shimizu, Masao and Katsuki, Atsushi, NMR, Magnetic Susceptibility and Electronic Specific Heat of Nb and Mo Metals and Nb-Tc and Nb-Mo Alloys, J. Phys. Soc. of Japan 18 (12) 1744-1754 (December 1963).

Walter, C. M., and Dickerman, C. E., TREAT Study of the Penetration of Molten U/5 wt% Fs Alloy Through Type-304 Stainless Steel, Trans. ANS 6 (1) 104-105 (June 1963). [Summary]

Westlake, D. G., Enthalpy Data for the Zirconium-Hydrogen System, J. Nucl. Matls. 7 (3) 346-347 (December 1962). [Letter to Editor]

Westlake, D. G., Initiation and Propagation of Microcracks in Crystals of Zirconium-Hydrogen Alloys, Trans. ASM Quarterly 56 1-10 (March 1963).

Westlake, D. G., Egypt, (Fracture of a Zirconium Hydride Particle by a Mechanical Twin), Metal Prog. 83 108 (June 1963). [Letter to Editor]

White, George D., Sintering Studies of Uranium Monocarbide Powders, Bull. Am. Cer. Soc. 42 (4) 269 (April 1963). [Abstract]

Zegler, S. T., and Downey, J. W., Ternary Cr_3O-Type Phases with Vanadium, Trans. AIME 227 1407-1411 (December 1963).

Reports

ANL-5674 Kittel, J. H., Horak, J. A., Murphy, W. F., and Paine, S. H., Effects of Irradiation on Thorium and Thorium-Uranium Alloys (April 1963).

ANL-6103 Paine, S. H., Murphy, W. F., and Brown, F. L., Examination of Irradiated RaLa Source Fuel Rod (Prototype No. 2) for Los Alamos Scientific Laboratory (October 1963).

ANL-6107 Burt, W. R., Jr., Fabrication of the Fuel and Blanket for the Argonne Fast Source Reactor (AFSR) (January 1963).

ANL-6276 Carson, N. J., Grant, N. R., Hessler, N. F., Jelinek, H. F., Olp, R. H., and Shuck, A. B., Fabrication of EBR-II, Core I Fuel Elements (December 1962).

ANL-6489 Mayfield, R. M., Tope, W. G., and Shuck, A. B., The Facility 350 Helium-Atmosphere System (December 1962).

ANL-6550 Carson, N. J., Jr., Jelinek, H. F., and Shuck, A. B., The Manufacture of Supplemental Depleted Fuel Rods for FCF Startup (September 1963).

ANL-6591 Lloyd, Lowell T., Thermal Expansion of Alpha-Zirconium Single Crystals (January 1963).

ANL-6622 Burt, W. R., Jr., Hins, A. G., Mayfield, R. M., and Shuck, A. B., Development and Manufacture of Fuel, Blanket, and Thermocouple Rods for the Experimental Breeder Reactor I, Core IV (September 1963).

ANL-6630 diNovi, Roberta Ann, Lamb Waves: Their Use in Nondestructive Testing (March 1963).

ANL-6631 Kolar, D., Handwerk, J. H., and Beals, R. J., Investigations in the System Urania-Neodymia (December 1962).

ANL-6632 Selner, R. H., Renken, C. J., Perry, R. B. and Balasamamoorthy, K., Nondestructive Tests of Components of EBR-I, Core IV (October 1963).

ANL-6636 Brooks, E. J., Kramer, W. C., and McGowan, R. D , High-Temperature Sensors for Borax-V Boiling Fuel Rods (October 1962).

ANL-6651 Loomis, B. A., Swelling of Aluminum-Clad Aluminum-Plutonium Alloys on Postirradiation Annealing (November 1963).

ANL-6657 Myles, Kevin Michael, A Study of the Thermodynamic Properties of the Vanadium-Iron Alloy System (February 1963).

ANL-6659 Shuck, A. B., Hins, A. G., Burt, W. R., and Beatty, R. A., Breeding-Gain Specimens for EBR-I Core IV (September 1963).

ANL-6665 Reinke, C. F., Irradiation and Postirradiation Annealing of Some Aluminum-Base Fuels (September 1963).

ANL-6670 Carlander, R., Kittel, J. H., and Dunworth, R. J., Postirradiation Examination of EBR-I Core-IV Prototype Fuel Rods (September 1963).

ANL-6671 Blumenthal, B., Density Measurements in Gloveboxes (September 1963).

ANL-6676 Berndt, Alan F. and Lloyd, Lowell T., Tabulations of Calculated Crystallographic Data for Alpha Plutonium (June 1963).

ANL-6678 Kittel, J. H., Neimark, L. A., Carlander, R., Kruger, O. L. and Lied, R. C., Preliminary Irradiations of PuC and UC-PuC (September 1963).

ANL-6680 Berger, Harold and Dickens, R. E., A Review of Ultrasonic Imaging Methods, with a Selected, Annotated Bibliography (July 1963).

ANL-6699 Mueller, M. H., Clark, Fred, and Simonsen, S. H., Program for the Location of Fourier Peak Centers (July 1963).

ANL-6702 Savage, Howard and Seibel, Richard D., Heat Capacity Studies of Uranium and Uranium-Fissium Alloys (September 1963).

ANL-6711 Hill, D. C., Handwerk, J. H., and Beals, R. J., Phase Relationships in the System Uranium Oxide-Lanthanum Oxide (June 1963).

ANL-6712 Kruger, O. L., Hughes, J. P., and Schmitz, F. J., Variably Curing Resins for Mounting Metallographic Samples (September 1963).

ANL-6747 Atlas, L. M. and Moser, J. B., Tables of Oxygen Pressures Calculated from the Hydrogen-Water System and from the Dissociation of Cupric Oxide (July 1963).

ANL-6411 Yaggee, F. L., "Slumping Behavior of Pu-Al Alloy Under Compressive Loads," Appendix E, Safety Analysis Report, EBR-I, Mark IV, pp. 140-149 (February 1963).

ANL-6640 Bean, C. H. and McCuaig, F., "Fabrication of Fuel," Section VII, EBWR Fuel Design and Behavior, PROCEEDINGS OF THE AMU-ANL SUMMER STUDY PROGRAM, JUNE 19-JULY 14, 1961, pp. 165-183 (November 1962).

Kittel, J. and Reinke, C., "Irradiation Testing and Examination of Fuel," pp. 184-198, ibid.

Rossin, A. D., "Safety and Hazards," Section XII, Operations, Hazards and Containment, pp. 349-350, ibid.

ANL-6708 Smaardyk, A., Bump, T. R., Handwerk, J., Kann, W. J., Martinec, E. L., Persiani, P. J., Popper, G. F., and Skladzien, S. B., Interim Report: FARET Experimental Program (April 1963).

ANL-6797 Mueller, M. H., Sidhu, S. S., Heaton, L., Hitterman, R. L., and Knott, H. W., "Coherent Nuclear Scattering Amplitudes and Cross Sections as Determined by Neutron-Diffraction Techniques," International Conference on Nuclear Physics with Reactor Neutrons, pp. 393-396 (November 1963).

COO-267 Ruther, W. E., "Corrosion of Stainless Steel in Superheated Steam," Proceedings of the Nuclear Superheat Meeting, No. 8, March 20, 21, and 22, 1963, Idaho Falls, Idaho, pp. 8-10 (April 15, 1963).

Kramer, W. C., "BORAX-V Superheat Fuel Fabrication," pp. 31-34, ibid.

GEAP-4089 (Vol. II) Misch, R. D. and VanDrunen, C., "The Oxidation of Zirconium Binary Alloys in 700°C Oxygen for Times up to 200 Days," Proceedings of the USAEC Symposium on Zirconium Alloy Development, November 12-14, 1962, Castlewood, Pleasanton, California, pp. 15.0-15.46 (November 30, 1962).

HW-75007 Foote, Frank G., "Plutonium Fuel Programs at Argonne National Laboratory," Proceedings, Plutonium as a Power Reactor Fuel, ANS Topical Meeting, Richland, Washington, September 1962, pp. 7.1-7.21 (December 1962).

TID-7620 (Pt. 1) Stone, C. C. and Noland, R. A., "The Welding of 2.25 Cr-0.5 Mo Heat Exchangers," Minutes of the Annual Atomic Energy Commission Welding Conference Held in San Antonio, Texas, October 3-6, 1960, pp. 193-205 (May 1963).

TID-7642 (Book 2) Kittel, J. H., Gavin, A. P., Crothers, C. C., and Carlander, R., "Performance of Aluminum-Uranium Alloy Fuel Plates Under High Temperature and High Burnup Conditions," Research Reactor Fuel Element Conference, September 17-19, 1962, Gatlinburg, Tennessee, pp. 425-443 (1963).

Ruther, W. E. and Draley, J. E., "Aluminum Alloy Corrosion," pp. 601-611, ibid.

Perry, Ronald B., "Applications of Scintillation Spectrometry to Research Reactor Fuel Assay," pp. 716-733, ibid.

TID-7650 (Book II) Blumenthal, B., "Metallurgical Studies of Thorium-Uranium-Plutonium Alloys," Proceedings of the Thorium Fuel Cycle Symposium, Gatlinburg, Tennessee, December 5-7, 1962, pp. 543-552 (July 1963).

TID-17940 Draley, J. E., Young, F. W., Jr., Visit to Soviet Corrosion Chemistry Institutes, June 25-July 4, 1962 (March 15, 1963).

WASH-1036 Macherey, R. E., "U.K. Fast Reactor Fuel Development," Report on Fast Reactor Activities of the U.K.A.E.A. and French Commissariat l'Energie Atomique by the 1962 U.S.A. Fast Reactor Team, March 26-April 5, 1962, pp. 18-37 (May 1962).

Kittel, J. H., "U.K. Irradiation Evaluation and Testing," pp. 38-47, ibid.

Macherey, R. E., "Fast Reactor Fuel Development in France," pp. 91-92, ibid.

Kittel, J. H., "Carbide Development," pp. 92-94, ibid.

Kittel, J. H., "Irradiation Evaluation and Testing," pp. 94-96, ibid.

Patents

Bean, Charles H. and Karasek, Frank J., Refractory Metal Tube Drawing, Patent No. 3,075,637 (January 29, 1963).

Zegler, Sylvester T. and Darby, Joseph B., Process of Producing a Niobium-Tin Compound, Patent No. 3,084,041 (April 2, 1963).

Walker, David E. and Matras, Steve, Control Rod, Patent No. 3,087,879 (April 30, 1963).

Foote, F. G. and Jette, Eric R., Fuel Elements for Neutronic Reactors, Patent No. 3,088,891 (May 7, 1963).

Noland, Robert A. and Walker, David E., Foil Element for Nuclear Reactor, Patent No. 3,098,025 (July 16, 1963).

Zegler, Sylvester T., Ductile Uranium Fuel for Nuclear Reactors and Method of Making, Patent No. 3,109,730 (November 5, 1963).

Kittel, John Howard, Dimensionally Stable, Corrosion Resistant Nuclear Fuel, Patent No. 3,089,768 (May 14, 1963).